RECENT ADVANCEMENTS IN X-RAY AND NEUTRON IMAGING OF DYNAMIC PROCESSES IN EARTH SCIENCES

EDITED BY: Lucia Mancini, Fabio Arzilli, Margherita Polacci and Marco Voltolini
PUBLISHED IN: Frontiers in Earth Science

frontiers Research Topics

frontiers

ISSN 1664-8714
ISBN 978-2-88966-137-4
DOI 10.3389/978-2-88966-137-4

About Frontiers

Frontiers is more than just an open-access publisher of scholarly articles: it is a pioneering approach to the world of academia, radically improving the way scholarly research is managed. The grand vision of Frontiers is a world where all people have an equal opportunity to seek, share and generate knowledge. Frontiers provides immediate and permanent online open access to all its publications, but this alone is not enough to realize our grand goals.

Frontiers Journal Series

The Frontiers Journal Series is a multi-tier and interdisciplinary set of open-access, online journals, promising a paradigm shift from the current review, selection and dissemination processes in academic publishing. All Frontiers journals are driven by researchers for researchers; therefore, they constitute a service to the scholarly community. At the same time, the Frontiers Journal Series operates on a revolutionary invention, the tiered publishing system, initially addressing specific communities of scholars, and gradually climbing up to broader public understanding, thus serving the interests of the lay society, too.

Dedication to Quality

Each Frontiers article is a landmark of the highest quality, thanks to genuinely collaborative interactions between authors and review editors, who include some of the world's best academicians. Research must be certified by peers before entering a stream of knowledge that may eventually reach the public - and shape society; therefore, Frontiers only applies the most rigorous and unbiased reviews.
Frontiers revolutionizes research publishing by freely delivering the most outstanding research, evaluated with no bias from both the academic and social point of view. By applying the most advanced information technologies, Frontiers is catapulting scholarly publishing into a new generation.

What are Frontiers Research Topics?

Frontiers Research Topics are very popular trademarks of the Frontiers Journals Series: they are collections of at least ten articles, all centered on a particular subject. With their unique mix of varied contributions from Original Research to Review Articles, Frontiers Research Topics unify the most influential researchers, the latest key findings and historical advances in a hot research area! Find out more on how to host your own Frontiers Research Topic or contribute to one as an author by contacting the Frontiers Editorial Office: researchtopics@frontiersin.org

RECENT ADVANCEMENTS IN X-RAY AND NEUTRON IMAGING OF DYNAMIC PROCESSES IN EARTH SCIENCES

Topic Editors:
Lucia Mancini, Elettra Sincrotrone Trieste, Italy
Fabio Arzilli, The University of Manchester, United Kingdom
Margherita Polacci, The University of Manchester, United Kingdom
Marco Voltolini, Lawrence Berkeley National Laboratory, United States

Citation: Mancini, L., Arzilli, F., Polacci, M., Voltolini, M., eds. (2020). Recent Advancements in X-Ray and Neutron Imaging of Dynamic Processes in Earth Sciences. Lausanne: Frontiers Media SA. doi: 10.3389/978-2-88966-137-4

Table of Contents

frontiers in Earth Science

EDITORIAL
published: 11 September 2020
doi: 10.3389/feart.2020.588463

Editorial: Recent Advancements in X-Ray and Neutron Imaging of Dynamic Processes in Earth Sciences

Lucia Mancini[1,4], *Fabio Arzilli*[2], *Margherita Polacci*[2] *and Marco Voltolini*[3]*

[1] Elettra-Sincrotrone Trieste S.C.p.A., Trieste, Italy, [2] School of Earth and Environmental Sciences, University of Manchester, Manchester, United Kingdom, [3] Lawrence Berkeley National Laboratory, Berkeley, CA, United States, [4] Lund Institute for Neutron and X-Ray Science, Lund, Sweden

Keywords: 4D imaging, X-ray computed tomography, neutron imaging, volcanic systems, fluid transport, porous rocks

Editorial on the Research Topic

Recent Advancements in X-Ray and Neutron Imaging of Dynamic Processes in Earth Sciences

Earth is a dynamic system; therefore, the study of geological processes in function of time is of paramount importance. Also, geological systems often evolve at non-ambient conditions, thus limiting the applications of the most common imaging techniques.

Many processes in different scenarios: volcanic, metamorphic, and reservoirs, but also man-made cement-based materials and ceramics, are inherently dynamic and require an investigation in 4D (three-dimensions, 3D + time) to be fully understood. These processes are subject to changes due to mechanical stress, reactive transport, heating, etc. The high-penetrating power of hard X-rays and neutrons, coupled with the recent advances in instrumentation and computational methods, fostered the growth of novel imaging approaches, making microradiography and computed microtomography (microCT) unique tools to observe internal structures of materials undergoing different processes.

This Research Topic is focused on hard X-ray and neutron-based imaging studies carried out under controlled conditions, representing the next generation of *in-situ* time-resolved experiments, with applications in different fields of Earth Sciences, as shown in this Research Topic.

A large number of contributions are related to the investigation of fluid flow and transport properties in porous rocks. The high sensitivity of neutrons to hydrogen-based fluids has been exploited by Cordonnier et al. to investigate the subsurface transport of pollutants, such as cadmium, in limestone samples by using *in-situ* neutron imaging. Their experiments allow constraining parameters such as local hydraulic conductivity and sorption properties of the dissolved cadmium by the solid matrix, showing that cadmium transport follows preferential pathways. Dynamic neutron imaging has been also used by Zambrano et al. to characterize the geometrical properties of the pore network in carbonate reservoirs. In this study, the complementary results provided by neutron and X-ray imaging are used as an input for computational fluid dynamics simulation. This integrated approach provided novel information about fluid storage and migration in reservoir rocks.

The mineral dissolution in porous diamond has been analyzed by Eckley and Ketcham using laboratory-based X-ray microCT during a sequential acid leaching procedure. The formation of fluorides during acid digestion, which can persist throughout acid leaching procedures, is observed. This can drastically affect yields for geochemical measurements of certain elements. Different segmentation procedures are tested showing that the utilization of CT number information to discern partial porosity below the resolution limit is more reliable than purely binary segmentation.

OPEN ACCESS

Edited by:
Valerio Acocella,
Roma Tre University, Italy

Correspondence:
Marco Voltolini
mvoltolini@lbl.gov

Specialty section:
This article was submitted to Volcanology, a section of the journal Frontiers in Earth Science

Received: *28 July 2020*
Accepted: *20 August 2020*
Published: *11 September 2020*

Citation:
Mancini L, Arzilli F, Polacci M and Voltolini M (2020) Editorial: Recent Advancements in X-Ray and Neutron Imaging of Dynamic Processes in Earth Sciences. Front. Earth Sci. 8:588463. doi: 10.3389/feart.2020.588463

Finally, the comparison of mass and X-ray attenuation loss allowed estimating the relative heavy-metal content of the leached material.

Tonai et al. propose a new systematic method for quality control of X-ray CT data (based on downhole radiodensity profiles from mean CT-values) to analyze core samples from scientific drilling. Thanks to this approach, lithologies and deformation structures can be identified within a geological core, with the potential for an automatic procedure. Numerical measures to CT slices are proposed in order to obtain data reflective of core quality. This method has been applied to data from International Ocean Discovery Program Expedition 370 Site C0023 located at the toe of the Nankai accretionary complex.

Two different works involve studies on Opalinus Clay (OPA). Stavropoulou et al. features a combined X-ray and neutron study about water absorption in a OPA core. The imbibition front advancement is visualized and its effect on the sample microstructure (swelling) is studied via digital volume correlation, providing important information about the use of the material as a sealant. Voltolini and Ajo-Franklin instead addresses the closure of a single fracture in an OPA mini-core with synchrotron X-ray microCT, under flow of CO_2-saturated water in a mini-triaxial cell. The study identified the different phenomena involved in the evolution of the sample (swelling, fracturing, generation of choke points, etc.) in function of hydration and stress, and quantified their role on the progressive loss of fracture conductivity.

Marone et al. describe the current hardware and software capabilities in X-ray imaging available at the TOMCAT beamline of SLS (PSI, Switzerland) and highlight their relevance for Earth Sciences studies providing three different examples. 1) 4D visualization of solute transport in a synthetic porous medium in a flow cell, following the evolution of the solute plume. 2) Deformation of a complex evaporate sample at subsurface P/T conditions in a heated triaxial cell. The authors identify the mechanisms underlying the microstructure changes in the sample. 3) Magmatic processes at high temperature, focusing on the deformation of bubbles in foamed volcanic rock samples, in a laser-heated cell with torsional deformation capabilities.

Tripoli et al. and Dobson investigate the effect of strain-rate and associated deformation on magma at high temperature and ambient pressure. The former paper reports how strain-rate increases crystallization kinetics in basaltic magmas compared to a magma that is not deformed. Deformation increases crystal nucleation and growth rates, and decreases incubation time. Increasing strain-rate, however, does not show a discernible effect on crystallization kinetics. The latter presents an experimental apparatus and analytical toolkit for the *in situ* X-ray tomography based quantification of magmatic microstructural evolution during rheological testing, showing how textures evolve heterogeneously within a shearing magma. Both contributions have implications on magma rheology, and, therefore, on magma transport dynamics and eruption initiation/cessation.

Finally, in this Research Topic the combination of 2D X-ray chemical mapping with laboratory-based 3D X-ray microCT was applied to the study of metamorphic transformations and fabric evolution in Western Italian Alps (Corti et al.). The resulting parameters allows them to perform dynamic modeling of metamorphic processes showing that samples preserve 100% of the pre-alpine granulite fabric, while the alpine eclogitic static assemblage corresponds to 78% though no new fabric is developed.

The examples of 4D imaging presented in this Research Topic clearly display how this approach can reveal unique information about dynamic processes in very diverse branches of Earth Sciences, such as volcanology, structural geology, hydrogeology. Future developments both in the hardware (radiation source, *in situ* cells, combined techniques) and software (image processing, digital rock physics, modeling) fields will further open new opportunities to understand complex evolving systems.

AUTHOR CONTRIBUTIONS

All authors listed have made a substantial, direct and intellectual contribution to the work, and approved it for publication.

FUNDING

MV was supported by DOE-BES under Award # DE-AC02-05CH11231.

ACKNOWLEDGMENTS

We thank the Editorial Board and Editorial Office of Frontiers in Earth Science for the kind invitation to edit this Research Topic and their support in organizing and managing the topic.

Conflict of Interest: The authors declare that the research was conducted in the absence of any commercial or financial relationships that could be construed as a potential conflict of interest.

frontiers in Earth Science

METHODS
published: 31 May 2019
doi: 10.3389/feart.2019.00117

A New Method for Quality Control of Geological Cores by X-Ray Computed Tomography: Application in IODP Expedition 370

Satoshi Tonai[1,2], Yusuke Kubo[3], Man-Yin Tsang[4], Stephen Bowden[2], Kotaro Ide[1], Takehiro Hirose[5], Nana Kamiya[6], Yuzuru Yamamoto[7], Kiho Yang[8], Yasuhiro Yamada[9,10,11], Yuki Morono[5], Verena B. Heuer[12], Fumio Inagaki[5,9,10] and Expedition 370 Scientists*

[1] Faculty of Science and Technology, Kochi University, Kochi, Japan, [2] Department of Geology and Petroleum Geology, University of Aberdeen, Aberdeen, United Kingdom, [3] Center for Deep Earth Exploration, Japan Agency for Marine-Earth Science and Technology, Yokosuka, Japan, [4] Department of Earth Sciences, University of Toronto, Toronto, ON, Canada, [5] Kochi Institute for Core Sample Research, Japan Agency for Marine-Earth Science and Technology, Nankoku, Japan, [6] Department of Urban Management, Kyoto University, Kyoto, Japan, [7] Department of Mathematical Science and Advanced Technology, Japan Agency for Marine-Earth Science and Technology, Yokosuka, Japan, [8] Korea Institute of Ocean Science and Technology, Uljin, South Korea, [9] Research and Development Center for Ocean Drilling Science (ODS), Japan Agency for Marine-Earth Science and Technology, Yokosuka, Japan, [10] Mantle Drilling Promotion Office (MDP), Institute for Marine-Earth Exploration and Engineering (MarE3), Japan Agency for Marine-Earth Science and Technology, Yokosuka, Japan, [11] Graduate School of Science, Kochi University, Kochi, Japan, [12] MARUM - Center for Marine Environmental Sciences and Faculty of Geosciences, University of Bremen, Bremen, Germany

OPEN ACCESS

Edited by:
Lucia Mancini, Elettra Sincrotrone Trieste, Italy

Reviewed by:
Richard Ketcham, University of Texas at Austin, United States
Alessandro Maria Michetti, University of Insubria, Italy
Miller Zambrano, University of Camerino, Italy

***Correspondence:**
Satoshi Tonai
s-tonai@kochi-u.ac.jp

Specialty section:
This article was submitted to Structural Geology and Tectonics, a section of the journal Frontiers in Earth Science

Received: *19 February 2019*
Accepted: *06 May 2019*
Published: *31 May 2019*

Citation:
Tonai S, Kubo Y, Tsang M-Y, Bowden S, Ide K, Hirose T, Kamiya N, Yamamoto Y, Yang K, Yamada Y, Morono Y, Heuer VB, Inagaki F and Expedition 370 Scientists (2019) A New Method for Quality Control of Geological Cores by X-Ray Computed Tomography: Application in IODP Expedition 370. Front. Earth Sci. 7:117. doi: 10.3389/feart.2019.00117

X-ray computed tomography (XCT) can be used to identify lithologies and deformation structures within geological core, with the potential for the identification processes to be applied automatically. However, because of drilling disturbance and other artifacts, the use of large XCT-datasets in automated processes requires methods of quality control that can be applied systematically. We propose a new systematic method for quality control of XCT data that applies numerical measures to CT slices, and from this obtains data reflective of core quality. Because the measures are numerical they can be applied quickly and consistently between different sections and cores. This quality control processing protocol produces downhole radiodensity profiles from mean CT-values that can be used for geological interpretation. The application of this quality control protocols was applied to XCT data from International Ocean Discovery Program (IODP) Expedition 370 Site C0023 located at the toe of the Nankai accretionary complex. The evaluation of core quality based on this protocol was found to be a good fit to standard-evaluations based on the visual description of core, and could be used to select samples free from drilling disturbance or contamination. The quality-controlled downhole mean CT-value profile has features that can be used to identify lithologies within a formation, the presence and type of deformation structures and to distinguish formations.

Keywords: X-ray computed tomography, scientific drilling, International Ocean Discovery Program, Nankai Trough, accretionary complex

1. INTRODUCTION

Studies of structural geology and mountain building processes have benefitted enormously from the drilling of deep sea sediments and the recovery of rock and sediment cores. However, visual core description (VCD) only utilizes a part of the information recorded in sediments. For example, even though microscopy can resolve small features, the measurements

of lithological or small structural features across sampling distances that are a kilometer or more in length are impractical for many reasons; time, scale and also the 3D volume involved (e.g., internal surfaces are not exposed at the surface). The physical properties of core (e.g., bulk density, P-wave velocity) can also be measured and used to generate downhole profiles, but these also have a low spatial resolution. It is an aim of scientific drilling to completely document and acquire all of the information present in geological cores, but the achievement of this aim is held back by an inability to use all the data available, whilst at the same time taking into consideration the fine and large scales. The capability to measure and use all geological features at the greatest resolution possible would be of great benefit.

X-ray computed tomography (XCT) is a radiological imaging method initially developed for medical applications (Hounsfield, 1973) and subsequently applied to many fields of Earth Sciences. Areas of application within Earth Science include paleontology, sedimentology, structural geology and petrophysics (e.g., Johns et al., 1993; Row, 1996; Ketcham and Carlson, 2001; Mees et al., 2003; Tanaka et al., 2011; Watanabe et al., 2011; Yun et al., 2013) with microfocus XCT scanners also seeing widespread use (e.g., Van Geet et al., 2000; Nakashima and Kamiya, 2007; Uramoto et al., 2014; Nomaki et al., 2015). For some time scientific drilling has also used three-dimensional XCT images of cores to support interpretations of lithology and structure as well as to preserve a digital record of core prior to destructive analyses (e.g., Ashi , 1997; Ujiie et al., 2004).

Most recently the potential of CT measurements to provide downhole profiles of radiodensity has been recognized as the physical properties of geological formations vary and thus CT-value profiles lend themselves to geological interpretations (e.g., Støren et al. , 2010; Tanaka et al., 2011; Fortin et al., 2013; Reilly et al., 2017). However, cores can be broken by fractures or drilling disturbance, and the broken intervals show anomalies within the CT-value profiles and prevent accurate geological interpretations. Thus, systematic quality control is needed for so that reliable radiodensity profiles can be obtained.

Systematic quality control of XCT data is also useful for selecting high-quality sample, where "high quality" means free from artificial disturbance and free from and contamination by drilling fluids (fractured intervals are more permeable and more easily contaminated by drilling fluids). Additionally, many analyses that are concerned with contamination are also time-sensitive and notably sensitive to procedures such as core-splitting or opening core lines, and thus contamination tests should preferably be performed without sample destruction. Non-destructive and quick XCT techniques are suitable for such sample selection (e.g., Inagaki et al., 2015). An improvement could be made by developing a systematic XCT-based method for contamination monitoring that could be applied consistently between cores, as well as potentially between projects or expeditions.

Here, we introduce a new method for processing of full XCT datasets and show the potential of XCT scanning as an automated core logging tool for the identification of structural features in geological archives. Our method consists of the following data processing steps: (1) Assignment of slice quality (SQ) to each CT slice by image processing; (2) Assignment of a mean CT number (MCN) to each CT slice, characterizing its average radiodensity; (3) Creation of quality-controlled mean radiodensity profiles from MCN values of filtered CT slices. In order to test whether automated processing for XCT data can capture fine-scale lithological features and natural deformation structures, and whether it correctly recognizes drilling disturbances, we applied our method to XCT-images that were generated from sediment cores during Expedition 370 of the International Ocean Discovery Program (IODP) (Heuer et al., 2017b). The expedition drilled and cored sediments in the Nankai Trough Subduction Zone off Muroto, Japan, where a drastic change in sedimentation rate, volcaniclastic ash layers, hydrothermal veins and faults have yielded characteristic geological features.

2. METHODS

2.1. X-Ray CT Image

Tomographic images of XCT are reconstructed by inversion of the Radon transform (Radon, 1917, 1986) of the X-ray Linear Attenuation Coefficient (LAC). The LAC is a physical index describing the reduction of X-ray beam intensity during transmission through objects and mainly relates to density, but also chemical composition and state. A transmitted X-ray intensity varies as a function of X-ray path length and the LAC of the object and is expressed by Beer's law:

$$I = I_0 \exp(-\mu_t L), \tag{1}$$

where I and I_0 are the transmitted and initial X-ray intensity, respectively. μ_t and L are functions of the LAC of the object and X-ray path length through the object. The CT number is given by the following equation:

$$\text{CT number} = [(\mu_t - \mu_w)/\mu_w] \times 1000, \tag{2}$$

where μ_w is the LAC of water.

2.2. Slice Quality (SQ)

The proposed slice quality (SQ) is measured for an interval of a core using scanned Digital Imaging and Communications in Medicine (DICOM) slice images. In other literature and contexts the term "section" might refer to an interval of core or other geological span, but here we use the term "interval" to refer to an arbitrary selected interval of core samples, and the term "section" within the IODP convention of dividing core into a number of sections, which are up to 1.5 m long.

Figure 1 illustrates a processing and measurement workflow for SQ. First, for a defined interval (e.g., a standard IODP section or a specific interval of subsampling), a circular area is visually selected by a researcher for a given interval, and the CT number of each voxel within that area examined using an image processing program (**Figure 1A**). A voxel is a value on a regular grid in three-dimensional space, and represents the basic unit of CT data.

Second, a quality threshold of CT number is determined for a given interval using a histogram of CT numbers (**Figure 1B**). The major material within an interval will have a dominant

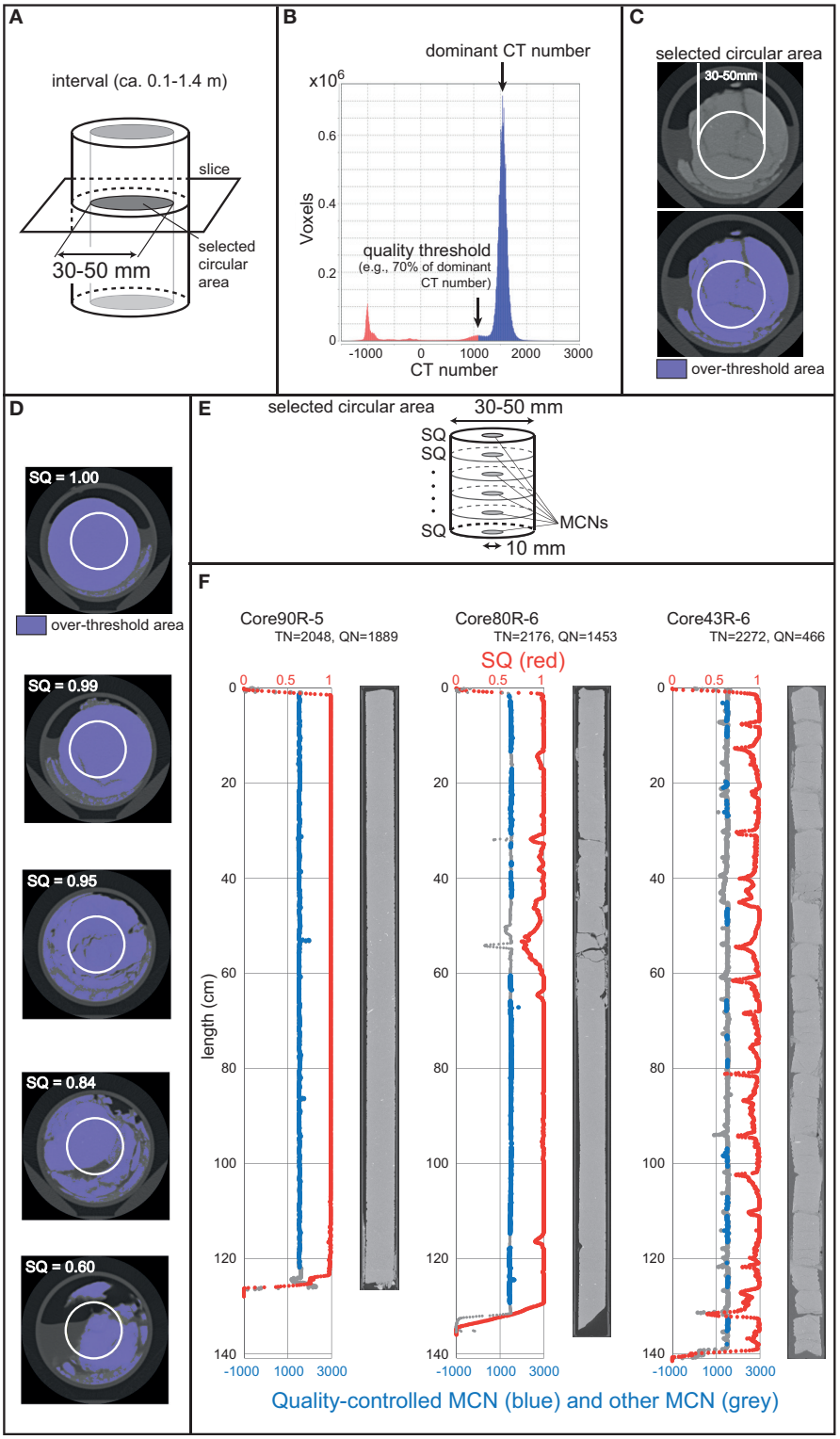

FIGURE 1 | Processing and measurement flow of slice quality (SQ) and quality-controlled mean CT number (MCN) profiles. **(A)** A selected circular area of a CT slice for SQ. **(B)** A histogram of voxel numbers against CT numbers for a selected interval. **(C)** Over-threshold areas of a CT slice. **(D)** CT slices showing different SQ. **(E)** Schematic image showing areas of SQ and MCNs. **(F)** SQs and MCNs of some typical intervals in the core samples of International Ocean Discovery Program (IODP) Expedition 370 Hole C0023A. TN, total slice number; QN, quality-controlled slice number.

CT number which is visualized as a peak in the histogram (**Figure 1B**). The quality threshold for the interval can be determined based on the dominant CT number (e.g., 70% of the dominant CT number taking into consideration the variation) and the voxels with CT numbers greater than the threshold are considered "over-threshold areas" (**Figure 1C**). Finally, the proportion of over-threshold areas for the selected circular area of a slice in the interval is used to determine the SQ (**Figure 1D**). When a slice has a SQ higher than a slice quality threshold, it is regarded as a "over-threshold slice." This process is repeated for all slices in an interval (**Figure 1E**) and the slices are subsequently designated as "over-threshold" or "under-threshold" (**Figure 1F**). This process was automated by performing measurements on slices using a plugin for ImageJ, a free open access image processing program (Schneider et al., 2012).

2.3. Mean CT Number (MCN) Profile

To create quality-controlled radiodensity profiles from CT-values, the mean CT number (MCN) was calculated for each CT slice. In terms of lithological composition, MCN better captures the physical property of a whole CT slice than the CT number of single voxels, as typically a rock will comprise a mixture of mineral components and pore spaces. Furthermore, even within a single homogenous slice, the CT-values of the outer rim of a slice may show anomalies because of beam-hardening during CT-scanning (e.g., Ketcham and Carlson, 2001). Therefore, the MCN of each slice in this study was measured using a 10 mm-diameter circular area at the center of the selected areas (**Figure 1E**).

In this study, CT slices regarded as under-threshold due to their lower SQs were removed because they would generate anomalies (suppressed-values) within MCN profiles. Additionally, the higher MCNs anomalies that would be caused by the presence of heavy-mineral assemblages also complicate the interpretation of lithological and/or deformational characteristics of drilling cores from MCN profiles and thus such anomalous slices must also be removed. The effects of processing to removing CT slices that are anomalously high or low are illustrated in **Figure 1F**.

2.4. Application to a Natural Dataset (IODP Expedition 370)

The XCT data used for this study was measured on core samples acquired at Site C0023 of IODP Expedition 370, Temperature-Limit of the Deep Biosphere off Muroto, Japan (**Figure 2**). This expedition was conducted in the Nankai Trough Subduction Zone, where the Philippine Sea Plate is subducting beneath the Japan Archipelago (Heuer et al., 2017a). The borehole reached 1,180 meters below the sea floor (mbsf), penetrating the frontal portion of the décollement (plate boundary fault) zone at 758.2–796.4 mbsf and basement igneous rocks at 1125.9 mbsf (**Figure 3**). Sediment thickness and type vary along the Nankai Trough (e.g., Ike et al., 2008; Underwood, 2018), and six sediment facies are recognized at the site; axial trench-wedge facies, outer trench-wedge facies, trench-to-basin facies, Upper Shikoku Basin facies, Lower Shikoku Basin facies and acidic volcaniclastic facies

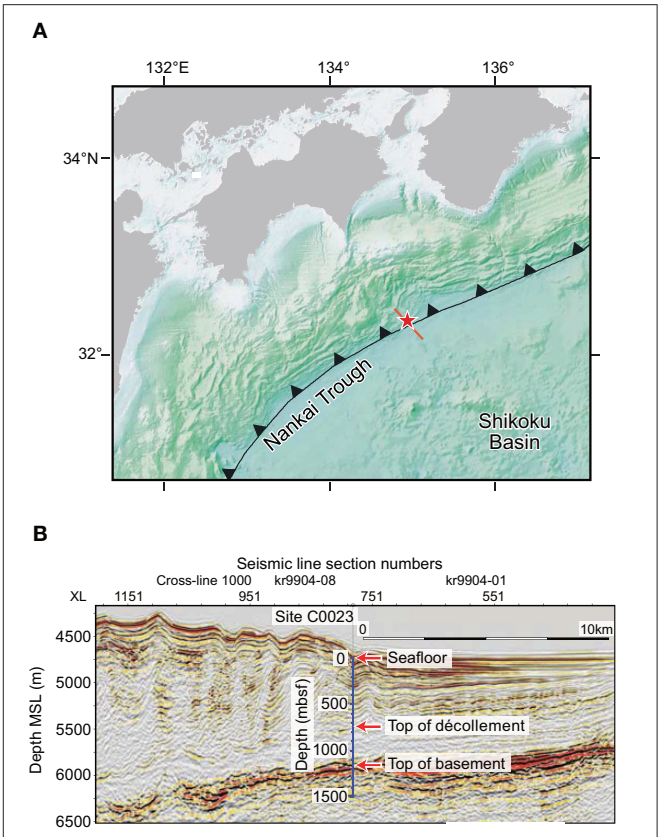

FIGURE 2 | (A) Regional map around IODP Site C0023 (Heuer et al., 2017b). The star symbol and red line show the locations of the site and seismic line section of **(B)**, respectively. **(B)** A seismic section at the toe portion of the Nankai Trough off Muroto (Heuer et al., 2017b). The arrows indicate the horizons of the sea floor, the top of the décollement zone, and the top of the oceanic basement.

(Heuer et al., 2017b). 112 cores were recovered in total and core recovery was 76% on average (Heuer et al., 2017a) (**Figure 3**).

XCT measurements were performed on the D/V *Chikyu* using a Discovery CT 750HD (GE Medical Systems) which is capable of generating thirty-two 0.625 mm thick slice images every 0.4 s. Data generated for each core-section consist of core-axis-normal planes of X-ray attenuation with dimensions of 512 × 512 voxels, corresponding to an area of 90 mm × 90 mm. To calculate CT numbers of samples standards were used; air (CT number = -1000), water (CT number = 0) and aluminum (2,477 < CT number < 2,487). All three standards were run once a day during the measurement period. For each standard analysis, the CT number was determined for a 24.85 mm^2 area at fixed coordinates near the center of the cylinder. The scanning was done immediately after dividing the core into sections and before splitting each section (Heuer et al., 2017b).

The circular area selected for SQ measurements ranges from 30 to 50 mm diameter depending on the diameter of the core (**Figure 1A**) and the quality threshold for CT numbers in an interval was set to 70% of the dominant CT number within that interval (**Figure 1B**). Based on the relationship between SQ and the degree of fractures, the slice was regarded as a "over-threshold slice" if the SQ was greater than 0.99 (**Figure 1D**). When CT

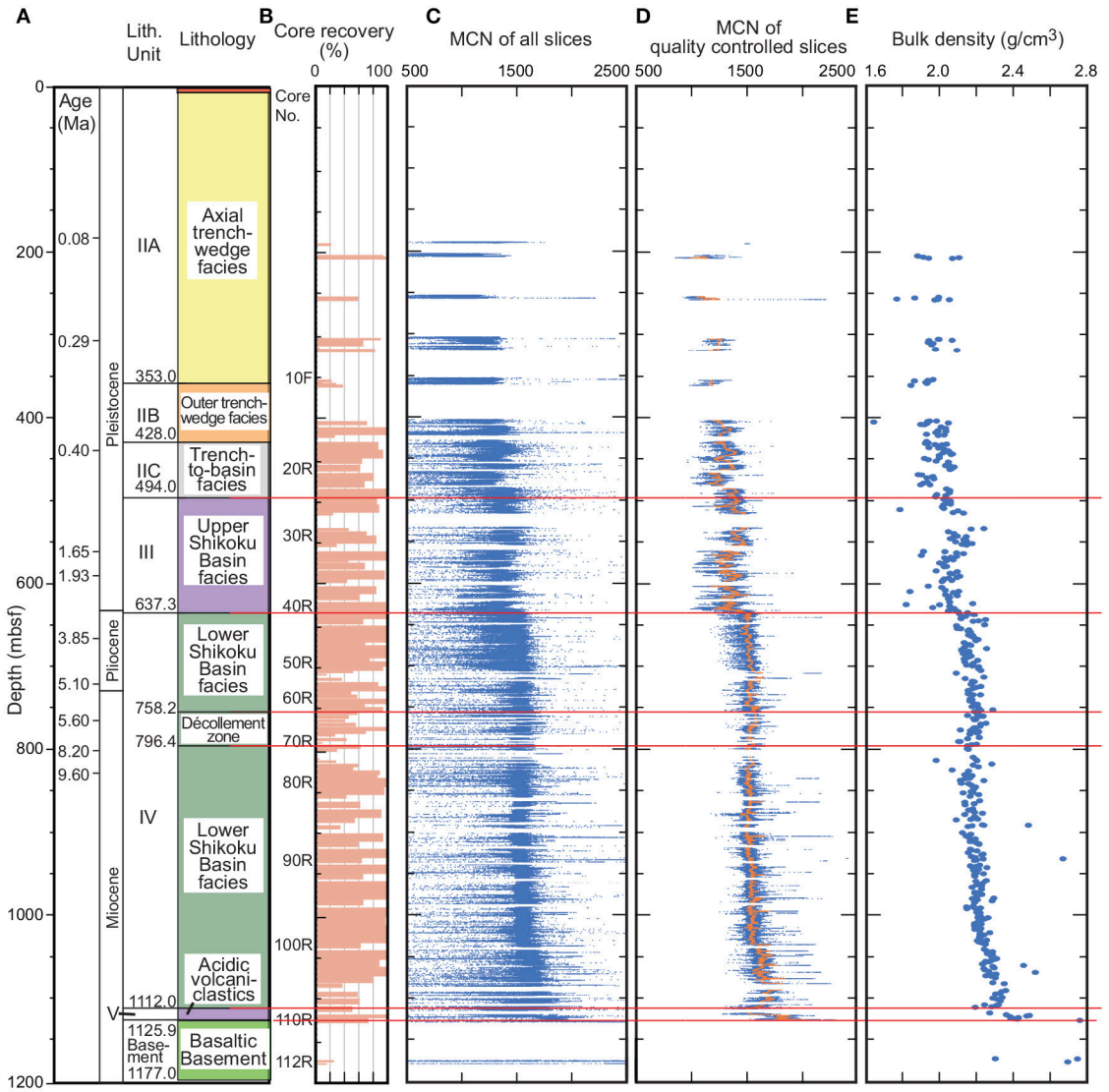

FIGURE 3 | Site summary diagram of X-ray CT scanning for Site C0023 from 0 to 1,200 mbsf. Original data are from Heuer et al. (2017b). **(A)** Lithological facies. **(B)** Core recovery. **(C)** Mean CT number (MCN) profile using all CT slices. **(D)** Quality-controlled MCN profile. Orange plots are 500-slices moving averages of MCN. **(E)** Bulk density. mbsf, meter below sea floor; Lith. Unit, Lithological Unit.

images and VCD are compared, the majority of the core has CT numbers less than 2,500, on the other hand, CT numbers of the area composed of heavy-mineral assemblages are greater than 3,000. Thus, the final selection criteria used to determine "over-threshold" slices was a SQ greater than 0.99 without a CT number area more than 3,000 (**Figure 1F**). Slices not meeting these criteria were removed from the radiodensity profile and 42.4% of the total CT slices remained.

3. RESULTS AND DISCUSSIONS

3.1. General Trends in MCN

Figure 3 summarizes MCN and other information for Site C0023. Comparing **Figures 3C,D** it can be seen that the quality-controlled MCN radiodensity profile shows a much clearer trend, after the removal of the many slices within a low SQ and low MCN. The quality-controlled MCNs show generally increase with increasing depth, and MCN mostly ranges from 1,200 to 1,900 and appears to co-vary with bulk density downhole (**Figures 3D,E**). Bulk densities of a downhole core normally increase with depth due to diagenesis (compaction, cementation and mineral replacement) and this is probably the main cause of the general increase of the quality-controlled MCNs with depth at the site. The main lithology of the site is mud and mudstone, and there is no significant variation in elemental or mineralogical composition (Heuer et al., 2017b). Consequently, it is likely that the MCNs of slices comprising mud or mudstone mainly reflect their bulk density. The bulk densities of mud and mudstone are compared to MCN in **Figure 4**, and the greater part of the 316 measurements cluster around values of 2.1–2.3 g/cm^3 and

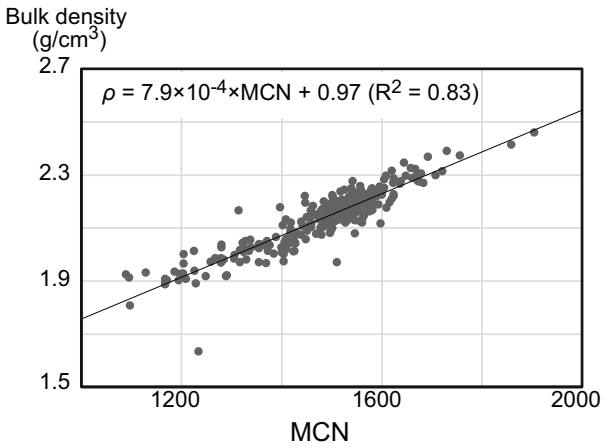

FIGURE 4 | Relationship between mean CT number (MCN) and bulk density (ρ) data of the mud/mudstone of the IODP Site C0023. Bulk density data are from Heuer et al. (2017b).

1,500–1,600 for bulk density and MCN, respectively. There is a positive correlation (**Figure 4**), the results of which give the following equation:

$$\rho = 7.9 \times 10^{-4} \times \mathrm{MCN} + 0.97 \qquad (R^2 = 0.83), \qquad (3)$$

where ρ and MCN are bulk density and MCN value, respectively. The positive correlation between bulk density and CT number of mud/mudstone or marine sediments seen at Site C0023 has also been observed at other ODP (Ocean Drilling Program) sites in the Nankai Trough (Ujiie et al., 2004) and other areas (Orsi et al., 1994; Ashi , 1997; Orsi and Anderson, 1999; Tanaka et al., 2011).

In addition, the quality-controlled MCNs correspond to lithologies of the cores very well. **Figure 5** shows the MCNs of CT slices comprising mud or mudstone, calcareous mud or mudstone, tuffaceous rocks and hydrothermally altered sediments. Among them tuffaceous rocks show lower MCNs than adjacent mud or mudstones, and hydrothermally altered sediments show higher MCNs than stratigraphically adjacent rocks. Some units of mudstone reacted strongly to 10% hydrochloric acid, and thus were logged as calcareous mud or mudstones and separated from other mud or mudstone (Heuer et al., 2017b). It can be seen that in some instances the radiodensities of these different mud or mudstones overlap, but in other instances such as at 650 to 750 mbsf and 1,000 to 1,100 mbsf the calcareous mudstones have the highest densities within an interval (blue triangles) and the mud the lowest (**Figure 5**).

3.2. Comparison MCN to Lithologies and Deformation Structures

In addition to a general increase of MCN with depth, there are distinctive features in the downhole quality-controlled radiodensity profile of Site C0023, namely; (1) positive spikes, (2) negative spikes, (3) abrupt downhole increases or decreases of 30–200 in the MCN value and (4) intervals with tiny cyclic negative anomalies. Correspondence between these characteristics and individual features of the lithologies and/or deformation structures are discussed in the following subsections.

3.2.1. Positive Spikes

Positive MCN spikes of 3–30 cm thickness are present throughout the hole. They are relatively rare in the shallower facies, but frequent below the décollement zone of the Lower Shikoku Basin facies (**Figure 3**). These positive spikes mainly represent lithologies other than mud or mudstone. For example, positive spikes in the trench-to-basin facies and the Upper Shikoku Basin facies are about 5–10 cm thick and some of them correspond to whitish discolored intervals and healed faults (**Figures 6**, **7**). Below the décollement zone of the Lower Shikoku Basin facies, some large positive spikes correspond to the hydrothermal alternation of sediments (**Figure 8**) or the mineral veins filling fractures or faults.

In the case of intervals logged as hydrothermally altered sediments, their radiodensities are notably higher (**Figure 5**). In these intervals authigenic or epigenetic heavy-mineral assemblages (pyrite, barite, anhydrite, rhodochrosite, etc.), fill pores and fractures or replace specific sedimentary structures e.g., burrows (Heuer et al., 2017b). CT numbers of such heavy-minerals are usually much higher than those of the dominant rock forming minerals because of their higher grain densities. When a greater part of a CT slice comprises heavy-mineral assemblages, the MCN of the slice becomes significantly higher than the maximum threshold for a quality-controlled MCN profile (3,000 in this study) and is removed from the profile. However, if these mineral phases and individual crystals constitute a small volume, for example a volume less than a voxel, the MCN of the slice will reflect the CT number of the other rock forming minerals as well as the authigenic mineral phases and thus range between the MCN of the slices and the maximum threshold. As a result, the slice will make a positive anomaly and in most instances it will still be present in the quality-controlled radiodensity profile based on MCN.

3.2.2. Negative Spikes

Negative spikes in the radiodensity profile 3–30 cm thick are notable in the trench-to-basin facies and the Upper Shikoku Basin facies (**Figures 3**, **6**, **7**). These negative spikes are typically around 5–10 cm thick with MCNs less than 1,100 and correspond to tuffaceous rocks. The MCN profiles above and below the negative spikes often show no great change with depth. However, intervals above negative spikes exhibit a decrease of 50–200 downwards toward the spikes. At 560.0–587.2 mbsf and 624.0–631.0 mbsf, many negative spikes are observed, and other MCNs in the intervals are also slightly lower than that of other intervals within the same facies (**Figure 6**).

The CT slices comprised of tuffaceous rocks show lower MCNs (**Figure 5**) due to the higher porosities, and thus, lower bulk densities. Bulk densities of the tuffaceous rocks in the trench-to-basin and the Upper Shikoku Basin facies are 1.80–1.90 g/cm^3 and obviously lower than that of adjacent mud or mudstone (1.88–2.20 g/cm^3) (Heuer et al., 2017b). In the acidic

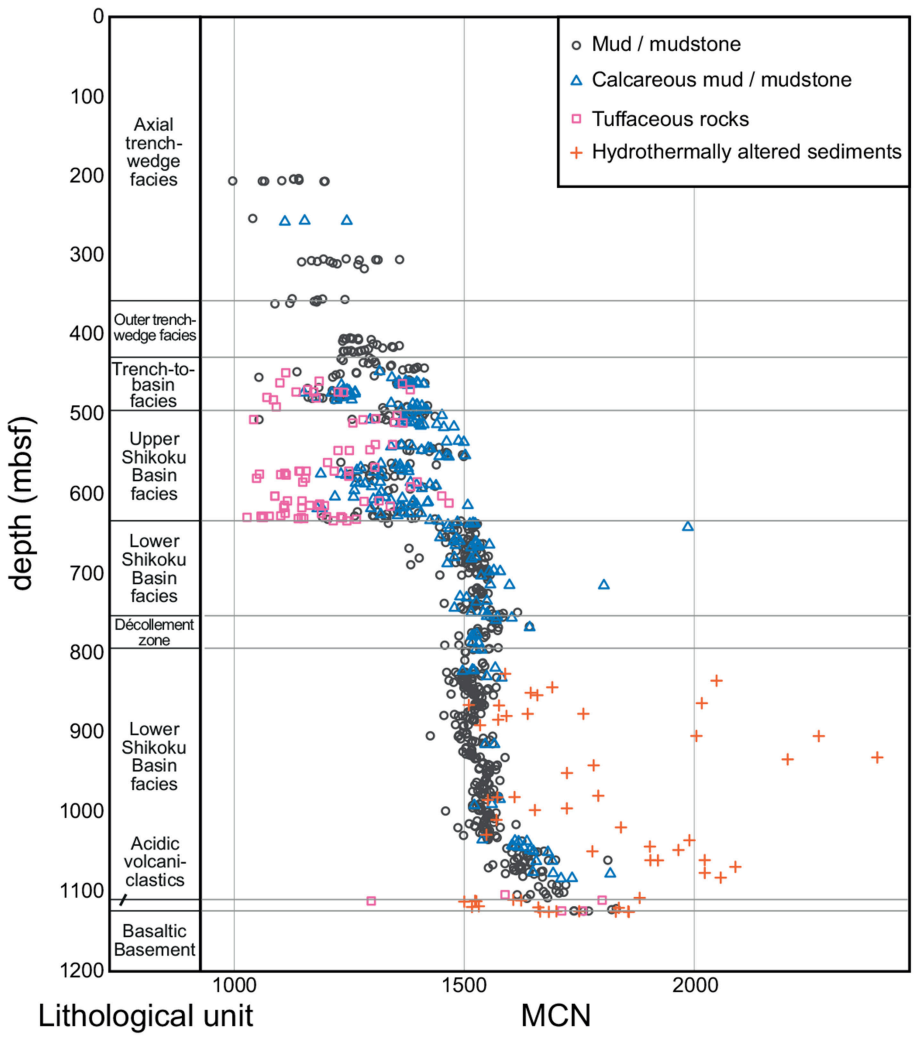

FIGURE 5 | Relationship between graphic lithology and MCN of the IODP Site C0023. Graphic lithology data are from Heuer et al. (2017b).

volcaniclastic facies and the deeper part of Lower Shikoku Basin facies, bulk densities of the tuffaceous rocks are 2.18–2.40 g/cm^3 which is lower than that of adjacent lithologies, although data in this interval is sparse. Thus, the CT numbers of the tuffaceous rocks are lower than that of the muds or mudstones, and are often lower than the quality threshold of the interval. As a result, CT slices comprising tuffaceous rocks may have lower SQ and may be classified as under-threshold. Even if they pass the SQ filtering, they show lower MCNs than adjacent slices and can be seen as negative spikes within the quality-controlled MCN profile (**Figure 6**).

3.2.3. Abrupt Downhole Increases or Decreases

Abrupt downhole increases or decreases of 30–200 in the MCN value are prominent in the trench-to-basin facies and the Upper Shikoku Basin facies (**Figures 3**, **6**, **7**). For example, CT images show faulting from 450.95 to 451.1 mbsf and the MCNs abruptly increase with depth from 1,200 to 1,300 through the fault (**Figure 6**). Another example is found immediately above a fracture zone at 586.8 mbsf (can be seen in CT images), where MCNs abruptly increase with depth from 1,200 to 1,400 (**Figure 7**). The detailed shape of some excursion in radiodensity profile are unclear because of lack of core recovery and slices that pass quality-control protocol. But in other intervals change and excursions in MCN are abrupt, and occur across distances of a few tenths of centimeters, and can clearly be shown to correspond to faults. In the region below the décollement zone, within the Lower Shikoku Basin facies, there are several abrupt increases in MCN with depth, for example 1034.4–1035.6 mbsf and 1047.0–1050.5 mbsf. Such increases in radiodensity correspond with occurrences of mudstones with a calcareous matrix, indicating cementation of intraformational breccias.

The abrupt changes of MCNs with depth are geologically meaningful. Based on the correlation between bulk density and MCN of Site C0023 measurements (Equation 3), a MCN value of one is roughly comparable to about 0.001 g/cm^3. Inazaki et al.

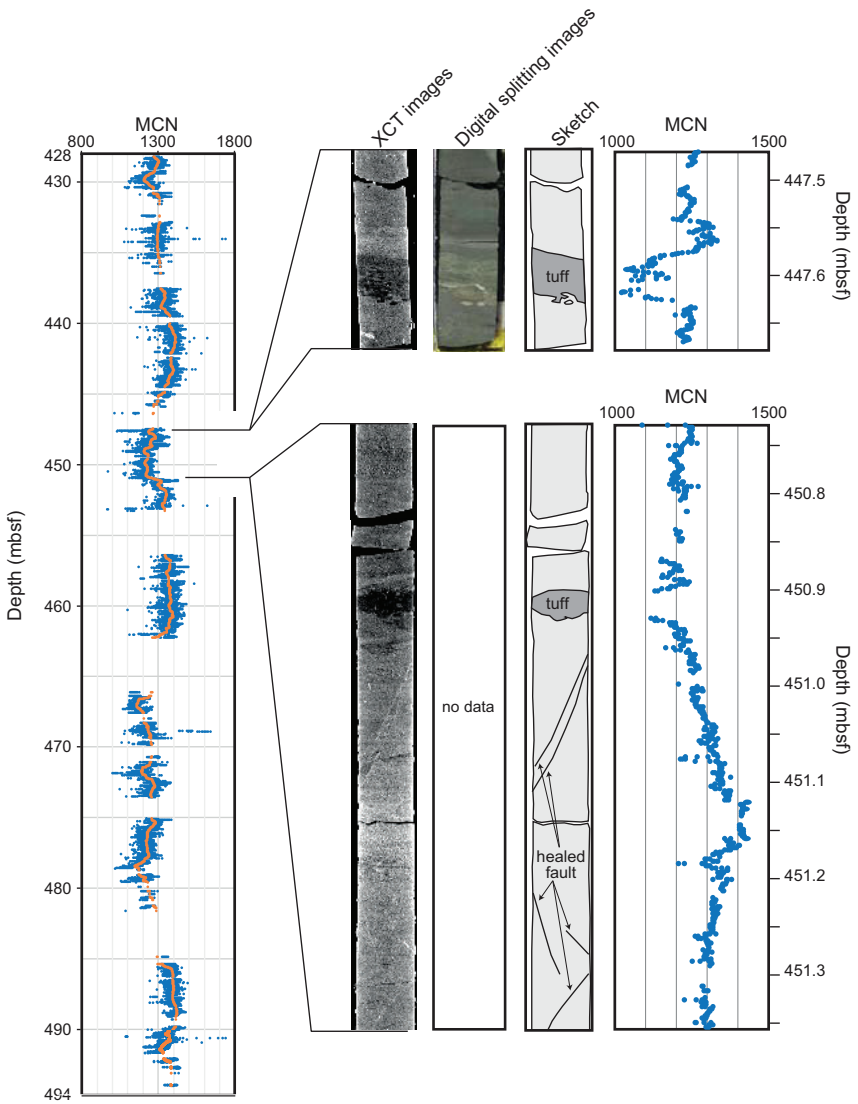

FIGURE 6 | Downhole quality-controlled MCN profile of the trench-to-basin facies (428.0–494.0 mbsf). Orange plots are 500-slices moving averages of MCN. XCT images, digital splitting images, sketches and close up MCN profiles around typical negative (core C0023A-20R-1, 48–67 cm) and positive spikes (from core C0023A-20R-3, 116 cm to core C0023A-20R-4, 52 cm) of the facies are shown.

(1995) indicated that the precision of bulk density measurements estimated from the CT number is better than ±0.02 g/cm^3 on a medical X-ray CT system (TCT-700S) at 120 kV/55–200 mA. The abrupt changes at Site C0023 range from 30 to 200 in MCN (i.e., CT number), which roughly corresponds to 0.03–0.20 g/cm^3 . Therefore, they are statistically significant and reflect true material changes.

Lithological boundaries that are sedimentary or deformational in origin might be expected to cause sudden jumps in radiodensity profile. At Site C0023 few such jumps are evident, but there are many abrupt changes that correspond to fracture assemblages or fracture zones. Some of these assemblages or zones accompany lithological changes as mentioned above. In addition, faults with vertical displacement, some of which accompanied with fractures, could also generate MCN (i.e., bulk density) gaps. Such vertical displacement and accompanied lithological changes probably cause the abrupt MCN-changes in the site. There are also fracture zones without significant MCN-changes, and a lack of response in the radiodensity profile may be due to a small vertical displacement for the zones concerned.

The deposition or redeposition of sediments by mass transport may also bring about sedimentary horizons that record abrupt changes in a downhole MCN profile. Mass transport deposits are reported from the Nankai Trough (e.g., Strasser et al., 2011; Kitamura and Yamamoto, 2012), and this is indeed the likely mode of emplacement for many of the tuffaceous rocks at the site (Heuer et al., 2017b). However, no thick mass transport deposits which might be expected to cause formation-scale changes in

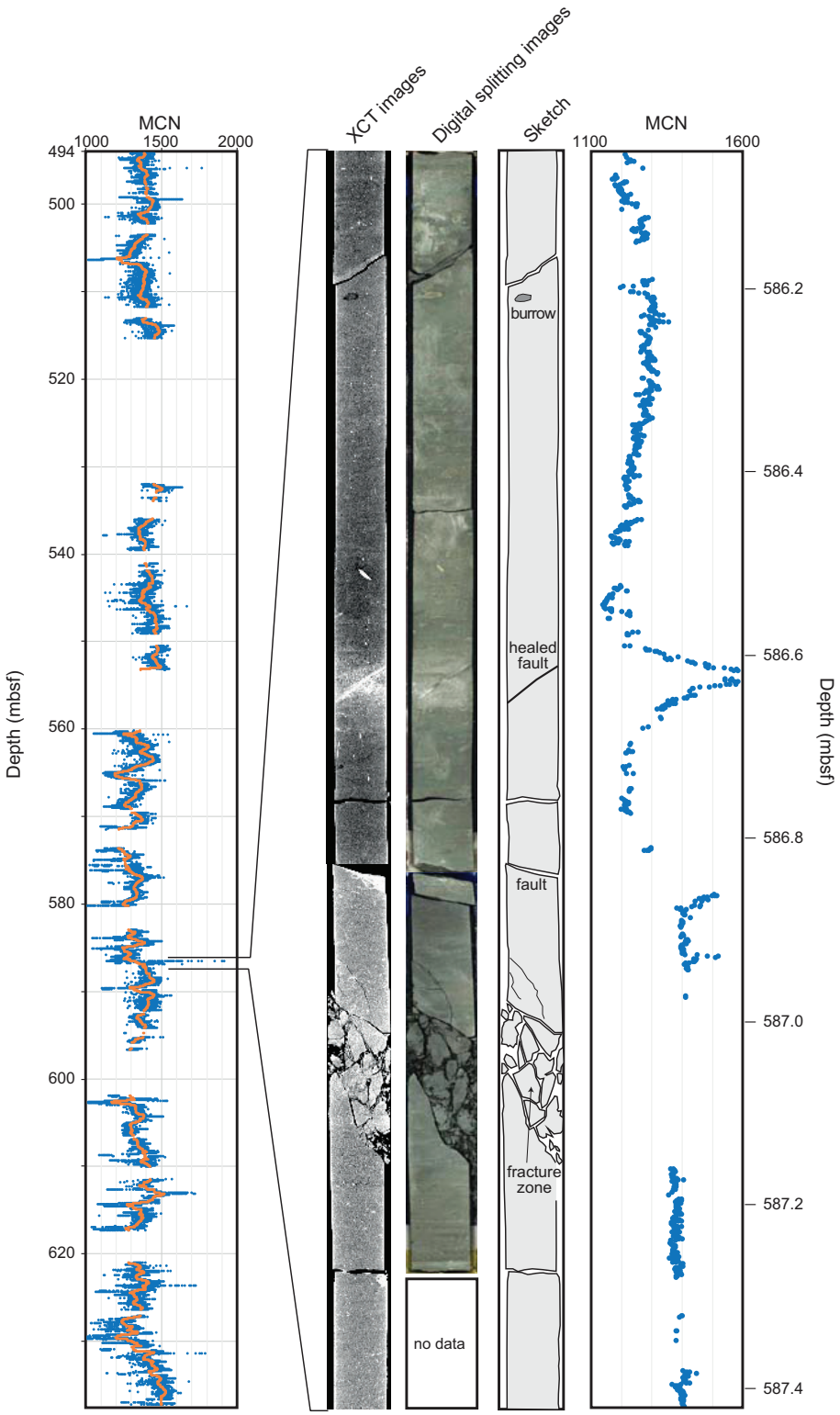

FIGURE 7 | Downhole quality-controlled MCN profile of the Upper Shikoku Basin facies (494.0–637.3 mbsf). Orange plots are 500-slices moving averages of MCN. XCT images, digital splitting images, a sketch and a close up MCN profile of an abrupt increase around a positive spike are shown (from core C0023A-36R-3, 64 cm to core C0023A-36R-4, 57 cm).

bulk density have been observed during visual core inspection of Site C0023, and thus significant perturbations of downhole MCN profile cannot be demonstrated in this case.

3.2.4. Intervals With Tiny Cyclic Negative Anomalies

Intervals with tiny cyclic negative anomalies in the MCN profile are noticeable in the shallower part of the Lower Shikoku Basin facies (**Figure 8**), but they can also be seen in some hydrothermally altered sediments in the deeper part of the Lower Shikoku Basin and in the acidic volcaniclastic facies. These anomalies are in 5–30 cm intervals and correspond to the presence of drilling biscuits (**Figure 8**). Drilling biscuits are drilling-induced discrete blocks typically several centimeters thick (Leggett, 1982) and are identified by their cyclic separation and the presence of circular striations at the top and the bottom of the core pieces (biscuits). The biscuits often sit in a matrix of mud which results from grinding of the biscuits. The mud that fills the gaps between biscuits has a lesser radiodensity than the biscuits. Although the CT slices measured within the mud-filled fractures were mostly identified by SQ and filtered, some of them pass the filtering because of small area of the mud-fill (less than 1% of the slice) and form tiny cyclic negative excursions (**Figure 8**).

3.3. Implications

3.3.1. On the Methodology

It can thus be shown that the quality-controlled MCN data yields downhole radiodensity profiles in which lithological and structural features can readily be seen. This implies that fractures (including drilling artifacts) have largely been identified by their SQ and removed because they no longer dominate the radiodensity profile. Consequently, SQ is an effective measure to evaluate the quality of core and useful for creating clear and reliable MCN profiles. There are further advantages to using SQ to evaluate core and these are explained below.

Firstly, SQ enables a consistent quality-evaluation of samples that does not rely solely on visual identification of features. Certainly a two- or three-dimensional XCT image can be helpful or even a substitute for visual inspection of core. But even a visual interpretation of core in this way may be too intricate or too complex a job to perform at a level necessary for a high number of small subsamples of core for example. Additionally, different scientists may apply different recognition criteria, or criteria may vary from site to site. SQ is a simplified numerical measures based on relatively consistent criteria, and once it has been trued or calibrated it can be applied by any user to evaluate core quality.

Secondly, XCT data has a high spatial resolution and covers a high volume of sample; higher than both conventional contamination tests and physical property data. The size of a voxel of XCT data in this study is about 0.176 × 0.176 × 0.625 mm. Thus, lithological components and fractures up to a millimeter in size can be detected. The detection and measurement of all fractures this size would be impracticable if only visual confirmation on CT images or by VCD was used.

The third advantage is that the method is quick. In many cases a quick selection of samples is better because it reduces contamination by fluids diffusion through core. Other contamination tests such as using sulfate as a proxy for seawater or PFC concentration take far longer to provide results, and thus are retrospectively applied to screen samples. A method based on XCT requires a relatively short time and is ideal because it is nondestructive and therefore will not forward contaminate samples, and if automated can be applied to screen samples ahead of their potential consideration for further analysis.

Although numerical, the process remains subjective to a certain extent due to the setting of some parameters; the interval range over which SQ-criteria are applied, the processing area of a CT slice, the quality threshold for CT numbers and the selection criteria for over-threshold slices (**Figure 1**). For example, in the current iteration of the method used for this study, the area of analysis taken from a CT slice is visually selected to take account of variations due to core cutting. However, this approach has an arbitrary element and might be considered non-reproducible. A selection process, applied automatically and based on non-visual criteria, might yield a more objective process with respect to its application to different core, although the choice of one criterion or another is still a subjective decision. Repeated iterations of similar XCT processing methods in different contexts should help identify which criteria are most valid or matter most in a given situation. Choices concerning the area of analysis or other thresholds are effectively choices about the strictness of the level of quality control to be perused, so an alternative perspective would be that flexible criteria permit reasonable adaption to circumstance or purposes (e.g., different users in different circumstances may accept different risks). What is important is that the same set of parameters and same process can be repeated to all cores or samples. The simple and adaptable concept of the method we present is applicable not only to medical XCT data but also potentially micro XCT data. Thus, as the method we present here is applied in different contexts, improvement with respect to processing criteria would be expected.

SQ also allows for an objective assessment of core quality. For example, core quality factor (CQF) can be calculated based on the ratio of over-threshold slices to all slices within a given interval of recovered cores. CQF is convenient to select intervals for sensitive analyses or to consider later drilling conditions.

3.3.2. Geological Implications

The radiodensity gradient (change in MCN with respect to depth) varies by unit or formation-level, dividing the site into several intervals where gradients are similar (**Figures 3**, **5**). Although an accurate analysis is not provided here, some aspects of radiodensity gradient are notable, such as the transition from the trench-to-basin to the Upper Shikoku Basin facies, and from the Upper Shikoku Basin facies to Lower Shikoku Basin facies (**Figures 3**, **5**). The most likely explanation for the change in MCN during the transition from basin to trench facies is the change in sedimentation rate which is significantly higher under trench conditions (Hagino and Expedition 370 Scientists, 2018).

Another noteworthy change in radiodensity gradient occurs around the deepest part of the Lower Shikoku Basin facies (1030.0–1050.0 mbsf). Particularly, in the lower part of the acidic volcaniclastic facies (1121.0–1125.0 mbsf), MCNs abruptly increase with depth and are remarkably higher than in other intervals of the site (**Figures 3**, **5**). Although the sedimentation rate below 1050.0 mbsf is not constrained by age-data, a

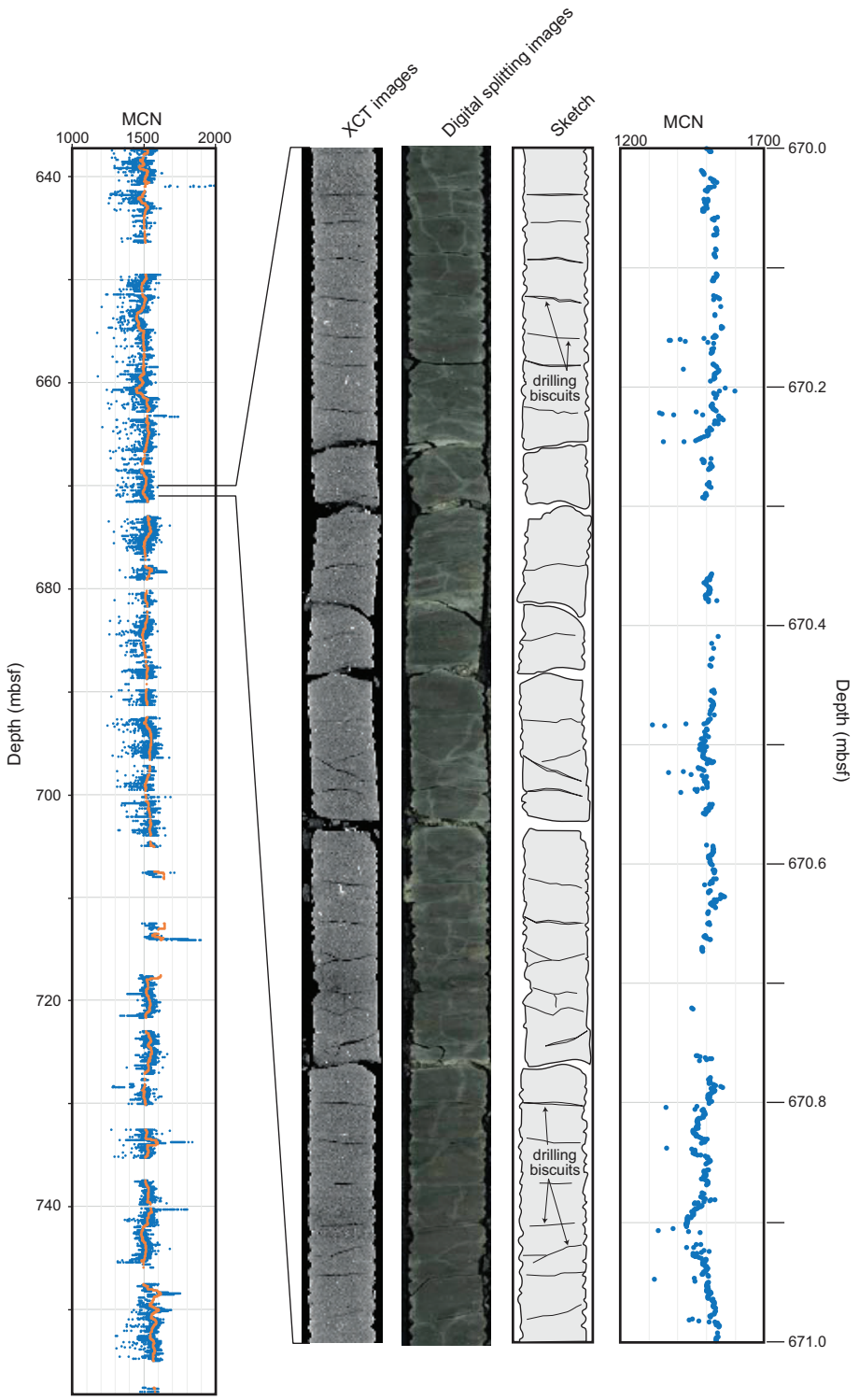

FIGURE 8 | Downhole quality-controlled MCN profile of the shallower part of the Lower Shikoku Basin facies (637.3–758.2 mbsf). Orange plots are 500-slices moving averages of MCN. Selected XCT images, digital splitting images, a sketch and a close up MCN profile of the interval where there are tiny negative anomalies corresponding to drilling biscuits are shown (from core C0023A-45R-2, 29-129 cm).

hemipelagic depositional environment would not be likely to see high rates of sedimentation. In this case it is plausible that a lithological change that has been caused by diagenesis or hydrothermal alteration which involves cementation. The *in-situ* strength of sediments in this interval was calculated from drilling parameters and shows an abrupt increase with depth below about

1,050 mbsf (Hamada et al., 2018), and this is consistent with a lithological change brought about by cementation.

The downhole quality-controlled MCN profile of Site C0023 evidences high abundances of faults in the trench-to-basin and the Upper Shikoku Basin facies (**Figures 3**, **6**, **7**). The presence of abrupt positive and negative shifts suggests that these are both normal faults and thrusts in these facies. Normal faults in these facies were observed within core (Heuer et al., 2017b) and have also been observed in seismic reflection studies seaward of Site C0023 (Heffernan et al., 2004). The seismic sections of the trench-to-basin and the Upper Shikoku Basin facies at Site C0023 are unclear. Fewer thrusts have been described in these facies, and one possibility is a poor recovery of core samples with fault planes or zones. Although Site C0023 is located within the imbricate thrust zone (Moore et al., 2001), frontal thrusts do not significantly penetrate the site. Thus, the thrusts that are observed may be minor thrusts branched from the main frontal thrusts. The many negative abrupt changes in the MCN profile are indicative such minor thrusts.

The MCN profile also implies a concentration of normal faults in the deeper part (below the décollement zone) of the Lower Shikoku Basin facies (**Figure 3**). Positive abrupt changes are dominant in the interval and correspond to the presence of normal faults within core (Heuer et al., 2017b). Normal faulting developed between the deeper part of the Lower Shikoku Basin facies and the shallower part of the basement around the site, which are speculated to be constrained by ridge topography (Ike et al., 2008). The positive abrupt changes may reflect this normal faulting.

4. CONCLUSIONS

XCT data can be used to evaluate the quality of core obtained during scientific drilling and to generate downhole radiodensity profiles. When slice quality (SQ) is used as part of a processing protocol to filter XCT data, there are several benefits:

(1) Numerical evaluation of data quality becomes consistent between cores, formations and sites.

(2) Evaluation of core quality with respect to drilling disturbance becomes a rapid and non-destructive process that can be applied *a priori*.

(3) Large numbers of core samples can be assessed easily with a high spatial resolution.

When used to process XCT data, SQ provides well-filtered and reliable downhole profiles of quality-controlled mean CT numbers (MCNs). Data processed in this way reflect characteristics of lithologies and deformation structures. For core samples from IODP Site C0023, the MCN profile identifies lithologies, matches physical properties and can measure features meters to millimeters in size. This is potentially transformative because it permits the measurement of high numbers of small features, for example fault-concentrations. Measurement of these small features at high abundances over large distances would not be possible with conventional core logging because of the scales involved. Thus, the quality-controlled MCN data has the potential to provide consistent measures of lithologies and deformation structures.

DATA AVAILABILITY

The datasets generated for this study are available on request to the corresponding author.

AUTHOR CONTRIBUTIONS

ST, YK, YM, VH, FI, and Expedition 370 Scientist conceived the idea. ST, YK, M-YT, and KI conducted the analyses of the XCT data. ST, YK, M-YT, SB, YuY, and KY participated in the method setup discussion. ST, TH, and NK participated in the comparing XCT data to bulk density data. ST, M-YT, SB, YaY, VH, and Expedition 370 Scientists wrote and edited the manuscript.

FUNDING

ST acknowledges financial support from IODP Exp.370 After Cruise Research Program, JAMSTEC. M-YT acknowledges funding from the ECORD Research Grant and the Centre for Global Change Science (Toronto). SB acknowledges IODP NERC award NE/P015182/1. VH acknowledges funding of her research by the Cluster of Excellence: The Ocean Floor - Earth's Uncharted Interface and DFG Project Grant HE8034/1-1.

ACKNOWLEDGMENTS

This research used data provided by the International Ocean Discovery Program (IODP). We are grateful to the IODP and thank crew, drilling team, geologists and lab technicians on *Chikyu* and the staff of the Kochi Institute for Core Sample Research for supporting IODP 370-operations. We would like to thank Lucia Mancini for handling the editorial process and the three reviewers for submitting their helpful comments and improving the manuscript.

Expedition 370 Scientists

Lena Maeda, Margaret Cramm, Susann Henkel, Kira Homola, Tatsuhiko Hoshino, Akira Ijiri, Hiroyuki Imachi, Masanori Kaneko, Lorenzo Lagostina, Hayley Manners, Harry-Luke McClelland, Kyle Metcalfe, Natsumi Okutsu, Donald Pan, Maija Jocelyn Raudsepp, Justine Sauvage, Florence Schubotz, Arthur Spivack, Tina Treude, Bernhard Viehweger, David T. Wang, Emily Whitaker, Masataka Kinoshita.

REFERENCES

Ashi, J. (1997) "Computed tomography scan image analysis of sediments," in *Proceedings of the Ocean Drilling Program, Scientific Results*, eds T. H. Shipley, Y. Ogawa, and P. Blum, Vol. 156 (College Station, TX: Ocean Drilling Program), 151–159.

Fortin, D., Francus, P., Gebhardt, A. C., Hahn, A., Kliem, P., Lisé-Pronovost, A., et al. (2013). Destructive and non-destructive density determination: method comparison and evaluation from the Laguna Potrok Aike sedimentary record. *Quat. Sci. Rev.* 71, 147–153. doi: 10.1016/j.quascirev.2012.08.024

Hagino, K., and Expedition 370 Scientists (2018). "Data report: calcareous nannofossils from the middle Miocene to Pleistocene, IODP Expedition 370

Site C0023," in *Proceedings of the International Ocean Discovery Program Volume 370* (College Station, TX: International Ocean Discovery Program).

Hamada, Y., Hirose, T., Ijiri, A., Yamada, T., Sanada, Y., Saito, S., et al. (2018). *In-situ* mechanical weakness of subducting sediments beneath a plate boundary décollement in the Nankai Trough. *Prog. Earth Planet. Sci.* 5:70. doi: 10.1186/s40645-018-0228-z

Heffernan, A. S., Moore, J. C., Bangs, N. L., Moore, G. F., and Shipley, T. H. (2004). Initial deformation in a subduction thrust system: polygonal normal faulting in the incoming sedimentary sequence of the Nankai subduction zone, southwest Japan. *Geol. Soc. Lond. Mem.* 29, 143–148. doi: 10.1144/GSL.MEM.2004.029.01.14

Heuer, V. B., Inagaki, F., Morono, Y., Kubo, Y., Maeda, L., and Expedition 370 Scientists (2017a). International Ocean Discovery Program Expedition 370 Preliminary Report: temperature limit of the deep biosphere off muroto. *Int. Ocean Discov. Prog.* doi: 10.14379/iodp.pr.370.2017

Heuer, V. B., Inagaki, F., Morono, Y., Kubo, Y., Maeda, L., and Expedition 370 Scientists (2017b). "Temperature limit of the Deep Biosphere off Muroto," in *Proceedings of the International Ocean Discovery Program, 370* (College Station, TX: International Ocean Discovery Program).

Hounsfield, G. N. (1973). Computerized transverse axial scanning (tomography): part I. Description of system. *Brit. J. Radiol.* 46, 1016–1022. doi: 10.1259/0007-1285-46-552-1016

Ike, T., Moore, G. F., Kuramoto, S., Park, J., Kaneda, Y., and Taira, A. (2008). Variation in sediment thickness and type along the northern Philippine Sea Plate at the Nankai Trough. *Island Arc* 17, 342–357. doi: 10.1111/j.1440-1738.2008.00624.x

Inagaki, F., Hinrichs, K. U., Kubo, Y., Bowles, M. W., Heuer, V. B., Hong. W. L., et al. (2015). Exploring deep microbial life in coal-bearing sediment down to 2.5 km below the ocean floor. *Science* 349, 420–424. doi: 10.1126/science.aaa6882

Inazaki, T., Inouchi, Y., and Nakano, T. (1995). Use of medical X-ray CT scanner for nondestructive and quantitative analysis of lake sediments. *Bull. Geol. Surv. Jpn.* 46, 629–642.

Johns, R. A., Steude, J. S., Castanier, L. M., and Roberts, P. V. (1993). Nondestructive measurements of fracture aperture in crystalline rock cores using X ray computed tomography. *J. Geophys. Res.* 98, 1889–1900. doi: 10.1029/92JB02298

Ketcham, R. A., and Carlson, W. D. (2001). Acquisition, optimization and interpretation of X-ray computed tomographic imagery: applications to the geosciences. *Comput. Geosci.* 27, 381–400. doi: 10.1016/S0098-3004(00)00116-3

Kitamura, Y., and Yamamoto, Y. (2012). "Records of submarine landslides in subduction input recovered by IODP Expedition 322, Nankai Trough, Japan," in *Submarine Mass Movements and Their Consequences*, Vol. 31. Advances in Natural and Tecnological Hazards Research, eds Y. Yamada, K. Kawamura, K. Ikehara, Y. Ogawa, R. Urgeles, D. Mosher, J. Chaytor, and M. Strasser (Dordrecht: Springer), 659–670.

Leggett, J. K. (1982). 18. Drilling-induced structures in Leg 66 Core. *Init. Reports Deep Sea Drilling Project* 66, 531–538.

Mees, F., Swennen, R., Geet, M. V., and Jacobs, P. (2003). Applications of X-ray computed tomography in the geosciences. *Geol. Soc. Lond. Spec. Publ.* 215, 1–6. doi: 10.1144/GSL.SP.2003.215.01.01

Moore, G. F., Taira, A., Klaus, A., Becker, L., Boeckel, B., Cragg, B. A., et al. (2001). New insights into deformation and fluid flow processes in the Nankai Trough accretionary prism: results of Ocean Drilling Program Leg 190. *Geochem. Geophys. Geosyst.* 2:2001GC000166. doi: 10.1029/2001GC000166

Nakashima, Y., and Kamiya, S. (2007). Mathematica programs for the analysis of three-dimensional pore connectivity and anisotropic tortuosity of porous rocks using X-ray computed tomography image data. *J. Nucl. Sci. Technol.* 44, 1233–1247. doi: 10.1080/18811248.2007.9711367

Nomaki, H., Toyofuku, T., Tsuchiya, M., Matsuzaki, T., Uematsu, K., and Tame, A., (2015). Three-dimensional observation of foraminiferal cytoplasmic morphology and internal structures using uranium–osmium staining and micro-X-ray computed tomography. *Mar. Micropaleontol.* 121, 32–40. doi: 10.1016/j.marmicro.2015.09.003

Orsi, T. H., and Anderson, A. L. (1999). Bulk density calibration for X-ray tomographic analyses of marine sediments. *Geo-Marine Lett.* 19, 270–274. doi: 10.1007/s0036700501

Orsi, T. H., Edwards, C. M., and Anderson, A. L. (1994). X-ray computed tomography: a nondestructive method for quantitative analysis of sediment cores. *J. Sediment. Res. A* 64, 690–693.

Radon, J. (1917). Über die Bestimmuug von Funktionen durch ihre Integralwerte längs gewisser Mannigfaltigkeiten. *Berichte der Sächsischen Akadamie Wissenschaft* 69, 262–277.

Radon, J. (1986). On the determination of functions from their integral values along certain manifolds. *IEEE Trans. Med. Imaging* MI-5, 170–176. doi: 10.1109/TMI.1986.4307775

Reilly, B. T., Stoner, J. S., and Wiest, J. (2017). SedCT: MATLAB^{TM} tools for standardized and quantitative processing of sediment core computed tomography (CT) data collected using a medical CT scanner. *Geochem. Geophys. Geosyst.* 18, 3231–3240. doi: 10.1002/2017GC006884

Row, T. (1996). Coevolution of the mammalian middle ear and neocortex. *Science* 273, 651–654. doi: 10.1126/science.273.5275.651

Schneider, C. A., Rasband, W. S., and Eliceiri, K. W. (2012). NIH Image to ImageJ: 25 years of image analysis. *Nat. Methods* 9, 671–675. doi: 10.1038/nmeth.2089

Støren, E. N., Dahl, S. O., Nesje, A., and Paasche, Ø. (2010). Identifying the sedimentary imprint of high-frequency Holocene river floods in lake sediments: development and application of a new method. *Quat. Sci. Rev.* 29, 3021–3033. doi: 10.1016/j.quascirev.2010.06.038

Strasser, M., Moore, G. F., Kimura, G., Kopf, A. J., Underwood, M. B., Guo, J., et al. (2011). Slumping and mass transport deposition in the Nankai fore arc: evidence from IODP drilling and 3-D reflection seismic data. *Geochem. Geophys. Geosyst.* 12:Q0AD13. doi: 10.1029/2010GC003431

Tanaka, A., Nakano, T., and Ikehara, K. (2011). X-ray computerized tomography analysis and density estimation using a sediment core from the Challenger Mound are in the Porcupine Seabight, off Western Ireland. *Earth Planet. Space* 63, 103–110. doi: 10.5047/eps.2010.12.006

Ujiie, K., Maltman, A. J., and Sánchez-Gómez, M. (2004). Origin of deformation bands in argillaceous sediments at the toe of the Nankai accretionary prism, southwest Japan. *J. Struct. Geol.* 26, 221–231. doi: 10.1016/j.jsg.2003.06.001

Underwood, M. B. (2018). The origin of strata within the inner accretionary prism of Nankai Trough: evidence from clay mineral assemblages along the NanTroSEIZE transect. *Island Arc* 27:e12252. doi: 10.1111/iar.12252

Uramoto, G., Morono, Y., Uematsu, K., and Inagaki, F. (2014). An improved sample preparation method for imaging microstructures of fine-grained marine sediment using microfocus X-ray computed tomography and scanning electron microscopy. *Limnol. Oceanogr. Method* 12, 469–483. doi: 10.4319/lom.2014.12.469

Van Geet, M., Swennen, R., and Wevers, M. (2000). Quantitative analysis of reservoir rocks by microfocus X-ray computerised tomography. *Sediment. Geol.* 132, 25–36. doi: 10.1016/S0037-0738(99)00127-X

Watanabe, N., Ishibashi, T., Ohsaki, Y., Tsuchiya, Y., Tamagawa, T., Hirano, N., et al. (2011). X-ray CT based numerical analysis of fracture flow for core samples under various confining pressures. *Eng. Geol.* 123, 338–346. doi: 10.1016/j.enggeo.2011.09.010

Yun, T. S., Jeong, Y. J., Kim, K. Y., and Min, K., (2013). Evaluation of rock anisotropy using 3D X-ray computed tomography. *Eng. Geol.* 163, 11–19. doi: 10.1016/j.enggeo.2013.05.017

Conflict of Interest Statement: The authors declare that the research was conducted in the absence of any commercial or financial relationships that could be construed as a potential conflict of interest.

frontiers in Earth Science

ORIGINAL RESEARCH
published: 27 September 2019
doi: 10.3389/feart.2019.00250

The Effects of Deformation on the Early Crystallization Kinetics of Basaltic Magmas

Barbara Tripoli[1]†, Michael Manga[1]*†, Jerome Mayeux[1] and Harold Barnard[2]*

[1] Department of Earth and Planetary Science, University of California, Berkeley, Berkeley, CA, United States, [2] Advanced Light Source, Lawrence Berkeley National Laboratory, Berkeley, CA, United States

Crystals and bubbles nucleate and grow in a magma that experiences a range of temperatures, pressures and strain-rates. We have a good conceptual and sometimes quantitative understanding of how crystallization and bubble nucleation are controlled by decompression and cooling. Here we explore the effect of strain-rate on the crystallization kinetics of magmas. In order to understand the interaction between deformation and crystallization, samples of basalt were deformed during their crystallization. We made measurements at subliquidus conditions (1160°C) and deformed samples in compression at strain-rates varying from 0 to 2×10^{-4} s^{-1} for a total strain of 0.31. We simultaneously imaged the samples using X-ray micro-tomography. Without deformation, no crystallization was observed over the course of a 260 min experiment. Once deformation was applied, crystallization initiated. Deformation increased the nucleation rate, increased crystal growth rates, and decreased the incubation time. Increasing the strain-rate, however, does not show a discernable effect of crystallization kinetics. We hypothesize that deformation may have an effect on the parameters that govern the crystallization kinetics of magmas, such as activation energy and diffusion by changing chemical potentials.

Keywords: deformation, crystallization, X-ray micro-tomography, activation energy, diffusion, chemical potential

OPEN ACCESS

Edited by:
Fabio Arzilli,
The University of Manchester, United Kingdom

Reviewed by:
Matteo Masotta,
University of Pisa, Italy
Stephan Kolzenburg,
Ludwig Maximilian University of Munich, Germany

****Correspondence:***
Barbara Tripoli
barbara.tripoli01630@gmail.com
Michael Manga
manga@seismo.berkeley.edu

†ORCID:
Barbara Tripoli
orcid.org/0000-0002-1663-3991
Michael Manga
orcid.org/0000-0003-3286-4682

Specialty section:
This article was submitted to Petrology, a section of the journal Frontiers in Earth Science

Received: *11 June 2019*
Accepted: *05 September 2019*
Published: *27 September 2019*

Citation:
Tripoli B, Manga M, Mayeux J and Barnard H (2019) The Effects of Deformation on the Early Crystallization Kinetics of Basaltic Magmas. Front. Earth Sci. 7:250. doi: 10.3389/feart.2019.00250

INTRODUCTION

Considerable effort has been devoted to studying magma rheology in order to understand the transport of magma into and through the Earth's crust and the eruptions of volcanoes. From magma reservoirs to Earth's surface, magmatic liquids are subject to various deformation processes including shearing, extension and compression. The response of magma to this deformation is a function of intensive parameters (e.g., melt composition, crystal and bubble fraction) and extensive conditions (temperature, pressure) and has been widely studied (e.g., Shaw et al., 1968; Spera et al., 1988; Pinkerton and Stevenson, 1992; Caricchi et al., 2007; Cordonnier et al., 2009; Pistone et al., 2012). On the way to the surface, magmatic liquids also undergo textural and structural changes generated by depressurization, cooling and changes in oxygen fugacity leading to disequilibrium rheology (e.g., Giordano et al., 2007; Kolzenburg et al., 2016, 2017, 2018a,b,c; Vetere et al., 2019) and crystallization (e.g., Arzilli and Carroll, 2013; Vetere et al., 2013, 2015). Crystals and bubbles thus nucleate and grow in a magma that experiences a range of temperatures, pressures and strain-rates.

We have a good conceptual and sometimes quantitative understanding of how crystallization and bubble nucleation are controlled by decompression and cooling. Since all magmas have deformed during their ascent, understanding if and why deformation affects their crystallization are relevant for relating observations in natural samples to those from laboratory experiments that

only vary pressure, temperature and composition. The effect of deformation on the crystallization kinetics of basaltic magma has been studied experimentally at high strain-rates and strains (Kouchi et al., 1986; Vona and Romano, 2013; Kolzenburg et al., 2018b). Shear-enhanced crystallization can in some cases have a large effect on the evolution of rheology and hence magma and lava flow (e.g., Kolzenburg et al., 2018b).

Although flow-enhanced nucleation in polymer melts has been well-documented experimentally and probed with molecular simulations (e.g., Nicholson and Rutledge, 2019 for a recent review), fewer studies have been performed on silicate melts. Kouchi et al. (1986) deformed basaltic melts in torsion at a constant sub-liquidus temperature. By comparing the obtained microstructure with an undeformed sample, they noticed that the crystal nucleation rate is higher and that the nucleation incubation time is shorter in deformation experiments. The crystalline phases are small and acicular in all dynamic experiments performed at low undercooling, which is in contrast to the theory of the dependence of crystal morphologies upon undercooling (Lofgren, 1974; Kirkpatrick et al., 1979). Instead, we expect euhedral crystals at low undercooling and acicular crystals at high undercooling (e.g., Shea and Hammer, 2013; Pontesilli et al., 2019).

An increase in crystal growth rate was also observed in concentric cylinder experiments by Vona and Romano (2013) in basaltic melts, by Chevrel et al. (2015) in andesitic melts, and by Campagnola et al. (2016) in tephriphonolitic melts. The authors of these studies explained their results by the thinning of the diffusion boundary layer around the growing crystals. The induced flow in the silicate liquid facilitates the transport of elements close to the liquid/crystal interface and thus favors crystal growth by supplying to the crystal surface fresh liquid that has not been depleted of components compatible in crystalline phases. In these three studies, however, the samples were deformed using a concentric cylinder apparatus which promotes highly efficient advection. The role of other parameters influencing the crystallization kinetics, such as the activation energy, are thus difficult to assess.

Here we first review the equations governing the nucleation and growth rates of crystals in melts and their incubation time. Then we present new results on the crystallization kinetics of spinel and Fe-Ti oxides in basaltic melts undergoing deformation by unconfined uniaxial compression. The influence of strain-rate on crystal nucleation and growth is characterized *in situ* using X-ray micro-tomography.

Crystal Nucleation and Growth

The steady state nucleation rate J of crystals in melt follows an Arrhenius equation and its simplified form is:

$$J = A \exp\left(-\frac{E}{K_B T}\right), \tag{1}$$

where T is the temperature, K_B is the Boltzmann constant, A is the pre-exponential term and E is the energy term. Although the equations used for calculating A and E differ in different studies, the parameters included in these equations are similar. The pre-exponential term A represents the transport of atoms to the crystal nuclei and includes the frequency of attachment attempts and the concentration of atoms in the vicinity of the nuclei (e.g., Hammer, 2008). Other studies include as well in the pre-exponential term A the energy at the interface between the nuclei and the melt σ_{int} (e.g., Fokin et al., 2006). The energy term E generally includes the activation energy necessary for the incorporation of atoms in the nuclei, the bulk free energy decrease driving crystallization, and the interfacial free energy between nuclei and the melt.

If the nucleus forms spontaneously in the melt, i.e., homogeneous nucleation, it needs to reach a certain critical size to grow further. Otherwise, it becomes unstable and collapses (e.g., Swanson, 1977). The time needed for these stable nuclei to form is called the incubation time and is calculated using (Fokin et al., 2007):

$$\tau = \frac{16 K_B T \sigma_{int}}{3 \Delta G_v^2 a^2 D}, \tag{2}$$

where ΔG_v is the thermodynamic driving force for crystallization, a is a size parameter, D is the diffusion coefficient and σ_{int} is the interfacial energy between nuclei and melt.

The growth rate of crystals in silicate melts is limited by two main processes: the migration efficiency of compatible elements through the melt and their attachment efficiency to the crystal surface (Loomis, 1981). If the attachment rate is slower than the transport of elements in the melt, the growth rate G of crystals is "interface-controlled" and the equation takes a form similar to the nucleation rate:

$$G = B \exp\left(-\frac{E}{K_B T}\right). \tag{3}$$

As for the nucleation rate, the pre-exponential term B represents the transport of atoms across the crystal-melt interface and includes the frequency of attachment attempts, the thickness of the molecular layer, and the fraction of sites available for attachment on the crystal surface (Kirkpatrick, 1975). If the migration of elements is slower than the attachment rate, the growth rate of crystals is "diffusion-controlled" and scales as:

$$G = k \left(\frac{D}{t}\right)^{\frac{1}{2}}, \tag{4}$$

where t is time and k is a constant (Müller-Krumbhaar, 1975).

MATERIALS AND METHODS

In order to study the effects of deformation on the crystallization of magmas, we used a high temperature deformation apparatus developed at the Advanced Light Source, Lawrence Berkeley National Laboratory (**Figure 1**). This hot cell has been designed to image samples using X-ray micro-tomography during mechanical loading (maximum force of 2.2 kN) at temperatures up to 2300°C (Haboub et al., 2014). Six infrared halogen lamps are symmetrically arranged to focus light, and

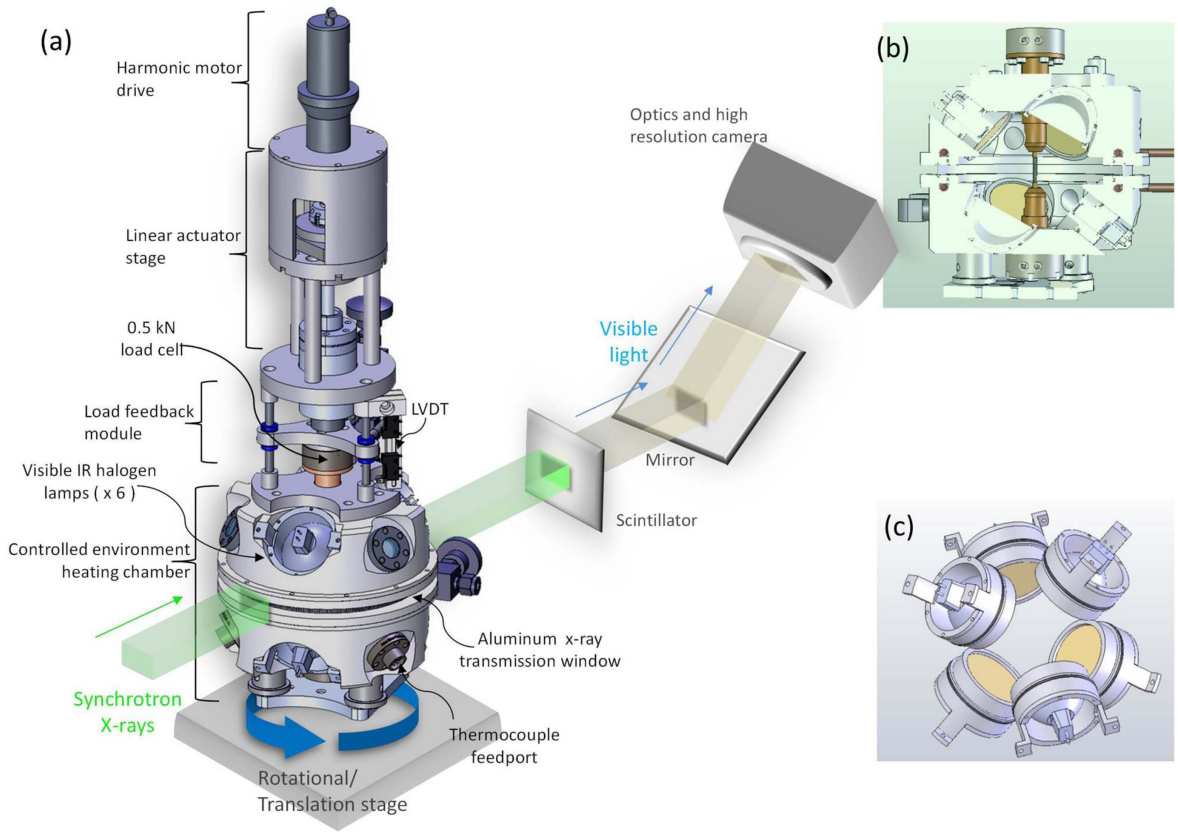

FIGURE 1 | Drawing showing the deformation apparatus developed by Haboub et al. (2014). **(a)** Complete view of the apparatus placed on a rotation and translation stage for X-ray micro-tomography. **(b)** Cross section through the heating chamber. Diameter of the cylindrical X-ray transmission window in a (and shown in b) is 15 cm. **(c)** View of six halogen lamps positioned around the heating chamber. Reprinted from Haboub et al. (2014), with the permission of AIP Publishing.

thus heat, in the central part of the chamber, where samples are held between two water-cooled grippers. The combination of the focused heat and the cooling system produces a hot zone on the sample of approximately 8 mm length, with the central 5 mm having a constant temperature. As the heat absorption of the sample depends on the sample's surface properties, temperature calibration for different applied lamp currents was performed by placing a K-type thermocouple in the middle of the hot zone of our selected basaltic samples. Our experiments complement direct observations of crystallization in basalt made using 4D X-ray microtomography (Polacci et al., 2018) and imaged optically in a moissanite cell (Schiavi et al., 2009; Ni et al., 2014) by documenting the effects of deformation.

The sample selected for this study is the mid-Miocene Lovejoy basalt, the product of a large flood eruption in Northern California (Garrison et al., 2008). Its homogeneous composition and nearly aphyric texture favor the *in situ* melting of its microlites of plagioclase, olivine, pyroxene and iron oxides (**Figure 2B**). Five cylindrical cores of 30 mm length and 3.42 mm diameter were drilled and their extremities were cut perpendicular to the long axis and polished. As a first step, we melted the central part of the cored samples in the hot cell. The temperature was first increased up to 1000°C at a rate of 200°C/min, then from 1000 to 1250°C at a rate of 4°C/min, and finally held for 30 min at 1250°C. We selected this method to remove crystals for two main reasons: (1) Drilling a long and thin core in glass as well as obtaining a large amount of basaltic glass free of crystals are difficult to achieve; (2) Longer times at 1250°C were not possible as the melt would flow downward under the influence of gravity and separate from the upper part of the sample (**Figure 2A**). These times should be long enough for at least local chemical heterogeneity to be removed. Following the 30 min at 1250°C, the sample was rapidly quenched by powering down the lamps. After this first step, the melted zone measured 8 mm in length and contained a volume fraction of 0.02 (± 0.01) of spinel and less than 0.01 of iron oxides. No quenched microlites were observed in Secondary Electron Microscopy images (**Figure 2C**).

During the second step, these melted samples of basalt were deformed during their crystallization. We selected a temperature of 1160°C in order to image the crystallization of spinel and oxides, minerals that we could reliably image because their density is higher than the melt. Indeed, at temperatures lower than 1160°C, the crystallizing phase, i.e., plagioclase, is not readily distinguishable from the melt due to its similar density (e.g., Arzilli et al., 2015). Using the high temperature deformation apparatus, we deformed four samples in compression at four different strain-rates: 2×10^{-5}, 6×10^{-5}, 1×10^{-4}, and 2×10^{-4} s^{-1}. After every 500 μm of displacement, we

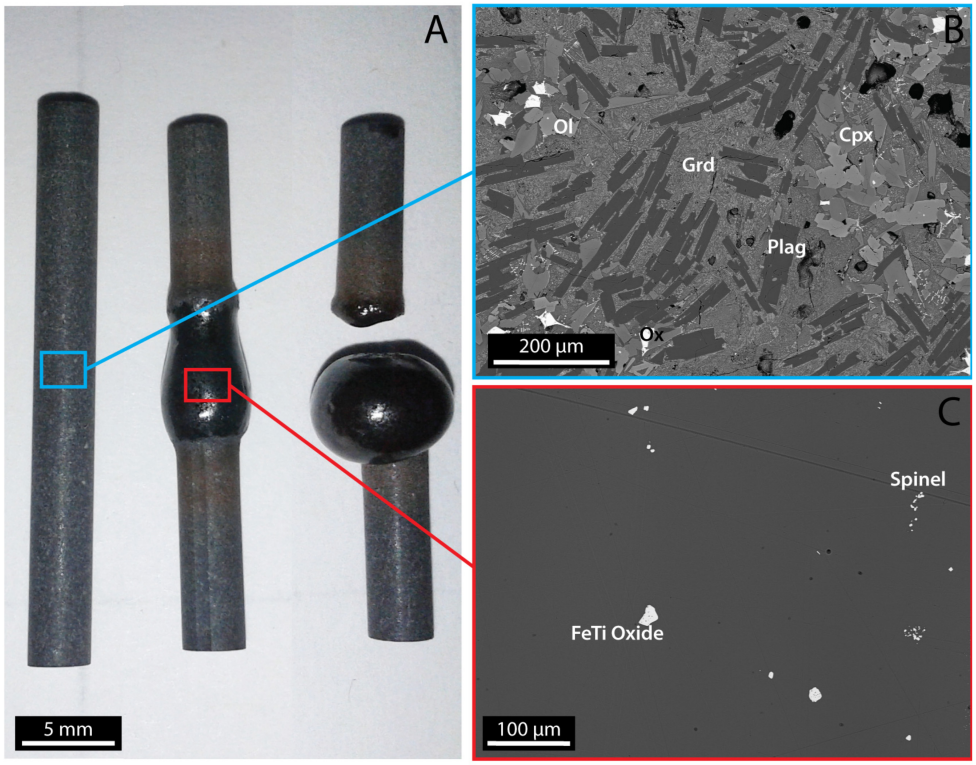

FIGURE 2 | (A) Cores of the Lovejoy basalt before (on the left) and after (in the middle) the melting phase at 1250°C. The core on the right is an example of a melt separating from the top part due to its lower viscosity at higher temperature. **(B)** SEM images of the Lovejoy basalt before the melting phase. **(C)** SEM images of the Lovejoy basalt showing the structure of the zone melted at 1250°C. Cpx: clinopyroxene; Grd: groundmass; Plag: plagioclase; Ol: olivine.

quenched the samples to room temperature by powering off the lamps, which permitted a cooling rate reaching 50°C/s between the investigated temperature (1160°C) and the glass transition (678°C). We then imaged the cores using X-ray micro-tomography (XRT) (see **Supplementary Material S.A.** for details). We used monochromatic X-rays with energies of 33 kev and a voxel linear dimension of 1.28 microns. As the time required to scan the sample was about 15 min, we decided to not image the sample at high temperature as any bubbles move upward and additional crystallization may occur during the scans – any motion of a few pixels creates image artifacts. After each scan, the sample was reheated rapidly by switching the lamps back on with heating rates reaching approximately 50°C/s. This cycle, involving a sequence of heating, deforming, quenching and scanning the sample, was repeated five times until the total strain reached 0.31. This total strain corresponds to the ratio of the five applied deformations (total of 2.5 mm) to the hot zone length (8 mm). Experiments at higher strains were not performed in order to avoid the accumulation of stress located near the interface between the melted and the unmelted parts of the sample (Mogi, 2007). Although a load cell records the applied stress (**Figure 1**), the viscosity of our samples is so low that instrument noise prevents us from measuring rheology on these samples. In order to characterize the crystallization at static conditions, one sample was held at 1160°C without applying any deformation. This sample was quenched for XRT imaging every 52 min, which corresponds to the time elapsed during one deformation step at the lowest strain rate. The total duration at 1160°C was 260 min.

The obtained XRT images were first segmented for spinels, Fe-Ti oxides and melt using the Fiji plugin *Trainable Weka Segmentation* (Arganda-Carreras et al., 2017). We then used the volume obtained from these XRT images for measuring the number densities and the volume fractions of Fe-Ti oxides and spinels using the Fiji plugin *Particle Analyzer* within *BoneJ* (Doube et al., 2010).

After the experiments, samples were cut horizontally through the hot zone and embedded in epoxy for chemical analyses. The composition of the minerals and their surrounding melts, i.e., within 25 µm distance, were measured using a Scanning Electron Microscope (SEM) located in the Department of Earth Sciences, at ETH Zurich (Switzerland). In order to determine the stable mineral assemblage at these P-T conditions, we repeated the same temperature sequence on the sample of basalt in a high temperature furnace and kept the sample at 1160°C without deforming it for 65 h, corresponding to an amount of time significantly long to more closely reach equilibrium. After quenching, this sample was then imaged using X-ray microtomography. The measurement parameters of energy beam, resolution and exposure time, as well as the image processing, were kept the same as during the deformation experiments. These results were then compared to the mineral

assemblage estimated by thermodynamic calculations using MELTS (Gualda et al., 2012) at a temperature of 1160°C and atmospheric pressure and fO_2 (see **Table 1** and **Supplementary Material S.B.** for more details).

The main advantage of the micro-tomography experiments is that the imaging is non-destructive and hence we can document the progression of nucleation and crystal growth on the same samples in a device that also allows us to apply deformation. Further the crystals are characterized in three dimensions. There are also disadvantages. First, the spatial resolution of the microtomography is lower than SEM or Transmission Electron Microscopy images, and nucleation by definition begins at small scales. Second, because the density of the dominant mineral, plagioclase is so similar to the melt, we are only able to document the first phases that crystallize at the highest temperatures, limiting the temperatures and crystallizing phases we could explore. Third, the finite time available for imaging and the requirement that the sample not flow too fast under the influence of gravity, further limit the range of compositions and temperatures that we could consider.

RESULTS

Under static conditions there was no additional crystallization during the 260 min experiment. The spinel and iron oxide fractions and number densities remain constant throughout the experiment. By increasing the strain-rate up to 1.0×10^{-4} s^{-1}, within 50 min crystallization occurs on preexisting surfaces, such as bubbles and crystals, as noted by Pleše et al. (2018), and in the melt, where no preexisting surfaces were visible. Number densities and volume fractions of both crystal phases increase rapidly after 50 min (**Figure 3** and **Table 2**). After 50 min of deformation, spinel number density stays constant and amounts to 17 ($\pm$ 1) $\times$ 10^3 mm^{-3}. Their volume fraction reaches a constant value of 0.08 ($\pm$ 0.01) after 150 min (slightly larger than the MELTS equilibrium value of 0.05). The Fe-Ti oxide number density continuously increases up to 6 ($\pm$ 1) $\times$ 10^3 mm^{-3} and their volume fraction reaches a constant value of 0.016 ($\pm$ 0.002) after 50 min.

In our experiments, varying the strain-rate during deformation has no clear effect. Indeed, the increase in number densities and volume fractions of the lower strain-rate experiments are similar, i.e., the measured values for different strain-rates are within the error bars during crystallization (**Figure 3**). All dynamic experiments with a duration over 50 min have newly formed crystals. At the highest strain-rate (2.0×10^{-4} s^{-1}), no additional crystallization is observed after reaching the highest crystallinity. However, as the total strain applied in all experiments was kept constant (0.31), the experimental time for the sample deformed at 2.0×10^{-4} s^{-1} was only 26 min and thus did not reach the 50 min required for crystallization under deformation in the other experiments.

TABLE 1 | Composition of the crystals and the residual melt of the Lovejoy basalt modeled by MELTS (Gualda et al., 2012) and measured by Secondary Electron Microprobe (SEM).

Bulk rock		MELTS calculations		SEM measurements		
		Melt	Spinel	Melt	Spinel	Fe-Ti oxide
SiO_2	51.51	56.38	0.00	54.60	0.42	0.46
TiO_2	2.53	2.55	2.28	2.23	1.76	11.55
Al_2O_3	14.12	14.92	5.67	14.67	5.64	2.02
Fe_2O_3	11.71	6.59	65.85	9.32	81.83	82.29
FeO	1.55	0.62	11.43	ND	ND	ND
MnO	0.24	0.26	0.00	0.22	0.63	0.17
MgO	4.11	3.10	14.76	4.19	9.38	3.13
CaO	7.93	8.68	0.00	8.27	0.19	0.17
Na_2O	3.14	3.44	0.00	3.56	0.02	0.01
K_2O	1.99	2.18	0.00	1.87	0.02	0.02
P_2O_5	1.17	1.28	0.00	1.04	0.00	0.00

The values are given in wt%. Iron content is reported as Fe_2O_3 for the SEM measurements. ND, not determined. Bulk rock is the average from Garrison et al. (2008). At the experimental temperature of 1160°C, MELTS computes a crystal volume fraction of 5% and the only solid phase is spinel.

TABLE 2 | Summary of the experiments.

			Volume fraction [n.u.]		CND [mm^{-3}]	
Strain rate [s^{-1}]	Strain [n.u.]	Time [min]	Spinel	TiFeO	Spinel	TiFeO
0	0.00	0	0.017	0.005	5278	1255
	0.00	52	0.019	0.005	6501	1100
	0.00	104	0.018	0.004	6637	889
	0.00	156	0.010	0.005	7343	1390
	0.00	208	0.018	0.005	6780	1242
	0.00	260	0.017	0.004	7705	1171
2×10^{-4}	0.00	0	0.023	0.005	8378	1401
	0.06	5	0.021	0.004	8984	1417
	0.13	10	0.020	0.005	8461	1508
	0.19	16	0.027	0.004	8531	1641
	0.25	21	0.020	0.005	7558	1617
	0.31	26	0.021	0.004	8219	920
1×10^{-4}	0.00	0	0.015	0.007	8776	1391
	0.06	10	0.024	0.006	9294	1778
	0.13	20	0.021	0.009	10141	2167
	0.19	30	0.021	0.005	8091	1076
	0.25	40	0.017	0.006	11812	1219
	0.31	50	0.032	0.007	10276	1298
6×10^{-5}	0.00	0	0.016	0.008	7528	2062
	0.06	18	0.024	0.009	9067	2201
	0.13	36	0.019	0.013	8228	2107
	0.19	54	0.039	0.010	12837	3894
	0.25	72	0.058	0.015	12613	3314
	0.31	90	0.058	0.016	13307	4186
2×10^{-5}	0.00	0	0.027	0.006	9128	1698
	0.06	52	0.048	0.011	17703	2840
	0.13	104	0.060	0.015	15392	3675
	0.19	156	0.083	0.017	15934	4822
	0.25	208	0.078	0.015	15548	4138
	0.31	260	0.084	0.018	15876	5928

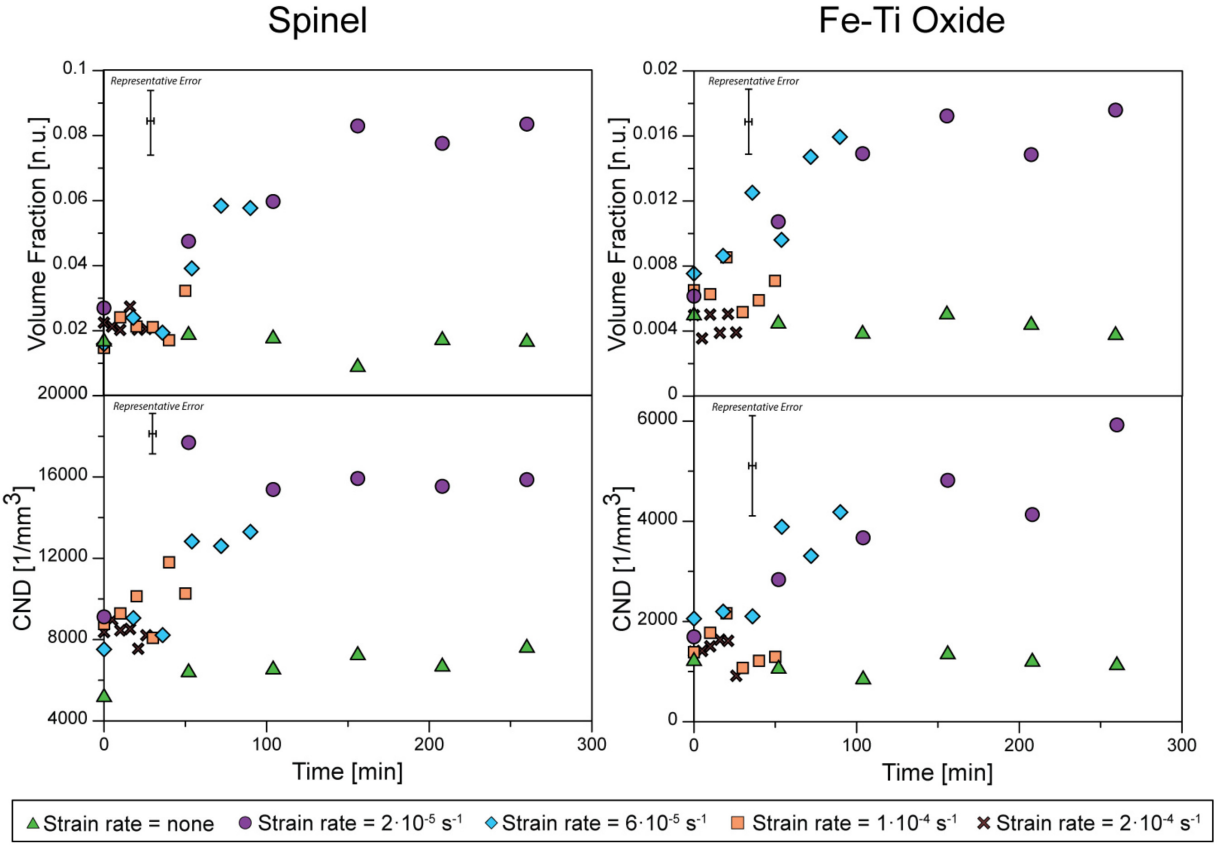

FIGURE 3 | Microstructure evolution of the spinel (on the **left**) and Fe-Ti oxide (on the **right**) determined using the XRT images. The volume fraction and the crystal number density (CND) are plotted for each strain rate applied during the experiments.

The sample left for 65 h at 1160°C contains a spinel volume fraction of 0.05 and no iron oxide. Thermodynamic calculations using MELTS predicts the same fraction of spinel (**Supplementary Material**), i.e., 0.05, having a composition similar to the one measured by SEM (**Table 1**), and no iron oxide. We can thus assume that the thermodynamic equilibrium assemblage for this basalt at 1160°C and atmospheric pressure and fO_2 is composed uniquely of spinel at a volume fraction of about 0.05. As this spinel fraction is higher than the spinel fraction in the undeformed sample, we can also assume that the incubation time under static conditions is longer than 260 min.

The newly formed spinels are recognized from older ones by their shape. The spinels grown during deformation are platy (white crystals in **Figure 4A**) whereas those already present have a vermiform structure (colored crystals in **Figure 4A**). The spinels grown during the 65 h static experiment have more commonly an octahedral shape.

Secondary Electron Microscopy on the recovered samples reveals some features not observable during X-ray imaging. During the second step of the experiments, iron-rich microlites with a diameter of less than 1 μm (are assumed to) form in the melt during quenching (e.g., Zhou et al., 2000). The resolution of 1.28 μm prevents us from recognizing these features during the X-ray imaging. Interestingly, we observe in the deformed samples the presence of a microlite-free zone around the crystals (**Figure 5**) in addition to the depletion of iron around newly formed crystals.

DISCUSSION

Our experiments were performed over time scales comparable to the incubation time, allowing us to document the effects of deformation on incubation, nucleation rates, and crystal growth. Our results show that deformation has an effect on the crystallization kinetics of magmas by (1) increasing the nucleation rate (variation in CND), (2) increasing the growth rate (variation in crystal fraction) and (3) decreasing the incubation time (corresponding to 50 min under dynamic conditions and more than 260 min under static conditions). Our experiments confirm that deformation affects crystallization in basaltic melts, not just for large strains and strain-rates where advection is important (Kouchi et al., 1986; Vona and Romano, 2013; Kolzenburg et al., 2018b).

Each parameter used in the nucleation and growth models (Eq. 1–4) is assessed to understand the potential origins of the observed variations.

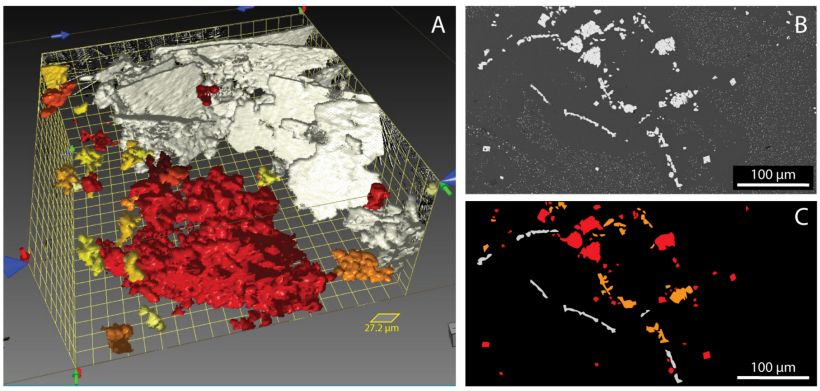

FIGURE 4 | Images displaying features associated with the spinels. **(A)** 3D reconstruction, performed using Dragonfly software, of newly formed spinel (in white) and already present spinel (in red) in the sample deformed at 2×10^{-5} s^{-1} at t = 260 min. The different colors represent the aspect ratio of the crystals and are used here only for visualization purposes. **(B)** Elongated spinel crystals nucleated during deformation [white crystals in panel **(C)**] and vermicular spinel crystals already present [colored crystals in panel **(C)**] grew during deformation and have an aureole of microlite-free melt visible in SEM images.

Possible Origins of Deformation-Induced Crystallization

During our crystallization experiments, the temperature is held constant. The difference in nucleation rate between the deformed and undeformed samples must thus be linked to A and/or E. Previous studies proposed that A increases during deformation because there is a higher flow of elements to the crystal-melt interface (Kouchi et al., 1986; Vona and Romano, 2013; Kolzenburg et al., 2018b). In this case, deformation favors chemical homogenization of the melt. However, our deformed samples display a zone around the newly formed crystals which is depleted in iron, i.e., a zone that is free of quenched microlites (**Figure 4**). As the undeformed sample did not further crystallize during the experiment and does not present any aureole of microlite-free melt around its crystals, we interpreted this feature as the diffusion boundary layer depleted in iron. Kouchi et al. (1986) observed that the thickness of the boundary layer decreased with increasing deformation rate. This discrepancy between our and their observations might be linked to the experimental method employed. Previous studies considered much larger strain-rates and strains (Kouchi et al., 1986; Vona and Romano, 2013; Kolzenburg et al., 2018b) which would increase the advection efficiency. In our compression experiments, the concentration of reactant atoms is not increased by deformation.

Another possibility involves a variation in the energy state of the system. Minimization of the Gibbs free energy can be used to establish phase equilibria at fixed temperature and pressure using changes in state functions of a system, such as enthalpy and entropy, and/or intensive properties, such as chemical potentials and activities (Ghiorso and Sack, 1995). Since the local description of chemical equilibrium at an interface can be modified by stresses

$$\mu = F + \sigma_n V \tag{5}$$

where μ is the chemical potential, F is the Helmholtz free energy, σ_n is the normal stress across the interface and V is the molar volume, variations in stress may also change properties such as diffusion and mineralogy that are influenced by chemical potential (e.g., Wheeler, 2017).

The rate of a chemical reaction is influenced by the concentration of the reactant molecule and the activation energy, i.e., the minimum energy required to start a chemical reaction. For crystallization, the activation energy is better defined as the energy barrier that must be overcome to produce a stable crystal nucleus. Molecules commonly absorb thermal energy to overcome this barrier. In the case of crystallization from melt, this energy is used to rearrange, break and/or build bonds in the chains of silica tetrahedra present in the melt (Kirkpatrick, 1983) and when the less energetic, more stable crystal nucleus is formed, energy is released in the form of latent heat of crystallization.

Stress may help molecules overcome the activation energy. Indeed, the activation strain model states that the activation energy can be decomposed into the energy associated with the structural deformation undergone by the reactant molecules, i.e., strain energy, and the energy resulting from the bonding of these molecules, i.e., interaction energy (Van Zeist and Bickelhaupt, 2010; Fernández and Bickelhaupt, 2014). An applied stress during melt deformation may thus bring strain energy into the system and helps to distort and/or disrupt chains of silica tetrahedra that ultimately favor the formation of crystal nuclei. A decrease in activation energy during deformation-induced crystallization has been observed in various type of material such as polymers (Sun et al., 1984; Chien and Weiss, 1988; Kumaraswamy et al., 1999; Xu et al., 2011), metal alloys (Lee et al., 2006; Wang et al., 2015), oil and butter (Yang et al., 2011), and metals (e.g., Donovan and Stobbs, 1981; Chen et al., 1994) and might explain impact-induced vesiculation of magmas (Rothery et al., 2007; Carey et al., 2012).

The activation energy is present in the energy term of Eqs. (1) and (3) and thus influences nucleation and growth rates. However, we observed as well a decrease in incubation time for crystallization in our experiments. Variations in the normal stress on interfaces produced by deformation give rise to gradients in

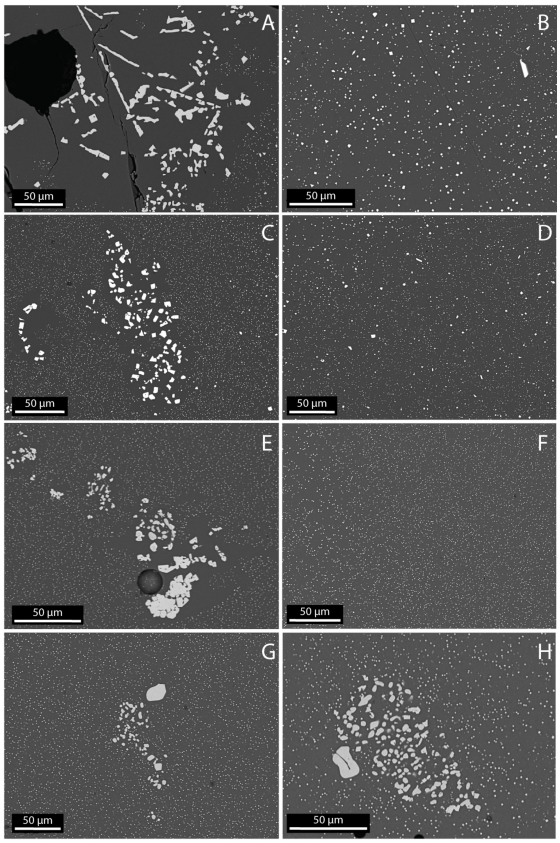

FIGURE 5 | SEM images of the samples recovered after the deformation experiment. Elongated spinel crystals nucleated during deformation or vermicular spinels grown during deformation have an aureole of microlite-free melt visible in SEM images. **(A)** Phenocrysts of spinels in the sample deformed at 2×10^{-5} s^{-1} and its groundmass **(B)**. **(C)** Phenocrysts of spinels in the sample deformed at 6×10^{-5} s^{-1} and its groundmass **(D)**. **(E)** Phenocrysts of spinels in the sample deformed at 1×10^{-5} s^{-1} and its groundmass **(F)**. **(G)** Phenocrysts of spinels in the sample deformed at 2×10^{-4} s^{-1}. **(H)** Phenocrysts of spinels in the undeformed sample. In panels **(G,H)**, no aureole of microlite-free melt is visible.

chemical potential (Eq. 5), and can promote diffusion (Eqs. 2, 4), in turn increasing both the nucleation rates and decreasing the incubation time. The diffusion coefficient can be calculated using the Arrhenius relation $D = D_0 \exp(-\frac{E}{K_B T})$, where E is the activation energy for diffusion and D_0 is the diffusion coefficient at high temperature where $K_B T >> E$ (Zhang, 2010). The crystallizing phases in our experiments contain Fe, Mg, Ti and Al (**Table 1**) and their activation energy for diffusion in basaltic melts are 264 ± 17 kJ/mol (Lowry et al., 1982), 240 ± 20 (Chen and Zhang, 2009), 255 ± 86 and 313 ± 26 kJ/mol [determined by Zhang (2010) from data produced by Chen and Zhang (2009)], respectively. Burkhard (2005) determined the activation energy for the nucleation and the growth of Fe-Ti oxides in basaltic melt and their values, i.e., 292 and 343 (± 7) kJ/mol, respectively, are particularly close to the activation energy for diffusion. We may thus assume that strain energy provided during deformation was sufficient to promote a higher diffusivity of elements by the same mechanism presented before, i.e., distortion and/or breaking of chains of silica tetrahedra.

Variation in the Mineral Assemblage

Our studies, combined with previous studies, show that deformation increases nucleation and growth rates and reduces the incubation time of crystals in silicate melts. In addition, we observed the growth of Fe-Ti oxides that did not disappear during the melting phase of the sample preparation as well as the nucleation of new crystals of the same composition. These Fe-Ti oxides are not present in the sample left 65 h at 1160°C and are not predicted by thermodynamic modeling using MELTS. This suggests that deformation might also promote the formation of metastable phases that leads to kinetic-controlled crystallization, rather than only the thermodynamically favored phases (e.g., Woodward and Baer, 1944; Cölfen and Mann, 2003). In this case, the activation energy for the nucleation of the metastable phase needs to be lower than the activation energy of the stable phase. As no Fe-Ti oxides crystallized in the undeformed samples, deformation may be the external factor lowering activation energy for crystallization of metastable and stable phases by changing the chemical potential of the various interfaces present (Eq. 5). Our experiments, however, do not document an effect of the metastable phases on stable phases.

Implications for Natural Samples

The texture (mineralogy, crystal shape and number density) of erupted magmas are commonly used to infer ascent dynamics by comparing natural samples with those created experimentally (e.g., Castro and Dingwell, 2009; Brugger and Hammer, 2010; Riker et al., 2015 for some examples). Our findings that deformation changes the mineralogy, growth rate, and number density imply that an additional variable may need to be considered when connecting lab studies and natural samples. In some cases, the deformation-enhanced growth and nucleation of crystals (here over several 10 s of minutes) may be negligible compared to those produced by the large changes in pressure that accompany rapid ascent. However, in lava flows where pressure changes are small, deformation may play a relatively greater role in promoting crystallization and natural strain-rates are typically much larger than those we considered. For the basalt we considered, for example, in 260 min the static sample did not change crystallinity but does approach a different steady value of about 10% after several 10 s of minutes in the presence of deformation. Our experimental apparatus and imaging constraints limited the range of strain-rates, temperatures and compositions we could study. Further experimental and theoretical analyses may lead to a better quantification of the role of deformation and thus identify when and how deformation affects the interpretation of natural samples.

CONCLUSION

Deformation enhances the crystallization kinetics in magmas. Based on X-ray images collected during the experiments, we

observed that the nucleation and growth rates of spinels and Fe-Ti oxides increase when deformation is applied to a basaltic melt. A decrease in the incubation time is also observed during deformation. These changes in the crystallization kinetics upon deformation do not depend on the strain rate, at least for the temperatures and range of strain rates investigated. We suggest that the applied stress helps the system to overcome the activation energy involved in crystallization kinetics and in diffusion of elements by changing chemical potentials. Models might be tested in the future by exploring a broader range of temperatures, achieving greater spatial resolution in the imaging, finding approaches to image low absorption contrast minerals, and considering a longer spectrum of time scales.

DATA AVAILABILITY STATEMENT

All datasets for the plots in this paper are included in the manuscript.

AUTHOR CONTRIBUTIONS

BT conceived the study and acquired, analyzed, and interpreted the data. MM acquired and interpreted the data. JM acquired and analyzed the data. HB acquired the data.

FUNDING

The authors acknowledge the financial support of the Swiss National Science Foundation (grant P2EZP2_162226) with additional support from the US NSF EAR 1615203.

ACKNOWLEDGMENTS

We would like to thank Dilworth Parkinson and Kristen Fauria for their instructions and recommendations for tomography analyses at the Advanced Light Source and Eric Reusser and Lukas Martin for their help using the SEM at ETHZ. We also thank the ALS for providing many days of beamtime between 2016 and 2017 for performing these experiments. We also thank the two reviewers for thorough reviews and identifying ways to clarify the presentation and interpretation. The raw images and automated reconstructions acquired using the X-ray tomography are stored by the United States Department of Energy at spot.nersc.gov.

SUPPLEMENTARY MATERIAL

The Supplementary Material for this article can be found online at: https://www.frontiersin.org/articles/10.3389/feart.2019.00250/full#supplementary-material

REFERENCES

Arganda-Carreras, I., Kaynig, V., Rueden, C., Eliceiri, K. W., Schindelin, J., Cardona, A., et al. (2017). Trainable Weka segmentation: a machine learning tool for microscopy pixel classification. *Bioinformatics* 33, 2424–2426. doi: 10.1093/bioinformatics/btx180

Arzilli, F., and Carroll, M. R. (2013). Crystallization kinetics of alkali feldspars in cooling and decompression-induced crystallization experiments in trachytic melt. *Contrib. Mineral. Petrol.* 166, 1011–1027. doi: 10.1007/s00410-013-0906-1

Arzilli, F., Mancini, L., Voltolini, M., Cicconi, M. R., Mohammadi, S., Giuli, G., et al. (2015). Near-liquidus growth of feldspar spherulites in trachytic melts: 3D morphologies and implications in crystallization mechanisms. *Lithos* 216-217, 93–105. doi: 10.1016/j.lithos.2014.12.003

Brugger, C. R., and Hammer, J. E. (2010). Crystallization kinetics in continuous decompression experiments: implications for interpreting natural magma ascent processes. *J. Petrol.* 51, 1941–1965. doi: 10.1093/petrology/egq044

Burkhard, D. J. (2005). Nucleation and growth rates of pyroxene, plagioclase, and Fe-Ti oxides in basalt under atmospheric conditions. *Eur. J. Mineral.* 17, 675–685.

Campagnola, S., Vona, A., Romano, C., and Giordano, G. (2016). Crystallization kinetics and rheology of leucite-bearing tephriphonolite magmas from the Colli Albani volcano (Italy). *Chem. Geol.* 424, 12–29. doi: 10.1016/j.chemgeo.2016.01.012

Carey, R. J., Manga, M., Degruyter, W., Swanson, D., Houghton, B., Orr, T., et al. (2012). External triggered renewed bubble nucleation in basaltic magma: the October 12 2008 eruption at Halemaʻumaʻu Overlook vent, Kilauea, HawaiʻI, USA. *J. Geophys. Res.* 117:B11202. doi: 10.1029/2012JB009496

Caricchi, L., Burlini, L., Ulmer, P., Gerya, T., Vassalli, M., and Papale, P. (2007). Non-newtonian rheology of crystal-bearing magmas and implications for magma ascent dynamics. *Earth Planet. Sci. Lett.* 264, 402–419. doi: 10.1016/j.epsl.2007.09.032

Castro, J. M., and Dingwell, D. B. (2009). Rapid ascent of rhyolitic magma at Chaiten volcano. Chile. *Nature* 461, 780–783. doi: 10.1038/nature08458

Chen, H., He, Y., Shiflet, G. J., and Poon, S. J. (1994). Deformation-induced nanocrystal formation in shear bands of amorphous alloys. *Nature* 367, 541–543. doi: 10.1038/367541a0

Chen, Y., and Zhang, Y. (2009). Clinopyroxene dissolution in basaltic melt. *Geochim. Cosmochim. Acta* 73, 5730–5747. doi: 10.1016/j.gca.2009.06.016

Chevrel, M. O., Cimarelli, C., deBiasi, L., Hanson, J. B., Lavallée, Y., Arzilli, F., et al. (2015). Viscosity measurements of crystallizing andesite from Tungurahua volcano (Ecuador). *Geochem. Geophys. Geosyst.* 16, 870–889. doi: 10.1002/2014gc005661

Chien, M. C., and Weiss, R. (1988). Strain-induced crystallization behavior of poly (ether ether ketone)(PEEK). *Polym. Eng. Sci.* 28, 6–12. doi: 10.1002/pen.760280103

Cölfen, H., and Mann, S. (2003). Higher-order organization by mesoscale self-assembly and transformation of hybrid nanostructures. *Angew. Chem. Int. Ed.* 42, 2350–2365. doi: 10.1002/anie.200200562

Cordonnier, B., Hess, K.-U., Lavallee, Y., and Dingwell, D. (2009). Rheological properties of dome lavas: case study of Unzen volcano. *Earth Planet. Sci. Lett.* 279, 263–272. doi: 10.1016/j.epsl.2009.01.014

Donovan, P., and Stobbs, W. (1981). The structure of shear bands in metallic glasses. *Acta Metallurgica* 29, 1419–1436. doi: 10.1016/0001-6160(81)90177-2

Doube, M., Kłosowski, M. M., Arganda-Carreras, I., Cordelières, F. P., Dougherty, R. P., Jackson, J. S., et al. (2010). BoneJ: free and extensible bone image analysis in ImageJ. *Bone* 47, 1076–1079. doi: 10.1016/j.bone.2010.08.023

Fernández, I., and Bickelhaupt, F. M. (2014). The activation strain model and molecular orbital theory: understanding and designing chemical reactions. *Chem. Soc. Rev.* 43, 4953–4967. doi: 10.1039/c4cs00055b

Fokin, V. M., Schmelzer, J. W., Nascimento, M. L., and Zanotto, E. D. (2007). Diffusion coefficients for crystal nucleation and growth in deeply undercooled glass-forming liquids. *J. Chem. Phys.* 126:234507. doi: 10.1063/1.2746502

Fokin, V. M., Zanotto, E. D., Yuritsyn, N. S., and Schmelzer, J. W. (2006). Homogeneous crystal nucleation in silicate glasses: a 40 years perspective. *J. Non Cryst. Solids* 352, 2681–2714. doi: 10.1016/j.jnoncrysol.2006.02.074

Garrison, N. J., Busby, C. J., Gans, P. B., Putirka, K., and Wagner, D. L. (2008). A mantle plume beneath California? The mid-Miocene Lovejoy flood basalt, northern California. *Geol. Soc. Am. Spec. Pap.* 438, 551–572. doi: 10.1130/2008.2438(20)

Ghiorso, M. S., and Sack, R. O. (1995). Chemical mass transfer in magmatic processes IV. A revised and internally consistent thermodynamic model for the interpolation and extrapolation of liquid-solid equilibria in magmatic systems at elevated temperatures and pressures. *Contrib. Mineral. Petrol.* 119, 197–212. doi: 10.1007/s004100050036

Giordano, D., Polacci, M., Longo, A., Papale, P., Dingwell, D. B., Boschi, E., et al. (2007). Thermo-rheological magma control on the impact of highly fluid lava flows at Mt. Nyiragongo. *Geophys. Res. Lett.* 34: L06301.

Gualda, G. A., Ghiorso, M. S., Lemons, R. V., and Carley, T. L. (2012). Rhyolite-MELTS: a modified calibration of MELTS optimized for silica-rich, fluid-bearing magmatic systems. *J. Petrol.* 53, 875–890. doi: 10.1093/petrology/egr080

Haboub, A., Bale, H. A., Nasiatka, J. R., Cox, B. N., Marshall, D. B., Ritchie, R. O., et al. (2014). Tensile testing of materials at high temperatures above 1700°C with in situ synchrotron X-ray micro-tomography. *Rev. Sci. Instrum.* 85:083702. doi: 10.1063/1.4892437

Hammer, J. E. (2008). Experimental studies of the kinetics and energetics of magma crystallization. *Rev. Mineral. Geochem.* 69, 9–59. doi: 10.2138/rmg.2008.69.2

Kirkpatrick, R. J. (1975). Crystal growth from the melt: a review. *Am. Mineral.* 60, 798–814.

Kirkpatrick, R. J. (1983). Theory of nucleation in silicate melts. *Am. Mineral.* 68, 66–77.

Kirkpatrick, R. J., Klein, L., Uhlmann, D., and Hays, J. F. (1979). Rates and processes of crystal growth in the system anorthite-albite. *J. Geophys. Res. Solid Earth* 84, 3671–3676. doi: 10.1029/jb084ib07p03671

Kolzenburg, S., Di Genova, D., Giordano, D., Hess, K. U., and Dingwell, D. B. (2018a). The effect of oxygen fugacity on the rheological evolution of crystallizing basaltic melts. *Earth Planet. Sci. Lett.* 487, 21–32. doi: 10.1016/j.epsl.2018.01.023

Kolzenburg, S., Giodano, D., Hess, K. U., and Dingwell, D. B. (2018b). Shear rate-dependent disequilibrium rheology and dynamics of basalt solidification. *Geophys. Res. Lett.* 45, 6466–6475. doi: 10.1029/2018gl077799

Kolzenburg, S., Giordano, D., Di Muro, A., and Dingwell, D. (2018c). Equilibrium viscosity and disequilibrium rheology of a high magnesium basalt from piton De La Fournaise volcano, La Reunion, Indian Ocean, France. *Ann. Geophys.* 61:18.

Kolzenburg, S., Giordano, D., Cimarelli, C., and Dingwell, D. B. (2016). In Situ thermal characterization of cooling/crystallizing lavas during rheology measurements and implications for lava flow emplacement. *Geochim. Cosmochim. Acta* 195, 244–258. doi: 10.1016/j.gca.2016.09.022

Kolzenburg, S., Giordano, D., Thordarson, T., Höskuldsson, A., and Dingwell, D. B. (2017). The rheological evolution of the 2014/2015 eruption at Holuhraun, central Iceland. *Bull. Volcanol.* 79:45.

Kouchi, A., Tsuchiyama, A., and Sunagawa, I. (1986). Effect of stirring on crystallization kinetics of basalt: texture and element partitioning. *Contrib. Mineral. Petrol.* 93, 429–438. doi: 10.1007/bf00371713

Kumaraswamy, G., Issaian, A. M., and Kornfield, J. A. (1999). Shear-enhanced crystallization in isotactic polypropylene. 1. Correspondence between in situ rheo-optics and ex situ structure determination. *Macromolecules* 32, 7537–7547. doi: 10.1021/ma990772j

Lee, S.-W., Huh, M.-Y., Chae, S.-W., and Lee, J.-C. (2006). Mechanism of the deformation-induced nanocrystallization in a Cu-based bulk amorphous alloy under uniaxial compression. *Scripta Materialia* 54, 1439–1444. doi: 10.1016/j.scriptamat.2006.01.002

Lofgren, G. (1974). An experimental study of plagioclase crystal morphology; isothermal crystallization. *Am. J. Sci.* 274, 243–273. doi: 10.2475/ajs.274.3.243

Loomis, T. P. (1981). An investigation of disequilibrium growth processes of plagioclase in the system anorthite-albite-water by methods of numerical simulation. *Contrib. Mineral. Petrol.* 76, 196–205. doi: 10.1007/bf00371959

Lowry, R. K., Henderson, P., and Nolan, J. (1982). Tracer diffusion of some alkali, alkaline-earth and transition element ions in a basaltic and an andesitic melt, and the implications concerning melt structure. *Contrib. Mineral. Petrol.* 80, 254–261. doi: 10.1007/bf00371355

Mogi, K. (2007). *Experimental Rock Deformation*. London: Taylor and Francis group. 378.

Müller-Krumbhaar, H. (1975). Diffusion theory for crystal growth at arbitrary solute concentration. *J. Chem. Phys.* 63, 5131–5138. doi: 10.1063/1.431321

Nicholson, D. A., and Rutledge, G. C. (2019). An assessment of models for flow-enhanced nucleation in an n-alkane melt by molecular simulation. *J. Rheol.* 63, 465–475. doi: 10.1122/1.5091945

Ni, H., Keppler, H., Walte, N., Schiavi, F., Chen, Y., Masotta, M., and Li, Z. (2014). In situ observation of crystal growth in a basalt melt and the development of crystal size distribution in igneous rocks. *Contrib. Mineral. Petrol.* 167:1003. doi: 10.1007/s00410-014-1003-9

Pinkerton, H., and Stevenson, R. J. (1992). Methods of determining the rheological properties of magmas at sub-liquidus temperatures. *J. Volcanol. Geotherm. Res.* 53, 47–66. doi: 10.1016/0377-0273(92)90073-m

Pistone, M., Caricchi, L., Ulmer, P., Burlini, L., Ardia, P., Reusser, E., et al. (2012). Deformation experiments of bubble-and crystal-bearing magmas: rheological and microstructural analysis. *J. Geophys. Res. Solid Earth* 117, 1–39.

Pleše, P., Higgins, M., Mancini, L., Lanzafame, G., Brun, F., Fife, J., et al. (2018). Dynamic observations of vesiculation reveal the role of silicate crystals in bubble nucleation and growth in andesitic magmas. *Lithos* 296, 532–546. doi: 10.1016/j.lithos.2017.11.024

Pontesilli, A., Masotta, M., Nazzari, M., Mollo, S., Armienti, P., Scarlato, P., et al. (2019). Crystallization kinetics of clinopyroxene and titanomagnetite growing from a trachybasaltic melt: new insights from isothermal time-series experiments. *Chem. Geol.* 510, 113–129. doi: 10.1016/j.chemgeo.2019.02.015

Polacci, M., Arzilli, F., La Spina, G., Le Gall, N., Cai, B., Hartley, M. E., et al. (2018). Crystallisation in basaltic magmas revealed via in situ 4D synchrotron X-ray microtomography. *Sci. Rep.* 8:8377. doi: 10.1038/s41598-018-26644-6

Riker, J. M., Cashman, K. V., Rust, A. C., and Blundy, J. D. (2015). Experimental constraints on plagioclase crystallization during H2O- and H2O-CO2-saturated magma decompression. *J. Petrol.* 56, 1967–1998. doi: 10.1093/petrology/egv059

Rothery, D. A., Sumner, J. M., Spieler, O., and Dingwell, D. B. (2007). Impact vesiculation – A new trigger for volcanic bubble growth and degassing. *eEarth Discuss.* 2, 151–167. doi: 10.5194/eed-2-151-2007

Schiavi, F., Walte, N., and Keppler, H. (2009). First in situ observation of crystallization processes in a basaltic-andesitic melt with the moissanite cell. *Geology*, 37, 963–966. doi: 10.1130/g30087a.1

Shaw, H., Wright, T., Peck, D., and Okamura, R. (1968). The viscosity of basaltic magma; an analysis of field measurements in Makaopuhi lava lake, Hawaii. *Am. J. Sci.* 266, 225–264.

Shea, T., and Hammer, J. E. (2013). Kinetics of cooling-and decompression-induced crystallization in hydrous mafic-intermediate magmas. *J. Volcanol. Geothermal Res.* 260, 127–145. doi: 10.1016/j.jvolgeores.2013.04.018

Spera, F. J., Borgia, A., Strimple, J., and Feigenson, M. (1988). Rheology of melts and magmatic suspensions: 1. Design and calibration of concentric cylinder viscometer with application to rhyolitic magma. *J. Geophys. Res. Solid Earth* 93, 10273–10294. doi: 10.1029/jb093ib09p10273

Sun, T., Pereira, J., and Porter, R. S. (1984). Crystallization kinetics for poly (ethylene terephthalate) oriented by solid-state coextrusion. *J. Polym. Sci. Part B Polym. Phys.* 22, 1163–1171. doi: 10.1002/pol.1984.180220702

Swanson, S. (1977). Relation of nucleation and crystal-growth rate to the development of granitic textures. *Am. Mineral.* 62, 966–978.

Van Zeist, W.-J., and Bickelhaupt, F. M. (2010). The activation strain model of chemical reactivity. *Organ. Biomol. Chem.* 8, 3118–3127.

Vetere, F., Iezzi, G., Behrens, H., Cavallo, A., Misiti, V., Dietrich, M., et al. (2013). Intrinsic solidification behaviour of basaltic to rhyolitic melts: a cooling rate experimental study. *Chem. Geol.* 354, 233–242. doi: 10.1016/j.chemgeo.2013.06.007

Vetere, F., Iezzi, G., Behrens, H., Holtz, F., Ventura, G., Misiti, V., et al. (2015). Glass forming ability and crystallisation behaviour of sub-alkaline silicate melts. *Earth Sci. Rev.* 150, 25–44. doi: 10.1016/j.earscirev.2015.07.001

Vetere, F., Murri, M., Alvaro, M., Domeneghetti, M. C., Rossi, S., Pisello, A., et al. (2019). Viscosity of pyroxenite melt and its evolution during cooling. *J. Geophys. Res. Planets* 124, 1451–1469.

Vona, A., and Romano, C. (2013). The effects of undercooling and deformation rates on the crystallization kinetics of Stromboli and Etna basalts. *Contrib. Mineral. Petrol.* 166, 491–509. doi: 10.1007/s00410-013-0887-0

Wang, Y., Yu, M., Qiao, Q., You, F., Li, C., Xu, Z., et al. (2015). Effect of plastic deformation on the crystal structure and crystallization activation energy of Ni-WP alloy coating. *J. Mater. Eng. Perform.* 24, 2653–2657. doi: 10.1007/s11665-015-1551-9

Wheeler, J. (2017). The effects of stress on reactions in the Earth: sometimes rather mean, usually normal, always important. *J. Metamorphic Petrol.* 36, 439–461. doi: 10.1111/jmg.12299

Woodward, R., and Baer, H. (1944). Studies on Diene-addition reactions. II. 1 The reaction of 6, 6-pentamethylenefulvene with maleic anhydride. *J. Am. Chem. Soc.* 66, 645–649. doi: 10.1021/ja01232a042

Xu, J.-Z., Chen, C., Wang, Y., Tang, H., Li, Z.-M., and Hsiao, B. S. (2011). Graphene nanosheets and shear flow induced crystallization in isotactic polypropylene nanocomposites. *Macromolecules* 44, 2808–2818. doi: 10.1021/ma1028104

Yang, D., Hrymak, A. N., and Kamal, M. R. (2011). Crystal morphology of hydrogenated castor oil in the crystallization of oil-in-water emulsions: part II. Effect of shear. *Ind. Eng. Chem. Res.* 50, 11594–11600. doi: 10.1021/ie1025997

Zhang, Y. (2010). Diffusion in minerals and melts: theoretical background. *Rev. Mineral. Geochem.* 72, 5–59. doi: 10.2138/rmg.2010.72.2

Zhou, W., Van der Voo, R., Peacor, D. R., and Zhang, Y. (2000). Variable Ti-content and grain size of titanomagnetite as a function of cooling rate in very young MORB. *Earth Planet. Sci. Lett.* 179, 9–20. doi: 10.1016/s0012-821x(00)00100-x

Conflict of Interest: The authors declare that the research was conducted in the absence of any commercial or financial relationships that could be construed as a potential conflict of interest.

frontiers in Earth Science

ORIGINAL RESEARCH
published: 01 November 2019
doi: 10.3389/feart.2019.00288

4D Imaging of Mineral Dissolution in Porous Carbonado Diamond: Implications for Acid Digestion and XCT Measurement of Porosity and Material Properties

Scott A. Eckley and Richard A. Ketcham*

Jackson School of Geosciences, The University of Texas at Austin, Austin, TX, United States

OPEN ACCESS

Edited by:
Lucia Mancini,
Elettra Sincrotrone Trieste, Italy

Reviewed by:
Katherine Dobson,
Durham University, United Kingdom
Benoit Cordonnier,
Nationaal Archief of the Netherlands, Netherlands

****Correspondence:***
Scott A. Eckley
seckley@utexas.edu

Specialty section:
This article was submitted to Earth and Planetary Materials, a section of the journal Frontiers in Earth Science

Received: *21 June 2019*
Accepted: *21 October 2019*
Published: *01 November 2019*

Citation:
Eckley SA and Ketcham RA (2019) 4D Imaging of Mineral Dissolution in Porous Carbonado Diamond: Implications for Acid Digestion and XCT Measurement of Porosity and Material Properties. Front. Earth Sci. 7:288. doi: 10.3389/feart.2019.00288

In this study, we utilize high-resolution X-ray computed tomography (XCT) to track the progress of a leaching process within a pore network. Dissolution and leaching are difficult processes to observe with combined temporal and spatial context, particularly when dissolving material within a non-reactive pore network, and XCT is a uniquely suited technique for observing dissolution *in situ*, and extracting quantitative data on pore networks and the material in them in 3D. We XCT image two samples of porous diamond (carbonado) during a sequential acid leaching procedure designed to remove a diverse assemblage of pore-filling minerals. This experiment provides a unique perspective for observing mineral dissolution in 4D, allowing us to identify differences in mineral inclusions and pore network topology between carbonado samples based on dissimilar dissolution styles and rates. We are also able to observe the formation of fluorides during acid digestion, which can persist throughout acid leaching procedures and drastically affect yields for geochemical measurements of certain elements, most importantly REEs, U, Th, and Pb. We test various approaches to measuring porosity, finding that methods based on quantitative interpretation of CT numbers as partial porosity give more accurate results than purely binary segmentation, and that attempts to segment the pore network using visual criteria are scattered and unreliable. We document how image quality can be locally affected by material properties, with filled pores measurably blurrier than empty ones. Such local variation in point-spread function is important when segmenting XCT data for the purposes of quantification. Finally, we demonstrate that by comparing mass and X-ray attenuation loss it is possible to estimate the relative heavy-metal content of the leached material.

Keywords: X-ray CT, 4D imaging, pore networks, carbonado diamond, acid digestion, porosity segmentation

INTRODUCTION

Rock preparation methods for determining bulk elemental abundances and isotopic compositions involve either fusion or digestion and result in the complete destruction of the sample. Several acid digestion procedures exist (Potts and Cresser, 1987) and are optimized for dissolving a specific mineralogy (Pinto et al., 2012). Most involve sequential dissolution steps in various acids at high temperatures and usually use a hydrofluoric (HF) acid step to break down more refractory mineral phases (e.g., garnet, spinel, zircon, rutile, etc.). However, it has long been recognized that insoluble Ca, Mg, and Al fluoride complexes precipitate during this step and can incorporate significant amounts of rare earth elements (REEs), Rb, Sr, Y, Cs, Ba, Pb, Th, and U (Yokoyama et al., 1999; Krachler et al., 2002; Makishima and Nakamura, 2006). Precipitation of these insoluble fluorides can result in reduced yields of these elements, which can affect interpretation of rock petrogenesis and/or age (Boer et al., 1993). Several studies have quantified the composition of these precipitates using X-ray diffraction (XRD) and have developed digestion methods to avoid their formation or at least effectively dissolve them in a subsequent leaching step (Yokoyama et al., 1999; Krachler et al., 2002).

Because of the destructive nature of acid digestion, it is difficult to observe the dissolution process directly. Although most procedures are conducted on powders and complete dissolution is desired, intermediate phases like the aforementioned fluorides can precipitate during digestion, or some phases can persist through the entire process. In cases where the target for dissolution is mixed or embedded within a non-reactive matrix, spatial context can be important, as it provides the ability to study internal variation in acid digestion due to mineralogy or pore network topology. For instance, it is possible for refractory minerals to withstand a complete acid digestion procedure and result in incomplete yields of high field-strength elements (HFSEs) and REEs (Pinto et al., 2012). Similarly, the connectivity and permeability of a pore network can vary locally, leading to variation in reaction front penetration. Currently, there is no method for *in situ* determination of the effectiveness of acid digestion methods.

In this study, we provide the first time-integrated 3D imaging (i.e., 4D) of acid digestion in a porous medium using high-resolution X-ray computed tomography (XCT). XCT is a uniquely effective tool for imaging acid digestion, as other imaging techniques are destructive and/or simply not feasible given the nature of the material and process being imaged.

The medium we are studying is carbonado, a porous, polycrystalline diamond with an exceptionally diverse mineral assemblage filling and lining its pores. Using XCT, we are able to image the effects of reactive transport of various acids through a porous medium without altering the matrix, as diamond is inert to the acids used.

This experiment also presents a unique opportunity to examine how to best quantify the pore network and the materials within it using XCT data. We evaluate various strategies for measuring the filled and unfilled pores, and the effect of pore fillings on image sharpness. We also evaluate the ability of CT to discern information about the composition of leached material based on internal changes in X-ray attenuation. The results from this study not only contribute to a better understanding of acid digestion methods, but also shed light on properties of XCT data that affect quantitative interpretations.

MATERIALS AND CT DATA

Samples

Carbonado is an enigmatic variety of polycrystalline diamond found only in placer deposits and Mesoproterozoic metaconglomerates in Bahia, Brazil and the Central African Republic, with unknown primary origin (Trueb and Butterman, 1969; Trueb and De Wys, 1969, 1971). These highly porous dark nodules possess a narrow range of isotopically light carbon ($\delta^{13}C$ −31 to −24 ‰), an inclusion suite reflecting crustal pressure-temperature conditions (e.g., kaolinite and florencite – a REE-rich aluminophosphate commonly formed from the hydrothermal breakdown of monazite) and unusually enriched in REEs and actinides filling the pore spaces, a loosely constrained crystallization age between 2.6 and 3.8 Ga (Ozima and Tatsumoto, 1997; Sano et al., 2002), and other atypical features. This unusual assortment of properties has led to a variety of formation theories, from extra-solar to deep mantle (Haggerty, 2014). The pore network in some carbonado specimens has been shown to be interconnected based on the successful removal of all inclusion-hosted magnetism after intense acid leaching (Dismukes et al., 1988). However, the origin of the inclusion material, whether as a product of the *in situ* breakdown of primary phases or as precipitates from infiltrating crustal fluids, remains unknown.

We have collected new 3D textural, geochemical, and isotopic data to investigate the age and origin of several carbonado specimens (Eckley, 2018). To acquire bulk geochemical and isotopic data on the pore-filling material, we subjected one African (C-16-C; 0.715 g) and one Brazilian sample (1–3; 1.001 g), both shown in **Figure 1**, to a multi-stage acid digestion procedure. We will refer to sample C-16-C and 1–3 as "sample A" and "sample B", respectively, for the remainder of this paper. The samples were XCT imaged prior to leaching and after each acid leaching step to document the effects of the various acids on the mineral inclusion suite hosted within the pore network, and trace the progress of the reaction.

XCT Scanning

All scans were acquired at the University of Texas High-Resolution X-ray CT Facility using a Zeiss Xradia microXCT 400. X-rays were set at 80 kV and 10 W with 4 s (sample A; C-16-C in Eckley, 2018) and 2.5 s (sample B; 1–3 in Eckley, 2018) acquisition times per view (1261 views) using the LFOV objective; scan times were 1.8 and 1.1 h, respectively. X-rays were pre-filtered with a 0.35 mm SiO_2 filter for sample A and unfiltered for sample B. The reconstructed data have a voxel size of 14.36 and 14.35 μm, respectively. Software corrections were applied to compensate for ring and beam hardening artifacts. The same reconstruction parameters were used for each scan.

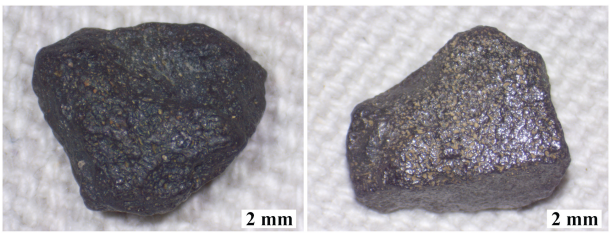

FIGURE 1 | Stereomicroscope images of carbonado nodules used in this study (sample A, **left**; and sample B, **right**).

X-ray computed tomography produces a continuous sequence of two-dimensional (2D) 16-bit images (slices), which when stacked together create a three-dimensional (3D) volume reflecting X-ray attenuation within the sample. X-ray attenuation is a function of a material's atomic number and density, as well as the X-ray energy; denser, more attenuating material is assigned a higher CT number, which is usually visualized with brighter grayscales (Ketcham and Carlson, 2001). Ideally, each data voxel (pixel with volume) has a value proportional to the average X-ray linear attenuation coefficient of the material comprising that voxel. In reality, because of the finite resolution of XCT, the attenuation signal is blurred somewhat, and thus the signal within a voxel is also influenced by material in surrounding voxels (i.e., its neighborhood). The size of the neighborhood can be described by a point-spread function (PSF), the extent of which is affected by several inherent properties of XCT imaging (ASTM, 2011). This phenomenon is most important when features of interest are small with respect to the PSF, as the blurring will affect their detectability and appearance, and the appropriate strategy for measuring them (Ketcham and Mote, 2019).

Acid Digestion Procedures

After initial XCT imaging, samples were subjected to the following acid digestion procedure:

(Step 1) Cleaning: (6 N HCl for 2 h, 4:1 HF:HNO_3 for 72 h; and aqua regia for 72 h at 110°C)
(Step 2) 7 days of 6 N HCl at 110°C
(Step 3) 7 days of 4:1 HF:HNO_3 at 110°C
(Step 4) 7 days of aqua regia at 110°C

All steps were performed in sealed 15 mL Savillex^{TM} beakers with screw tops in a ventilated oven using optima-grade 12 M HCl, optima-grade concentrated HF, and doubly-distilled 15.6 M HNO_3. Before each step, sample masses were measured using a microbalance with 1 μg precision. Leachates were saved and the samples were ultrasonically rinsed in ultrapure water for 30 min. The water was combined with the leachate and saved for analysis. All leachates were evaporated to dryness on a hot plate at 110°C, re-dissolved in 1 mL of 1 N HNO_3, and transferred in acid-cleaned 1.5 mL microcentrifuge tubes for subsequent dilution and geochemical analysis. All sample preparation was performed in the Radiogenic Isotope Clean Lab at the University of Texas at Austin. After each step, the samples were dried for at least 72 h on a hot plate at 140°C and reweighed. Next, to observe the effectiveness of each leaching step, both samples were rescanned using the same XCT parameters.

XCT Data Processing

The samples were scanned at random orientations at each stage, which required the TIFF slices for each scan to be reoriented, registered, and resampled to align with the initial XCT data sets. This task was performed in Avizo^{TM} using the *Register Images* and *Resample Transformed Image* modules. The former is an automated registration function that computes an affine transformation to match a transformed image to a reference image using an iterative optimization algorithm that employs a hierarchical approach proceeding from coarse to fine quality. For computational efficiency, the two 3D volumes were manually pre-aligned as closely as possible using isosurfaces prior to using the alignment function. The newly registered dataset was then resampled to the original one so that they share the same coordinate system.

To exclude air-filled voxels exterior to the sample from the analysis, a mask encompassing the exterior was created in Avizo^{TM} and expanded into the sample by two voxels. This was performed on the initial scans of both samples, and the respective masks were applied to all data volumes collected after the acid leaching steps. The results of image registration and masking are illustrated in **Figure 2**. Next, image subtraction calculations were performed in ImageJ to examine what material was removed during each acid leaching step.

RESULTS

Dissolution

Progressive XCT imaging the effects of acid digestion provides a 4D perspective of reactant infiltration and diffusion and dissolution styles. **Figure 2** illustrates the effects of each step. The cleaning procedure (Step 1) removed pore-filling material from a relatively uniform ∼1 mm annulus in sample A; in sample B the annulus is somewhat more uneven, with shallower penetration in some regions such as the top, while on the left several bright inclusions remain after removal of the surrounding material. Nevertheless, in both scans there is a distinct boundary delineating the dissolution front and most affected pores are completely empty. For sample A, the extended HCl step (Step 2) penetrated deeper, but was not as effective as the cleaning step in completely removing all pore-filling material from the affected volume. There is a broad, 6-mm-diameter central region where inclusions remain but show much lower X-ray attenuation than evident in the same region in step 1. A smaller ∼2-mm-diameter core appears unaffected. In the intermediate region, the smaller pores appeared less distinct and the walls of the larger pores are lined with material. For sample B, the HCl step penetrated relatively uniformly by an additional ∼0.5 mm, and even removed some of the previously stranded inclusions. The dissolution front is well defined and, in contrast to sample A, there is no obvious region of partially demineralized pores. The HF:HNO_3 step (Step 3) penetrated only slightly more deeply

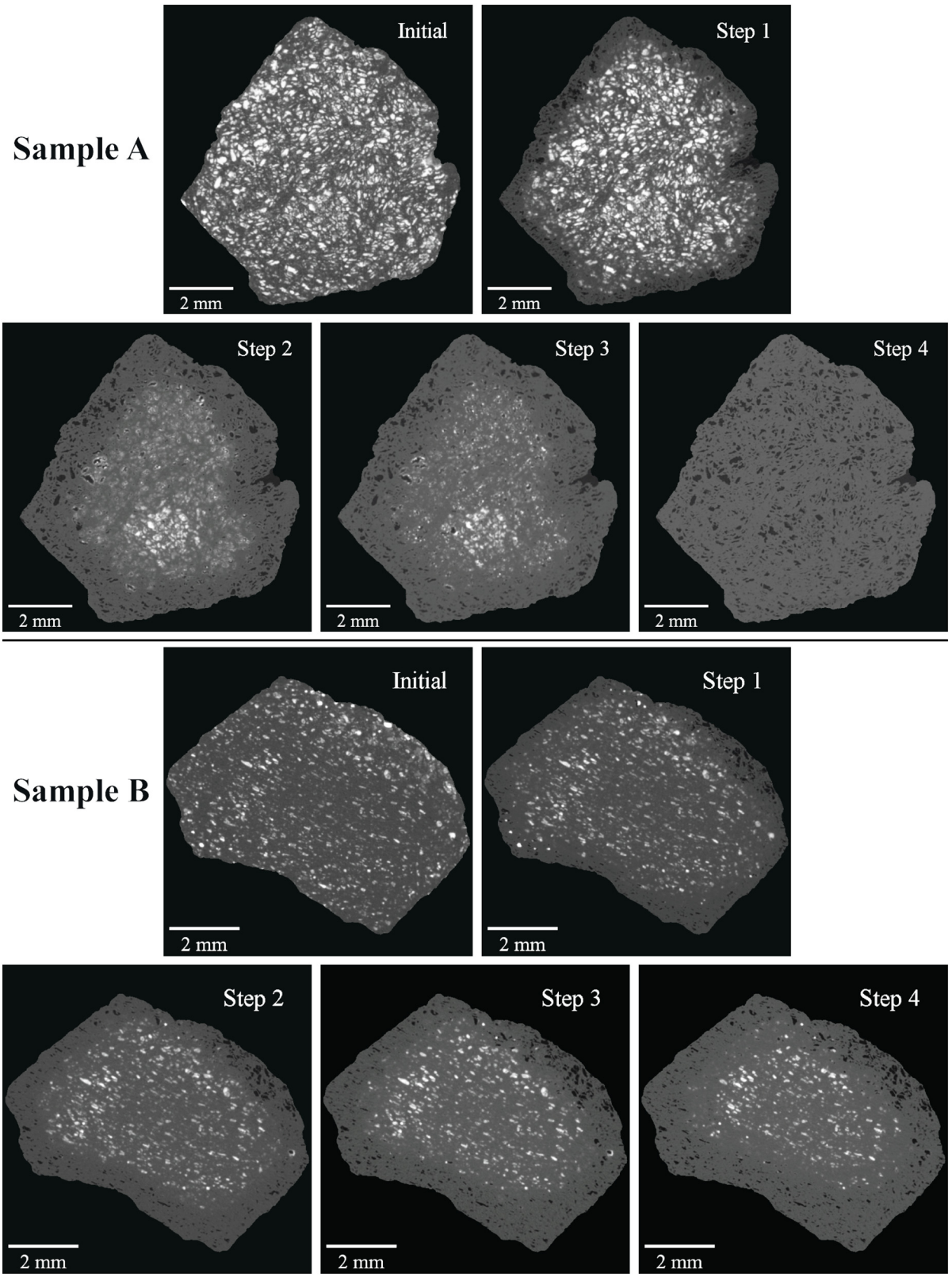

FIGURE 2 | Example XCT slices from sequential acid leaching steps of samples A **(top)** and B **(bottom)** after volume registration, resampling, and masking.

in sample A, and left most of the ∼2 mm core unaffected. Similar to Step 2, smaller pores are cloudy and some of the pore-lining material in larger pores was removed. Interestingly, randomly distributed, highly attenuating phases formed during this step, indicating dissolution, transfer, and re-precipitation of some high-Z material. **Figure 3** highlights some of the largest instances of these new phases, as well as smaller ones that are more representative of the others in the remainder of the volume. For sample B, the HF:HNO_3 step was similarly ineffective in removing material. Finally, the aqua regia step (Step 4) fully penetrated sample A and removed all remaining pore-filling material. For sample B, the aqua regia step penetrated slightly deeper and left an ∼0.5 mm annulus with cloudy smaller pores. The combined acid digestion procedure penetrated relatively uniformly, but left a large volume unaffected. Furthermore, in the affected rind, small, isolated, highly attenuating material remains in areas otherwise cleared in steps 2–4, similar to the remnants observed after the cleaning step (Step 1).

Figure 4 shows a close-up of the same region in sample A before and after leaching. The variation of CT numbers in the pores of the unleached sample reflect mixtures of various minerals of various compositions. Some pore fillings (for example, just above and to the left of the scale bar) have central regions with CT numbers close to the value for diamond; these are likely to be kaolinite (Ketcham and Koeberl, 2013). In the leached image the pores are fully empty; small pores appear less distinct from the diamond matrix than larger ones, but this is almost certainly due to blurring, not residual material. Interestingly, the pore-matrix boundaries for the empty pores in the leached sample appear sharper and more distinct than in the unleached specimen, even for those filled pores that have no obvious evidence of being multi-mineralic. The cause of this apparent increased blurring in the unleached sample may be due to local variation in the PSF (discussed later) and/or a heterogeneous distribution of mineral inclusions in the micro-porosity of the diamond matrix.

Figure 5 shows the histograms for each data set at each stage of the experiment, calculated using a 3D mask that captured only the diamond and omitted the outside air and container. The diamond peak is evident as the mode on the left side of each histogram, and the values to the right reflect the pore-filling material. The different shapes of these regions between sample B and A reflect the different amounts of low-Z and high-Z elements and minerals, and the extent to which they are intermixed in the pores. As the reaction progresses, the brighter values are progressively lost, with larger pores moving to the left side of the diamond mode. The precipitation of high-Z-concentrating fluorides resulted in rearranging the histogram values somewhat between sample A steps 2 and 3.

QUANTITATIVE ANALYSIS

Quantifying Blurring in CT Data

Background

Blurring in XCT data is caused by the finite resolution of the technique stemming from various factors, including X-ray focal spot size, shape, and stability; detector size, crosstalk, and latency; gantry alignment and precision; image noise; and reconstruction algorithm and filter (Ketcham et al., 2010, ASTM, 2011; Ketcham and Mote, 2019). It can be usefully quantified as a blurring kernel. Various parameterizations are possible, but we keep to the convention introduced by Ketcham et al. (2010) of defining the PSF radius (r_{PSF}) as 4σ for a standard Gaussian kernel, which corresponds visually to the approximate number of voxels required to pass fully from one material to another, or the number of voxels across which a flat interface will be blurred. Ketcham and Hildebrandt (2014) present a method for measuring r_{PSF} using flat interfaces within a CT data set, and document minor but systematic variation within scans based on position, with areas closer to the center of rotation being slightly less blurry than edge regions due to greater data density. However, although the cited factors underlying r_{PSF} are geometric in nature with no obvious relation to sample material, whether there is a link between r_{PSF} and material properties has not been tested.

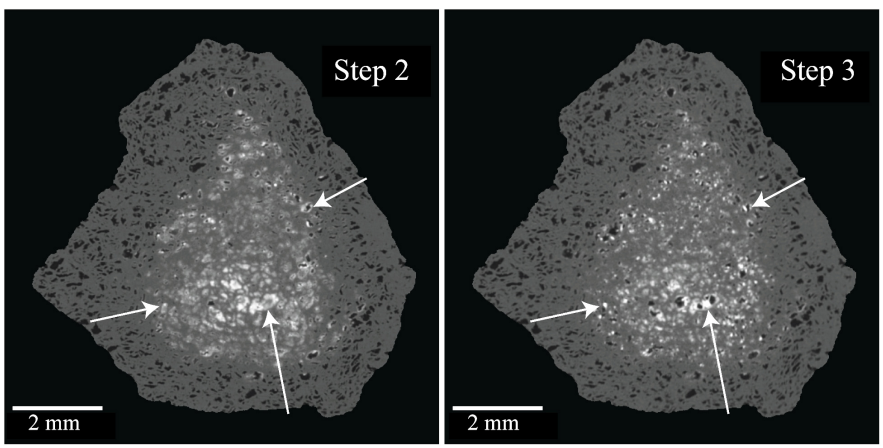

FIGURE 3 | XCT slices through same location in samples A before **(left)** and B after **(right)** HF digestion step highlighting the formation of highly attenuating phases.

Knowledge of r_{PSF} is not directly required for other calculations described below, but it does inform choices in data segmentation and interpretation. First, and most simply, it provides a simple and quantitative means of evaluating and comparing data quality and resolution. Second, it describes the extent of the region over which the signal from a given object is distributed, aiding the segmentation method described in the next section. Third, it helps determine when shape metrics may be impacted by blurring (Ketcham and Mote, 2019).

Measuring the Point-Spread Function

We measured the pore-diamond r_{PSF} of mineral-filled and empty pores within a single XCT scan. After XCT imaging the cleaning step (Step 1), there was a ∼1 mm rind of completely empty pores in each sample, while interior pores seemed visually unaffected. We used the *Line Traverse* tool in Blob3D (Ketcham, 2005; Ketcham and Hildebrandt, 2014), which measures the PSF from the edge response function across a flat interface separating two materials, to measure the r_{PSF} of empty and filled pores within these scans. We only measured the most visually homogeneous mineral-filled pores, as material heterogeneity can lead to excess apparent blurring. At least 10 traverses for both filled and empty pores were accumulated and only measurements with uncertainties around 1.0 voxel and angle between the traverse and interface normal less than 36° were accepted.

Point-Spread Function Results

The appearance of greater sharpness in the images of leached regions (**Figure 4**) is borne out in our PSF analysis (**Figure 6**). The r_{PSF} values measured in the Step 1 scans for both samples were smaller for empty pores than for filled pores. The average r_{PSF} for the empty pores is 2.61 and 2.11 voxels for samples A and B, respectively, whereas averages for the filled pores are almost double at 4.80 and 4.03 voxels, respectively. **Figure 6** shows r_{PSF} plotted against the absolute value of the percent difference between the normalized CT numbers ($|\Delta CT_{norm}|$%) for adjacent phases in each traverse. While the data for sample A suggest a continuously rising r_{PSF} with respect to $|\Delta CT_{norm}|$, the sample B analyses, which extend to much higher $|\Delta CT_{norm}|$ values reflecting more attenuating inclusions, suggest a plateau.

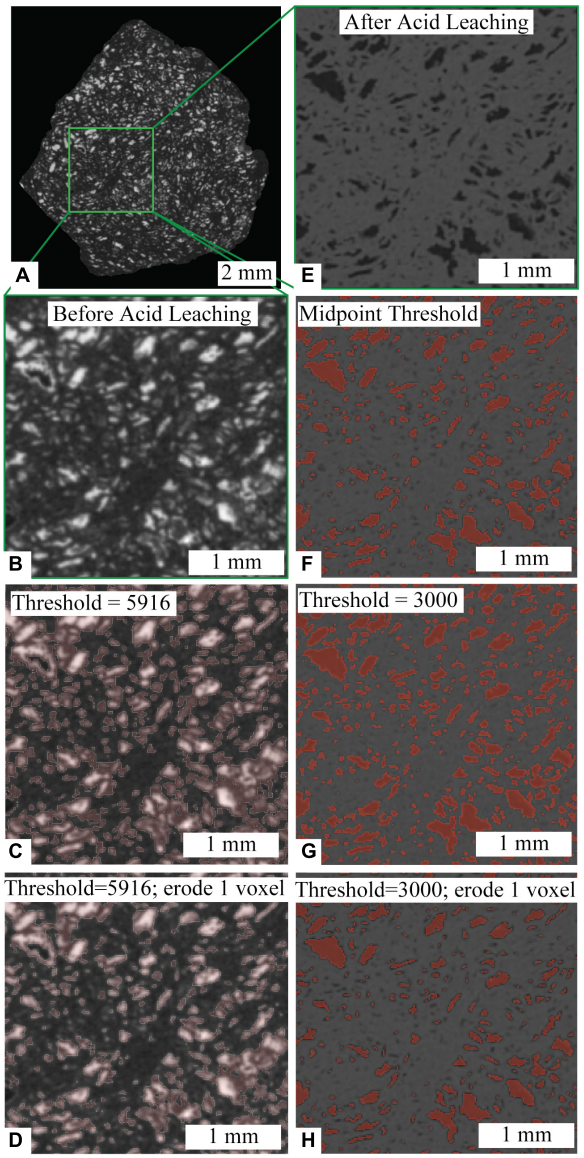

FIGURE 4 | (A) XCT slice of sample A before acid leaching with **(B)** zoomed in area and **(C,D)** segmentation attempts (outlined in semi-transparent pink). **(E)** Same zoomed in area after acid leaching procedure with **(F–H)** segmentation attempts (filled in semi-transparent red).

Measuring Porosity

Background

Porosity is not a straightforward quantity to measure in XCT data. In porous media, pore and throat sizes can vary over orders of magnitude, and almost always range down to near and below the XCT resolution limit. Several reviews discuss the challenges of quantifying XCT-imaged porosity, and illustrate the importance of careful analysis (Ashbridge et al., 2003; Taud et al., 2005; Iassonov et al., 2009; Brun et al., 2010; Wildenschild and Sheppard, 2013). Despite these limitations, multiple studies document the unique capabilities of XCT for visualizing and quantifying porosity in 3D (Wellington and Vinegar, 1987; Mooney, 2002; Taud et al., 2005; Wildenschild and Sheppard, 2013).

There are two general approaches to quantifying porosity using XCT: direct or binary segmentation, which delineates which voxels are porosity and which are not (Iassonov et al., 2009); and utilization of CT number information to discern partial porosity below the resolution limit (Wellington and Vinegar, 1987; Withjack, 1988). Binary segmentation is more conducive to pore network visualization and modeling, and when individual pores are visually evident in the data, it is usually the approach chosen, implicitly assuming that the below-resolution component of porosity can be neglected. Typically in such cases the segmentation is done using a global threshold CT number, with voxels below the threshold classified as porosity; ideally this threshold should be at the midpoint between the end-member CT numbers for pores and the solid matrix (ASTM, 2011), under

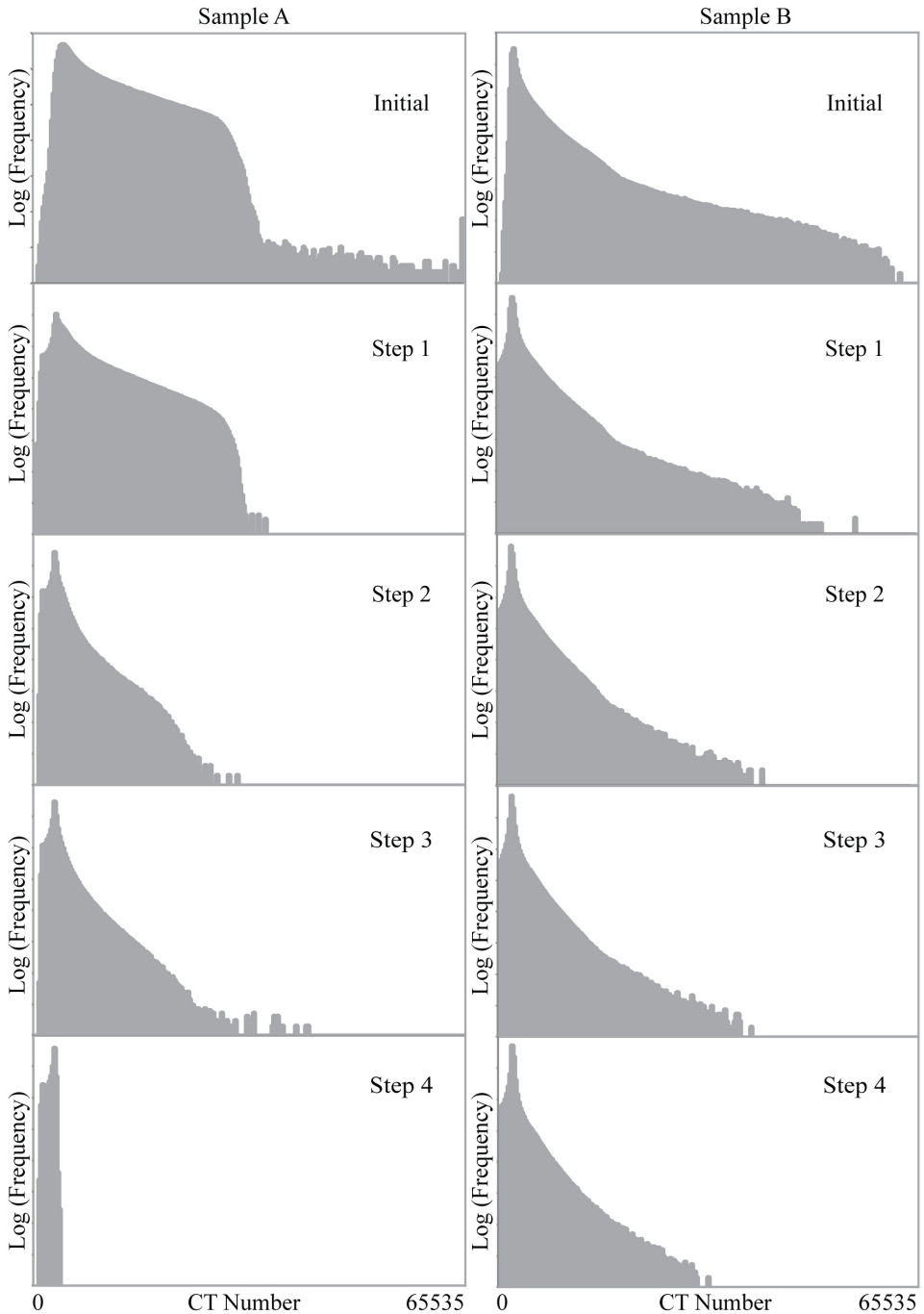

FIGURE 5 | Histograms of voxel CT number values for both samples after each acid leaching step.

the assumption that net attenuation is conserved. However, a strict midpoint will usually underestimate porosity, due to resolution effects. As pores approach the resolution limit, they begin to blur, appearing to grow fainter in the XCT data; this effect can be characterized as a convolution of the true specimen structure with the PSF (Ketcham and Mote, 2019). A segmentation that omits these small and dim but still visually evident pores is unsatisfying, and an analyst may be tempted to adjust the threshold to capture them. Some more sophisticated segmentation methods attempt to do a more careful job of distinguishing borderline voxels based on neighborhood criteria (Oh and Lindquist, 1999) or other local properties such as gradient, correlation, or entropy, but these are based on general statistical or mathematical models that do not necessarily reflect the actual physical situation. Iassonov et al. (2009) review and compare a range of these segmentation methods, and find that

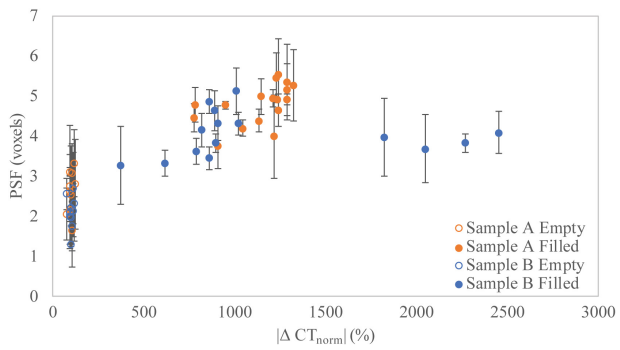

FIGURE 6 | Relationship between PSF size (r_{PSF}, voxels) versus attenuation difference ($|\Delta CT_{norm}|$%) for individual traverses of empty and filled pores in both samples.

significant supervision and adaptation by a skilled operator is necessary to achieve good results.

The alternative quantification approach typically consists of calculating partial porosity on a voxel-by-voxel basis by assuming CT numbers are a linear mixture between solid and void, or whatever the pore-filling phase is (e.g., Withjack, 1988; Ketcham and Iturrino, 2005). This linear average method captures sub-voxel porosity more completely, but is degraded by image noise or by having multiple solid phases. It also does not provide a straightforward starting point to determine a pore-size distribution or conduct pore-network modeling.

An intermediate possibility is to combine segmentation with utilization of local CT number information. In the PVB (Partial Volume and Blurring) method (Ketcham and Mote, 2019), a broad segmentation is used to capture the entire CT number anomaly associated with a feature, including any attenuation dispersed among adjacent voxels by partial volume and blurring effects. The volume and shape of the feature are then determined based on a linear interpretation of the CT numbers within each segmented region. This approach has been successfully used to measure fracture apertures at sub-voxel resolution (Johns et al., 1993), and has more recently been adapted to measuring discrete small features such as gold particles (Ketcham and Mote, 2019). As the porosity in carbonado consists of virtually isolated pores connected only by very narrow sinuous passages along grain boundaries in the polycrystalline diamond matrix, we attempted to apply the PVB method for the first time to quantify porosity.

Application to Carbonado

We demonstrate the above methods and their outcomes on the scans for sample A, with both filled and empty (leached) porosity. Generally, porosity is measured on air- or fluid-filled voids, but occasionally samples may have partially or completely filled or mineralized pore space. By imaging a porous diamond before and after removal of pore-filling material with no matrix deformation, we are able to quantify how estimates vary depending on the nature of the pore-filling material (i.e., mineral inclusions or air). While measuring a mineral-filled pore seems counterintuitive for estimating porosity, the situation is analogous to studies that infiltrate a sample with a highly attenuating fluid (e.g., KI, NaI, Wood's metal) to characterize porosity (Wellington and Vinegar, 1987; Withjack, 1988; Ramandi et al., 2016), or a case where an analyst needs to estimate pre-mineralization pore structure.

Carbonado porosity is highly variable as illustrated in **Figure 3**; pore sizes range from hundreds of μm to well below the XCT resolution limit, and the pore-filling material is a polymineralic assemblage that varies between and within individual pores (Ketcham and Koeberl, 2013). One of the dominant minerals, florencite, can contain several weight percent of rare earth and other elements with high atomic numbers (Z). Such high-Z phases are far more attenuating than other common pore-filling minerals such as kaolinite. Because of the diversity of pore-filling phases, no single CT number value can accurately represent the mineral-filled pore space for the initial scan. Nevertheless, we attempted to measure the effective porosity in the non-leached scan (**Figure 3B**) using a threshold (5916) that segmented the majority of XCT-resolvable filled pores. This threshold (**Figure 3C**) was arbitrarily determined using visual and geological criteria, recognizing that some pore-filling phases are only slightly more attenuating than diamond. This threshold omitted some locally bright regions representing diamond matrix with a relatively higher concentration of below-resolution filled pores, while also apparently over-segmenting larger pores filled with more attenuating material. In an attempt to compensate for the latter effect, we adjusted the initial segmentation by eroding it by one voxel in 3D (**Figure 3D**).

Segmenting pore space in the final scan was more straightforward, as there are only two phases, diamond and air (**Figure 3E**). Endmember CT number values for diamond (3479 ± 20) and air (1670 ± 35) were determined by measuring the average CT number value of several regions across multiple slices. For air, regions within larger, interior pores were used. For diamond, visually "flat" regions with no identifiable pores were used, although it is likely that even these regions had a small component of micro-porosity.

We experimented with segmenting the pore space in the final scan using various global thresholds determined both visually and mathematically. Our first attempt (**Figure 3F**) used the recommended midpoint CT number value (2575) between the two calculated end-member components. As expected, this value visually failed to include smaller pores, and so we simulated a typical user response by increasing threshold to 3000 (**Figure 3G**). This, however, led to over-segmented large pores, so a third attempt sought to compensate by eroding the selection by one voxel (**Figure 3H**). While the erosion step eliminated some very small pores, these were assumed to be volumetrically insignificant.

We also used the PVB method as implemented in Blob3D analysis software (Ketcham, 2005; Ketcham and Mote, 2019). In this workflow, pore space is slightly over-segmented (in this case, threshold at 3000 (**Figure 4G**), and expanding by one more voxel during the final data extraction step) to encompass the entire attenuation anomaly of every individual pore; i.e., out to an annular ring approximately r_{PSF} beyond the central, unblurred region of the pore. Rather than simply counting all voxels selected as pore space, a partial porosity is calculated for each selected

voxel using a linear interpolation between the endmember CT values for diamond and air. Volumes of individual pores are then determined as the sum of partial porosities within 3D-connected sets of voxels (blobs).

Finally, instead of directly segmenting XCT-resolvable pores, we used the linear average approach with endmember air and diamond values to calculate porosity globally. This calculation can be performed efficiently by simply using the sample-wide average CT number, excluding the exterior masked region. Intuitively, this method is most useful when quantifying the volume percentage of a phase of interest in a binary system (i.e., air and matrix).

We benchmarked these estimates using a simple bulk density method. As the fully leached diamond is a nearly pure mixture of diamond and air, we can determine porosity accurately based on its density deficit relative to solid diamond (3.51 g/cm^3). To calculate the density of sample A after the complete digestion procedure, we measured its volume using Avizo^{TM} and its mass using a microbalance with 10 μg precision. The diamond frame volume was segmented by using a midpoint CT number threshold between proximal exterior air and diamond near the sample boundary. To measure the entire sample's envelope volume (diamond frame + pore space), we used the "fill volume" function in Avizo^{TM}. Pores 3D-connected to the exterior had to be manually segmented and added to the sample volume; this increased the envelope volume by <0.1%.

Porosity Results

Estimates for porosity between and within the initial and final XCT scans for sample A varied greatly (**Table 1**). Based on mass and volume measurements, the density of the leached specimen was 2.98 g/cm^3; assuming a diamond density of 3.51 g/cm^3, this results in a porosity of 15.9%, which we take as the benchmark against which the other methods are evaluated (**Table 1**, bottom row).

Our "visually reasonable" threshold value for the initial scan with filled pores yielded a porosity of 45%; eroding that same threshold by one voxel reduced it to 29%. Because of the wide range of CT number values that comprise the pore-filling material, there is no appropriate global threshold for segmenting all of the XCT-resolvable pore space in the initial scan. Moreover, very small pores near r_{PSF} are more affected by blurring, and some diamond regions may be made slightly brighter due to dispersed filled microporosity. Thus, as illustrated in **Figure 3**, in the attempt to capture small pores and low-Z pore fillings, the larger pores were grossly over-segmented, and even the attempt to scale back the overselection by erosion did not prevent a substantial overestimate of porosity.

The final scan for sample A is essentially pure air and diamond, allowing for more accurate quantification. The standard thresholding using the midpoint CT number between the two endmembers yielded a porosity of 13.7%, a slight underestimate of the benchmark value reflecting missed small pores. Thresholding based on a visually "reasonable" adjustment to capture these yielded an over-estimate of 22.6%, and the subsequent 1-voxel erosion step overcompensated, reducing the value to 9.3%. Finally, the PVB method improved on the standard segmentation value somewhat, probably due to capturing some of the smaller pores in an appropriate way, yielding a value of 14.2%. The linear average method using only mean CT numbers yielded a value of 16.8%, slightly above the density-derived benchmark.

TABLE 1 | XCT-based and physical porosity measurements for sample C-16-C.

Method	Porosity (%)	Bulk volume (mm^3)	Pore volume (mm^3)
Initial Scan (filled pores)			
Visual threshold (CT Threshold [CT] = 5916)	45.0	201.2	90.5
Visual threshold (CT = 5916; erode 1 voxel)	28.9	201.2	58.2
Final Scan (empty pores)			
Midpoint threshold (CT = 2575)	13.7	201.2	27.6
Visual threshold (CT = 3000)	22.6	201.2	45.5
Visual threshold (CT = 3000; erode 1 voxel)	9.3	201.2	18.7
Partial-volume and blurring method (PVB)	14.2	201.2	28.5
Linear average	16.8	–	–
Density	15.9	–	–

Linking CT and Geochemical Data

Mass and Attenuation Loss

Mass loss was tracked by weighing the specimen after each leaching and drying step. We also performed geochemistry on the leaching acids (Eckley, 2018), to track the composition of lost material. Leachates were analyzed for a broad suite of elements, including all REE's, Rb, Sr, Y, Zr, Nb, Cs, Ba, Hf, Ta, Pb, Th, U. We refer this suite of elements as "high-Z", to distinguish them from other less dense, lower-attenuation elements extracted during leaching. During the cleaning step some insoluble residues formed in the dried HF acid, preventing a full accounting of the extracted high-Z elements in that step, but based on analysis of other another leached carbonado we estimate the missing material as roughly 23% of the amount measured in the other acids.

Attenuation loss was calculated by simply measuring the net drop in mean CT number in the masked regions of each scan. Because the two specimens were scanned with slightly different reconstruction parameters, we normalized the two measurement series by their respective differences between endmember diamond and air CT numbers.

Mass Versus Attenuation Loss Results

Figure 7 shows mean attenuation loss, normalized for the mean CT number difference between diamond and air for each sample, plotted versus total mass loss and lost mass of high-Z elements for each sample. As expected, higher amounts of removed mass are generally reflected in higher net loss of attenuation, demonstrating that CT can directly quantify material loss. However, the correlation is poorer with total loss than with the loss of high-Z elements. For sample A, the two lowest-attenuation-loss points (corresponding to leaching steps 4 and 3) are inverted with respect to total mass loss, but positively correlated as expected with respect to high-Z mass loss. The overall trends for both samples are also much more similar when only high-Z elements are considered. Note that the open

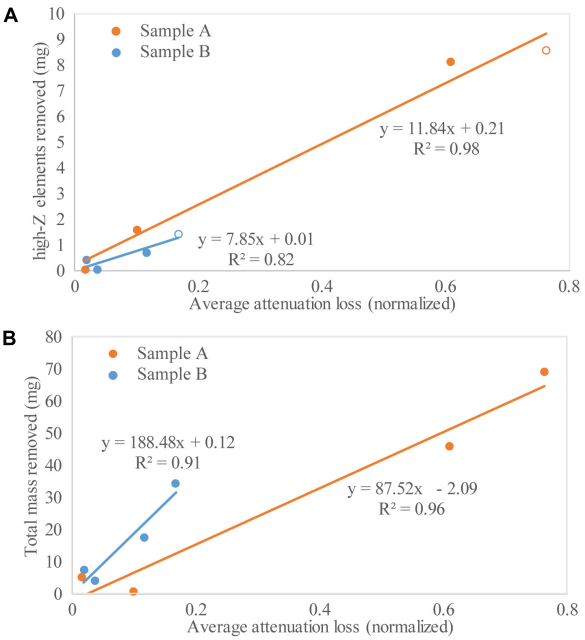

FIGURE 7 | High-Z elements removed **(A)** and total mass removed **(B)** during acid leaching steps vs. average normalized attenuation loss for both samples.

high-Z-loss points in **Figure 7A** reflect that fact that some leached material remains unanalyzed, and thus these points under-report the true mass removal; moving them both slightly upward to account for the missing material would increase consistency within sample A and between samples. In sum, these features indicate that the high-Z component dominates the attenuation removal signal.

DISCUSSION

Dissolution Styles

Time-resolved XCT imaging provides a unique perspective for imaging acid digestion in carbonado in 4D. In sample A, there are no preferential fluid pathways that facilitated enhanced mineral dissolution, and acid transport is dominated by bulk volume diffusion through the pore network and along grain boundaries. The extended HCl and HF:HNO_3 steps (Steps 2 and 3) resulted in a pair of reaction fronts, an outer one for total dissolution, and an inner one for partial removal of predominantly high-Z material. High-Z phases were preferentially leached and removed during Step 2 compared to Step 3, in which they were mostly just redistributed. This variation in behavior is likely due to a polymineralic assemblage dominated by disseminated silicate, phosphate, and oxide minerals (Ketcham and Koeberl, 2013). The partially cleared pores after Steps 2 and 3 were caused by different solubilities and reactivities of the diverse inclusion materials in the respective acids. Finally, the complete evacuation of the pores indicates that the entire sample A pore network is interconnected.

In sample B the dissolution front is less even, and some near-boundary inclusions were unaffected, likely reflecting a different pore structure, with tighter pathways to some portions of the sample and lower overall permeability, leading to locally and globally lower dissolution rates. Preferential dissolution of high-Z phases and partially cleared pores in Steps 2 and 3 as observed in sample A are not present, likely reflecting differences in both internal mineralogy and pore network topology. Although sample B did not fully leach, the steady progress of the reaction front indicates that the great majority of its pore network is probably also connected. Isolated inclusions bypassed by the reaction front across multiple leaches, however, may indicate one or more insoluble phases, or possibly small cavities not connected to the pore network and thus potentially containing primary material formed with the diamond.

Fluoride Precipitation

We observed the formation of highly attenuating phases after the HF:HNO_3 digestion in sample A (**Figure 3**). Our 4D technique allowed us to observe how acids migrate and interact with the pore-filling material differently. There are three main processes during acid digestion: (1) infiltration of acid throughout the sample, (2) dissolution of material, and (3) diffusion of dissolved material throughout the solvent. However, during digestion where excess HF is present, it is known that Ca, Mg, and Al fluoride complexes precipitate out of solution and can remain insoluble in the HF-bearing solution. These newly formed compounds can incorporate significant amounts of high-Z elements (REEs, U, Th, and Pb), which we know comprise several wt.% of the bulk inclusion material. Thus, it is likely that these newly formed highly attenuating phases are fluorides with significant concentrations of high-Z elements. We are aware of no prior study where the formation of these compounds has been imaged *in situ*. Fortunately for our subsequent geochemical analyses, we were also able to observe that following HF digestion with an aqua regia digestion was effective at removing these materials, as insoluble fluorides can often persist throughout an entire acid digestion procedure.

Variation of Porosity Calculations

The nature of pore-filling material has a strong control on the quality of segmentation for calculating porosity using XCT. Significantly different values (up to 36%) were calculated between the initial and final scans. The high values for the initial scan were a result of several issues: a heterogeneous pore-filling material, a large range of pore sizes, and greater blurring of pore boundaries. Notably, both of our arbitrary but "reasonable" porosity estimates for the filled scan were highly inaccurate by a factor of 2–3×.

The binary nature (diamond and air) of the final scan allowed for more accurate segmentation and estimates for porosity closer to the density-derived benchmark value. The standard technique to threshold at the midpoint value yielded results comparable to the benchmark, and the estimate was further improved by the PVB method, which enabled appropriate quantification of some of the smaller pores. On the other hand, the visually assessed threshold resulted in a value ∼40% too high, and trying to compensate by eroding the result by one voxel overcorrected to a value ∼40% too low. Again, the "visual assessment" approach resulted in largely arbitrary values poorly linked to

the actual porosity, demonstrating that porosity estimation is much sounder when based on physical principles than even informed guesswork.

Although demonstrated here on a simple two-phase system, the PVB method can be applied to more complex systems with little difficulty due to the simplicity of its underlying model. The input parameter it absolutely requires is an endmember CT number for the phase of interest, in this case air. It also requires the CT number of the surrounding material, which can also be entered by the user, or for complex materials it can be estimated adequately by averaging the CT numbers in the region immediately surrounding each segmented blob.

PSF Variation

Contrary to the assumption that the PSF can be considered generally uniform across a scan volume, we found it to be higher for filled versus unfilled pores (**Figures 4B** vs. **4E**, **6**). This is an interesting and unexpected observation and suggests that the PSF may be more complicated than previously thought, and affected by factors (discussed below) beyond scanning and reconstruction parameters.

Some component of excess blurring may be due to the pore fillings being inhomogeneous, but we were careful to only choose measurement locations where there was no obvious evidence of inhomogeneity, which would be apparent as an irregular transition. The most likely explanation lies in the unusually high amount of high-Z material in the pore fillings. One possibility is that the excess blurring is similar in origin to "metal artifacts" caused by photon starvation and edge gradient effects, although such artifacts usually appear directionally variable, which we do not observe here. Another, perhaps related, is that there may be additional blurring caused by coherent, or elastic scattering, in which the photon changes direction without losing energy. Coherent scattering is a second-order attenuation process compared to Compton scattering and the photoelectric effect, but it dominates over Compton scattering at low X-ray energies (∼30–100 keV) in high-Z materials, and can constitute several percent of total attenuation. Coherent scattering is more likely to occur at low angles, meaning that some photons with undiminished energy and only slight displacement are likely to reach the detector, the expected result of which would be blurring around high-scattering features.

Locally or contextually variable r_{PSF} within a single scan can affect segmentation and quantitative measurements derived from XCT, including volume, surface area, and axis lengths. This concern is not only applicable to porous media, but to any XCT-based measurement.

Tracking Attenuation Loss

Although it is generally not practical to extract detailed compositional information from polychromatic XCT data, our experiments demonstrate some interesting new possibilities. In particular, we can distinguish that the high-Z component constitutes a major proportion of our leached attenuation signal, and by comparing attenuation with mass loss we may be able to derive quantitative information. In **Figure 7**, the fitted lines for sample B have a ∼3.3× greater change in slope from the total mass loss to the high-Z loss case compared to the change for sample A, implying that sample B has a lower high-Z content (a zero high-Z content would show the maximum change). This relation is corroborated in our geochemical data, which shows sample A to have a ∼8× greater high-Z content than sample B. Of course, this relation is only approximate, and a more rigorous calculation would require accounting for the different attenuation coefficients of each species as they vary over the X-ray spectrum used for scanning. However, it is clear that the general approach of comparing mass change to attenuation change in this manner has excellent potential for quick and spatially sensitive evaluation of leached heavy-metal content.

CONCLUSION

We present the first 4D imaging of acid digestion of pore-filling minerals in an inert porous medium. This technique not only allows us to further understand the physical nature of acid digestion, but also sheds light on inherent properties of XCT scanning. We find that, at least in carbonado, reactant infiltration is dominated by bulk volume diffusion through the pore network and along grain boundaries and is not focused along preferential reaction pathways, though it can be impeded by locally low permeability. For the first time, we image fluoride formation and subsequent destruction *in situ*. We demonstrate an approach for using CT to infer when and where preferential heavy metal leaching occurs. Finally, while the observations on dissolution style and pore network topology relate to carbonado, our experiments also provide general insights into the basics of XCT and the processing and interpretation of XCT data. We show that estimating porosity with XCT using seemingly reasonable but arbitrary criteria can be problematic, and that more reliable results are obtained by adhering to a more structured approach accounting for material end-members and blurring. We also document that the local degree of blurring within a scan can vary as a function of the material properties. This is important to consider not only when measuring porosity, but in any study where 3D quantitative data are extracted from discrete phases that have been segmented using general thresholding techniques.

DATA AVAILABILITY STATEMENT

The datasets generated for this study can be found in the Digital Rocks Portal repository http://www.digitalrocksportal.org/projects/219, http://doi.org/10.17612/MPGF-FC78.

AUTHOR CONTRIBUTIONS

SE planned and conducted the dissolutions and chemical analyses, conducted the image processing and analysis, and participated in data interpretation and writing. RK conceived of the experiment, provided the samples and funding, advised on image processing and analysis, and participated in data interpretation and writing.

FUNDING

This research was supported by the Geology Foundation of the Jackson School of Geosciences and UTCT facility was provided by the National Science Foundation grant EAR-1762458 to RK.

ACKNOWLEDGMENTS

We thank J. Maisano for conducting the CT scans, and S. Loewy and N. Miller for overseeing the acid digestion and geochemical work.

REFERENCES

Ashbridge, D. A., Thorne, M. S., Rivers, M. L., Muccino, J. C., and O'day, P. A. (2003). Image optimization and analysis of synchrotron X-ray computed microtomography (CμT) data. *Comput. Geosci.* 29, 823–836. doi: 10.1016/s0098-3004(03)00081-5

ASTM, (2011). *Standard Gudie for Computed Tomography (CT) Imaging. ASTM Designation E* 1441–1411. West Conshohocken, PA.: ASTM International.

Boer, R., Beukes, G., Meyer, F., and Smith, C. (1993). Fluoride precipitates in silicate wet-chemistry: implications on REE fractionation. *Chem. Geol.* 104, 93–98. doi: 10.1016/0009-2541(93)90144-8

Brun, F., Mancini, L., Kasae, P., Favretto, S., Dreossi, D., and Tromba, G. (2010). Pore3D: a software library for quantitative analysis of porous media. *Nucl. Instrum. Methods Phys. Res. Sec. A* 615, 326–332. doi: 10.1016/j.nima.2010.02.063

Dismukes, J., Gaines, P., Witzk, H., Leta, D., Kear, B., Behal, S., et al. (1988). Demineralization and microstructure of carbonado. *Mater. Sci. Eng. A* 105, 555–563. doi: 10.1016/0025-5416(88)90743-4

Eckley, S. A. (2018). *3D Textural and Geochemical Analyses on Carbonado Diamond: Insights from Pores and the Minerals within Them*, Master's Thesis, The University of Texas, Austin.

Haggerty, S. E. (2014). Carbonado: physical and chemical properties, a critical evaluation of proposed origins, and a revised genetic model. *Earth Sci. Rev.* 130, 49–72. doi: 10.1016/j.earscirev.2013.12.008

Iassonov, P., Gebrenegus, T., and Tuller, M. (2009). Segmentation of X-ray computed tomography images of porous materials: a crucial step for characterization and quantitative analysis of pore structures. *Water Resour. Res.* 45:W09415.

Johns, R. A., Steude, J. S., Castanier, L. M., and Roberts, P. V. (1993). Nondestructive measurements of fracture aperture in crystalline rock cores using X ray computed tomography. *J. Geophys. Res.* 98, 1889–1900. doi: 10.1029/92jb02298

Ketcham, R., and Mote, A. (2019). Accurate measurement of small features in X-ray Ct data volumes, demonstrated using gold grains. *J. Geophys. Res.* 124, 3508–3529.

Ketcham, R. A. (2005). Computational methods for quantitative analysis of three-dimensional features in geological specimens. *Geosphere* 1, 32–41.

Ketcham, R. A., and Carlson, W. D. (2001). Acquisition, optimization and interpretation of X-ray computed tomographic imagery: applications to the geosciences. *Comput. Geosci.* 27, 381–400. doi: 10.1016/s0098-3004(00)00116-3

Ketcham, R. A., and Hildebrandt, J. (2014). Characterizing, measuring, and utilizing the resolution of CT imagery for improved quantification of fine-scale features. *Nucl. Instrum. Methods Phys. Res. Sec. B* 324, 80–87. doi: 10.1016/j.nimb.2013.08.064

Ketcham, R. A., and Iturrino, G. J. (2005). Nondestructive high-resolution visualization and measurement of anisotropic effective porosity in complex lithologies using high-resolution X-ray computed tomography. *J. Hydrol.* 302, 92–106. doi: 10.1016/j.jhydrol.2004.06.037

Ketcham, R. A., and Koeberl, C. (2013). New textural evidence on the origin of carbonado diamond: an example of 3-D petrography using X-ray computed tomography. *Geosphere* 9, 1336–1347. doi: 10.1130/ges00908.1

Ketcham, R. A., Slottke, D. T., and Sharp, J. M. Jr. (2010). Three-dimensional measurement of fractures in heterogeneous materials using high-resolution X-ray computed tomography. *Geosphere* 6, 499–514. doi: 10.1130/ges00552.1

Krachler, M., Mohl, C., Emons, H., and Shotyk, W. (2002). Influence of digestion procedures on the determination of rare earth elements in peat and plant samples by USN-ICP-MS. *J. Anal. At. Spectrom.* 17, 844–851. doi: 10.1039/b200780k

Makishima, A., and Nakamura, E. (2006). Determination of major/minor and trace elements in silicate samples by ICP-QMS and ICP-SFMS applying isotope dilution-internal standardisation (ID-IS) and multi-stage internal standardisation. *Geostand. Geoanal. Res.* 30, 245–271. doi: 10.1111/j.1751-908x.2006.tb01066.x

Mooney, S. J. (2002). Three-dimensional visualization and quantification of soil macroporosity and water flow patterns using computed tomography. *Soil Use Manag.* 18, 142–151. doi: 10.1111/j.1475-2743.2002.tb00232.x

Oh, W., and Lindquist, B. (1999). Image thresholding by indicator kriging. *IEEE Trans. Pattern Anal. Mach. Intell.* 21, 590–602. doi: 10.1109/34.777370

Ozima, M., and Tatsumoto, M. (1997). Radiation-induced diamond crystallization: origin of carbonados and its implications on meteorite nano-diamonds. *Geochim. Cosmochim. Acta* 61, 369–376. doi: 10.1016/s0016-7037(96)00346-8

Pinto, F. G., Junior, R. E., and Saintpierre, T. D. (2012). Sample preparation for determination of rare earth elements in geological samples by ICP-MS: a critical review. *Anal. Lett.* 45, 1537–1556. doi: 10.1080/00032719.2012.677778

Potts, P., and Cresser, M. (1987). A handbook of silicate rock analysis. *Anal. Chim. Acta* 201, 363–363.

Ramandi, H. L., Mostaghimi, P., Armstrong, R. T., Saadatfar, M., and Pinczewski, W. V. (2016). Porosity and permeability characterization of coal: a micro-computed tomography study. *Int. J. Coal Geol.* 154, 57–68. doi: 10.1016/j.coal.2015.10.001

Sano, Y., Yokochi, R., Terada, K., Chaves, M. L., and Ozima, M. (2002). Ion microprobe Pb–Pb dating of carbonado, polycrystalline diamond. *Precambrian Res.* 113, 155–168. doi: 10.1016/s0301-9268(01)00208-x

Taud, H., Martinez-Angeles, R., Parrot, J., and Hernandez-Escobedo, L. (2005). Porosity estimation method by X-ray computed tomography. *J. Petrol. Sci. Eng.* 47, 209–217. doi: 10.1016/j.petrol.2005.03.009

Trueb, L., and Butterman, W. (1969). Carbonado: a microstructural study. *Am. Mineral.* 54, 412–425.

Trueb, L., and De Wys, E. (1969). Carbonado: natural polycrystalline diamond. *Science* 165, 799–802. doi: 10.1126/science.165.3895.799

Trueb, L., and De Wys, E. (1971). Carbon from Ubangi-A microstructural study. *Am. Mineral.* 56, 1252–1256.

Wellington, S. L., and Vinegar, H. J. (1987). X-ray computerized tomography. *J. Pet. Technol.* 39, 885–898.

Wildenschild, D., and Sheppard, A. P. (2013). X-ray imaging and analysis techniques for quantifying pore-scale structure and processes in subsurface porous medium systems. *Adv. Water Resour.* 51, 217–246. doi: 10.1016/j.advwatres.2012.07.018

Withjack, E. (1988). Computed tomography for rock-property determination and fluid-flow visualization. *SPE Format. Eval.* 3, 696–704. doi: 10.2118/16951-pa

Yokoyama, T., Makishima, A., and Nakamura, E. (1999). Evaluation of the coprecipitation of incompatible trace elements with fluoride during silicate rock dissolution by acid digestion. *Chem. Geol.* 157, 175–187. doi: 10.1016/s0009-2541(98)00206-x

Conflict of Interest: The authors declare that the research was conducted in the absence of any commercial or financial relationships that could be construed as a potential conflict of interest.

frontiers in Earth Science

ORIGINAL RESEARCH
published: 26 November 2019
doi: 10.3389/feart.2019.00306

Neutron Imaging of Cadmium Sorption and Transport in Porous Rocks

Benoît Cordonnier[1], Anne Pluymakers[2], Alessandro Tengattini[3,4], Sina Marti[5], Anders Kaestner[6], Florian Fusseis[5] and François Renard[1,7]*

[1] Departments of Geosciences and Physics, The Njord Centre, Physics of Geological Processes, University of Oslo, Oslo, Norway, [2] Department of Geoscience and Engineering, Faculty of Civil Engineering and Geosciences, TU Delft, Delft, Netherlands, [3] Univ. Grenoble Alpes, CNRS, Grenoble INP, 3SR, Grenoble, France, [4] Institute Laue-Langevin, Grenoble, France, [5] University of Edinburgh, School of Geosciences, Edinburgh, United Kingdom, [6] Paul Scherrer Institute, ICON, Villigen, Switzerland, [7] University Grenoble Alpes, ISTER, University Savoie Mont Blanc, CNRS, IRD, IFFSTTAR, ISTerre, Grenoble, France

Understanding fluid flow in rocks is crucial to quantify many natural processes such as ground water flow and naturally triggered seismicity, as well as engineering questions such as displacement of contaminants, the eligibility of subsurface waste storage, geothermal energy usage, oil and gas recovery and artificially induced seismicity. Two key parameters that control the variability of fluid flow and the movement of dissolved chemical species are (i) the local hydraulic conductivity, and (ii) the local sorption properties of the dissolved chemical species by the solid matrix. These parameters can be constrained through tomography imaging of rock samples subjected to fluid injection under constrained flow rate and pressure. The neutron imaging technique is ideal to explore fluid localization in porous materials due to the high but variable sensitivity of neutrons to the different hydrogen isotopes. However, until recently, this technique was underused in geology because of its large acquisition time. With the improved acquisition times of newly set-up neutron beamlines, it has become easier to study fluid flow. In the current set of experiments, we demonstrate the feasibility of *in-situ* 2D and 3D time-lapse neutron imaging of fluid and pollutant percolation in rocks, in particular that of cadmium salt. Cadmium is a hazardous compound that is found in many electronic devices, including batteries and is a common contaminant in soil and groundwater. It also exhibits higher contrast in neutron attenuation with respect to heavy water, and is therefore an ideal tracer. Time-lapse 2D radiographies and 3D neutron tomographies of the samples were acquired on two neutron beamlines (ILL, France and SINQ, Switzerland). We performed two sets of experiments, imbibition and injection experiments, where we imaged *in-situ* flow properties, such as local permeability and interactions between cadmium and the solid rock matrix. Our results indicate that even within these cm-scale porous rocks, cadmium transport follows preferential pathways, and locally interacts within the limestone samples. Our results demonstrate that the use of neutron imaging provides additional insights on subsurface transport of pollutants.

Keywords: neutron imaging, cadmium, porous rocks, pollutant transport, sorption, advection

OPEN ACCESS

Edited by:
Lucia Mancini, Elettra Sincrotrone Trieste, Italy

Reviewed by:
Burkhard Schillinger, Technical University of Munich, Germany
Branko Bijeljic, Imperial College London, United Kingdom

****Correspondence:***
Benoît Cordonnier
cordonnier.benoit@gmail.com

Specialty section:
This article was submitted to Earth and Planetary Materials, a section of the journal Frontiers in Earth Science

Received: *21 June 2019*
Accepted: *04 November 2019*
Published: *26 November 2019*

Citation:
Cordonnier B, Pluymakers A, Tengattini A, Marti S, Kaestner A, Fusseis F and Renard F (2019) Neutron Imaging of Cadmium Sorption and Transport in Porous Rocks. Front. Earth Sci. 7:306. doi: 10.3389/feart.2019.00306

1. INTRODUCTION

Historically, laboratory measurements on fluid flow properties through rocks had to rely on data from sensors at the end surfaces of the rock specimen. Such data only yields bulk flow properties and information about spatial heterogeneity or non-linearity of flow within the sample is not accessible. Additionally uncertainties linked with these circuitous observations force researchers to recursively confirm the experiments before stating potential causality. These limitations of the classical approach have pushed experimental geologists toward new *in-situ* measurements techniques. Recent advances in tomographic measurements, specifically, X-rays, neutrons and magnetic resonance imaging techniques, allow a more detailed observation of the rock internal structure and its evolution through time (Carlson, 2006). Additionally, 3D image analysis, such as Digital Volume Correlation (DVC), provides local strain tensors showing localization and strain distribution within the specimens (Viggiani et al., 2007; Tudisco et al., 2015, 2019; Macente et al., 2018). Among the different approaches to obtain 3D tomograms, X-ray imaging is traditionally preferred over neutron as it allows higher spatial and temporal resolution (Pacureanu et al., 2012; Cnudde and Boone, 2013; Olbinado and Rack, 2019). Additionally, the recent increase in number of X-ray computed tomography desktop facilities in universities and research institutes has made X-ray imaging more accessible. As a consequence, this technique is becoming more and more widespread in the geoscience community (Desrues et al., 2006 and references therein). X-rays interact with the atom's electronic cloud while neutrons interact with the atom's nuclei, providing alternative attenuation and diffraction spectra. It results in that, compared to X-rays, neutrons allow imaging of alternative elements with high properties of absorption (e.g., metals) or scattering (e.g., hydrogen). Since hydrogen, present in most geological fluids, strongly attenuates neutrons, neutron imaging is ideal to study rocks with small fluid fractions (i.e., low porosity, Lanza et al., 1991). Neutron imaging in geomaterials historically started more than 20 years ago and from the very beginning focused on flow in porous media (Jasti et al., 1987; Lanza et al., 1991; Degueldre et al., 1996). One of the main interests has been put on imbibition tests, performed either with time-lapse 2D radiography or 3D tomography (Masschaele et al., 2004; Middleton et al., 2005; Carminati et al., 2007; Cnudde et al., 2008; Hall et al., 2010; Zhang et al., 2010; Trtik et al., 2011; Sedighi-Gilani et al., 2012; Derluyn et al., 2013; Kang et al., 2013; Cheng et al., 2015; DiStefano et al., 2017). Additional geologically relevant fields were investigated such as deformed and cracked samples (Hall, 2013; Tudisco et al., 2015, 2019), drying concrete (De Beer et al., 2004; Poulikakos et al., 2013; Toropovs et al., 2015; Dauti et al., 2018) or fossils (Dawson et al., 2014). However, to date, following dynamic processes in 3D time series has remained scarce due to long acquisition times of most neutron facilities. Moreover, experimental devices that allow studying rock samples under confining pressures, i.e., geologically relevant conditions, were rare (Yehya et al., 2018). Recent developments in neutron tomography techniques now allow for faster tomography and enable scientists to capture fluid and contaminant flow at high spatial and temporal resolution (Masschaele et al., 2004; Kaestner et al., 2007, 2016; Lehmann et al., 2007; Tötzke et al., 2011; Tremsin et al., 2011; Tudisco et al., 2019). In our study, we present an experimental set-up which can study fluid flow and cadmium contaminant flow through porous rocks under confining pressures (Pc) relevant to shallow subsurface aquifers (Pc=1 MPa).

Pollution of soil and ground-water is a serious health threat where heavy metals express one of the highest hazards. Cadmium (Cd) is a resilient heavy metal which is among the top six pollutants worldwide. It is used in many electronic devices, including batteries. Its unique toxicological profile makes it dangerous also at low concentrations (Satarug and Moore, 2004; Shen et al., 2019). It affects brain cells, lungs and is strongly carcinogenic (Waalkes, 2003; Bertin and Averbeck, 2006; Subramanian and Govindan, 2007). With high rates of transfer from soils to plants (Das et al., 1997; Benavides et al., 2005) compared to other "non-essential elements" (e.g., lead or mercury), cadmium easily accumulates in all biological forms as it is hardly affected by metabolic degradation (An et al., 2001; Satarug et al., 2003; Joseph, 2009; Jiang et al., 2010; Sari and Tuzen, 2014). It is thus a persistent and ubiquitous health risk. Sources of cadmium can be both geogenic or anthropic with hydrological or aeolian transport. Metal fractionation may lead to relatively natural high concentration of Cd in soils and rocks (i.e., limestones) while electronic waste, smelting, metal extraction and tanneries are the main anthropogenic sources (Fishbein, 1981).

Heavy metal transfer and transport occur in all rocks, and the specific properties depend on the rocks' physical and geochemical properties. Soils can be both an accumulating source and buffer for heavy metals or a simple inert porous media. Soils able to accumulate heavy metals may be used as a natural sorbent to treat and prevent pollution from industrial waste effluents (Ghazy et al., 2008; Sari and Tuzen, 2014). If bio-sorbents are also considered, natural rocks offer a strong potential in storing cadmium. Among them phyllosilicates like smectite (bentonite, montmorillonite) (Barbier et al., 2000; Papini et al., 2004; Sneddon et al., 2006; Bhattacharyya and Gupta, 2007; El Mouzdahir et al., 2007; Karapinar and Donat, 2009; Kuo and Lin, 2009; Vázquez et al., 2009) or sepiolite (Kocaoba, 2009) are used. Furthermore, limestones are also identified as common sorbent for heavy metals and particularly were used to mitigate cadmium pollution (Rangel-Porras et al., 2010). By comparing common sandstones (which likely will act as inert porous medium) with limestones (capable of sorbing cadmium), one may discriminate if the mechanisms of cadmium retention are to be linked to the differences in porous network characteristics or to chemical and mineralogical properties.

Therefore, understanding and quantifying the retention and sorption mechanisms of cadmium in rocks is of tremendous importance for both risk prediction and hazardous waste treatment. Common experimental strategies include tests with various environmental conditions strongly influencing the sorption mechanisms such as flow rate, pH, initial pollutant concentration, or rock composition (Joseph et al., 2019). Here we present results of *in-situ* neutron imaging of flow experiments (imbibition and injection) in limestone and sandstone samples.

We used Indiana limestone and Fontainebleau-, Eselfuhrter-, and Bentheim sandstones, which are all porous sedimentary rocks considered to be homogeneous on the centimeter-scale. We rather used heavy than common water for the lower neutron attenuation of deuterium compared to protium. Taking two of the most classic experimental approaches, namely imbibition tests as well as fluid injection, we determined the potential of neutron imaging to improve our understanding of cadmium interaction mechanisms in confined rocks. For the injection experiments we first saturated the samples with heavy water before introducing cadmium (dissolved in heavy water) within the system, and subsequently rewashed the samples with heavy water. We explored the potential and limits of *in-situ* neutron imaging in porous rocks in the presence of cadmium. Strongly interacting with neutrons, cadmium brings all the potential of neutron imaging. Our experimental set-up (**Figure 1**) confines the samples to a few MPa and thus reproduces the flow of pollutant in rocks at a few tens of meters depth.

2. METHODS

Experiments were performed on three different sandstones (Eselfuhrter, Bentheim, Fontainebleau) and one limestone (Indiana). The cylindrical samples were prepared by coring rock blocks perpendicularly to the sedimentary layering with water cooled diamond drill bits, and rectifying the upper and lower surface of the cylinders to ensure parallelism. The Eselfuhrter sandstone (ES), Bentheim sandstone (BS) and Fontainebleau Sandstone (FS) hold a porosity fraction of 0.21, 0.25, and 0.07 (±0.03), respectively (Peksa et al., 2015; Barnhoorn et al., 2018). The Indiana limestone (IL) has been measured with a He-pycnometer to a porosity fraction of 0.16 (Barnhoorn et al., 2018).

For all samples, pore fraction was in the range 0.15–0.25. Therefore, when the neutron beam traverses a sample with a diameter of 5 cm, 7.5–12.5 mm of the path will occur through the water phase in the center of the sample when full fluid saturation of the sample is attained. To optimize the signal to noise ratio we ensured that the fluid used would neither be too transparent, neither too opaque to neutrons but used a reasonable portion of the sensor dynamic range. A series of calibration have been performed to identify the most suitable fluids for the injection (**Figure 2**). We successively filled 8 mm inner diameter aluminum crucibles with H_2O, D_2O (deuterium heavy water) and solutions of either H_2O or D_2O with cadmium under concentrations of 0.05 and 0.5 mol/L. The cadmium solution was prepared by dissolving a $CdCl_2$ salt into D_2O. Taking into account the relatively high porosity of the rock samples, the sample size and relative neutron absorptions properties of all the components of the experimental set-up, the optimal dynamic range for the acquired image was obtained when using deuterium water (see **Figure 2** and caption for further details).

Series of flow-through experiments have been performed at two different neutron sources: the D50 beamline (Tengattini et al., 2017) of the Institut Laue-Langevin (Grenoble, France) and the ICON beamline of SINQ (Kaestner et al., 2011a) at the Paul Scherrer Institut (Villigen, Switzerland). The first one is a fission type source where neutron flux can be as high as 1.5 10^{15} n/cm^2/s, while the second one is a spallation type source with a flux as high as 10^{14} n/cm^2/s. During our experiment time, the ILL nuclear core was only at half of its optimal flux, thus bringing it closer to the flux values of SINQ. Imbibition tests were performed at ILL, the injection ones at PSI.

In order to complete the fluid injection experiments, three experimental core holders have been developed. Two were made of ALAA5083, an aluminum alloy known for its low neutron activation and high transparency with neutrons, and Teflon pistons. The third core holder was built with grade 2 titanium, also transparent to neutrons. Having three separate core holders allowed an efficient management of the experimental time as

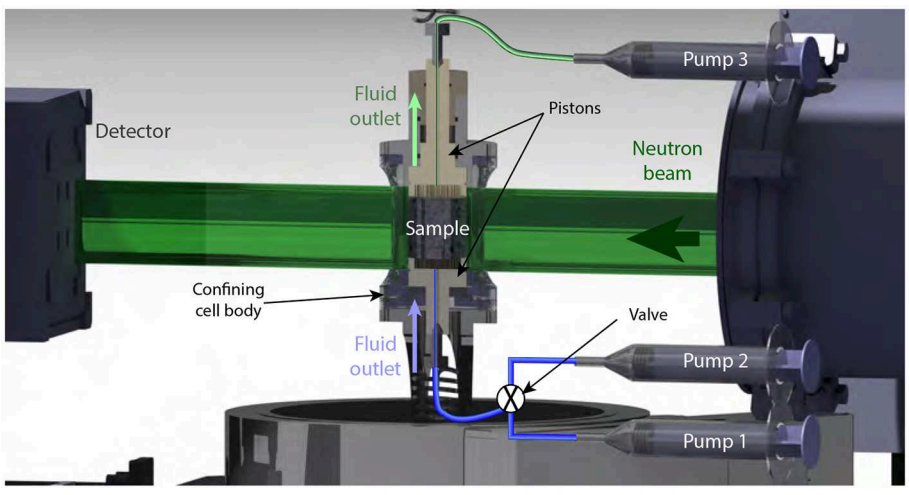

FIGURE 1 | Experimental set-up. A core holder pressurized with nitrogen gas is placed on the rotary stage of the neutron beamline. The sample in the autoclaveA is filled from its bottom side by using one of the two injection pumps. The fluid is recovered by the third pump connected to the top of the sample.

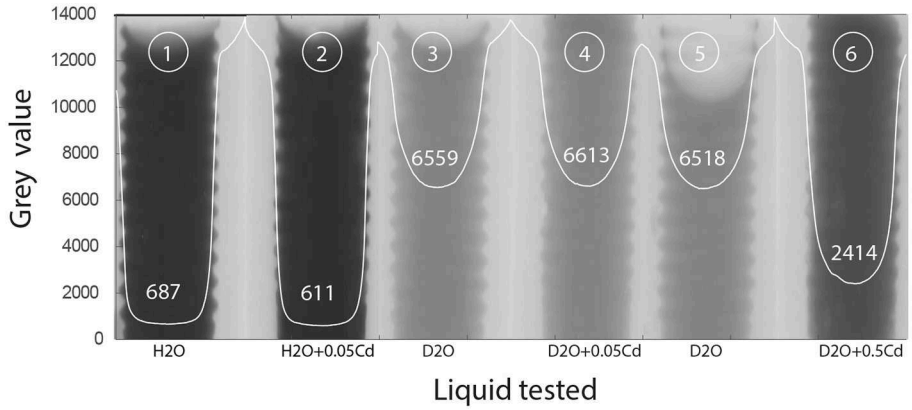

FIGURE 2 | Radiographies and attenuation of injected fluids with, from left to right: (1) H_2O, (2) solution of H_2O with 0.05 mol/L cadmium, (3) D_2O, (4) solution of H_2O with 0.05 mol/L cadmium, (5) D_2O, and (6) solution of H_2O with 0.5 mol/L cadmium. Fluids are placed into 8 mm diameter aluminum crucibles (light gray). Protium based water (1) is attenuating too much and lowers our image projection dynamic range while adding only 0.05 mol/L cadmium to the solution does not give enough contrast (2,4) and falls into the detection method error bar. Hence we ran the experiment with deuterium based water and 0.5 mol/L cadmium concentration (5,6) which are the optimized fluids for the image acquisition of our sample characteristics and optical set-up.

TABLE 1 | List of experiments and experimental conditions.

Experiment number	Experiment name	Sample	Scan type	# proj	Exp. time [s]	Binning	av.	t.d.	ac. time [s]	# volumes [s]	Duration [ml/h]	Flow rate	Liquid
1 (ILL)	Eselfuhrter sandstone	ES01	TomoF	650	0.03	4	3	0	58.5	15	877.5	15	Imbibition test
2 (ILL)	Bentheim Sandstone	BS01	TomoF	900	0.03	4	3	0	81	18	1458	15	Imbibition test
3 (ILL)	Indiana Limestone	IL01	Radio	5548									Imbibition test
4 (ILL)	Indiana Limestone	IL01	Tomo	1599									
5 (SINQ)	Indiana Limestone	IL03	Radio	3145	10	1	1	3.8	43401		0	8	Injection D_2O; Injection D_2O +Cd; Washing D_2O; reinjection D_2O+Cd
6 (SINQ)	Indiana Limestone	IL03	Tomo	627	10	1	1	3.8	8652.6	2	17305.2	0	After D_2O injection, After D_2O +Cd reinjection
7 (SINQ)	Fontainebleau Sandstone	FB02	Radio	2360	10	1	1	3.8	32568			3	Injection D_2O; Injection D_2O+Cd; Washing D_2O
8 (SINQ)	Fontainebleau Sandstone	FB02	Tomo	626	10	1	1	3.8	8638.8	1		1	After D_2O+Cd reinjection

The neutron source used is indicated with the number of each experiment. Scan types are: fast time-lapse 3D tomography (TomoF), high resolution 3D tomography (Tomo), and time-lapse 2D radiography acquisitions (Radio). The averaged frame (av.), time delay between each acquisition (t.d.) and the average acquisition time in seconds (ac. time) are also provided.

one experiment may be prepared while another was running. Additionally, although the rigs were designed for low activation (i.e., low radioactivity level after exposure to neutrons), they still required a so-called radioactive cooling time after each experiment, before being handled at radioactivity levels below the recommended safety limit. All of the cells were composed of a confining cell pressurized to 1 MPa, using nitrogen as a confining medium. The combined use of pressurized gas as a confining medium and neutrons, to our knowledge, for the first time, allows a more transparent apparatus compared to fluid based pressurized cells. The cell had a volume of 240 cm^3 and hosted a 5 by 5 cm cylindrical sample. Two pistons with centered capillary holes on top and bottom of the cylindrical sample allowed fluid circulation (**Figure 1**). Three syringe pumps (Aladdin AL-1000HP) were used, two at the inlet and one at the outlet, allowing the separate injection of two different fluids during the experiments. A given flow rate was imposed on the inlet pump whereas the outlet pump was controlled with a fixed pressure (0.1 MPa). Samples were isolated from the confining medium via Fluorinated Ethylene Propylene (FEP) jackets. After pressurizing the cell, the nitrogen bottle was closed and left at rest for an hour to verify for pressure drops and presence of leaks.

All experiments and experimental conditions are listed in **Table 1**. At the ILL beamline, we performed imbibition tests on initially dry Eselfuhrter and Bentheim sandstones with fast scan tomography where 15 and 18 time-lapse neutron 3D tomography volumes were acquired, respectively (**Table 1**, exp. 1 and 2). Tests consisted in placing the samples in Petri dishes filled with D_2O. Progression of the imbibition front was then imaged by setting the camera in a 4 × 4 binning mode and an exposure time of 0.03 s. Each projection (512 × 512 pixels) was calculated by averaging of three 2D radiographs. For both samples, 650 and

900 projections were acquired, respectively, while the sample was rotated over 360 degrees, resulting in a total acquisition time of 1 min and 1 min 20 s for each volume. Reconstructed volumes, cropped to the Region Of Interest (ROI), resulted in 300 × 300 × 250 voxels with a resolution of 1700 μm. A supplementary imbibition test has been performed on Indiana limestone but this time with time-lapse 2D radiography to be able to follow rapid changes within the sample (**Table 1**, exp. 3). Prior to this test, a full tomography of the IL sample before experiment has been performed (**Table 1**, exp. 3) which provided information on its 3D structure.

For the injection experiments at the ICON beam line (PSI, Switzerland) samples were placed in the apparatus and pressurized at 1 MPa confining pressure with a nitrogen bottle. Two pore volumes of D_2O were first injected for both one Fontainebleau sample and one Indiana sample at a flow rate of 3 and 8 mL/h, respectively. Then, two pore volumes of D_2O+Cd were injected at similar flow rates. We then "washed" the sample by injecting again two pores volumes of D_2O. In the case of the Indiana limestone sample a second injection of the cadmium solution was performed for comparison with the first injection. Two series of radiographs acquisitions were successively performed on both samples (**Table 1**, exp. 5 and 7). Additionally, three 3D tomographies were acquired; two on the Indiana limestone sample after the injection of D_2O and D_2O+Cd (**Table 1**, exp. 6), and one on Fontainebleau sandstone after the injection of D_2O+Cd (**Table 1**, exp. 8). For both radiography and tomography acquisitions, the exposure time was 10 s with no binning nor averaging of projections and a delay of 3.8 s. between each acquisition. Each projection was acquired with a size of 2160 × 2560 pixels and each tomography was composed of 625 projections acquired over a rotation of 180 degrees, leading to a resolution of 250 μm. Unfortunately, several failures of the camera controlling computer led to several hiatuses in the time series, but trends over time could still be followed.

Once the acquisition was performed, radiography raw images were enhanced as follows: (1) First, flat field correction was performed to remove the source contribution and extract only the attenuation of the sample. Beer-Lambert relation was applied on the raw images by normalizing with the bright and dark field references. (2) A second normalization was performed with the initial image averaged over a minimum of 10 projections. With these operations, most of the signal coming from the rock could be removed, enhancing the signal from the injected fluid. (3) The common logarithm of the resulting image was then weighted and divided by the sample thickness at each point of the projection to correct for the variable neutron path length in a cylindrical sample. We used the assumption that samples are perfect cylinders, so thickness was estimated using the cylinder axis and the position of the edges was determined from the overall attenuation of the sample. Up to these three steps, the operations are summarized in Equations (1, 4) Last, for time curve plots each image was averaged and reduced to a 13x13 pixels image. Local averages allowed smoothing heterogeneous effects of the sample while keeping the general trend of the flow for each region.

Summing up the first three steps leads to:

$$ImFin_{i,j} = \frac{log\left(\frac{ImRaw_{i,j} - DF_{i,j}}{BF_{i,j} - DF_{i,j}}\right)}{2\left(R^2 - r_{i,j}^2\right)^{\frac{1}{2}}} \quad (1)$$

where *ImFin* is the resulting image, *ImRaw* the raw original image, *DF* is the dark field image reference, *BF* is the bright field image reference, *R* is the radius of the sample and $r_{i,j}$ is the pixel radius from the center of sample at the given coordinates *i* and *j*.

3. RESULTS

Imbibition tests of Indiana limestone and Eselfuhrter and Fontainebleau sandstones exhibited relatively short flooding times of 45, 15, and 10 min, respectively, corresponding to flow rates between 10 to 150 ml/h. These numbers evidence the variability of the permeability of the samples. Imbibition tests have been widely used in previous studies as a first characterization of the samples (**Figure 3**). Semi-analytical solutions and experimental results demonstrated that the front progression is known to scale with the square root of time (Middleton et al., 2005; Kang et al., 2013; Cheng et al., 2015; DiStefano et al., 2017). From the saturation index of the sample, capillary pressures may be estimated vs. the sample saturation and a relative permeability calculated (Li and Horne, 2005; Haugen et al., 2014; Alyafei and Blunt, 2016, 2018). Complete calculation may be found in Alyafei and Blunt (2018). In the present study, even with a few tomograms, the front progression may easily be estimated. It also linearly scales with the square root

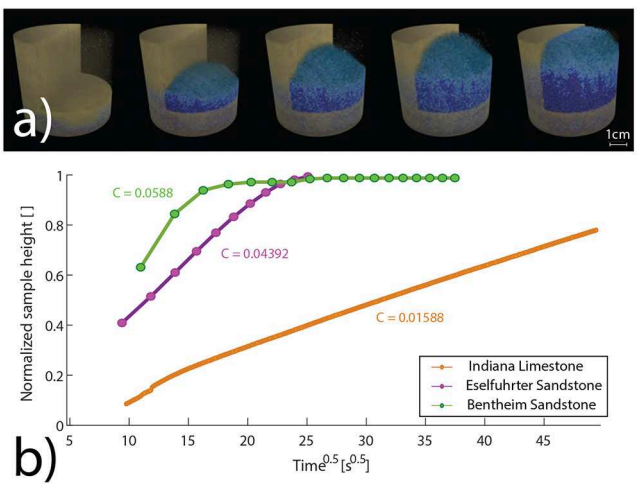

FIGURE 3 | Neutron imaging of the imbibition of porous rocks with D_2O. **(a)** Three-dimensional rendering time series of Eselfuhrter sandstone. The sample has been virtually cropped to evidence the progression of waterfront, represented in blue. **(b)** Progression of the waterfront along the normalized sample height vs. the square root of time for Indiana limestone, Eselfuhrter sandstone and Bentheim sandstone. The slope of the front progression defines the commonly called "sorptivity" constant, here marked as C.

of time and from the slope calculated we may easily sort the Indiana limestone, the Eselfuhrter sandstone and the Fontainebleau sandstone samples as having an increasing relative permeability.

From the results of the injection experiments at the ICON beamline, we observed the evolution, dispersion and alteration of the cadmium concentration from the two different injected fluids into the Indiana limestone and Fontainebleau sandstone. Assuming that the linear attenuation coefficients of cadmium and deuterium are constant through time, we can use the Beer-Lambert law to estimate the cadmium concentration and its relative evolution with time. Note however that our method, based on the data from the dry samples, remains simplified. A more elaborated approach would first attempt reducing the polychromatism of the neutron beam in order to correct the beam hardening effect and so the intensity profile on the sides of the sample. Then another correction would be on the scattering of the sample with and without fluid but also the background scattering (Boillat et al., 2018; Carminati et al., 2019). Such a correction would reduce the cupping effect generated by scattered neutrons. Cupping and beam hardening effects induce some bias on the data from the radial sides of our samples and so only the central region of the sample was used in the analysis. Finally, a further correction must be made to account for the fluid thickness crossed at each point of the radiography. This implies that a true quantification of the cadmium concentration requires performing these experiments with a full tomographic time series to obtain the knowledge of the pore thickness at each point of the projection. This could be achieved by performing prior to the experiment a registered tomography or acquiring a few projections at different angles during the experiment. A third approach could be a mixture of the two with the method of the golden ratio (Kaestner et al., 2011b; Wang et al., 2017). Nevertheless, the image processing as presented here [see Equation (1)] provides a general trend to estimate the cadmium concentration.

In **Figure 4** are presented The two radio-projection time series of both Fontainebleau sandstone (**Figure 4A**) and Indiana limestone (**Figure 4B**). In **Figure 4A**, the first two lines, slides 1 to 6, display the injection of D_2O, while slides 7 to 9 show the injection of D_2O+Cd. Note that during the first D_2O injection, the water front is slightly brighter, which may be due to some cadmium left over into the injecting tube from previous experiments. The last three slides visualize the washing phase with injection of D_2O. One may note that slides 6 and 12, both final stages of the D_2O injection, are extremely comparable and this suggests that most of the cadmium has been removed during this washing phase. In **Figure 4B**, slides 1 to 5 display the injection of D_2O, slides 6 to 8 show the injection of D_2O+Cd and slides 9 to 11 display the washing phase. We may observe numerous bright spots remaining after the washing phase, suggesting that some Cd remained trapped in the sample. Slide 12 is the onset of the new D_2O+Cd injection. **Figure 5** shows, for each injection experiment in the Fontainebleau sandstone and Indiana limestone, the time evolution of cadmium at different locations of the sample. From the 13 × 13 pixels averaged images we selected a grid covering the central area of the sample (see **Figure 5**). Distinct vertical sections of the sample are presented with different colors. Different radial positions are presented with different color saturations. The center of the sample is displayed with thicker curves. From these data, a vertical gradient, almost linear, is observed across the height of the sample. This linear trend may be interpreted as a lower water saturation and concentration of cadmium at the top of the sample compared to the bottom part once the fluid and pollutant were injected. This is in stark contrast with the Fontainebleau sandstone, which does not display any significant horizontal gradient (the cadmium concentration on the sides of

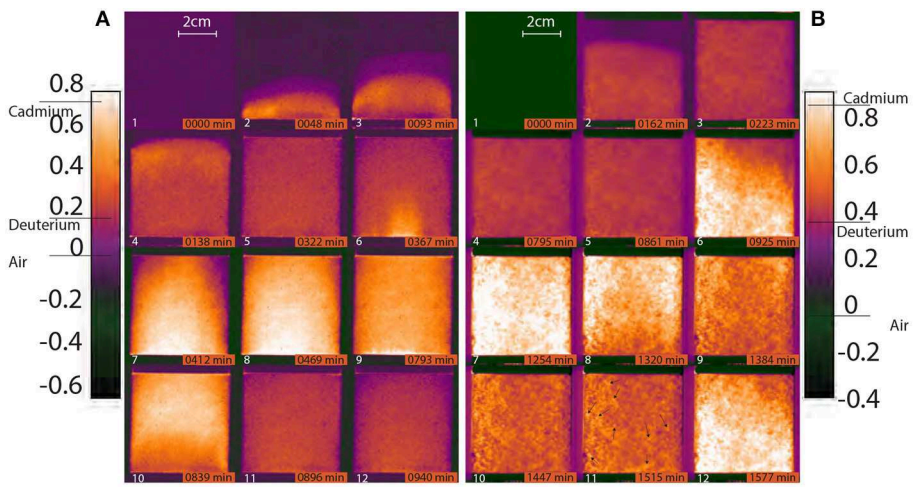

FIGURE 4 | Time-lapse 2D radiographs of injection of cadmium in **(A)** Fontainebleau sandstone and **(B)** Indiana limestone. The first injection of D_2O was followed by an injection of D_2O +Cd. Samples were then washed with a second injection of D_2O. For the limestone only, a second injection of D_2O+Cd has been performed at the end of the experiment. The color code shows the range expected for air, D_2O, and D_2O+Cd. Black arrows in slide 11, **(B)**, evidence the spots where "unwashed" cadmium is maximum. Note, however, that comparing slide 11 and 5, most of the sample contains some unwashed cadmium.

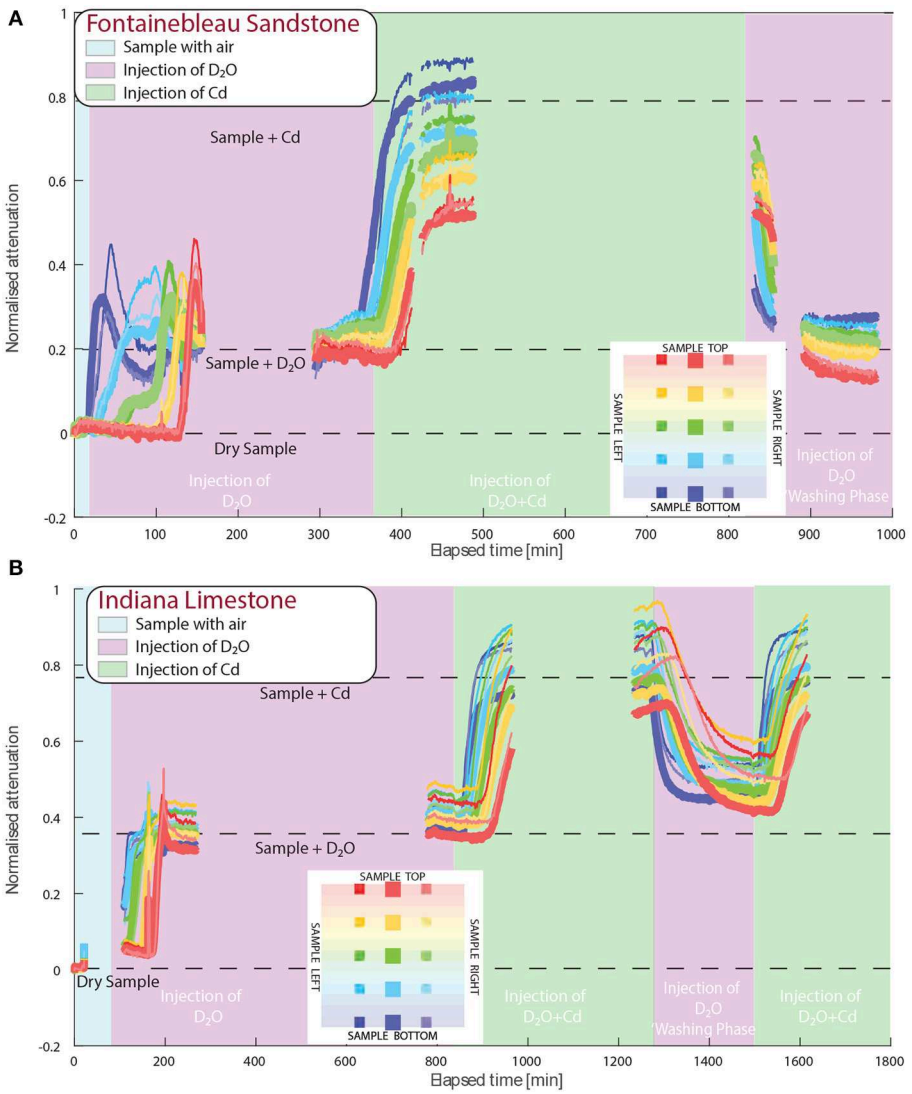

FIGURE 5 | Normalized neutron attenuation in the samples vs. time. Hiatuses in the data correspond to failures of the camera system or tomography acquisition. The different curves display different regions in the sample, as mapped in the figure inset. The central region of the sample has an increased thickness for easier visualization. **(A)** Fontainebleau sandstone experiment. The first injection of D_2O shows a slight overshoot before 200 min. due to some left-over cadmium from the previous experiment still present in the tubing system. **(B)** Indiana limestone experiment.

the samples nearly superimposes the curves from the center of the sample). Conversely, the Indiana limestone sample displays a horizontal gradient from the left to right side. Even though the limestone and sandstone samples display overall very similar behaviors, careful observation indicates that only for limestone, the cadmium is not completely removed during the D_2O washing phase as the curves do not come back to their initial values (**Figure 5B**). By normalizing the curve drop during the washing phase with the stable values of D_2O+Cd and D_2O during the first and second injection phases, one may measure how much of the cadmium was removed during the washing phase. The curve drop during the washing phase evidences that about 60% of the total cadmium is quickly removed and then stabilizes to a value of 70%, indicating that 30% of the injected cadmium is still present in the sample. On the other side, in less than 200 min of D_2O injection, the Fontainebleau sandstone recovered the original D_2O value and we conclude that the sample has been fully washed and all the pollutant flushed out. Within the Indiana limestone, local areas are seen to have captured and preserved the cadmium. They appear as brighter spots, on **Figure 4** highlighted by arrows on slide 11, section b. Further analyses on these specific areas have been performed and revealed that these locations retained 42 to 55 % of the cadmium originally injected with an average of 48±4% (standard deviation), see arrows in **Figure 4**. Note however that the projections of these spots are influenced by the material in front and behind them. Despite picking the darkest areas where the sample is the thinnest and less influenced, this estimation represents a lower bound

on the amount of trapped cadmium. For the same reasons, these cadmium locations were mostly visible on the sides of the samples where they were less affected by cleaned (i.e., Cd-free) rock material. Nevertheless one side of the sample remained predominantly contaminated (see **Figure 4**). This is also reflected by the preferential infiltration of both the D_2O and D_2O + Cd injection front (**Figure 4B**). This observation indicates that even for this Indiana limestone, usually considered to be a relatively homogeneous medium in terms of composition and grain size at the scale of laboratory samples, a variation of permeability is present within the sample. Such heterogeneities can not be observed by conventional flow-through tests. Previous experiment did not evidence any pronounced tailing on Indiana limestone (Gist et al., 1990) but numerical simulations already evidenced a large range of fluid velocities (Bijeljic et al., 2013). Our results therefore present the first evidence of *in-situ* non-Fickian transport of pollutants in porous rocks.

4. DISCUSSION

Solute transport is normally described by advection dispersion equations. The plume of a pollutant through porous media can consequently be modeled accordingly if one knows the mean velocity of the fluid. When anomalies are observed, transport is then described as non-Fickian (Becker and Shapiro, 2003; Levy and Berkowitz, 2003; Gouze et al., 2008). Sources of non-Fickian behavior may vary, such as fluids trapped or delayed in the pore network or sorption of the pollutant within the host rock. In order to be sorbed in rocks, inorganic pollutants must first move from the bulk solution to the fluid boundary layer within the rock pores and then from the boundary layer to the rock surface. From there, they may adsorb to an active site of the surface, following either a chemical reaction or an exchange of ions with the surface. Eventually, if the surface is sufficiently porous, it will allow these pollutants to diffuse and to be incorporated inside the solid elements of the rock. These four steps will have different efficiencies depending on the flow rate, pH, initial concentration of the pollutant, chemical composition of the rock and the amount of active sorption: sites present. The use of different existing models (e.g., Langmuir model or Freundlich model), which are based on different assumptions, may help determining the sorption mechanisms. The Langmuir model is based on the assumption that the number of sites is limited compared to the amount of solute material. The Freundlich model assumes a greater number of active sites compared to the available solute material. Indiana limestone itself has been identified among other carbonates to be a rock with a wide range of flow velocities (Bijeljic et al., 2013), interpreted to be a result from the bimodal porosity distribution. The throats connecting the pores have been evidenced with two characteristic diameters of 20 and 0.4 μm. The dispersion of the fluid within the porosity connected by thin throats may lead to pockets of slow or stagnant fluids. Finally, diffusion coefficients of cadmium in water may be approximated in the range of $710^{-10} m^2 s^{-1}$ (Lide and Kehiaian, 1994; Furukawa et al., 2007). Hence considering spherical or cylindrical diffusion (i.e., pore or throats), from Indiana limestone network characteristics, cadmium will be diffused to the host rock-fluid interface in much less than an hour. Such pockets may consequently ease the sorption process. At the current stage of our study it is not yet possible of distinguishing if the remaining cadmium has been sorbed or trapped in a stagnant fluid pocket. Further experiments are necessary to determine the mechanisms behind the local interaction of the cadmium with the rock. A post-experimental X-ray tomography acquisition of the Indiana limestone sample, oriented along the projection of the radiography, provides some explanation on the reasons why the permeability and potentially sorption were higher on the sides of the sample. In **Figure 6**, one may observe a vertically heterogeneous layering. On the left side, several large pores and fragments of marine organisms are present. On the right side a similar composition but with lower pore size, is observed. Indiana limestone is known for being a homogeneous and quasi exclusively calcite limestone (Handin et al., 1971; Barnhoorn et al., 2018). In between the rock matrix, the fragments appear to be less attenuating either due to a different composition or a lower density. Hence, we propose that the differences in attenuation are due to the density variations of the background rock matrix and pore network. This effect could be explained by some of the large marine fragments that were crushed, filling the large pores and creating microporosity in between the fragments. Overall, the total pore

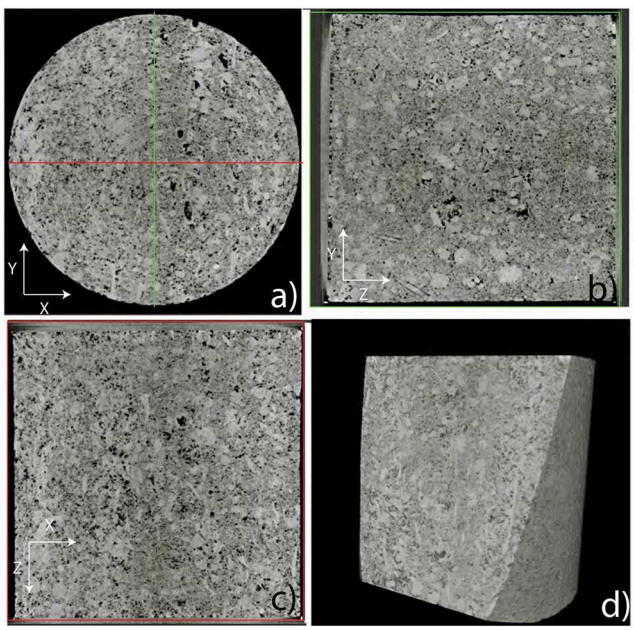

FIGURE 6 | X-ray tomography of the Indiana limestone sample IL3 (exp. 5). The sample is a cylinder with dimensions of 5 × 5 cm. **(a)** Slice in the middle of the sample, top view. **(b)** Slice in the middle of the sample, right side view. **(c)** Slice in the middle of the sample, front view. **(d)** 3D volume rendering. The pores in the sample are represented in black while fossil and sediment fragments are represented in bright or light gray. A darker gray domain, mostly in the center of the sample corresponds to lower density, fossil fragments are difficult to distinguish. They probably corresponds to fragments reduced into powder with consequently a higher inner porosity than the intact fragments.

fraction throughout the sample may not have changed but the polydispersity of the poresize distribution has been modified. The mixture of fragments with small pores is shown in **Figure 6** with lower gray values as their overall density is lower than the density of the intact fragments. It would offer a bimodal permeability, distinguishing the main flow from smaller pockets where the fluid would be delayed or approximated as stagnant over the experimental time-scale. It would make these sites ideal for cadmium sorption within the host rock. This shows that sample-scale sorption experiments, such as been performed in the past on dolomitic and calcitic limestones, can therefore be significantly improved with *in-situ* imaging, which can take into account the small-scale heterogeneities that affect flow and sorption. Neutron imaging, with its remarkable sensitivity to fluids, has now reached a level of technicality where fast time-series of tomographies can be acquired. Moreover, the recent advance on the correction of scattering bias has improved the quantitative possibilities of the method (Boillat et al., 2018; Carminati et al., 2019).

5. CONCLUSIONS

With the present study we demonstrated that neutron beamlines are ready for the use of *in-situ* experimental devices with confining pressure that allow to study contaminant transport in rocks. Radiography and tomography time-series can be acquired and image geological processes under earth-like conditions. Using cadmium as a tracer, we investigated the case study of pollutant flow in different porous rocks. Moreover, we have also demonstrated that the use of either protium- or deuterium-based water allows for greater flexibility when choosing sample-type and sample size, with respect to the expected ranges in porosity and permeability. We used a centimetersized sample, which is generally considered to be homogeneous using traditional set-ups for flow experiments. Our neutron tomography experiments indicate that even at this small scale localization of flow and preferential adsorption takes place, indicating non-Fickian transport of the aqueous species. Now the feasibility of neutron usage has been ascertained to study cadmium transport in porous rocks, the next step will be to perform similar experiments with different initial concentrations in order to further understand which mechanisms prevail (retention or sorption), as a function of experimental conditions, space and time. Additionally, further experiments need to be performed with tomography time series in order to better localize the areas where the residual cadmium is maximum and to investigate further these locations. Regardless of improvements of the imaging methods, this study demonstrates that Indiana limestone has a real potential in cadmium retention. It therefore provides a new perception of pollutant capture, where only a fraction of the rock structure contributes to the retention of heavy metal pollutants.

DATA AVAILABILITY STATEMENT

The datasets (2D and 3D neutron data) are available in the public repository NORSTORE (https://doi.org/10.11582/2019.00021, Renard, 2019).

AUTHOR CONTRIBUTIONS

All authors listed have made a substantial, direct and intellectual contribution to the work, and approved it for publication.

FUNDING

This study received funding from the Norwegian Research Council (project ARGUS, grant 272217). AP was currently support by a VENI project, with grant number 016.Veni.181.036, funded by the Dutch Foundation for Scientific Research (NWO).

ACKNOWLEDGMENTS

We thank Auke Barnhoorn at TU Delft for providing several rock samples.

REFERENCES

Alyafei, N., and Blunt, M. J. (2016). The effect of wettability on capillary trapping in carbonates. *Adv. Water Resour.* 90, 36–50. doi: 10.1016/j.advwatres.2016.02.001

Alyafei, N., and Blunt, M. J. (2018). Estimation of relative permeability and capillary pressure from mass imbibition experiments. *Adv. Water Resour.* 115, 88–94. doi: 10.1016/j.advwatres.2018.03.003

An, H. K., Park, B. Y., and Kim, D. S. (2001). Crab shell for the removal of heavy metals from aqueous solution. *Water Res.* 35, 3551–3556. doi: 10.1016/S0043-1354(01)00099-9

Barbier, F., Duc, G., and Petit-Ramel, M. (2000). Adsorption of lead and cadmium ions from aqueous solution to the montmorillonite/water interface. *Colloids Surf. A Phys. Eng. Aspects* 166, 153–159. doi: 10.1016/S0927-7757(99)00501-4

Barnhoorn, A., Douma, L., and Janmahomed, F. (2018). Experimental load cycling in the brittle field produces a more distributed fracture network. *Geophys. Res. Abstr.* 20.

Becker, M. W., and Shapiro, A. M. (2003). Interpreting tracer breakthrough tailing from different forced-gradient tracer experiment configurations in fractured bedrock. *Water Resour. Res.* 39. doi: 10.1029/2001WR001190

Benavides, M. P., Gallego, S. M., and Tomaro, M. L. (2005). Cadmium toxicity in plants. *Braz. J. Plant Physiol.* 17, 21–34. doi: 10.1590/S1677-04202005000100003

Bertin, G. and Averbeck, D. (2006). Cadmium: cellular effects, modifications of biomolecules, modulation of DNA repair and genotoxic consequences (a review). *Biochimie* 88, 1549–1559. doi: 10.1016/j.biochi.2006.10.001

Bhattacharyya, K. G., and Gupta, S. S. (2007). Adsorptive accumulation of Cd(II), Co(II), Cu(II), Pb(II), and Ni(II) from water on montmorillonite: influence of acid activation. *J. Coll. Interface Sci.* 310, 411–424. doi: 10.1016/j.jcis.2007.01.080

Bijeljic, B., Mostaghimi, P., and Blunt, M. J. (2013). Insights into non-fickian solute transport in carbonates. *Water Resour. Res.* 49, 2714–2728. doi: 10.1002/wrcr.20238

Boillat, P., Carminati, C., Schmid, F., Grünzweig, C., Hovind, J., Kaestner, A., et al. (2018). Chasing quantitative biases in neutron imaging with scintillator-camera detectors: a practical method with black body grids. *Optics Express* 26, 15769–15784. doi: 10.1364/OE.26.015769

Carlson, W. D. (2006). Three-dimensional imaging of earth and planetary materials. *Earth Planet. Sci. Lett.* 249, 133–147. doi: 10.1016/j.epsl.2006.06.020

Carminati, A., Kaestner, A., Hassanein, R., Ippisch, O., Vontobel, P., Flü Hler, H., et al. (2007). Infiltration through series of soil aggregates: neutron radiography and modeling. *Adv. Water Resour.* 30, 1168–1178. doi: 10.1016/j.advwatres.2006.10.006

Carminati, C., Boillat, P., Schmid, F., Vontobel, P., Hovind, J., Morgano, M., et al. (2019). Implementation and assessment of the black body bias correction in quantitative neutron imaging. *PLoS ONE* 14:e0210300. doi: 10.1371/journal.pone.0210300

Cheng, C.-L., Perfect, E., Donnelly, B., Bilheux, H., Tremsin, A., McKay, L., et al. (2015). Rapid imbibition of water in fractures within unsaturated sedimentary rock. *Adv. Water Resour.* 77 82–89. doi: 10.1016/j.advwatres.2015.01.010

Cnudde, V., and Boone, M. N. (2013). High-resolution X-ray computed tomography in geosciences: a review of the current technology and applications. *Earth Sci. Rev.* 123, 1–17. doi: 10.1016/j.earscirev.2013.04.003

Cnudde, V., Dierick, M., Vlassenbroeck, J., Masschaele, B., Lehmann, E., Jacobs, P., et al. (2008). High-speed neutron radiography for monitoring the water absorption by capillarity in porous materials. *Nuclear Instrum. Methods Phys. Res. B* 266, 155–163. doi: 10.1016/j.nimb.2007.10.030

Das, P., Samantaray, S., and Rout, G. R. (1997). Studies on cadmium toxicity in plants: a review. *Environ. Pollut.* 98, 29–36. doi: 10.1016/S0269-7491(97)00110-3

Dauti, D., Tengattini, A., Dal Pont, S., Toropovs, N., Briffaut, M., and Weber, B. (2018). Analysis of moisture migration in concrete at high temperature through *in-situ* neutron tomography. *Cement Concrete Res.* 111, 41–55. doi: 10.1016/j.cemconres.2018.06.010

Dawson, M., Francis, J., and Carpenter, R. (2014). New views of plant fossils from Antarctica: a comparison of X-ray and neutron imaging techniques. *J. Paleontol.* 88, 702–707. doi: 10.1666/13-124

De Beer, F. C., Middleton, M. F., and Hilson, J. (2004). Neutron radiography of porous rocks and iron ore. *Appl. Radiat. Isotopes* 61, 487–495. doi: 10.1016/j.apradiso.2004.03.089

Degueldre, C., Pleinert, H., Maguire, P., Lehman, E., Missimer, J., Hammer, J., et al. (1996). Porosity and pathway determination in crystalline rock by positron emission tomography and neutron radiography. *Earth Planet. Sci. Lett.* 140, 213–225. doi: 10.1016/0012-821X(96)00043-X

Derluyn, H., Griffa, M., Mannes, D., Jerjen, I., Dewanckele, J., Vontobel, P., et al. (2013). Characterizing saline uptake and salt distributions in porous limestone with neutron radiography and X-ray micro-tomography. *J. Build. Phys.* 36, 353–374. doi: 10.1177/1744259112473947

Desrues, J., Viggiani, G., and Besuelle, P. (eds.) (2006). *Advances in X-ray Tomography for Geomaterials*. ISTE.

DiStefano, V. H., Cheshire, M. C., McFarlane, J., Kolbus, L. M., Hale, R. E., Perfect, E., et al. (2017). Spontaneous imbibition of water and determination of effective contact angles in the Eagle Ford Shale Formation using neutron imaging. *J. Earth Sci.* 28 874–887. doi: 10.1007/s12583-017-0801-1

El Mouzdahir, Y., Elmchaouri, A., Mahboub, R., ElAnssari, A., Gil, A., Korili, S. A., et al. (2007). Interaction of stevensite with Cd2+ and Pb2+ in aqueous dispersions. *Appl. Clay Sci.* 35, 47–58. doi: 10.1016/j.clay.2006.08.002

Fishbein, L. (1981). Sources, transport and alterations of metal compounds: an overview. I. Arsenic, beryllium, cadmium, chromium, and nickel. *Environ. Health Perspect.* 40, 43–64. doi: 10.1289/ehp.814043

Furukawa, K., Takahashi, Y., and Sato, H. (2007). Effect of the formation of EDTA complexes on the diffusion of metal ions in water. *Geochim. Cosmochim. Acta* 71, 4416–4424. doi: 10.1016/j.gca.2007.07.009

Ghazy, S. E., Gabr, I. M., and Gad, A. H. (2008). Cadmium(II) sorption from water samples by powdered marble wastes. *Chem. Spec. Bioavailabil.* 20, 249–260. doi: 10.3184/095422908X382152

Gist, G. A., Thompson, A. H., Katz, A. J., and Higgins, R. L. (1990). Hydrodynamic dispersion and pore geometry in consolidated rock. *Phys. Fluids A Fluid Dyn.* 2, 1533–1544. doi: 10.1063/1.857602

Gouze, P., Borgne, T. L., Leprovost, R., Lods, G., Poidras, T., and Pezard, P. (2008). Non-fickian dispersion in porous media: 1. multiscale measurements using single-well injection withdrawal tracer tests. *Water Resour. Res.* 44. doi: 10.1029/2007WR006278

Hall, S., Hughes, D., and Rowe, S. (2010). Local characterisation of fluid flow in sandstone with localised deformation features through fast neutron imaging. *EPJ Web Conf.* 6:22008. doi: 10.1051/epjconf/20100622008

Hall, S. A. (2013). Characterization of fluid flow in a shear band in porous rock using neutron radiography. *Geophys. Res. Lett.* 40, 2613–2618. doi: 10.1002/grl.50528

Handin, J., Friedman, M., Logan, J. M., Pattison, L. J., and Swolfs, H. S. (1971). "Experimental folding of rocks under confining pressure: buckling of single-layer rock beams," in *Geophysical Monograph Series Flow and Fracture of Rocks*, 1–28.

Haugen, A., Fernø, M. A., Mason, G., Morrow, N. R., Haugen, Å., Fernø, M. A., et al. (2014). Capillary pressure and relative permeability estimated from a single spontaneous imbibition test. *J. Petrol. Sci. Eng.* 115, 66–77. doi: 10.1016/j.petrol.2014.02.001

Jasti, J., Lindsay, J., and Fogler, H. (1987). "Flow imaging in porous media using neutron radiography," in *SPE Annual Technical Conference and Exhibition* (Dallas, TX: Society of Petroleum Engineers), 8.

Jiang, M.-q., Jin, X.-y., Lu, X.-Q., and Chen, Z.-l. (2010). Adsorption of Pb(II), Cd(II), Ni(II) and Cu(II) onto natural kaolinite clay. *Desalination* 252, 33–39. doi: 10.1016/j.desal.2009.11.005

Joseph, L., Jun, B.-M., Flora, J. R., Park, C. M., and Yoon, Y. (2019). Removal of heavy metals from water sources in the developing world using low-cost materials: a review. *Chemosphere* 229, 142–159. doi: 10.1016/j.chemosphere.2019.04.198

Joseph, P. (2009). Mechanisms of cadmium carcinogenesis. *Toxicol Appl Pharmacol.* 238, 272–279. doi: 10.1016/j.taap.2009.01.011

Kaestner, A., Hassanein, R., Vontobel, P., Lehmann, P., Schaap, J., Lehmann, E., et al. (2007). Mapping the 3D water dynamics in heterogeneous sands using thermal neutrons. *Chem. Eng. J.* 130, 79–85. doi: 10.1016/j.cej.2006.06.013

Kaestner, A. P., Hartmann, S., Kühne, G., Frei, G., Grünzweig, C., Josic, L., et al. (2011a). The ICON beamline – a facility for cold neutron imaging at SINQ. *Nuclear Instrum. Methods Phys. Res. A* 659, 387–393. doi: 10.1016/j.nima.2011.08.022

Kaestner, A. P., Munch, B., and Trtik, P. (2011b). Spatiotemporal computed tomography of dynamic processes. *Opt. Eng.* 50, 1–10. doi: 10.1117/1.3660298

Kaestner, A. P., Trtik, P., Zarebanadkouki, M., Kazantsev, D., Snehota, M., Dobson, K. J., et al. (2016). Recent developments in neutron imaging with applications for porous media research. *Solid Earth* 7, 1281–1292. doi: 10.5194/se-7-1281-2016

Kang, M., Perfect, E., Cheng, C., Bilheux, H., Gragg, M., Wright, D., et al. (2013). Diffusivity and sorptivity of berea sandstone determined using neutron radiography. *Vadose Zone J.* 12. doi: 10.2136/vzj2012.0135

Karapinar, N., and Donat, R. (2009). Adsorption behaviour of Cu2+ and Cd2+ onto natural bentonite. *Desalination* 249, 123–129. doi: 10.1016/j.desal.2008.12.046

Kocaoba, S. (2009). Adsorption of Cd(II), Cr(III) and Mn(II) on natural sepiolite. *Desalination* 244, 24–30. doi: 10.1016/j.desal.2008.04.033

Kuo, C.-Y., and Lin, H.-Y. (2009). Adsorption of aqueous cadmium (II) onto modified multi-walled carbon nanotubes following microwave/chemical treatment. *Desalination*, 249(2):792–796. doi: 10.1016/j.desal.2008.11.023

Lanza, R. C., Mcfarland, E. W., and Poulos, G. W. (1991). "Computerized neutron tomography for core analysis," in *SCA-9128, in 5th Annual Conference Transactions: Society of Professional Well Log Analysts, Society of Core Analysts Chapter-at-Large*, 12. Available online at: http://www.jgmaas.com/SCA/1991/SCA1991-28.pdf

Lehmann, E. H., Frei, G., Kühne, G., and Boillat, P. (2007). The micro-setup for neutron imaging: a major step forward to improve the spatial resolution. *Nuclear Instrum. Methods Phys. Res. A* 576, 389–396. doi: 10.1016/j.nima.2007.03.017

Levy, M., and Berkowitz, B. (2003). Measurement and analysis of non-fickian dispersion in heterogeneous porous media. *J. Contaminant Hydrol.* 64, 203–226. doi: 10.1016/S0169-7722(02)00204-8

Li, K., and Horne, R. N. (2005). Computation of capillary pressure and global mobility from spontaneous water imbibition into oil-saturated rock. *SPE J.* 10, 458–465. doi: 10.2118/80553-PA

Lide, D. R., and Kehiaian, H. V. (1994). *CRC Handbook of Thermophysical and Thermochemical Data.* Chicago, IL; Washington, DC: American Library Association.

Macente, A., Fusseis, F., Butler, I. B., Tudisco, E., Hall, S. A., and Andò, E. (2018). 4D porosity evolution during pressure-solution of NaCl in the presence of phyllosilicates. *Earth Planet. Sci. Lett.* 502, 115–125. doi: 10.1016/j.epsl.2018.08.032

Masschaele, B., Dierick, M., Cnudde, V., Hoorebeke, L., Delputte, S., Gildemeister, A., et al. (2004). High-speed thermal neutron tomography for the visualization of water repellents, consolidants and water uptake in sand and lime stones. *Radiat. Phys. Chem.* 71, 807–808. doi: 10.1016/j.radphyschem.2004.04.102

Middleton, M., Li, K., and de Beer, F. (2005). *Spontaneous Imbibition Studies of Australian Reservoir Rocks With Neutron Radiography*. Irvine, CA: Society of Petroleum Engineers.

Olbinado, M. P., and Rack, A. (2019). "Recent advances on *in situ* materials characterization using ultra high-speed x-ray imaging at The European Synchrotron ESRF," in *32nd International Congress on High-Speed Imaging and Photonics*, eds M. Versluis and E. Stride (Enschede: SPIE), 16.

Pacureanu, A., Langer, M., Boller, E., Tafforeau, P., and Peyrin, F. (2012). Nanoscale imaging of the bone cell network with synchrotron X-ray tomography: optimization of acquisition setup. *Med. Phys.* 39, 2229–2238. doi: 10.1118/1.3697525

Papini, M. P., Saurini, T., Bianchi, A., Majone, M., and Beccari, M. (2004). Modeling the competitive adsorption of Pb, Cu, Cd, and Ni onto a natural heterogeneous sorbent material (Italian "Red Soil"). *Indus. Eng. Chem. Res.* 43, 5032–5041. doi: 10.1117/12.2524607

Peksa, A. E., Wolf, K.-H. A., and Zitha, P. L. (2015). Bentheimer sandstone revisited for experimental purposes. *Marine Petrol. Geol.* 67, 701–719. doi: 10.1016/j.marpetgeo.2015.06.001

Poulikakos, L. D., Sedighi Gilani, M., Derome, D., Jerjen, I., and Vontobel, P. (2013). Time resolved analysis of water drainage in porous asphalt concrete using neutron radiography. *Appl. Radiat. Isotopes* 77, 5–13. doi: 10.1016/j.apradiso.2013.01.040

Rangel-Porras, G., García-Magno, J. B., and González-Muñoz, M. P. (2010). Lead and cadmium immobilization on calcitic limestone materials. *Desalination* 262, 1–10. doi: 10.1016/j.desal.2010.04.043

Renard, F. (2019). *Neutron Imaging of Cadmium Sorption and Transport in Porous Rocks.* [Data set]. Norstore. doi: 10.11582/2019.00021

Sari, A. and Tuzen, M. (2014). Cd(II) adsorption from aqueous solution by raw and modified kaolinite. *Appl. Clay Sci.* 88–89, 63–72. doi: 10.1016/j.clay.2013.12.021

Satarug, S., Baker, J. R., Urbenjapol, S., Haswell-Elkins, M., Reilly, P. E., Williams, D. J., et al. (2003). A global perspective on cadmium pollution and toxicity in non-occupationally exposed population. *Toxicol. Lett.* 137, 65–83. doi: 10.1016/S0378-4274(02)00381-8

Satarug, S., and Moore, M. R. (2004). Adverse health effects of chronic exposure to low-level cadmium in foodstuffs and cigarette smoke. *Environ. Health Perspect.* 112, 1099–1103. doi: 10.1289/ehp.6751

Sedighi-Gilani, M., Griffa, M., Mannes, D., Lehmann, E., Carmeliet, J., and Derome, D. (2012). Visualization and quantification of liquid water transport in softwood by means of neutron radiography. *Int. J. Heat Mass Transfer* 55, 6211–6221. doi: 10.1016/j.ijheatmasstransfer.2012.06.045

Shen, X., Liu, W., Chen, Y., Guo, Y., Gao, M., Chen, W., et al. (2019). Diagnostic significance of metallothionein members in recognizing cadmium exposure in various organs under low-dose exposure. *Chemosphere* 229, 32–40. doi: 10.1016/j.chemosphere.2019.04.192

Sneddon, I., Orueetxebarria, M., Hodson, M., Schofield, P., and Valsami-Jones, E. (2006). Use of bone meal amendments to immobilise Pb, Zn and Cd in soil: a leaching column study. *Environ. Pollut.* 144, 816–825. doi: 10.1016/j.envpol.2006.02.008

Subramanian, J., and Govindan, R. (2007). Lung cancer in never smokers: a review. *J. Clin. Oncol.* 25, 561–570. doi: 10.1200/JCO.2006.06.8015

Tengattini, A., Atkins, D., Giroud, B., Andò, E., Beaucour, J., and Viggiani, G. (2017). "NeXT-Grenoble, a novel facility for Neutron and X-ray Tomography in Grenoble NEXT-Grenoble," in *3rd International Conference on Tomograpgy of Materials and Structures* (Cairns, QLD).

Toropovs, N., Monte, F. L., Wyrzykowski, M., Weber, B., Sahmenko, G., Vontobel, P., et al. (2015). Real-time measurements of temperature, pressure and moisture profiles in High-Performance Concrete exposed to high temperatures during neutron radiography imaging. *Cement Concrete Res.* 68, 166–173. doi: 10.1016/j.cemconres.2014.11.003

Tötzke, C., Manke, I., Hilger, A., Choinka, G., Kardjilov, N., Arlt, T., et al. (2011). Large area high resolution neutron imaging detector for fuel cell research. *J. Power Sour.* 196, 4631–4637. doi: 10.1016/j.jpowsour.2011.01.049

Tremsin, A. S., McPhate, J. B., Vallerga, J. V., Siegmund, O. H. W., Feller, W. B., Lehmann, E., et al. (2011). Improved efficiency of high resolution thermal and cold neutron imaging. *Nuclear Instrum. Methods Phys. Res. A* 628, 415–418. doi: 10.1016/j.nima.2010.07.014

Trtik, P., Münch, B., Weiss, W. J., Kaestner, A., Jerjen, I., Josic, L., et al. (2011). Release of internal curing water from lightweight aggregates in cement paste investigated by neutron and X-ray tomography. *Nuclear Instrum. Methods Phys. Res. A* 651, 244–249. doi: 10.1016/j.nima.2011.02.012

Tudisco, E., Etxegarai, M., Hall, S. A., Charalampidou, E.-M., Couples, G. D., Lewis, H., et al. (2019). Fast 4-d imaging of fluid flow in rock by high-speed neutron tomography. *J. Geophys. Res. Solid Earth* 124, 3557–3569. doi: 10.1029/2018JB016522

Tudisco, E., Hall, S., Charalampidou, E., Kardjilov, N., Hilger, A., and Sone, H. (2015). Full-field measurements of strain localisation in sandstone by neutron tomography and 3D-volumetric digital image correlation. *Phys. Proc.* 69, 509–515. doi: 10.1016/j.phpro.2015.07.072

Vázquez, G., Sonia Freire, M., González-Alvarez, J., and Antorrena, G. (2009). Equilibrium and kinetic modelling of the adsorption of Cd2+ ions onto chestnut shell. *Desalination* 249, 855–860. doi: 10.1016/j.desal.2009.09.007

Viggiani, G., Lenoir, N., Bornert, M., Desrues, J., and Be, P. (2007). Volumetric digital image correlation applied to X-ray microtomography images from triaxial compression tests on argillaceous rock. *Strain* 43, 193–205. doi: 10.1111/j.1475-1305.2007.00348.x

Waalkes, M. (2003). Cadmium carcinogenesis. *Mutat. Res.* 533, 107–120. doi: 10.1016/j.mrfmmm.2003.07.011

Wang, H., Kaestner, A., Zou, Y., Lu, Y., and Guo, Z. (2017). Sparse-view reconstruction of dynamic processes by neutron tomography. *Phys. Proc.* 88, 290–298. doi: 10.1016/j.phpro.2017.06.040

Yehya, M., Andò, E., Dufour, F., and Tengattini, A. (2018). Fluid-flow measurements in low permeability media with high pressure gradients using neutron imaging: application to concrete. *Nuclear Instrum. Methods Phys. Res. A* 890, 35–42. doi: 10.1016/j.nima.2018.02.039

Zhang, P., Wittmann, F. H., Zhao, T. J., Lehmann, E. H., Tian, L., and Vontobel, P. (2010). Observation and quantification of water penetration into Strain Hardening Cement-based Composites (SHCC) with multiple cracks by means of neutron radiography. *Nuclear Instrum. Methods Phys. Res. A* 620, 414–420. doi: 10.1016/j.nima.2010.04.119

Conflict of Interest: The authors declare that the research was conducted in the absence of any commercial or financial relationships that could be construed as a potential conflict of interest.

frontiers in Earth Science

ORIGINAL RESEARCH
published: 19 December 2019
doi: 10.3389/feart.2019.00329

Implementation of Dynamic Neutron Radiography and Integrated X-Ray and Neutron Tomography in Porous Carbonate Reservoir Rocks

Miller Zambrano[1,2,3], Fareeha Hameed[4,5,6], Kaestner Anders[7], Lucia Mancini[4] and Emanuele Tondi[1,2,3]*

[1] Geology Division, School of Science and Technology, University of Camerino, Camerino, Italy, [2] Reservoir Characterization Project (www.rechproject.com), Camerino, Italy, [3] GeoMore s.r.l., Camerino, Italy, [4] Elettra-Sincrotrone Trieste S.C.p.A., Trieste, Italy, [5] The 'Abdus Salam' International Centre for Theoretical Physics, Trieste, Italy, [6] Forman Christian College University, Physics Department, Lahore, Pakistan, [7] Laboratory for Neutron Scattering and Imaging, Paul Scherrer Institut, Villigen, Switzerland

The textural and geometrical properties of the pore networks (i.e., such as pore size distribution, pore shape, connectivity, and tortuosity) provides a primary control on the fluid storage and migration of geofluids within porous carbonate reservoirs. These properties are highly variable because of primary depositional conditions, diagenetic processes and deformation. This issue represents an important challenge for the characterization and exploitation plan in this type of reservoirs. In this study, the complementary properties of neutrons and X-ray experiments are carried out to better understand the effects of pore network properties on the hydraulic behavior of porous carbonates. Neutrons have unique properties and are particularly suitable for this study due to the sensitivity of neutrons to hydrogen-based fluids. The used methodology combines dynamic neutron radiography (NR), integrated X-ray and neutron tomography (XCT, NCT), and computational fluid dynamics simulations (lattice-Boltzmann method) of porous carbonate reservoir analogs from central and southern Italy. Dynamic 2D NR images provide information regarding the fluid transport and the wetting front dynamics related to the effect of heterogeneities (e.g., fractures and deformation bands) at the microscale. The combination of NCT (dry and wet samples) and XCT (dry), generates more information regarding the effective pore space contribution to fluid flow. The fluid flow simulations generate information about the connected pore network and the permeability evaluated rock sample at saturated condition.

Keywords: neutron radiography, neutron tomography, X-ray microtomography, fluid flow, porous media, grainstones

OPEN ACCESS

Edited by:
Sung Keun Lee,
Seoul National University,
South Korea

Reviewed by:
Youngseuk Keehm,
Kongju National University,
South Korea
Yoshio Kono,
Ehime University, Japan

****Correspondence:***
Miller Zambrano
miller.zambrano@unicam.it

Specialty section:
This article was submitted to Earth and Planetary Materials, a section of the journal Frontiers in Earth Science

Received: *08 July 2019*
Accepted: *27 November 2019*
Published: *19 December 2019*

Citation:
Zambrano M, Hameed F, Anders K, Mancini L and Tondi E (2019) Implementation of Dynamic Neutron Radiography and Integrated X-Ray and Neutron Tomography in Porous Carbonate Reservoir Rocks. Front. Earth Sci. 7:329. doi: 10.3389/feart.2019.00329

INTRODUCTION

Porous carbonate rocks constitute important reservoirs for water and hydrocarbons. The characterization in terms of fluid storage and migration of these reservoirs is challenging because of their petrophysical variability related to both depositional environment and subsequent diagenetic processes (e.g., dissolution, cementation, mineral replacement, deformation). A microstructural

analysis of the rocks provides a better understanding of reservoir quality, decreasing both uncertainty and risk.

In general, the microscale assessment of rocks is based on two-dimensional (2D) microscopy techniques (e.g., Tondi et al., 2006; Tondi, 2007), however three-dimensional (3D) approaches such as X-ray and neutron tomography (XCT and NCT, respectively) are becoming more popular for evaluation in the oil industry due to their non-destructive nature. Recent investigations of carbonate rocks have focused on evaluating the internal architecture and their impact on fluid flow in porous samples at the microscale by the integration of X-ray microtomography image analysis (Blunt et al., 2013; Cilona et al., 2014; Ji et al., 2015; Arzilli et al., 2016; Baud et al., 2017; Voltolini et al., 2017; Zambrano et al., 2017; Kaminskaite et al., 2019; Riegel et al., 2019) and computational fluid dynamics (Zambrano et al., 2018).

Neutrons with their peculiar properties (such as ability to penetrate metals) and sensitivity to hydrogen (Schillinger et al., 2000), offer a valuable tool for such studies related to flow problems like capillarity-driven (e.g., Cnudde et al., 2008) or pressure-driven flow (e.g., Yehya et al., 2018). Several studies have used Neutron radiation images to characterize the porosity, moisture, and water absorption in different materials such as concrete (De Beer et al., 2005; Kanematsu et al., 2009; Zhang et al., 2010, 2011; Yehya et al., 2018), steel (Zawisky et al., 2010), building stones (Hameed et al., 2006, 2009; Cnudde et al., 2008; Zawisky et al., 2010; Dewanckele et al., 2014), porous asphalt (Lal et al., 2014), sandstones (De Beer and Middleton, 2006; Hall, 2013), clay-rock (Stavropoulou et al., 2019), dehydration of molding sand (Schillinger et al., 2011), and cultural heritage artifacts (Fedrigo et al., 2018; Schillinger et al., 2018).

X-rays being electromagnetic in nature, interact mainly with the electrons of an atom and their interaction with matter depends on the atomic number and density. Therefore, information on the elemental or chemical composition of the studied sample is not directly obtained using X-ray CT. In the case of fluid content, X-ray requires a contrast agent (e.g., iodine or bromine solutions) that may modify the rock under investigation (Cnudde et al., 2008). On the other hand, the use of Neutron radiations permits to use a less reactive fluid (e.g., deionized water). In contrast to X-rays, neutrons are neutral particles and therefore interact with the atomic nucleus. Neutron interaction thus does not have any relationship with the atomic number. The main advantages of neutrons are their high penetration and also their sensitivity to isotopes of the same element (Anderson et al., 2009).

Concerning the physics behind the methods, the XCT method is based on the attenuation of X-rays passing through a material (Bultreys et al., 2016), expressed by the Lambert–Beer law:

$$I = I_0 e^{-\int \mu(s) ds} \tag{1}$$

here, the transmitted X-ray intensity I is a function of the incident intensity I_0 and the linear attenuation coefficient $\mu(s)$ along the raypaths. Neutron imaging is based on the interactions of neutrons with matter. Despite this is a quantum mechanical interaction, we can consider it as a classical particle interaction and express neutron attenuation with Eq. 2 (Anderson et al., 2009).

$$I(x) = I_i e^{-n\sigma x} \tag{2}$$

This equation is based on the assumption that a collimated beam of neutrons is incident on a thin sample of thickness x cm. I_i is the incident neutron flux, $I(x)$ is the neutron flux transmitted after interaction with the sample. The units in both cases being $cm^{-2}s^{-1}$. n is the number density of atoms (in the sample) and units are atoms cm^{-3}. σis the microscopic cross-section (the effective interaction area for the neutron with a nucleus), the units being cm^2. A conventional unit for the microscopic cross-section is the barn 10^{-24} cm^2. The product of n and σ gives the macroscopic cross-section Σ with units cm^{-1}. Since samples can be composed of several elements and isotopes, a summation has to be performed over all the elements and isotopes as shown in Eq. 3.

$$\Sigma_{tot} = \sum_j n_j \sigma_j = \sum_J \Sigma_j \tag{3}$$

Hence, the attenuation equation is now given by Eq. (4)

$$I(x) = I_i e^{-\Sigma_{tot} x} \tag{4}$$

The sensibility (attenuation ratios) of both tomographic techniques, Neutron and X-ray, to the different phases (solid and fluid) involved in the study of carbonates are shown in terms of cross-sections of the studied materials (**Table 1**). The cross-section can be defined as the likelihood of the interaction of an incident particle beam (e.g., neutrons and X-rays) with a target object (e.g., sample). In this case the neutron cross-section is given by Σ (macroscopic cross-section), and the X-ray cross-section is given by the linear attenuation coefficient μ. In the case of Neutron, the attenuation contrast between the fluid phases (water and air) is more significant that for the X-rays. Similarly, the neutrons radiation can provide a better contrast between water and carbonate rock (mainly $CaCO_3$).

The general aim of this work is to map imbibition and saturation during imposed constant flux experiments (forced imbibition) in porous carbonate rocks. In addition, single-phase flow is evaluated as a complement of the laboratory experiment to cover the saturated conditions. In order to do that, this work integrates four different experiments: (1) Constant-flux dynamic NR, (2) XCT at dry conditions, (3) NCT at dry and wet (water

TABLE 1 | Comparison of the cross-sections for neutrons and X-rays.

Material	Neutron, macroscopic cross-section, Σ [cm^{-1}]	X-ray, linear attenuation coefficient, μ [cm^{-1}]
H_2O	5.621	0.1839
N_2 (air)	0.001	0.00020
O_2 (air)	0 (negligible)	0.00024
$CaCO_3$ (calcite)	0.357	0.6486

Source data from https://webapps.frm2.tum.de/intranet/neutroncalc/, https://physics.nist.gov/PhysRefData/FFast/html/form.html.

saturated) conditions, and (4) Single-phase Lattice-Boltzmann simulations at saturated conditions.

Studied samples correspond to the Orfento (Maiella Mountain, Italy) and Favignana (Sicily, Italy) grainstones, which are important reservoirs for water and oil in Central and Southern Italy and have been widely studied from the macro (e.g., Tondi et al., 2006, 2016; Tondi, 2007; Antonellini et al., 2014) to the microscale (e.g., Baud et al., 2009; Zhu et al., 2010; Cilona et al., 2012; Ji et al., 2015; Arzilli et al., 2016; Zambrano et al., 2017, 2018). According to these authors, the studied rocks can be affected by both deformation features (i.e., fractures and deformation bands) and diagenesis (i.e., dissolution and cementation of calcite) causing some heterogeneities in the pore network.

The first aim of this work is to map the wetting front as a function of time through the studied rocks by means of constant-flux dynamic NR. By fixing the flux rate, the experiment represents a forced imbibition where the saturation of the wetting phase (deionized water) will increase during the time replacing the non-wetting phase (air). Since samples are initially dry, a significant capillarity driven flow is expected. Capillary forces control the spontaneous absorption, migration and retention of fluids in porous materials. Since both capillary force and velocity of capillary rise are controlled by pore network properties (e.g., porosity, average pore radius, connectivity) in complex pore-network geometries, the implementation of dynamic image experiments may help to better understand these processes (e.g., Cnudde et al., 2008). The interaction of capillary forces with heterogeneities (different pore structure) produces local variation of the saturation during immiscible displacement experiments (Chang and Yortsos, 1992). This phenomenon is called capillary heterogeneity and it is evaluated by the spatial variability of the capillary pressure-saturation function (Chaouche et al., 1994; Huang et al., 1995; Hejazi et al., 2019). The capillarity heterogeneity has been a topic of recent investigation in heterogeneous carbonates by combining experimental and numerical characterization of the capillary pressure (Hejazi et al., 2019). Despite we did not provide measures of capillarity pressure, our results may provide information about the imbibition front velocity and relative wetting phase saturation during time.

It is expected that during imbibition process in a dry porous material some air/gas will be trapped and eventually diffused into the wetting fluid (Cnudde et al., 2008). Therefore, the second aim of this work is to investigate the distribution of pores and fluid phases (i.e., air, deionized water) after the imbibition experiments. To do that, neutrons and X-ray tomographic techniques are integrated benefiting from their complementary properties. The X-rays are suitable for the grain distribution and pores, whereas neutrons provide a good contrast among the different phases. The last aim of this work is to investigate the fluid flow at saturated conditions which have been covered by performing computational fluid dynamics experiments. Direct flow simulations are ordinarily used to investigate single phase flow and transport in complex porous media (e.g., Blunt et al., 2013; Bultreys et al., 2016, and references therein). As an alternative to classical computational fluid dynamics approaches (finite difference, finite element method, finite volume method), the lattice-Boltzmann method (LBM) is well-established for modeling flow in complex geometries without need of any simplification (e.g., De Rosis, 2014; Ren et al., 2016; Yang et al., 2016; Benioug et al., 2017; Xie et al., 2017). The LBM describes the flow of a large number of particles interacting with the medium

TABLE 2 | Porosity and permeability data for the studied rocks.

	Favignana grainstones	Orfento grainstones
Permeability, k [m^2]	6.8×10^{-11} (3.1×10^{-11}–1.3×10^{-10}) *[k_{sa}; Tondi et al., 2016]*	4.4×10^{-13} (2.6×10^{-13}–7.4×10^{-13}) *[k_{sa}; Tondi et al., 2016]*
	4.0×10^{-11} (2.9×10^{-11}–6.0×10^{-11}) *[k_{lb}; Zambrano et al., 2018]*	3.9×10^{-13} (3.6×10^{-13}–4.2×10^{-13}) *[k_{lb}; Zambrano et al., 2018]*
		4.8×10^{-13} (9.9×10^{-15}–1.3×10^{-12}) *[k_{lg}; Sekti, 2010]*
		1.0×10^{-13} (4.2×10^{-15}–2.7×10^{-13}) *[k_{lw}; Sekti, 2010]*
		3.1×10^{-13} (1.1×10^{-13}–6.5×10^{-13}) *[k_{lw}; Marchesini, 2015]*
Porosity, Φ [%]	30.0 *[Pw; Φ_t; Tondi et al., 2012]*	*31.0–32.0 [Ph; Φ_c; Tondi et al., 2016]*
	26.72 ± 1.31 *[Px; Φ_c; Zambrano et al., 2017]*	31.9 (26.0–41.0) *[Ph; Φ_c; Sekti, 2010]*
	0.74 ± 0.05 *[Px; Φ_i; Zambrano et al., 2017]*	30.1 (27.0–34.0) *[Ph; Φ_c; Marchesini, 2015]*
	50.0 * *[Pw; Φ_t; Tondi et al., 2012]*	21.9 (15.3–28.5) *[Pw; Φ_t; Tondi et al., 2006]*
	45.0–50.0 * *[Ph; Φ_c; Tondi et al., 2016]*	*30.0–32.0 [Pw; Φ_t; Baud et al., 2009; Zhu et al., 2010; Cilona et al., 2012]*
		19.6 [Px; Φ_m; Ji et al., 2015]
		11.4 [Px; Φ_M; Ji et al., 2015]
		9.97 [Px; Φ_c; Ji et al., 2015]
		14.75 ± 0.15 *[Px; Φ_c; Zambrano et al., 2017]*
		0.6 *[Px; Φ_i; Zambrano et al., 2017]*

*Methods applied for permeability: [k_{sa}] in situ air-permeameter, [k_{lg}] laboratory gas-permeameter, [k_{lw}] laboratory water-permeameter, [k_{lb}] lattice-Boltzmann simulation. Methods applied for porosity: [Pw] triple weight porosity, [Ph] Helium pycnometer porosity, [Px] 3D X-ray micro-CT image analysis. Types of porosities: [Φ_t] total, [Φ_c] connected, [Φ_i] isolated, [Φ_M] macroporosity, [Φ_m] microporosity. *Lithofacies and facies different from the ones evaluated in this work.*

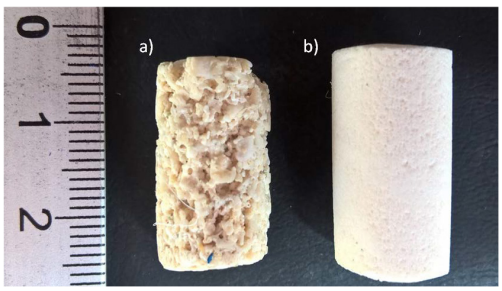

FIGURE 1 | Studied samples are made of carbonate grainstones. **(a)** Favignana grainstones **(b)** Orfento Grainstones, characterized by different texture and permeability (**Table 1**). Samples have a diameter of about 10 mm with a height of about 20 mm.

and among themselves following the Navier-Stokes equation at the macroscopic scale (Ladd, 1994). The LBM has been used to investigate transport and to compute permeability using as input 3D X-ray micro-CT images of rocks and soft sediments (e.g., Degruyter et al., 2010; Khan et al., 2012; Andrä et al., 2013; Shah et al., 2016; Zambrano et al., 2018) showing a good agreement with laboratory measurements over a wide range of permeability values (e.g., Keehm et al., 2004; Zambrano et al., 2018). The simplest LBM is based on the Bhatnagar-Gross-Krook (BGK) collision operator, which consists of a single relaxation time approximation (Bhatnagar et al., 1954). A more accurate alternative is the implementation of multiple relaxation times (MRTs) methods, which are more stable and solve the drawbacks (e.g., results depends on viscosity) of the BGK method (e.g., d'Humières, 1992; d'Humières et al., 2002).

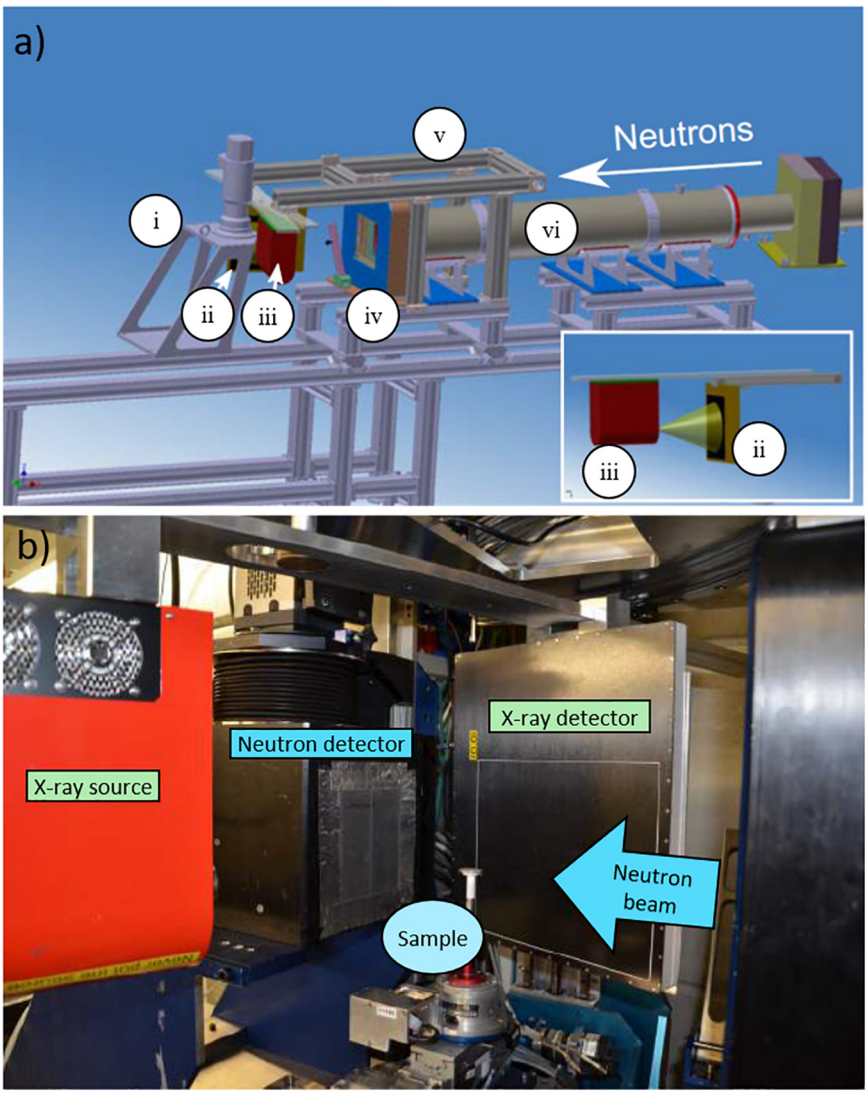

FIGURE 2 | Experimental setup. **(a)** A view showing the arrangement of the neutron source and detector and also the X-ray source and detector used for bimodal imaging (Kaestner et al., 2017). In detail, (i) Neutron camera detector, (ii) Flat panel detector, (iii) X-ray source, (iv) Neutron beam limiter, (v) Frame for X-ray beamline, and (vi) Neutron flight tubes. **(b)** A photograph showing the arrangement that was used for neutron and X-ray imaging (Kaestner et al., 2016).

The main interest of this study is related to enhanced gas recovery by imbibition process and residual gas saturation. However, the methodology is also relevant to applications like moisture assessment in construction stones.

MATERIALS AND METHODS

Samples

In this work, porous carbonate rocks from Maiella Mountain (Abruzzo, Italy) and Favignana Island (Sicily, Italy) were investigated. The Favignana grainstones (Early Pleistocene in age) consist of well-preserved bioclasts composed of *Vermetus*, *Serpula*, bivalves, echinoids, red algae, and corals ranging in size from submillimeter to centimeter (Tondi et al., 2012). The host rock is poorly cemented with the cement limited to the grain contacts, around echinoids, or within intragranular pores (Tondi et al., 2012). Its pore-network is mainly composed of well-connected intergranular pores characterized by a dominant diameter ranging between 100 and 400 μm (Tondi, 2007). In addition, isolated porosity is represented by intragranular space within the bioclast (Zambrano et al., 2017). The Favignana grainstones experienced a shallow burial depth of approximated 30 m (Tondi et al., 2012; Antonellini et al., 2014).The carbonate grainstones from the Maiella Mountain (Campanian to Maastrichtian in age), here after called Orfento grainstones, mainly consist of rudist fragments interpreted as a package of proximal bioclastic turbidites (Mutti, 1995). Detailed X-ray micro-CT analyses indicated that the pore space is characterized by both micro- and macro- pores (Tondi et al., 2006; Ji et al., 2015; Zambrano et al., 2017), however permeability is mainly controlled by pores with diameter larger than ca. 10 μm (Zambrano et al., 2018). These rocks experienced a maximum burial depth between 0.5 and 3 km (Ori et al., 1986; Graham et al., 2003; Rustichelli et al., 2016).

In general, both rocks have similar total porosity values (near 30%), however their permeability differs by two orders of magnitude (for details see **Table 2**). Zambrano et al. (2017, 2018) have explained these differences in permeability as related to diverse values of connected porosity, connectivity, pore size distribution, and tortuosity. In fact, the connected porosity observed by means of X-ray micro-CT (pixel size 9 μm) for the Favignana grainstones is near 27%, whereas the Orfento grainstones is less than 15% (Zambrano et al., 2017). Also, connectivity density (a value representing the number of redundant connections between pores) is higher for the Favignana grainstones. On the other hand, the specific surface area is greater (indicating a smaller grain size) for the Orfento grainstone (near 79.6 mm^{-2}) in comparison to the Favignana one (18.1–38.1 mm^{-2}). Moreover, the tortuosity is almost double for the Orfento grainstones in front of the Favignana one (Zambrano et al., 2018).

For the experiments, cylindrical samples were prepared with a diameter of 10 and 20 mm in height (**Figure 1**). These dimensions were chosen so that the cross-sectional water thickness would not be greater than 5 mm in order to get suitable neutron transmission. Considering the previous reported porosity (**Table 2**), it was estimated a maximum water thickness of 4.5 mm. Samples were placed in cylindrical holders made from Polytetrafluoroethylene (PTFE), commercially known as Teflon, with 12 mm of inner diameter closing the remaining space between sample and holder with Teflon tape. The choice of Teflon, for both sample holder and tape, was due to its suitability for both neutron and X-ray imaging (Domanus, 1992[1]). The water container was attached to a rotation stage by means of an adapter that allows the connection of a pipe for water without interfering with the experiment.

TABLE 3 | Neutron imaging parameters used at ICON.

Beam aperture (mm)	**20**
Experimental position	2
L/D ratio	343
Mean neutron energy	8.53 meV/3.1 Å
Neutron intensity φ ($n\ cm^{-2}s^{-1}mA^{-1}$)	1.3×10^7
Scintillator	Gadox + 6Li; Thickness 20 μm
Camera	Andor DW436K-BV SN: CCD-4544, (2048 pixel)
Exposure time	80 s
Number of projections for NCT	625 over 360 degrees
Dark images	5
Open beam images	5

Experimental Setup

The experiments were performed at the beamline for Imaging with COld Neutrons (ICON) at Swiss spallation neutron source (SINQ) of the Paul Scherrer Institut (PSI[2]) in Switzerland. Details of the ICON facilities and available instrumentations have been described by Kaestner et al. (2011). Bimodal imaging was performed using neutrons and X-rays, sequentially. The schematic layout is given in **Figure 2a** (Kaestner et al., 2017) and a photo of the setup is given in **Figure 2b** (Kaestner et al., 2016).

Neutron Imaging Experimental Setup

Neutrons were used for two-dimensional (2D) dynamic neutron radiography (NR) and three-dimensional (3D) neutron computed tomography (NCT measurements). These experiments were carried out at position number 2 at the ICON instrument (Kaestner et al., 2011). The parameters for these measurements are given reported in **Table 3**.

X-Ray Imaging Experimental Setup

Bimodal imaging was performed using neutrons and X-rays. **Figures 2a,b** illustrate the experimental setup. The X-ray source delivers a polychromatic cone-beam. The specifications of the X-ray source and detector are given in **Table 4**. In our case, XCT was performed at a voltage of 80 kV, a current of 200 μA and X-ray spot size was 5 μm. The detection system used for XCT in this case was the same as that used for the NCT. The source-to-detector distance was 185 mm while the source-to-object distance

[1]http://henke.lbl.gov/optical_constants/atten2.html

[2]https://www.psi.ch/en/niag/comparison-to-x-ray

TABLE 4 | X-ray imaging parameters for bimodal imaging at ICON (Kaestner et al., 2017).

X-ray source	
Model	Hamamatsu L212161-07
Tube voltage	40–150 kV
Tube current	500 μA
Max power	75 W
Spot size available	7–50 μm
Cone angle	43°

was 165 mm. A set of 625 projections over a total scan angle of 360° was acquired with an exposure time/projection of 40 s. A total of 10 dark-field and 10 flat-field images we acquired prior to the tomographic scan acquisition.

Dynamic Neutron Radiography

Time-lapsed or dynamic NR was performed for two different samples pertaining to Favignana and Orfento grainstones. Similar to Cnudde et al. (2008), we have performed a dynamic NR experiments to investigate the position of the wetting front as a function of time. Our experiments differ from Cnudde et al. (2008) in that we did not use the gravity as force for triggering the flow, instead we used only constant flux rate (forced imbibition). In order to introduce deionized water into the system, a dual syringe pump (Pharmacia P-500) was used with a flow rate set to 1 ml/h. The pumping device can provide a maximum pressure of 5.0 MPa. Since the studied samples are highly porous and pervasive, it was expected (and tested) that the threshold pressure was not be reached during the experiments.

The output data consist of a time series of 2D NR images. With the aim to map the dynamic flow front in each sample, at the selected flow rate, about 26 neutron radiographs (one radiograph every 90 s) were acquired until the sample was filled with water. For corrections, 5 images of dark current, 5 flat field beam images, and a radiograph of the dry sample were taken before the experiment started. To indicate the presence of water, the original dry condition image is subtracted to radiograph to the n-time radiograph. During the processing, the noise was removed with a median filter by using the freeware ImageJ (Schneider et al., 2012).

For estimating a pseudo water saturation trough time, a series of profiles were made in each photograph. The first intention of this analysis is to roughly estimate the advancement of water flow

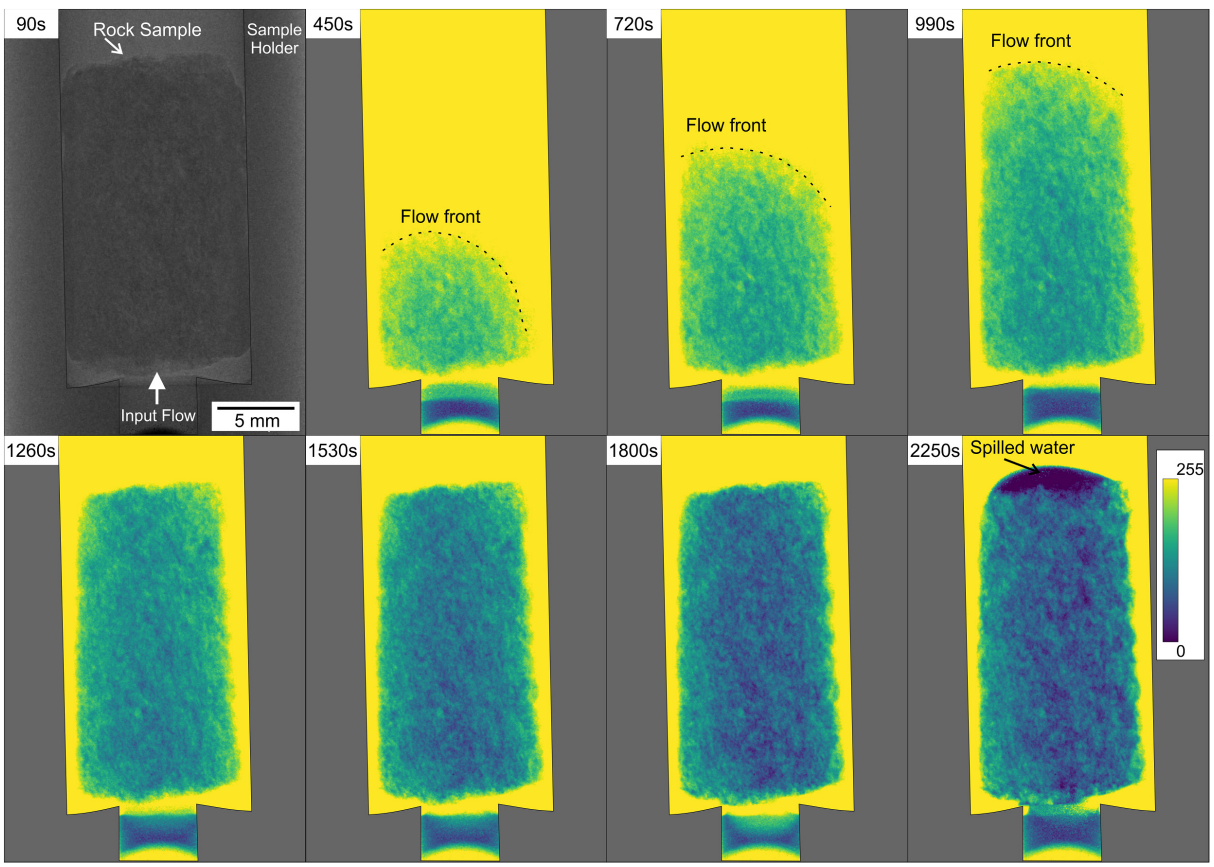

FIGURE 3 | Time lapsed neutron radiographs showing the flow of deionized water for the sample corresponding to a Favignana grainstone. The image at 90 s (in original gray scale color) corresponds to a stage where the water still not entered into the rock sample. The rest of the images (in false color) correspond to input fluid into the sample obtained by subtracting the original dry condition (90 s) to radiograph to the n-time radiograph. The stages from 450 to 990 s show the fluid filling the rock sample. The stages from 1260 to 2250 s show an increment in the fluid saturation until the water is spilled due to oversaturation.

and to distinguish important heterogeneities within the samples. The pseudo water saturation was estimated by processing the raw data X_{awr} voxel by voxel following the equation (partially modify) proposed by Riaz et al. (2007):

$$S = 1 - \left(\frac{X_{awr} - X_{wr}}{X_{ar} - X_{wr}} \right) \quad (5)$$

Where the subscripts *ar* and *wr* refer to air-filled and water-filled rock, respectively. The first case corresponds to images taken before the flow started (dry condition), whereas the water-filled stage was arbitrary selected as the time when the water started to spill out of the sample. The rate of water volume injected into the sample is given by the flux rate of the pump. In comparison, it was estimated the fraction of water within the invaded volume of rock a certain time. This data is useful to distinguish when the imbibition is dominated by capillarity forces or the constant flux rate.

Dual Modality XCT and NCT Imaging

For the static tomographic experiments, a single sample corresponding to Favignana grainstones was selected. This approach consists of three steps: (1) XCT of a sample in dry condition, (2) NCT of the same sample in dry, and (3) wet conditions (water-filled).

An XCT scan was recorded with a pixel size of 13.5 μm. A set of 375 projections were taken over 360 degrees with air on both sides of the sample. The exposure time per projection was 30 s. For the NCT at dry and wet conditions, the pixel size was also set to 13.5 μm. A total of 625 projections were planned over 360°; however, for the dry case the acquisition was stopped after about 280 degrees due to time limitations. The exposure time was 80 s per projection. Before every CT scan, 5 dark current and 5 open beam images were acquired.

The reconstruction was done by the Octopus 8.8 software (Vlassenbroeck et al., 2006). The beam was chosen as having a cone-beam geometry although it was nearly parallel, but this option was better as the beam is slightly divergent. Then, the noise was removed using a 3D Median filter in ImageJ. Ring artifacts on the reconstructed slices were removed using the modified Sijbers & Postonov algorithm (Brun et al., 2011) which is part of the *Pore3D* software library (Brun et al., 2010; Zandomeneghi et al., 2010). For the NCT with incomplete projections, the MuhRec

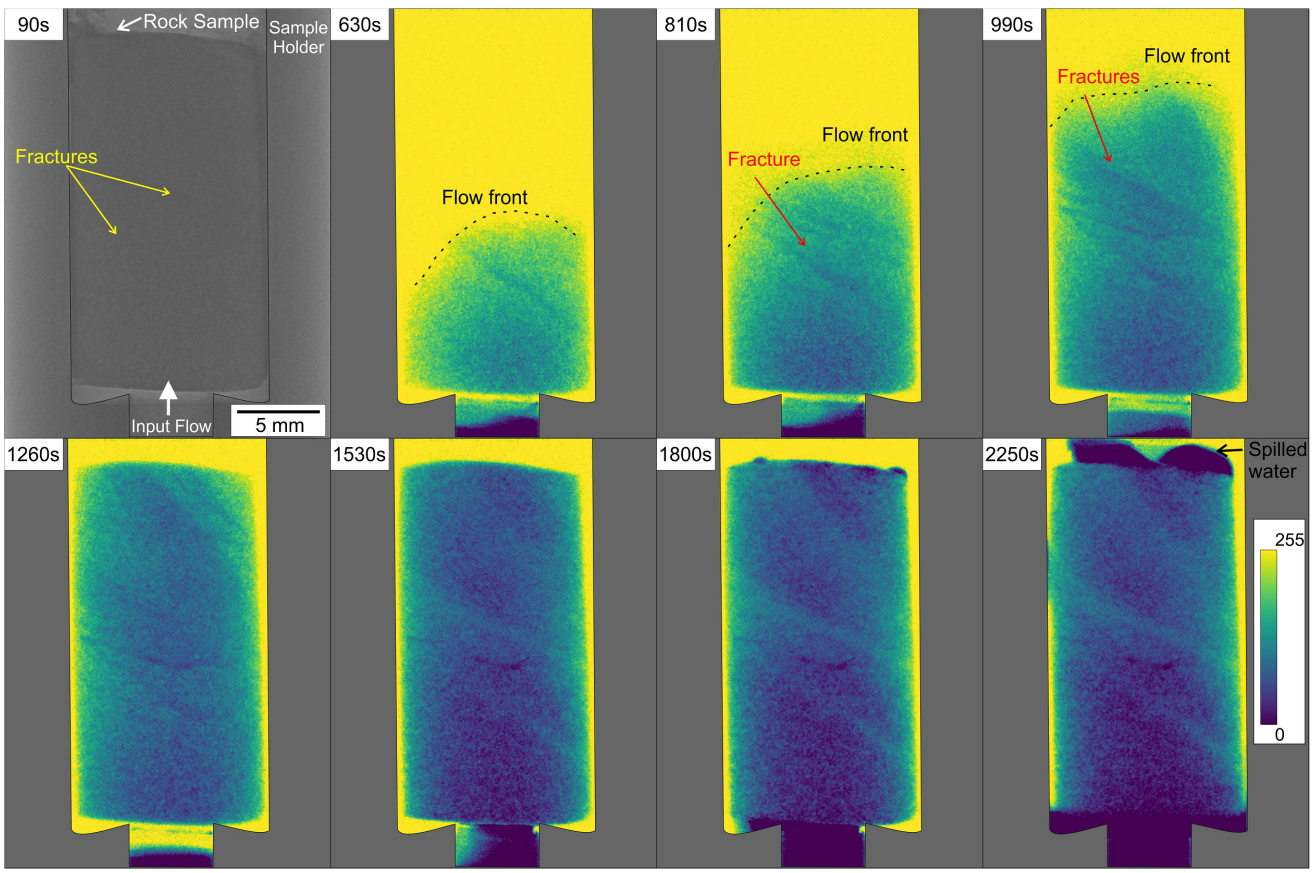

FIGURE 4 | Time lapsed neutron radiographs showing the flow of deionized water for the sample corresponding to the Orfento grainstone containing fractures. The image at 90 s (in original gray scale color) corresponds to a stage where the water still not entered into the rock sample. The rest of the images (in false color) correspond to input fluid into the sample obtained by subtracting the original dry condition (90 s) to radiograph to the n-time radiograph. The stages from 630 to 1260 s show the fluid filling the rock sample. The stages from 1530 to 2250 s show an increment in the fluid saturation until the water is spilled due to oversaturation.

tomographic reconstruction software was used (Kaestner, 2011). The filtering of the data was done using the ISS filter in KipTool (the in-house developed image processing tool at ICON).

For the segmentation of the X-ray images in dual components, voids, and solid phase (framework grains and cement), the automatic multiphase k-means clustering algorithm (Hartigan, 1975; Hartigan and Wong, 1979) was used. The algorithm was set to 4 classes and implemented twice in order to get most of the visible pores. Results are binary images composed of voids and grains. After this, the tool 'Find Connected Structures' of the open source Fiji software (Schindelin et al., 2012) was used for dividing the pore space into two components: (i) connected pores and (ii) isolated pores. For the simulations, only the connected pore networks were used for facilitating the computation.

Considering the attenuation factors for the different studied phases (water, air, and carbonate rock; **Table 1**), a rough indicator of the water content was founded by using the difference of NCT wet-dry images. In the gray color intensity scale, wet zones tend to have a more whitish color in comparison to air or carbonate rock. Therefore, warmer colors indicate a higher saturation of water.

Lattice-Boltzmann Method and Permeability Calculation

Since the laboratory experiments were performed on dry samples, Lattice-Boltzmann simulations were useful to investigate the flow at saturated condition. The simulations were executed by means of the open-source computational fluid dynamics software PALABOS (Latt, 2009) using the methodology introduced by Degruyter et al. (2010) and later modified by Zambrano et al. (2018). The methodology consists of imposing a single-phase fluid flow through the segmented 3D images by maintaining a fixed pressure gradient between the inlet and outlet faces of the volume, while the rest of the faces were padded. The interface pore-voids was converted to bounce-back boundary conditions. The main difference with the methodology proposed

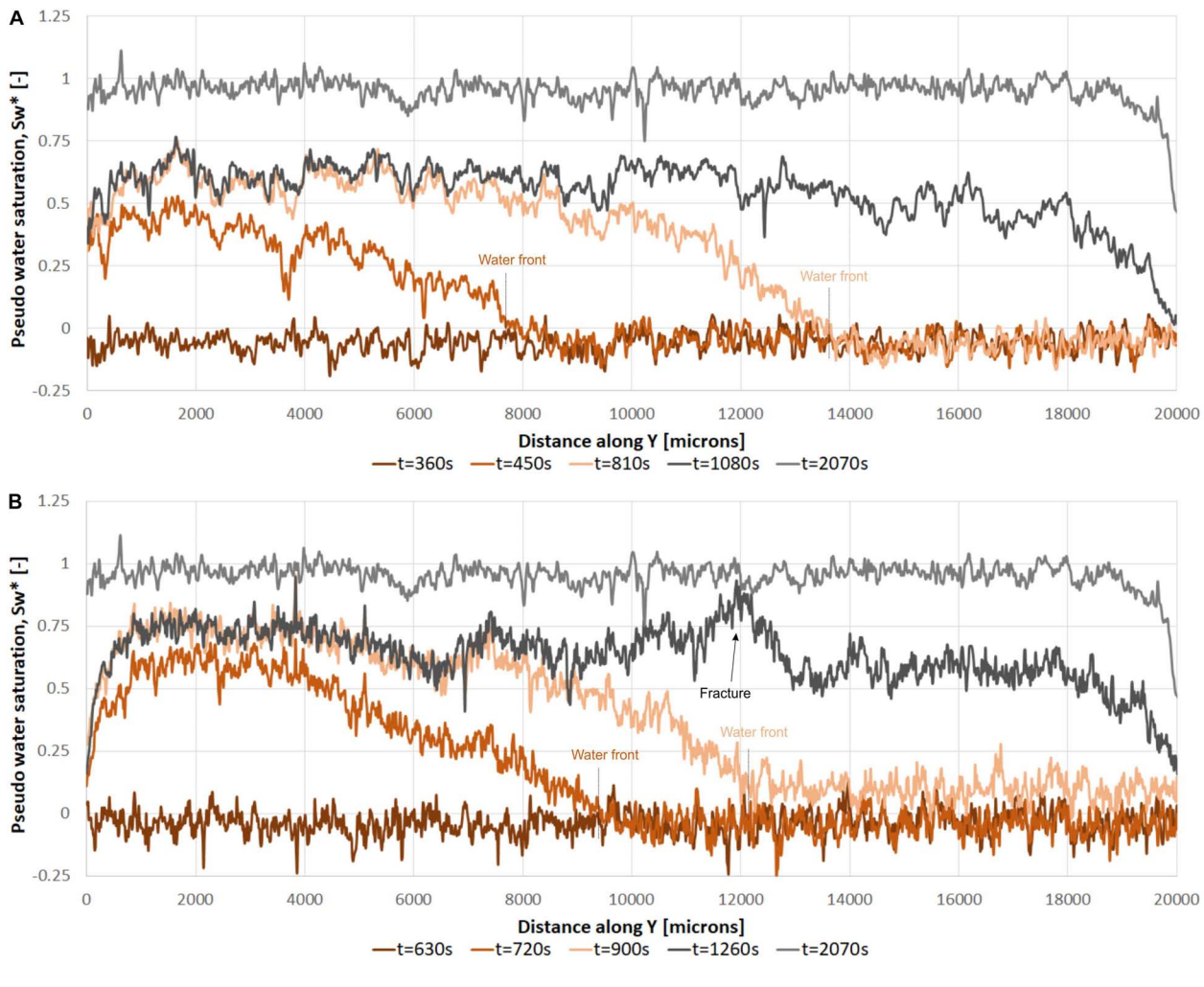

FIGURE 5 | Longitudinal profiles indicating the migration of the flow front and the relative pseudo saturation of the **(A)** Favignana grainstones, and **(B)** Orfento grainstones samples, indicating and anomalous increase of the saturation due to fractures (t = 1260 s).

by Degruyter et al. (2010) is the replacement of the collisional operator BGK by an MRT (d'Humières et al., 2002) with a D3Q19 lattice, which guarantees results viscosity independent (Zambrano et al., 2018). The steady state condition of the simulation is considered after the standard deviation of the average energy falls blow 10^{-4} after 1000 time-steps, Degruyter et al., 2010). After that, the permeability component parallel to the imposed flow can be computed applying the Darcy's law,

$$\frac{\delta P}{\delta x} = \frac{\mu}{k} U \tag{6}$$

where, $\delta P/\delta x$ is the pressure gradient, μ the fluid kinematic viscosity, and U the average fluid velocity per unit of area. All the variables are handled in lattice units before the permeability computation, results are transformed to SI units multiplying by the effective length of the voxel side in meters.

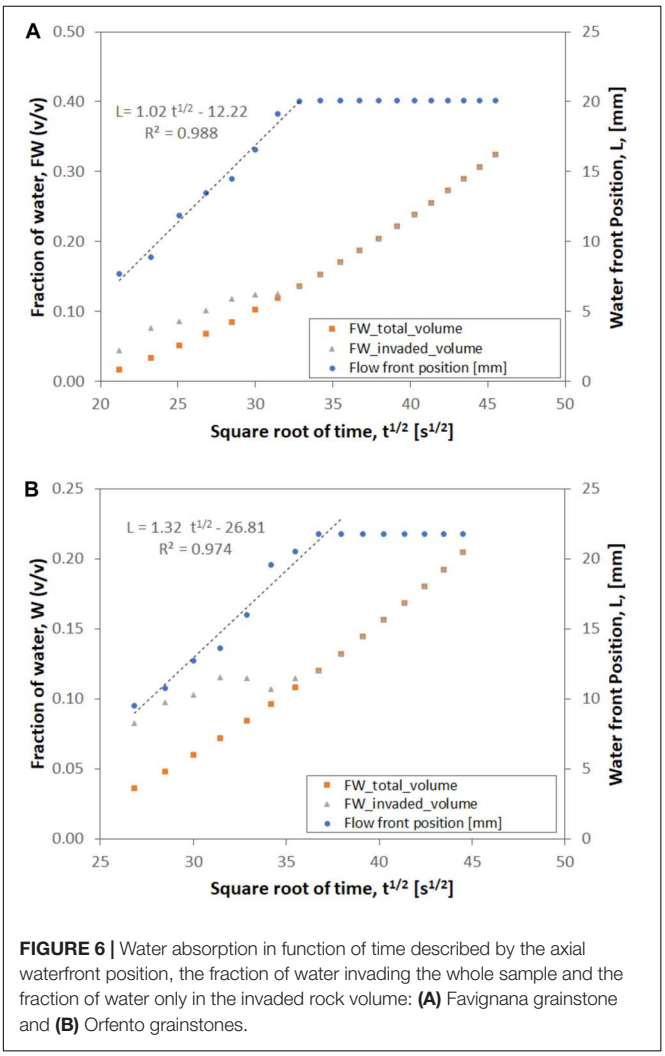

FIGURE 6 | Water absorption in function of time described by the axial waterfront position, the fraction of water invading the whole sample and the fraction of water only in the invaded rock volume: **(A)** Favignana grainstone and **(B)** Orfento grainstones.

RESULTS

Dynamic Neutron Radiography

The results of the experiment consist of a series of time lapse neutron radiographs obtained at a time interval of 90 s indicating the flow front trough time (**Figures 3**, **4**). In addition, longitudinal profiles, flow front progression and water saturation graphs were plotted to show the results in a more quantitative manner (**Figures 5**, **6**).

In the case of the Favignana grainstones, the studied sample seems homogeneous at initial dry conditions (NR 90s). However, the time-lapsed neutron radiographs (**Figure 3**) show that the flow front is slightly inclined (NR 90s -NR 990s). Initially the water invaded the rock sample rapidly, however the invaded volume is not highly saturated (NR 90s -NR 990s). The saturation increment is more evident in the **Figures 5A**, **6A**. After the sample is totally invaded by water, the water saturation increases (NR 1290s – NR 1800s) until the water spilled out (NR 2250s). The profiles confirm both the initial rapid migration of the flow front and continuous saturation of the sample trough time until the water spilled out (**Figures 5A**, **6B**). The profiles also indicate the heterogeneities in the sample associated with local porosity variation. In general, these heterogeneities are kept in time but their general intensity changes as an indicator of an increment of the water saturation.

In the case of the Orfento grainstone, the initial image in dry conditions (NR 90 s) shows a sample with smaller grain/pore size with respect to Favignana grainstone. Whereas, the time lapsed neutron radiographs, once the flow started (**Figure 4**), rapidly show the presence of lineations (fractures) characterized by an earlier saturation. These fractures could be created during the preparation of the sample or likely of natural origin. These features control an anisotropic distribution of the flow. The fractures are also recognized as important heterogeneities controlling the fluid flow in the longitudinal profiles (**Figure 5B**). In this graph, an 'anomalous' rapid increment in water saturation is observed at the time 1260s in correspondence to the presence of fractures. A similar migration of the flow front and increment of the relative saturation is showed by the profiles through time (**Figure 6B**).

We have observed that water saturation was driven by to mechanism: capillarity and constant flux rate. The limit between the two flows mechanism correspond to the time when the water reaches the top of the rock samples. After that, the saturation starts to increase uniformly according to the constant flux rate provided by the pump. This limit seems to be preceded by an inflection of the fraction of water curve. During the capillarity driven flow, the waterfront velocity for the Favignana samples is slightly lower (0.0202 mm/s) than for the Orfento sample (0.0208 mm/s). In the **Figure 6**, the flow front vs. square root of time presented some scattering and variability with the expected best fit line. This variability is more important for the Orfento grainstones, which is characterized by the presence of fractures.

The maximum fraction of water absorbed by the samples seems a good indicator of the connected porosity. In the case of Favignana sample, the fraction of water reached during the capillarity driven flow is near 12.53%, whereas the maximum,

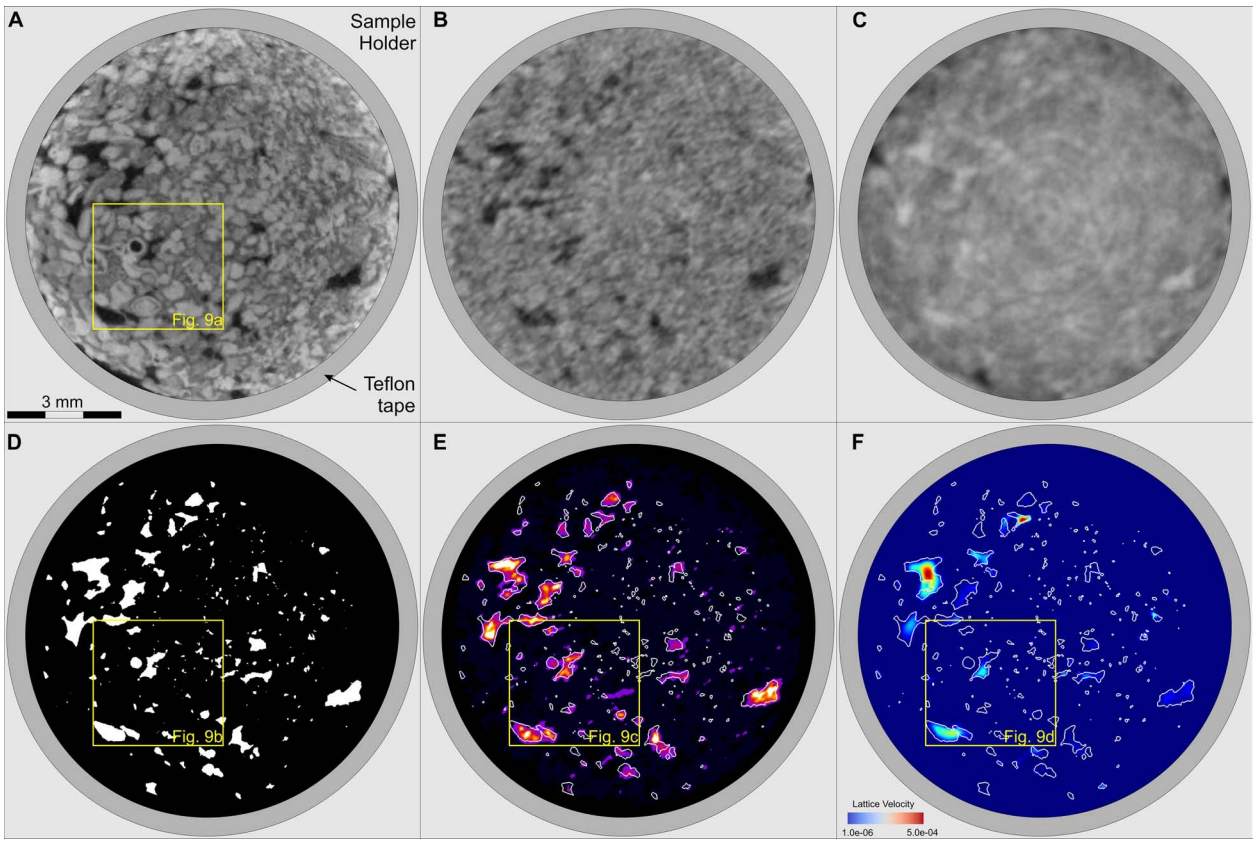

FIGURE 7 | Comparison of resulting images near the middle of the sample. **(A)** XCT at dry conditions, **(B)** NCT at dry conditions, **(C)** NCT at wet conditions, **(D)** segmented pores from XCT, **(E)** Difference of NCT wet-dry images using as mask the segmented macropores from the XCT data, warmer colors indicate a higher saturation of water, **(F)** Lattice velocity images obtained by using LBM fluid flow simulation, warmer colors indicate a higher lattice velocity of the simulated flow. The pixel size is set to 13.5 μm for both NCT and XCT images.

after the saturation of the sample, is near 32.4%. For the Orfento sample the fraction of water reached during the capillarity driven flow is near 11.5%, and the maximum at the end of the experiment is near 20.45%.

Integrated XCT an NCT Imaging

Imaged from both methods were aligned and presented with the same nominal resolution (pixel size equal to 13.5 μm) for comparing and integrating the results (**Figure 7**). The XCT data provides a good evaluation of rock components (framework grains, matrix, cement, and pores). Particularly the resolution of the images allows to distinguish and segment the macropores (diameters between 50 and 800 μm) contained in the sample (**Figure 7A**). It is expected that some pores below the nominal resolution (pixel size equal to 13.5 μm) are present in the sample.

The strength of neutron imaging is its sensitivity to hydrogen and hence to the fluid in the sample. As shown in the **Table 1** neutrons give a very high contrast between the three main phases in the studied samples (i.e., water, air, and carbonate rock). The limitation of the neutron image is that the pores/grains are not very well-defined (images are blurry in comparison to XCT). However, the method proved useful for comparing the wetting-phase saturation after the inhibition experiment. In fact, NCT images at dry and wet conditions look very different (**Figures 7B,C**, respectively). In the use gray color bar, wet zones tend to have a more whitish color in comparison to air or carbonate rock. This is likely due to the sensitivity of NR to hydrogen and the different attenuation factors for the different studied phases (water, air, and carbonate rock). A rough estimation of the relative concentration of water considering the difference of NCT wet-dry images (**Figure 7E**). In this figure, warmer colors indicate a higher saturation of water.

Some differences between the pores extracted from X-ray images and the pores filled by water (differences of NCT wet-dry images) were observed (**Figures 7**, **8**). The first case some detected pores are not filled by water, this could be related to the presence of isolated intragrain (e.g., bioclast) pores previously reported by Zambrano et al., 2017). Also, this could be attributed to the presence of air bubbles trapped due to a 'rapid' and low-pressure water flow. This fact may explain the presence of macropores partially filled with water. In addition, the water could have taken preferable pathways like the borders of the sample even though it was well-sealed by Teflon tape. Another important difference, correspond to apparent zones filled by water that do not correspond to the observed pores. This is more likely due to the presence of micropores (sub-resolvable pore by XCT) that are

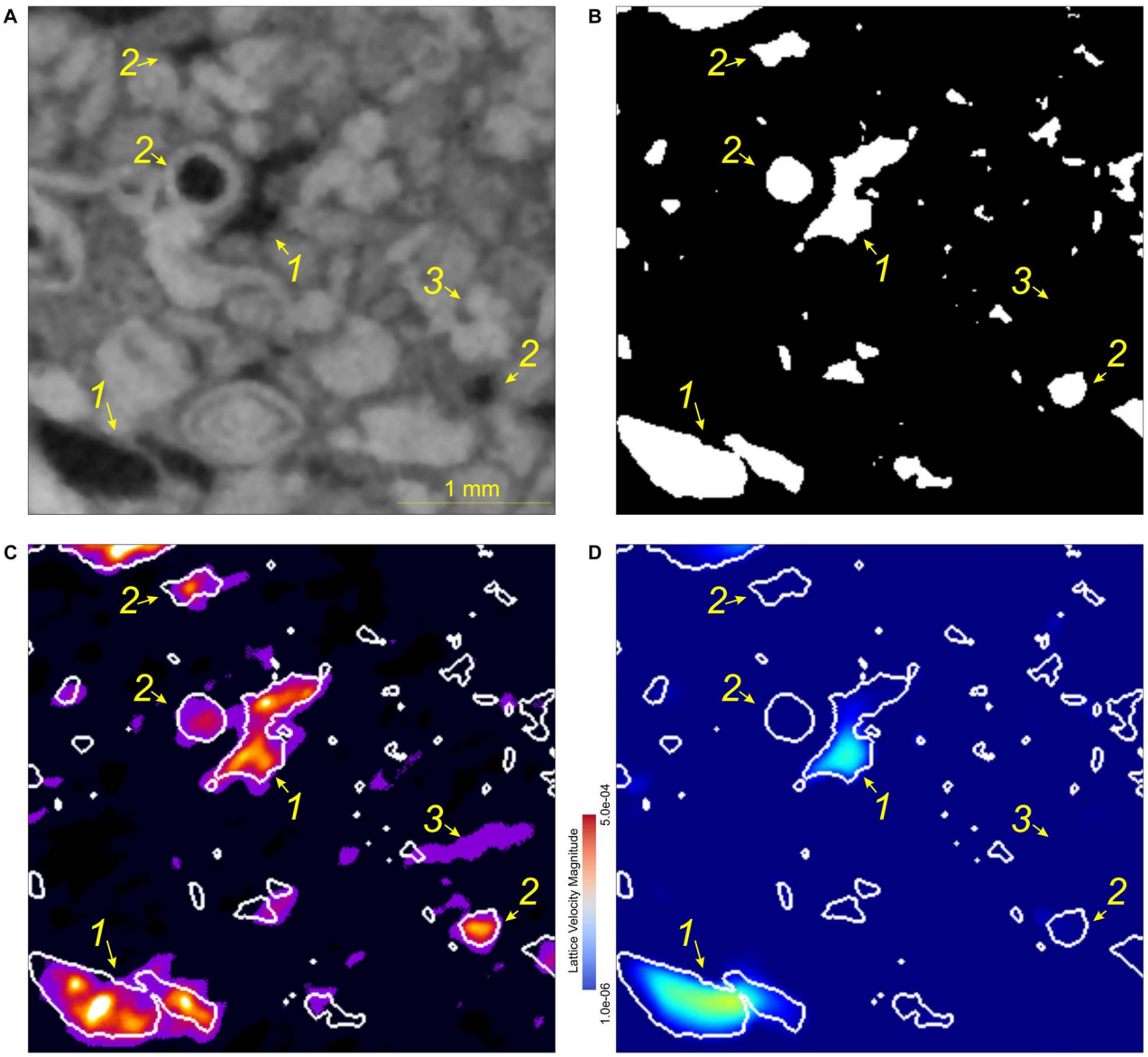

FIGURE 8 | Detail of the comparison of resulting images (**Figure 7**). **(A)** XCT at dry conditions, **(B)** segmented pores from XCT, **(C)** Difference of NCT wet-dry images using as mask the segmented macropores from the XCT data, warmer colors indicate a higher saturation of water, **(D)** Lattice velocity images obtained by using LBM fluid flow simulation, warmer colors indicate a higher lattice velocity of the simulated flow. Three different cases are observed: (1) Macropores filled by water and connected according to LB simulation, (2) Macropores filled by water and poorly connected according to LB simulation, and (3) XCT sub-resolvable pores/throats filled by water only observed in Neutron experiments.

contributing to the water flow. The structure of these pores may be not clearly defined in the images, however the water presence within the pores can be mapped.

Fluid Flow Simulation

The fluid flow simulations provide information about the possible behavior of the flow through time after saturated conditions. In steady state conditions we compared the velocity field (**Figure 7F**) with the connected pore network (**Figure 7D**) extracted from the X-ray micro-CT images. Results indicate that some pores do not contribute to the flow in simulation; however, in reality these pores are connected (**Figure 8**, label 2). This is likely an issue of image resolution of the XCT. Similarly, some pores below the resolution (XCT) contributing to the flow (NCT) are not detected and therefore not included in the simulation (**Figure 8**, label 3). Also, pores located at the lateral edges could be excluded if they are not connected to the top and base of the sample. Therefore, the pores contributing to flow in the simulation are only macropores clearly connected (**Figure 9**). In these regards, the computed permeability ($1.29 \times 10^{-13}\ m^2$) is slightly lower than the values obtained by Zambrano et al. (2018) using X-ray micro-CT at higher resolution (see **Table 2**). In fact, the calculated

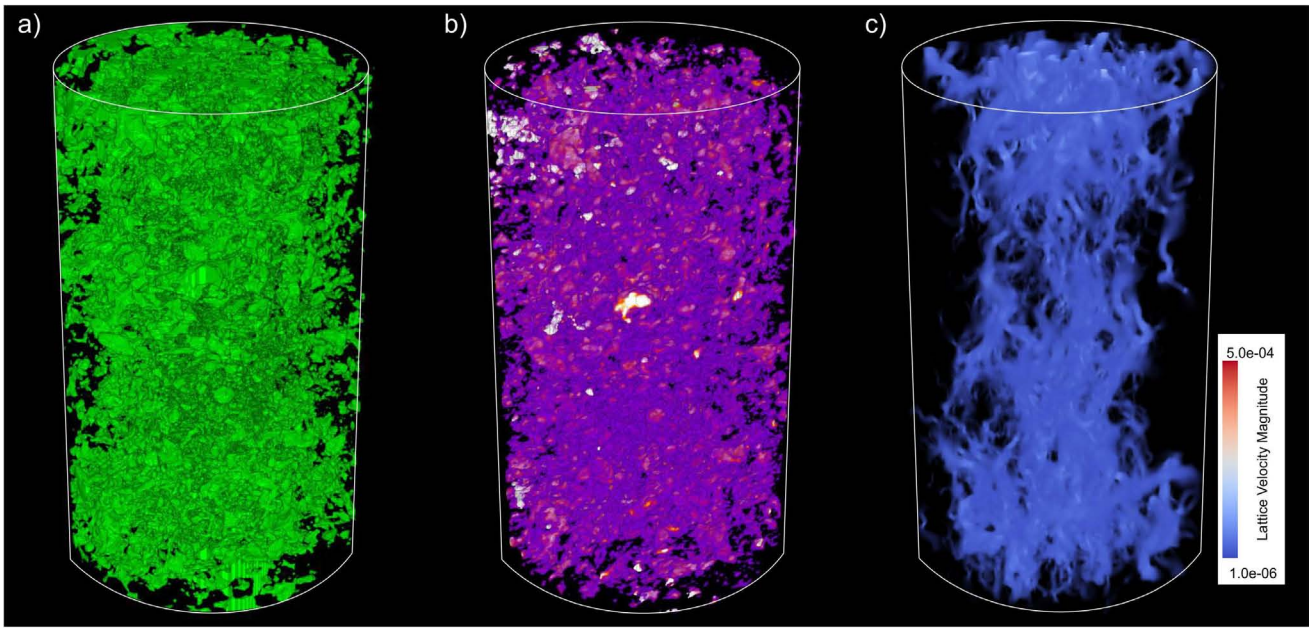

FIGURE 9 | Comparison of resulting 3D renderings of **(a)** Segmented pores from XCT (in green), **(b)** Difference of wet-dry NCT images, **(c)** Lattice velocity images obtained by LBM fluid flow simulation.The sample size is ca. 10 mm × 20 mm (diameter × height), whereas the pixel size was set to 13.5 μm.

permeability tends to be underestimated at low spatial resolution of pore network model (see Zambrano et al., 2018).

DISCUSSION

Methodology Implications

The dynamic 2D NR permits the evaluation of the front of the fluid flow as a function of time. However, we detected an initial front likely driven by capillarity forces and later increment of the saturation on the wetting phase. The latter is likely driven by a forced imbibition caused by the constant flux rate. The limit of these domains is given by the time when the waterfront reaches the top of the sample. Also, it was possible to observe the influence of sample heterogeneities on the fluid flow. These heterogeneities can be the intergranular pores or fractures. Particularly, some fractures observed in the Orfento sample could be natural or related to the sample preparation. In contrast to some sandstone samples investigated by Cnudde et al. (2008) we did not observe any 'abnormal' dual-waterfront due to these heterogeneities. Nevertheless, the NR methodology provides information in two-dimensions resulting in a smooth boundary water/air. As a consequence, the detail control on the surface geometry and roughness (e.g., Alava et al., 2004) was not possible. This issue could be solved by implementing time-step NCT in further investigations. We found that final values of water absorbed by the samples are near and slightly higher that the reported values of connected porosity using XCT (Zambrano et al., 2017). Therefore, the reached water saturation in the experiments should be close to the available porosity. However, some air bubbles should remain trapped in the rock.

The dynamic 2D NR experiments showed differences regarding pore structure between the two evaluated rocks that have been reported by previous authors (Tondi et al., 2016; Zambrano et al., 2017, 2018). In the case of Favignana grainstones a high heterogeneity of the gray values in the image profiles was observed, whereas the Orfento grainstones were more regular and homogeneous. This is related to the huge differences in texture, grains and pores sizes being near 10 times larger in the Favignana grainstones in comparison to the Orfento ones. This difference in texture (specific surface area, connectivity, tortuosity) is responsible that Favignana grainstones have a permeability two orders of magnitude higher than the Orfento grainstones. Since both rocks have similar porosity, but different pore-throat sizes. The capillarity forces driving the flow at this first stage are expected to be very different. In fact, lithofacies with larger pore-throat sizes are expected to have small initial displacement pressures, and therefore the air phase can be easily displaced by the injected water. Major initial displacement pressures are expected in lithofacies with smaller pore-throat sizes, which may buffer the displacement of air by water phase. Therefore, differences in the flow velocity in the capillarity driven flow domain, may be related to both the difference in permeability and pore geometry (diameter, connectivity, tortuosity) between the two rocks as have been reported by Zambrano et al. (2017, 2018).

The combined use of XCT and NCT methodologies can provide information regarding the pore space architecture (X-rays) and the fluid contents (neutrons). According to our results, X-rays can define the geometry of the solid components of the rocks (framework grains, cements, and matrix). Neutrons, however, show images more diffused and only a few macropores are distinguished. On the other hand, comparing NCT in dry

and wet conditions allows to discriminate the presence of water within pores. In fact, the method seems to provide information on micropores contributing to fluid flow even below the actual spatial resolution of the images. On the other hand, the NCT at wet conditions reveled air trapped in the pores. This issue may be related to the initial unsaturated and low-pressure conditions of the experiment.

This approach using NR and integrated XCT an NCT is relevant for the study of petroleum systems, where the capillarity governs the initial distribution of the different phases of fluids within the reservoir (Brown, 1951), control the relative permeabilities, pressure and saturation of different phases during production (Jerauld and Rathmell, 1997; Christiansen, 2001). Particularly, the implemented approaches were useful for mapping fluid flow as a function of time, wetting phase (water) saturation dynamically and at the end of the experiments. In these regards, the methodology finds uses to the study of spontaneous and forced imbibition gas recovery (e.g., Di Stefano et al., 2017), irreducible water estimation useful for petrophysical evaluations and oil recovery planning (e.g., Treiber and Owens, 1972; Salathiel, 1973; Morrow and Melrose, 1991). Another important application of this method could be the evaluation of moisture inside building stones (e.g., Cnudde et al., 2008). Here the absorption of water by capillarity can cause important degradation of in building materials (e.g., carbonate rocks).

CONCLUSION

In this work we have applied a combined approach (X-ray and neutron imaging) for mapping the fluid flow within porous carbonates rocks and estimated the effective pore space properties. The methodology includes dynamic neutron radiography (NR), integrated X-ray and neutron tomography (XCT and NCT, respectively), and computational fluid dynamics simulations.

The dynamic NR was very useful for mapping water flow through the studied samples. From these experiments we conclude that: (i) Fractures presented in samples generate a non-uniform flow front, indicating some anisotropy on permeability, and (ii) in unsaturated samples, water fills rapidly part of the pore-structure which may indicate a capillary control of the flow. Lately, the sample is uniformly saturated until the water spills out, indicating a control of macropores on fluid flow and storage.

The combined tomographic experiments including X-ray- and neutron-based techniques were useful for mapping the three-dimensional distribution of pores, and the fluids within them. In particular, the difference between NCT images in dry and wet conditions allows the determination of water, even in partially filled pores and pores with sizes below the spatial resolution. In fact, the limitations (i.e., missing pores and throats, undervalued connectivity) of performing fluid flow simulations using X-ray images can be overcome with neutron-based methods.

DATA AVAILABILITY STATEMENT

The datasets generated for this study are available on request to the corresponding author.

AUTHOR CONTRIBUTIONS

MZ: collection and preparation of samples and experiments in site. FH: experiments in site and elaboration of data. KA: setup preparation, experiments in site, and elaboration of data. LM and ET: interpretation and elaboration of data.

FUNDING

This research was supported by the FAR ('Fondi di Ateneo per la Ricerca,' University of Camerino research funds) Project 2014 "Characterization and modelling of natural reservoirs of geofluids in fractured carbonate rocks" and the Reservoir Characterization Project (www.rechproject.com). FH acknowledges the receipt of a fellowship from the ICTP Programme for Training and Research in Italian Laboratories, Trieste, Italy.

ACKNOWLEDGMENTS

This work is based on experiments performed at the Swiss spallation neutron source SINQ of the Paul Scherrer Institute in Villigen (Switzerland). We acknowledge Prof. Giulio Lupidi for providing the syringe pump used in the experiments. We also acknowledge Elettra synchrotron facility (Italy) for allowing us to use the *Pore3D* software and the related training. We also thank the staff of a local company (Meccanica Matelicese s.r.l., Matelica, Italy) who kindly provided support for the design and creation of the sample holders.

REFERENCES

Alava, M., Dubé, M., and Rost, M. (2004). Imbibition in disordered media. *Adv. Phys*. 53, 83–175. doi: 10.1080/00018730410001687363

Anderson, I. S., McGreevy, R. L., and Bilheux, H. Z. (2009). *Neutron Imaging and Applications*, Vol. 2209. Berlin: Springer Science+ Business Media, 980–987.

Andrä, H., Combaret, N., Dvorkin, J., Glatt, E., Han, J., Kabel, M., et al. (2013). Digital rock physics benchmarks—Part II: computing effective properties. *Comput. Geosci*. 50, 33–43. doi: 10.1016/j.cageo.2012.09.008

Antonellini, M., Cilona, A., Tondi, E., Zambrano, M., and Agosta, F. (2014). Fluid flow numerical experiments of faulted porous carbonates, Northwest Sicily (Italy). *Mar. Petrol. Geol.* 55, 185–201. doi: 10.1016/j.marpetgeo.2013.12.003

Arzilli, F., Cilona, A., Mancini, L., and Tondi, E. (2016). Using synchrotron X-ray microtomography to characterize the pore network of reservoir rocks: a case study on carbonates. *Adv. Water Resour.* 95, 254–263. doi: 10.1016/j.advwatres.2015.07.016

Baud, P., Exner, U., Lommatzsch, M., Reuschlé, T., and Wong, T. F. (2017). Mechanical behavior, failure mode, and transport properties in a porous carbonate. *J. Geophys. Res. Solid Earth* 122, 7363–7387. doi: 10.1002/2017jb014060

Baud, P., Vinciguerra, S., David, C., Cavallo, A., Walker, E., and Reuschlé, T. (2009). Compaction and failure in high porosity carbonates: mechanical data and microstructural observations. *Pure Appl. Geophys.* 166, 869–898. doi: 10.1007/978-3-0346-0122-1_7

Benioug, M., Golfier, F., Oltéan, C., Buès, M. A., Bahar, T., and Cuny, J. (2017). An immersed boundary-lattice Boltzmann model for biofilm growth in porous media. *Adv. Water Resour.* 107, 65–82. doi: 10.1016/j.advwatres.2017.06.009

Bhatnagar, P. L., Gross, E. P., and Krook, M. (1954). A model for collision processes in gases. I. Small amplitude processes in charged and neutral one-component systems. *Phys. Rev.* 94:511. doi: 10.1103/physrev.94.511

Blunt, M. J., Bijeljic, B., Dong, H., Gharbi, O., Iglauer, S., Mostaghimi, P., et al. (2013). Pore-scale imaging and modelling. *Adv. Water Resourc.* 51, 197–216. doi: 10.1016/j.advwatres.2012.03.003

Brown, H. W. (1951). Capillary pressure investigations. *J. Pet. Technol.* 3, 67–74. doi: 10.2118/951067-G

Brun, F., Kourousias, G., Dreossi, D., Mancini, L., and Tromba, G. (2011). "A comparative evaluation of ring artifacts reduction filters for X-ray computed microtomography images," in *Proceedings of the 2011 18th IEEE International Conference on Image Processing*, (Brussels: IEEE), 405–408.

Brun, F., Mancini, L., Kasae, P., Favretto, S., Dreossi, D., and Tromba, G. (2010). Pore3D: a software library for quantitative analysis of porous media. *Nucl. Instrum. Methods Phys. Res. A* 615, 326–332. doi: 10.1016/j.nima.2010.02.063

Bultreys, T., De Boever, W., and Cnudde, V. (2016). Imaging and image-based fluid transport modeling at the pore scale in geological materials: a practical introduction to the current state-of-the-art. *Earth Sci. Rev.* 155, 93–128. doi: 10.1016/j.earscirev.2016.02.001

Chang, J., and Yortsos, Y. C. (1992). Effect of capillary heterogeneity on Buckley-Leverett displacement. *SPE Reserv. Eng.* 7, 285–293. doi: 10.2118/18798-pa

Chaouche, M., Rakotomalala, N., Salin, D., Xu, B., and Yortsos, Y. C. (1994). Capillary effects in drainage in heterogeneous porous media: continuum modelling, experiments and pore network simulations. *Chem. Eng. Sci.* 49, 2447–2466. doi: 10.1016/0009-2509(94)e0040-w

Christiansen, R. L. (2001). *Two-Phase Flow Through Porous Media*, Vol. 31. Littleton, CO: Colorado School of Mines, Golden, 2–4.

Cilona, A., Baud, P., Tondi, E., Agosta, F., Vinciguerra, S., Rustichelli, A., et al. (2012). Deformation bands in porous carbonate grainstones: field and laboratory observations. *J. Struct. Geol.* 45, 137–157. doi: 10.1016/j.jsg.2012.04.012

Cilona, A., Faulkner, D. R., Tondi, E., Agosta, F., Mancini, L., Rustichelli, A., et al. (2014). The effects of rock heterogeneity on compaction localization in porous carbonates. *J. Struct. Geol.* 67, 75–93. doi: 10.1016/j.jsg.2014.07.008

Cnudde, V., Dierick, M., Vlassenbroeck, J., Masschaele, B., Lehmann, E., Jacobs, P., et al. (2008). High-speed neutron radiography for monitoring the water absorption by capillarity in porous materials. *Nucl. Instrum. Methods Phys. Res. B* 266, 155–163. doi: 10.1016/j.nimb.2007.10.030

De Beer, F. C., Le Roux, J. J., and Kearsley, E. P. (2005). Testing the durability of concrete with neutron radiography. *Nucl. Instrum. Methods Phys. Res. A* 542, 226–231.

De Beer, F. C., and Middleton, M. F. (2006). Neutron radiography imaging, porosity and permeability in porous rocks. *S. Afr. J. Geol.* 109, 541–550. doi: 10.2113/gssajg.109.4.541

De Rosis, A. (2014). A lattice Boltzmann-finite element model for two-dimensional fluid–structure interaction problems involving shallow waters. *Adv. Water Resour.* 65, 18–24. doi: 10.1016/j.advwatres.2014.01.003

Degruyter, W., Burgisser, A., Bachmann, O., and Malaspinas, O. (2010). Synchrotron X-ray microtomography and lattice Boltzmann simulations of gas flow through volcanic pumices. *Geosphere* 6, 470–481. doi: 10.1130/ges00555.1

Dewanckele, J., De Kock, T., Fronteau, G., Derluyn, H., Vontobel, P., Dierick, M., et al. (2014). Neutron radiography and X-ray computed tomography for quantifying weathering and water uptake processes inside porous limestone used as building material. *Mater. Charact.* 88, 86–99. doi: 10.1016/j.matchar.2013.12.007

d'Humières, D. (1992). "Generalized Lattice-Boltzmann equations," in *Rarefied Gas Dynamics: Theory and Simulations, 159*, eds B. D. Shizgal, and D. P. Weave, (Washington, DC: American Institute of Aeronautics and Astronautics), 450–458. doi: 10.2514/5.9781600866319.0450.0458

d'Humières, D., Ginzburg, I., Krafczyk, M., Lallemand, P., and Luo, L-S. (2002). Multiple-relaxation-time lattice Boltzmann models in three dimensions. *Philos. Trans. A Math. Phys. Eng. Sci.* 360, 437–451. doi: 10.1098/rsta.2001.0955

Di Stefano, V. H., Cheshire, M. C., McFarlane, J., Kolbus, L. M., Hale, R. E., Perfect, E., et al. (2017). Spontaneous imbibition of water and determination of effective contact angles in the Eagle Ford Shale Formation using neutron imaging. *J. Earth Sci.* 28, 874–887. doi: 10.1007/s12583-017-0801-1

Domanus, J. C. (1992). *Practical Neutron Radiography*. Dordrecht: Kluwer Academic Publishers.

Fedrigo, A., Strobl, M., Williams, A. R., Lefmann, K., Lindelof, P. E., Jørgensen, L., et al. (2018). Neutron imaging study of 'pattern-welded'swords from the Viking Age. *Archaeol. Anthropol. Sci.* 10, 1249–1263. doi: 10.1007/s12520-016-0454-5

Graham, B., Antonellini, M., and Aydin, A. (2003). Formation and growth of normal faults in carbonates within a compressive environment. *Geology* 31, 11–14.

Hall, S. A. (2013). Characterization of fluid flow in a shear band in porous rock using neutron radiography. *Geophys. Res. Lett.* 40, 2613–2618. doi: 10.1002/grl.50528

Hameed, F., Rohatsch, A., Weber, J., Zamani, B., and Zawisky, M. (2006). *Investigation of Calcareous Arenites From St. Stephan's Cathedral, Vienna*. Gaithersburg, MD: NIST.

Hameed, F., Schillinger, B., Rohatsch, A., Zawisky, M., and Rauch, H. (2009). Investigations of stone consolidants by neutron imaging. *Nucl. Instrum. Methods Phys. Res. A* 605, 150–153. doi: 10.1016/j.nima.2009.01.139

Hartigan, J. A. (1975). *Clustering Algorithms*. New York, NY: Wiley.

Hartigan, J. A., and Wong, M. A. (1979). A K-means clustering algorithm. *Appl. Stat.* 28, 100–108.

Hejazi, S. A. H., Shah, S., and Pini, R. (2019). Dynamic measurements of drainage capillary pressure curves in carbonate rocks. *Chem. Eng. Sci.* 200, 268–284. doi: 10.1016/j.ces.2019.02.002

Huang, Y., Ringrose, P. S., and Sorbie, K. S. (1995). Waterflood displacement mechanisms in a laminated rock slab: validation of predicted capillary trapping mechanisms. *SPE Reserv. Eng.* 10, 287–292. doi: 10.2118/28942-pa

Jerauld, G. R., and Rathmell, J. J. (1997). Wettability and relative permeability of Prudhoe Bay: a case study in mixed-wet reservoirs. *SPE Reserv. Eng.* 12, 58–65. doi: 10.2118/28576-PA

Ji, Y., Hall, S., Baud, P., and Wong, T.-f. (2015). Characterization of pore structure and strain localization in Majella limestone by X-ray computed tomography and digital image correlation. *Geophys. J. Int.* 200, 701–719. doi: 10.1093/gji/ggu414

Kaestner, A., Mannes, D., Hovind, J., Boillat, P., and Lehmann, E. (2016). "Combined neutron and x-ray imaging on different length scales," in *Proceedings of the 6th Conference on Industrial Computed Tomography*, Wels.

Kaestner, A. P. (2011). MuhRec—A new tomography reconstructor. *Nucl. Instrum. Methods Phys. Res. A* 651, 156–160. doi: 10.1016/j.nima.2011.01.129

Kaestner, A. P., Hartmann, S., Kühne, G., Frei, G., Grünzweig, C., Josic, L., et al. (2011). The ICON beamline–A facility for cold neutron imaging at SINQ. *Nucl. Instrum. Methods Phys. Res. A* 659, 387–393. doi: 10.1016/j.nima.2011.08.022

Kaestner, A. P., Hovind, J., Boillat, P., Muehlebach, C., Carminati, C., Zarebanadkouki, M., et al. (2017). Bimodal imaging at ICON using neutrons and X-rays. *Phys. Proc.* 88, 314–321. doi: 10.1016/j.phpro.2017.06.043

Kaminskaite, I., Fisher, Q. J., and Michie, E. A. H. (2019). Microstructure and petrophysical properties of deformation bands in high porosity carbonates. *J. Struct. Geol.* 119, 61–80. doi: 10.1016/j.jsg.2018.12.001

Kanematsu, M., Maruyama, I., Noguchi, T., Iikura, H., and Tsuchiya, N. (2009). Quantification of water penetration into concrete through cracks by neutron radiography. *Nucl. Instrum. Methods Phys. Res. A* 605, 154–158. doi: 10.1016/j.nima.2009.01.206

Keehm, Y., Mukerji, T., and Nur, A. (2004). Permeability prediction from thin sections: 3D reconstruction and Lattice-Boltzmann flow simulation. *Geophys. Res. Lett.* 31:L04606.

Khan, F., Enzmann, F., Kersten, M., Wiegmann, A., and Steiner, K. (2012). 3D simulation of the permeability tensor in a soil aggregate on basis of nanotomographic imaging and LBE solver. *J. Soils Sedim.* 12, 86–96. doi: 10.1007/s11368-011-0435-3

Ladd, A. J. (1994). Numerical simulations of particulate suspensions via a discretized Boltzmann equation. Part 1. Theoretical foundation. *J. Fluid Mech.* 271, 285–309. doi: 10.1017/s0022112094001771

Lal, S., Poulikakos, L. D., Gilani, M. S., Jerjen, I., Vontobel, P., Partl, M. N., et al. (2014). Investigation of water uptake in porous asphalt concrete using neutron radiography. *Trans. Porous Media* 105, 431–450. doi: 10.1007/s11242-014-0376-6

Latt, J. (2009). *Palabos, Parallel Lattice Boltzmann Solver*. Lausanne: FlowKit.

Marchesini, P. (2015). Visualization and Quantification of Fluid Dynamics in Fractured Carbonates using 4D Ground Penetrating Radar (4D GPR. Available at: http://scholarlyrepository.miami.edu/oa_dissertations/1529 (accessed February, 2018).

Morrow, N. R., and Melrose, J. C. (1991). "Application of capillary pressure measurements to the determination of connate water saturation," in *Interfacial Phenomena in Petroleum Recovery*, ed. N. R. Morrow, (New York, NY: Marcel Dekker Inc), 257–287.

Mutti, M. (1995). Porosity development and diagenesis in the Orfento supersequence and its bounding unconformities (Upper Cretaceous, Montagna della Majella, Italy). *Am. Assoc. Petrol. Geol. Spec. Publ.* 63, 141–158.

Ori, G. G., Roveri, M., and Vannoni, F. (1986). "Plio-Pleistocene sedimentation in the Apennine–Adriatic foredeep (central Adriatic Sea, Italy)," in *Foreland Basins*, eds P. A. Allen, and P. Homewood, (Oxford: Blackwell), 183–198. doi: 10.1002/9781444303810.ch9

Ren, F., Song, B., and Sukop, M. C. (2016). Terminal shape and velocity of a rising bubble by phase-field-based incompressible Lattice Boltzmann model. *Adv. Water Resour.* 97, 100–109. doi: 10.1016/j.advwatres.2016.08.012

Riaz, A., Tang, G. Q., Tchelepi, H. A., and Kovscek, A. R. (2007). Forced imbibition in natural porous media: comparison between experiments and continuum models. *Phys. Rev. E* 75:036305.

Riegel, H., Zambrano, M., Balsamo, F., Mattioni, L., and Tondi, E. (2019). Petrophysical properties and microstructural analysis of faulted heterolithic packages: a case study from miocene turbidite successions, Italy. *Geofluids* 2019:9582359.

Rustichelli, A., Torrieri, S., Tondi, E., Laurita, S., Strauss, C., Agosta, F., et al. (2016). Fracture characteristics in cretaceous platform and overlaying ramp carbonates: an outcrop study from Maiella mountain (central Italy). *Mar. Petrol. Geol.* 76, 68–87. doi: 10.1016/j.marpetgeo.2016.05.020

Salathiel, R. A. (1973). Oil recovery by surface film drainage in mixed-wettability rocks. *J. Petrol. Technol.* 25, 1216–1224. doi: 10.2118/4104-pa

Schillinger, B., Beaudet, A., Fedrigo, A., Grazzi, F., Kullmer, O., Laaß, M., et al. (2018). Neutron imaging in cultural heritage research at the FRM II reactor of the Heinz Maier-Leibnitz center. *J. Imaging* 4:22. doi: 10.3390/jimaging4010022

Schillinger, B., Calzada, E., Eulenkamp, C., Jordan, G., and Schmahl, W. W. (2011). Dehydration of moulding sand in simulated casting process examined with neutron radiography. *Nucl. Instrum. Methods Phys. Res. Sect. A* 651, 312–314. doi: 10.1016/j.nima.2011.02.103

Schillinger, B., Lehmann, E., and Vontobel, P. (2000). 3D neutron computed tomography: requirements and applications. *Phys. B Condens. Matter* 276, 59–62. doi: 10.1016/s0921-4526(99)01254-5

Schindelin, J., Arganda-Carreras, I., Frise, E., Kaynig, V., Longair, M., Pietzsch, T., et al. (2012). Fiji: an open-source platform for biological-image analysis. *Nat. Methods* 9:676e682. doi: 10.1038/nmeth.2019

Schneider, C. A., Rasband, W. S., and Eliceiri, K. W. (2012). NIH image to ImageJ: 25 years of image analysis. *Nat. Methods* 9:671. doi: 10.1038/nmeth.2089

Sekti, R. P. (2010). *3-D Stratigraphy and Fracture Characterization in Late Cretaceous Carbonates (Madonna della Mazza, Italy*. Available at: http://scholarlyrepository.miami.edu/oa_theses/38 (accessed February, 2018).

Shah, S. M., Gray, F., Crawshaw, J. P., and Boek, E. S. (2016). Micro-computed tomography pore-scale study of flow in porous media: effect of voxel resolution. *Adv. Water Resourc.* 95, 276–287. doi: 10.1016/j.advwatres.2015.07.012

Stavropoulou, E., Andò, E., Tengattini, A., Briffaut, M., Dufour, F., Atkins, D., et al. (2019). Liquid water uptake in unconfined Callovo Oxfordian clay-rock studied with neutron and X-ray imaging. *Acta Geotechn.* 14, 19–33. doi: 10.1007/s11440-018-0639-4

Tondi, E. (2007). Nucleation, development and petrophysical properties of faults in carbonate grainstones: evidence from the San Vito Lo Capo peninsula (Sicily. Italy). *J. Struct. Geol.* 29, 614–628. doi: 10.1016/j.jsg.2006.11.006

Tondi, E., Antonellini, M., Aydin, A., Marchegiani, L., and Cello, G. (2006). The role of deformation bands, stylolites and sheared stylolites in fault development in carbonate grainstones of Majella Mountain, Italy. *J. Struct. Geol.* 28, 376–391. doi: 10.1016/j.jsg.2005.12.001

Tondi, E., Cilona, A., Agosta, F., Aydin, A., Rustichelli, A., Renda, P., et al. (2012). Growth processes, dimensional parameters and scaling relationships of two conjugate sets of compactive shear bands in porous carbonate grainstones, Favignana Island, Italy. *J. Struct. Geol.* 37, 53–64. doi: 10.1016/j.jsg.2012.02.003

Tondi, E., Rustichelli, A., Cilona, A., Balsamo, F., Storti, F., Napoli, G., et al. (2016). Hydraulic properties of fault zones in porous carbonates, examples from central and southern Italy. *Ital. J. Geosci.* 135, 68–79. doi: 10.3301/ijg.2015.08

Treiber, L. E., and Owens, W. W. (1972). A laboratory evaluation of the wettability of fifty oil-producing reservoirs. *Soc. Petrol. Eng. J.* 12, 531–540. doi: 10.2118/3526-PA

Vlassenbroeck, J., Masschaele, B., Cnudde, V., Dierick, M., Pieters, K., Van Hoorebeke, L., et al. (2006). "Octopus 8: a high performance tomographic reconstruction package for X-ray tube and synchrotron micro-CT," in *Advances in X-ray Tomography for Geomaterials*, eds J. Desrues, G. Viggiani, and P. Bésuelle (London: ISTE), 167–173. doi: 10.1002/9780470612187.ch13

Voltolini, M., Kwon, T. H., and Ajo-Franklin, J. (2017). Visualization and prediction of supercritical CO2 distribution in sandstones during drainage: an in situ synchrotron X-ray micro-computed tomography study. *Int. J. Greenhouse Gas Control* 66, 230–245. doi: 10.1016/j.ijggc.2017.10.002

Xie, C., Raeini, A. Q., Wang, Y., Blunt, M. J., and Wang, M. (2017). An improved pore-network model including viscous coupling effects using direct simulation by the lattice Boltzmann method. *Adv. Water Resour.* 100, 26–34. doi: 10.1016/j.advwatres.2016.11.017

Yang, X., Mehmani, Y., Perkins, W. A., Pasquali, A., Schönherr, M., Kim, K., et al. (2016). Intercomparison of 3D pore-scale flow and solute transport simulation methods. *Adv. Water Resour.* 95, 176–189. doi: 10.1016/j.advwatres.2015.09.015

Yehya, M., Andò, E., Dufour, F., and Tengattini, A. (2018). Fluid-flow measurements in low permeability media with high pressure gradients using neutron imaging: application to concrete. *Nucl. Instrum. Methods Phys. Res. A* 890, 35–42. doi: 10.1016/j.nima.2018.02.039

Zambrano, M., Tondi, E., Mancini, L., Arzilli, F., Lanzafame, G., Materazzi, M., et al. (2017). 3D Pore-network quantitative analysis in deformed carbonate grainstones. *Mar. Petrol. Geol.* 82, 251–264. doi: 10.1016/j.marpetgeo.2017.02.001

Zambrano, M., Tondi, E., Mancini, L., Lanzafame, G., Trias, F. X., Arzilli, F., et al. (2018). Fluid flow simulation and permeability computation in deformed porous carbonate grainstones. *Adv. Water Resour.* 115, 95–111. doi: 10.1016/j.advwatres.2018.02.016

Zandomeneghi, D., Voltolini, M., Mancini, L., Brun, F., Dreossi, D., and Polacci, M. (2010). Quantitative analysis of X-ray microtomography images of geomaterials: application to volcanic rocks. *Geosphere* 6, 793–804. doi: 10.1130/ges00561.1

Zawisky, M., Hameed, F., Dyrnjaja, E., Springer, J., and Rohatsch, A. (2010). Digitized neutron imaging with high spatial resolution at a low power research reactor: applications to steel and rock samples. *Nucl. Instrum. Methods Phys. Res. B* 268, 2446–2450. doi: 10.1016/j.nimb.2010.04.020

Zhang, P., Wittmann, F. H., Zhao, T., and Lehmann, E. H. (2010). Neutron imaging of water penetration into cracked steel reinforced concrete. *Phys. B Condens. Matter.* 405, 1866–1871. doi: 10.1016/j.physb.2010.01.065

Zhang, P., Wittmann, F. H., Zhao, T. J., Lehmann, E. H., and Vontobel, P. (2011). Neutron radiography, a powerful method to determine time-dependent moisture distributions in concrete. *Nucl. Eng. Design* 241, 4758–4766. doi: 10.1016/j.nucengdes.2011.02.031

Zhu, W., Baud, P., and Wong, T. F. (2010). Micromechanics of cataclastic pore collapse in limestone. *J. Geophys. Res. Solid Earth* 115, 1–17. doi: doi:10.1029/2009JB006610

Disclaimer: Elettra-Sincrotrone Trieste S.C.p.A. is an institute of research and non-profit organization.

Conflict of Interest: MZ and ET were employed by company GeoMore s.r.l.

The remaining authors declare that the research was conducted in the absence of any commercial or financial relationships that could be construed as a potential conflict of interest.

frontiers in Earth Science

ORIGINAL RESEARCH
published: 19 December 2019
doi: 10.3389/feart.2019.00327

Integrating X-Ray Computed Tomography With Chemical Imaging to Quantify Mineral Re-crystallization From Granulite to Eclogite Metamorphism in the Western Italian Alps (Sesia-Lanzo Zone)

Luca Corti[1], Michele Zucali[1,2], Roberto Visalli[3], Lucia Mancini[4] and Mohammad Sayab[5]*

[1] Department of Earth Sciences, University of Milano, Milan, Italy, [2] Department of Earth and Atmospheric Sciences, University of Houston, Houston, TX, United States, [3] Department of Biological, Geological and Environmental Sciences, University of Catania, Catania, Italy, [4] Elettra-Sincrotrone Trieste S.C.p.A., Trieste, Italy, [5] Geological Survey of Finland, Espoo, Finland

OPEN ACCESS

Edited by:
Scott Andrew Whattam, King Fahd University of Petroleum and Minerals, Saudi Arabia

Reviewed by:
Laixi Tong, Northwest University, China
Omar Bartoli, University of Padova, Italy

***Correspondence:**
Luca Corti
luca.corti@unimi.it

Specialty section:
This article was submitted to Petrology, a section of the journal Frontiers in Earth Science

Received: *23 July 2019*
Accepted: *27 November 2019*
Published: *19 December 2019*

Citation:
Corti L, Zucali M, Visalli R, Mancini L and Sayab M (2019) Integrating X-Ray Computed Tomography With Chemical Imaging to Quantify Mineral Re-crystallization From Granulite to Eclogite Metamorphism in the Western Italian Alps (Sesia-Lanzo Zone). Front. Earth Sci. 7:327. doi: 10.3389/feart.2019.00327

Metamorphic transformations and fabric evolution are the consequence of thermo-dynamic processes, lasting from thousands to millions of years. Relative mineral percentages, their grain size distribution, grain orientation, and grain boundary geometries are first-order parameters for dynamic modeling of metamorphic processes. To quantify these parameters, we propose a multidisciplinary approach integrating X-ray computed microtomography (μ-CT) with X-ray chemical mapping obtained from an Electron MicroProbe Analyzer (EMPA). We used a metapelitic granulite sample collected from the Alpine HP-LT metamorphic rocks of the Mt. Mucrone (Eclogitic Micaschists Complex, Sesia-Lanzo Zone, Western Alps, Italy). The heterogeneous Alpine deformation and metamorphism allowed the preservation of pre-alpine structural and mineralogical features developed under granulite-facies conditions. The inferred granulitic mineral association is Grt + Bt + Sil + Pl + Qtz ± Ilm ± Kfs ± Wm. The subsequent pervasive static eclogite-facies re-equilibration occurred during the alpine evolution. The inferred alpine mineral association is Wm + Omp ± Ky + Qtz + Grt though local differences may occur, strongly controlled by chemistry of microdomains. X-ray μ-CT data extracted from centimeter-sized samples have been analyzed to quantify the volumetric percentage and shape preferred orientation (SPO) for each mineral phase. By combining tomographic phase separation with chemical variation and microstructures (i.e., different grain-size classes for the same phase and morphology of different pre-alpine microdomains) the pre-alpine mineralogical phases from the alpine overprint have been distinguished and quantified. Moreover, the sample preserves 100% of the pre-alpine granulite fabric, which surprisingly corresponds to less than 22% of the corresponding pre-alpine metamorphic assemblages, while the alpine eclogitic static assemblage corresponds to 78% though no new fabric is developed. This contribution

demonstrates that the combined use of EMPA X-ray chemical mapping with the X-ray μ-CT shape analysis permits a dynamic approach to constrain the chemistry of the mineral phases linked to the development of metamorphic-related static and dynamic fabrics.

Keywords: X-ray microtomography, X-ray chemical maps, shape preferred orientation, granulite metamorphism, pre-alpine fabrics, Sesia-Lanzo Zone

INTRODUCTION

The knowledge of crust and mantle dynamics is mostly based on the study of fabric elements, metamorphic assemblages and their relationships within the rock-volume, now exposed after the subduction- and collision-related processes. The metamorphic basements are usually affected by strong heterogeneities in the degree of fabric and metamorphic evolution (Salvi et al., 2010; Corti et al., 2017), mainly due to the strain partitioning and consequent heterogeneous distribution of metamorphic assemblages (e.g., Myers, 1970; Mørk, 1985; Spalla and Zucali, 2004; Spalla et al., 2005; Pearce and Wheeler, 2010). Detailed multiscale correlation between deformation and metamorphism has been shown to be of primary importance to constrain the relationships between fabric and metamorphism (e.g., Turner and Weiss, 1963; Park, 1969; Hobbs et al., 1976, 2010; Williams, 1985; Lardeaux and Spalla, 1990; Passchier et al., 1990; Johnson and Vernon, 1995; Spalla et al., 1999; Salvi et al., 2010; Gosso et al., 2015; Corti et al., 2017).

Classical structural geology studies have been progressively reinforced by a collection of quantitative data through texture analysis (e.g., Zucali et al., 2014a; Frassi et al., 2017), synchrotron X-ray computed microtomography (e.g., Zucali et al., 2014a) and chemical mapping of superimposed structures in metamorphic rocks (Lanari et al., 2014; Ortolano et al., 2014a; Visalli, 2017). In this view, the quantitative analysis of the metamorphic textures related to the superimposed fabrics allows the evaluation of the mechanically and chemically reacting volume percentage, during successive tectono-metamorphic stages. In particular, the estimation of relative mineral percentages, their grain size distribution, grain orientation, and grain boundary geometries for each tectono-metamorphic stage are the first-order parameters for dynamic modeling of metamorphic processes.

To quantitatively investigate the textural and chemical heterogeneities developing during deformation and metamorphism partitioning we propose a novel approach integrating X-ray computed microtomography (μ-CT) with X-ray chemical mapping obtained from an Electron MicroProbe Analyzer (EMPA). This procedure combines (1) the quantitative calibration of the X-ray chemical map for selected microdomains using the Q-XRMA (i.e., Quantitative X-Ray Map Analyzer) statistical approach (Ortolano et al., 2018) to determine different compositional regions within the rock and minerals associated to the superposed metamorphic assemblages; (2) the high-resolution thin section optical scanning to determine the mineral grain-size distribution and perform the orientation analysis using the Min-GSD (Mineral-Grain Size Distribution) method (Visalli, 2017); and (3) the X-ray μ-CT capability to resolve the three-dimensional (3D) shape and spatial distribution of minerals marking different fabrics in metamorphic rocks (e.g., Denison et al., 1997; Huddlestone-Holmes and Ketcham, 2010; Voltolini et al., 2011; Baker et al., 2012; Sayab et al., 2015; Macente et al., 2017).

We applied this approach to a metapelitic granulite sample (i.e., kinzigite gneiss) surfacing within the poly-deformed metamorphic basements of the Mt. Mucrone, Eclogitic Micaschists Complex, Sesia-Lanzo Zone, Western Alps (Hy, 1984; Koons et al., 1987; Ridley, 1989; Ildefonse et al., 1990; Zucali et al., 2002; Babist et al., 2006; Cenki-Tok et al., 2011; Delleani et al., 2013). The sample pervasively records the pre-alpine granulite fabric, but the original pre-alpine granulite mineral assemblages were extensively replaced by static eclogite facies minerals, recording the alpine subduction-related evolution.

In this contribution, we show how to quantify the modal percentage, the mineral chemical variation, the grain-size distribution, the grain orientation, and the grain boundary geometries of the mineral phases recording the metamorphic evolution from pre-alpine granulitic- to the eclogitic-facies conditions. This approach allows a detailed and reliable discrimination of these parameters for the pre-alpine and alpine stages.

MATERIALS AND METHODS

Geological Outline

The Sesia-Lanzo Zone, in the Western Alps (SLZ, **Figures 1A,B**), is a portion of continental crust, which recorded high pressure (HP) metamorphic conditions during the alpine subduction (e.g., Dal Piaz et al., 1972; Compagnoni et al., 1977; Pognante, 1991; Babist et al., 2006; Meda et al., 2010; Roda et al., 2012; Regis et al., 2014). Its alpine metamorphic history comprises a prograde blueschist- to eclogite-facies stage followed by blueschist- and greenschist-facies retrograde re-equilibrations (e.g., Compagnoni and Maffeo, 1973; Compagnoni, 1977; Gosso, 1977; Lardeaux, 1981; Lardeaux et al., 1982a, 1983; Spalla et al., 1983; Pognante, 1989a; Castelli and Rubatto, 2002; Zucali et al., 2004; Rebay and Messiga, 2007; Zanoni et al., 2008; Zucali and Spalla, 2011; Giuntoli and Engi, 2016; Corti et al., 2018; Giuntoli et al., 2018a; Roda et al., 2018a, 2019). The metamorphic evolution ended at Oligocene with the intrusion of large intrusive bodies which produced contact metamorphic aureole (Zanoni et al., 2008). The alpine eclogite-facies peak has been dated between 90 and 65 Ma (Rubatto et al., 1999; Cenki-Tok et al., 2011; Regis et al., 2014; Giuntoli et al., 2018b; Halama et al., 2018). The early-alpine HP imprints range between 500–625°C and 1.3–2.5 GPa (see

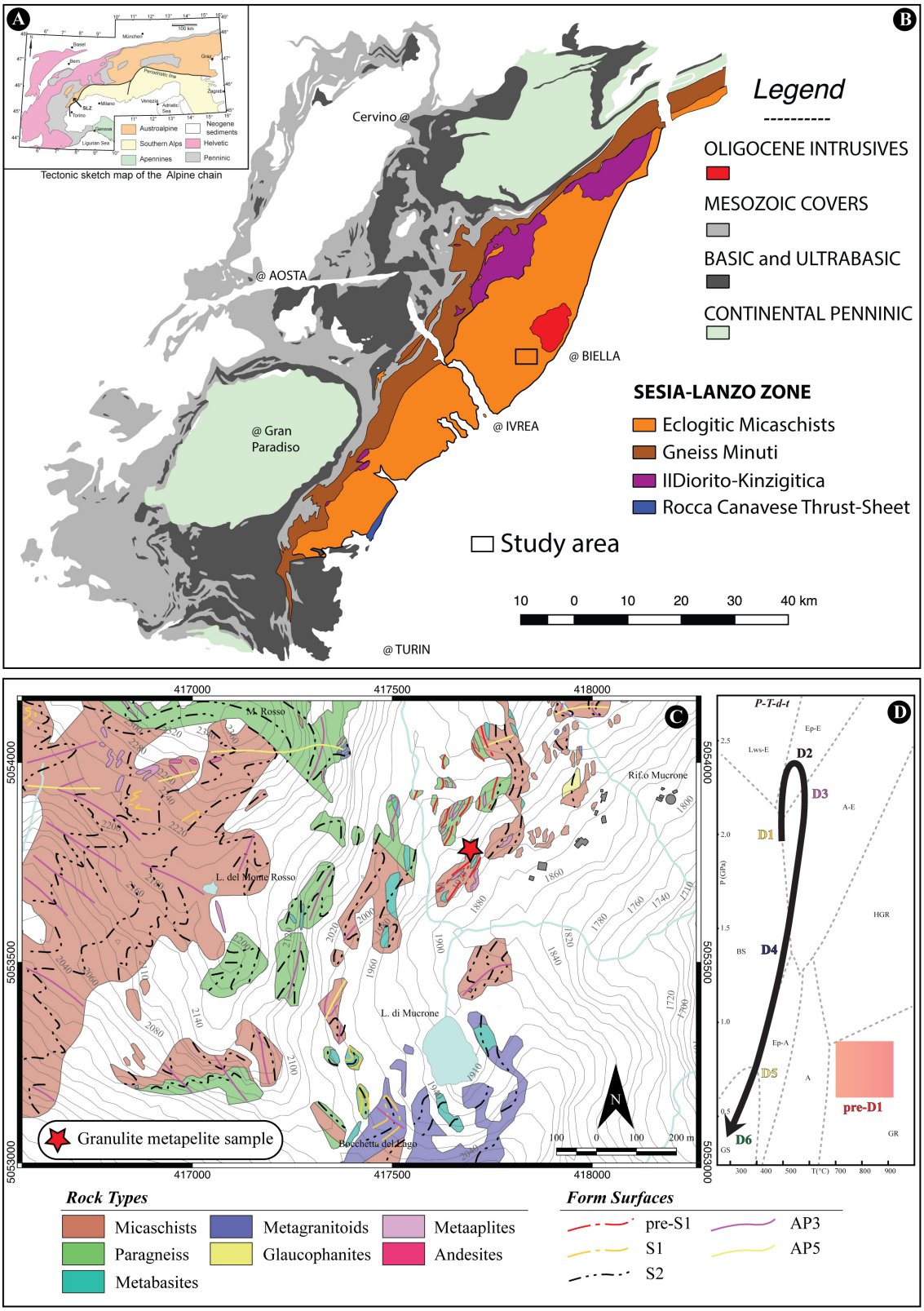

FIGURE 1 | (A) Tectonic outline of the major domain of the alpine chain. **(B)** Tectonic scheme of the Western Alps with the different metamorphic complexes of the Sesia-Lanzo Zone. The studied area is located. **(C)** Rock-types and foliation trajectories around the Mt. Mucrone. The metapelitic granulite sample is located. **(D)** P-T-d-t path modified after Zucali et al. (2002) and Delleani et al. (2013).

Roda et al., 2012 for a review of P-T estimates). The eclogitized ophiolitic relics of the Liguria-Piedmont Ocean, the Piedmont Zone, bound the external margin of the SLZ, while the SLZ internal margin is a thick mylonitic belt (the Canavese Line) (**Figure 1**); the Canavese Line puts in contact the SLZ from the lower crustal rocks of the Southalpine Ivrea Zone (e.g., Bigi et al., 1990; Rebay et al., 2018; Balestro et al., 2019). The SLZ is subdivided into four main units (**Figure 1B**): the Eclogitic Micaschist Complex (EMC), the Gneiss Minuti Complex (GMC), the II Dioritic–Kinzigitic Zone (IIDK) and the Rocca Canavese Thrust Sheets (RCT) (e.g., Compagnoni et al., 1977; Pognante, 1989a,b; Spalla et al., 1991; Cantù et al., 2016; Roda et al., 2018a, 2019). Eclogitic parageneses are widely described both in EMC and GMC with a strong difference in relative volume affected by the retrograde greenschist re-equilibration. The GMC is widely re-equilibrated under greenschist facies conditions, while the EMC, constituting the internal part of the SLZ, records the greenschist-facies re-equilibration along discrete shear zones (Spalla et al., 1983, 1991; Stünitz, 1989; Giuntoli and Engi, 2016). The IIDK consists of kilometric lenses of paragneisses, marbles and metabasites between EMC and GMC. The pre-alpine high-temperature evolution is well preserved and the alpine eclogitic assemblages are described only in the Vogna Valley, where the tectonic contact between IIDK and EMC is marked by eclogitic mylonites (Lardeaux, 1981; Lardeaux et al., 1982b).

The EMC protoliths, composed by high-grade paragneisses, granulites, amphibolites and minor marbles and quartzites, constitute the country rocks of the Permian granitoids and gabbros (Compagnoni and Maffeo, 1973; Callegari et al., 1976; Compagnoni et al., 1977; Lardeaux, 1981; Oberhänsli et al., 1985; Castelli, 1987; Bussy et al., 1998; Cenki-Tok et al., 2011; Zucali, 2011; Corti et al., 2017); the Mt. Mucrone is one of these Permian bodies and the most renown. The deformation history of EMC, in the area of Mt. Mucrone and studied samples, comprises four generations of alpine folds (**Figure 1C**), two of which are associated with the HP mineral assemblages, and two generations of shear zones synchronous with the blue- and greenschist-facies re-equilibration, respectively (Hy, 1984; Zucali et al., 2002; Delleani et al., 2012, 2013).

A pre-alpine polyphasic metamorphic evolution, from granulite- to amphibolite-facies conditions, has been recognized in marbles, metapelites, metagranitoids and metabasics of the SLZ (Compagnoni et al., 1977; Lardeaux et al., 1982b; Castelli, 1991; Lardeaux and Spalla, 1991; Rebay and Spalla, 2001). This pre-alpine stage, marked by biotite-, sillimanite-, garnet-rich foliation in paragneiss (pre-D1 in **Figure 1D**), is found as relict in paragneiss close to the Mt. Mucrone (i.e., metapelitic granulite sample in **Figure 1C**). The pre-alpine stage has been constrained at T = 730–830°C P = 0.7–0.9 GPa for acid and basic granulites surfacing in other localities of the SLZ (Lardeaux and Spalla, 1991). Pre-D1 has been interpreted as the result of an extension-related uplift of a portion of the Variscan crust; this extensional tectonics is inferred to be of Permian–Triassic time, during the lithospheric thinning leading to the Tethys opening (e.g., Lardeaux and Spalla, 1991; Marotta et al., 2009; Roda et al., 2018b).

Sample Description

The analyzed samples are pre-alpine granulite-facies metapelites, characterized by gneissic fabric (i.e., kinzigite). They were collected from the EMC, NW of the Lago del Mucrone (**Figure 1C**, UTM32N – WGS84 417517.69 m E, 5053493.35 m N). They occur as lenses within the eclogitic gneisses and micaschists, country rocks of the Permian Mt. Mucrone metaintrusive body (Eclogitic Micaschists Complex, Sesia-Lanzo Zone, Western Alps). The heterogeneous alpine deformation and metamorphism allowed the preservation of pre-alpine granulite-facies relicts in country rocks, preserving a foliation (pre-S1 in **Figure 1C**) at meter-scale, wrapped by the eclogite-facies S1 and S2 foliations (**Figure 1C**). The pre-alpine fabrics are mostly defined by alternating microfilms and microlithons, which are marked, respectively, by red-brown biotite, elongated ex-sillimanite domain, ilmenite, rare white mica and garnet porphyroblasts, K-feldspars, ex-plagioclase domain, quartz, and decussate arcs of red-brown biotite (**Figure 2A**). The pre-S1 foliation (**Figure 2A**) is characterized by S-C-like geometry where the C planes, spaced by 2–3 mm, deflect the S planes marked by biotite and ex-sillimanite domains, the latter being characterized by diagnostic columnar shape and transversal fractures (**Figure 2D**). Garnet porphyroclasts are wrapped by the pre-S1 foliation; they are commonly associated with biotite, quartz and white mica (WmI) inclusions (**Figures 2B,C**). Ex-plagioclase domains are characterized by thin-grained aggregates of white mica and/or a high-relief mineral (omphacite) and may occur as elongated domain, mainly parallel to the S-planes, locally wrapping porphyroblasts, or as coronas of the garnet porphyroblasts (**Figure 2B**). Biotite also marks the pre-S1 foliation; biotite is well preserved in microfilm domains and displays (001) cleavage mainly parallel to the foliation; its red-color at parallel nicols suggests a preserved composition, probably related to the pre-alpine high-temperature conditions (e.g., Hayama, 1959; Wu and Chen, 2015). Locally, isolated grains of white mica co-exist with biotite, suggesting also a pre-alpine age for the white mica (WmI in **Figure 2E**). The pre-S1 pre-alpine fabric is pervasively replaced by static eclogite facies mineral association, namely garnet, white mica, omphacite, kyanite, and rutile. Alpine generation of garnet (GrtII in **Figure 2B**) occurs as corona over garnet porphyroblasts (GrtI) or biotite (**Figure 2B**) or as new grains (**Figure 2**). Alpine white mica (WmII, **Figures 2C,E**) defines thin-grained aggregates likely replacing feldspar, biotite or white mica pre-alpine domains. Omphacite (OmpI) fine-grained aggregates replace pre-alpine plagioclase (**Figure 2B**); large individuals may also occur as in **Figure 2D**. Kyanite occurs as fine-grained aggregates replacing sillimanite in ex-sill domains (**Figure 2D**). The fine grain-size made the recognition of optical characters sometimes hard. The different alpine metamorphic assemblages or replacements seem to be strongly controlled by the chemistry of microdomains. Typical examples are kyanite and omphacite that preferentially grow only in specific pre-alpine domains. This is also confirmed by the comparison of the eclogitic assemblages of these rocks with those of eclogitic micaschists where no kyanite occur, likely due to the effect of chemical homogenization of the

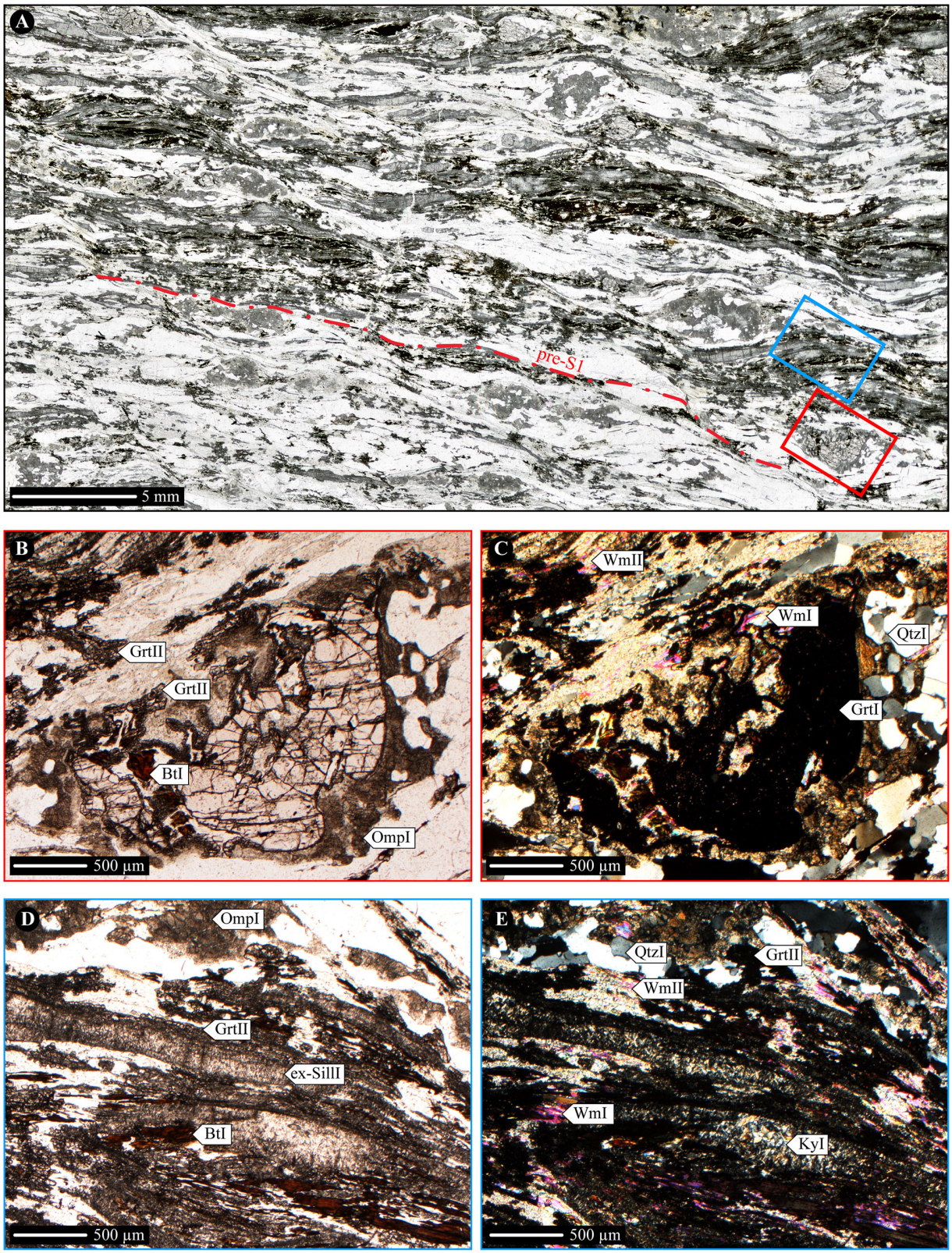

FIGURE 2 | (A) High-resolution optical scan of the entire thin section characterized by well-developed pre-S1 foliation, plane polarized light. **(B)** pre-alpine Grt microdomains, plane polarized light. **(C)** pre-alpine Grt microdomains, crossed polars. **(D)** pre-alpine Sill and Pl microdomains, plane polarized light. **(E)** pre-alpine Sill and Pl microdomains, crossed polars.

alpine deformation. The inferred eclogitic mineral association WmII + OmpI ± KyI + Qtz + GrtII + Rt indicate T = 500–600°C and $P \geq$ 1.5–2.2 GPa conditions (Zucali et al., 2002) while the pre-alpine granulitic stage is characterized by the mineral assemblage GrtI + BtI + SillI + Pl + Qtz ± Ilm ± Kfs ± WmI, but no thermo-barometric estimates are available so far.

Methods

Chemical Imaging and Fabric Analysis

Three different image processing tools (i.e., GSD, Q-XRMA and Min-GSD) developed at the Geoinformatics and Image Analysis Lab of the Biological, Geological, and Environmental Sciences Department at the University of Catania (Italy), have been applied both at the scale of the entire thin section and of the microdomain one. In this last case, two microdomains (i.e., C1, C2) have been selected as the best candidates to execute the tools. These tools are based on various scripts and functions adopted for images analysis, implemented within the most common GIS software, which have been increasingly used in solving various geoscientific issues (e.g., Li et al., 2010; DeVasto et al., 2012; Pradhan, 2013; Ortolano et al., 2014a,b; Belfiore et al., 2016; Fiannacca et al., 2017; Berrezueta et al., 2019).

The first tool adopted is the Grain Size Detector (GSD – Visalli, 2017). Such tool permits the users to trace a map of polygonal features representative of the grains composing the rock, by processing high-resolution thin section optical scans. In such a way, a database containing several data of grain sizes and shapes (e.g., area, axial ratio, orientation with respect the foliation and others) is obtained. With this aim, a 24 bit-depth optical scan has been acquired with a resolution of 4800 dpi via an Epson V750 dual lens system scanner. According to Visalli (2017), the above scan resolution was selected as the best setting for acquiring an image at high quality, reducing, at the same time, the required hard drive space storage and image processing time.

The analytical procedure of the tool is based on the sequential application of four image-processing steps, within the GIS environment: (i) the filtering step, to improve the quality of the input scan, by emphasizing grains boundaries and reducing noise; (ii) the image segmentation step, required to distinguish, select and extract boundaries of different grains; (iii) the vectorization step, needed to create polygon features that trace the original grains of the thin section; and, finally, (iv) the quantification step, useful to calculate grain sizes and shape parameters.

The second tool applied is the Quantitative X-Ray Map Analyzer (Q-XRMA – Ortolano et al., 2018). In this case, users are able to classify rock-forming minerals starting from an array of X-ray maps as well as to calibrate these maps for deriving pixel-based chemical data and end-member fraction maps, by using a sufficient number of spot chemical analyses as internal standards (De Andrade et al., 2006). With this aim, major element X-ray maps (i.e., Al, Ca, Cr, Fe, K, Mg, Mn, Na, Si, Ti) of the entire thin section (c. 38*20 mm) have been acquired using a JEOL 8200 electron microprobe equipped with five WDS spectrometers located at the Department of Earth Science, University of Milan. Operating conditions were 160 ms dwell time, 15 kV accelerating voltage and a probe current of 100 nA. A spatial resolution of about 60 μm in both x and y directions was used for acquiring an image with a resolution of 360 × 610 pixels. X-ray maps of the C1 and C2 microdomains were acquired with a dwell time of 130 ms and pixel matrices of 650 × 700 and 600 × 770, where the pixel size was equaled to 4 and 5 μm, respectively. Spot chemical analyses used as internal standards to calibrate X-ray maps were performed using the JEOL 8200 EMPA. Operating conditions were: ∼1 μm beam spot, 15 kV accelerating voltage, and 5 nA beam current. Natural minerals and synthetic oxides were used as standards. Adopted mineral abbreviations are from Siivola and Schmid (2007), whereas mineral formulae were calculated according to Deer et al. (1992) by the jPTGUI software (Zucali, 2005). Representative mineral analyses and structural formulae of garnet, biotite, pyroxene and white mica are given as **Supplementary Table S1**. The analytical procedure of the Q-XRMA tool is subdivided into three different cycles: (i) the first cycle consists of various stages implying a multivariate statistical data handling of the X-ray maps, based on the sequential application of the Principal Components Analysis (PCA) and the supervised Maximum Likelihood Classification (MLC) (Ortolano et al., 2014b). As a result, users can distinguish mineral phases constituting the analyzed thin section/microdomain as well as extrapolate the associated modal percentages; (ii) the second cycle comprises two sub-procedure allowing to perform, on one hand, an in-depth analysis of a selected phase identified during the first cycle for detecting occurrences of sub-phases (e.g., mineral zoning) and, on the other hand, to calibrate native X-ray maps through a multiple linear regression algorithm. In this last case, the element concentration values (expressed as atoms per formula unit, a.p.f.u) can be predicted for each pixel representative of a specific investigated mineral phase; (iii) the third cycle permits users to manage the calibrated X-ray maps obtained during the second cycle, for constructing maps of end-member proportions as well as quantifying chemical variations within the investigated phases.

The third tool adopted is the Mineral Grain Size Detector (Min-GSD – Visalli, 2017). This tool allows users to merge together the outputs of the GSD and Q-XRMA in order to label each grain polygon feature with the appropriate mineral name, as the GSD tool alone is not capable to make any division between grains of the same/different minerals, unless the user manually renames each polygon. The analytical procedure requires the sequential application of three different steps: (i) a preliminary manual georeferencing stage, in ArcGIS® environment, between the GSD and Q-XRMA outputs. This is in order to ensure a valid overlap between the two images; (ii) a raster to point conversion of the Q-XRMA output, with the aim to convert each classified pixel in a point feature storing the datum of the mineral name; and finally, (iii) a spatial join operation between the GSD output and the Q-XRMA point converted image in order to attach the correct mineral name to each polygon feature. In this view, the tool calculates the highest frequency of the pixels having the same label enclosed within a polygon.

X-Ray Computed Tomography

X-ray computed microtomography (μ-CT) is a non-destructive technique based on the 3D mapping of the X-ray attenuation coefficient across the investigated sample (Baruchel et al., 2000). Using X-ray μ-CT based on a cone-beam geometry it is possible to achieve a maximum spatial resolution close to the focal spot size of the microfocus X-ray source. Moreover, it has been demonstrated (Wilkins et al., 1996) that by using a tomographic instrument based on a microfocus source, it is possible to take advantage of phase-contrast effects at the edges of the different features present within the sample volume (phase objects). This could allow to improve the contrast and spatial resolution in the images, obtaining sharper borders of the sample features and detecting details smaller than the pixel size of the detector (Mancini et al., 1998). Phase-contrast X-ray μ-CT measurements based on synchrotron and microfocus X-ray sources applied in the Earth science domain represent a powerful tool for the non-destructive characterization of the internal microstructures and the mineral phases separation thanks to their different density and/or chemical composition (Polacci et al., 2010; Zandomeneghi et al., 2010; Baker et al., 2012; Cnudde and Boone, 2013). Through virtual slicing of the sample volume and applying image processing and analysis 3D tools, it is possible to achieve a quantitative shape preferred orientation (SPO) analysis by means of the extraction of geometrical, morphological, and orientation parameters (Voltolini et al., 2011; Zucali et al., 2014b).

Phase-contrast X-ray μ-CT data have been acquired on centimeter-sized samples at the TomoLab station at the Elettra synchrotron facility in Basovizza (Trieste, Italy)[1]. This station is equipped with a sealed microfocus source (Hamamatsu, Japan) which guarantees a minimum focal spot size of 5 μm. For each sample, a set of 2400 projections was acquired over a total scan angle of 360°. A water-cooled, 12-bit, 4008 × 2672 pixels CCD camera (Photonic Science, United Kingdom) was used as detector applying a 2 × 2 binning to the pixels. Scanning acquisition conditions were: Voltage = 130 kV, current = 61 μA, filter = 1.5 mm of Al, exposure time per projection = 6.5 s, source-to-sample distance = 220 mm and source-to-detector distance = 311 mm. The reconstruction of the tomographic slices was done using the commercial software COBRA (Exxim, United States) with an isotropic voxel size of 17.7 μm. The reconstructed slices were visualized by using the freeware ImageJ (Schneider et al., 2012), while the 3D visualization, through volume rendering procedure, was obtained by the Pergeos software[2]. PerGeos software allows the mineral quantification through user-friendly 3D visual imaging and mineral phases segmentation by mapping gray value to specific colors. To reduce imaging noise, the reconstructed μ-CT data (**Figure 3A**) was pre-filtered using variance weighted mean filter (**Figure 3B**; noise variance = 400, radius = 2 pixels; Gonzalez and Woods, 2002). Prior to the volume data processing, we crop out a sub-volume (VOI: Volume of Interest) suitable for the analysis avoid the dark background masking the slices with respect to the outer region of the sample. The mineral phases are separated from each other using 3D Marked-Watershed segmentation (MBW; Meyer and Beucher, 1990). The algorithm is based on semi-automatic thresholding, where the boundary between mineral is defined by using the gradient function (i.e., the local deviation) as the gray-values delimiters (**Figures 3C,D**). The material to be segmented is marked using the manual Interactive Overlay Thresholding function seeded with local maxima of distance map. During the procedure it is possible to have areas with multiple adjacent local maxima. This issue can be minimized taking only the largest local maxima (Sayab et al., 2017). The MBW algorithm then expand the seeded markers over the related mineral phases (**Figures 3E,F**) using a landscape function which is defined by the gradient volume (i.e., active contours algorithm). Once the segmentation is achieved post-segmentation filtering was needed to improve the edge preservation and to remove the background voxels. The filtering was retained to a minimum level to preserve the shape of the objects. In this view, we used the closing procedure for avoid dark "unclassified" voxels (Sayab et al., 2016). Thanks to this imaging analysis we separated seven mineral phases: garnet, pyroxene, kyanite, quartz, micas, and opaque minerals. The 3D grain size distribution and the SPO analysis for each mineral phase have been calculated along with the entire rock volume and for each *XY* plane thanks to the Separate Object procedure using the Skeleton algorithm. Through the labeling tool it is possible to extract the useful parameters, i.e., length, width, volume, orientation angles, eigenvalue, and eigenvector, for each object.

[1]https://www.elettra.trieste.it/it/lightsources/labs-and-services/tomolab/tomolab.html

[2]https://www.thermofisher.com/electron-microscopy

RESULTS

2D Chemical and Fabric Results

The first cycle of Q-XRMA allows the modal percentage of the entire thin section (98.41% classified pixels) to be calculated. The identified mineral phases are Qtz (43.04%), Cpx (23.45%), Wm (12.35%), Bt (8.99%), Ky (6.61%), Op (Ilm) (1.64%), Pl (1.38%), and Grt (0.95%) (**Figure 3**), which correspond to the pre-alpine Bt, Qtz, Grt, Op, Pl, and alpine Qtz, Cpx, Wm, Ky, Grt mineral associations.

Combining the mineral classification (**Figure 4**) with the grain size distribution (i.e., GSD output) using the Min-GSD, all grains were clustered as a function of each rock-forming mineral (**Figure 4A**). The procedure can distinguish 35,138 Qtz-grains, 32,030 Cpx-grains, 11,380 Wm-grains, 8,006 Ky-grains, 6,916 Bt-grains, 1,124 Op-grains, 731 Pl-grains, and 249 Grt-grains. This technique allows the quantitative estimation of the mineral orientation with respect to the pre-S1 foliation and the calculation of the mineral shape parameters (e.g., grain-size, width, length, and aspect-ratio; see **Supplementary Table S1** for details). The orientation analysis shows as the pre-alpine fabric (i.e., pre-S1 foliation and S-C fabric) is the most preserved. Although the alpine metamorphic mineral association is the most diffused, the orientation analysis reveals that the forming-minerals are still organized in the pre-alpine S-C-like geometry (**Figure 5**). In particular, the Bt, Wm, Qtz, Ky, and Cpx grains show two orientation clusters that can be correlated to the

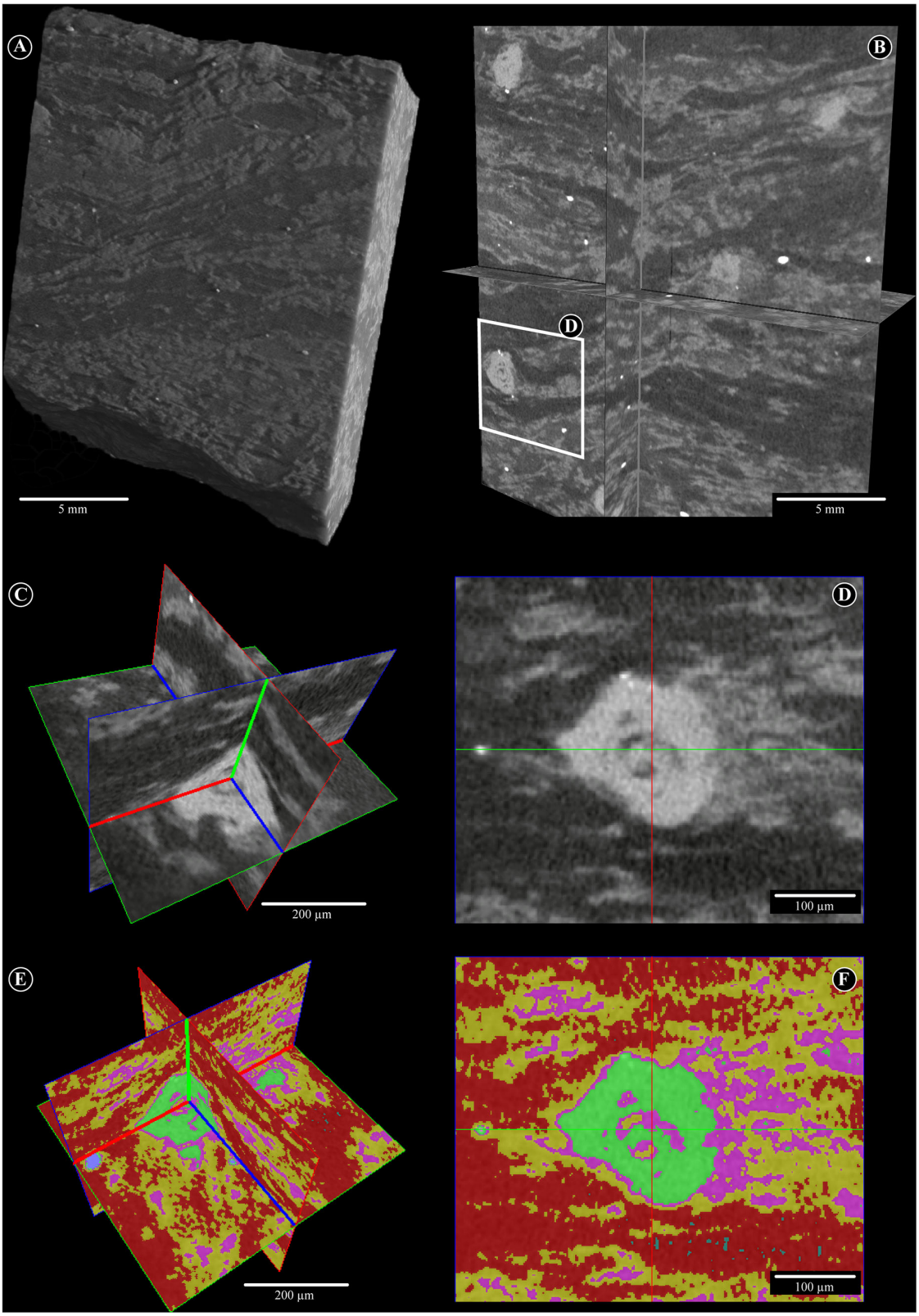

FIGURE 3 | Segmentation procedure. **(A)** Volume rendering of the original VOI obtained from the X-ray microtomography experiments. **(B)** Visual inspection of the gray levels related to the mineral phases. The sub-volume used as a target for the segmentation is located (white rectangle). Visual inspection of the gray levels related to the mineral phases within the **(C)** sub-volume and along **(D)** *XZ* plane. 3D Marked-Watershed segmentation procedure for the target **(E)** sub-volume and along **(F)** XZ plane.

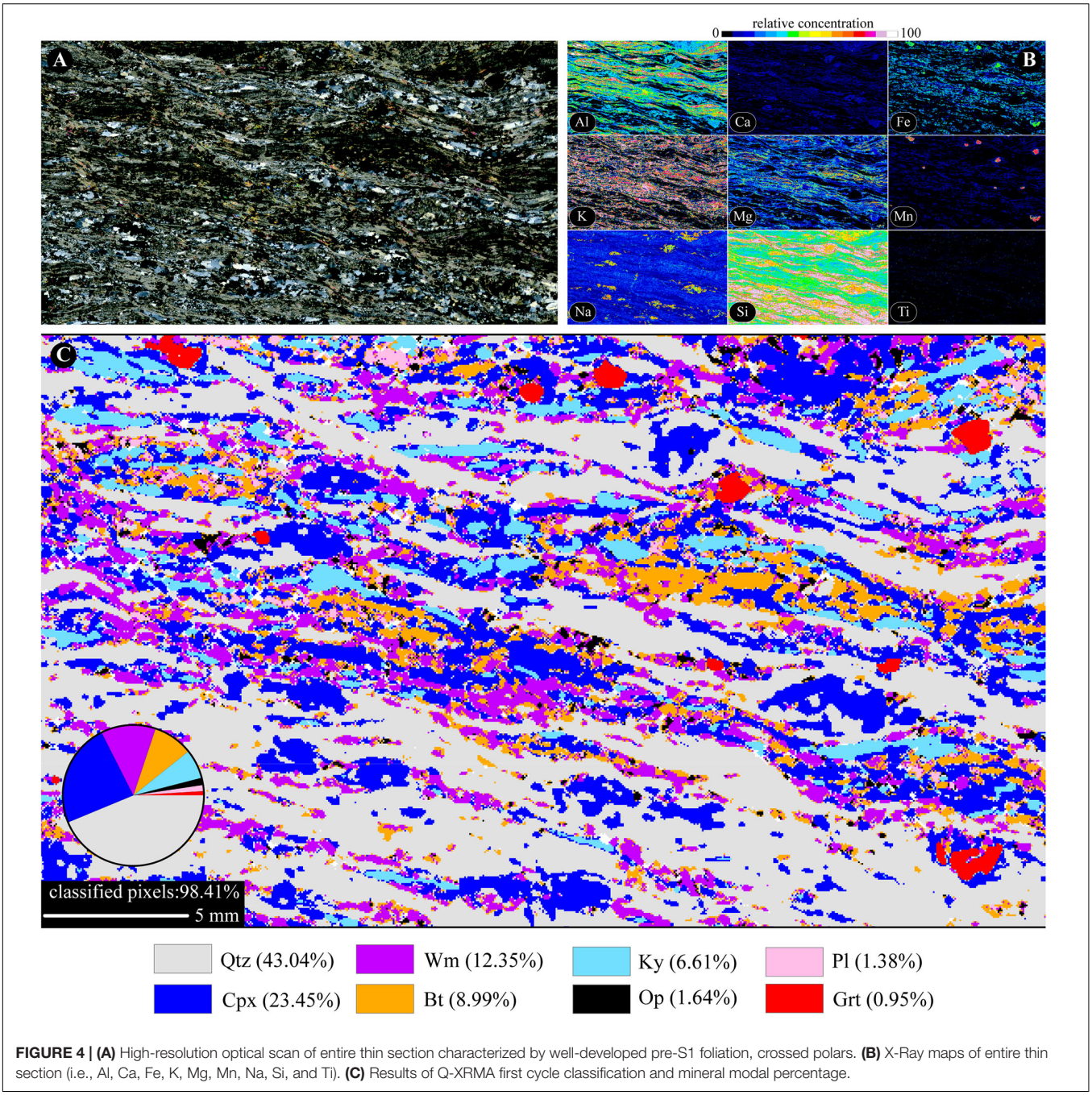

FIGURE 4 | (A) High-resolution optical scan of entire thin section characterized by well-developed pre-S1 foliation, crossed polars. **(B)** X-Ray maps of entire thin section (i.e., Al, Ca, Fe, K, Mg, Mn, Na, Si, and Ti). **(C)** Results of Q-XRMA first cycle classification and mineral modal percentage.

S and C structures. The S-related includes 28–35% of grains aligned at 2–13° with respect to the pre-S1. The C-related comprising 20–23% of grains laying at 34–46° from the pre-S1 orientation. The microstructural knowledge about the different microsites and about the variation in size and in shape of every mineral species it is crucial to archive the processed mineral grains to the alpine or pre-alpine metamorphic assemblage. For example, **Figure 5B** shows the quantification of the Grt generations (i.e., GrtI and GrtII) in relation to their grainsize and microstructural positions.

The microstructural analysis allows to assume the 0.1 mm^2 as the area-threshold value between the pre-alpine and alpine garnets and to estimate that only the 4.03% of the Grt grains refers to the pre-alpine metamorphic assemblage. Furthermore, the ArcGIS classification functions are useful to obtain 2D maps of the Aspect Ratio (AsR) for the different mineralogical species. The AsR visualization and estimation are shown for the Qtz (**Figure 5C**) and Cpx (**Figure 5D**) grains. The 60.17% of Qtz grains are characterized by the AsR equals to 0.70 ± 0.10 and the 60.80% of Cpx grains have an AsR of

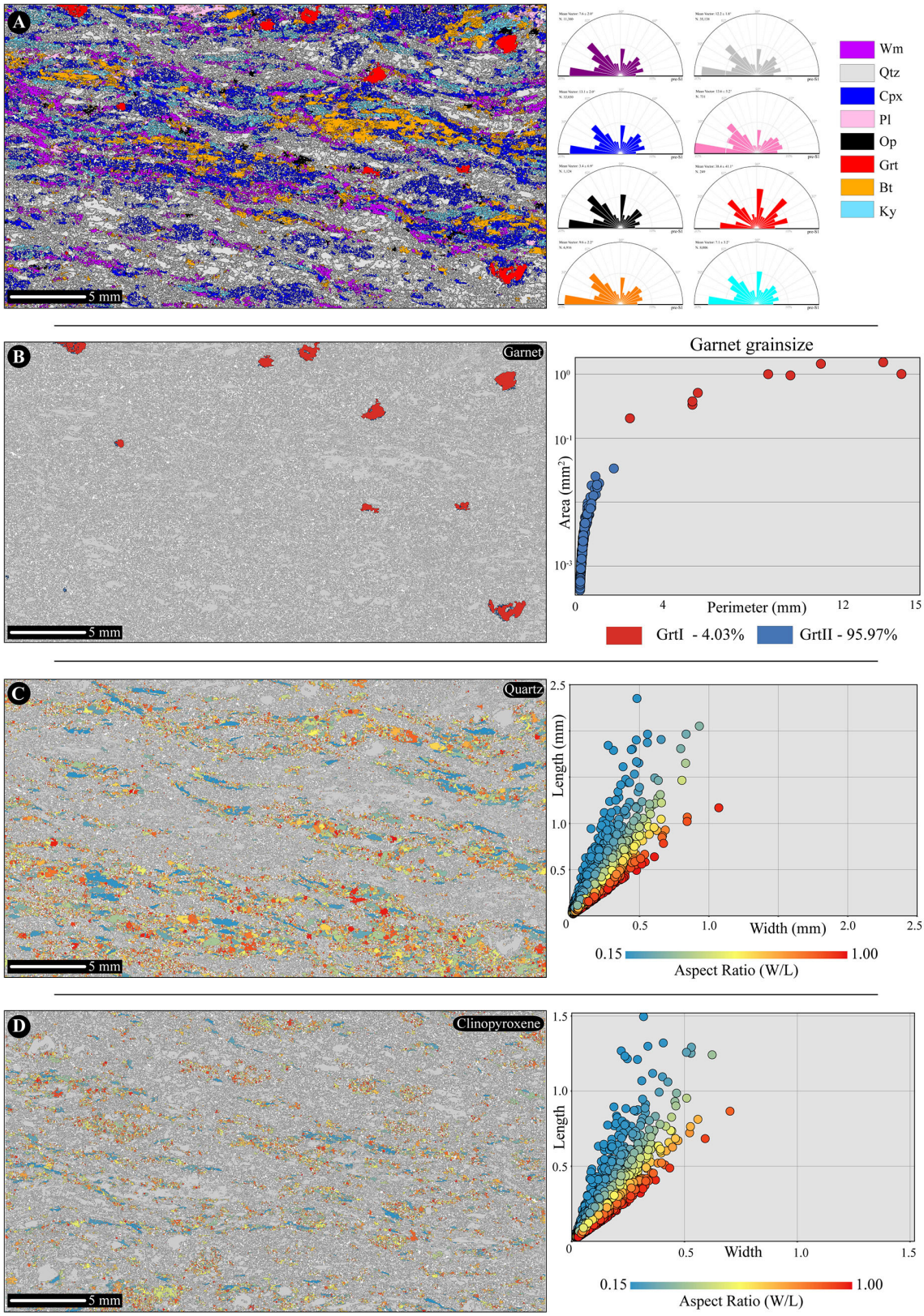

FIGURE 5 | (A) Results of Min-GSD and grains orientation with respect to pre-S1 foliation for each mineral phase. **(B)** Garnet grainsize map and grainsize vs. perimeter plot. **(C)** Aspect Ratio map of Qtz and Length vs. Width plot for all Qtz grains. **(D)** Aspect Ratio map of Cpx and Length vs. Width plot for all Cpx grains.

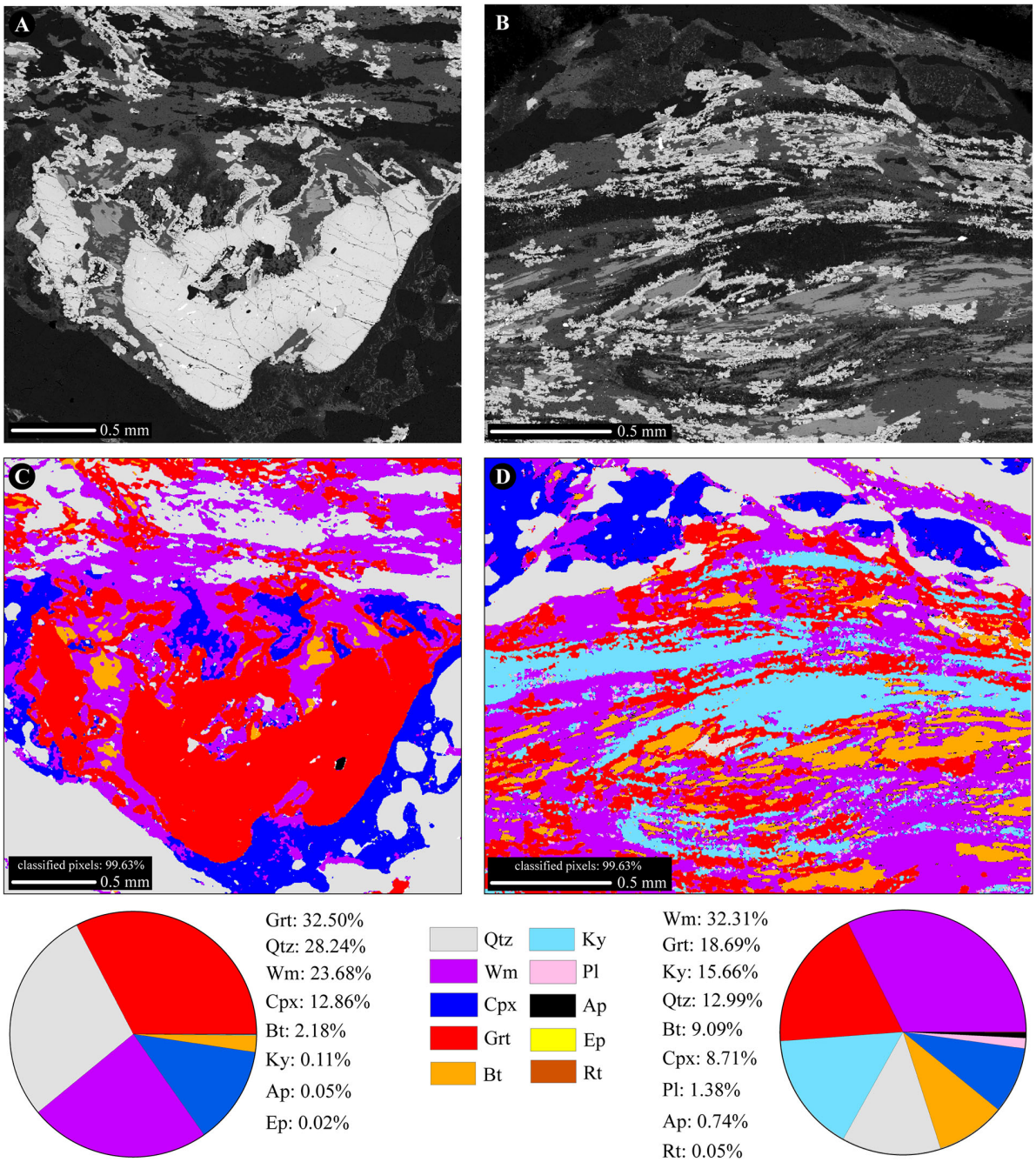

FIGURE 6 | (A) BSE image of pre-alpine Grt microdomain. **(B)** BSE image of pre-alpine Sill microdomain. **(C)** Results of Q-XRMA first cycle classification and mineral modal percentage for pre-alpine Grt microdomain. **(D)** Results of Q-XRMA first cycle classification and mineral modal percentage for pre-alpine Sill microdomain.

0.70 ± 0.10 denoting a low degree of alpine fabric evolution at the grain-scale.

The mineral chemical variation of the pre-alpine and alpine paragenesis are quantitatively explored in the GrtI (C1; **Figure 6A**) and ex-Sill (C2; **Figure 6B**) microdomains using the Q-XRMA software. The C1 forming-minerals and their modal percentage (**Figure 6C**) are Grt (32.50%), Qtz (28.24%), Wm (23.68%), Cpx (12.86%), Bt (2.18%), Ky (0.11%), Ap (0.05%), and Ep (0.02%). The C2 classified minerals and their modal abundance (**Figure 6D**) are Wm (32.31%); Grt (18.69%), Ky (15.66%), Qtz (12.99%), Bt (9.09%), Cpx (8.71%), Pl (1.38%), Ap (0.74%), and Rt (0.05%).

Garnet and clinopyroxene were selected due to their chemical composition distribution and as target minerals to highlight pre-alpine and alpine metamorphic evolution, respectively. With the aim of highlighting the maximum

range of compositional variability in the selected zoned garnet porphyroblast and the garnet coronae, 35 spot analyses (**Supplementary Table S2**) were acquired in both the chosen microdomains.

For each calculated pixel, the stoichiometry is in agreement with the structural formula of garnet [i.e., X3Y2(ZO4)3]. In the same manner, X-Ray maps of clinopyroxene were calibrated using 20 spot analyses (**Supplementary Table S3**) of different grains to highlight and quantify mineral chemical variations in relation to which pre-alpine microsite they replaced. The sum of cations is coherent with the structural formula of clinopyroxene (i.e., XYZ2O6).

Figure 7 shows the modal percentage of the Grt and Cpx sub-phase within the C1 microdomain and their calibrated chemical composition. The results of the calibration process for Grt divalent cations (**Figure 7A**; i.e., Ca, Fe, Mg, and Mn) highlight four distinct Grt sub-phases. The pre-alpine GrtI covers the 51% of the C1-garnets and it is characterized by high Fe content (2.31 ± 0.04 a.p.f.u.), the higher Mn content (0.23 ± 0.03 a.p.f.u.), Mg content of 0.37 ± 0.03 a.p.f.u., and the lowest Ca content (0.10 ± 0.05 a.p.f.u.). The three-type of alpine Grt show a wider chemical variability in depends on the microstructural location. Higher Ca content (i.e., maximum value of 1.23 a.p.f.u.) is observed where GrtII developed in contact with Cpx. Toward the pre-alpine biotite, GrtII is characterized by a continuous decrease of Mn and Fe contents and a corresponding increase of Mg and Ca contents. The GrtII grown in the pre-alpine Sill microdomain increase their Mg and Fe contents up to 0.89 and 1.91 a.p.f.u., respectively.

This mineral chemical variability was probably caused by differential diffusive exchange of the divalent cations in relation with pre-alpine microdomains replaced. Cpx replacing pre-alpine plagioclase microdomains (e.g., CpxI) displays two chemical trends. **Figure 7B** shows these trends by the calibrated maps of Ca, Fe, Mg, and Na, occupying the *X* and *Y* site in CpxI. They show higher Na content (0.89 ± 0.07 a.p.f.u.) in CpxI grown with Qtz than Cpx grown close to pre-alpine Grt porphyroblasts.

Figure 8 shows the modal percentage of the Grt and Cpx sub-phase within the C1 microdomain and their calibrated chemical composition. The calibrated elemental maps of the Grt show a continuous Ca content enrichment and Mg and Fe contents depletion from the pre-alpine Sill and Bt to the Pl microdomains (**Figure 8A**). In details, the Grt IIc is characterized by the highest Mg content (0.61 ± 0.13 a.p.f.u.) and the lowest Ca content (0.05 ± 0.03 a.p.f.u.). The Ca content reaches the maximum values of 0.68 a.p.f.u. and minimum Fe content (i.e., 1.86 a.p.f.u.) at the contact with the ex-Pl microdomains which is replace by the Cpx and Qtz assemblage during the alpine metamorphic evolution.

The results of the calibration process for Cpx (**Figure 8B**; Ca, Fe, Mg, and Mn) highlight three sub-phases. Cpx Ia are characterized by the higher Na content (0.91 ± 0.07 a.p.f.u.) than the Cpx Ib (0.68 ± 0.05 a.p.f.u.) and the Cpx Ic (0.57 ± 0.04 a.p.f.u.). The Fe content of 0.61 ± 0.02 a.p.f.u., the Ca content of 0.69 ± 0.06 a.p.f.u., and the absence of Mg content distinguish the Cpx Ic, whereas the Mg enrichment up to 0.28 a.p.f.u. discriminate the Cpx Ib. The third analytical cycle of Q-XRMA allow to obtain for C1 microdomain (**Figure 9A**) the end-member maps of Grt (**Figure 9B**; almandine, grossular, pyrope, and spessartine) and the end-member maps of Cpx (**Figure 9C**; diopside, hedenbergite, and jadeite) which were also used to extract chemical profiles (**Figure 9D**) from the calibrated outputs.

The GrtI is high in almandine content and low in the other three endmembers ranging from $Alm_{83}Grs_{0}Prp_{11}Sps_{6}$ to $Alm_{73}Grs_{5}Prp_{13}Sps_{9}$. The Grt IIa is characterized by a sharp discontinuity defined by a steep increase in grossular content and simultaneous depletion in almandine content, clearly visible in the compositional profile of **Figure 9D**. Toward the ex-Pl microdomain, the Grt IIa compositions vary from $Alm_{56}Grs_{31}Prp_{11}Sps_{2}$ to $Alm_{50}Grs_{40}Prp_{4}Sps_{6}$. The Grt IIb and Grt IId consist in a continuous corona around Grt I and Bt grains and they are generally characterized by gradual decrease in Alm content and increase in Prp and in Grs contents, respectively. Grt IIb developed toward Grt I and Bt grains exhibiting an average composition of $Alm_{59}Grs_{9}Prp_{24}Sps_{8}$. Whereas, Grt IId growth between the Grt I and the pre-alpine Sill microdomains shows an end-member composition of $Alm_{53}Grs_{30}Prp_{11}Sps_{6}$. The Grt IIc is developed outside of Grt I microdomain showing a gradual reduction of almandine and grossular components and enrichment in Prp and Sps contents toward pre-alpine Sill microdomain. The composition ranging from $Alm_{47}Grs_{2}Prp_{30}Sps_{21}$ to $Alm_{46}Grs_{2}Prp_{5}Sps_{47}$. The clinopyroxene phase mostly consists in jadeite component ranging from 50 to 96%. When Cpx is developed in contact with garnet shows a Jd contents up to 78% with an average value of 93%. Toward pre-alpine Sill microdomain, the Cpx is characterized by low content in Jd and corresponding enrichment in Hed and Di end-members up to 30 and 12%, respectively.

The end-member components variation for garnet and clinopyroxene within the C2 microdomain (**Figure 10A**) has been explored through the Q-XRMA third cycle. The garnet component maps (**Figure 10B**) and chemical profile (**Figure 10D**) highlight a gradual enrichment in grossular and depletion in almandine and pyrope from Grt IIc (average composition: $Alm_{70}Grs_{0}Prp_{29}Sps_{1}$) to Grt IIb (average composition: $Alm_{66}Grs_{9}Prp_{23}Sps_{2}$).

Grt IId developed in contact with clinopyroxene and quartz assemblage and it is characterized by a sharp discontinuity defined by a steep increase in grossular and simultaneous decrease in almandine and pyrope contents. The Grt IId component composition varies from $Alm_{63}Grs_{18}Prp_{18}Sps_{1}$ to $Alm_{61}Grs_{22}Prp_{15}Sps_{2}$.

The assemblage consists of clinopyroxene plus quartz developed within the pre-alpine Pl-microdomains. Although the clinopyroxene is generally high in jadeite composition, the component maps (**Figure 10C**) show a composition variability related to the distance from the pre-alpine biotite and alpine garnet. Cpx Ia is characterized by a gradual increase of Jd content from 82% at the core to 97% at the rim in contact with Grt IId. Cpx Ib develop in contact with white-mica and it is characterized by a Di content of 33%, whereas Cpx Ic shows a sharp discontinuity defined by a steep increase of Hed up to 73%

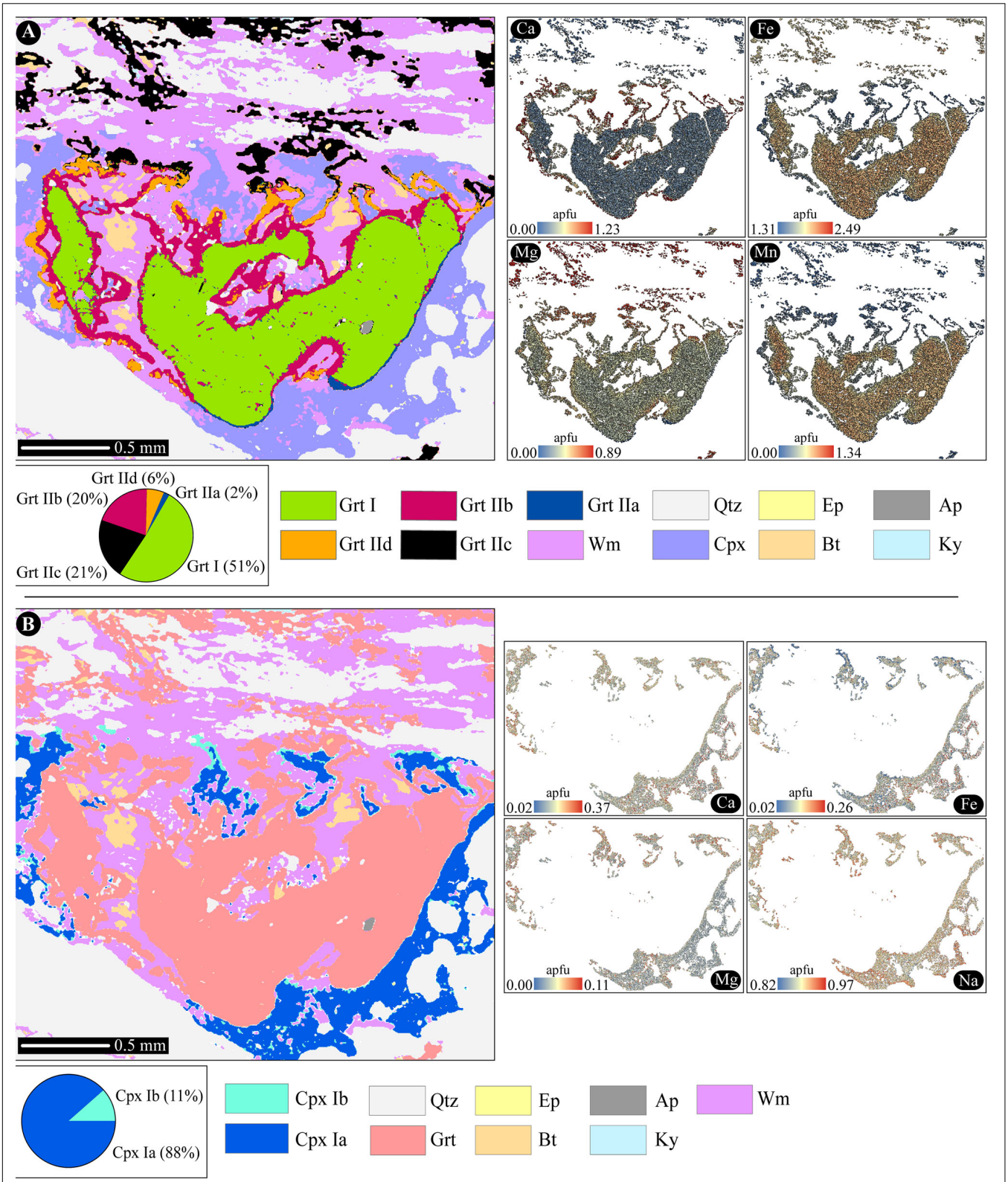

FIGURE 7 | Results of second cycle of Q-XRMA procedure for pre-alpine Grt microdomain. **(A)** Grt sub-phases classification and their modal percentage. Calibration maps of Ca, Fe, Mg, and Mn contents in Grt. **(B)** Cpx sub-phases classification and their modal percentage. Calibration maps of Ca, Fe, Mg, and Na contents in Cpx.

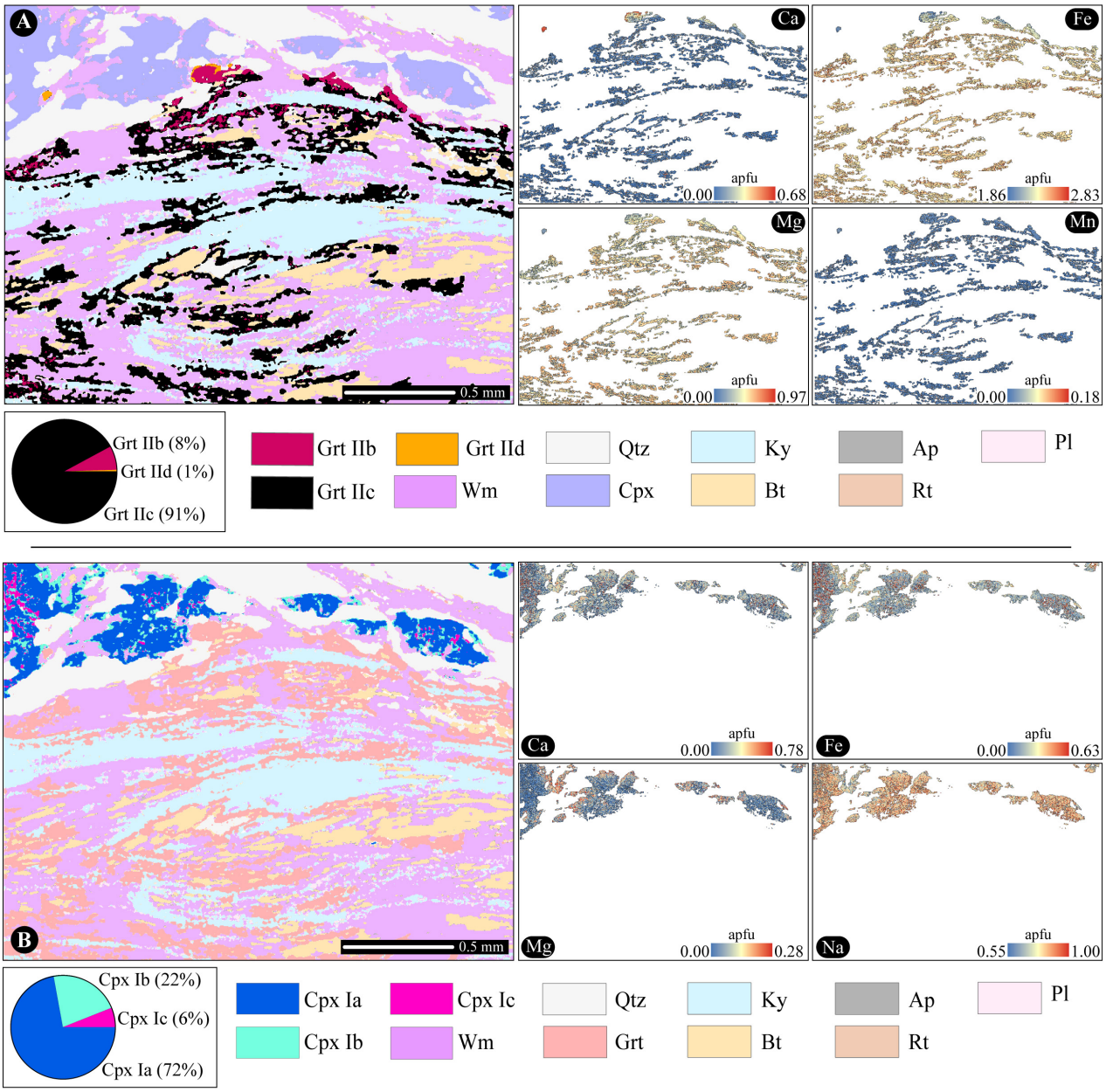

FIGURE 8 | Results of second cycle of Q-XRMA procedure for pre-alpine Sill microdomain. **(A)** Grt sub-phases classification and their modal percentage. Calibration maps of Ca, Fe, Mg, and Mn contents in Grt. **(B)** Cpx sub-phases classification and their modal percentage. Calibration maps of Ca, Fe, Mg, and Na contents in Cpx.

and simultaneous depletion in Jd content (i.e., minimum value of 27%), clearly visible in the compositional profile of **Figure 10D**.

3D Fabric and Metamorphic Results

The X-ray μ-CT data can be segmented into six components. The brightest regions in the images have been attributed to opaque and garnet, followed by the clinopyroxene-kyanite-micas (i.e., biotite and white mica) aggregates, and the darkest layers to quartz. **Figure 11A** shows the volume rendering of the segmented phases and the volumetric quantification of each phase processed with the PerGeos software. The segmentation of the Qtz volume (**Figure 11B**) allows to observe how the pre-alpine S-C-like geometry is well-preserved and the pervasive mylonitic fabric is overprinted by static alpine re-equilibration. By combining mineral phase segmentation based on gray-scale threshold with the characterization of microstructures (i.e., different grain-size classes for the same phase and morphology of different pre-alpine microdomains) allowed to distinguish the pre-alpine mineralogical phases from the alpine overprint and to quantify their ratio (**Supplementary Table S4**). For instance, the volume rendering of the specimen with 127,073 highlighted garnets (**Figure 11C**) and the garnet grainsize analysis (**Figure 11D**)

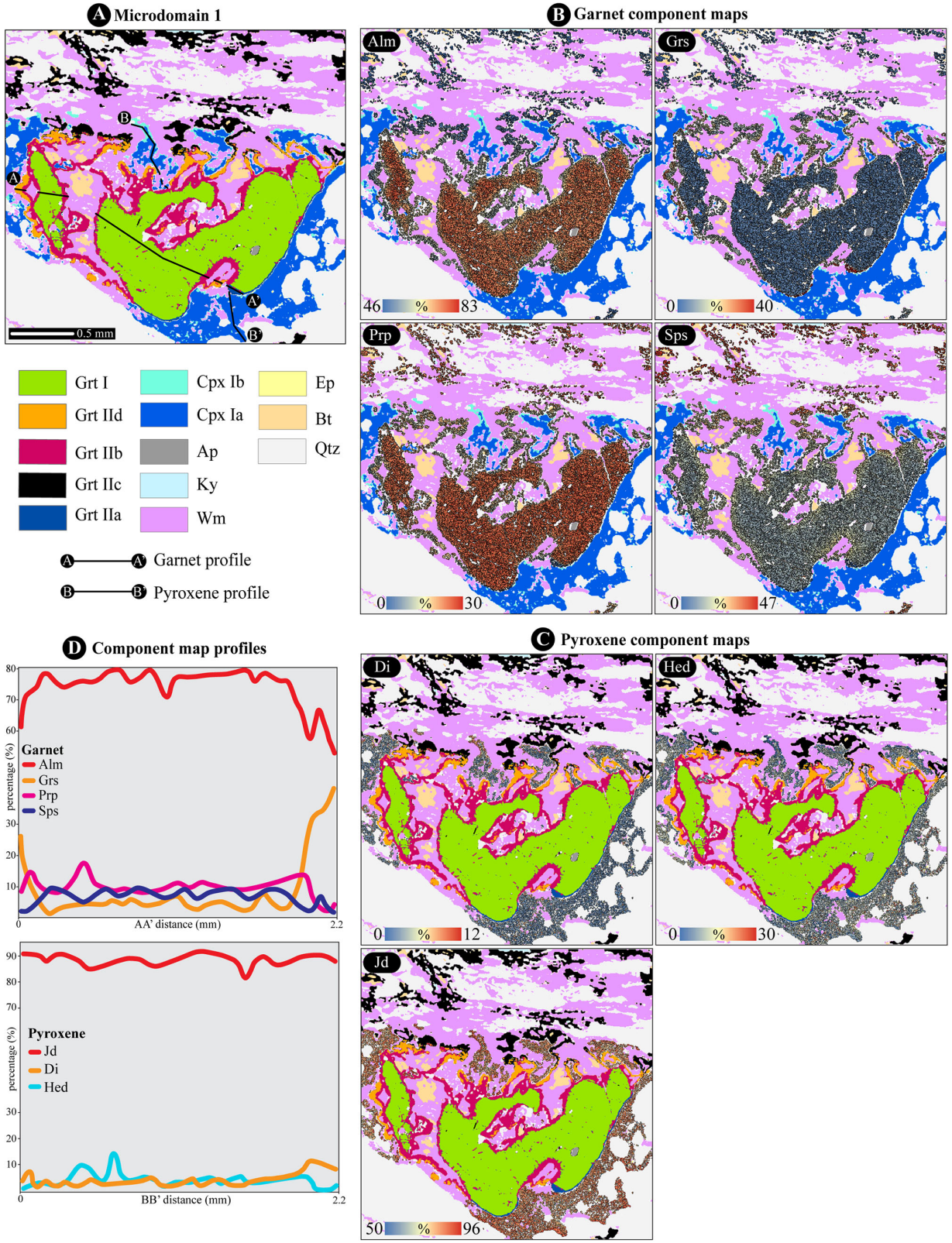

FIGURE 9 | (A) Results of third cycle of Q-XRMA for pre-alpine Grt microdomain and localization of chemical profiles. **(B)** Component maps for Grt (i.e., Alm, almandine; Grs, grossular; Prp, pyrope; Sps, spessartine). **(C)** Component maps for Cpx (i.e., Di, diopside; Hed, hedenbergite; Jd, jadeite). **(D)** Component profiles for Grt and Cpx.

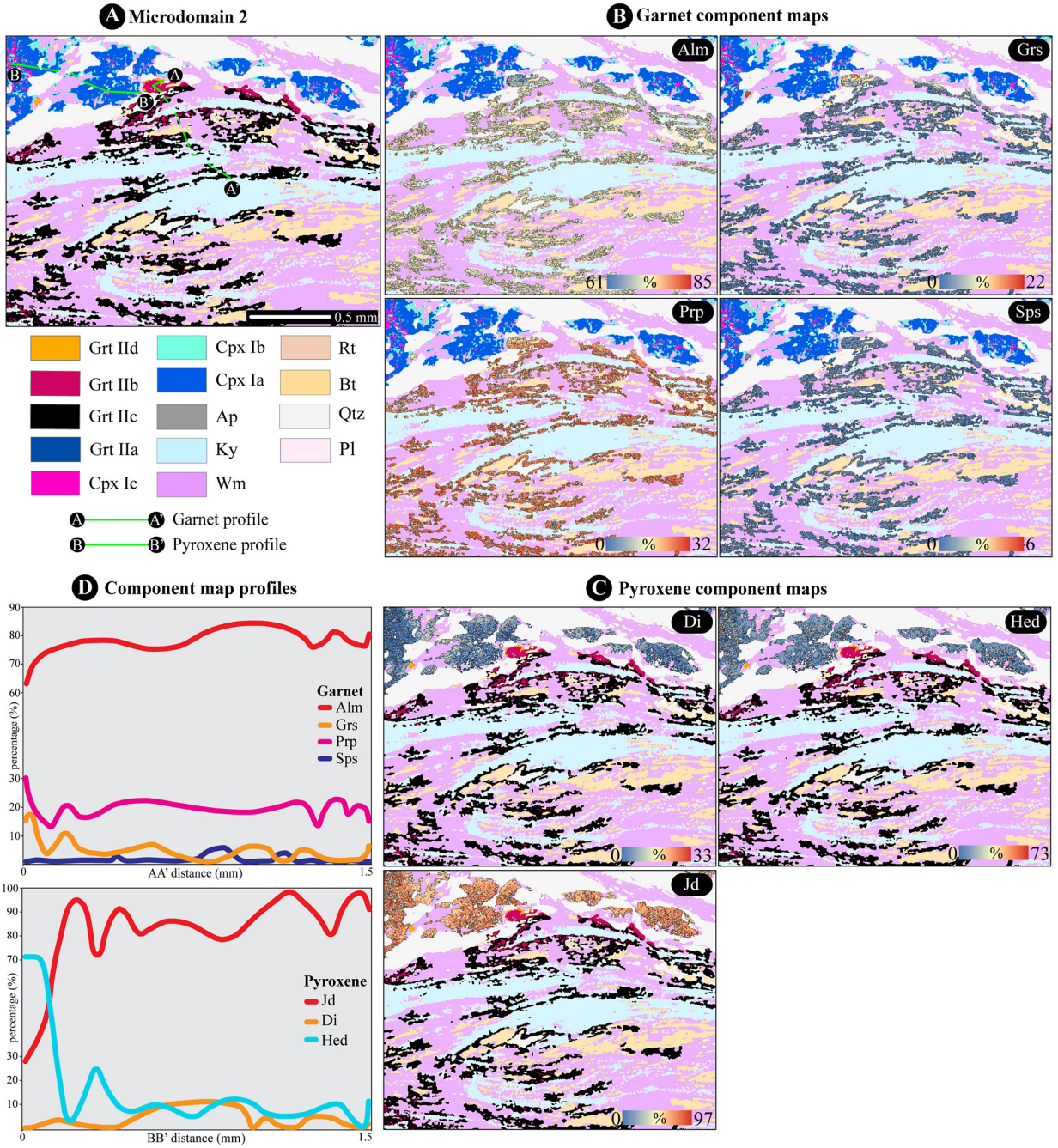

FIGURE 10 | (A) Results of third cycle of Q-XRMA for pre-alpine Sill microdomain and localization of chemical profiles. **(B)** Component maps for Grt (i.e., Alm, almandine; Grs, grossular; Prp, pyrope; Sps, spessartine). **(C)** Component maps for Cpx (i.e., Di, diopside; Hed, hedenbergite; Jd, jadeite). **(D)** Component profiles for Grt and Cpx.

clearly display two distinct classes (**Supplementary Table S5**). The Grt I is characterized by a volume of 108 μm^3 and a more marked anhedral morphology than Grt II, as can be visualized by high pseudo-grain surface (**Figure 11D**). Using this approach for each segmented mineralogical phase permits to quantify the volume of pre-alpine assemblage (Grt I + Wm I + Bt I) and the alpine overprints. The volumetric analysis shows that the pre-alpine-related phases represent 21.91% of the volume (**Figure 11A**) and mostly consist in Bt I and Wm I. The alpine-related phases, comprising the 78.09% of the volume, involve Wm II/Bt II (41.73%), Qtz (30.46%), Cpx (3.86%), Ky (2.04%), and Grt II (0.01%).

The distribution patterns, and the SPO analysis for Qtz and Cpx are shown in **Figures 1**, **12,** and **Supplementary Table S5**.

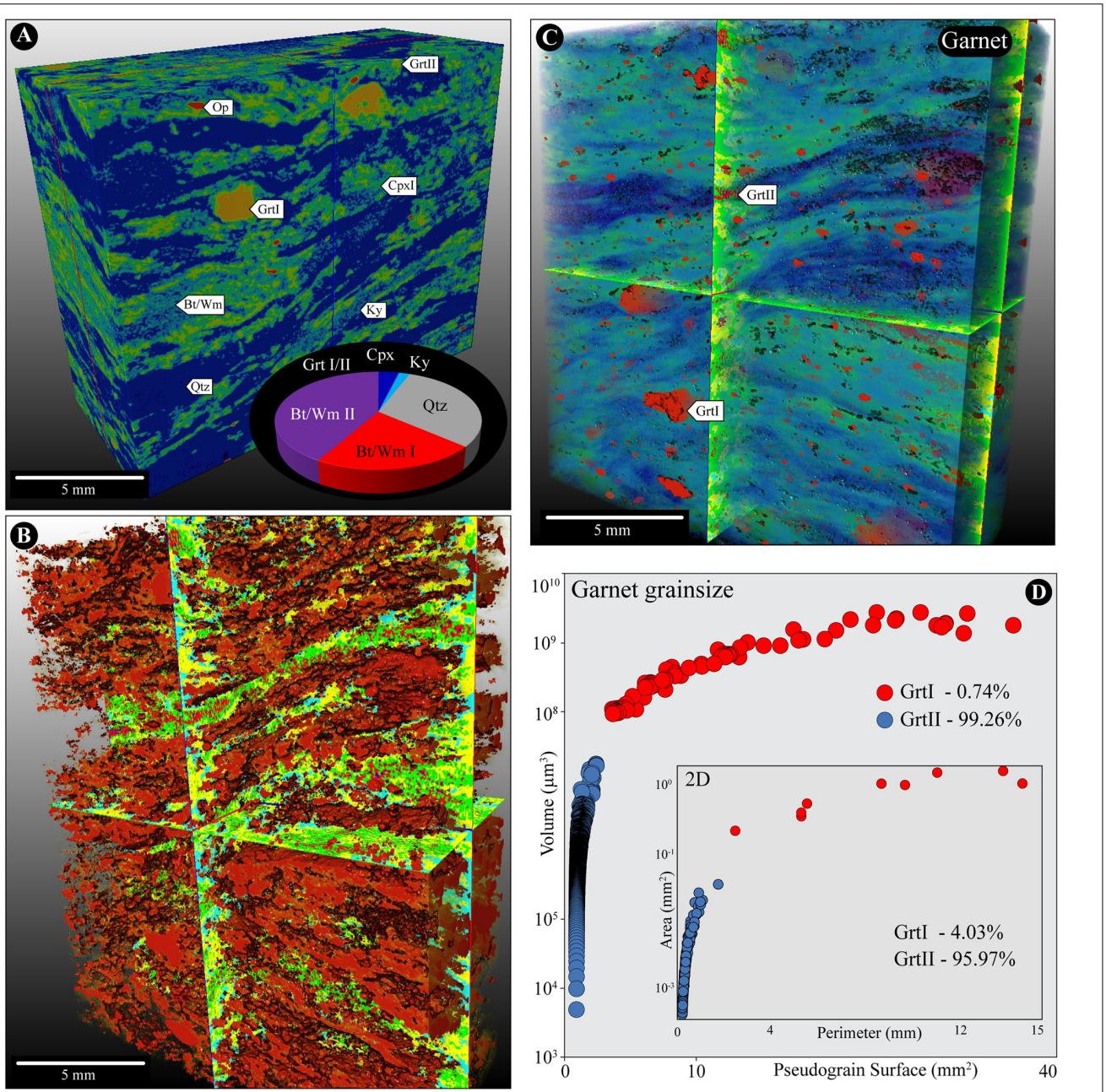

FIGURE 11 | (A) Volume rendering of the segmented phases and the volumetric quantification of each phase. **(B)** Example of mineral segmentation (e.g., Qtz) showing the preservation of pre-S1 fabric. **(C)** Garnet pseudo-grains are highlighted within the entire rock-volume. **(D)** Grainsize vs. surface of Grt pseudo-grains.

3D grain-shape anisotropy and orientation were measured using best-fit ellipsoids to Qtz and Cpx outer surfaces, from which the mean radius was calculated based on a spherical geometry (i.e., *X*, *Y*, and *Z* from longest to shortest axis). A total of 65,5361 quartz and 92,0316 clinopyroxene were measured as enclosed within the sample volume (**Figures 12A,B**) and are both characterized by an aspect ratio (Z/X) ranging from 0.15 to 1.00 (**Figures 12C,D**). The distribution of Cpx and Qtz aspect ratios (**Figures 13A,B**) has an average value of 0.52 ± 0.19 and 0.67 ± 0.26, respectively, persisting among all grain-size classes (**Figures 12C,D**).

Qtz and Cpx shapes can be summarized with a Flinn plot (**Figures 13C,E**) and Zingg shape diagram (**Figures 13D,F**), which suggest a weak planar-type fabric orientation of pseudo-grains roughly distributed among blade-like shapes. Even though the weak SPO and the blade-like shape arrangement of alpine Cpx and Qtz pseudo-grains, the anisotropic aspect ratios may be the results of pre-alpine high SPO inheritance. The SPO and the volumetric measurements verified and quantified the observed weak grain-shape anisotropy and high metamorphic overprint during the alpine tectono-metamorphic evolution.

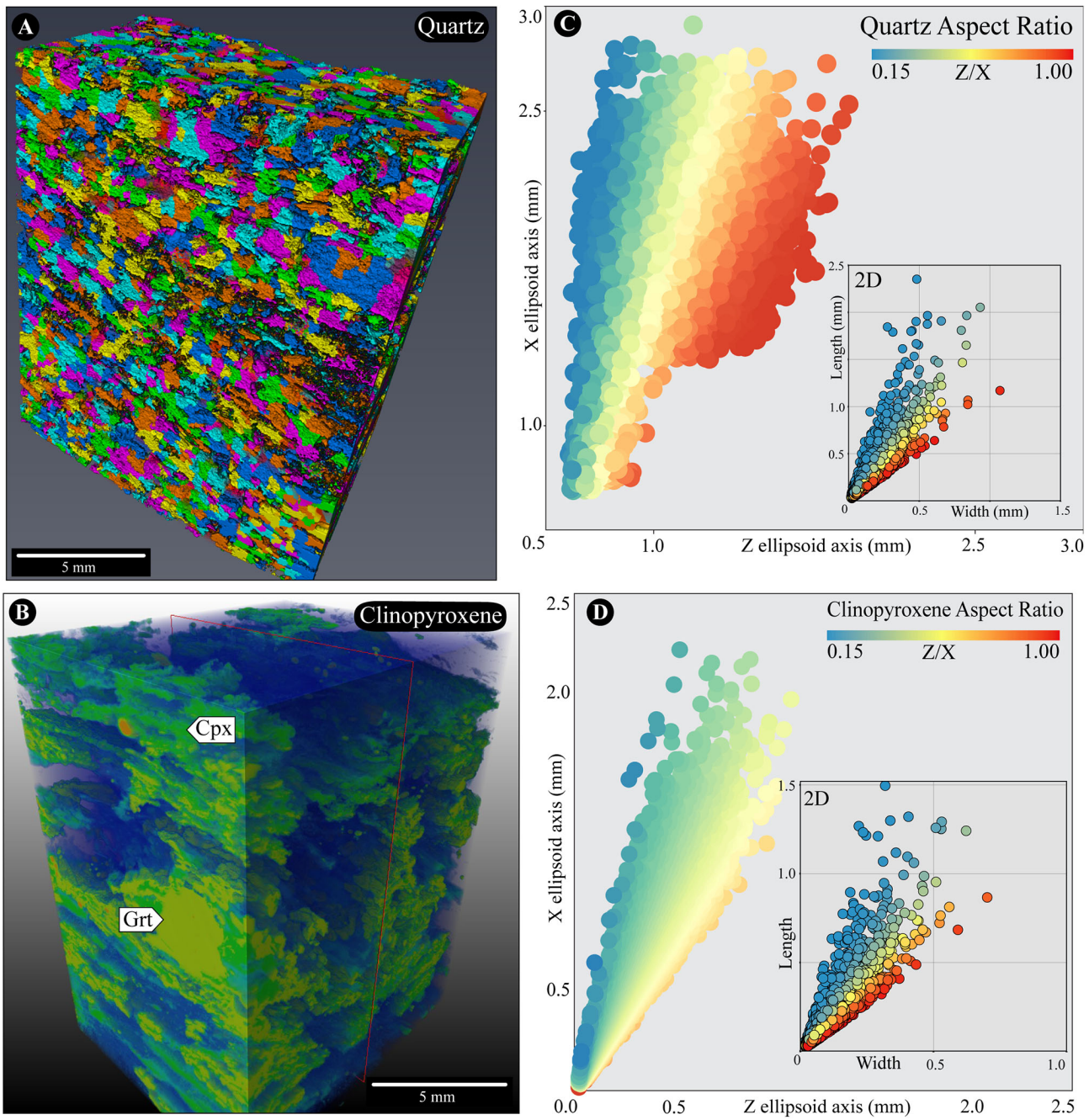

FIGURE 12 | (A) 3D visualization of the Qtz pseudo-grains arrangement. **(C)** Qtz aspect ratio plot defined by the *Z* ellipsoid axis and *X* ellipsoid axis ratio. The 2D aspect ratio plot is reported. **(B)** 3D visualization of the Grt (yellow), Qtz (blue), and Cpx (green) relationships. **(D)** Cpx aspect ratio plot defined by the *Z* ellipsoid axis and *X* ellipsoid axis ratio. The 2D aspect ratio plot is reported.

DISCUSSION AND CONCLUSION

Micro-Scale and Kinetics Implications

The 3D visualization and analysis of fabrics and metamorphic minerals achieved by the X-ray μ-CT are well constrained by the 2D micro-structural analysis. In fact, despite the large gap between the two techniques in terms of number of analyzed grains, the results are comparable as shown by 2D vs. 3D description of shape parameters (**Figures 12**, **13**). The reproducibility shown by the comparison of the shape analysis results allowed us to improve mineral phases identification, during the segmentation procedure, thanks to the knowledge from the 2D analysis, where not only shape parameters were known but also optical properties and

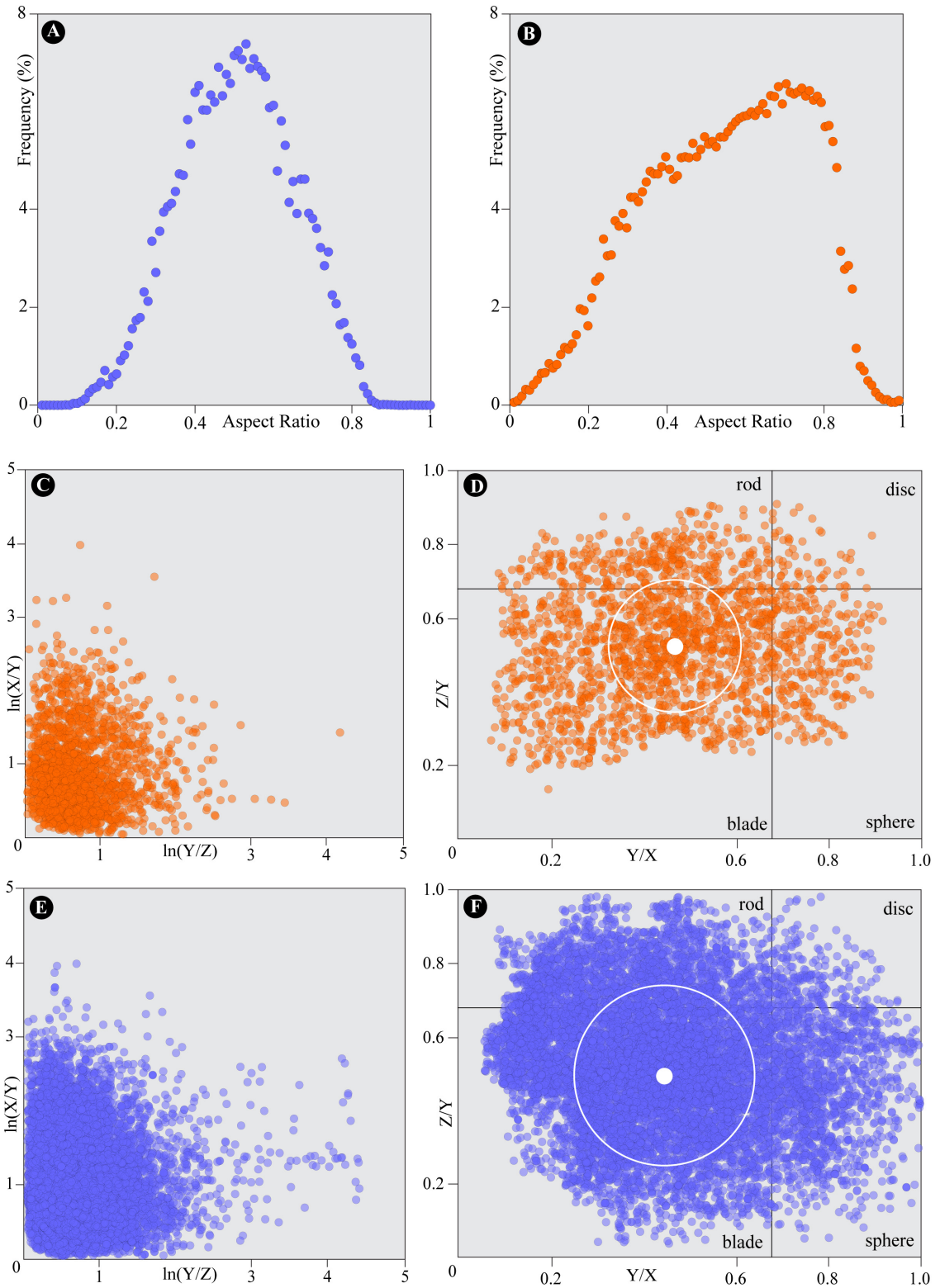

FIGURE 13 | 3D quantitative fabric analysis. **(A)** Frequency of Cpx aspect ratio. **(B)** Frequency of Qtz aspect ratio. **(C)** Flinn diagram of Qtz pseudo-grains. **(D)** Zingg diagram of Qtz pseudo-grains. The average and the standard deviation are reported. **(E)** Flinn diagram of Cpx pseudo-grains. **(F)** Zingg diagram of Cpx pseudo-grains. The average and the standard deviation are reported.

mineral chemistry. Consequently, the quantitative chemical information obtained by the Q-XRMA tool were extended to the whole 3D volume.

Figures 11, **12** may also be used to quantitatively support the pervasiveness of the pre-alpine fabrics (100% of the rock fabric) within the investigated volume. Even though the pre-alpine fabric is so well preserved the pre-alpine minerals surprisingly correspond only to less than 22% (**Figure 11A**). Pre-alpine minerals mostly consist of GrtI, BtI and WmI and their compositions are known, and the P-T estimates might be easily depicted and used as first-order input data for dynamic numerical modeling for geodynamic reconstructions (e.g., Roda et al., 2012).

Similar contrasting relations between degree of fabric development and mineral associations have been described for eclogitized rocks in the same area, where Permian intrusive preserve their igneous fabrics, estimated as >90% of the rock fabric (Zucali et al., 2002; Zucali, 2011), but the mineral association related to the magmatic stage is almost totally replaced by eclogite facies minerals, up to 80–90% of the investigated portions (Koons, 1982; Zucali et al., 2002; Corti et al., 2017).

In the investigated case, the alpine-related mineral phases, comprising the 78.09% of the volume, involve WmII/BtII (41.73%), Qtz (30.46%), Cpx (3.86%), Ky (2.04%), and GrtII (0.01%), and do not mark a new fabric, but statically replace specific pre-alpine microdomains. The static replacement is also quantitatively shown by the heterogeneous grain-size distribution (**Figures 11**, **12**), suggesting a dominant control of the growth domain over dynamic recrystallization that would have induced more pronounced shapes preferred orientations (Bell and Hayward, 1991). For example, GrtII grows as corona over GrtI, or Ky grows as aggregates replacing pre-alpine Sill-microdomains. The volumetric reconstruction of the shape and spatial distribution of alpine-related phases clearly demonstrate that metamorphic reactions may occur even in absence of deformation, and in the virtual absence of fluid as chemical medium. This was demonstrated by the unchanged bulk chemistry within the selected microsites. As an example, GrtII increases its Fe and Ca content in the ex-sillimanite domain and ex-plagioclase domains, respectively. Similarly, the Ky phase only occurs as pseudomorphic fine-grained aggregates in ex-sill domains. In the same way, the symplectite textures occurring in the ex-Pl domains are defined by high Jd contents (82–97%) Cpx, Ca-rich Grt (highest Grs component around 22%), and Qtz. All these features suggest that even at low temperature conditions (nominally below 550°C) and in low-strain domains the activation energy of many metamorphic reactions, energetically less favored (e.g., sillimanite to kyanite reaction), may be overstepped.

General Implications

A relative age of the two generations of minerals (i.e., pre-alpine and alpine) can be inferred, using their chemistry and microstructural relationships. In fact, GrtII, Cpx and WmII mineral chemistry strongly overlap with those expected for similar phases growth at eclogite-facies conditions (Zucali et al., 2002; Zucali and Spalla, 2011), attributed to an age range of 80–60 Ma (Cenki-Tok et al., 2011; Regis et al., 2014). The chemistry of GrtI and BtI overlaps the compositions known for similar rocks, as the Ivrea-Zone (e.g., Barboza and Bergantz, 2000), the Serie di Valpelline and the Dent-Blance Unit (Manzotti et al., 2012; Manzotti and Zucali, 2013), and other Austroalpine or Southalpine slices which they preserve the pre-alpine (Permian) high-temperature imprint (Roda et al., 2018c).

The investigated 3D microstructures exhibit complex overprinting relationships that are only partially reflected by outcrop-scale structures. In particular, the Bt, Wm, Qtz, Ky, and Cpx grains show two orientation clusters that can be correlated to the S and C mylonitic structures. The S-related structure includes 35% of grains aligned at 2–13° with respect to the pre-S1. The C-related structure comprises 23% of grains laying at 34–46° from the pre-S1 orientation. These S-C fabrics may be compared to pre-alpine features described by previous authors at the map-scale (Zucali, 2002; Corti et al., 2017) and preserved in similar low-strain volumes of the Sesia-Lanzo Zone. Still remains unclear how those meter-scale domains might preserve such clean fabrics even where no mechanical barriers have been described at the map-scale.

In conclusion, similar to what described at km-scale by 3D geological modeling (e.g., Salvi et al., 2010; Zucali et al., in press), a volumetric quantification is fundamental to improve our knowledge of the tectono-metamorphic evolution of active margins (e.g., subduction zone). In particular, the 3D reconstruction of grain shape distribution through X-ray microtomography on centimeters-sized samples allows to improve the knowledge of the metamorphic texture development. Moreover, the combined use of EMPA X-ray chemical mapping with the X-ray μ-CT technique can further permit to dynamically constrain the chemistry of the mineral phases linked to the metamorphic transformation.

DATA AVAILABILITY STATEMENT

All datasets generated for this study are included in the article/**Supplementary Material**.

AUTHOR CONTRIBUTIONS

LC and MZ conceived the presented idea. MZ, LM, and LC carried out the experiment. LM, RV, and MS verified the analytical methods. MZ, RV, LM, and MS contributed to the interpretation of the results. LC wrote the manuscript with support from MZ, RV, LM, and MS. All authors discussed the results and contributed to the final manuscript.

FUNDING

This work was funded by Ph.D. School in Earth Sciences from University of Milan; Elettra Proposal (SYRMEP) #20170147, "Toward a geologically meaningful quantification of 3D grains shape distribution in natural rocks" to MZ and the University of Milano: Linea 2, Azione A – fondi giovani ricercatori "*Analisi strutturale delle catene collisionali*" (PSR2018_DZANONI). Results here presented have been developed in the frame of the MIUR Project "Dipartimenti di Eccellenza 2017 – Le Geoscienze per la società: risorse e loro evoluzione (work-package 3, tasks 3.3, and 3.4)." Elettra Sincrotrone Trieste is acknowledged for financial support to open access publication.

ACKNOWLEDGMENTS

The authors thank A. Risplendente for assistance during the WDS/EDS-EPMA analysis and Dr. J. Kuva for support during the tomography data analysis with PerGeos in GTK.

SUPPLEMENTARY MATERIAL

The Supplementary Material for this article can be found online at: https://www.frontiersin.org/articles/10.3389/feart.2019.00327/full#supplementary-material

REFERENCES

Babist, J., Handy, M. R., Konrad-Schmolke, M., and Hammerschmidt, K. (2006). Precollisional, multistage exhumation of subducted continental crust: the Sesia Zone, western Alps. *Tectonics* 25:TC6008. doi: 10.1029/2005TC001927

Baker, D. R., Mancini, L., Polacci, M., and Higgins, M. D. (2012). An introduction to the application of X-ray microtomography to the three-dimensional study of igneous rocks. *Lithos* 148, 262–276. doi: 10.1016/j.lithos.2012.06.008

Balestro, G., Festa, A., and Dilek, Y. (2019). Structural architecture of the Western alpine ophiolites, and the Jurassic Seafloor spreading tectonics of the alpine Tethys. *J. Geol. Soc.* 176, 913–930. doi: 10.1144/jgs2018-099

Barboza, S. A., and Bergantz, G. W. (2000). Metamorphism and anatexis in the mafic complex contact Aureole, Ivrea Zone, Northern Italy. *J. Petrol.* 41, 1307–1327. doi: 10.1093/petrology/41.8.1307

Baruchel, J., Buffiere, J. Y., and Maire, E. (2000). *X-ray Tomography in Material Science*. Paris: Hermes science publications.

Belfiore, C. M., Fichera, G. V., Ortolano, G., Pezzino, A., Visalli, R., and Zappalà, L. (2016). Image processing of the pozzolanic reactions in Roman mortars via X-Ray map analyser. *Microchem. J.* 125, 242–253. doi: 10.1016/j.microc.2015.11.022

Bell, T. H., and Hayward, N. (1991). Episodic metamorphic reactions during orogenesis: the control of deformation partitioning on reaction sites and reaction duration. *J. Metamorph. Geol.* 9, 619–640. doi: 10.1111/j.1525-1314.1991.tb00552.x

Berrezueta, E., Domínguez-Cuesta, M. J., and Rodríguez-Rey, Á. (2019). Semi-automated procedure of digitalization and study of rock thin section porosity applying optical image analysis tools. *Comput. Geosci.* 124, 14–26. doi: 10.1016/j.cageo.2018.12.009

Bigi, G., Castellarin, A., Coli, M., Dal Piaz, G. V., Sartori, R., Scandone, P., et al. (1990). *Structural Model of Italy, Sheets 1-2. In: Progetto Finalizzato Geodinamica del CNR*. Firenze: SELCA.

Bussy, F., Venturini, G., Hunziker, J., and Martinotti, G. (1998). U–Pb ages of magmatic rocks of the western Austroalpine Dent-Blanche-Sesia Unit. *Schweitz. Mineral. Petrogr. Mitt.* 78, 163–168.

Callegari, E., Compagnoni, R., Dal Piaz, G. V., Frisatto, V., Gosso, G., and Lombardo, B. (1976). Nuovi affioramenti di metagranitoidi nella zona Sesia-Lanzo. *Rend. Soc. Ital. Miner. Petrol.* 32, 97–111. doi: 10.1140/epjc/s10052-018-6290-2

Cantù, M., Spaggiari, L., Zucali, M., Zanoni, D., and Spalla, M. I. (2016). Structural analysis of a subduction-related contact in southern Sesia-Lanzo Zone (Austroalpine Domain, Italian Western Alps). *J. Maps* 12, 22–35. doi: 10.1080/17445647.2016.1155925

Castelli, D. (1987). *Il Metamorfismo Alpino delle Rocce Carbonatiche della Zona Sesia-Lanzo (Alpi Occidentali)*. Ph.D. thesis, Consorzio Universitario di CA-GE-TO, Ragusa.

Castelli, D. (1991). Eclogitic metamorphism in carbonate rocks: the example of impure marbles from the Sesia-Lanzo Zone, Italian Western Alps. *J. Metam. Geol.* 9, 61–77. doi: 10.1111/j.1525-1314.1991.tb00504.x

Castelli, D., and Rubatto, D. (2002). Stability of Al- and F-rich titanite in metacarbonate: petrologic and isotopic constraints from a polymetamorphic eclogitic marble of the internal Sesia Zone (Western Alps). *Contrib. Miner. Petrol.* 142, 627–639. doi: 10.1007/s00410-001-0317-6

Cenki-Tok, B., Oliot, E., Rubatto, D., Berger, A., Engi, M., and Janots, E. (2011). Preservation of Permian allanite within an alpine eclogite facies shear zone at Mt Mucrone, Italy: mechanical and chemical behavior of allanite during mylonitization. *Lithos* 125, 40–50. doi: 10.1016/j.lithos.2011.01.005

Cnudde, V., and Boone, M. N. (2013). High-resolution X-ray computed tomography in geosciences: a review of the current technology and applications. *Earth Sci. Rev.* 123, 1–17. doi: 10.1016/j.earscirev.2013.04.003

Compagnoni, R. (1977). The Sesia-Lanzo zone: high-pressure low-temperature metamorphism in the Austroalpine continental margin. *Ren. Soc. Ital. Miner. Petrol.* 33, 335–374.

Compagnoni, R., Dal Piaz, G. V., Hunziker, J. C., Gosso, G., Lombardo, B., and Williams, P. F. (1977). The Sesia Lanzo zone, a slice of continental crust with alpine high pressure-low temperature assemblages in the Western Italian Alps. *Rend. Soc. It. Min. Petr.* 33, 281–334.

Compagnoni, R., and Maffeo, B. (1973). Jadeite bearing metagranites ls. and related rocks in the Mount Mucrone Area (Sesia-Lanzo zone, Western Italian Alps). *Schweiz. Mineral. Petrogr. Mitt.* 53, 355–378.

Corti, L., Alberelli, G., Zanoni, D., and Zucali, M. (2017). Analysis of fabric evolution and metamorphic reaction progress at Lago della Vecchia-Valle d'Irogna, Sesia-Lanzo Zone, Western Alps. *J. Maps* 13, 521–553. doi: 10.1080/17445647.2017.1331177

Corti, L., Alberelli, G., Zanoni, D., and Zucali, M. (2018). Tectonometamorphic evolution of the Lago della Vecchia meaintrusive and its country rocks, Sesia-Lanzo Zone, Western Alps. *Ital. J. Geosci.* 137, 188–207. doi: 10.3301/IJG.2018.08

Dal Piaz, G. V., Hunziker, J. C., and Martinotti, G. (1972). La Zona Sesia-Lanzo e l'evoluzione tettonico-metamorfica delle Alpi Nord-occidentali interne. *Mem. Soc. Geol. Ltal.* 11:433.

De Andrade, V., Vidal, O., Lewin, E., O'Brien, P., and Agard, P. (2006). Quantification of electron microprobe compositional maps of rock thin sections: an optimized method and examples. *J. Metamorph. Geol.* 24, 655–668. doi: 10.1111/j.1525-1314.2006.00660.x

Deer, W., Howie, R., and Zussman, J. (1992). *An Introduction to the Rock-Forming Minerals*. Essex: Longman Scientific and Technology.

Delleani, F., Spalla, M. I., Castelli, D., and Gosso, G. (2012). Multiscale structural analysis in the subducted continental crust of the internal Sesia-Lanzo Zone (Monte Mucrone, Western Alps). *J. Vir. Explor.* 41:7. doi: 10.3809/jvirtex.2011.00287

Delleani, F., Spalla, M. I., Castelli, D., and Gosso, G. (2013). A new petro-structural map of the Monte Mucrone metagranitoids (Sesia-Lanzo Zone, Western Alps). *J. Maps* 9, 410–424. doi: 10.1080/17445647.2013.800004

Denison, C., Carlson, W. D., and Ketcham, R. A. (1997). Three-dimensional quantitative textural analysis of metamorphic rocks using high-resolution computed X-ray tomography: Part I. Methods and techniques. *J. Metamorph. Geol.* 15, 29–44. doi: 10.1111/j.1525-1314.1997.00006.x

DeVasto, M. A., Czeck, D. M., and Bhattacharyya, P. (2012). Using image analysis and ArcGIS® to improve automatic grain boundary detection and quantify geological images. *Comp. Geosci.* 49, 38–45. doi: 10.1016/j.cageo.2012.06.005

Fiannacca, P., Ortolano, G., Pagano, M., Visalli, R., Cirrincione, R., and Zappalà, L. (2017). IG-Mapper: a new ArcGIS® toolbox for the geostatistics-based automated geochemical mapping of igneous rocks. *Chem. Geol.* 470, 75–92. doi: 10.1016/j.chemgeo.2017.08.024

Frassi, C., Musumeci, G., Zucali, M., Mazzarini, F., Rebay, G., and Langone, A. (2017). The Cotoncello Shear Zone (Elba Island, Italy): the deep root of a fossil oceanic detachment fault in the Ligurian ophiolites. *Lithos* 278, 445–463. doi: 10.1016/j.lithos.2017.02.015

Giuntoli, F., and Engi, M. (2016). Internal geometry of the central Sesia Zone (Aosta Valley, Italy): HP tectonic assembly of continental slices. *Swiss. J. Geosci.* 109, 445–471. doi: 10.1007/s00015-016-0225-4

Giuntoli, F., Lanari, P., and Engi, M. (2018a). Deeply subducted continental fragments – Part 1: fracturing, dissolution–precipitation, and diffusion processes recorded by garnet textures of the central Sesia Zone (western Italian Alps). *Solid Earth* 9, 167–189. doi: 10.5194/se-9-167-2018

Giuntoli, F., Lanari, P., Burn, M., Kunz, B. E., and Engi, M. (2018b). Deeply subducted continental fragments - Part 2: insight from petrochronology in the central Sesia Zone (western Italian Alps). *Solid Earth* 9, 191–222. doi: 10.5194/se-9-191-2018

Gonzalez, R., and Woods, R. (2002). *Digital Image Processing*. Upper Saddle River, NJ: Prentice Hall, doi: 10.1016/0734-189X(90)90171-Q

Gosso, G. (1977). Metamorphic evolution and fold history in the eclogite micaschists of the upper Gressoney valley (Sesia-Lanzo zone, Western Alps). *Rend. Soc. It. Mineral. Petrol.* 33, 389–407.

Gosso, G., Rebay, G., Roda, M., Spalla, M. I., Tarallo, M., Zanoni, D., et al. (2015). Taking advantage of petrostructural heterogeneities in subduction-collisional orogens, and effect on the scale of analysis. *Per. Miner.* 84:779. doi: 10.2451/2015PM0452

Halama, R., Glodny, J., Konrad-Schmolke, M., and Sudo, M. (2018). Rb-Sr and in situ 40Ar/39Ar dating of exhumation-related shearing and fluid-induced recrystallization in the Sesia zone (Western Alps, Italy). *Geosphere* 14, 1425–1450. doi: 10.1130/GES01521.1

Hayama, Y. (1959). Some considerations on the color of biotite and its relation to metamorphism. *J. Geol. Soc. Jpn* 65, 21–30. doi: 10.5575/geosoc.65.21

Hobbs, B. E., Means, W. D., and Williams, P. F. (1976). *An Outline of Structural Geology*. New York, NY: Wiley.

Hobbs, B. E., Ord, A., Spalla, M. I., Gosso, G., and Zucali, M. (2010). The interaction of deformation and metamorphic reactions. *Geol. Soc. Lond. Special Pub.* 332, 189–223. doi: 10.1144/SP332.12

Huddlestone-Holmes, C. R., and Ketcham, R. A. (2010). An X-ray computed tomography study of inclusion trail orientations in multiple porphyroblasts from a single sample. *Tectonophysics* 480, 305–320. doi: 10.1016/j.tecto.2009.10.021

Hy, C. (1984). *Métamorphisme Polyphasé et Evolution Tectonique dans la Croûte Continentale Éclogitisée: les Series Granitiques et Pélitiques du Monte Mucrone (zone Sesia-Lanzo, Alpes italiennes)*. Ph.D. thesis, Université Paris VI, Paris.

Ildefonse, B., Lardeaux, J. M., and Caron, J. M. (1990). The behavior of shape preferred orientations in the metamorphic rocks: amphiboles and jadeites from the Monte Mucrone Area (Sesia-Lanzo Zone, Italian Western Alps). *J. Struct. Geol.* 12, 1005–1011. doi: 10.1016/0191-8141(90)90096-H

Johnson, S. E., and Vernon, R. H. (1995). Inferring the timing of porphyroblast growth in the absence of continuity between inclusion trails and matrix foliations; can it be reliably done? *J. Struct. Geol.* 17, 1203–1206. doi: 10.1016/0191-8141(95)00021-5

Koons, P. O. (1982). *An Investigation of Experimental and Natural High-Pressure Assemblages From Sesia Zone, Western Alps, Italy*. Ph.D. thesis, ETH Zürich, Zurich.

Koons, P. O., Rubie, D. C., and Frueh-Green, G. (1987). The effects of disequilibrium and deformation on the mineralogical evolution of quartz-diorite during metamorphism in the eclogite facies. *J. Petrol.* 28, 679–700. doi: 10.1093/petrology/28.4.679

Lanari, P., Vidal, O., De Andrade, V., Dubacq, B., Lewin, E., Grosch, E. G., et al. (2014). XMapTools: a MATLAB© -based program for electron microprobe X-ray image processing and geothermobarometry. *Comp. Geosci.* 62, 227–240. doi: 10.1016/j.cageo.2013.08.010

Lardeaux, J. M. (1981). *Evolution Tectono-Métamorphique de la Zone Nord du Massif de Sesia-Lanzo (Alpes Occidentales): Un exemple d'éclogitisation de croûte continentale*. Ph.D. thesis, Université Paris VI, Paries.

Lardeaux, J. M., Gosso, G., Kienast, J. R., and Lombardo, B. (1982a). Chemical variations in phengitic micas of successive foliations within the Eclogitic Micaschists complex, Sesia-Lanzo zone (Italy, Western Alps). *Bull. Minéral.* 106, 673–689. doi: 10.3406/bulmi.1983.7689

Lardeaux, J. M., Gosso, G., Kienast, J. R., and Lombardo, B. (1982b). Relations entre le métamorphisme et la déformation dans la zone Sésia-Lanzo (Alpes Occidentales) et le problème de l'éclogitisation de la croûte continentale. *Bull. Soc. Géol. Fr.* 7, 793–800. doi: 10.2113/gssgfbull.s7-xxiv.4.793

Lardeaux, J. M., Lombardo, B., Gosso, G., and Kienast, J. R. (1983). Découverte de paragenèses à ferro-omphacites dans les orthogneiss de la zone Sesia-Lanzo septentrionale (Alpes Italiennes). *C. R. Acad. Sci. Paris* 296:453.

Lardeaux, J. M., and Spalla, M. I. (1990). Tectonic significance of P-T-t paths in metamorphic rocks: examples from ancient and modern orogenic belts. *Mem. Soc. Geol. Ital.* 45, 51–69.

Lardeaux, J. M., and Spalla, M. I. (1991). From granulites to eclogites in the Sesia zone (Italian western Alps): a record of the opening and closure of the Piedmont ocean. *J. Metam. Geol.* 9, 35–59. doi: 10.1111/j.1525-1314.1991.tb00503.x

Li, X., Di, L., Han, W., Zhao, P., and Dadi, U. (2010). Sharing geoscience algorithms in a Web service-oriented environment (GRASS GIS example). *Comp. Geosci.* 36, 1060–1068. doi: 10.1016/j.cageo.2010.03.004

Macente, A., Fusseis, F., Menegon, L., Xiao, X., and John, T. (2017). The strain-dependent spatial evolution of garnet in a high-P ductile shear zone from the Western Gneiss Region (Norway): a synchrotron X-ray microtomography study. *J. Metamorph. Geol.* 35, 565–583. doi: 10.1111/jmg.12245

Mancini, L., Reinier, R., Cloetens, P., Gastaldi, J., Härtwig, J., Schlenker, M., et al. (1998). Investigation of structural defects and inhomogeneities in Al-Pd-Mn icosahedral quasicrystals by combined synchrotron X-ray topography and phase radiography. *Phil. Mag.* 78, 1175–1194. doi: 10.1080/01418619808239982

Manzotti, P., Rubatto, D., Darling, J., Zucali, M., Cenki-Tok, B., and Engi, M. (2012). From Permo-Triassic lithospheric thinning to Jurassic rifting at the Adriatic margin: petrological and geochronological record in Valtournenche (Western Italian Alps). *Lithos* 146, 276–292. doi: 10.1016/j.lithos.2012.05.007

Manzotti, P., and Zucali, M. (2013). The pre-alpine tectonic history of the Austroalpine continental basement in the Valpelline unit (Western Italian Alps). *Geol. Mag.* 150, 153–172. doi: 10.1017/S0016756812000441

Marotta, A. M., Spalla, M. I., and Gosso, G. (2009). Upper and lower crustal evolution during lithospheric extension: numerical modelling and natural footprints from the European Alps. *Geol. Soc. Lond. Spec. Publ.* 321, 33–72. doi: 10.1144/SP321.3

Meda, M., Marotta, A. M., and Spalla, M. I. (2010). The role of mantle hydration into the continental crust recycling in the wedge region. *Geol. Soc. Lond. Spec. Pub.* 332, 149–172. doi: 10.1144/SP332.10

Meyer, F., and Beucher, S. (1990). Morphological segmentation. *J. Vis. Commun. Image Represent.* 1, 21–46. doi: 10.1016/1047-3203(90)90014-M

Mørk, M. B. (1985). A gabbro eclogite transition of Flemsoy, Suamore, western Norway. *Chem. Geol.* 50, 283–310. doi: 10.1016/0009-2541(85)90125-1

Myers, J. S. (1970). Gneiss types and their significance in the repeatedly deformed and metamorphosed Lewisian complex of Western Harris, Outer Hebrides. *Scot. J. Geol.* 6, 186–199. doi: 10.1144/sjg06020186

Oberhänsli, R., Hunziker, J. C., Martinotti, G., and Stern, W. B. (1985). Geochemistry, geochronology and petrology of Monte Mucrone: an example of Eo-alpine eclogitization of Permian granitoids in the Sesia-Lanzo Zone, Western Alps, Italy. *Chem. Geol.* 52, 165–184. doi: 10.1016/0168-9622(85)90016-8

Ortolano, G., Visalli, R., Godard, G., and Cirrincione, R. (2018). Quantitative X-ray Map Analyser (Q-XRMA): a new GIS-based statistical approach to Mineral Image Analysis. *Comp. Geosci.* 115, 56–65. doi: 10.1016/j.cageo.2018.03.001

Ortolano, G., Zappalà, L., and Mazzoleni, P. (2014a). X-Ray Map Analyser: a new ArcGIS® based tool for the quantitative statistical data handling of X-ray maps (Geo-and material-science applications). *Comp. Geosci.* 72, 49–64. doi: 10.1016/j.cageo.2014.07.006

Ortolano, G., Visalli, R., Cirrincione, R., and Rebay, G. (2014b). PT-path reconstruction via unraveling of peculiar zoning pattern in atoll shaped garnets via image assisted analysis: an example from the Santa Lucia del Mela garnet micaschists (northeastern Sicily-Italy). *Period. Mineral.* 83, 257–297. doi: 10.2451/2013PM0015

Park, R. G. (1969). Structural correlations in metamorphic belts. *Tectonophysics* 7, 323–338. doi: 10.1016/0040-1951(69)90077-8

Passchier, C. W., Myers, J. S., and Kroner, A. (1990). *Field Geology of High-Grade Gneiss Terrains*. Berlin: Springer.

Pearce, M. A., and Wheeler, J. (2010). Modelling grain-recycling zoning during metamorphism. *J. Metam. Geol.* 28, 423–437. doi: 10.1111/j.1525-1314.2010.00872.x

Pognante, U. (1989a). Lawsonite, blueschist and eclogite formation in the southern Sesia Zone (Western Alps, Italy). *Eur. J. Miner.* 1, 89–104. doi: 10.1127/ejm/01/1/0089

Pognante, U. (1989b). Tectonic implications of lawsonite formation in the Sesia zone (Western Alps). *Tectonophysics* 162, 219–227. doi: 10.1016/0040-1951(89)90245-X

Pognante, U. (1991). Petrological constraints on the eclogite- and blueschist-facies metamorphism and P-T-t paths in the Western Alps. *J. Metam. Geol.* 9, 5–17. doi: 10.1111/j.1525-1314.1991.tb00501.x

Polacci, M., Mancini, L., and Baker, D. R. (2010). The contribution of synchrotron X-ray computed microtomography to understanding volcanic processes. *J. Synchrotron Rad.* 17, 215–221. doi: 10.1107/S0909049509048225

Pradhan, B. (2013). A comparative study on the predictive ability of the decision tree, support vector machine and neuro-fuzzy models in landslide susceptibility mapping using GIS. *Comp. Geosci.* 51, 350–365. doi: 10.1016/j.cageo.2012.08.023

Rebay, G., and Messiga, B. (2007). Prograde metamorphic evolution and development of chloritoid-bearing eclogitic assemblages in subcontinental metagabbro (Sesia-Lanzo Zone, Italy). *Lithos* 98, 275–291. doi: 10.1016/j.lithos.2007.04.002

Rebay, G., and Spalla, M. I. (2001). Emplacement at granulite facies conditions of the Sesia–Lanzo metagabbros: an early record of Permian rifting? *Lithos* 58, 85–104. doi: 10.1016/S0024-4937(01)00046-9

Rebay, G., Zanoni, D., Langone, A., Luoni, P., Tiepolo, M., and Spalla, M. I. (2018). Dating of ultramafic rocks from the Western Alps ophiolites discloses Late Cretaceous subduction ages in the Zermatt-Saas Zone. *Geol. Mag.* 155, 298–315. doi: 10.1017/S0016756817000334

Regis, D., Rubatto, D., Darling, J., Cenki-Tok, B., Zucali, M., and Engi, M. (2014). Multiple metamorphic stages within an eclogite-facies terrane (Sesia Zone, Western Alps) revealed by Th–U–Pb petrochronology. *J. Petrol.* 55, 1429–1456. doi: 10.1093/petrology/egu029

Ridley, J. (1989). Structural and metamorphic history of a segment of the Sesia-Lanzo Zone, and its bearing on the kinematics of alpine deformation in the Western Alps. *Geol. Soc. Lond. Spec. Publ.* 45, 189–201. doi: 10.1144/GSL.SP.1989.045.01.10

Roda, M., De Salvo, F., Zucali, M., and Spalla, M. I. (2018a). Structural and metamorphic evolution during tectonic mixing: is the Rocca Canavese Thrust Sheet (Italian Western Alps) a subduction-related melange? *Ital. J. Geosci.* 137, 311–329. doi: 10.3301/IJG.2018.17

Roda, M., Regorda, A., Spalla, M. I., and Marotta, A. M. (2018b). What drives alpine Tethys opening? Clues from the review of geological data and model predictions. *Geol. J.* 54, 2646–2664. doi: 10.1002/gj.3316

Roda, M., Zucali, M., Li, Z., and Spalla, M. I. (2018c). Pre-alpine contrasting tectono-metamorphic evolutions within the Southern Steep Belt, Central Alps. *Lithos* 310, 31–49. doi: 10.1016/j.lithos.2018.03.025

Roda, M., Spalla, M. I., and Marotta, A. M. (2012). Integration of natural data within a numerical model of ablative subduction: a possible interpretation for the alpine dynamics of the Austroalpine crust. *J. Metam. Geol.* 30, 973–996. doi: 10.1111/jmg.12000

Roda, M., Zucali, M., Regorda, A., and Spalla, M. I. (2019). Formation and evolution of a subduction-related mélange: the example of the Rocca Canavese Thrust Sheets (Western Alps). *Geol. Soc. Am. Bull.* doi: 10.1130/B35213.1

Rubatto, D., Gebauer, D., and Compagnoni, R. (1999). Dating of eclogite-facies zircons: the age of alpine metamorphism in the Sesia-Lanzo zone (western Alps). *Earth Planet. Sci. Lett.* 167, 141–158. doi: 10.1016/S0012-821X(99)00031-X

Salvi, F., Spalla, M. I., Zucali, M., and Gosso, G. (2010). Three-dimensional evaluation of fabric evolution and metamorphic reaction progress in polycyclic and polymetamorphic terrains: a case from the Central Italian Alps. *Geol. Soc. Lond. Spec. Pub.* 332, 173–187. doi: 10.1144/SP332.11

Sayab, M., Miettinen, A., Aerden, D., and Karell, F. (2017). Orthogonal switching of AMS axes during type-2 fold interference: insights from integrated X-ray computed tomography, AMS and 3D petrography. *J. Struct. Geol.* 103, 1–16. doi: 10.1016/j.jsg.2017.09.002

Sayab, M., Suuronen, J. P., Hölttä, P., Aerden, D., Lahtinen, R., and Kallonen, A. P. (2015). High-resolution X-ray computed microtomography: a holistic approach to metamorphic fabric analyses. *Geology* 43, 55–58. doi: 10.1130/G36250.1

Sayab, M., Suuronen, J. P., Molnár, F., Villanova, J., Kallonen, A., et al. (2016). Three-dimensional textural and quantitative analyses of orogenic gold at the nanoscale. *Geology* 44, 739–742. doi: 10.1130/G38074.1

Schneider, C. A., Rasband, W. S., and Eliceiri, K. W. (2012). NIH Image to ImageJ: 25 years of image analysis. *Nat. Methods* 9, 671–675. doi: 10.1038/nmeth.2089

Siivola, J., and Schmid, R. (2007). Recommendations by the IUGS Subcommission on the Systematics of Metamorphic Rocks: List of Mineral Abbreviations. Web Version 01.02.07. Available at: http://www.bgs.ac.uk/scmr/docs/papers/paper_12.pdf (accessed February 26, 2019).

Spalla, M. I., Carminati, E., Ceriani, S., Oliva, A., and Battaglia, D. (1999). Influence of deformation partitioning and metamorphic re-equilibration on P-T path reconstruction in the pre-alpine basement of central Southern Alps (Northern Italy). *J. Metam. Geol.* 17, 319–336. doi: 10.1046/j.1525-1314.1999.00199.x

Spalla, M. I., De Maria, L., Gosso, G., Miletto, M., and Pognante, U. (1983). Deformazione e metamorfismo della Zona Sesia-Lanzo meridionale al contatto con la falda piemontese e con il massiccio di Lanzo, Alpi occidentali. *Mem. Soc. Geol. Ital.* 26, 499–514.

Spalla, M. I., Lardeaux, J. M., Dal Piaz, G. V., and Gosso, G. (1991). Metamorphisme et tectonique a la marge externe de la Zone Sesia - Lanzo (Alpes Occidentales). *Mem. Sci. Geol. Padova.* 43, 361–369.

Spalla, M. I., and Zucali, M. (2004). Deformation vs. metamorphic re-equilibrium heterogeneities in polymetamorphic rocks; a key to infer quality P-T-d-t path. *Period. Mineral.* 73, 249–257.

Spalla, M. I., Zucali, M., Di Paola, S., and Gosso, G. (2005). A critical assessment of tectono-thermal memory of rocks and definition of tectonometamorphic units: evidence from fabric and degree of metamorphic transformation. *Geol. Soc. Lond Spec. Publ.* 243, 227–247. doi: 10.1144/GSL.SP.2005.243.01.16

Stünitz, H. (1989). *Partitioning of Metamorphism and Deformation in the Boundary Region of the "Seconda Zona Diorito-Kinzigitica", Sesia Zone, Western Alps*. Ph.D. thesis, ETH, Zurich.

Turner, F. J., and Weiss, L. E. (1963). *Structural Analysis of Metamorphic Tectonites*. New York, NY: MacGraw-Hill.

Visalli, R. (2017). *Innovative Numerical Petrological Methods for Definition of Metamorphic Timescale Events of Southern European Variscan Relicts via Thermodynamic and Diffusion Modelling of Zoned Garnets*. Ph.D. Thesis, University of Catania, Catania.

Voltolini, M., Zandomeneghi, D., Mancini, L., and Polacci, M. (2011). Texture analysis of volcanic rock samples: quantitative study of crystals and vesicles shape preferred orientation from X-ray microtomography data. *J. Volcanol. Geoth. Res.* 202, 83–95. doi: 10.1016/j.jvolgeores.2011.02.003

Wilkins, S. W., Gureyev, T. E., Gao, D., Pogany, A., and Stevenson, A. W. (1996). Phase-contrast imaging using polychromatic hard X-rays. *Nature* 384, 335–338. doi: 10.1038/384335a0

Williams, P. F. (1985). Multiply deformed terrains - problems of correlation. *J. Struct. Geol.* 7, 269–280. doi: 10.1016/0191-8141(85)90035-5

Wu, C. M., and Chen, H. X. (2015). Revised Ti-in-biotite geothermometer for ilmenite-or rutile-bearing crustal metapelites. *Sci. Bull.* 60, 116–121. doi: 10.1007/s11434-014-0674-y

Zandomeneghi, D., Voltolini, M., Mancini, L., Brun, F., Dreossi, D., and Polacci, M. (2010). Quantitative analysis of X-ray microtomography images of geomaterials: application to volcanic rocks. *Geosphere* 6, 793–804. doi: 10.1130/GES00561.1

Zanoni, D., Bado, L., Spalla, M. I., Zucali, M., and Gosso, G. (2008). Structural analysis of the Northeastern margin of the Tertiary intrusive stock of Biella (Western Alps, Italy). *Ital. J. Geosci.* 127, 125–140.

Zucali, M. (2002). Foliation map of the "Eclogitic Micaschists Complex" (Monte Mucrone-Monte Mars-Mombarone, Sesia-Lanzo Zone, Italy). *Mem. Sci. Geol.* 54:86.

Zucali, M. (2005). *JPT-Mineral Formula Calculation and Geo-Thermobarometry*. Available at: https://michelezucali.wixsite.com/michelezucali/jpt (accessed March 10, 2019).

Zucali, M. (2011). Coronitic microstructures in patchy eclogitised continental crust: the Lago della Vecchia Permian metagranite (Sesia-Lanzo Zone,

Western Italian Alps). *J. Virtual. Expl.* 38:7. doi: 10.3809/jvirtex.2011.00286

Zucali, M., Barberini, V., Voltolini, M., Ouladdiaf, B., Chateigner, D., and Mancini, L. (2014a). Quantitative 3D microstructural analysis of naturally deformed amphibolite from the Southern Alps (Italy): microstructures, CPO and seismic anisotropy from a fossil extensional margin. From: Faulkner, D. R., Mariani, E., and Mecklenburgh, J. (Eds). Rock Deformation from Field, Experiments and Theory: a Volume in Honour of Ernie Rutter. *Geol. Soc.* 409, 201–222. doi: 10.1144/SP409.5

Zucali, M., Voltolini, M., Ouladdiaf, B., Mancini, L., and Chateigner, D. (2014b). The 3D quantitative lattice and shape preferred orientation of a mylonitised metagranite from Monte Rosa (Western Alps): combining neutron diffraction texture analysis and synchrotron X-ray microtomography. *J. Struct. Geol.* 63, 91–105. doi: 10.1016/j.jsg.2014.02.011

Zucali, M., and Spalla, M. I. (2011). Prograde lawsonite during the flow of continental crust in the alpine subduction: strain vs. metamorphism partitioning, a field-analysis approach to infer tectonometamorphic evolutions (Sesia-Lanzo Zone, Western Italian Alps). *J. Struct. Geol.* 33, 381–398. doi: 10.1016/j.jsg.2010.12.006

Zucali, M., Spalla, M. I., and Gosso, G. (2002). Strain partitioning and fabric evolution as a correlation tool: the example of the eclogitic micaschists complex in the Sesia-Lanzo Zone (Monte Mucrone-Monte Mars, Western Alps, Italy). *Schweiz. Miner. Petrogr. Mitt.* 82, 429–454.

Zucali, M., Spalla, M. I., Gosso, G., Racchetti, S., and Zulbati, F. (2004). Prograde Lws-Ky transition during subduction of the alpine continental crust of the Sesia-Lanzo Zone: the Ivozio Complex. *J. Virtual. Expl.* 16, 1–21. doi: 10.3809/jvirtex.2004.00105

Zucali, M., Corti, L., Delleani, F., Zanoni, D., and Spalla, M. I. (in press). 3D reconstruction of fabric and metamorphic domains in a slice of continental crust involved in the alpine subduction system: the example of Mt. Mucrone (Sesia-Lanzo Zone, Western Alps). *Int. J. Earth. Sci.*

Conflict of Interest: The authors declare that the research was conducted in the absence of any commercial or financial relationships that could be construed as a potential conflict of interest.

frontiers in Earth Science

METHODS
published: 14 January 2020
doi: 10.3389/feart.2019.00346

Time Resolved *in situ* X-Ray Tomographic Microscopy Unraveling Dynamic Processes in Geologic Systems

Federica Marone[1†], Christian M. Schlepütz[1†], Sina Marti[2], Florian Fusseis[2], Andrés Velásquez-Parra[3,5], Michele Griffa[4], Joaquín Jiménez-Martínez[3,5], Katherine J. Dobson[6,7] and Marco Stampanoni[1,8]*

[1] Swiss Light Source, Paul Scherrer Institut, Villigen, Switzerland, [2] School of Geosciences, The University of Edinburgh, Edinburgh, United Kingdom, [3] Department of Water Resources and Drinking Water, EAWAG, Dübendorf, Switzerland, [4] Swiss Federal Laboratories for Materials Science and Technology (Empa), Dübendorf, Switzerland, [5] Department of Civil, Environmental and Geomatic Engineering, ETH Zürich, Zurich, Switzerland, [6] Department of Earth Sciences, Durham University, Durham, United Kingdom, [7] Department of Civil and Environmental Engineering, University of Strathclyde, Glasgow, United Kingdom, [8] Institute for Biomedical Engineering, ETH Zürich, Zurich, Switzerland

OPEN ACCESS

Edited by:
Marco Voltolini, Lawrence Berkeley National Laboratory, United States

Reviewed by:
Fabrizio Bardelli, Institute of Nanotechnology (NANOTEC), Italy
Alexander Rack, European Synchrotron Radiation Facility, France

***Correspondence:**
Marco Stampanoni
stampanoni@biomed.ee.ethz.ch

[†] *These authors have contributed equally to this work*

Specialty section:
This article was submitted to Earth and Planetary Materials, a section of the journal Frontiers in Earth Science

Received: *09 September 2019*
Accepted: *12 December 2019*
Published: *14 January 2020*

Citation:
Marone F, Schlepütz CM, Marti S, Fusseis F, Velásquez-Parra A, Griffa M, Jiménez-Martínez J, Dobson KJ and Stampanoni M (2020) Time Resolved in situ X-Ray Tomographic Microscopy Unraveling Dynamic Processes in Geologic Systems. Front. Earth Sci. 7:346. doi: 10.3389/feart.2019.00346

X-ray tomographic microscopy is a well-established analysis technique in different fields of the Earth Sciences to access volumetric information of the internal microstructure of a large variety of opaque materials with high-spatial resolution and in a non-destructive manner. Synchrotron radiation, with its coherence and high flux, is required for pushing the temporal resolution into the second and sub-second regime and beyond, and therefore moving from the investigation of static samples to the study of fast dynamic processes as they happen in 3D. Over the past few years, several hardware and software developments at the TOMCAT beamline at the Swiss Light Source contributed to establishing its highly flexible and user-friendly fast tomography endstation, making a large variety of new dynamic *in situ* and operando investigations possible. Here we present an overview of the different devices, including an in-house developed detector, a new highly efficient macroscope and a programmable fast rotation stage. Their tight interplay and synchronization are key for lifting experimental design compromises and follow dynamic processes with high spatial and temporal resolution unfolding over prolonged periods of time, as often required by many applications. We showcase these new capabilities for the Earth Sciences community by presenting three different geological studies, which make use of different sample environments. With a tri-axial deformation rig, chemo-mechanical-hydraulic feedbacks between gypsum dehydration and halite deformation have been studied, while the spatio-temporal evolution of a solute plume has been investigated for the first time in 3D with a flow cell. A laser-based heating system available at the beamline provides access to the high temperatures required to address bubble growth and collapse as well as bubble-bubble interaction and

coalescence in volcanological material. With the integration of a rheometer, information on bubble deformation could also be gained. In the near future, upgrades of most large-scale synchrotron radiation facilities to diffraction-limited storage rings will create new opportunities, for instance through sub-second tomographic imaging capabilities at sub-micron length scales.

Keywords: synchrotron radiation, tomographic microscopy, time-resolved, *in situ*, high-temperature, high-pressure, fluid flow, volcanology

INTRODUCTION

X-ray tomographic microscopy (XTM) provides access to volumetric information of the internal microstructure of a large variety of opaque materials with high-spatial resolution and in a non-destructive manner. During the past decade, XTM has become a widespread analysis technique and invaluable tool in different branches of the Earth Sciences in laboratory settings with conventional sources and at synchrotron facilities (Cnudde and Boone, 2013). Typical applications cover the 3D morphological characterization of micro- and macro-fossils (Friis et al., 2015; Lindgren et al., 2018; Voeten et al., 2018) for new insights into their anatomy, development and preservation, leading to a deeper understanding of the paleobiology of extinct organisms and related evolutionary theories (Cunningham et al., 2014). Detailed microstructural and compositional analyses of extraterrestrial materials (Hanna and Ketcham, 2017) are fundamental for advancing our knowledge regarding, e.g., their formation. Direct access to complex 3D pore networks at multiple scales in different geological bodies and soils provides key structural information for numerical modeling of, for instance, fluid flow in porous media (Munawar et al., 2018). Recently, XTM has been successfully used to document metamorphic reactions (Zhu et al., 2016; Bedford et al., 2017), for digital rock (and reservoir) petrophysical property predictions and direct insight into micro-scale phenomena (Fusseis et al., 2012; Blunt et al., 2013), and in volcanology, where it has been providing insights into, for example, crystallization and degassing processes in magma evolution (Moretti et al., 2019), bubble growth in basaltic foams (Baker et al., 2012) and magma rheology (Pistone et al., 2015c).

Although XTM for static samples and post-mortem specimens is nowadays a well-established technique for geological materials, many dynamic geological processes are still not fully understood due to the lack of adequate investigation tools. Tomographic analyses require sample stability during the data acquisition process, which typically lasts several minutes to a few hours. Microstructural changes during dynamic processes are usually investigated in *in situ* experiments by "freezing" the ongoing process at different intermediate conditions. In this way, it was for instance possible to image metallic melt migration at high pressure and temperature conditions (Berg et al., 2018). Only recently, experiments with a higher temporal resolution have become possible, in particular at tomography beamlines of synchrotron facilities, thanks to the high brilliance and flux of their beams (Di Michiel et al., 2005). Time-resolved tomographic microscopy experiments at pore scales with a time resolution of a few tens of seconds have also been performed with conventional sources (Bultreys et al., 2016), but, for studying faster processes with dynamics in the sub-second regime and beyond, a third generation synchrotron source is a must. In addition to the higher flux, which for a specific scan time intrinsically leads to a higher quality tomographic volume, synchrotron radiation is also characterized by at least partial coherence. This feature unlocks the possibility of phase retrieval, a key tool to further enhance the image quality in particular in time-resolved applications (Mokso et al., 2013), with usually sparse noisy data.

Several hard X-ray tomographic microscopy beamlines have developed time-resolved capabilities over the past few years, and have demonstrated XTM measurements with a time resolution in the sub-second regime (e.g., ID15 at the ESRF, TOPO-TOMO at ANKA, JEEP i12 at the Diamond Light Source, TOMCAT at the Swiss Light Source, BL13W at SSRL, EDDI at BESSY II, BL28B2 at SPring-8) (Salvo et al., 2012; dos Santos Rolo et al., 2014; Dobson et al., 2016; Maire et al., 2016; Xu et al., 2016; García-Moreno et al., 2018; Yashiro et al., 2018). Despite these successful sub-second tomographic experiments, their widespread use in the imaging community and a further increase of the achievable temporal resolution has been hampered by several fundamental and technical limitations that need to be overcome in those measurements. Firstly, the available X-ray flux and optical efficiency of the image acquisition process determine the achievable imaging contrast, thus setting a lower limit on the necessary exposure time for a measurement. This is application-dependent and systems exhibiting a high inherent X-ray contrast (e.g., between hard matter and gases) generally require shorter acquisition times than those with lower contrast (e.g., between different crystalline phases). Secondly, the scanning time for a full 3D volume is also limited by how fast the sample can be rotated through 180° (assuming the parallel beam geometry available at the synchrotron). Fortunately, most modern high-precision rotation stages can reach continuous angular velocities of 600–900 rpm, corresponding to 20–30 180° rotations per second. A further bottleneck are the high-speed imaging detectors. To reach the high frame rates (1–20 kHz) needed to acquire several tomographic datasets per second, it is often necessary to reduce the read-out region of interest with respect to the full detector frame, severely compromising the available overall field-of-view (FOV) of the measurement.

Additionally, commercial high-frame rate CMOS detectors are usually designed for a burst operation, utilizing fast on-board memory of at maximum a few hundreds of GBs in size. Thus, only a few seconds of the studied dynamics can be captured before the internal memory is full and the data need to be downloaded from the camera, a process taking typically several minutes during which no further acquisitions are possible. The achievable acquisition durations and intervals are therefore insufficient to investigate many dynamic phenomena, which can instead span time periods of several minutes if not hours. Another obstacle is that most dynamic measurements require complex sample environments, which may simply not be compatible with a fast or a continuous sample rotation, for example, due to external electric or fluid connections. Back-and-forth scanning avoids coiling up of connection lines, but comes at a significant cost in speed due to the additional time required to accelerate and decelerate the rotation stage for every scan, and potential sample motion associated with changes in direction. Lastly, available software tools and computing infrastructures are not always adequate to efficiently transfer, store, reconstruct, visualize and analyze the tens of TBs of data generated during extended fast time-resolved experiments.

The most intriguing dynamical phenomena tend to occur under environments far from ambient conditions, such as high temperatures, high pressures, reactive atmospheres, etc. This is particularly true for the Earth Sciences, where, for example, sub-surface conditions at elevated pressures and temperatures comprise a major part of the research activities. To gain access to these conditions, the user community has been actively developing dedicated sample environments that are compatible with the restrictions imposed by the tomographic data acquisition protocol, namely the need to rotate a sample while guaranteeing an unobstructed pathway for the X-rays to the sample region to be imaged from all viewing directions (e.g., Renard et al., 2016; Glatz et al., 2018; Voltolini et al., 2019, to mention but a few). Dedicated devices with a range of capabilities are even available from commercial companies (e.g., Deben[1]). To optimally exploit these developments in a very active community, the experimental stations at synchrotron beamlines need to be designed such that they provide sufficient space and load capacity to accommodate these chambers as well as the required signal processing and connectivity capabilities to synchronize the control and monitoring signals from the sample cell with the imaging data.

Recent hardware and software developments at the TOMCAT beamline at the Swiss Light Source (SLS) (Stampanoni et al., 2006) helped in consolidating its cutting-edge fast tomography endstation and dynamical tomographic microscopy program (Lovric et al., 2016). In the following, we first describe these hardware and software advancements and highlight their relevance for Earth Sciences studies (**Table 1**). We then present three different respective applications, making use of different sample environments. Finally, we discuss current limitations and future plans also related to the scheduled SLS machine upgrade (Streun et al., 2018).

[1] deben.co.uk

TIME-RESOLVED X-RAY TOMOGRAPHIC MICROSCOPY ENDSTATION

Hardware

Source

X-ray radiation to the TOMCAT fast tomography endstation is delivered by a 2.9 T bending magnet with a critical energy of 11.1 keV (Stampanoni et al., 2006). The higher magnetic field of the TOMCAT source compared to the normal SLS bending magnets (1.8 T) enhances the flux at energies higher than 20 keV by more than an order of magnitude. This aspect is highly relevant for most *in situ* experiments, for which the sample diameter is often 5 mm or more (also to avoid excessive boundary effects) and the beam might have to penetrate a sample environment, sometimes consisting of X-ray absorbing materials, in addition to the sample itself.

XTM measurements using monochromatic radiation provide superior image quality compared to those using a polychromatic spectrum, in particular for strongly absorbing samples, since beam-hardening artifacts can be avoided. However, the final image quality is also strongly coupled to the number of photons available for imaging. For time-resolved experiments in the sub-second regime, the monochromatic flux at energies higher than 20 keV, as mostly required in Earth Sciences applications, is usually insufficient to achieve the necessary image quality required to perform accurate data quantification. Therefore, despite possible minor beam-hardening artifacts, fast imaging at TOMCAT is almost exclusively performed with polychromatic radiation.

The integrated flux over $2.75 \times 2.75\ \mu m^2$ (typical pixel area for dynamic experiments) on axis at 25 m from the source delivered by the TOMCAT superbend is shown in **Figure 1A** (blue curve). A large portion of this flux consists of low energy photons (<10 keV), which would not contribute to the image formation since they would be completely absorbed by the sample (and possibly contribute to radiation damage) but lead to enhanced beam hardening. For this reason, the full beam as delivered by the source (blue curve in **Figure 1A**) is never used for the experiments, but it is always filtered at least to some degree. At TOMCAT, we have different options to modify the beam spectrum. In **Figure 1A**, the flux is presented as a function of energy, after different routinely used filters. Usually, an attenuator (5 mm Sigradur), cutting at least 50% of the beam power, is inserted into the beam, also to prevent sample and optics damage. Additional filters are used to further condition the beam and in particular to achieve a narrower bandwidth, so to further reduce (beam hardening) artifacts, when required.

It should also be noted that the beam spectrum (and therefore also the flux) is not constant over the entire FOV, but it varies off-axis along the vertical direction, since the vertical photon source divergence is energy dependent (**Figure 1B**). To mitigate

TABLE 1 | Summary of the features of recent hardware and software developments at the TOMCAT beamline and their relevance for time-resolved Earth Sciences applications.

	Features	Relevance for time-resolved Earth Sciences applications
Hardware		
Source *2.9 T bending magnet*	High energies (up to 40 keV) Large fan opening angle High flux Coherence	High material penetration (thick samples, sample environments) Large horizontal field-of-view (22 mm) High temporal resolution Monochromatic option (higher image quality, quantitative information) Phase contrast
Optics *Different microscopes*	Different magnifications High numerical aperture	Flexible experimental design High efficiency, high temporal resolution
Detector *GigaFRoST*	High frame-rate (max. 1.25 kHz) High streaming rate (7.7 GB/s) Custom acquisition and triggering modes	High acquisition speed Sustained data acquisition High experimental flexibility
Rotation stage *ABRT-200, Aerotech Inc.*	High rotation speed (600 rpm) Small error motions (<200 nm) Electrical slip ring Different scanning protocols	High temporal resolution Micrometer spatial resolution Compatibility with complex sample environments High experimental flexibility
Software		
Data acquisition	Graphical user interfaces Ipython command line interface	User-friendly High flexibility, user-friendly
Data preview	Flexible display of 2D projections Display of arbitrarily selected tomographic slices	Optimal experimental control Increased experimental control and steering options Data information maximization
Data reconstruction	Fast reconstruction pipeline Phase retrieval Routines for artifact reduction	Rapid access to tomographic volumes for beamline and experimental parameter optimization Efficient handling of large amount of data Improved signal-to-noise and contrast-to-noise ratios High image quality

this dependence and the resulting artifacts, a vertical FOV larger than 5 mm is usually avoided. Horizontally, the maximum fan opening angle is instead as large as 2 mrad (50 mm at sample position 25 m downstream from the source). Contingent to the available optics and detectors, however, a horizontal FOV larger than 22 mm is never used.

Optics

At TOMCAT, different microscopes compatible with polychromatic beam applications are available. For high spatial resolution experiments requiring a pixel size of 1 μm or less, a microscope (Optique Peter, Lentilly, France) equipped with interchangeable long-working distance Mitutoyo objective lenses is used and features a discrete set of magnification values ranging from 5× up to 26×. For very low-resolution experiments, a system with a high numerical aperture tandem 1:1 configuration (Optique Peter, Lentilly, France) is available [pixel size of 11 μm if coupled to the GigaFRoST detector (see Section Detector)].

The workhorse for many dynamic experiments, in particular when a high time resolution is required, is, however, a recently procured high efficiency custom-made macroscope (Optique Peter, Lentilly, France) (Bührer et al., 2019). This system has a fixed 4× intermediate magnification, which is suitable for the investigation of many systems at a relatively high spatial resolution of a few μm while at the same time capturing a representative volume of interests of several mm. The key aspect of this new optical component is its high numerical aperture of 0.35, which boosted the efficiency compared to a previously used system by nearly a factor of 5, while at the same time providing a far superior image quality (the effective spatial resolution, defined as the 10% modulation transfer function bandwidth values for the high temporal resolution setup is 2.5 pixels). The design of the macroscope is modular, with independent camera and front modules which can be rotated into different positions. The system can also be mounted with its principal optical axis oriented both horizontally and vertically. This flexibility is important for optimally accommodating complex sample environments, as it is often the case for Earth Sciences applications.

Detector

Commercially available detectors capable of reaching kHz frame-rates are normally designed for burst operation and are therefore equipped with an internal memory of typically at maximum a few hundreds of GBs, while the data download to storage happens *a posteriori* via a communication protocol standard. This architecture severely limits the optimal design of time resolved experiments in several ways. The recorded FOV and number of projections per scan often need to be compromised in favor of increasing the total number of frames (hence of scans) that can be stored in memory in order to gain a sufficient time duration of the recording. Even then, an accurate synchronization of the few second-long possible acquisition period to match an unpredictable and sometimes still unexplored dynamical process is often difficult to achieve, bearing the risk of missing the

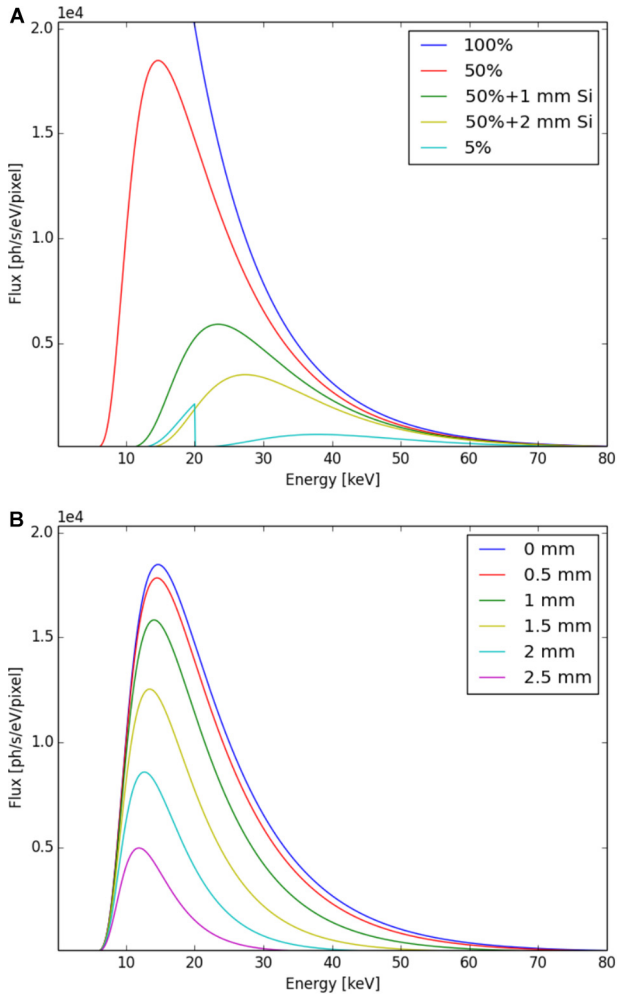

FIGURE 1 | Integrated flux over 2.75 × 2.75 μm^2 (typical pixel area for dynamic experiments) at 25 m from the source delivered by the TOMCAT superbend **(A)** on-axis and filtered by different attenuators (50%: 5 mm Sigradur, 5%: 20 mm Sigradur and 75 μm Mo), **(B)** off-axis at different vertical positions attenuated by the 50% filter. The flux is expressed per eV (instead of per 0.1% bandwidth) so that the absolute number of photons at a specific energy can be directly read from the plot.

time point of interest. Furthermore, inspections of the acquired data to validate beamline and experimental settings are delayed by the relatively long download times, leading to unwanted unutilized beamtime.

Efficient and reliable investigations of dynamic processes, instead, require a sustained data acquisition capability over extended periods of time, coupled with real-time availability of the current image frame. The GigaFRoST (Mokso et al., 2017) detection and read-out system, developed in-house and based on a commercial CMOS imaging sensor, can acquire and stream data with a rate as high a 7.7 GB/s directly to a backend system in a sustained manner, eliminating any experimental design compromise necessary with commercial systems. Further advantages of the GigaFRoST include its customized acquisition and triggering modes, which provide a high flexibility in the experimental execution. A highly useful feature for most high-speed experiments, which is provided by the GigaFRoST, is the possibility of monitoring the ongoing process by previewing the acquired projections while simultaneously storing the relevant data to disk. This option enables a direct insight into the investigated phenomena and the means to adjust the acquisition protocol to the actual dynamics in real-time. Additional details relevant to the specific applications are discussed in Section "Applications" and summarized in **Table 2**.

Rotation Stage

The TOMCAT sample manipulator (Lovric et al., 2016) has been custom designed to satisfy the stringent requirements of time-resolved high-resolution tomographic microscopy in terms of sample translational and rotational precision over a broad range of rotation velocities. At the same time, sufficient degrees of freedom are required to accurately align the rotation axis with respect to the beam and detector as well as to choose the desired volume of interest in the investigated sample.

A key component for reaching a temporal resolution in the sub-second regime is the high-precision air-bearing rotation stage (ABRT-200, Aerotech Inc.). It couples a maximum continuous rotational speed as high as 800 rpm (finally limited to 600 rpm by other mechanical components) with axial and radial error motions below 200 nm, totally acceptable for experiments with pixel sizes of 2–3 μm. In parallel beam geometry, as it is the case at the TOMCAT beamline, a maximum rotational speed of 10 full turns per second (600 rpm) corresponds to a maximum time resolution of 20 tomograms per second (tps). If a higher time resolution is required, a faster rotation unit provided by the user group can easily be integrated in the beamline infrastructure. In this way, an experiment requiring the acquisition of more than 200 tomograms per seconds has recently been carried out at TOMCAT (García-Moreno et al., 2019).

The air-bearing rotation stage is synchronized with a mechanical rotation stage (ADRS-150, Aerotech Inc.) which drives an electrical slip-ring with 60 lead-throughs. This slip-ring decouples the spinning top part of the stage from the static portion below. This is essential for achieving a high temporal resolution with sample environments which require analog or digital signals, since fast continuous rotation with dragged cables is not feasible. In addition to providing the connectivity for two linear translation stages mounted on top of the rotation axis used for region-of-interest alignment, the slip-ring also serves 2 D-sub/DB-9 connectors available for easily interfacing user-specific sample cells in the beamline environment. A slip-ring for gases or fluids as well as a slip-ring positioned above the rotating sample is not yet part of the beamline equipment, but can be integrated in collaboration with user groups on demand.

The rotation stage is integrated in the EPICS beamline control system and can be operated in different modes, providing and/or accepting multiple TTL triggering signals to and from detectors and other external devices (Lovric et al., 2016). The highest possible temporal resolution in tomography is achieved by a continuous data acquisition over many rotation cycles during a high-speed steady sample rotation. The tomographic reconstruction of each time point requires image data covering

TABLE 2 | Summary of the technical details key to each presented Earth Sciences application.

Use case[a]	Beam	Rotation protocol	Scanning protocol[b]	Sample environment	Contrast mechanism
Section "Solute Transport Through Porous Media" Soil analog Ø 4 mm	Monochromatic (21 keV)	Back-and-forth	1.2 s 2.4 s 10 min	Flow cell	Absorption Phase
Section "Evaporite Deformation" Evaporites Ø 3.2 mm	Polychromatic	Back-and-forth	2 s 0.5–1 min/5–10 min 30–240 min	Tri-axial deformation rig Elevated temperature	Absorption
Section "Capturing Instabilities in Bubble Interactions in 4D" Obsidian Ø 3.2 mm	Polychromatic	Sequence scan	2 s 1 min 145 min	Laser heating system	Absorption
Section "Quantification of Flow in Bubbly Magmatic Fluids" Synthetic basalt Ø 7 mm	Polychromatic	Sequence scan	1 s 7 s 10–90 min	Laser heating system Rheological testing apparatus	Absorption

[a]*Relevant paper section, sample material and diameter.* [b]*Scan time, interval between 2 scans, experiment duration.*

an angular range of 180°. The full dataset can thus be subdivided into consecutive ranges of 180°, each one representing one discrete time step, as shown in **Figure 2A**. However, while a short scan time for each individual volume is crucial to avoid any motion artifacts caused by the evolving system, the relevant structural changes can often still be clearly resolved with a scanning interval for consecutive time points a few times longer than the individual scan time. To this end, one of the most used triggering modes is the so-called "sequence mode," lending a great amount of flexibility for defining customized time-structures for a series of (non-continuous) scans. In this mode, multiple triggering sequences, typically to be used as a gating signal for the detector, can be defined, so that tomographic scans can be easily acquired at different time intervals to best match the investigated dynamics. This mode is shown schematically in **Figure 2B**.

As mentioned earlier, many *in situ* sample environments are unfortunately not compatible with a continuous sample rotation due to external fluid or electrical connections. In such cases, assuming that the external connections safely allow for rotations of somewhat more than 180°, one can fall back on back-and-forth scanning modes. Data can either be acquired both during the forward and backward rotation (**Figure 2C**), or always in the same rotation direction by rewinding the sample orientation in between (**Figure 2D**). However, these modes are decreasing the achievable temporal resolution considerably to scan intervals upwards of about 1 s. For faster scan times, the acceleration and deceleration times and distances for the back-and-forth motion are becoming prohibitive, both taking increasingly more time than the scan itself and requiring acceleration distances of several multiples of 180° for realistic acceleration rates available in high-precision rotation stages.

The flexibility in choosing the most adequate scanning protocol for each specific application is crucial to accommodate a wide variety of use cases. In Section "Applications" and **Table 2**, additional details specific for each of the showcase applications are given.

Sample Environments

The TOMCAT endstation for time-resolved tomography is highly flexible and features sufficient space around the sample position to enable the easy installation and integration of user-specific sample environments, including, for example, a humidity chamber (Derome et al., 2011), a cell for *in situ* methane hydrate growth (Sahoo et al., 2018), a tensile rig (Maire et al., 2016), a flow cell (Armstrong et al., 2014), a cold chamber (Maus et al., 2011), electrochemical cells for *in situ* battery (Ebner et al., 2013) and fuel cell (Eller et al., 2015) operation, as well as complex setups for *in vivo* experiments, e.g., on insects (Walker et al., 2014) or mice (Lovric et al., 2017).

A Measurement Computing USB Analog/Digital IO Module, integrated in EPICS, is also available to acquire, process and output electronic signals. This multi-function device is particularly suited to record analog electronic (high-speed) signals (e.g., for monitoring and logging temperatures or pressures during an investigation), as well as send custom-defined signal sequences to control an experiment.

For studies at elevated temperature, a laser-based heating system (Fife et al., 2012) can be mounted in a short time on top of the standard sample manipulator. In addition to the two laser heads with a small rectangular focus of 1×0.2 mm^2 described in Fife et al. (2012), a pair of laser heads with a larger focal spot have been procured (Apollo Instruments, Irvine, CA, United States) and can be interchanged with the original set. The focus of the new lasers is oval with a Gaussian-like power distribution and 6×4 mm^2 in size at a working distance of 150 mm. They are better suited to achieve near isothermal heating of samples with a size in the order of $5 \times 5 \times 5$ mm^3, typical for time-resolved experiments (Pleše et al., 2018). Both class IV diode laser sets operate at the same wavelength (980 nm) with a power output of 150 W per laser head.

The original pyrometry approach for measuring the sample temperature is limited to temperatures above 350°C. To cover lower temperature ranges, important, for instance, for oil shale pyrolysis investigations (Saif et al., 2019), a new

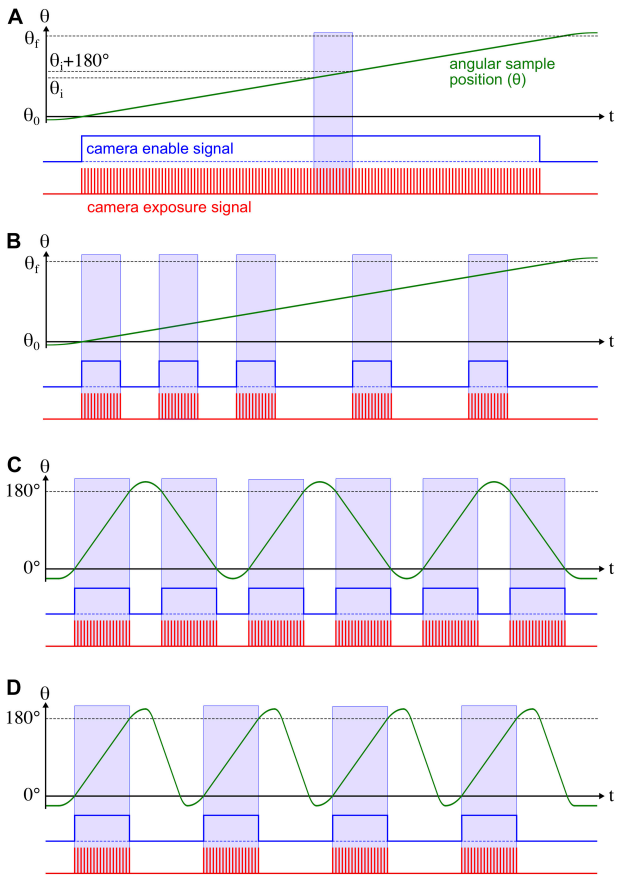

FIGURE 2 | Illustration of different data acquisition modes for fast tomographic measurements. The angular position of the sample is displayed by the green line as a function of time in the θ(t) coordinate system. Below this plot, typical TTL control signal sequences are represented by the blue line for the camera enable signal and the red line for individual camera frame exposure signals. The translucent blue rectangles mark the boundaries for individual tomographic scans. Four different acquisition modes are shown: **(A)** continuous acquisition during a continuous rotation of the sample. The total rotation angle covers many times the 180° range required to reconstruct a single volume. **(B)** The so-called "sequence scan," where acquisition windows can be programed to occur at configurable positions of the continuous rotation, allowing for a tighter control of the time series properties and scanning intervals. **(C,D)** Where a continuous rotation of the sample is not possible, scans can be acquired in a back-and-forth motion of the sample, either in both movement directions **(C)** or only along one direction with a rewinding operation in between **(D)**.

option to use a K-type thermocouple (Omega Engineering, Stamford, CT, United States) has been implemented and can be used simultaneously with the pyrometer. The thermocouple is typically inserted through the bottom of the sample holder and located at or near the base of the sample. The signals are read out through the slip-ring by a signal conditioner box (Omega Engineering, Stamford, CT, United States). As opposed to the pyrometer, which measures at different locations on the surface of the sample or sample holder during rotation, the thermocouple sensor remains stationary with respect to it, leading to a significantly more stable temperature measurement. The disadvantage of the thermocouple is the impossibility to position the sensor directly at the heating (and imaging) position, resulting in an offset of the measured temperature.

Temperature control is achieved either through the direct definition of laser current profiles or by dynamically adjusting the heating power using a PID-based feedback-loop on the measured temperature. The latter approach is very susceptible to variations in the temperature readings of the pyrometer due to material inhomogeneities, changes of the emissivity and sample wobble or the slow response of the thermocouple system, rendering a stable tuning of the PID parameters very difficult and often resulting in large unwanted temperature fluctuations. For this reason, most experiments rely on the direct control of the laser power. This approach requires a calibration step at the beginning of each experiment, but results in significantly more stable temperature profiles.

For experiments at high temperatures, the samples are usually contained in (relatively) X-ray transparent boron nitride or alumina crucibles or quartz capillaries. A gas diffuser positioned above the sample can be used to control the sample atmosphere during the measurement.

While the fast tomography endstation at TOMCAT can accommodate a large palette of user-provided devices, for safety reasons it was not possible to integrate external laser systems in the same way until now. With the ongoing development of a new laser safety and integration concept, this limitation will soon be lifted and lasers with different characteristics than those presently available at the beamline could be used for tomographic experiments.

Software

In addition to outstanding imaging performance, one of the key guiding principles for the development of the hardware for the fast TOMCAT endstation has been its flexibility. Adaptations of the application-specific sample setups required to match the beamline infrastructure are kept to a minimum, while the choice and combination of different endstation components and tools (sample environment, microscope, detector, etc.) enables an optimal match of the measurement system to the investigation needs. These same principles, together with a focus on user-friendliness, are also used as a precept for all software developments.

Data Acquisition

All major hardware components (slits, shutters, detectors, microscopes, rotation stage and sample environments) at the beamline are integrated in the EPICS beamline control system. Manual manipulation and monitoring of individual components is available via graphical user interface panels for EPICS (caqtdm). For the development and automation of more complex data acquisition protocols, libraries and bindings for EPICS exist for various programing and scripting languages (python, java, MATLAB, etc.).

The tight synchronization of data acquisition and measurement devices required for fast tomography, however, is not achievable by software communication between these sets of devices. Instead, electronic control signals need to be used to

send signals triggering or enabling different parts of the process chain. Both the rotation stage controller and the GigaFRoST detector can be programed to accept and output TTL signals in a variety of different modes (Lovric et al., 2016; Mokso et al., 2017). The synchronization is aided by a custom-designed TTL signal distribution box and the Measurement Computing DAQ device to record the signal trains.

Measurements with the GigaFRoST are controlled via an ipython command line interface. It allows the configuration of all measurement parameters (e.g., number of images to be acquired, region of interests, exposure time, rotation mode, etc.) and controls all of the necessary beamline devices during experiments. After the initial setup, users usually need to learn but a handful of different simple commands (4–6) to control their complex experiments.

To increase the flexibility with regards to the integration of user-specific equipment as part of the measurements, a plugin-system to communicate with additional external devices on demand, as part of the experimental workflow, is currently under development.

Raw experimental data is saved in an HDF5 file structured according to the Data Exchange format (De Carlo et al., 2014), including the metadata information describing the acquisition parameters of the measurement.

Data Preview

With the GigaFRoST detector, it is possible to preview radiographic projections while data are acquired (Mokso et al., 2017). This feature is key for the optimal control of fast tomographic experiments, where often the time scales of the dynamics under investigation are not yet well known. The option to display only selected images, for instance projections only at a specific angle to effectively suppress the rotational motion of the sample in the preview, makes it possible to even better observe and assess ongoing changes.

Although 2D X-ray projections of the sample already provide very insightful information to control and steer the experiment, for several applications they are unfortunately not sufficient to detect subtle but important changes indicating for instance the onset of a particular event. To expand the controlling and steering options, a previewing tool outputting selected arbitrarily oriented tomographic slices on-the-fly is currently being developed (Buurlage et al., 2019). This tool enables the optimization of the beamline and of experimental parameters as well as for instance the real-time selection of a region of interest in a larger volume, an operation often very difficult to achieve from 2D projections only. In a proof-of-concept experiment, the water uptake by a yarn sample and the filling of its pore space with liquid could be followed in real-time through selected tomographic slices. Per contra, the arrival of water at the measurement position remained invisible in the corresponding 2D projections.

Dynamic processes can be very sample- and experimental parameter-dependent and it is not always possible to predict when an event (e.g., crack opening) in the imaged region will occur. Furthermore, different mechanisms with different characteristic velocities, including very abrupt changes, could be present at the same time (e.g., slow plastic deformation and abrupt failure) requiring therefore the acquisition of single tomographic volumes as fast as possible to optimally image also the fastest processes. To avoid the collection of a large amount of useless data as well as putting the streaming and storage infrastructure under unnecessary load, it is of utmost importance to match the data acquisition to the dynamics of the studied process.

This new tool not only leads to information maximization in the acquired data, but opens up new options for an active experimental control, e.g., stabilizing a temperature ramp as soon as a magma starts vesiculating, or adjusting the tensile or compressive force when a particular microstructure starts to develop, further enhancing the flexibility of the endstation and helping in the realization of complex time-resolved tomographic studies.

Data Reconstruction

The sustained data rates provided by the GigaFRoST can be as high as 7.7 GB/s, leading to the collection of tens to hundreds of TBs of raw data per day. To fully exploit the potential of the TOMCAT fast tomography endstation, these large amounts of acquired data need to be efficiently handled and, in particular, tomographically reconstructed. Full access to the 3D microstructure shortly after the experiment is in addition important for decisions on beamline and experimental parameters. Computational tools for post-processing raw tomographic data have unfortunately not experienced the same rapid developments as high frame rate detectors. At TOMCAT we have developed a fast and user-friendly tomographic reconstruction pipeline delivering full tomographic volumes just a few seconds to minutes after data acquisition completion (Marone et al., 2017). In addition to several routines for the reduction of artifacts (e.g., ring and zinger removal), phase retrieval according to the Paganin algorithm (Paganin et al., 2002) is part of the pipeline and key for improving the signal-to-noise and contrast-to-noise ratios of sub-second time-resolved tomographic experiments (Mokso et al., 2013). With a combination of dedicated and shared computing infrastructures, it is possible to simultaneously reconstruct selected tomographic volumes almost in real-time for fast data assessment as well as post-process TBs of raw tomographic projections in an efficient manner.

APPLICATIONS

Solute Transport Through Porous Media

The transport of substances dissolved in liquids and their chemical reactions in topologically complex environments, such as porous media, play an important role in many environmental and industrial applications, including, for example, contaminant remediation (e.g., Williams et al., 2009), nuclear waste disposal (e.g., Winograd, 1981), enhanced oil recovery (e.g., Jiménez-Martínez et al., 2016) and geothermal energy production (e.g., Barbier, 2002), among many others. The majority of natural and man-made porous media exhibits a high degree

of spatial heterogeneity in terms of flow dynamics, with development of both preferential paths (high velocity regions) and stagnation zones (low velocity regions). Such a degree of heterogeneity makes solute transport very complex and difficult to understand and characterize, and therefore to be controlled (Dentz et al., 2011).

Dispersion and mixing are two of the main transport processes of solutes through porous media. Dispersion describes the continuous increase through time of the spatial extent of a solute (generically called "solute plume" in what follows) within the media. It is mostly a consequence of the high degree of spatial heterogeneity in the fluid flow velocity, which enhances the spatial heterogeneity of the solute concentration within the liquid. Mixing, in contrast, is the process that increases the actual total volume occupied by the solute, i.e., a spatial smoothing of the solute concentration field (Ottino, 1989; Kitanidis, 1994; Dentz et al., 2011). Mixing can also be defined as the process in which two solutes (e.g., resident and incoming solution) tend to occupy the same volume in space. The characterization of dispersion is important to predict the spatial extent of a solute plume. However, it does not provide any information about the actual mixing of solutes (i.e., the distribution of the solute concentrations) within the plume. This is a major problem because concentration fields control chemical reactions (Flühler et al., 1996; Dentz et al., 2011; Chiogna et al., 2012; de Barros et al., 2012; de Anna et al., 2014). Indeed, mixing plays a key role in controlling both fluid-fluid and fluid-solid reactions. Since in porous media both mixing and chemical reactions intrinsically occur at the pore-scale, i.e., at the length scale of the space between the components of the solid skeleton, mixing also needs to be characterized at this length scale. The relative importance of transport to chemical reactions, either within the liquid or with the hosting solid environment, is measured by the Damköhler number (*Da*), representing the ratio of advection to reaction time scales. Chemical reactions can thus be classified as mixing-driven (or mixing-limited), when the reaction is fast compared to advection ($Da>>1$), or kinetics-driven ($Da<<1$) in the opposite case.

The experimental characterization of mixing and chemical reactions in porous media has been so far very difficult, mainly due to technological bottlenecks in visually accessing these "hidden" environments. While microfluidics enables the visualization and quantification of, e.g., concentration gradients with high temporal and spatial resolution (e.g., Jiménez-Martínez et al., 2015), it is experimentally limited to 2D, with obvious and expected differences in the observed phenomenology compared with the reality. As an example, a recent theoretical and numerical study has suggested that the additional degree of freedom offered by the third dimension affects mixing and mixing-driven processes (Lester et al., 2013, 2016). Time-resolved synchrotron-based XTM provides the means to advance in the investigation of solute dispersion and mixing through partially or fully saturated porous media, at the actual pore-scale, beyond the 2D model case studies employed so far.

In this study, we have been focusing on a fluid-fluid solute system to characterize the impact of the third dimension, i.e., of a larger tortuosity in the pore space (Ghanbarian et al., 2013) compared with that achievable in a 2D microfluidics model, on the dispersion front's geometrical and topological properties and on the concentration gradients distribution, therefore on the mixing. The physical model used in our *in situ* experiment during XTM consisted of a packing of sintered, irregularly shaped borosilicate glass beads, manufactured by Hilgenberg GmbH. We chose such a bead packing as an analog of soil. As a porous medium, it possesses a spatially heterogeneous pore space with a size distribution in the range of 40–100 μm. The bulk porosity of the whole bead packing is about 28% and its permeability is 10^{-10} m^2. For this *in situ* experiment, we manufactured a flow cell consisting of three pieces: two conic containers, at the top and bottom of the cell, used as flow inlet and outlet, and a central, cylindrical container, within which the bead packing was fixed (**Figure 3**). Paraffin film was set between the bead packing and the container to minimize boundary effects. Any of the three parts of the flow cell was printed in 3D by stereo-lithography (DWS) using a photosensitive resin composed of acrylic monomers (Vitra 429). The central part of the cell, containing the bead packing, has an external diameter of 4 mm and is 8 mm high. The whole flow cell with the bead packing was mounted on the TOMCAT fast tomography endstation rotation stage, its inlet and outlet parts being connected to PEEK tubes (790 μm OD, 250 μm ID) (**Figure 3**). The *in situ* experiment consisted in pushing a liquid (called herein "tracer fluid") through the inlet into the bead packing, after having partially saturated the sample in advance with another liquid (herein called "resident background fluid"). Both the saturation with the background fluid and the further injection of the tracer fluid occurred via an automatically controlled syringe pump (by Harvard Apparatus) connected to the inlet and pumping at a constant flow rate (0.015 mL min^{-1}). The pressure difference between the inlet and the outlet was simultaneously measured using microfluidics pressure sensors (MPS by Elveflow). As background fluid, we used a KI water-based solution with 0.06 M concentration. The tracer was also a KI water-based solution, but with a much higher concentration (0.9 M). We chose KI as the solute to be transported because of (1) its lack of chemical reactivity with the borosilicate beads and (2) because of its high effective atomic number Z_{eff}, mainly due to presence of the I^- ion. It allowed creating a sufficient X-ray absorption and phase contrast on the voxel length scale inside the regions of the pore space saturated with the liquids during dispersion and mixing of the tracer within the background fluid.

Since the tubes were directly connected to the inlet and outlet of the flow cell without a slip ring, it was not possible to continuously rotate the flow cell mounted on the TOMCAT X-ray tomographic rotation stage. Instead, the flow cell was rotated around its vertical axis of 180° during the tomographic data acquisition, then it was rotated back to the 0° orientation before starting the tomographic acquisition at the next point in the time series (cf. **Figure 2D**, back-and-forth rotation protocol). The tomographic acquisition settings were kept constant throughout the time series. As in most time-resolved experiments, the high-efficiency 4× macroscope coupled to the GigaFRoST detector was used. Since achieving quantitative information about the solution concentration from the voxel values was an essential point for this study, we decided to use monochromatic radiation (21 keV)

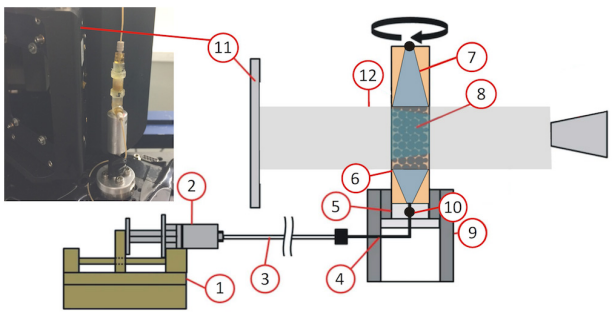

FIGURE 3 | Experimental setup used to study solute transport through porous media (modified from Setiawan et al., 2014), which includes: **(1)** syringe pump, **(2)** syringe, **(3)** tubing, **(4)** connector, **(5)** bottom cap, **(6)** flow cell printed in resin, **(7)** cone at the inlet and outlet, **(8)** sintered irregular glass beads, **(9)** holder, **(10)** pressure sensor, **(11)** X-ray detector, and **(12)** parallel beam.

so to avoid beam hardening artifacts, despite the significant flux reduction. Thanks to the high quality and efficiency of the used optics, it was nonetheless possible to keep the scan time around 1 s. Indeed, the actual acquisition of a single tomographic dataset, including rotation acceleration and deceleration, took about 1.2 s. The experiment consisted in acquiring a time series of such datasets at a sampling frequency of one tomogram about every 2.4 s, while the tracer was continuously pushed into the flow cell at the constant flow rate mentioned above. This high acquisition frequency achievable at the TOMCAT fast tomography endstation is essential in capturing the targeted processes. Indeed, the time scale of the tomographic acquisition (τ_{ac}) must be smaller than the time scale of both the solute's advection (τ_a) and of its diffusion (τ_d) over a pore length ($\tau_{ac} << \tau_a << \tau_d$). The sustained acquisition possibilities offered by the GigaFRoST enabled the acquisition of a tomographic time series with 80 time-frames, of which about 50 were necessary to displace the tracer from the inlet to the bottom of the bead packing. The voxel size of each tomogram was 2.75 μm, with an effective spatial resolution of approximately 2 voxels (5.5 μm). This resolution allowed us to get access to a sufficient level of details of the pore space as well as of the concentration gradients and geometrical features of the tracer plume. All tomograms were reconstructed (including phase retrieval) using the beamline hardware and software infrastructure (**Table 2**).

Figure 4 shows the spatio-temporal evolution of the solute plume at 4 out of the 80 available time frames. The time frame of **Figure 4A** was designated as time = 0 s and depicts the tracer fluid starting to enter into the porous medium. Each panel in **Figure 4** shows, by 3D rendering, about one quarter of a reconstructed tomogram as two overlapped volumes: the bead packing volume (in gray tones) and the volume occupied by the liquids (in colors). Both volumes were selected via a customized 3D image segmentation workflow. The gray tone scale used to represent the bead packing voxel values was associated to the same voxel value range fixed for any time frame. The same was done for the representation of the liquid voxel values. In **Figure 4**, only the color scale bar describing the liquid volume is shown, normalized to its maximum value in space and time. Such a color scale represents a proxy of the physical tracer concentration scale. Thus, bluish colors mean lower concentration, while more reddish colors are associated with a higher concentration of KI in water. The arrow in each inset indicates the flow direction through the porous medium. For providing better evidence of the successful resolution of the tracer concentration gradients inside the liquid volume, each inset shows a planar cross-section parallel to the flow direction depicting the complete sample's volume and adopting the same color scale of the 3D rendering.

The insets in **Figure 4** represent a small excerpt of the complete concentration field temporal evolution, showcasing the very heterogeneous chemical landscape. The dispersion (spreading along the main flow direction) increases with time, as does the existence of a larger volume of fluid with concentration different from 0 and 1, indicating a temporal increase of mixing between the two fluids. Note that the co-existence of high and low fluid flow velocity regions induces an incomplete mixing behind the plume's front. In the low velocity regions, high concentrations are mainly reached by molecular diffusion. The spatial distribution of the phases and the imposed boundary conditions allow estimating the local flow velocities with the help of a computational fluid dynamics solver. Incomplete mixing has implications in the global reactivity of the system, i.e., the existence of concentration gradients promotes reactions. Although the main purpose of this first proof-of-concept study was to infer dispersion and mixing, in addition to testing the potential of the experimental approach for this purpose, the chemical reactivity could be also investigated. Assuming a fast reversible reaction, i.e., a mixing-driven reaction ($Da << 1$), of known equilibrium constant, the local reaction rate can be inferred from the mixing of the tracer with the background liquid using the method presented by De Simoni et al. (2005, 2007) and Willmann et al. (2010), already successfully applied to 2D experimental data by Jiménez-Martínez et al. (2015). This allows quantifying the 3D spatial distribution of local reaction rates from the measured tracer concentration fields.

Evaporite Deformation

The processes that allow for km-scale rock deformation and mountain building are taking place on the grain scale. "Thin-skinned" foreland mountain belts like the Swiss Jura Mountains usually form where km thick sediment stacks get detached from underlying rock units along evaporitic rock sequences (e.g., Jordan, 1992; Vergés et al., 1992). Evaporites are a type of sedimentary rock that forms due to the evaporation of saline water in isolated basins, and are mostly composed of calcite ($CaCO_3$), halite (NaCl) and calcium sulfates such as gypsum ($CaSO_4 \cdot 2H_2O$). In the course of diagenesis (with increasing pressure and temperature during burial), gypsum dehydrates to bassanite ($CaSO_4 \cdot 0.5H_2O$) and anhydrite ($CaSO_4$).

The exact grain-scale mechanisms operating in evaporitic detachments are still debated. There is consensus on the significance of the low mechanical strength and low permeability of rock salt. The exact role of the gypsum dehydration reaction,

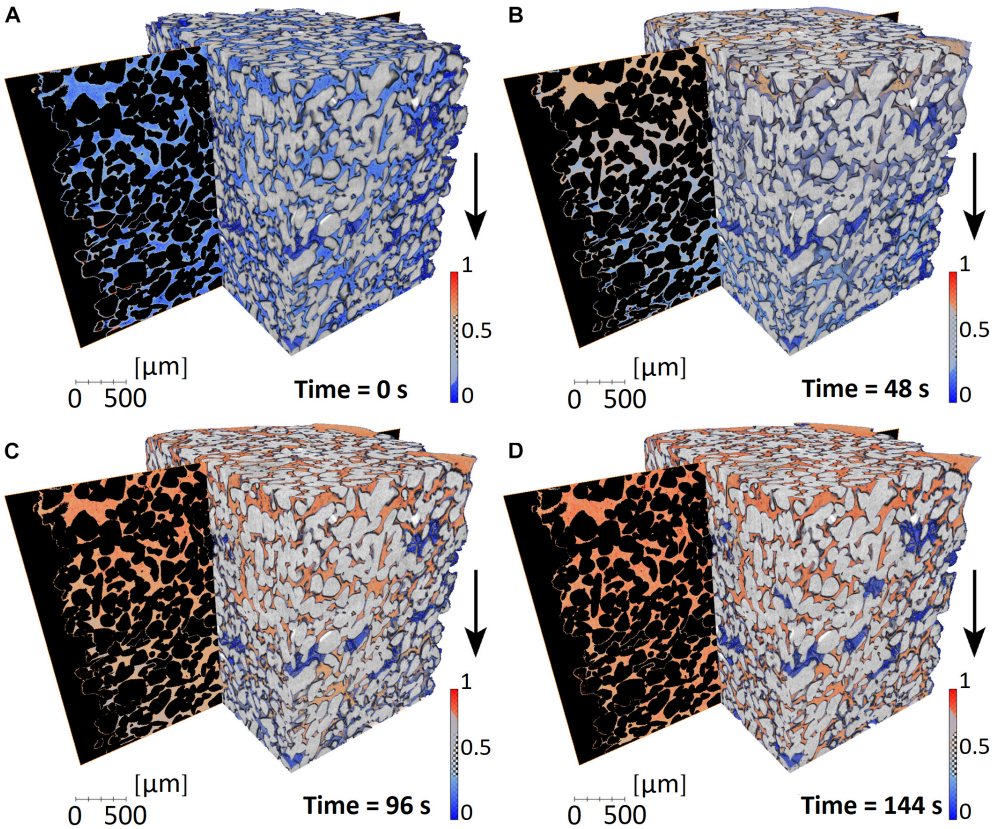

FIGURE 4 | Graphical rendering of the time series of tomographic datasets during the solute transport through a porous medium. Each panel refers to a distinct point in the time series. The time scale was set to 0 s for the dataset in panel **(A)**, corresponding to the time when the tracer starts to penetrate the porous medium. Each panel (**B** for time = 48 s, **C** for time = 96 s, **D** for time = 144 s) shows the 3D rendering of two distinct and complementary sub-sets of the acquired X-ray phase contrast tomogram: the glass beads volume (in gray scale) and the liquid (in colors). Approximately one quarter of the porous medium volume is shown, while the rest was cut out in order to better show the liquid distribution inside the pore space. The arrows indicate the main flow direction. The color mapping is identical for all time points, and the liquid phase value range was renormalized to its maximum value in space and time during the overall experiment duration. The corresponding color bar is shown in each inset. More bluish colors correspond to smaller (normalized) solute concentration values while more reddish ones indicate higher concentrations. Additionally, a planar cross-section through the full extent of the liquid volume along the flow direction is shown in each panel. All voxels not belonging to the liquid phase are rendered in black in these vertical slices.

which releases large quantities of pressurized water and affects the effective stress in detachment faults, is still being explored.

In a pressure and temperature dependent reaction, gypsum dehydrates to form bassanite:

$$CaSO_4 \cdot 2H_2O \text{ (gypsum)} \rightarrow CaSO_4 \cdot 0.5H_2O \text{ (bassanite)} + 1.5H_2O \text{ (water)}$$

The reaction is accompanied by a solid volume reduction of ∼29%, which usually causes the formation of porosity around the nucleating and growing bassanite grains. However, the total volume of the reaction is positive with +8%, due to the large volume of the released water. Where the water cannot drain, pore fluid pressure will build up.

Although, individually, gypsum dehydration and salt deformation have been studied extensively, little is known about the complex chemo-mechanical-hydraulic feedbacks between gypsum dehydration and halite deformation. The (i) reduction in solid volume during the dehydration reaction which produces porosity, (ii) hydraulic fracturing induced by fluid overpressure, which reduces the pore fluid pressure and lets the dehydration reaction progress, and (iii) the expected low permeability of salt affect the transport properties and influence the deformability of the rock. Ultimately, it is these coupled processes on the grain scale that determine the role of evaporites in tectonic processes. *In situ* experiments documented with time-resolved (4D) synchrotron-based X-ray tomography are ideally suited to study feedback processes in evaporites with the necessary temporal and spatial resolution.

To investigate the chemo-mechano-hydraulical feedbacks during evaporite deformation and dehydration, rock deformation experiments have been performed at SLS's TOMCAT beamline. These experiments were enabled by the X-ray-transparent tri-axial deformation rig *Mjölnir* (**Figure 5**, Butler et al., 2017), integrated at the beamline just for this specific experiment. *Mjölnir* deforms cylindrical samples with a diameter of 3.2 mm and 8–10 mm height. At ambient temperatures,

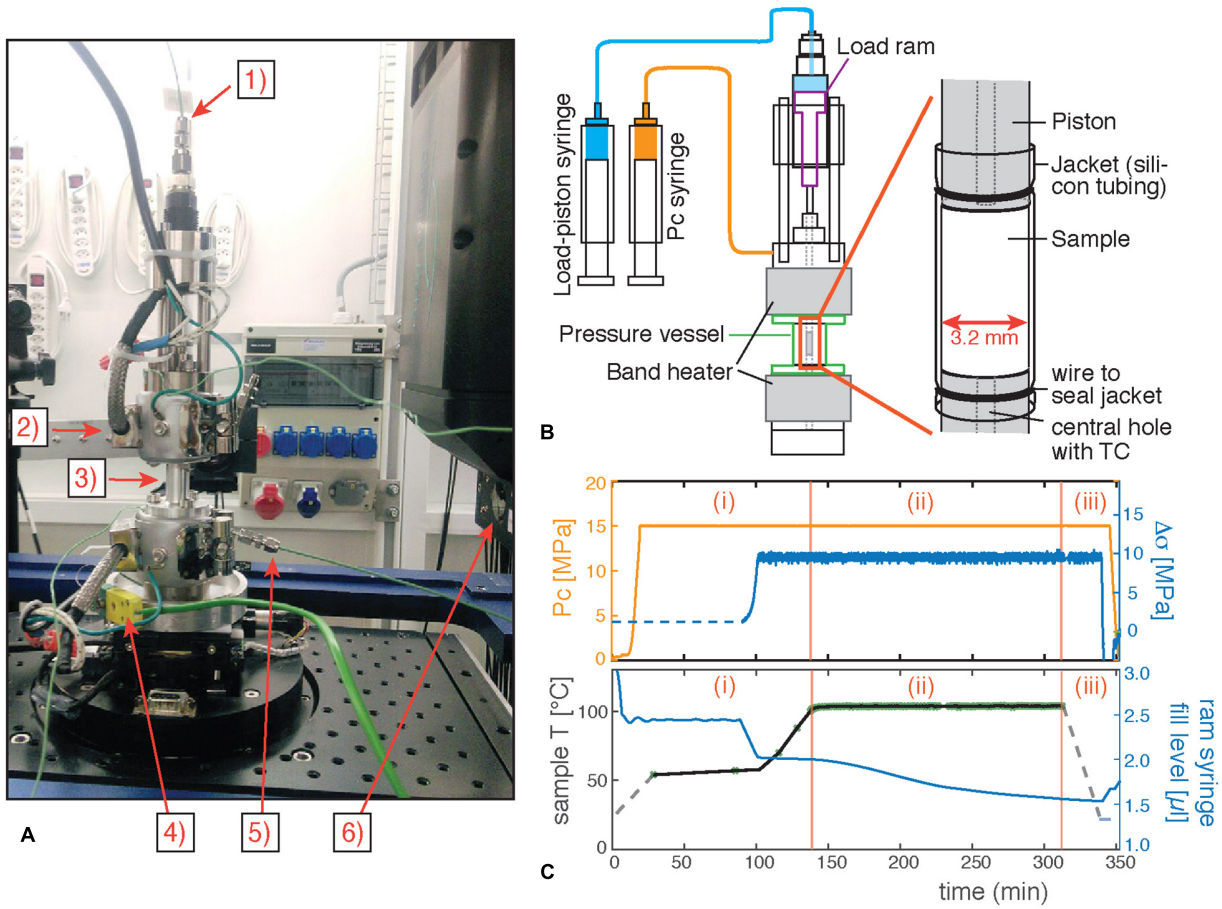

FIGURE 5 | Experimental setup. **(A)** Photograph of the deformation rig *Mjölnir* installed at the TOMCAT beamline. **(1)** Fluid inlet to load ram. **(2)** Upper band heater. **(3)** X-ray transparent pressure vessel (sample located inside). **(4)** Thermocouple connector. **(5)** Confining fluid inlet. **(6)** Scintillator. **(B)** Schematic sketch of *Mjölnir*, the high-pressure syringes controlling load and confining pressure, and the inner sample assembly. **(C)** Data derived from high-pressure pumps and temperature log. Stages of an experiment are indicated: **(i)** Initiation of the experiment: Pressurization, loading and heating **(ii)** Main part of the experiment with XTM scans at short intervals. Semi-transparent green crosses on temperature log curve (black) indicate time of XTM scan acquisition. **(iii)** End of experiment. De-pressurization and cooling. The ram syringe fill level curve is a proxy for load piston displacement. Decrease of the syringe fill level during the experiment indicates advance of the piston into the sample chamber as response to sample shortening/deformation.

it allows the application of a confining pressure (Pc) of up to 50 MPa via a confining fluid, and axial loads of more than 600 MPa. The axial load is applied via a piston that is driven by a hydraulic actuator. Both, the confining pressure and axial load are remotely controlled via two high-pressure syringe pumps (**Figure 5B**). For the experiments described here, the rig was equipped with band heaters (**Figures 5A,B**) to perform experiments at sample temperatures of up to 110°C. Higher temperatures are possible but were not necessitated by the experiments described here.

We deformed/dehydrated solid samples composed of either homogeneous mixtures of NaCl and gypsum or alternating NaCl – gypsum layers. Samples were pressurized to a Pc of 15 MPa, loaded to 8 MPa of differential stress and heated to 96–110°C (**Figure 5C**). The Pc and the axial load were logged at 1 Hz. The temperature was logged every time a tomographic scan was acquired. The FOV was ∼5 mm wide and 3.3 mm high, at a voxel resolution of 2.75^3 µm^3.

The coupled dehydration/deformation processes investigated in this study involve non-linear positive feedbacks and transient, run-away behavior can occur. Consequently, a good balance between fast data acquisition and data quality was very important to us to avoid motion artifacts and minimize noise in the XTM data. On the basis of previous experiments, we further anticipated that the relevant processes would unfold over prolonged periods of time, where the capability to continuously stream data from the camera would be critical. The GigaFRoST camera coupled to the highly efficient 4x macroscope allowed us to meet both requirements. Individual XTM datasets were acquired in ∼2 sec, rotating *Mjölnir* over 180° while collecting 2000 projections. White/dark field images were acquired every 3–5 h. At the start of an experiment, the scan interval was chosen to be high, at either every 0.5–1 min. In later stages of the experiment, where the rate of microstructural change slowed down, acquisition intervals were reduced to every 5–10 min. 3D data were reconstructed from the projections at the beamline (**Table 2**).

With the acquired time resolved 3D data it is possible to closely follow the spatial and temporal advance of the dehydration reaction in the gypsum layers and its link to the microstructural changes observed in the sample. The high quality of the data, especially in terms of absorption contrasts, allowed the use of largely unsupervised segmentation algorithms to extract pores and bassanite confidently. Tracking the discrete evolution of these two phases in the large 4D datasets is critical for the quantification of the different feedback mechanisms.

Heating the sample over the gypsum stability field destabilizes the gypsum and causes it to dehydrate. This destabilization of the system triggers a number of coupled transient developments. In these experiments, dehydration reaction in the gypsum initiates at the contact to the salt layer, and reaction spreads over the whole gypsum layer on the order of a few tens of minutes (**Figure 6**). Whereas porosity formation in the gypsum layer is an expected result of the dehydration reaction (e.g., Fusseis et al., 2012; Bedford et al., 2017), porosity and permeability changes can also be observed within the salt layer (**Figure 7**). There, the changes can be correlated to the fluid release and pore fluid pressure buildup caused by the dehydration reaction in the gypsum layer, showing an example of a coupled process. Further developments that feed into grain-scale feedbacks include the (i) temporary fluid release until the dehydration reaction has completed, (ii) the formation and, at least partly, subsequent compaction of porosity, or (iii) increased salt deformation rates where water enters the system from the dehydration reaction. It is during these transient stages that the rock is most likely to weaken significantly and where/when we expect to find the processes that explain the susceptibility of evaporitic rocks to function as detachment horizons.

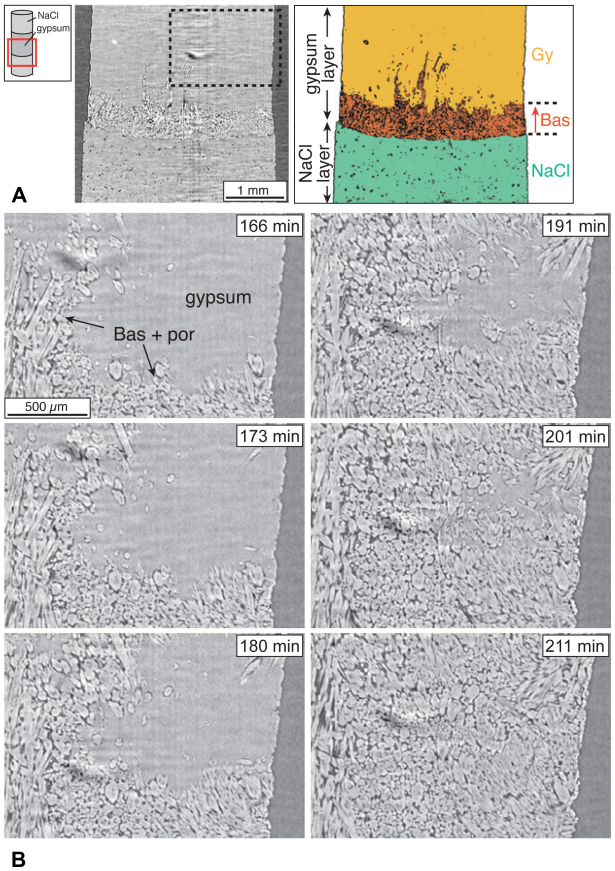

FIGURE 6 | Microstructural development overview. **(A)** Left: sketch of sample assembly with indicated FOV, which captures the interface between an upper gypsum and a lower NaCl layer. Middle: tomographic reconstruction. Vertical slice through the sample. Right: Same as middle image, but segmented for the different phases for better visibility. Orange: Gypsum, Red: Bassanite, Green: NaCl. The dehydration reaction, forming bassanite, initiates at the gypsum – NaCl interface and travels upwards into the gypsum layer. **(B)** Time-series showing the advance of the dehydration reaction.

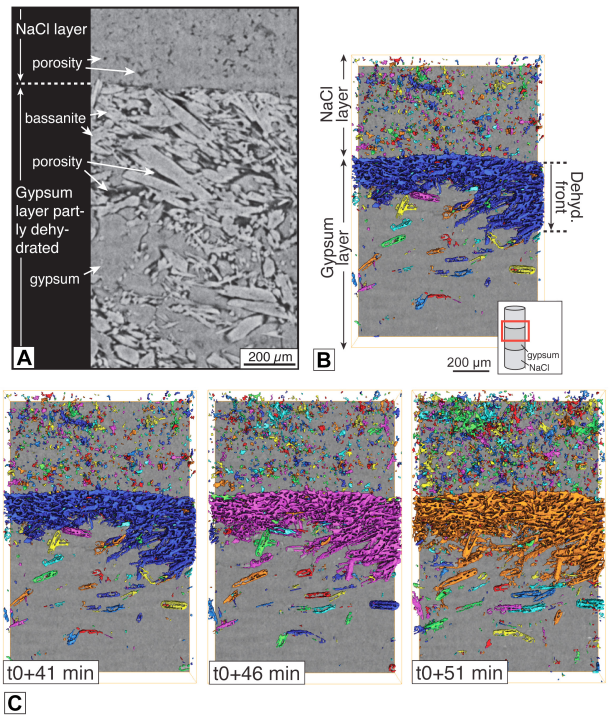

FIGURE 7 | Porosity evolution. **(A)** Microstructure overview. Sub-area of reconstructed XTM scan, vertical cross section. **(B)** Explanatory image for how to read data in **(C)**. 3D subvolume of segmented porosity. To each pore, an individual color is assigned (although colors repeat). The subvolume contains part of an NaCl layer to the top, a gypsum layer to the bottom and a dehydrated layer traveling from the NaCl – gypsum interface downwards into the gypsum layer. The large connected pore volume (large blue pore) shows how porosity in the dehydrated layer is well connected. **(C)** Time-series of pore network evolution with a time step of 5 min between successive time points.

Magmatic Processes

Modern volcanology uses a wide range of field and laboratory techniques, analyzing and comparing cooled natural samples with experimental products, real time geophysical measurements and field observations to improve our understanding of magmatic behavior. However, many of the key sub-surface

processes that control magma mobility and influence eruption behavior remain extremely challenging to constrain. This is because of the multiple spatial and temporal scales over which the processes operate, and the range of physical and chemical heterogeneity in the magmatic systems; a level of complexity further compounded by overprinting and alteration of the microstructural information during all subsequent stages of formation, storage, mobilization and transport of magma. The natural and experimental samples we can analyze *post mortem* will not retain the textures that controlled behavior at depth, or those that existed under experimental conditions.

Understanding what triggers eruptions, what controls eruption explosivity, and how the coupled physical, chemical and thermal evolution of the magma control its eruptability remain core challenges in the discipline. This includes the nucleation and growth of multiple mineral and bubble populations through time; how crystal and bubble "cargoes" control magmatic mobility; the mechanisms of mixing and mobilization of magmas during recharge; and how bubble growth and coalescence control permeability and outgassing during magma ascent and therefore influence eruption explosivity. Fragmentation, welding or sintering, and understanding how deformation and flow can affect the rheological behavior and mobility are also targets of ongoing investigation.

Making advances in these areas requires real-time, direct observations of the processes operating at all stages of magmatic evolution. Analysis of post-emplacement natural samples or experimental charges both include a component of overprinting, with early processes obscured or obliterated by later stages of the evolution, and neither allow us to capture the dynamics of the processes involved. X-ray tomography at synchrotron facilities such as TOMCAT now gives us the capability to perform these much needed *in situ* experiments, and allow us to observe and quantify processes that have hitherto been inaccessible. This continues to lead to new advances in conceptual understanding and the development of new empirical and numerical models to describe magmatic evolution.

In recent years the TOMCAT time-resolved endstation has been used with great effect in a number of high temperature volcanology studies, including work that has identified the mechanism of volcanic sintering (Wadsworth et al., 2017, 2019), tracked bubble growth (Baker et al., 2012; Pistone et al., 2015b; Pleše et al., 2018), and melt segregation mechanisms (Pistone et al., 2015a). In many of these cases, the starting point of the processes under investigation and its duration are unknown or hard to predict prior to the experiment. Often, the kinetics of the processes has a strong thermal dependence, or is controlled by the initial sample microstructure. In these cases, the ability to exploit the GigaFRoST to capture multiple, pre-registered 3D datasets at a variable image frequency over the course of an experiment is invaluable, as is the absence of any delay for data download from the camera before starting another acquisition, should additional data be required. To briefly highlight the capability of the TOMCAT endstation for volcanological research, we present two exemplar datasets that show the range of high-temperature experimental conditions that can be achieved. For the purposes of this study, we focus here on the power of the temporal resolution of the data, and the information that can then be extracted from such data, rather than giving a detailed analysis and interpretation in any volcanological context.

Capturing Instabilities in Bubble Interactions in 4D

Capturing the bubble growth and collapse along with bubble-bubble interaction and coalescence is key to understanding degassing and out-gassing of magmas, which in turn controls the build-up and release of the over-pressure that drives explosive eruptions. The TOMCAT endstation has been instrumental in shedding light on the evolution of permeability and porosity.

Samples were loaded into an Al_2O_3 ceramic crucible and mounted on the TOMCAT rotation stage. The laser heating system (Fife et al., 2012) was used to heat the samples at 15°C/min to a fixed dwell temperature. The isothermal dwell was varied systematically (550–1200°C depending on sample) to constrain the process dynamics. During the testing phase, the continuous rotation provided the capability to move between temperatures without the need for a cooling step. The complex experimental charges used for this kind of experiment can be challenging to produce, and their behavior can be influenced by their initial heterogeneous microstructure and the cooling paths they have experienced. The ability to image the behavior of the same sample while changing temperature or deformation can therefore be extremely useful for cross-correlation of behavior between initial microstructures or between multiple samples under the same conditions. The evolving microstructure strongly influences the behavior at any time step, so the rate of change observed in the structural evolution can vary. Where progression occurs at a rate different to that predicted, the GigaFRoST allows for additional acquisition periods at different tomography acquisition frequencies without the need to stop rotation or quench the sample. In the example illustrated here, images were collected during heating, regularly through the isothermal dwell at 900°C, and during the sample cooling. 1000 projections were acquired per 3D data set, with an exposure time of 2 ms and a total scan acquisition time of 2 s. A 3D scan was started every 60 s throughout the experiment (**Table 2**). The reconstructed data have a voxel edge length of 3.7 μm. Although we acquired successive tomographies at low frequency (1/min), we obtain the individual tomographies with short exposures as scan times larger than a few seconds introduce significant motion blur into some regions of the reconstructed image.

In this foam collapse scenario, we use a natural obsidian sample (Newberry volcano) that had been foamed in the lab (*ex situ*), and exploit the TOMCAT endstation to capture the bubble-bubble interactions during a second phase of heating. In the *ex situ* experiments, this heating schedule causes significant collapse of the already degassed foam. The data from the foam collapse experiment (**Figure 8**, left), shows small sections of the reconstructed 2D slices at different time points (t = 1 min to t = 80 min shown) through the 4D data set and allows us to trace the geometric evolution of a particular bubble assemblage. The entire sample is contracting heterogeneously, but generally radially inwards in the images shown (the figure shows the

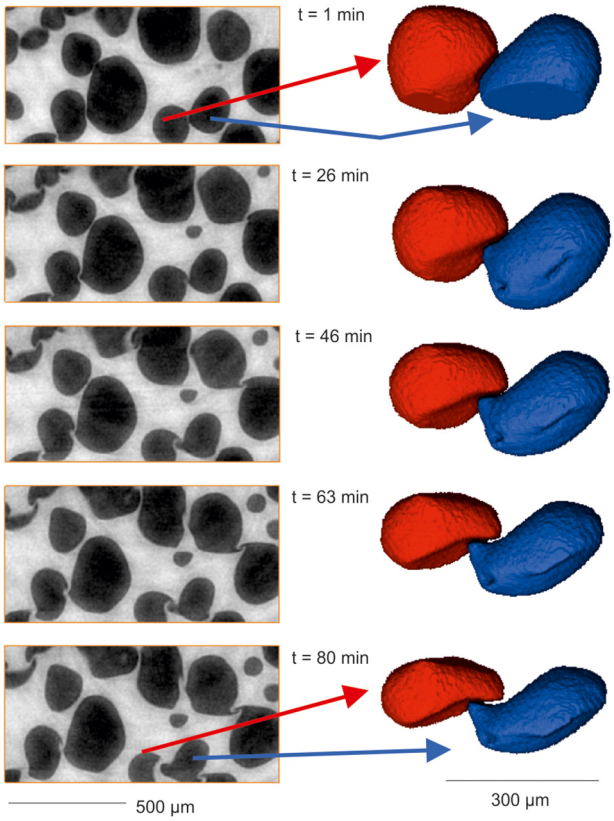

FIGURE 8 | Tracking bubble interactions during foam collapse. The panels on the left show a 2D axial slice through a sub-volume of the 4D data set at five time points during the experiment. The 3D renderings on the right show the changing interaction and complex "handshake" between two typical bubbles. Note the comparable near symmetric deformation of both bubbles around the interface. Most bubbles in the sample show some degree of dimpling at multiple bubble-bubbler interfaces, although some do have truly planar films. No thinning of the dimpled films is seen during this experiment, and no coalescence is observed despite the volume reduction in the foam.

central region of a slice perpendicular to the rotation axis, from the central region of the sample). The data, as illustrated by these typical 2D time slices and the 3D rendered pairs of bubbles (**Figure 8**, right), show that, despite the onset of collapse, we see no coalescence, even where high curvature bubble-bubble contacts are undergoing deformation. Such textures have previously been suggested as indicative of nascent coalescence. Yet, while we see significant but incomplete collapse over the 145 min heating schedule, we see no coalescence where these complex bubble interactions are observed.

Quantification of Flow in Bubbly Magmatic Fluids

Moving beyond simple static systems, the TOMCAT endstation and laser furnace system have also been integrated with a rheological testing apparatus (XRheo, see Dobson et al., submitted) to investigate the response of magmas to deformation. In the more challenging torsional experiments, the bubbly melt undergoes deformation in a miniaturized wide gap concentric cylinder rheometer (**Figure 9**, upper left). The beamline rotation stage is used to control the cup, with the XRheo providing the differential load for deformation. Given the high speed of individual coalescence events in these samples (simulating a fully degassed basaltic magma with an initial porosity of ∼40%), there remains some motion blur, even when working with short tomography acquisition times of 0.25 s. Speeds of 0.25 s per tomogram were achievable, but the slight reduction in motion blur was outweighed by the increase in detrimental image noise from shorter exposure times or fewer projections (see Dobson et al., submitted for details). Using an acquisition protocol with 1000 projections per scan at a speed of 1 tps (1 ms exposure time) with a 3.7 µm voxel size, the quality of the data is sufficient to perform a qualitative assessment of the bubble motion, and detailed quantitative analysis using the latest Digital Volume Correlation (DVC) techniques (3Dmagination and Avizo, Thermo Fisher) to define the accommodation of displacement and strain across the sample volume (**Figure 9**). The 2D images from three consecutive time steps at the same slice position (**Figure 9**, top right) clearly show the motion and deformation of the bubbles (with minimal motion blur), and the quantitative DVC analysis for the same time points (**Figure 9**, bottom) shows the 3-dimensional distribution and heterogeneity of the displacement vector field.

DISCUSSION AND OUTLOOK

XTM is an established analysis technique in different fields of the Earth Sciences and an increasing number of institutes in these fields are nowadays equipped with their own tomographic scanners (or even entire X-ray tomography facilities) for the on-site investigation of static samples. Synchrotron radiation, with its coherence and high flux, is instead required for studying fast dynamic processes as they happen in 3D. Hardware and software developments (**Table 1**) over the past decade have pushed the time resolution for tomographic microscopy investigations at large scale facilities well into the sub-second regime, opening up a wealth of new possibilities for addressing scientific questions outside reach until recently.

Since the advent on the market of the first high-quality, high-frame-rate detectors (Mokso et al., 2010), the TOMCAT beamline has been at the forefront of the time-resolved tomographic microscopy activities. In addition to its highly flexible design, able to accommodate the most diverse applications, a few key unique hardware devices made new groundbreaking experiments (Walker et al., 2014; García-Moreno et al., 2019) at the TOMCAT fast tomography endstation possible. The high field bending magnet source and the relatively short beamline (samples typically located at 25 m from the source of the radiation) lead to a large (∼20 × 5 mm^2) but at the same time intense beam, even though the used FOV is typically more around 5 × 5 mm^2. These beam sizes are not always available at other imaging beamlines based on undulator sources, unless the endstation is far away from the source outside the main building or a beam expander is used. The recently procured custom-made high-efficiency 4× optical component coupled to the in-house developed GigaFRoST detector is essential to best exploit the

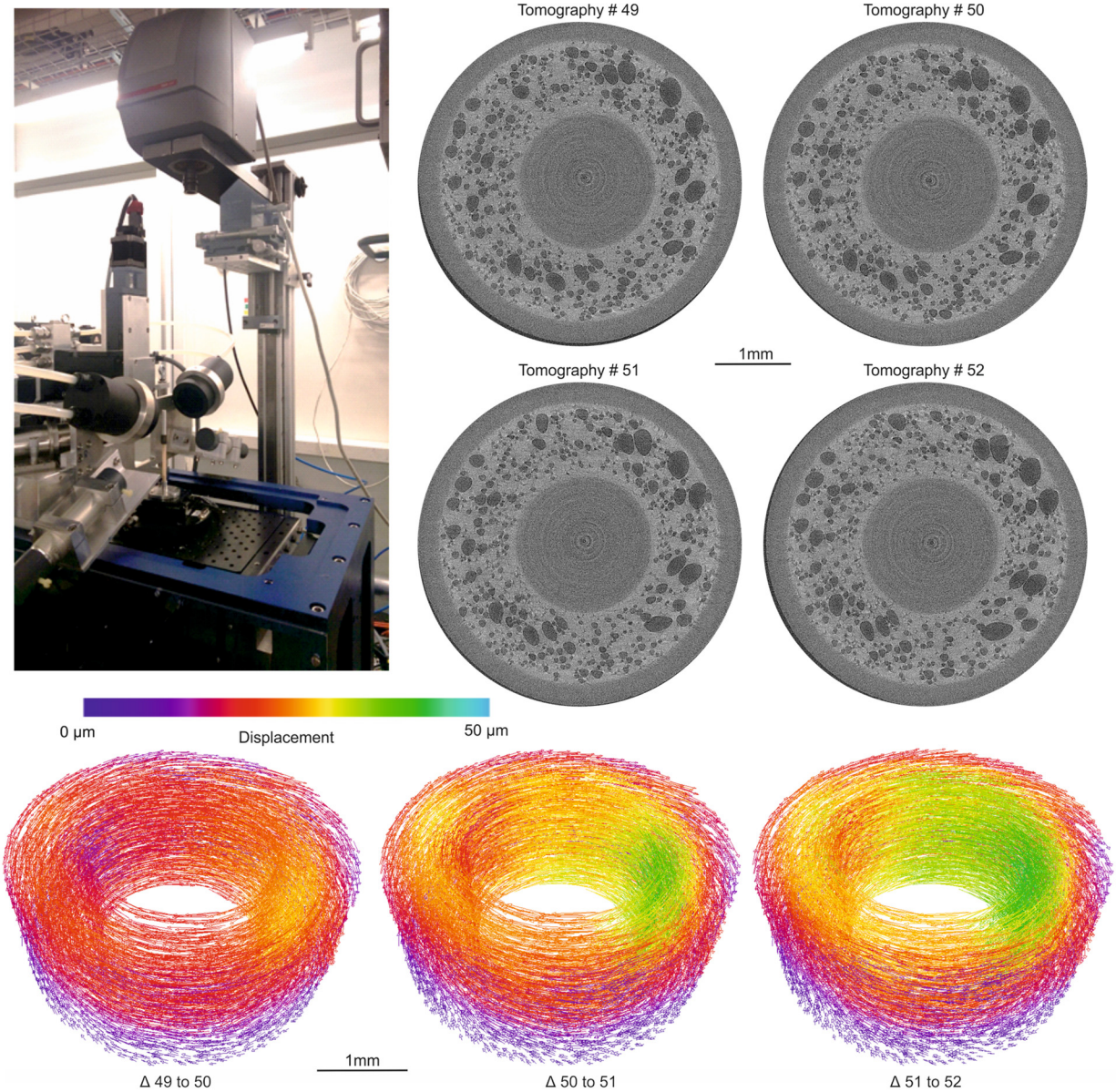

FIGURE 9 | Capturing deformation during rotational deformation. (TOP LEFT) Photograph showing the XRheo and the SLS laser system installed at TOMCAT (See Dobson et al., submitted for further details). (TOP RIGHT) Mid-section axial slices from four time steps through the measured volume (each image is 7 s apart). The cup and spindle are the mid gray cylindrical regions bounding the bubble-bearing melt (pale gray). Highly heterogeneous motion of bubbles (black) can be seen between all four images (especially in the bottom right quadrant). Data quality is sufficient to allow these displacements to be quantified using Digital Volume Correlation (BOTTOM), with the displacement vectors of the mesh centers shown colored by displacement magnitude.

available photon flux and push time-resolved imaging to the 20 Hz regime and beyond. The flexible hardware integration makes planning and designing a variety of different experiments with the most diverse requirements possible, while efficient data handling and reconstruction tools provide rapid access to post-processed data, facilitating and speeding up decisions affecting the on-ongoing experiment, a feature strongly appreciated by the scientific user community.

The study of the most diverse transient geological processes across different Earth Sciences disciplines has strongly benefited from these new capabilities. In particular the high spatial and temporal resolutions coupled to the potential for long duration experiments have proved essential for the investigation of highly dynamic systems where critical developments occur over several minutes, as it is often the case. Compromises on the experimental design (e.g., a higher number of projections or scans to the detriment of a smaller FOV) and on the portion of the processes to be investigated are no longer necessary. These new opportunities have also strongly contributed to pushing fields beyond the 2D approach and support with experimental

evidence the behavior of phenomena in 3D at unprecedented spatio-temporal resolution. This newly unlocked knowledge will be invaluable for the validation and advancement of theoretical and numerical models in different Earth Sciences communities, key tools for addressing several environmental, industrial and medical applications.

Although 20 Hz tomographic experiments with a few micron spatial resolution are routine at TOMCAT (Maire et al., 2016), investigations of sub-second dynamic processes with a higher-spatial resolution are still borderline due to insufficient photon flux leading to unsatisfactory data quality. A high-quality, high-efficiency microscope lens as the one described in Section "Optics," but with a higher magnification (e.g., 10×) would directly lead to an increase of time resolution by a few times. The in-line arrangement (Mokso et al., 2013) of two different efficient optics coupled to two GigaFRoST detectors, actually available in-house, would also make time-resolved multi-resolution studies a reality. This arrangement would enable the simultaneous acquisition of overview and zoomed-in scans of exactly the same sample and process, providing important simultaneous 3D information on the relationship between microstructural details and the overall structure or permitting the observation of processes at two different length scales. The immediate benefits for studies of pore scale flow processes in heterogeneous multiscale porous media are obvious for a wide range of geological settings, including volcanology, where the behavior of thin bubble films (elucidating the processes of bubble nucleation and coalescence) could be captured alongside the larger scale bubble evolution. Similarly, in rock deformation experiments, both grain scale and continuum behaviors in the same sample could be captured simultaneously under identical conditions.

With a 2.4 GeV ring and a 2.9 T bending magnet, the high energy photons available at TOMCAT are limited (**Figure 1**). For energies above 40 keV the flux is strongly reduced and at 80 keV it approaches 0. Although the beam on sample could be wider than 22 mm, the low number of high energy photons restrains the maximum sample size for typical geological materials like rocks to 5–7 mm, at times not satisfactory for *in situ* experiments, both because small cells could be difficult to realize and the observed processes could be dominated by boundary effects.

The SLS is planning an upgrade to a diffraction-limited storage ring for 2023–2024 (Streun et al., 2018). For the current TOMCAT fast tomography endstation, the proposed upgrade opens the doors to experiments with larger samples since the flux at higher energies should significantly increase by placing a bending magnet with a stronger magnetic field in the new ring. Furthermore, the portfolio of imaging options of the new ring (still under discussion) could potentially offer new opportunities as, for instance, sub-second tomographic imaging capabilities in the sub-micron regime if a new tomography endstation could be located at an undulator beamline. Additional envisaged hardware upgrades include a new modular sample manipulator and a faster high-frame rate detector.

Despite the efficient tools developed for handling, reconstructing and post-processing the large amount of data produced during time-resolved experiments, a margin for improvement still exists. While new technological solutions (e.g., more powerful computational hardware and larger bandwidths) will naturally ease the work with TBs of experimental data, we believe that with smarter acquisition strategies and new software solutions as those provided by the emerging deep learning field, a higher image quality, temporal and spatial resolution will be within reach with actually less data.

Currently, in time-resolved experiments, the data acquisition is often performed essentially blindly, resulting in large amounts of data without any information of interest. Not only is this large amount of useless data produced, transferred, stored and reconstructed in the first place, but these multiple TB of data need to be interrogated, either manually or semi-automatically, to identify its small useful portion, before any actual analysis can start. The synchronization possibilities offered at TOMCAT (see Sections "Rotation Stage" and "Data Acquisition") at least partially mitigate this data deluge. The 3D preview currently under development (Buurlage et al., 2019) opens up new opportunities for an active experimental feedback and should enable smarter experiment control, thereby significantly reducing the amount of acquired data while maximizing its information content.

Until now, it has mostly been possible to tomographically reconstruct the acquired data using standard approaches based on analytical solutions (Marone et al., 2017), even for under-sampled and noisy datasets typical for investigations with a high temporal resolution. Yet, iterative reconstruction techniques incorporating *a priori* knowledge about the sample's microstructure or time-evolution (Van Eyndhoven et al., 2015) and deep learning methods for image denoising and post-processing (e.g., segmentation) (Pelt et al., 2018) have the potential to further decrease the size of the raw datasets (by reducing the number of projections required to achieve a given data quality) or to increase the quality of tomographic volumes (for a given number of projections or scan time), thus improving and enabling automation of post-processing segmentation and quantification workflows. The current lack of reliable automatic data post-processing procedures still hinders the development of more streamlined large data quantification pipelines. Improvements to the data quality are expected to increase the level of automation for interrogating big data. This should lead to a net decrease of the delay between experiments and publication of the results, which can currently amount to several years.

DATA AVAILABILITY STATEMENT

The raw data supporting the conclusions of this article will be made available by the authors, without undue reservation, to any qualified researcher.

AUTHOR CONTRIBUTIONS

FM, CS, and MS were involved over the years in the development of the different aspects of the TOMCAT fast tomography

endstation. JJ-M, MG, and FM performed the experiments for Section "Solute Transport Through Porous Media." AV-P, MG, and JJ-M performed the 3D image analysis. SM and FF developed and provided the deformation rig for Section "Evaporite Deformation." SM, FF, and CS performed the experiments. SM and FF post-processed the data. KD developed the XRheo rheology setup for Section "Magmatic Processes." KD and FM (see Dobson et al., submitted) carried out the experiments. KD post-processed and analyzed the data. All authors contributed in drafting and revising the manuscript.

FUNDING

SM and FF acknowledge funding from the Swiss National Science Foundation (SNF) (early postdoc Mobility grant Nr. 178615). Financial support is gratefully acknowledged from the Swiss National Science Foundation (SNF, grant Nr. 200021_178986) and from the Swiss Light Source, PSI (TOMCAT beamtime Nr. 20170607) for AV-P, MG, and JJ-M. KD was supported by NERC NE/M018687/1, and European Research Council Advanced Grant (EVOKES-247076).

ACKNOWLEDGMENTS

AV-P, MG, and JJ-M acknowledge Dr. Rolf Kaufmann, Dr. Selina Kolokhyta, Mahdieh Shakoorioskooie, and Bekmurza Beisenov (Empa) for their help during the experiments. They also acknowledge the usage of the Empa Platform for Image Analysis (https://www.empa.ch/web/s499/software-/-imaging-platform) at Empa's Center for X-ray Analytics and of the Ra computer cluster at PSI (funded by the Data Analysis As Service, DaaS, project Nr. 142-004 of the *swissuniversities* SUC P-02 program) for part of the software and hardware resources used for the performed 3D image analysis. KD acknowledges the XRheo team for help during beamtime. We acknowledge the Paul Scherrer Institut, Villigen, Switzerland for provision of synchrotron radiation beamtime at the TOMCAT beamline X02DA of the SLS, and all the researchers and technical staff who assisted with the many beam time experiments that have contributed to this manuscript.

REFERENCES

Armstrong, R. T., Ott, H., Georgiadis, A., Rücker, M., Schwing, A., and Berg, S. (2014). Subsecond pore-scale displacement processes and relaxation dynamics in multiphase flow. *Water Resour. Res.* 50, 9162–9176. doi: 10.1002/2014wr015858

Baker, D. R., Brun, F., O'Shaughnessy, C., Mancini, L., Fife, J. L., and Rivers, M. (2012). A four-dimensional X-ray tomographic microscopy study of bubble growth in basaltic foam. *Nat. Commun.* 3:1135. doi: 10.1038/ncomms2134

Barbier, E. (2002). Geothermal energy technology and current status: an overview. *Renew. Sustain. Energy Rev.* 6, 3–65. doi: 10.1016/S1364-0321(02)00002-3

Bedford, J., Fusseis, F., Leclère, H., Wheeler, J., and Faulkner, D. (2017). A 4D view on the evolution of metamorphic dehydration reactions. *Sci. Rep.* 7:6881. doi: 10.1038/s41598-017-07160-7165

Berg, M. T. L., Bromiley, G. D., Le Godec, Y., Philippe, J., Mezouar, M., Perrillat, J. P., et al. (2018). Rapid core formation in terrestrial planets by percolative flow: in-situ imaging of metallic melt migration under high pressure/temperature conditions. *Front. Earth Sci.* 6:77. doi: 10.3389/feart.2018.00077

Blunt, M. J., Bijeljic, B., Dong, H., Gharbi, O., Iglauer, S., Mostaghimi, P., et al. (2013). Pore-scale imaging and modelling. *Adv. Water Resour.* 51, 197–216. doi: 10.1016/j.advwatres.2012.03.003

Bührer, M., Stampanoni, M., Rochet, X., Büchi, F., Eller, J., and Marone, F. (2019). High-numerical-aperture macroscope optics for time-resolved experiments. *J. Sync. Radiat.* 26, 1161–1172. doi: 10.1107/S1600577519004119

Bultreys, T., Boone, M. A., Boone, M. N., De Schryver, T., Masschaele, B., Van Hoorebeke, L., et al. (2016). Fast laboratory-based micro-computed tomography for pore-scale research: illustrative experiments and perspectives on the future. *Adv. Water Resour.* 95, 341–351. doi: 10.1016/j.advwatres.2015.05.012

Butler, I. B., Flynn, M., Fusseis, F., and Cartwright-Taylor, A. (2017). "Mjölnir: a novel x-ray transparent triaxial rock deformation apparatus," in *Proceedings of the 3rd International Conference on Tomography and Materials and Structures*, Lund.

Buurlage, J.-W., Marone, F., Pelt, D. M., Palestijn, W. J., Stampanoni, M., Batenburg, K. J., et al. (2019). Real-time reconstruction and visualization towards dynamic feedback control during time-resolved tomography experiments at TOMCAT. *Sci. Rep.* 9:18379. doi: 10.1038/s41598-019-54647-4

Chiogna, G., Hochstetler, D. L., Bellin, A., Kitanidis, P. K., and Rolle, M. (2012). Mixing, entropy and reactive solute transport. *Geophys. Res. Lett.* 39:GL053295. doi: 10.1029/2012GL053295

Cnudde, V., and Boone, M. N. (2013). High-resolution X-ray computed tomography in geosciences: a review of the current technology and applications. *Earth Sci. Rev.* 123, 1–17. doi: 10.1016/j.earscirev.2013.04.003

Cunningham, J. A., Rahman, I. A., Lautenschlager, S., Rayfield, E. J., and Donoghue, P. C. J. (2014). A virtual world of paleontology. *Trends Ecol. Evol.* 29, 347–357. doi: 10.1016/j.tree.2014.04.004

de Anna, P., Jimenez-Martinez, J., Tabuteau, H., Turuban, R., Le Borgne, T., Derrien, M., et al. (2014). Mixing and reaction kinetics in porous media: an experimental pore scale quantification. *Environ. Sci. Technol.* 48, 508–516. doi: 10.1021/es403105b

de Barros, F. P. J., Dentz, M., Koch, J., and Nowak, W. (2012). Flow topology and scalar mixing in spatially heterogeneous flow fields. *Geophys. Res. Lett.* 39:L08404. doi: 10.1029/2012GL051302

De Carlo, F., Gursoy, D., Marone, F., Rivers, M., Parkinson, D. Y., Khan, F., et al. (2014). Scientific data exchange: a schema for HDF5-based storage of raw and analyzed data. *J. Sync. Radiat.* 21, 1224–1230. doi: 10.1107/S160057751401604X

De Simoni, M., Carrera, J., Sánchez-Vila, X., and Guadagnini, A. (2005). A procedure for the solution of multicomponent reactive transport problems. *Water Resour. Res.* 41:W11410. doi: 10.1029/2005WR004056

De Simoni, M., Sanchez-Vila, X., Carrera, J., and Saaltink, M. W. (2007). A mixing ratios-based formulation for multicomponent reactive transport. *Water Resour. Res.* 43:W07419. doi: 10.1029/2006WR005256

Dentz, M., Le Borgne, T., Englert, A., and Bijeljic, B. (2011). Mixing, spreading and reaction in heterogeneous media: a brief review. *J. Contam. Hydrol.* 12, 1–17. doi: 10.1016/j.jconhyd.2010.05.002

Derome, D., Griffa, M., Koebel, M., and Carmeliet, J. (2011). Hysteretic swelling of wood at cellular scale probed by phase-contrast X-ray tomography. *J. Struct. Biol.* 173, 180–190. doi: 10.1016/j.jsb.2010.08.011

Di Michiel, M., Merino, J. M., Fernandez-Carreiras, D., Buslaps, T., Honkimaki, V., Falus, P., et al. (2005). Fast microtomography using high energy synchrotron radiation. *Rev. Sci. Instru.* 76:043702. doi: 10.1063/1.1884194

Dobson, K. J., Coban, S. B., McDonald, S. A., Walsh, J. N., Atwood, R. C., and Withers, P. J. (2016). 4-D imaging of sub-second dynamics in pore-scale processes using real-time synchrotron X-ray tomography. *Solid Earth* 7, 1059–1073. doi: 10.5194/se-7-1059-2016

dos Santos Rolo, T., Ershov, A., van de Kamp, T., and Baumbach, T. (2014). In vivo X-ray cine-tomography for tracking morphological dynamics. *Proc. Natl. Acad. Sci. U.S.A.* 111:3921. doi: 10.1073/pnas.1308650111

Ebner, M., Marone, F., Stampanoni, M., and Wood, V. (2013). Visualization and quantification of electrochemical and mechanical degradation in Li ion batteries. *Science* 342:716. doi: 10.1126/science.1241882

Eller, J., Marone, F., and Büchi, F. N. (2015). Operando sub-second tomographic imaging of water in PEFC gas diffusion layers. *ECS Trans.* 69, 523–531. doi: 10.1149/06917.0523ecst

Fife, J. L., Rappaz, M., Pistone, M., Celcer, T., Mikuljan, G., and Stampanoni, M. (2012). Development of a laser-based heating system for in situ synchrotron-based x-ray tomographic microscopy. *J. Sync. Radiat.* 19, 352–358. doi: 10.1107/S0909049512003287

Flühler, H., Durner, W., and Flury, M. (1996). Lateral solute mixing processes - A key for understanding field-scale transport of water and solutes. *Geoderma* 70, 165–183. doi: 10.1016/0016-7061(95)00079-78

Friis, E. M., Crane, P. R., Raunsgaard Pedersen, K., Stampanoni, M., and Marone, F. (2015). Exceptional preservation of tiny embryos documents seed dormancy in early angiosperms. *Nature* 528:551. doi: 10.1038/nature16441

Fusseis, F., Schrank, C., Liu, J., Karrech, A., Llana-Fúnez, S., Xiao, X., et al. (2012). Pore formation during dehydration of a polycrystalline gypsum sample observed and quantified in a time-series synchrotron X-ray micro-tomography experiment. *Solid Earth* 3, 71–86. doi: 10.5194/se-3-71-2012

García-Moreno, F., Kamm, P. H., Neu, T. R., and Banhart, J. (2018). Time-resolved in situ tomography for the analysis of evolving metal-foam granulates. *J. Sync. Radiat.* 25, 1505–1508. doi: 10.1107/S1600577518008949

García-Moreno, F., Kamm, P. H., Neu, T. R., Bülk, F., Mokso, R., Schlepütz, C. M., et al. (2019). Using X-ray tomoscopy to explore the dynamics of foaming metal. *Nat. Commun.* 10:3762. doi: 10.1038/s41467-019-11521-11521

Ghanbarian, B., Hunt, A. G., Ewing, R. P., and Sahimi, M. (2013). Tortuosity in porous media: a critical review. *Soil Sci. Soc. Am. J.* 77, 1461–1477. doi: 10.2136/sssaj2012.0435

Glatz, G., Lapene, A., Castanier, L. M., and Kovscek, A. R. (2018). An experimental platform for triaxial high-pressure/high-temperature testing of rocks using computed tomography. *Rev. Sci. Instrum.* 89:045101. doi: 10.1063/1.5030204

Hanna, R. D., and Ketcham, R. A. (2017). X-ray computed tomography of planetary materials: a primer and review of recent studies. *Geochemistry* 77, 547–572. doi: 10.1016/j.chemer.2017.01.006

Jiménez-Martínez, J., Anna, P. D., Tabuteau, H., Turuban, R., Borgne, T. L., and Méheust, Y. (2015). Pore-scale mechanisms for the enhancement of mixing in unsaturated porous media and implications for chemical reactions. *Geophys. Res. Lett.* 42, 5316–5324. doi: 10.1002/2015GL064513

Jiménez-Martínez, J., Porter, M. L., Hyman, J. D., Carey, J. W., and Viswanathan, H. S. (2016). Mixing in a three-phase system: enhanced production of oil-wet reservoirs by CO_2 injection. *Geophys. Res. Lett.* 43, 196–205. doi: 10.1002/2015GL066787

Jordan, P. (1992). Evidence for large-scale decoupling in the Triassic evaporites of Northern Switzerland: an overview. *Ecl. Geol. Helvetiae* 85, 677–693. doi: 10.5169/seals-167025

Kitanidis, P. K. (1994). The concept of the dilution index. *Water Resour. Res.* 30, 2011–2026. doi: 10.1029/94WR00762

Lester, D. R., Dentz, M., and Le Borgne, T. (2016). Chaotic mixing in three-dimensional porous media. *J. Fluid Mech.* 803, 144–174. doi: 10.1017/jfm.2016.486

Lester, D. R., Metcalfe, G., and Trefry, M. G. (2013). Is chaotic advection inherent to porous media flow? *Phys. Rev. Lett.* 111:174101. doi: 10.1103/PhysRevLett.111.174101

Lindgren, J., Sjövall, P., Thiel, V., Zheng, W., Ito, S., Wakamatsu, K., et al. (2018). Soft-tissue evidence for homeothermy and crypsis in a Jurassic ichthyosaur. *Nature* 564, 359–365. doi: 10.1038/s41586-018-0775-x

Lovric, G., Mokso, R., Arcadu, F., Vogiatzis Oikonomidis, I., Schittny, J. C., Roth-Kleiner, M., et al. (2017). Tomographic in vivo microscopy for the study of lung physiology at the alveolar level. *Sci. Rep.* 7:12545. doi: 10.1038/s41598-017-12886-12883

Lovric, G., Mokso, R., Schlepütz, C. M., and Stampanoni, M. (2016). A multi-purpose imaging endstation for high-resolution micrometer-scaled sub-second tomography. *Phys. Med.* 32, 1771–1778. doi: 10.1016/j.ejmp.2016.08.012

Maire, E., Le Bourlot, C., Adrien, J., Mortensen, A., and Mokso, R. (2016). 20 Hz X-ray tomography during an in situ tensile test. *Int. J. Fract.* 200, 3–12. doi: 10.1007/s10704-016-0077-y

Marone, F., Studer, A., Billich, H., Sala, L., and Stampanoni, M. (2017). Towards on-the-fly data post-processing for real-time tomographic imaging at TOMCAT. *Adv. Struct. Chem. Imaging* 3:1. doi: 10.1186/s40679-016-0035-39

Maus, S., Müller, S., Büttner, J., Brütsch, S., Huthwelker, T., Schwikowski, M., et al. (2011). Ion fractionation in young sea ice from Kongsfjorden, Svalbard. *Ann. Glaciol.* 52, 301–310. doi: 10.3189/172756411795931804

Mokso, R., Marone, F., Irvine, S., Nyvlt, M., Schwyn, D., Mader, K., et al. (2013). Advantages of phase retrieval for fast x-ray tomographic microscopy. *J. Phys. D Appl. Phys.* 46:494004. doi: 10.1088/0022-3727/46/49/494004

Mokso, R., Marone, F., and Stampanoni, M. (2010). Real Time Tomography at the Swiss Light Source. *AIP Conf. Proc.* 1234, 87–90.

Mokso, R., Schlepütz, C. M., Theidel, G., Billich, H., Schmid, E., Celcer, T., et al. (2017). GigaFRoST: the gigabit fast readout system for tomography. *J. Sync. Radiat.* 24, 1250–1259. doi: 10.1107/S1600577517013522

Moretti, R., Arienzo, I., Di Renzo, V., Orsi, G., Arzilli, F., Brun, F., et al. (2019). Volatile segregation and generation of highly vesiculated explosive magmas by volatile-melt fining processes: the case of the Campanian Ignimbrite eruption. *Chem. Geol.* 503, 1–14. doi: 10.1016/j.chemgeo.2018.10.001

Munawar, M. J., Lin, C., Cnudde, V., Bultreys, T., Dong, C., Zhang, X., et al. (2018). Petrographic characterization to build an accurate rock model using micro-CT: case study on low-permeable to tight turbidite sandstone from Eocene Shahejie formation. *Micron* 109, 22–33. doi: 10.1016/j.micron.2018.02.010

Ottino, J. M. (1989). *The Kinematics of Mixing: Stretching, Chaos, and Transport*. Cambridge: Cambridge University Press.

Paganin, D., Mayo, S. C., Gureyev, T. E., Miller, P. R., and Wilkins, S. W. (2002). Simultaneous phase and amplitude extraction from a single defocused image of a homogeneous object. *J. Microscopy* 206, 33–40. doi: 10.1046/j.1365-2818.2002.01010.x

Pelt, D. M., Batenburg, K. J., and Sethian, J. A. (2018). Improving tomographic reconstruction from limited data using mixed-scale dense convolutional neural networks. *J. Imaging* 4:128. doi: 10.3390/jimaging4110128

Pistone, M., Arzilli, F., Dobson, K. J., Cordonnier, B., Reusser, E., Ulmer, P., et al. (2015a). Gas-driven filter pressing in magmas: insights into in-situ melt segregation from crystal mushes. *Geology* 43, 699–702. doi: 10.1130/g36766.1

Pistone, M., Caricchi, L., Fife, J. L., Mader, K., and Ulmer, P. (2015b). In situ X-ray tomographic microscopy observations of vesiculation of bubble-free and bubble-bearing magmas. *Bull. Volcanol.* 77:108. doi: 10.1007/s00445-015-0992-1

Pistone, M., Cordonnier, B., Caricchi, L., Ulmer, P., and Marone, F. (2015c). The viscous to brittle transition in crystal- and bubble-bearing magmas. *Front. Earth Sci.* 3:71. doi: 10.3389/feart.2015.00071

Pleše, P., Higgins, M. D., Mancini, L., Lanzafame, G., Brun, F., Fife, J. L., et al. (2018). Dynamic observations of vesiculation reveal the role of silicate crystals in bubble nucleation and growth in andesitic magmas. *Lithos* 29, 532–546. doi: 10.1016/j.lithos.2017.11.024

Renard, F., Cordonnier, B., Dysthe, D. K., Boller, E., Tafforeau, P., and Rack, A. (2016). A deformation rig for synchrotron microtomography studies of geomaterials under conditions down to 10 km depth in the Earth. *J. Sync. Radiat.* 23, 1030–1034. doi: 10.1107/S1600577516008730

Sahoo, S. K., Madhusudhan, B. N., Marín-Moreno, H., North, L. J., Ahmed, S., Falcon-Suarez, I. H., et al. (2018). Laboratory insights into the effect of sediment-hosted methane hydrate morphology on elastic wave velocity from time-lapse 4-D synchrotron x-ray computed tomography. *Geochem. Geophys. Geosyst.* 19, 4502–4521. doi: 10.1029/2018gc007710

Saif, T., Lin, Q., Gao, Y., Al-Khulaifi, Y., Marone, F., Hollis, D., et al. (2019). 4D in situ synchrotron X-ray tomographic microscopy and laser-based heating study of oil shale pyrolysis. *Appl. Energy* 235, 1468–1475. doi: 10.1016/j.apenergy.2018.11.044

Salvo, L., Di Michiel, M., Scheel, M., Lhuissier, P., Mireux, B., and Suéry, M. (2012). Ultra fast in situ x-ray micro-tomography: application to solidification of aluminium alloys. *Mater. Sci. Forum* 70, 1713–1718. doi: 10.4028/www.scientific.net/msf.706-709.1713

Setiawan, A., Suekane, T., Deguchi, Y., and Kusano, K. (2014). Three-dimensional imaging of pore-scale water flooding phenomena in water-wet and oil-wet porous media. *J. Flow Control Measur. Vis.* 02, 25–31. doi: 10.4236/jfcmv.2014.22005

Stampanoni, M., Groso, A., Isenegger, A., Mikuljan, G., Chen, Q., Bertrand, A., et al. (2006). "Trends in synchrotron-based tomographic imaging: the

SLS experience," in *Developments in X-Ray Tomography V*, ed. U. Bonse (Bellingham: Spie-Int Soc Optical Engineering), U199–U212.

Streun, A., Garvey, T., Rivkin, L., Schlott, V., Schmidt, T., Willmott, P., et al. (2018). SLS-2 – the upgrade of the Swiss Light Source. *J. Sync. Radiat.* 25, 631–641. doi: 10.1107/S1600577518002722

Van Eyndhoven, G., Batenburg, K. J., Kazantsev, D., Van Nieuwenhove, V., Lee, P. D., Dobson, K. J., et al. (2015). An Iterative CT reconstruction algorithm for fast fluid flow imaging. *IEEE Trans. Image Proces.* 24, 4446–4458. doi: 10.1109/TIP.2015.2466113

Vergés, J., Muñoz, J. A., and Martínez, A. (1992). "South Pyrenean fold and thrust belt: The role of foreland evaporitic levels in thrust geometry," in *Thrust Tectonics*, ed. K. R. McClay (Dordrecht: Springer), 255–264. doi: 10.1007/978-94-011-3066-0_23

Voeten, D., Cubo, J., de Margerie, E., Roper, M., Beyrand, V., Bures, S., et al. (2018). Wing bone geometry reveals active flight in archaeopteryx. *Nat. Commun.* 9:923. doi: 10.1038/s41467-018-03296-3298

Voltolini, M., Barnard, H., Creux, P., and Ajo-Franklin, J. (2019). A new mini-triaxial cell for combined high-pressure and high-temperature in situ synchrotron X-ray microtomography experiments up to 400°C and 24 MPa. *J. Synch. Radiat.* 26, 238–243. doi: 10.1107/S1600577518015606

Wadsworth, F. B., Vasseur, J., Llewellin, E. W., Dobson, K. J., Colombier, M., von Aulock, F. W., et al. (2017). Topological inversions in coalescing granular media control fluid-flow regimes. *Phys. Rev.* 96:033113. doi: 10.1103/PhysRevE.96.033113

Wadsworth, F. B., Vasseur, J., Schauroth, J., Llewellin, E. W., Dobson, K. J., Havard, T., et al. (2019). A general model for welding of ash particles in volcanic systems validated using in situ X-ray tomography. *Earth Planet. Sci. Lett.* 525:115726. doi: 10.1016/j.epsl.2019.115726

Walker, S. M., Schwyn, D. A., Mokso, R., Wicklein, M., Müller, T., Doube, M., et al. (2014). In Vivo Time-Resolved Microtomography Reveals the Mechanics of the Blowfly Flight Motor. *PLoS Biol.* 12:e1001823. doi: 10.1371/journal.pbio.1001823

Williams, K. H., Kemna, A., Wilkins, M. J., Druhan, J., Arntzen, E., N'Guessan, A. L., et al. (2009). Geophysical monitoring of coupled microbial and geochemical processes during stimulated subsurface bioremediation. *Environ. Sci. Technol.* 43, 6717–6723. doi: 10.1021/es900855j

Willmann, M., Carrera, J., Sanchez-Vila, X., Silva, O., and Dentz, M. (2010). Coupling of mass transfer and reactive transport for nonlinear reactions in heterogeneous media. *Water Resour. Res.* 46:W07512. doi: 10.1029/2009WR007739

Winograd, I. J. (1981). Radioactive waste disposal in thick unsaturated zones. *Science* 212, 1457–1464. doi: 10.1126/science.212.4502.1457

Xu, L., Chen, R., Du, G., Yang, Y., Wang, F., Deng, B., et al. (2016). Anisotropic shrinkage of insect air sacs revealed in vivo by X-ray microtomography. *Sci. Rep.* 6:32380. doi: 10.1038/srep32380

Yashiro, W., Kamezawa, C., Noda, D., and Kajiwara, K. (2018). Millisecond-order X-ray phase tomography with a fringe-scanning method. *Appl. Phys. Express* 11:122501. doi: 10.7567/apex.11.122501

Zhu, W., Fusseis, F., Lisabeth, H., Xing, T., Xiao, X., De Andrade, V., et al. (2016). Experimental evidence of reaction-induced fracturing during olivine carbonation. *Geophys. Res. Lett.* 43, 9535–9543. doi: 10.1002/2016GL070834

Conflict of Interest: The authors declare that the research was conducted in the absence of any commercial or financial relationships that could be construed as a potential conflict of interest.

frontiers in Earth Science

ORIGINAL RESEARCH
published: 11 March 2020
doi: 10.3389/feart.2020.00006

Dynamics of Water Absorption in Callovo-Oxfordian Claystone Revealed With Multimodal X-Ray and Neutron Tomography

Eleni Stavropoulou[1], *Edward Andò*[1], *Emmanuel Roubin*[1], *Nicolas Lenoir*[1,2], *Alessandro Tengattini*[1,2], *Matthieu Briffaut*[1] *and Pierre Bésuelle*[1]*

[1] Univ. Grenoble Alpes, CNRS, Grenoble INP, 3SR, Grenoble, France, [2] Institute Laue-Langevin, Grenoble, France

The Callovo-Oxfordian claystone is a material with notoriously complex hydro-mechanical behaviour. Combined neutron and x-ray tomography modalities are used for the first time to characterise the dynamics of water absorption in this material by comparing material deformation as well as water arrival. Exploiting recent work on multimodal registration, neutron, and x-ray datasets are registered pairwise into a common coordinate system, meaning that a vector-valued field (i.e., neutron and x-ray reconstructed values) is available for each timestep, essentially making this a 5D dataset. The ability to cross-plot each field into a *joint histogram* (an inherent input into the registration) allows an improved identification of mineral phases in this complex material. Material deformation obtained from the application of Digital Volume Correlation on the x-ray timeseries data is *locally* compared to changes in water content available from the neutrons, opening the way toward a quantitative description of the hydro-mechanics of this process.

Keywords: multimodal tomography, timeseries analysis, digital volume correlation, hydro-mechanics, callovo-oxfordian claystone

OPEN ACCESS

Edited by:
Marco Voltolini, Lawrence Berkeley National Laboratory, United States

Reviewed by:
Harrison Lisabeth, Lawrence Berkeley National Laboratory, United States
Anh Minh Tang, École des Ponts ParisTech (ENPC), France

***Correspondence:**
Pierre Bésuelle
pierre.besuelle@3sr-grenoble.fr

Specialty section:
This article was submitted to Petrology, a section of the journal Frontiers in Earth Science

Received: *31 July 2019*
Accepted: *15 February 2020*
Published: *11 March 2020*

Citation:
Stavropoulou E, Andò E, Roubin E, Lenoir N, Tengattini A, Briffaut M and Bésuelle P (2020) Dynamics of Water Absorption in Callovo-Oxfordian Claystone Revealed With Multimodal X-Ray and Neutron Tomography. Front. Earth Sci. 8:6. doi: 10.3389/feart.2020.00006

1. INTRODUCTION

The beginning of the study of clay-rich formations as a potential geological barrier for the storage of nuclear waste dates back to a couple of decades (Bonin, 1998; Andra, 2005; Delay et al., 2010). In France, the Callovo Oxfordian claystone (COx) is being studied by Andra (The French radioactive Waste Management Agency) through an impressive volume of in-field and lab-scale work. This claystone's properties (low permeability, self-sealing properties) make it a favourable host rock, however, the complex couplings that govern its hydromechanical behaviour are still under investigation.

The mechanical response of the COx claystone is strongly related to its water content (Armand et al., 2017), the variation of which (drying-wetting process) has been related to the modification of its microstructure (Montes et al., 2004; Robinet et al., 2012). The non-linear response observed at high relative humidity has not only been related to damage (Chiarelli et al., 2000; Escoffier, 2002), but also to the non-linear swelling of the clay mineral (Wang et al., 2014) under these conditions. The swelling properties of the Callovo Oxfordian are linked to the presence of smectite in the clay matrix, which is very sensitive to water content changes and triggers swelling at high degrees of relative humidity (Homand et al., 2006).

A number of authors have studied the kinematics of clay-rich rocks due to wetting using different imaging tools, such as environmental scanning electron microscopy (ESEM) (Montes et al., 2004; Wang et al., 2015), scanning electron microscopy (SEM) (Desbois et al., 2017), optical

microscopy (Bornert et al., 2010), or x-ray tomography (Lenoir et al., 2007). All these methods allow structural modification due to water content changes to be captured and consequently the computation of strains, however, they do not provide direct information related to water presence.

Moisture change in geomaterials has been investigated through neutron tomography, since neutrons are sensitive to hydrogen (due to their high attenuation of cold neutrons itself due to elastic scattering of neutrons). DiStefano et al. (2017) measured imbibition into a shale using *in-situ* neutron imaging. Combined x-ray and neutron tomographies on shales Chiang et al. (2018) indicate that the combination of techniques allows a better identification of the composition of these complex materials. Stavropoulou et al. (2019) combined x-ray tomography and neutron radiography to study wate imbibition in COx (albeit on twin samples) linking the cracking and propagation to the water penetration. Even though interesting trends have been revealed, this study is limited by the use of similar but different samples, meaning that the characterisation of a mechanism linking crack opening and water penetration is difficult to quantify locally.

This paper presents a significant technical evolution of Stavropoulou et al. (2019) with the analysis of a wetting test on Callovo Oxfordian claystone using a simultaneous x-ray and neutron tomography on the same sample.

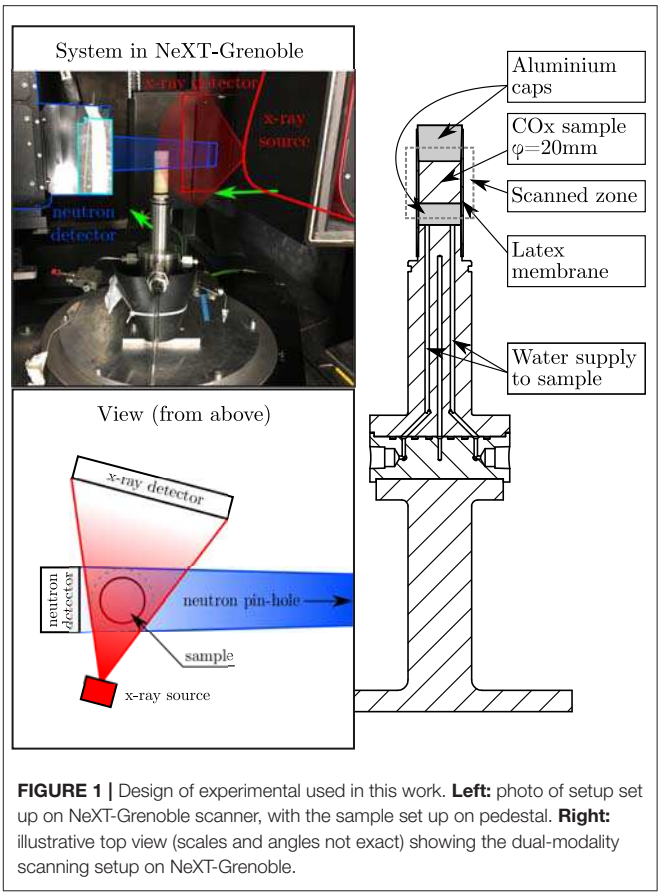

FIGURE 1 | Design of experimental used in this work. **Left:** photo of setup set up on NeXT-Grenoble scanner, with the sample set up on pedestal. **Right:** illustrative top view (scales and angles not exact) showing the dual-modality scanning setup on NeXT-Grenoble.

2. EXPERIMENTAL SETUP

2.1. Sample Preparation

For sample preparation, a fresh claystone core was used (EST57917, h = 300 mm, d = 120 mm) extracted from a depth of 490 m. The samples have been cut to a cylindrical shape (h = d = 20 mm) using a wire saw in neighbouring locations within the core. The average water content ($\frac{m_{\text{water}}}{m_{\text{dry}}}$) has been measured after drying at 105°C for at least 24 h equal to 6.54 %, a value a bit lower than what has been reported by Conil et al. (2018). This paper presents the analysis of the first sample of a series, the vertical axis of which is parallel to the bedding plane of the claystone.

Even though the experimental equipment that was designed and used for this study allows a confining pressure to be applied within a pressure vessel, this particular test is performed without confining pressure (other than that offered by the latex membrane). The experimental setup is shown in **Figure 1**. The sample is positioned on top of an aluminium base through which the water is supplied to the bottom of the sample. In order to ensure water arrival, a double hole and spiral passage is manufactured and placed on top of the aluminium base (see later **Figure 3** bottom), while the uniform distribution of the water supply to the sample is achieved using a filter paper at its bottom.

An initial tomography (numbered 001) with both modalities (details in next section) is acquired of the sample before starting water imbibition. Thereafter the air is vacuumed out of the water supply lines, and the imaging systems are readied. Water is supplied to the sample and back-to-back scans are immediately started. Tomographies are recorded back-to-back starting from number 002, which is used as the reference state for the following analysis.

2.2. Neutron and x-Ray Tomography Acquisition

X-ray and neutron tomographies were acquired simultaneously on NeXT-Grenoble (Tengattini et al., 2017, 2019), which is equipped with an almost-parallel cold neutron beam and now a micro-focus x-ray setup with a flat panel detector. The addition of the x-ray setup is a significant improvement from our preliminary study Stavropoulou et al. (2019) where twin samples were required for separate scanning with the two different modalities (neutrons and x-rays).

For the x-ray tomographies, the geometric pixel size is 42.70 µm/px. The Hamamatsu L-12161-07 x-ray source is operated at 140 kV and 130 µA. The source focuses its electron stream into a small point, creating a divergent conical beam. The Varex 2530HE Flat-panel detector records the beam with an exposure time of 1/9 s behind a B_4C filter. Each radiograph is the result of averaging 5 exposures.

Regarding neutron tomographies, NeXT-Grenoble is on a cold source, and the beam reaches the sample after going through a 30 mm diameter pinhole (with no filter). A very large collimation distance is used (around 10 m), meaning that at the sample the beam is practically parallel. A camera-mirror-scintillator system

is used to detect neutrons, with a 25 x 25 mm field of view. The Hamamastu Orca Flash V2 is equipped with Canon 180 mm F3.5 optics. The camera is used in binning 4 yielding a pixel size of approximately 50 μm/px. The camera is set to 0.6 s exposure. The scintillator used is a 50 μm thick LiF.

The x-ray and neutron acquisitions are controlled together by a proprietary RX-Solutions system. For both modalities 896 radiographs are acquired meaning scans last around 8 min. The two beams are oriented roughly perpendicular to each other (but not exactly at 90° to optimise the use of the x-ray cone beam).

During the test an interruption was necessary, meaning that seven scans are missing around the middle of the test. Due to probable neutron capture effects some greyscale corrections (detailed below) were necessary particularly after this pause.

3. DATA ANALYSIS

Both series of simultaneously acquired x-ray and neutron tomographies are reconstructed individually using the usual Filtered Back-Projection technique: the Feldkamp algorithm for the divergent x-rays and a parallel algorithm for the neutrons. The software used is RX-Solutions' UniCT, and a software correction for both beam-hardening and ring correction is applied. The resulting 3D fields of reconstructed values lumped attenuation coefficients for both modalities (henceforth referred to as μ_x for x-rays and μ_n for neutrons) are then saved on a 16-bit data range (scaling factors are kept constant for each modality).

In order to be able to simply compare noise levels between the two modalities, both tomographies of state 002 are linearly rescaled such that the mean value of the air (background) is 0.0 and the mean value of the clay matrix (foreground) is 1.0. After rescaling, the standard deviation of the background for μ_n is 0.069 and 0.011 for μ_x. The Signal to Noise Ratio can coarsely be taken as the reciprocal of these quantities since the claystone is scaled to 1.0, giving $\mathrm{SNR}_n = 14.5$ and $\mathrm{SNR}_x = 90$.

In order to denoise the μ_n field, each field is smoothed using the bilateral filter (Tomasi and Manduchi, 1998) offered in the Insight Toolkit (ITK) (Yoo et al., 2002) with a $\sigma_{\mathrm{domain}} = 1$ and $\sigma_{\mathrm{range}} = 3{,}000$. According to the definition above, the $\mathrm{SNR}_{n\text{-bilateral}}$ significantly increases to 36, at the cost of a small loss of sharpness. In what follows, these filtered images will be used for μ_n.

Since this study is mostly concerned with the entry of water into the claystone, the SNR is also computed taking the pure clay matrix as background (see later for the computation of its greylevel) and the water as the phase of interest. For safety the standard deviation of greyvalues is computed on the aluminium top cap (since the claystone has natural variations). This yields an $\mathrm{SNR}^{\mathrm{clay/water}}_{n\text{-bilateral}}=125$ and $\mathrm{SNR}^{\mathrm{clay/water}}_{x}=37$, which confirms the significant interest in the use of neutron tomography for following water.

3.1. Multimodal Registration

With a long time-series of both neutron and x-ray tomography it is very useful to be able to have a common coordinate system. If an exact match between μ_x and μ_n measurements can be achieved, the 3D data collected can be thought of as a *vector-valued* 3D field, where every voxel contains a value of μ_x and μ_n. Within the same modality the image registration problem can be written as the minimisation of the difference between the greyvalues, however since different modalities offer different contrast mechanisms, this subtraction no longer makes sense.

To this end a "multimodal registration" tool is used as first presented in Tudisco et al. (2017) and subsequently developed in Roubin et al. (2019). The inherent linearisation of the problem requires a good initial guess of the solution for registration to converge. The μ_x and μ_n volumes collected during this campaign are not easy to correlate, and the final result was found to be sensitive to the initial guess. A graphical user interface was implemented to allow an initial alignment by eye to be done, as illustrated in **Figure 2**.

The transformation to be applied to the neutron image by trilinear interpolation is described as a "linear deformation function" Φ (represented as a 4×4 matrix), meaning that rotations, shear and zoom changes of shapes can be described as well as sub-pixel translations.

For a few key states in the test (i.e., 002, 010, 020, 028, 040, 050) the entire multimodal registration procedure is performed (on 2-binned μ_x fields and μ_n fields), yielding the transformations presented in **Table 1**. It is important to stress that the Φ discussed here is the transformation between the μ_x and μ_n fields and *not* the deformation of the sample itself. Given the relatively coarse effective pixel-size used (2-binning implies 85.4 μm/px), practically no relative movement of the two imaging systems is expected. **Table 1** shows that the transformation is relatively stable, and allows a very coarse approximation of the registration error (assuming no relative movement between imaging systems) to be guessed, which is in the order of 0.1 px translation 0.2° for rotations and a factor 0.002 on "zoom." The fact that the "zoom" vector is not equal in the z direction to that found in the x and y directions may be explained by a 1% misalignment of the mirror of the neutron camera, stretching the pixels slightly in the z direction. The obtained transformations are averaged and this final transformation is then applied to *all* μ_n fields. Please note that the these registered data sets are made available, see "Data Availability Statement."

The result of this application is now a vector-valued timeseries which is valuable and complex to plot. **Figure 3** shows some selected horizontal slices from the registered volumes in state 002. The quality of the registration is apparent, as well as the complementarity of the fields measured with both modalities. Notably in the first slice, the denser aluminium attenuates the x-ray beam significantly whereas the membrane is hard to distinguish. The reverse is true for the neutron beam where the hydrogen-rich membrane attenuates enough to cause artefacts and where the aluminium is close to the background value for air.

These complementary measurements are also useful for identifying different types of inclusions in the sample studied. Furthermore, the neutron tomographies allow the identification of dry and water-filled cracks. **Table 2** shows a number of phases whose corresponding grey values have been identified by hand averaging over small homogeneous zones in the image. The table

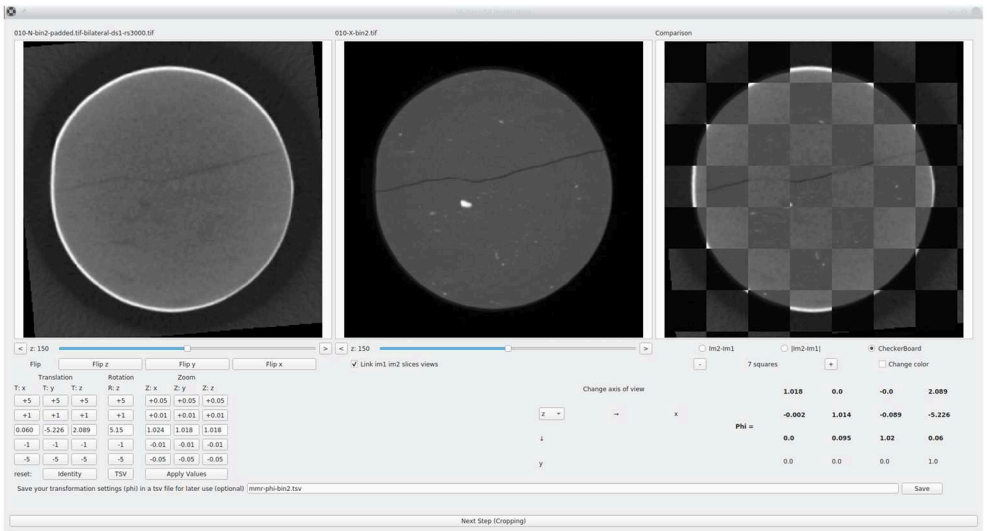

FIGURE 2 | Example of graphical tool (available in spam) developed in Qt allowing an accurate initial Φ to be manually applied to the neutrons to initialise the multimodal registration as close as possible to the correct solution. **Top row:** Horizontal slices through tomographies: (left) neutron (middle) x-rays (right) "checkerboard" allowing comparison. **Bottom row:** (left) Buttons to apply displacements, rotations and zooms to left image (middle) slice view settings (right) current Φ matrix. This software is free software and is included in the ''spam" python package.

TABLE 1 | Results of multiplicative polar decomposition of different Φ into translation, rotation, and "zoom" components to register μ_n fields onto μ_x fields for different imaged states.

State	$\begin{bmatrix} z \\ y \\ x \end{bmatrix}$ Translation vector (px)	$\begin{bmatrix} z \\ y \\ x \end{bmatrix}$ Rotation vector (degree)	$\begin{bmatrix} z \\ y \\ x \end{bmatrix}$ Zoom vector
002	2.147 –5.167 0.028	5.279 0.027 –0.077	1.018 1.018 1.028
010	2.132 –5.328 0.022	5.263 –0.003 –0.090	1.017 1.021 1.031
020	2.089 –5.226 0.060	5.152 –0.028 –0.053	1.018 1.018 1.024
028	2.190 –5.128 0.237	5.113 0.062 –0.102	1.018 1.019 1.026
040	2.291 –5.405 –0.096	5.457 –0.003 –0.157	1.020 1.020 1.035
050	2.293 –5.384 –0.095	5.462 –0.002 –0.179	1.020 1.020 1.033
Mean	2.190 –5.273 0.026	5.288 0.009 –0.110	1.019 1.019 1.030

Z is the vertical direction. Pixels of the translation vector are 2-binned (i.e., have a pixel size of 85.4 μm/px).

offers a numerical confirmation of the particular sensitivity of neutrons to water, which will be essential for the identification of the movements of water in this specimen. It is important to note that a small variation in the values of μ_x is observed throughout the timeseries, thus, a linear rescale of the values is applied to all images after 002, based on the grey values of air and water which should not vary in time. Considering air as the zero-intercept a linear correction is applied to all images such that the values of the air and the aluminium are always the same throughout the timeseries.

A powerful tool to look at the correspondence of greyvalues in these registered images is the *joint histogram* of μ_x and μ_n values. For two aligned voxelised volumes, the joint histogram is simply computed by discretising the greyvalues of μ_x and μ_n into bins, and for each voxel position in *both* volumes, adding 1 into the corresponding bin in μ_x and μ_n that two greylevels falls into. The result is a 2D space of discretised μ_x and μ_n values inside which counts are recorded. Large number of voxel pairs are expected to be found at the intersections of greylevels in **Table 2**. **Figure 4** shows the joint histogram for state 002, with the full 16-bit image range discretised into 128 bins. In fact, this joint histogram (and the fitting of each relevant peak with a bivariate Gaussian distribution) is a fundamental part of the multimodal registration presented above.

The images acquired during the wetting process in this material are numerous, so a subselection has been selected in **Figure 5**, which shows the evolution of a slice normal to the crack initially present in the sample, which is labelled as "Dry" crack in **Figure 3**. **Figure 5** also presents—in the black and white right column—the corresponding joint histograms for the entire

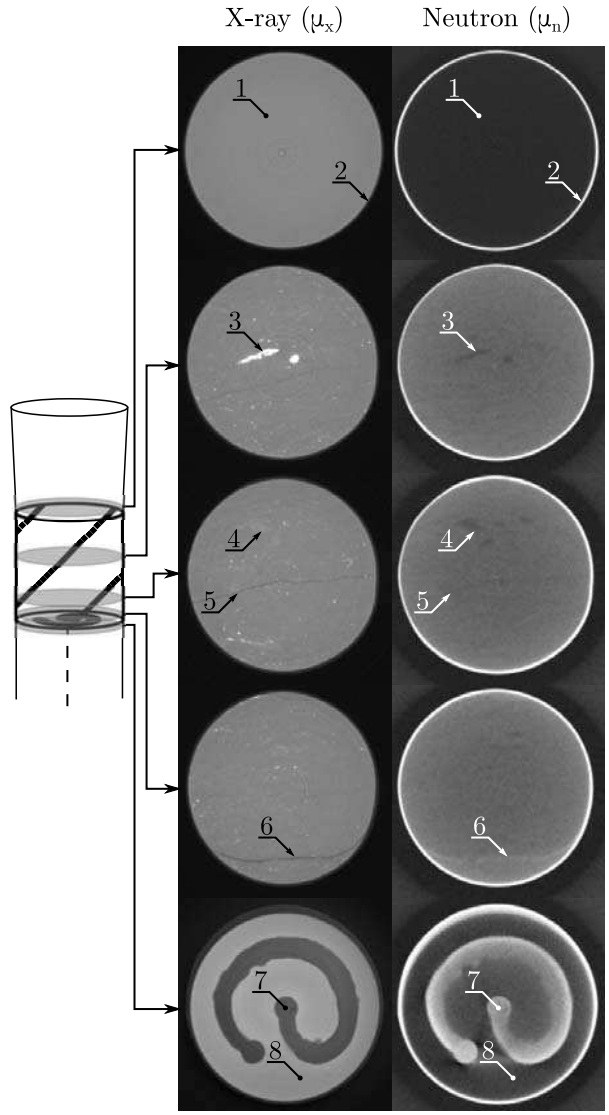

FIGURE 3 | Selected horizontal slices through registered μ_x and μ_n fields in state 002, highlighting the different phases in the material. The greylevels shown are [0–42,000] for μ_x and [0–52,000] for μ_n. As per convention, dark values in the slices represent lower values. 1. Aluminium top cap, 2. Latex membrane, 3. "Dense" inclusions, 4. "Less dense" inclusions, 5. "Dry" crack, 6. Water-filled crack, 7. Pure water, 8. Aluminium bottom cap.

TABLE 2 | Manually-measured average grey values of different phases visually present in μ_x and μ_n in state 002.

Phase	Grey value	
	μ_x	μ_n
Air	2,100	6,700
Membrane	5,900	49,400
Clay Matrix	16,000	22,500
Inclusions	47,000	15,300
Aluminium	17,000	8,800
Water (H_2O)	7,800	41,600

The high degree of complementarity between the two measurement is clear, with very different contrasts obtained for both water and inclusions, key elements in the process being studied.

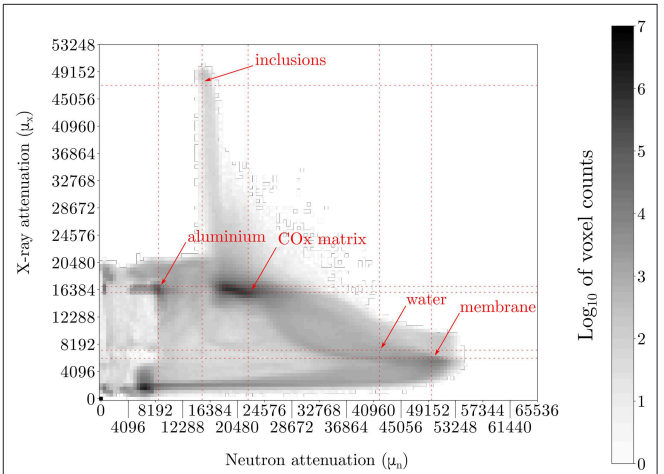

FIGURE 4 | Joint histogram of state 002, count values are presented in a $\log_{10}$ scale. Intersecting values from **Table 2** are highlighted.

volume of each pair. The changes in the joint histogram are rather subtle, however if attention is paid to the zone around the clay matrix, some changes can be observed.

For a better understanding of the evolution of the joint histograms, the difference between each time-step (005, 020, 039, 050) to the initial (002) has been calculated, indicating the increase of number of voxels in red and a decrease in blue (**Figure 5**). In addition, this difference of the joint histograms has been calculated on a cropped subvolume wholly within the sample, resulting in a range of values that cover a smaller area in the space of the joint greylevels. Similarly to **Figure 4**, the horizontal axis of these joint histograms corresponds the grey level values of the neutron images, while the vertical axis represents the grey level from x-rays, plotted in $\log_{10}$ scale.

As deduced from the incremental joint histograms, at the beginning (005–002), an increase of the number of voxels at the bottom of the vertical axis (x-ray axis) occurs in a location corresponding to the grey values of the "Dry" crack. This implies that between Scan 002 and Scan 005 an increase of the "quantity of Dry crack" is measured based on the amount of the corresponding grey level voxels from the x-ray images. Indeed, looking at the vertical slices, crack opening is well observed in the x-ray images—unlike the neutron ones.

In the following increment of joint histograms (020–002) crack opening is still observed—always along the vertical axis—however, an evolution along the horizontal axis (neutron axis) starts to appear around the same location. Increase of the grey values in the neutron images can be related to water appearance, an increase that becomes even more apparent in the following increments (039–002 and 050–002). When relating the observed evolution to the actual vertical slices, it can be confirmed that a clear water increase is depicted in the neutron image, with a

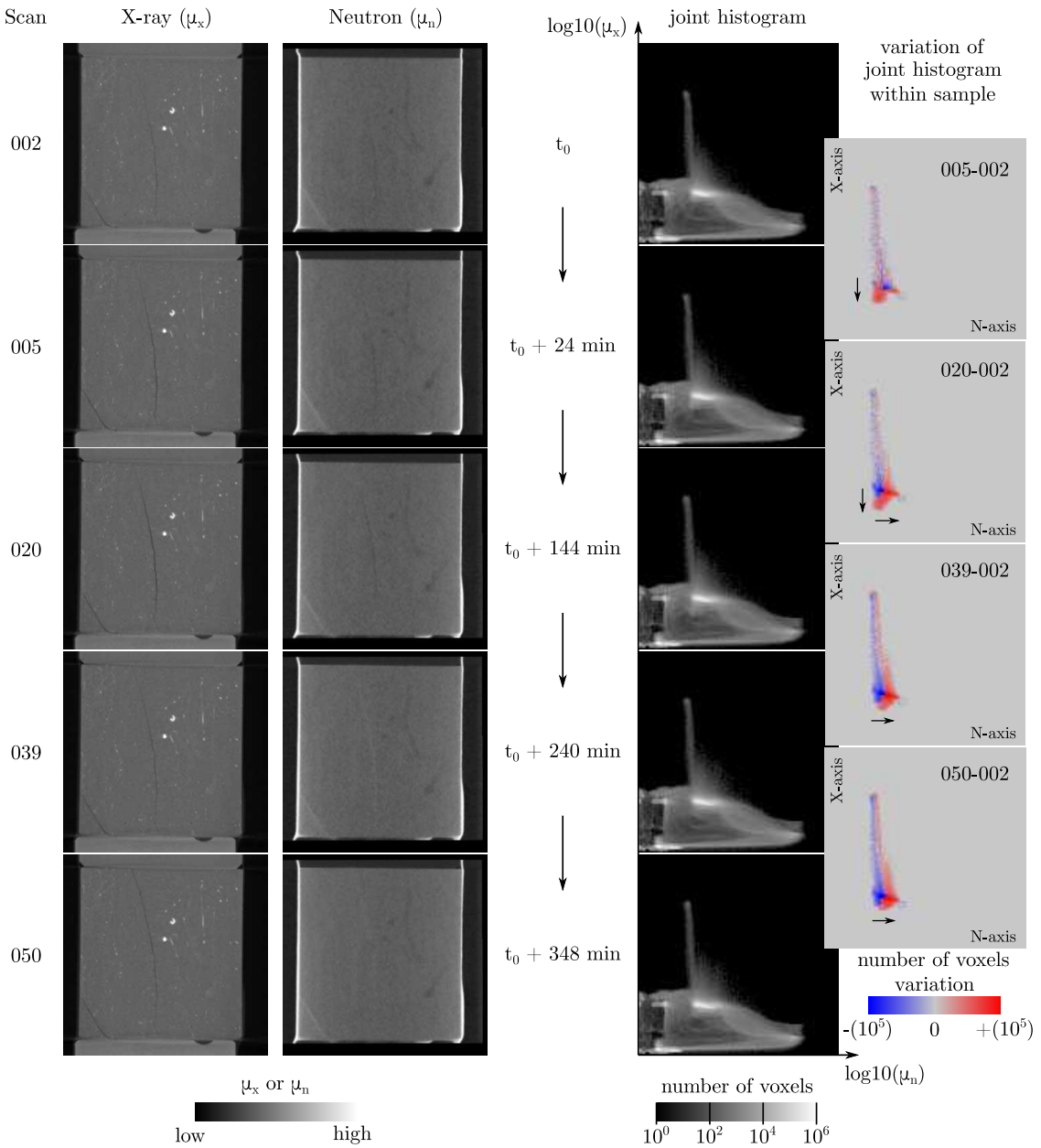

FIGURE 5 | Vertical slices through registered μ_x and μ_n fields throughout the wetting experiment. Slice has been chosen to be normal to the main crack present since the beginning of the experiment in the specimen. As per **Figure 3**, the greylevels shown are [0–42,000] for μ_x and [0-52,000] for μ_n. As per convention, dark values in the slices represent lower values. Columns 3 and 4 represent the joint histograms of the pairs of images: column 3 is the entire joint histogram of the two images, with the counts being presented in $\log_{10}$. Column 4 represents a difference in counts (also in $\log_{10}$) from 002 on a cropped zone within the specimen.

filled-up crack (high attenuation). From then on, a continued increase in water penetrating the clay matrix is revealed from the last increment of joint histograms (050–002).

3.2. Displacement and Strain Field Measurements

In order to measure the deformation of the material with time, a local-DVC code is first used (the `spam-ldic` script available in spam, Andò et al., 2017). With this technique, a regularly-spaced grid of points is spread through the "reference" 3D image (in this case the x-ray scan of state 002). A cubic subvolume, centred on each grid point is extracted from the 3D image and a transformation Φ is sought for each point to minimise:

$$\eta = \sum (\mathrm{ref}(\vec{X}) - \mathrm{def}(\Phi \cdot \vec{X})^2) \quad (1)$$

Here the Lucas and Kanade technique is used (Lucas and Kanade, 1981) with a deformation function (Grédiac and Hild, 2013; Tudisco et al., 2017). In this work, the x-ray volumes are used

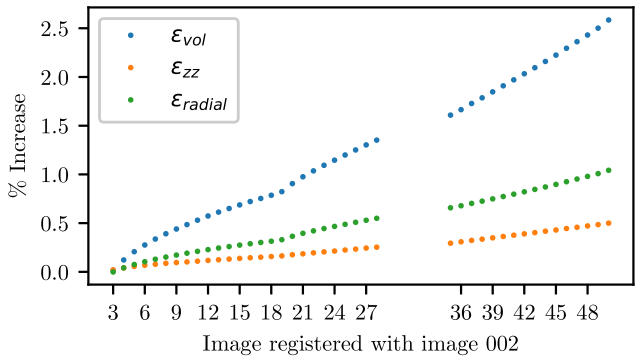

FIGURE 6 | Vertical and volumetric deformations obtained from registrations (i.e., a correlation yielding a single Φ for the entire 3D volume) with μ_x fields with state 002. Each tomography takes 8 min.

to measure the displacement, although in the future, the *vector-valued* (μ_x and μ_n) field could be used for the minimisation.

An initial time-saving step is the measurement of an overall Φ between the field of μ_x in state 002 and later states, which serves as an initial guess for the displacement of all points on the grid which will then be correlated. **Figure 6** shows the progression of ε_{zz}, ε_{radial}, and ε_{vol} with progressive registration with state 002. These scalars are obtained by extracting the displacement gradient tensor from the measured Φ: the component ε_{zz} is directly read out, the volume change is computed as the determinant of the displacement gradient tensor, and $\varepsilon_{radial} = \frac{1}{2}(\varepsilon_{vol} - \varepsilon_{zz})$ is computed as per Wood (1990).

Analysis of **Figure 6** immediately reveals that there is indeed swelling occurring *on average*. The extent of swelling is significantly less than what was expected from the previous study (Stavropoulou et al., 2019)—which is likely explained by a higher initial water content in the sample studied here, together with its different shape, size, and a potential confinement applied by the membrane.

In order to look at swelling locally, a displacement field must be measured and strains computed. Of particular interest is to be able to compare local strains to changes in μ_n, which should indicate—all other things being the same—water arrival. In this work, displacement fields are measured with two different image correlation techniques, non-rigid local correlation and global correlation, both available in the spam toolkit.

The local displacement field is measured by defining a regular grid of measurement points with an equal spacing of 40 pixels (in non-binned images, which means 1.7 mm) in all directions. Each point is represented by a cuboid subvolume of greylevels centred on the point. The overall registration is then used as an initial guess for the displacement of each measurement point. The volumetric strain can either be extracted from the determinant of a locally-measured Φ as above, or by deriving the displacement gradient from the translation part of Φ from neighbouring measurement points. The first approach is extremely noisy, and cannot be used meaningfully given the relatively subtle volumetric strains that are trying be to captured. The second technique works well, however since measurement points are represented by subwindows and are used multiple times to measure strains, the physical space represented by a strain point is not direct. However, the displacement fields measured are of excellent quality, and are added to the data uploaded to Zenodo for a variety of subvolume sizes (see Data Availability Statement).

The lack of a direct interpretation of the physical subvolume represented by a strain measurement point in local DVC motivates the use of global DVC (Leclerc et al., 2011), where a continuous mesh is deformed to best match two images (to minimise η as above). In this case a cubic tetrahedral mesh of 360 × 160 × 160 pixels or 15.4 × 6.8 × 6.8 mm within the specimen is used. The edges are avoided since the current implementation of the technique has no mechanical regularisation and therefore problematic behaviour can occur on the edges. A characteristic size of tetrahedron of 80 pixels or 3.4 mm is found to give sufficiently low-noise in the strain computation[1]. The global convergence criterion is the norm of the displacement vector and for the correlations performed here, the criterion is slowly relaxed from 0.01 px for the early steps to 0.15 px for the later ones. The mesh generated contains 448 tetrahedra, on which strains are computed from the obtained nodal displacements. **Figure 7** illustrates the quality of the measured global displacement field in the two penultimate increments of the images presented in **Figure 5** (the correlations of the last two images 002–049 and 002–050 present two diverging points on the boundary). Furthermore, **Figure 9** shows a part of the field measured.

3.3. Measurement of Local Greyscale Variations

Given the ability to follow material points through time with the displacement fields described above, the variation of the measured fields (μ_x and μ_n) will now be discussed. Considering as an example the case of thermal expansion with no mass transfer, the expectation would be for the density of the material to reduce, and for both μ_x and μ_n to decrease proportionally to the change in density. In this experimental configuration however, it is likely that the swelling is caused by water interaction with the material. This hypothesis will be evaluated for the process being studied by looking at change of μ_x and μ_n inside each tetrahedron, compared to the expected change due to the measured volume change. The particular sensitivity of neutrons to water should reveal water entry into the clay matrix.

During fluid entry, two major phenomena will cause a variation in the absorption levels of x-rays and neutrons. On one hand, if the material swells, assuming (for now) mass conservation of the solid part, this implies that the mass density of the solid part will decrease, leading to a decrease in the level of attenuation. On the other hand, if the swelling is associated with an increase in the water content, then the presence of the additional fluid will modify the material's attenuation level (and

[1]This validation is performed by "zooming" μ_x 002 by 1.01 in all directions and correlating the original image with the zoomed version of itself. The application of this 3 % volumetric strain to the greylevels of μ_x is done through interpolation which reduces noise. Variance is additive, so the variance is measured in the original image, and the missing noise is added to the zoomed image.

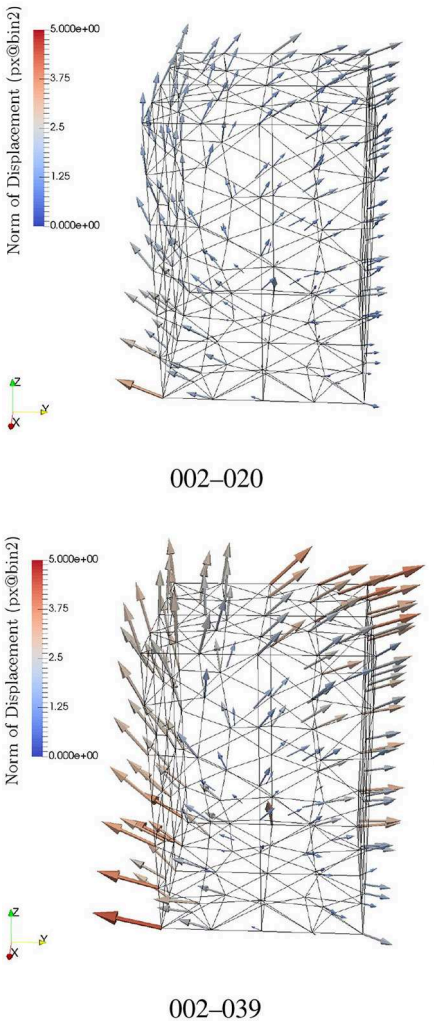

FIGURE 7 | Displacement field as measured with Global DVC. The displacement at the nodes of the mesh is shown with vectors scaled up by 25×, and whose colour represents the norm of the vector. The mesh is shown in its reference state (i.e., in 002).

may increase it if the attenuation coefficient of water is higher than the solid).

Considering that the infinitesimal volume can be decomposed into a solid part "s," a free water part "w_f," an adsorbed water part "w_a" and air "a," the decomposition in the initial configuration (time 0) and the deformed configuration (time t) is (in the style of Coussy, 2007):

$$\Omega_0 = \Omega_0^{\mathrm{s}} + \Omega_0^{\mathrm{w_f}} + \Omega_0^{\mathrm{w_a}} + \Omega_0^{\mathrm{a}} \tag{2}$$

and

$$\Omega_{\mathrm{t}} = \Omega_{\mathrm{t}}^{\mathrm{s}} + \Omega_{\mathrm{t}}^{\mathrm{w_f}} + \Omega_{\mathrm{t}}^{\mathrm{w_a}} + \Omega_{\mathrm{t}}^{\mathrm{a}} \tag{3}$$

with

$$\Omega_{\mathrm{t}} = J\Omega_0 \tag{4}$$

where J is the Jacobian of the transformation i.e., $J \approx 1 + \varepsilon_{\mathrm{v}}$. A number of hypotheses are made:

First it is assumed (common assumption in soil mechanics), that the volume of the solid skeleton does not change in time, leading to $\Omega_0^{\mathrm{s}} = \Omega_{\mathrm{t}}^{\mathrm{s}}$.

Furthermore, we assume that the density of free water is close to the density of adsorbed water, and consequently that the attenuation coefficients are the same: $\mu^{\mathrm{w_f}} \approx \mu^{\mathrm{w_a}} \approx \mu^{\mathrm{w}}$. This is supported by recent work at the nano-scale on the properties of adsorbed water, see Honorio et al. (2017) and Brochard (2019).

If we now consider a voxel ($\Omega_{\mathrm{voxel}} = \mathrm{cst}$), each phase will contribute to the total attenuation through what we name here "partial attenuation" β and thus,

$$\mu = \beta^{\mathrm{s}} + \beta^{\mathrm{w}} + \beta^{\mathrm{a}} \tag{5}$$

This assumes that the measured attenuation coefficient of the material is the result of a Gaussian mixture of the component attenuation coefficients. The partial attenuation of each phase is the attenuation of the phase weighted by the volume fraction of the phase as follows: $\beta^i = \mu^i \dfrac{\Omega^i}{\Omega}$ where i is {s, w, a}.

In the case of a fully saturated sample, $\Omega_{\mathrm{a}} = 0$ and thus,

$$\frac{\Omega_{\mathrm{t}}^{\mathrm{w}}}{\Omega_{\mathrm{t}}} = 1 - \frac{\Omega_{\mathrm{t}}^{\mathrm{s}}}{\Omega_{\mathrm{t}}} = 1 - \frac{1}{J}\frac{\Omega_0^{\mathrm{s}}}{\Omega_0} \tag{6}$$

In terms of solid partial attenuation, we have:

$$\beta_0^{\mathrm{s}} = \mu^{\mathrm{s}}\frac{\Omega_0^{\mathrm{s}}}{\Omega_0} \quad \text{and} \quad \beta_{\mathrm{t}}^{\mathrm{s}} = \mu^{\mathrm{s}}\frac{\Omega_{\mathrm{t}}^{\mathrm{s}}}{\Omega_{\mathrm{t}}} = \frac{1}{J}\beta_0^{\mathrm{s}} \tag{7}$$

In terms of water partial attenuation, we have initially:

$$\beta_0^{\mathrm{w}} = \mu^{\mathrm{w}}\frac{\Omega_0^{\mathrm{w}}}{\Omega_0} = \mu^{\mathrm{w}}\left(1 - \frac{\Omega_0^{\mathrm{s}}}{\Omega_0}\right) \quad \text{which leads to} \quad \frac{\Omega_0^{\mathrm{s}}}{\Omega_0} = 1 - \frac{\beta_0^{\mathrm{w}}}{\mu^{\mathrm{w}}} \tag{8}$$

and at time t:

$$\begin{aligned}\beta_{\mathrm{t}}^{\mathrm{w}} &= \mu^{\mathrm{w}}\frac{\Omega_{\mathrm{t}}^{\mathrm{w}}}{\Omega_{\mathrm{t}}} = \mu^{\mathrm{w}}\left(1 - \frac{1}{J}\frac{\Omega_0^{\mathrm{s}}}{\Omega_0}\right) = \mu^{\mathrm{w}}\left[1 - \frac{1}{J}\left(1 - \frac{\beta_0^{\mathrm{w}}}{\mu^{\mathrm{w}}}\right)\right] \\ &= \frac{1}{J}\beta_0^{\mathrm{w}} + \mu^{\mathrm{w}}\left(1 - \frac{1}{J}\right)\end{aligned} \tag{9}$$

Injecting these expressions of β into Equation (5) at time t gives:

$$\mu_{\mathrm{t}} = \beta_{\mathrm{t}}^{\mathrm{s}} + \beta_{\mathrm{t}}^{\mathrm{w}} = \frac{1}{J}\beta_0^{\mathrm{s}} + \frac{1}{J}\beta_0^{\mathrm{w}} + \mu^{\mathrm{w}}\left(\frac{J-1}{J}\right) \tag{10}$$

Finally, the change in attenuation will be:

$$\Delta\mu = \mu_{\mathrm{t}} - \mu_0 = \frac{1-J}{J}(\beta_0^{\mathrm{s}} + \beta_0^{\mathrm{w}} - \mu^{\mathrm{w}}) \tag{11}$$

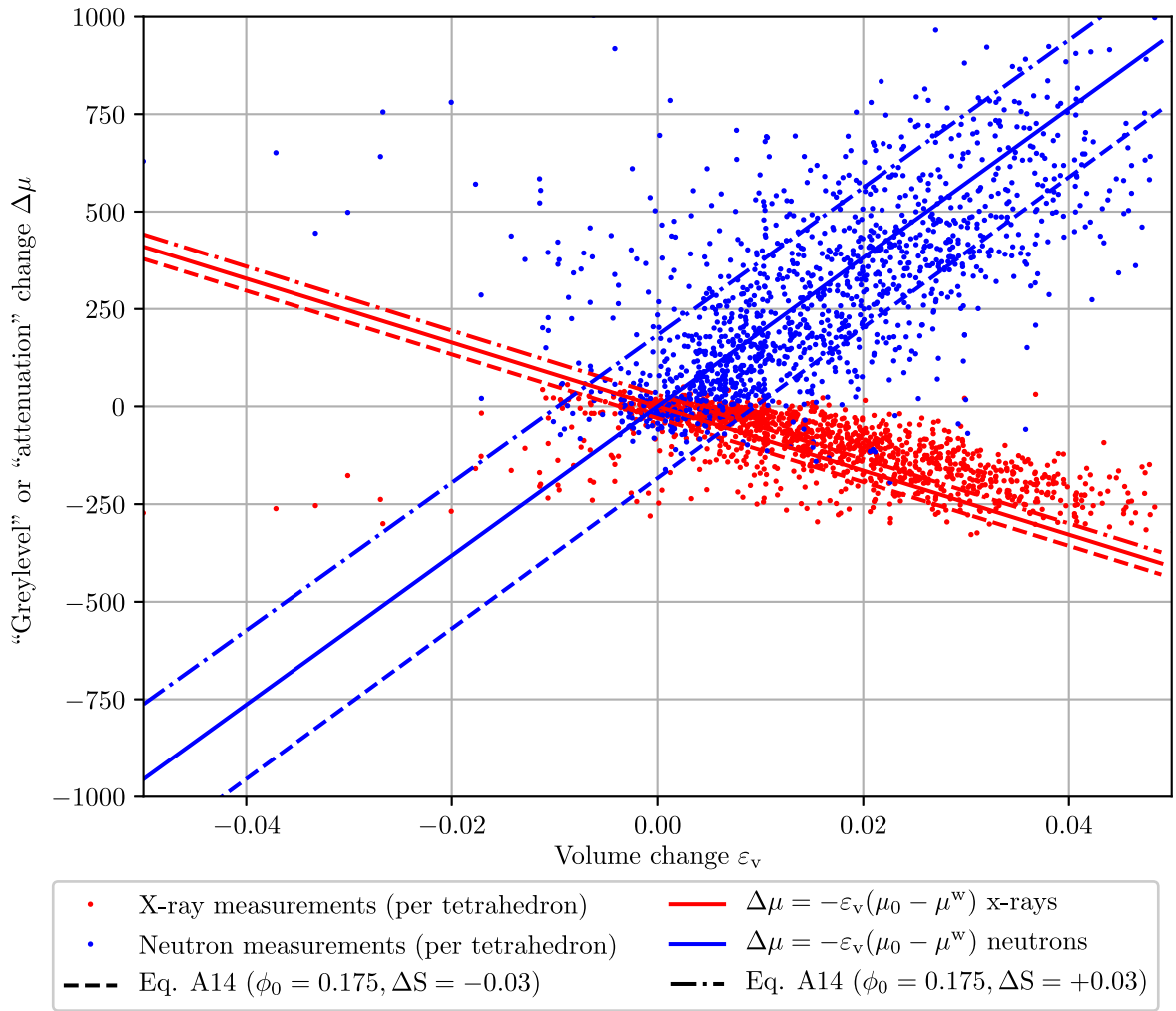

FIGURE 8 | Data from Global DVC on increments 002-020, 002-039, and 002-0045. Volumetric strain of each tetrahedron plotted against the measured greylevel change in each tetrahedron. Expected changes of greylevel due only to the solid are added as per Equation (12). These scattered values for x-rays and neutrons are fitted with a linear regression separately.

For small strains, $J \approx 1 + \varepsilon_v$, thus Equation (11) becomes,

$$\Delta\mu = -\varepsilon_v(\beta_0^s + \beta_0^w - \mu^w) = -\varepsilon_v(\mu_0 - \mu^w) \qquad (12)$$

This model indicates, *in fine* that the change in attenuation coefficient (for both x-ray and neutron tomographies) is a simple function of the volumetric strain and two easily measurable greyscale quantities. For x-ray tomography, μ_0 is higher than the water absorption coefficient μ^w (as detailed in **Table 2**), meaning that swelling due to water uptake should induce a decrease of the global absorption coefficient. This is the reverse for neutron tomography, where μ^w coefficient is much higher than μ_0 absorption coefficient, and so the swelling due to water uptake induce an increase of the global absorption coefficient.

Figure 8 presents two quantities plotted together:

x axis The volumetric strain measured locally (i.e., on the tetrahedra in the mesh discussed above) always taking image 002 as a reference. This measurement comes directly from the displacements of the mesh at the four nodes involving each tetrahedron.

y axis The change in greylevels $\Delta\mu_x$ and $\Delta\mu_n$ in each tetrahedron. This is computed as follows: All the voxels belonging to one tetrahedron are identified in the reference mesh, as well as in the deformed mesh. The mean value in the field corresponding to these voxels (which can be of different number in reference and deformed states) is recorded, and the difference is plotted here.

Each point in the space presented represents the evolution (of size and greyscale) of one tetrahedron.

Figure 8 also includes the prediction as per Equation (12) in solid lines, taking μ_0 as the mean measured value for the clay matrix from **Table 2**. The correspondence is quite satisfactory. The success of this simple model seems to indicate that the essential parts of the physics occurring have been captured adequately. Allowing a small change on the measured μ_0 for x-rays an even better correspondence can be obtained (not shown).

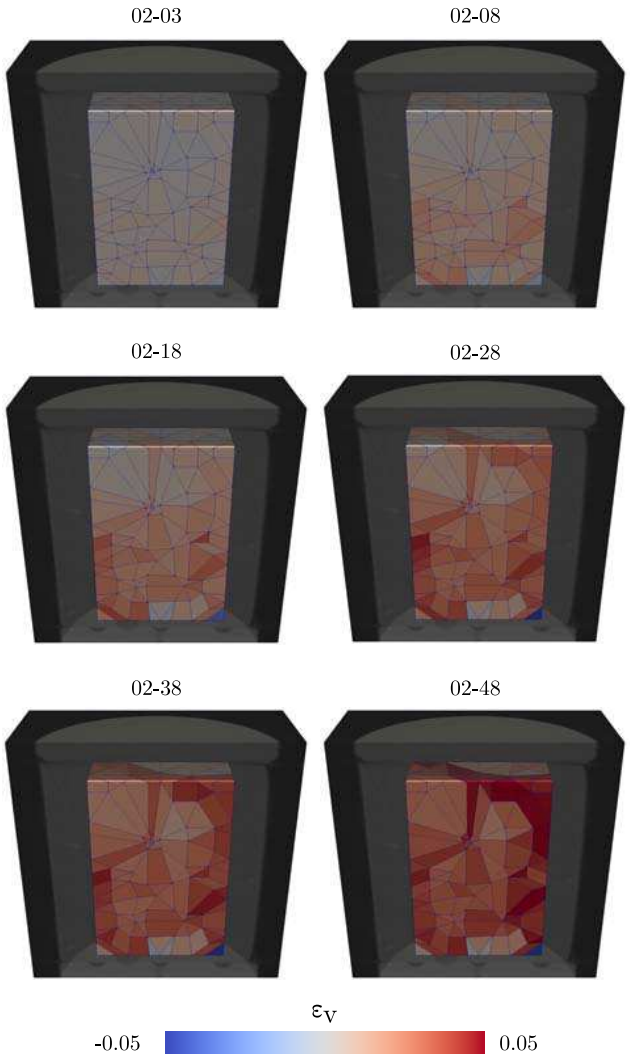

FIGURE 9 | Semi-transparent rendering of the x-ray graylevels of specimen (state 002) with the mesh used for the total global correlation with tetrahedra colored by their volumetric strain. Using Equation (12) and its assumptions, the color bar for ε_v corresponds to $\frac{\delta\Omega^w}{\delta\Omega}$.

A more sophisticated mathematical model is developed in the **Appendix** releasing the hypothesis that $\Omega^a = 0$ (thus allowing states of partial water saturation) and with the hypotheses that the volume of macro-voids does not change, and that swelling occurs only due to water adsorbed onto the clay aggregates $\Omega_t^{w_a} = \Omega_0^{w_a} + (J-1)\Omega_0$ (also valid above).

The upshot is that the change in greylevels can now be expressed as a function of volumetric strain (as before) and a new term linking the change of degree of saturation (ΔS) and the initial degree of open porosity (ϕ_0):

$$\Delta\mu = -\varepsilon_v(\mu_0 - \mu^w) + (1-\varepsilon_v)\Delta S\,\phi_0(\mu^w - \mu^a) \qquad (13)$$

This additional term allows the exploration of the influence of the change of degree of saturation during swelling. Taking ϕ_0 as 17.5 % from Conil et al. (2018), ΔS can be evaluated, and lines for $\pm$3 % are shown in **Figure 8**.

Returning to the fully saturated model, the spatial distribution of volumetric strain can be directly related to the increase of water ($\varepsilon_v = \frac{\Omega^w}{\Omega}$). **Figure 9** presents a slice through half the sample colouring the tetrahedra in the analysed zone according to their volumetric strain for a few selected time intervals. In the first time increments an increase of strain at the bottom of the sample (which is in contact with the water supply) is visible, whereas toward the end of the experiment high values are recorded all over, with some indication of inhomogeneous levels of swelling.

4. CONCLUSION

This paper has presented a combined neutron and x-ray tomography analysis of water absorption behaviour in Callovo-Oxfordian claystone. These complementary imaging techniques are first of all registered into a common coordinate system using previous work, as well as a specially-developed graphical user interface to provide an initial guess. The resulting registered neutron and x-ray images of each state allow first of all a fine identification of the material phases present in the sample.

To characterise the gentle swelling process observed (around 2.5 % overall volumetric increase after almost 6 h) again the combination of x-rays and neutrons is exploited: local swelling is measured with Digital Volume Correlation thanks to the sharpness and low noise of the x-ray volumes (although it is mentioned that a correlation on the joint x-ray and neutron field could be developed in future). A mathematical model is developed for the expected local changes of greylevels in saturated conditions with all volume changes associated with water entry. The measurements are compared to this model with a good degree of correspondence, indicating that for this experiment on this sample, the model appears sufficient. This indicates that there are limited amounts of swelling due to chemical interactions for example.

This initial hydromechanical analysis (performed on a single sample) will obviously benefit from repetition, but a number of technical improvements to the analysis can also be envisioned.

- Anisotropic swelling–Instead of a scalar (ε_v) representing the change of volume of the material, the stretch tensor itself could be used to measure anisotropic parts of swelling related to the bedding known to affect this material.
- Taking into account microstructure–here the analysis has focused on the averaged local behaviour of the clay matrix. Further steps in the analysis could identify different types of inclusions known to be present (carbonates, quartz, pyrite) from the joint histograms, and relate a local degree of swelling to the presence of these aggregates.
- Taking into different initial states–further experiments are certainly necessarily, and of chief interest is to study different initial water contents as well as different stress states.
- Taking into account permeability/swelling times–The analysis as it stands implies a "time-free" relationship between water arrival and volumetric strain, whereas the characteristic times related to the very low permeability in the material may be

interesting to include in the model, and which would explain long distance interactions through fluid pressure/suction.

Finally, a number of recommendations can be made for better estimations of the reconstructed attenuation coefficients:

1. Ensure that sufficient pure water is visible in a scan (on the neutron side in this case there are only 2 slices inside the spiral. Scanning a pure sample of water is also possible, but as far as neutron tomography is concerned, this must be a small cross-section to minimise the effects of scattering.
2. Given the importance that the mathematical model puts on the "physical" meaning of greyvalues, a long initial scan with lower noise provides a valuable reference for all μ values.
3. Selection of a less neutron-attenuating membrane material such as Teflon, or fluorinated silicons.

DATA AVAILABILITY STATEMENT

The raw datasets collected on NeXT-Grenoble are available at http://doi.ill.fr/10.5291/ILL-DATA.UGA-42 – the experiment analysed is 03-3N5. Furthermore, a number of key outputs from this paper are available on Zenodo https://zenodo.org/record/3628018 with doi: 10.5281/zenodo.3628018.

- **01-volumes** – Registered μ_x and μ_n fields at a pixel size of 85.4 µm/px – which is 2-binning for the x-ray volumes.
- **02-JH** – Dynamic Joint histograms for all pairs of registered μ_x and μ_n fields calculated over the mask available in folder 01.
- **03-DVC** – Results of registration, local Digital Volume Correlation with `spam-ldic` which describe a locally-measured Φ from scan 002 throughout the test for different half-window sizes, and Global DVC displacement fields.

AUTHOR CONTRIBUTIONS

All authors listed have made a substantial, direct and intellectual contribution to the work, and approved it for publication.

ACKNOWLEDGMENTS

Laboratoire 3SR is part of the LabEx Tec 21 (Investissements d'Avenir–grant agreement n°ANR-11-LABX-0030).

Tom Arnaud is gratefully acknowledged for his central role in the programming of the graphical interface to the multimodal registration tool.

The high precision machinists SMGOP in Fontaine are kindly thanked for their contribution to the building of the experimental setup.

The ANDRA (French radioactive Waste Management Agency) is thanked for providing the claystone core used in this work.

The absorption model has been developed in the framework of the EJP EURAD (WP Hitec) – grant agreement 847593.

REFERENCES

Andò, E., Cailletaud, R., Roubin, E., Stamati, O., and the Spam Contributors (2017). *spam: The Software for the Practical Analysis Of Materials.* Available online at: https://ttk.gricad-pages.univ-grenoble-alpes.fr/spam/.

Andra, S. (2005). *Dossier 2005 Argile: Synthesis: Evaluation of the Feasibility of a Geological Repository in an Argillaceous Formation, Meuse/Haute-Marne Site.* Technical report.

Armand, G., Conil, N., Talandier, J., and Seyedi, D. M. (2017). Fundamental aspects of the hydromechanical behaviour of callovo-oxfordian claystone: from experimental studies to model calibration and validation. *Comput. Geotech.* 85, 277–286. doi: 10.1016/j.compgeo.2016.06.003

Bonin, B. (1998). Deep geological disposal in argillaceous formations: studies at the tournemire test site. *J. Contam. Hydrol.* 35, 315–330. doi: 10.1016/S0169-7722(98)00132-6

Bornert, M., Vales, F., Gharbi, H., and Nguyen Minh, D. (2010). Multiscale full-field strain measurements for micromechanical investigations of the hydromechanical behaviour of clayey rocks. *Strain* 46, 33–46. doi: 10.1111/j.1475-1305.2008.00590.x

Brochard, L. (2019). "Revisiting thermo-poro-mechanics to explain the anomalous thermal pressurization of water in clay," in *Joint GeoMech-M2UN workshop on Upscalling for Strategic Materials* (Montpellier).

Chiang, W.-S., LaManna, J. M., Hussey, D. S., Jacobson, D. L., Liu, Y., Zhang, J., et al. (2018). Simultaneous neutron and x-ray imaging of 3D structure of organic matter and fracture in shales. *Petrophysics* 59, 153–161. doi: 10.30632/PJV59N2-2018A3

Chiarelli, A.-S., Ledesert, B., Sibai, M., Karami, M., and Hoteit, N. (2000). Influence of mineralogy and moisture content on plasticity and induced anisotropic damage of a claystone; application to nuclear waste disposals. *Bull. Soc. Géol.* 171, 621–627. doi: 10.2113/171.6.621

Conil, N., Talandier, J., Djizanne, H., de La Vaissière, R., Righini-Waz, C., Auvray, C., et al. (2018). How rock samples can be representative of *in situ* condition: a case study of callovo-oxfordian claystones. *J. Rock Mech. Geotech. Eng.* 10, 613–623. doi: 10.1016/j.jrmge.2018.02.004

Coussy, O. (2007). Revisiting the constitutive equations of unsaturated porous solids using a Lagrangian saturation concept. *Int. J. Num. Anal. Methods Geomech.* 31, 1675–1694. doi: 10.1002/nag.613

Delay, J., Lebon, P., and Rebours, H. (2010). Meuse/haute-marne centre: next steps towards a deep disposal facility. *Int. J. Num. Anal. Methods Geomech.* 2, 52–70. doi: 10.3724/SP.J.1235.2010.00052

Desbois, G., Höhne, N., Urai, J. L., Bésuelle, P., and Viggiani, G. (2017). Deformation in cemented mudrock (callovo-oxfordian clay) by microcracking, granular flow and phyllosilicate plasticity: insights from triaxial deformation, broad ion beam polishing and scanning electron microscopy. *Solid Earth* 8:291. doi: 10.5194/se-8-291-2017

DiStefano, V. H., Cheshire, M. C., McFarlane, J., Kolbus, L. M., Hale, R. E., Perfect, E., et al. (2017). Spontaneous imbibition of water and determination of effective contact angles in the eagle ford shale formation using neutron imaging. *J. Earth Sci.* 28, 874–887. doi: 10.1007/s12583-017-0801-1

Escoffier, S. (2002). *Caractérisation expérimentale du comportement hydromécanique des argilites de Meuse/Haute-Marne* (Ph.D. thesis). Institut National Polytechnique de Lorraine, Nancy, France.

Grédiac, M., and Hild, F. (2013). *Full-Field Measurements and Identification in Solid Mechanics*. London: Wiley Online Library.

Homand, F., Shao, J.-F., Giraud, A., Auvray, C., and Hoxha, D. (2006). Pétrofabrique et propriétés mécaniques des argilites. *Comptes Rendus Geosci.* 338, 882–891. doi: 10.1016/j.crte.2006.03.009

Honorio, T., Brochard, L., and Vandamme, M. (2017). Hydration phase diagram of clay particles from molecular simulations. *Langmuir* 33, 12766–12776. doi: 10.1021/acs.langmuir.7b03198

Leclerc, H., Périé, J.-N., Roux, S., and Hild, F. (2011). Voxel-scale digital volume correlation. *Exp. Mech.* 51, 479–490. doi: 10.1007/s11340-010-9407-6

Lenoir, N., Bornert, M., Desrues, J., Bésuelle, P., and Viggiani, G. (2007). Volumetric digital image correlation applied to x-ray microtomography images

from triaxial compression tests on argillaceous rock. *Strain* 43, 193–205. doi: 10.1111/j.1475-1305.2007.00348.x

Lucas, B. D., and Kanade, T. (1981). "An iterative image registration technique with an application to stereo vision," in *Proceedings DARPA Image Understanding Workshop* (Pittsburgh, PA), 121–130.

Montes, H., Duplay, J., Martinez, L., Escoffier, S., and Rousset, D. (2004). Structural modifications of callovo-oxfordian argillite under hydration/dehydration conditions. *Appl. Clay Sci.* 25, 187–194. doi: 10.1016/j.clay.2003.10.004

Robinet, J.-C., Sardini, P., Coelho, D., Parneix, J.-C., Prêt, D., Sammartino, S., et al. (2012). Effects of mineral distribution at mesoscopic scale on solute diffusion in a clay-rich rock: example of the callovo-oxfordian mudstone (Bure, France). *Water Resour. Res.* 48, 122–160. doi: 10.1029/2011WR011352

Roubin, E., Andò, E., and Roux, S. (2019). The colours of concrete as seen by x-rays and neutrons. *Cement Concrete Composites* 104:103336. doi: 10.1016/j.cemconcomp.2019.103336

Stavropoulou, E., Andò, E., Tengattini, A., Briffaut, M., Dufour, F., Atkins, D., et al. (2019). Liquid water uptake in unconfined callovo oxfordian clay-rock studied with neutron and x-ray imaging. *Acta Geotech.* 14, 19–33. doi: 10.1007/s11440-018-0639-4

Tengattini, A., Atkins, D., Giroud, B., Andò, E., and Beaucour, J. amd Viggiani, G. (2017). "Next-grenoble, a novel facility for neutron and x-ray tomography in grenoble," in *Proceedings ICTMS2017* (Lund).

Tengattini, A., Lenoir, N., Andò, E., Giroud, B., Atkins, D., Beaucour, J., et al. (2019). *Next-Grenoble, the Neutron and X-ray Tomograph in Grenoble*. ALERT Geomaterials, 47.

Tomasi, C., and Manduchi, R. (1998). "Bilateral filtering for gray and color images," in *Sixth international conference on computer vision (IEEE Cat. No. 98CH36271)* (IEEE), 839–846.

Tudisco, E., Jailin, C., Mendoza, A., Tengattini, A., Andò, E., Hall, S. A., et al. (2017). An extension of digital volume correlation for multimodality image registration. *Meas. Sci. Technol.* 28:095401. doi: 10.1088/1361-6501/aa7b48

Wang, L., Bornert, M., Héripré, E., Chanchole, S., Pouya, A., and Halphen, B. (2015). Microscale insight into the influence of humidity on the mechanical behavior of mudstones. *J. Geophys. Res. Solid Earth* 120, 3173–3186. doi: 10.1002/2015JB011953

Wang, L., Bornert, M., Héripré, E., Yang, D., and Chanchole, S. (2014). Irreversible deformation and damage in argillaceous rocks induced by wetting/drying. *J. Appl. Geophys.* 107, 108–118. doi: 10.1016/j.jappgeo.2014.05.015

Wood, D. M. (1990). *Soil Behaviour and Critical State Soil Mechanics*. Cambridge: Cambridge University Press.

Yoo, T. S., Ackerman, M. J., Lorensen, W. E., Schroeder, W., Chalana, V., Aylward, S., et al. (2002). Engineering and algorithm design for an image processing api: a technical report on itk-the insight toolkit. *Stud. Health Technol. Informatics* 85, 586–592. doi: 10.3233/978-1-60750-929-5-586

Conflict of Interest: The authors declare that the research was conducted in the absence of any commercial or financial relationships that could be construed as a potential conflict of interest.

APPENDIX – THEORETICAL TREATMENT OF PARTIALLY SATURATED CASE

In order to relax the previous hypothesis of full saturation, a non-zero air volume must be allowed: $\Omega^{a} \geqslant 0$.

Introducing ϕ_0 as the macro-porosity or "open" voids volume-fraction at time 0:

$$\Omega_0^{\text{voids}} = \Omega_0^{a} + \Omega_0^{w_f} = \phi_0 \Omega_0 \tag{A1}$$

A hypothesis is however needed for the evolution of the voids volume with time during swelling; here we assume that the macro-porosity *volume* remains constant in time.

$$\Omega_t^{a} + \Omega_t^{w_f} = \Omega_0^{a} + \Omega_0^{w_f} = \phi_0 \Omega_0 \tag{A2}$$

With S as the degree of saturation:

$$\Omega_0^{w_f} = S_0 \Omega_0^{\text{voids}} \quad \text{and} \quad \Omega_t^{w_f} = S_t \Omega_t^{\text{voids}} \tag{A3}$$

ΔS is then defined as the change in degree of saturation between time 0 and time t:

$$\Delta S = S_t - S_0 \tag{A4}$$

Moving onto partial attenuations, for the solid part nothing changes: $\beta_t^{s} = \frac{1}{J}\beta_0^{s}$

For the water part:

$$\beta_0^{w} = \mu^{w} \frac{\Omega_0^{w}}{\Omega_0} = \mu^{w}\left(S_0 \phi_0 + \frac{\Omega_0^{w_a}}{\Omega_0}\right) \tag{A5}$$

$$\beta_t^{w} = \mu^{w} \frac{\Omega_t^{w}}{\Omega_t} = \mu^{w}\left(\frac{S_t \phi_0}{J} + \frac{\Omega_t^{w_a}}{J\Omega_0}\right) \tag{A6}$$

With the hypothesis that only the adsorbed water changes in volume during swelling:

$$\Omega_t^{w_a} = \Omega_0^{w_a} + (J-1)\Omega_0 \tag{A7}$$

and factoring by $\frac{1}{J}$:

$$\beta_t^{w} = \frac{\mu^{w}}{J}\left(S_t \phi_0 + \frac{\Omega_0^{w_a}}{\Omega_0} + J - 1\right) \tag{A8}$$

Now splitting S_t into $S_0 + \Delta S$:

$$\beta_t^{w} = \frac{\mu^{w}}{J}\left(S_0 \phi_0 + \Delta S \phi_0 + \frac{\Omega_0^{w_a}}{\Omega_0} + J - 1\right) \tag{A9}$$

Combining with β_0^{w} finally yields:

$$\beta_t^{w} = \frac{1}{J}\beta_0^{w} + \mu^{w}\frac{\Delta S}{J}\phi_0 + \mu^{w}\frac{J-1}{J} \tag{A10}$$

Finally for the air:

$$\beta_0^{a} = \mu^{a}\frac{\Omega_0^{a}}{\Omega_0} = \mu^{a}(1 - S_0)\phi_0 \tag{A11}$$

$$\begin{aligned} \beta_t^{a} &= \mu^{a}\frac{\Omega_t^{a}}{\Omega_t} = \mu^{a}\frac{(1 - S_t)}{J}\phi_0 \\ &= \frac{1}{J}\mu^{a}(1 - S_0 - \Delta S) \\ \phi_0 &= \frac{1}{J}\beta_0^{a} - \mu^{a}\frac{\Delta S}{J}\phi_0 \end{aligned} \tag{A12}$$

The attenuation at time t, μ_t, can now be expressed as:

$$\mu_t = \frac{1}{J}(\beta_0^{s} + \beta_0^{w} + \beta_0^{a}) + \mu^{w}\left(\frac{\Delta S}{J}\phi_0\right) + \mu^{w}\left(\frac{J-1}{J}\right) - \mu^{a}\left(\frac{\Delta S}{J}\phi_0\right) \tag{A13}$$

Subtracting μ_0 in the same spirit as above:

$$\Delta\mu = \frac{1-J}{J}\mu_0 + \mu^{w}\left(\frac{\Delta S}{J}\phi_0\right) + \mu^{w}\left(\frac{J-1}{J}\right) - \mu^{a}\left(\frac{\Delta S}{J}\phi_0\right) \tag{A14}$$

In small strains:

$$\Delta\mu = -\varepsilon_v(\mu_0 - \mu^{w}) + (1 - \varepsilon_v)\Delta S \phi_0(\mu^{w} - \mu^{a}) \tag{A15}$$

frontiers in Earth Science

ORIGINAL RESEARCH
published: 16 June 2020
doi: 10.3389/feart.2020.00207

The Sealing Mechanisms of a Fracture in Opalinus Clay as Revealed by *in situ* Synchrotron X-Ray Micro-Tomography

Marco Voltolini and Jonathan B. Ajo-Franklin*

Lawrence Berkeley National Laboratory, Earth and Environmental Sciences Area, Energy Geosciences Division, Berkeley, CA, United States

The detailed mechanisms of the sealing of a single fracture, from hydration to almost complete closure by increase of confining pressure, as monitored from *in situ* synchrotron X-ray microtomography during the flow of carbonated water, is here shown for the first time. Different mechanisms play the key role at different stages in the evolution of the fracture. Hydration mechanically weakens the surfaces of the fracture and induces a first closure due to microcracking at the asperity contacts, increasing their size and creating choke points. Increase in confining stress promptly hydraulically seals the fracture by closing the main choke point, with a relative small deformation of the sample. Finally, the more pervasive mechanical deformation observed at higher stresses almost completely seals the whole fracture. The evolution of the sample has been described and quantified using 4D image processing, focusing on the evolution of aperture and digital volume correlation. Hydraulic properties of the sample at different stages have been modeled via Stokes flow simulation, and the results compared to the morphometric analysis, finding positive correlations with the average fracture aperture variation along the flowpath in function of confining pressure. Opalinus Clay is found to be a rock markedly prone to sealing in case of flow with carbonated water; this behavior is the result of the large fraction of clays and of its microstructure, lacking both cementing phases and large stiff particles. CO_2 in this sample has no evident role in the evolution of the fracture; chemically induced weathering on the surface has not been detected, in contrast with the behavior observed in samples with carbonates as cementing phase.

Keywords: opalinus clay, fracture sealing, caprocks, *in situ* synchrotron X-ray micro-computed tomography, digital rock physics

OPEN ACCESS

Edited by:
Marie Estelle Solange Violay, École Polytechnique Fédérale de Lausanne, Switzerland

Reviewed by:
Paul Josef Bossart, Swisstopo, Switzerland
Ben Laurich, Federal Institute for Geosciences and Natural Resources, Germany

****Correspondence:***
Marco Voltolini
mvoltolini@lbl.gov

Specialty section:
This article was submitted to Solid Earth Geophysics, a section of the journal Frontiers in Earth Science

Received: *18 June 2019*
Accepted: *19 May 2020*
Published: *16 June 2020*

Citation:
Voltolini M and Ajo-Franklin JB (2020) The Sealing Mechanisms of a Fracture in Opalinus Clay as Revealed by in situ Synchrotron X-Ray Micro-Tomography. Front. Earth Sci. 8:207. doi: 10.3389/feart.2020.00207

INTRODUCTION

Caprocks are geological bodies with low both intrinsic and effective permeability, forming a seal preventing the migration of fluids. Understanding the behavior of caprocks under different conditions is important for a variety of fields including oil and gas extraction, radioactive waste repositories, and geological carbon sequestration (GCS).

There are different types of caprocks and sealing rocks fulfilling the above requirements, with variable mineralogical compositions and textures. Two main groups of seal rocks can be considered: (i) seals comprised primarily of evaporitic minerals, such as halite, anhydrite, gypsum; and (ii) clay-bearing rocks such as shales, mudstones, and clay-rich carbonates (marls). Given their frequent occurrence in a geologic context, clay-rich rocks are particularly relevant to the applications mentioned previously. Rocks such as shales are common caprocks for conventional oil and gas reservoirs, given the high capillary pressure required for hydrocarbon migration in a material with such small pore/throat sizes and surface properties (e.g., Al-Bazali et al., 2005). Shales are also the primary sealing unit at many GCS sites (e.g., the Eau Claire Formation above the Mt. Simon sandstone reservoir, see Neufelder et al., 2012). In a GCS context, since CO_2-rich brines are potentially reactive, weathering of the caprock should also be considered when assessing long-term seal performance (e.g., Busch et al., 2009). The behavior of clay minerals with supercritical CO_2 can potentially have an impact in the sealing properties in deep reservoirs for both reactive clays, such as smectites (Loring et al., 2013) as well as conventionally stable clay minerals, including illite/muscovite (Wan et al., 2018).

The basic requirement for caprock sealing capacity is to display a very low *intrinsic* matrix permeability, on the order of the nanodarcy ($\sim$1e^{-14} cm^2), but the *effective* permeability of such rocks can be drastically increased by the presence of fractures. Increasing the permeability of such tight rocks by means of induced fracturing (hydrofracturing) is also the basis of modern unconventional oil and gas production. Since the presence of fractures can be detrimental to the effectiveness of a sealing unit, caprock integrity studies are a fundamental step in assessing the safety of a storage site (e.g., Busch et al., 2010). The presence of pre-existing fracture networks, or the generation of new ones due to stress changes in the reservoir, does not necessarily prevent the use of shales as caprocks, since the evolution of the fractures in time could lead to re-sealing of such structures. Fractures in caprocks intended for GCS can display different evolutionary paths, ranging from self-enhancing (i.e., progressive spontaneous enhancement of fracture conductivity due e.g., to the generation and enlargement of preferential flowpaths) to self-sealing (i.e., progressive spontaneous decrease in conductivity due e.g., to swelling of the material in contact with the fluid) or self-healing (i.e., the closure of the fracture with a complete recovery of the original properties of the rock prior to fracturing) behavior. This kind of behavior is complex in nature, and depends on a series of coupled processes, usually referred as THMC (thermal-hydraulic-mechanical-chemical) e.g., in the field of natural and engineered barriers (Tsang, 1991). The evolution of such a system is extremely complex to predict, given the coupling between the different parameters; a simplified approach based only on the mineralogical composition is presented in Bourg (2015) where the self-sealing vs. self-enhancing behavior is inferred only by the clay fraction of the caprock, which provides a proxy for behavior of a clay-rich rock. This approach seems to provide a starting point for evaluation, but quantitative estimates about how the fracture evolves requires a more detailed analysis. In particular, self-enhancing behavior (on short time scales) observed in Deng et al. (2016) has also been observed in "shales" rich in cementing carbonates and clays with a partial contribution due to erosion after the formation of channeling features due to reaction with carbonates (Deng et al., 2017). Broadly, the increase in clay fraction decreases the reactivity with aqueous CO_2, compared to carbonates, and the rock becomes mechanically weaker (ultimate tensile strength tends to decrease with the clay amount increase), thus facilitating the collapse of the contact areas in the fractures. In such conditions rapid self-sealing is generally observed [Figure 2 in Zhang (2011), Bourg and Ajo-Franklin (2017)]. Other sealing mechanisms can be present in caprocks: mineralization in fractures is a common behavior observed in the field, but rather difficult to replicate experimentally, since it often requires long paths along fractures to reach the saturation state needed to trigger crystallization, and often longer reaction times as well (Noiriel et al., 2010). Another important and frequently neglected process is pressure-solution (Yasuhara et al., 2004): in materials such as halite, pressure-solution is extremely fast and pervasive (Renard et al., 2004), but in carbonates, and more so in silicates, it is a slower process not easily observable in short laboratory experiments (Yasuhara and Elsworth, 2008); however, its contribution in the field can be important, given the long time scale considered. While clays, and phyllosilicates in general, have been found to facilitate pressure-solution (Renard et al., 1997), its role in shales is still not clear.

Most of previously cited fracture evolution studies utilize X-ray micro-computed tomography (XRμCT); over the last two decades, this experimental technique has proven to be an excellent tool for obtaining quantitative 3D information about the microstructure of geological materials (Cnudde and Boone, 2013). With steady improvements in both conventional and unconventional (synchrotron) X-ray sources, *in situ* time-resolved experiments are becoming more common and Earth scientists are taking advantage of such capabilities to probe the rapid evolution of geological systems at micron length scales (e.g., Voltolini et al., 2017a). In the field of subsurface studies, mini triaxial cells able to perform flow experiments at both high pressure and temperature have recently been developed, opening new opportunities for 4D X-ray imaging at P/T ranges not accessible until a few years ago (Renard et al., 2016; Voltolini et al., 2019).

In this study, we utilize *in situ* synchrotron XRμCT to monitor the evolution of a fractured Opalinus Clay sample at increasing differential pressure during flow with CO_2-saturated water in the mini-triaxial cell described in Voltolini et al. (2017b). The choice of Opalinus Clay (OPA) was driven by two reasons: (i) it provides an excellent model for a clay-based seal rock, with a large clay fraction, and therefore theoretically prone to fast (self-) sealing; (ii) it is an extremely well characterized formation due to exposure within the Mont Terri Underground Rock Laboratory in Canton Jura, Switzerland (Bossart et al., 2018). The aim of this work is to observe and quantify the mechanisms involved in the sealing of a single fracture in OPA as a function of differential pressure, and their impact on the hydrological properties of the fracture.

MATERIALS AND METHODS

The Opalinus Clay Sample

The OPA sample considered in this study was obtained from the Mont Terri URL. Opalinus Clay is shale (or claystone) of Toarcian-Aalenian age (upper Liassic- lower Dogger). The mineralogical composition of OPA, from the shaly facies used in our experiment, includes 40–70 wt.% clay minerals, 10–30 wt.% carbonates (mainly calcite, subordinate siderite, and ankerite), 10–30 wt.% quartz and accessory feldspars, pyrite, and organic matter. At smaller scale, inhomogeneities are largely layers enriched in silt or carbonate concretions, often including siderite. Calcite, the most abundant carbonate, is present in the form of isolated bioclasts (sometimes pyritized), and not in the form of cementing material. This has a strong impact on the mechanical as well as geochemical properties of the rock. The rock also displays a significant textural anisotropy, as quantified by X-ray diffraction for the crystalline part (Wenk et al., 2008) and by BIB-SEM for morphological analysis including pores (Houben et al., 2013, 2014).

The OPA core was obtained from the source wrapped in plastic wrap, aluminum foil, and sealed in a vacuum bag to preserve the original saturation. A section of the sample was sawn (slow speed cutting, with air cooling by use of a notched 1" diameter ultrathin blade) to obtain a manageable size piece. The block was fractured first, by compression between two blades, generating a single tensile fracture at ∼10 degrees relative to the average bedding plane; two half cylinders were then machined (dry) to obtain a 9 mm cylindrical core, 24 mm tall. To provide a small area of starting asperity contacts (and avoiding the perfect matching of the two halves), half of the sample was rotated by 180 degrees before re-assembly. This assembly was chosen to have a scenario where the fracture conductivity would be sustained longer than e.g., in a fracture with matching surfaces and to have more defined asperity contacts. A sustained conductivity would also allow for better observation of possible chemical reactions (e.g., dissolution of carbonates). Sample was prepared 2 days prior the experiment, and was kept in aluminum foil and in a sealed plastic bags to preserve the original saturation as much as possible.

The Synchrotron X-Ray Micro-Computed Tomography Experiment

When assembling the mini-triaxial cell, the sample was jacketed with heat-shrink polyvinylidene fluoride (PVDF) tubing, and fixed to the piston of the cell. The saturating fluid was deionized water saturated with CO_2 at 40 psi (0.28 MPa) for ∼8 h. This fluid was chosen to try to generate geochemical weathering (i.e., dissolution of the carbonates fraction close to the fracture surface) induced by the reaction with CO_2 during the flow. The cell and sample were pressurized by an array of three high-pressure syringe pumps (Teledyne-Isco 260D): the first pump was connected to both the water annulus and the vertical piston and worked in constant pressure mode, providing the confining stress conditions. The pressure of this pump was progressively increased to induce the closure of the fracture. The second pump was connected to the inlet of the cell, and contained the CO_2 saturated water. This pump was operated in constant flow rate mode. The third pump was connected to the outlet of the sample and worked as a fluid back-pressure regulator. This configuration allowed to operat at constant flow (before sample hydraulic sealing, when the flow was stopped) and pore pressure, being the only controlled variable the confining pressure.

Between each step of confining pressure increase the system was allowed to flow for ∼3 h to circulate ∼10 ml of solution through the sample (constant flow at 0.05 ml/min). Flow was of course stopped after the hydraulic sealing of the fracture. A first scan was run before flowing the solution, as a baseline, then after 1 h of saturation the series of increased confining pressure measurement started. The flow through the sample was kept constant, both in flowrate and pore pressure, through the two pumps system. This status was not sustainable anymore when the fracture sealing occurred, therefore the flow pump was stopped at that point to avoid an increase in pore pressure that would have damaged the sample environment. The sealing of the fracture was highlighted by a sudden increase in pressure at the inlet pump, which was then switched to constant pressure mode at the pore pressure value. The experiment lasted from the first assembly of the fracture sample until the complete occlusion of the fracture, with significant obliteration of the baseline microstructure. A total of seven confining pressure steps (plus one baseline scan of the sample with the as-received saturation) were collected. Measurements were run in a quasi-static fashion, stopping the flow and waiting until the sample was stable for scanning, i.e., when the sample motion observable was slower than the pixel size, at 3.22 μm, per tile scan time (15 min). Sample stabilization was relatively fast (less than 1 h) even at high confining pressures.

The experiment was conducted at beamline 8.3.2 (MacDowell et al., 2012) at the Advanced Light Source (Lawrence Berkeley National Laboratory). Data were collected using filter-hardened (6 mm Al, 0.5 mm Cu) white light. The detector system consisted of a conventional scintillator, visible light optics, and a sCMOS detector. More specifically, we used a 50 μm LuAG scintillator with a 2 × microscope objective (yielding a pixel size of 3.22 μm) optical system, recording the projection images with a low-noise sCMOS camera (PCO-Edge, Cooke Corporation, 2560 × 2560 px).

The data collection strategy at the beamline was to operate in continuous tomography mode, with 2049 projections over a 180 degrees rotation of the sample. A "local area" imaging setup (i.e., sample larger than the field of view) was used to collect the highest resolution dataset possible with the available optics: as a consequence an outer rim of the sample 50–100 μm thick was not measured. The choice of privileging this resolution vs. the larger field of view was done since from previous experience this resolution provides much better quality data in terms of subsequent data analysis and modeling (e.g., digital volume correlation). The significant loss in resolution (more than doubled) needed to image the whole sample is generally used when boundary conditions for modeling are critical. Given the small size of features in shales, we privileged the resolution (with enough detail to identify the evolution of microstructures, and enough fracture to compute a correct flow simulation)

with respect to the full boundary conditions. Exposure time was 400 ms per projection. Given that the vertical size of the sample exceeded the vertical size of the beam, a series of six vertical tiles for each measurement was collected for each time step to image the whole sample. From the raw projections, a conventional filtered back-projection approach (Kak and Slaney, 2001), as implemented in the software Octopus® (Dierick et al., 2004) was used to obtain the reconstructed slices for each dataset, finally the different tiles were combined to obtain the full sample volume for each time step.

RESULTS

Qualitative Observations of the Evolution

During the experiment, flow in the sample was obstructed early in the fracture closure process: after the saturation of the sample the pressure of the constant flow pump started to increase slowly, highlighting the presence of choke points in the sample making the flow more difficult. The flow stopped immediately and completely after increasing the differential pressure (confining minus pore pressure set by the backpressure pump) to 300 psi (2.07 MPa); at that point the pressure in the constant flow pump quickly increased to values close to the confining pressure, hence the pump was stopped and the system was kept at a constant pore pressure, set on both pumps [40 psi (0.28 MPa)]. After that threshold, no fluid was transferred through the sample.

This behavior can be qualitatively correlated to CT image features observed at the different closure steps. In **Figure 1**, volume renderings of the sample at the different stages during the flow of the carbonated water are shown (differential pressures are listed in psi). The closure of the fracture is progressive; at the first stages of the experiment, aperture reduction is more evident in the middle and lower sections of the sample.

In the lower row of **Figure 1** a horizontal section of this part of the sample looking from the lower inlet is also displayed to better appreciate the features present in the sample during the sealing of the fracture. Just under this section of the sample, the main choke point of the fracture is present. This choke point controls the flow along the fracture length. The sealing of the fracture seems to be a rather regular process, with the fracture monotonically decreasing in aperture, as seen in the subvertical sections on the top row in **Figure 1**, until the final stage where the seal is almost complete and significant vertical shortening of the sample due to pervasive microfracturing and shear is also observable.

In **Figure 2** a detail of the sample before and after hydraulic sealing is shown, in a vertical section of the sample (perpendicular with respect to the fracture plane) and a zoom of the most interesting region (middle column), with the main choke point at the bottom, and a large aperture zone of the fracture just above. A binarized version of the inset, better highlighting the morphology of the fracture in that section, is provided on the right. The deformation observable in the choke point area is small, but enough to completely obstruct flow: the original fracture plane before the sealing is still noticeable, while after the sealing it becomes difficult to distinguish from the unaltered OPA, in terms of CT number (which translates into gray value in the resulting image). The larger aperture zone deforms to a larger degree, with a progressive development of a microfractured zone, with most of the microfractures starting parallel to the bedding plane at, and around, the asperity contacts.

The carbonated water was circulated in order to observe eventual geochemical weathering, as for the shale sample documented in Deng et al. (2017), However, the facies of OPA studied in this experiment ("shaly facies"), in addition to having a lower fraction of carbonates, those carbonates are also not present as a microcrystalline cementing phase, but as bioclasts, making them less accessible to the reactive fluid. For this reason, no clear evidence of CO_2-induced weathering was observed in this experiment. Time, P/T conditions, and type of clays, also minimize significant interaction between the aqueous CO_2 and the clay minerals in OPA.

Stress-Induced Microstructures

The increase in differential pressure generated a variety of mechanical responses in the sample. During the sealing stage of the large aperture fracture, shown in **Figure 3A** (P = 500 psi [3.45 MPa]), the development of a pervasive microfracture network in the material around the fracture is evident, with the progressive filling of the fracture zone with microlithons. Most of the microfractures are subparallel to the bedding plane, but different mechanisms in the whole sample can be observed. In **Figure 3**, an example of purely tensile crack is shown in yellow: the behavior is highlighted by the presence of a bioclast, which is broken into two pieces. Fractures with a significant shear component are also present, as the one highlighted in light green. These fractures are difficult to observe, since the shearing action generates fines mixed with the pore fluid, resulting in a weak density (and consequently CT number) contrast. The presence of en echelon conjugated fracture systems, due to vertical shortening under load, are also observable in the sample (highlighted in light blue in **Figure 3A**). An eventual axial dilation of the bulk sample is not measurable given the "local area" setup used for the experiment. The deformation microstructures observed close to the fracture plane display affinities with those observed in the deformed zones at the Mont Terri site (Laurich et al., 2018).

In sections of the sample where deformation is more pronounced, a microstructure with a similarity to cataclasites is present, where angular-shaped microlithons and silt particles are surrounded by a mixture of clays and fluid. This microstructure is shown in **Figure 3B**, which focuses on the top of the sample at the last stage of the experiment. This pervasive microfracturing and the related deformation, starting at the asperity contacts of the fracture, is the mechanisms controlling the sealing of the system.

Quantitative Analysis of Local Deformation

In order to better quantify the mechanisms of the closure of the main choke point in the fracture, and hence the sealing, we used the digital volume correlation (DVC) technique, which has proven to be an effective analysis tool for rock deformation experiments in argillaceous rocks (Lenoir et al., 2007). The DVC

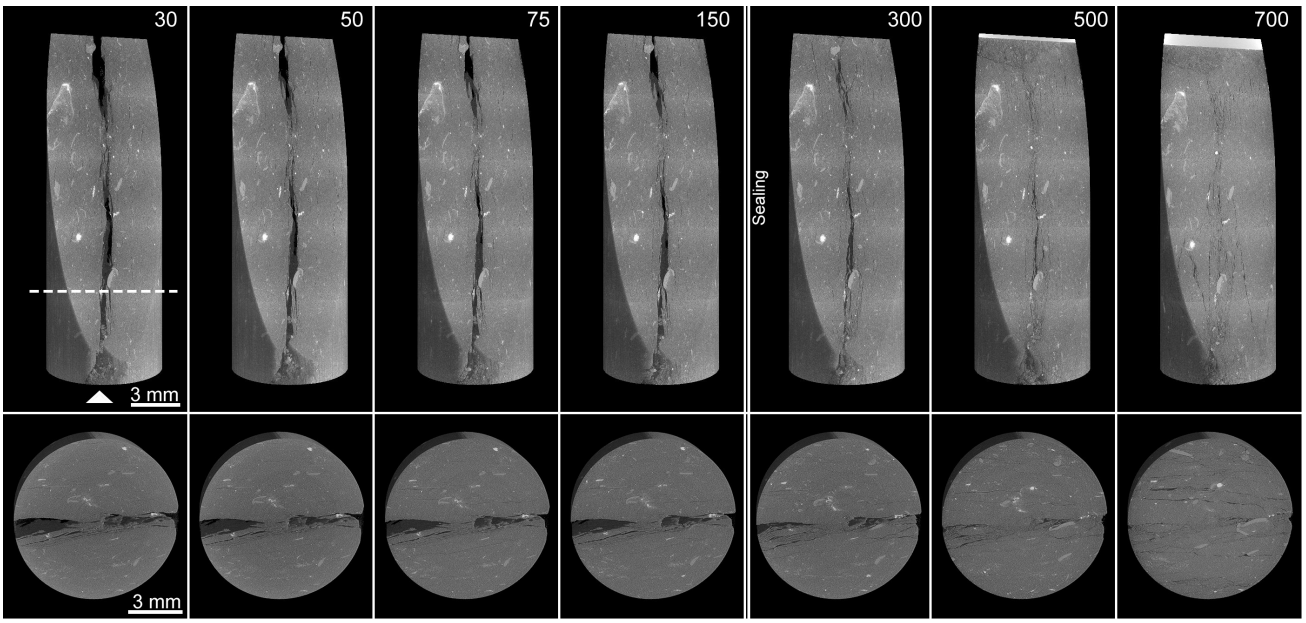

FIGURE 1 | Volume rendering of the sample during the flow experiment, while increasing the confining pressure (volumes in figure are labeled with differential pressure values, in psi). Inlet at the bottom (see arrow). On the top row a subvertical section of the sample is shown. The bottom row displays a slice of sample (at the dashed line) looking from the inlet direction.

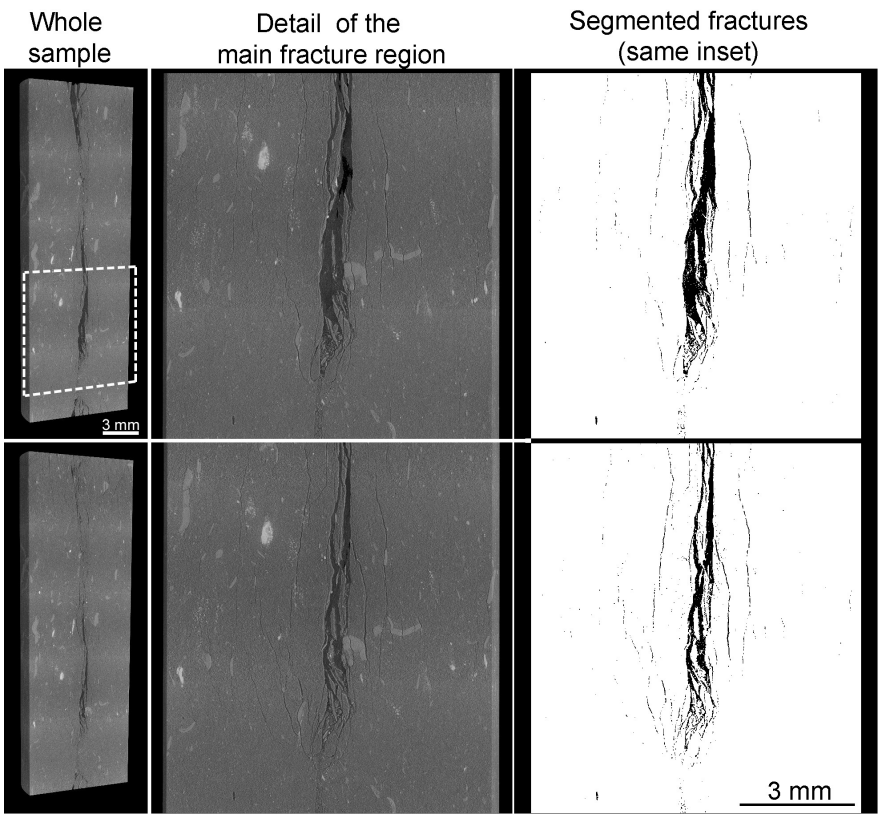

FIGURE 2 | Vertical section of the sample before and after hydraulic sealing. On the middle column, a detail of the part of the sample with the choke point and a large aperture section of the fracture are displayed. On the right, corresponding binarized images further highlight the fracture morphology in the sample.

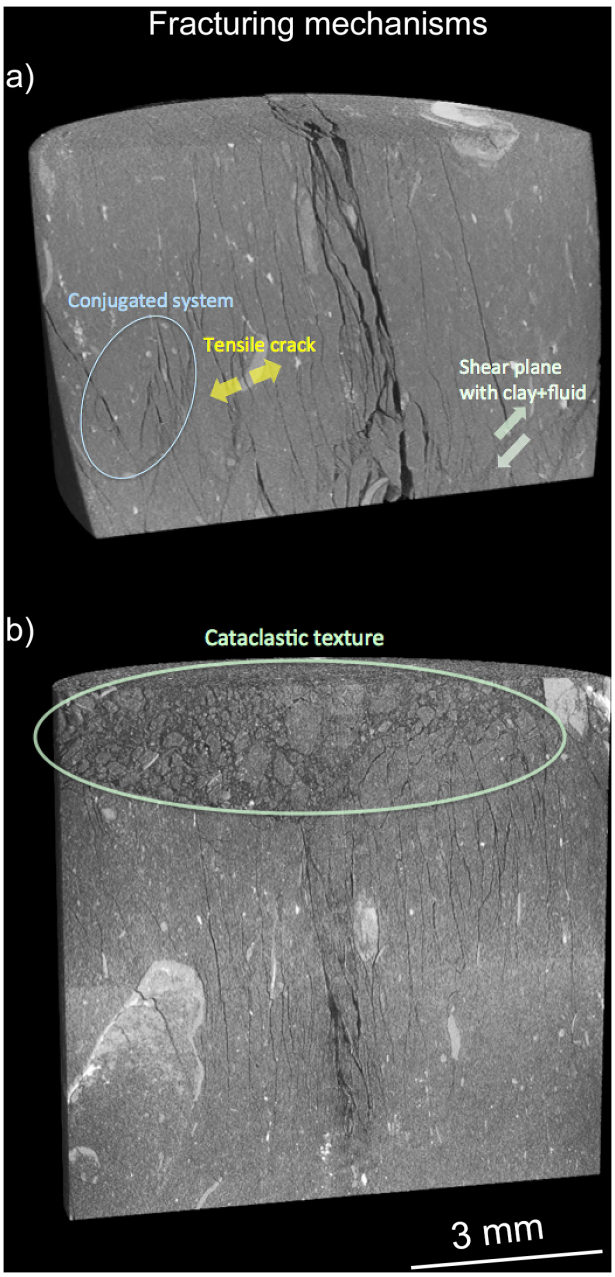

FIGURE 3 | Subsections of the sample at the latter stages of the experiment, where the mechanical deformation of the sample was more pronounced: different fracturing mechanisms are highlighted in the figures (see text for complete details). **(a)** middle section of the sample, **(b)** top section of the sample.

approach utilizes local patch-wise image correlation calculations between two volumetric datasets, such as the ones acquired via tomographic techniques, to estimate local vector displacements and volumetric deformation between the two (see Bay et al., 1999, for the first development on tomographic datasets). Using DVC, local displacements of the sample in the three directions were calculated for the lower section of the sample, where the main choke point and the large aperture zone are. We used the TomoWarp2 software (Tudisco et al., 2017) on the datasets collected before and after the sealing of the fracture.

The most interesting results are visible in the horizontal displacement maps, along the normal of the fracture plane, roughly corresponding to bedding plane. In **Figure 4** the volume rendering of the lower half of the sample is shown with the local displacement volume along the fracture normal superimposed. The look up table (LUT) chosen to label the DVC volume has two different colors for each displacement direction, and the color intensity is proportional to the displacement absolute value with a range of ± 130 µm. From the figure it is possible to observe how the two sample halves are pushed toward each other, with the half on the left displaying higher displacement values. This is evident in the section of the sample where the fracture has a larger effective aperture, with the largest displacement present at the very center of the volume where a new asperity contact is developing and the largest amount of open microfractures are

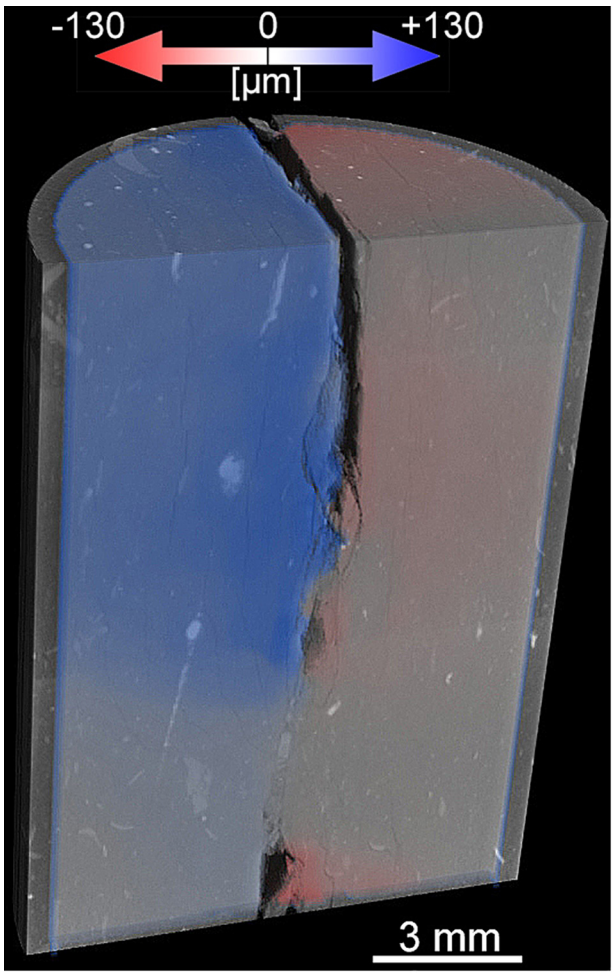

FIGURE 4 | Digital volume correlation of the sample before and after hydraulic sealing (lower half of the sample. A colormap of the local displacements along the direction perpendicular to the fracture plane has been superimposed to the sample volume rendering.

opening. The closure of the fracture in the zone of the choke point, in the lower part of the sample, where the asperity contacts are more developed, is much more limited; nevertheless, a very small displacement in this area, on the order of ∼30 μm, resulted in the complete hydraulic sealing of the fracture.

Local Evolution of the Fracture Aperture

The evolution of the aperture has a significant impact on the hydraulic properties of the fracture, therefore in this section we will address the morphological evolution of the fracture with a focus on the consequence on the flow field; we observed from the DVC analysis that a small displacement in an already constricted region resulted in sealing. To provide a more quantitative view of aperture evolution during the whole experiment, the slice-by-slice average aperture of the fracture has been calculated for the different steps.

The general results can be summarized by **Figure 5**. On the left part of the figure, in grays, a volume rendering of a virtual vertical section of the sample at the beginning of the flow experiment {differential pressure = 30 psi [(0.21 MPa)]} is displayed as a reference, to have a transversal section of the fracture in the sample. Superimposed to the volume rendering, the 3D Stokes flow field of the fracture has been plotted as well. The color-coding of the Stokes flow field corresponds to the flow velocity at any given voxel, and transparency has been added to better visualize the whole field in the context of the fracture. From this color-coding it is possible to see the main, small, choke point, close to the inlet (bottom) which results in the only orange-red color in the flow field. A larger section about 1 cm from the top (outlet) also exhibits high flow velocities to a lesser extent (green colors), due to the more constricted flow. The Stokes flow velocity field has been provided as a reference to the slice-by-slice aperture plots displayed on the right of **Figure 5** where the flow velocity plotted displays a very good agreement with the aperture variations along the flow direction plotted on the right. Observing the sample at the beginning of the flow experiment (red curve), starting from the inlet (bottom) we can see how the main choke point is immediately recognizable. Further along the flow path, the aperture gradually increases reaching a maximum; in this section of the fracture the flow is slower as would be expected. This local aperture-flow velocity correlation holds along the sample, where a secondary, and not as well developed as the first one, choke point is present, and where the fracture becomes larger again, going to the outlet.

Comparing the sequence of aperture measurements as a function of differential pressure, we see how the evolution of the aperture plots is not regular. The first important feature is the closure of the main choke point, visible on the local aperture plot (see arrow in figure): at 300 psi (2.07 MPa) that section of the plot goes sharply to values close to zero. The part of the sample above this choke point closes substantially, but never completely seals, even if the absolute changes in aperture are much larger than in the part of the sample with the main choke point. This behavior is in agreement with results obtained through DVC analysis, and it is also consistent with the evolution of the asperity contacts discussed later in this work. The secondary choke point in the upper half of the sample eventually seals the fracture as well. The top of the sample is where the most pronounced fracture closure is observed; as discussed previously, this is due primarily to the generation of a very pervasive fracturing of the OPA and the generation of the cataclastic texture (**Figure 3B**) which can deform and fill the fracture more efficiently when compared to the less pervasive mechanisms observed in the other parts of the sample.

Hydraulic Properties and Relationship With the Fracture Topology

A direct measurement of the permeability of the real sample in the experimental setup used in this study would be challenging at best, therefore we utilize the digital rock physics approach and calculate the single phase hydraulic properties of the sample directly from the tomographic datasets. To calculate the permeability of the fracture, the binarized volume of the fracture was directly used to calculate Stoke's flow, which results in a permeability value and volumes with the flow velocity fields in the three orthogonal directions. The calculation of Stokes flow velocity fields also is also helpful, since it facilitates understanding of controlling features such as channels, choke points, etc. To calculate the flow properties of the sample at the different stages we used the approach described in Zuo et al. (2017), with an updated version of the code used in that work, in a rescaled volume. The calculated permeability values, for comparison purposes, have been normalized with respect the starting permeability of the system (value = 100). The topological parameters of the fracture we calculated to compare the permeability are the average aperture and the percentage of contact areas in the fracture plane.

The permeability modeling results are summarized in **Figure 6**. The modeled permeability drops by 50% during the first increase in differential pressure (20 psi [0.14 MP]). After this first steep decrease, the permeability reductions becomes less pronounced, until the closure of the choke point, when the permeability goes to zero: this is in good agreement with the behavior observed during the experiment, since it's the point where flow was stopped due to the loss of hydraulic conductivity. The general trend in permeability modification follows the average aperture of the fracture, with the main difference being that such an averaged calculation cannot identify the closure of the choke point, and therefore the hydraulic sealing of the fracture. The increase in contact areas is rather regular during the sample evolution and it is not directly related to either the average aperture or permeability. An interesting detail is how the starting steep decrease in permeability is coupled with only a modest increase in asperity contacts in the fracture.

DISCUSSION

The evolution of the fractured OPA sample studied in this experiment depends on a series of different coupled processes. Mechanisms of localized and bulk strain have been observed, leading to the development of new microcracks and slaking at the fracture surface, and to bulk sealing of the main fracture, respectively. The loss in permeability occurs at relatively low

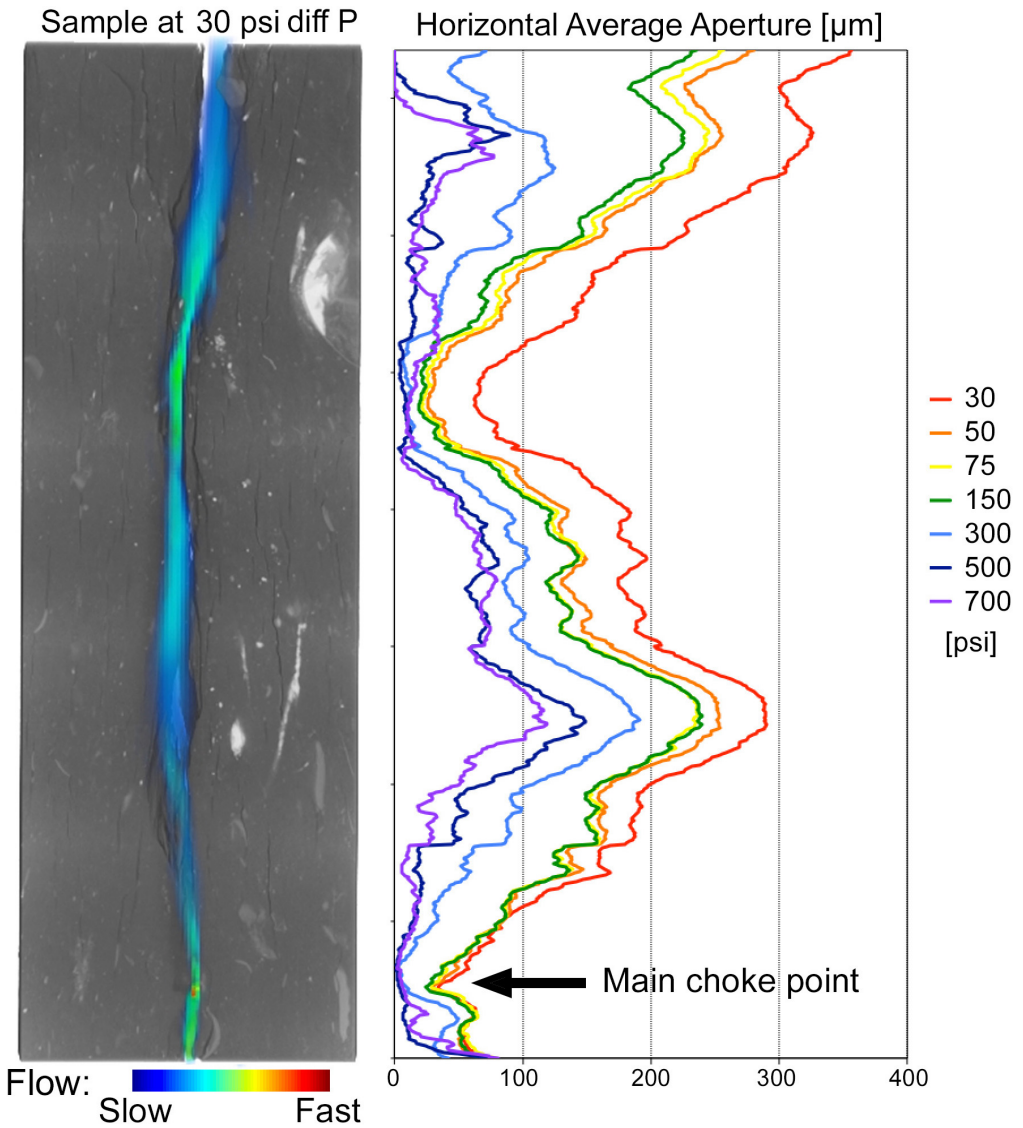

FIGURE 5 | Average aperture distributions along the vertical axis of the sample during the flow experiment. On the left, a vertical section of the sample at the beginning of the flow, with superimposed in colors the Stokes flow velocity field calculated for the fracture at that stage.

confining stress levels. At higher confining pressures (differential $P > 300$ psi [2.07 MPa]) the sample microstructure becomes noticeably distorted and aperture reduction is more extensive. The conductivity of the fracture studied is controlled by the evolution of a single feature of the system, the main choke point. This evolution is largely controlled by the evolution of the asperity contacts in that region of the fracture.

The effect of hydration of OPA has been shown to induce self-sealing in prior studies. In Bourg and Ajo-Franklin (2017) the sample displayed in **Figure 2** shows a self-sealing behavior, and the sealing happened at a constant differential pressure of 300 psi (2.07 MPa), the same value observed in this study, after less than 1 h of flowing carbonated water. The saturation of the sample seems to play a significant role. In Bastiaens et al. (2007) flow experiments, in an artificially fractured Boom Clay core, displayed a self-sealing/healing behavior due to sample hydration. The authors also found OPA behave in a similar fashion, only significantly slowly and to a lesser sealing extent. Hydration is an important process in assessing the sealing behavior of OPA and clay-bearing materials in general, concerning OPA, even complete self-sealing has been observed, as in the 2D cell of Laurich et al. (2019), where the fracture was optically sealed after as little as 1.4 h. This time is similar to the hydration period at constant flow and pressures allowed to our sample before increasing the confining pressure. In this timeframe we observed a clear partial sealing, but after that time the sample was considered "stable", meaning that during a scan no motion artifacts were observable. This translates to the fact that any motion in the sample (e.g., swelling) was -at that point- slower than the pixel size of the detector (3.22 µm)

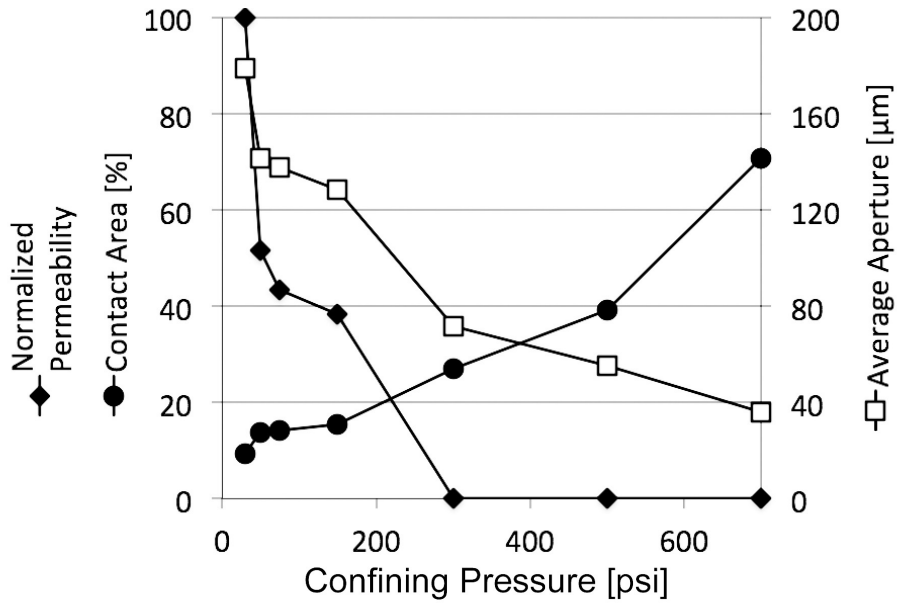

FIGURE 6 | Plots comparing hydraulic properties and morphometric parameters calculated for the fracture: normalized permeability [100 = value at the start of the experiment], asperity contacts area [%], and average aperture [µm].

in the timeframe of the tomographic scan, but slower swelling that would eventually seal the fracture by hydration alone cannot be excluded. The self-sealing properties of OPA are, as expected, increased as a function of the confining stress (Heitz et al., 2003; Bock et al., 2010). These experiments confirm the behavior observed in our study; however, with the addition of *in situ* imaging we have been able to both identify and quantify the sealing process in a case where shale hydration is combined with micromechanical alteration to inducing fracture sealing.

The role of hydration in our experiment is explored in **Figure 7**. The sample with "as received" saturation and the sample after flowing the carbonated water for ∼1 h (at the same differential pressure of 30 psi) are shown by way of the renderings on the left panel: the hydration of the shale at the asperity contacts weakened their mechanical properties. This results in localized microfracturing due to the swelling induced by the free water flow along the surface, with the consequent preferential failure along discontinuities parallel to the bedding plane. This results in a fast, partial sealing behavior due to hydration. Microfracturing induced by hydration is combined with the fracturing mechanisms induced by mechanical loading in the second phase of the experiment; fluid pressure built up and presumably slower pressure dissipation throughout the sample likely have caused local fluid over pressures. These, in conjunction with the proximity to the upper moving piston, might have favored cataclasis, as evident in the upper sample section shown in **Figure 3B**. The result of this combination is the generation of an extremely complex and pervasive deformation pattern.

Hydration of the shale close to the fracture surface seems to significantly impact the initial aperture distribution on the fracture plane. In **Figure 7** the aperture maps of the fracture before and after hydration are shown: from the volume rendering section, the closure of the fracture is evident, but the aperture maps show the phenomenon in a quantitative fashion and allow the identification of interesting details. The average aperture loss due to the hydration process is 44%, while contact area increases by a factor of 9. The evolution of aperture in the maps displays both a global decrease and some different behavior in specific areas. To better understand this evolution, the difference in aperture values and the newly formed asperity contacts are displayed on the right panel of **Figure 7**. The aperture decrease is roughly proportional to the aperture absolute values map, but there are some significant exceptions in the areas of the fracture with a low aperture starting value. Where both fracture surfaces come in contact, the subjected confining pressure might suppress any free clay mineral swelling. This suppression likely results in heterogeneous stress distributions and apparently enhances swelling and slaking around such wall-to-wall contacts. This fracturing and subsequent slaking of fragments is evident (for the largest fragments) in the difference aperture map, and three of these events have been highlighted with the green circles. The swelling of the material at the asperity contacts and in the zones with low aperture values had another effect, which was the most influential in the present experiment, from an hydraulic point of view: the generation of choke points. The single choke point controlling the evolution of the permeability, as calculated for this experiment, has been highlighted in yellow in the asperity contacts map. Before hydration, the area around the choke point displays low aperture values, with small asperity contacts surrounding it. After the hydration, swelling in that portion of the sample (coupled with the swelling-induced fracturing) generates a barrier with a few gaps where the fluid can pass through, setting thus the main choke point that will be sealed when increasing in

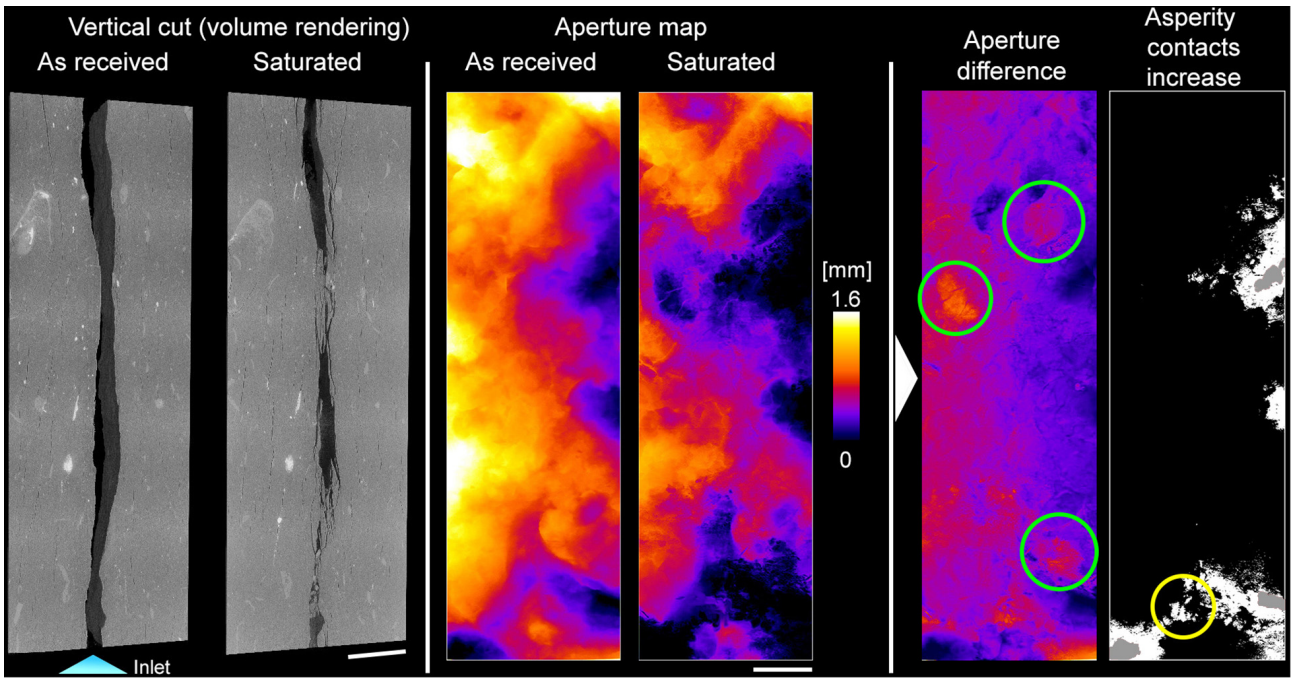

FIGURE 7 | Role of the hydration in the morphology of the fracture: volume renderings (left), and aperture maps (center) of the sample before and after hydration are shown. On the right, the difference in apertures and the evolution of asperity contacts is shown. In gray the starting contact areas are shown, and in white the new contact areas after saturation have been displayed. Areas of special interest have been highlighted: the generation of choke points because of the swelling and fracturing of material close to the fracture surface (green circles), and the generation of the main choke point which will be responsible of the hydraulic sealing on this specific sample (yellow circle) during the differential pressure increase.

confining pressure will be applied. The evolution of the hydraulic properties of the whole fracture was controlled by the evolution of that specific choke point: as we can observe, especially from the aperture maps, the asperity contacts generate this transverse "barrier" with respect to the flow direction. This barrier has a small channel left allowing flow to go through (highlighted with the yellow circle).

The hydration step seems to trigger the fast sealing behavior observed in OPA: the microfracturing due to the local swelling induced by the interaction of clays with the water, and the relative stress relief at the fracture surface, provides mechanically weaker asperity contacts, thus the closure of the fracture becomes easier. This process is also emphasized with the current sample geometry, where the bedding is subparallel to the fracture plane. Swelling strain measurements in OPA display a strongly anisotropic behavior, with the largest strain increase in the direction normal to the bedding plane (Wolter, 2003; Zhang et al., 2009), this results in preferential slaking along the lamination planes and the release of the stress with the expansion in the fracture space. This behavior is also highlighted by the DVC analysis, which detects a more pronounced local strain in the part of the sample closer to the fracture surface (and in the part of the surface with larger aperture), and presented in **Figure 4**. The changes of the sealing mechanisms in function of the bedding plane direction is an important topic, but is outside the scope of the present work, and would require a series of dedicated experiments. From the results found in our experiment we can indirectly obtain some insight about important factors: first, the slaking of the fracture surface due to hydration seems to be enhanced in the parallel configuration. Being the main detachment planes (planes between laminae) parallel to the fracture surface, the detachment is favored. This favored detachment of microlithons is also favored by the compression mechanisms around the contact areas, this is especially evident in **Figure 7**, both from the renderings and from the local aperture maps, where the decrease in aperture in specific parts of the fracture are due to the detachment of flat fragments parallel to the fracture surface. Such a behavior would not be possible, to this extent, in a sample where the fracture would be perpendicular to the bedding plane. Second, the layered nature of the microstructure, especially in presence of alternating laminae with different mechanical properties, would also become more important in fractures cutting those structures orthogonally: the mechanically stronger layers would control the evolution of the fracture, up to the point of acting as self-propping features, for example. An extended local variability of chemical properties, would also be important in a reactive environment, coupled with mechanics, in the evolution of the fracture (e.g., Ellis et al., 2011).

The sealing of the fracture starts with the weakening of the surface induced by hydration, and the mechanical response of the closure is also a result of this first event. The DVC analysis shows larger displacements (in the direction normal to the fracture plane/bedding) in the part of the sample close to the fracture surface, where water is more abundant. This

behavior can be explained by a combination of stress induced by the increase of confining pressure and the swelling due to hydration with the stress release at the fracture surface, resulting in the larger displacement values observed in this zone. At higher confining pressure values, the mechanisms become increasingly dominated by a primarily mechanical response of the sample, where different fracturing patterns are observable until the almost complete sealing of the sample. No true fracture healing processes have been observed, since the sealed zone displays bands composed of either microfractured OPA or bands and pockets of OPA fragments embedded in a clay and water mixture. These textures are expected to display low permeability values, being extremely rich in clays, but mechanical properties are expected to be significantly different than the unaltered OPA, also potentially acting as lubricant facilitating the development of preferential shear planes.

The mechanism responsible for hydraulically sealing the fracture seems to be the generation and the closure of choke points. This mechanism involves the area increase of specific asperity contacts. The increase in confining pressure is the most obvious way to start the process, but the effect of hydration weakening these areas due to swelling, and subsequent stress release by microfracturing, plays an important role in the pressure needed to seal the system, which is expected to be significantly smaller compared to a dry sample. The hydraulic sealing of the system happens well before the whole fracture is closed: when the calculated permeability in the fracture drops to zero, a substantial amount of open fracture is still present. The geometrical distribution of the starting contact (and close-to-contact) asperities seems to play a key role in the evolution of the fracture by generation (and closure) of choke points.

The sealing of OPA is complete at a relatively low differential pressure, and at these conditions fast self-sealing occurs as well, as observed in different experiments. The presence of large amounts of clays, combined with the absence of a cementing phase (carbonates), greatly increases the ease of sealing, by a synergistic effect of clay swelling/slaking with the decrease in strength of the asperity contacts. Also the absence of large and mechanically strong grains, (or laminae) with the exception for the few bioclasts, inhibits self-propping behavior in OPA fractures, and of course the low fraction of sand and silt particles prevents the development of a mechanically strong framework, therefore the system is controlled mostly by the behavior of clays. The presence of cementing phases would be detrimental for sealing properties as well; in a mechanically stronger matrix, the stress generated by the swelling of clays in contact with water would not result in the microfracturing and the subsequent weakening of the asperity contacts observed in this experiment. The presence of cementing phases seems to be instead a desirable feature in unconventional oil and gas recovery scenarios, where long-term high conductivity of fractures is the desired outcome: the pervasive weakening of the mechanical properties of the contacts of proppant grains and fracture surface does not occur, thus avoiding the embedment of the proppant in the shale and keeping the fracture open for production (Voltolini and Ajo-Franklin, 2020). In the case of OPA the weathering due to clay hydration is much more pervasive than the weathering due to the reaction with the CO_2 present in the fluid. This is exactly the opposite behavior observed in a strongly cemented "shale" (Deng et al., 2017), where the dissolution of calcite is triggered and carbonates dissolution geochemistry controls the evolution of the fracture. In our experiment the presence of dissolved CO_2 is in fact a negligible factor, and the hydraulic evolution is controlled by the mechanical response to hydration and stress increase of the asperity contacts alone.

CONCLUSION

The sealing of a fracture in OPA in function of hydration (1 h) and confining pressure (with datasets recorded every 3 h of flow, before sealing, after each pressure increase) has been observed via *in situ* SXRμCT. Different mechanisms play different key roles at the different stages of the evolution: first, the hydration of the sample induces a decrease in fracture aperture due to the hydration of the sample close to the fracture surfaces. Hydration induces swelling, and local stress is released via microfracturing. This generates the enlargement and mechanical weakening of the asperity contacts. After this first step, the increase in confining pressure induces the closure of the fracture; the mechanically weakened asperity contacts yield to the stress and the fracture progressively closes. The development of the asperity contacts completely controls the geometry of choke points, which in turn are the structures controlling the hydraulic properties of the fracture during sealing. At higher confining stresses, with the fracture already hydraulically sealed, more pervasive mechanical fracturing of the sample is observed: shear bands filled with fine clay mixed with water are observed; different fracturing mechanisms with conjugate fractures are present as well. In the parts of the sample with higher mechanical solicitation, material with a texture affine to cataclasites is observed as well, and the fracture becomes almost completely sealed.

As a formation able to self-seal after fracturing, OPA has proven, through both prior studies and the measurements presented in this work, to be a material with desirable characteristics for application where low-permeability seals are needed. The presence of CO_2 in this experiment seems to make no difference since the swelling induced by water is so fast and pervasive at this scale and time. In addition to that, the presence of swelling clays in OPA is limited, and clays such as montmorillonite are the most prone to react with CO_2. In a GCS scenario, the presence of supercritical CO_2 could influence the swelling properties of the clay fraction as has been observed, but in a scenario limited in time and at moderate P and T water plays the main role. While the observations about CO_2 are true in the temporal and spatial constraints of our experiment, evidence in nature, e.g., fractures sealed with calcite, clearly suggests that in given enough time and space different behaviors that can greatly influence the hydraulic properties of fractures can be also observed.

The present work has been able to identify and quantify the different processes involved in fracture sealing in a clay-rich rock such as the OPA, from the early stage of hydration until complete sealing due to confining stress progressive increase. The whole

process is a combination of different mechanisms (triggered at different stages) that influence the morphology of the fracture, and as a consequence its hydraulic properties. The large amount of clays and the microstructure of the sample (especially the lack of cementing phases) are the main factors influencing the sealing properties of this group of rocks. The mechanical weakening of asperity contacts is the key process controlling hydraulic properties: microfracturing due to hydration and local stress increase provide a rapid sealing of choke points, resulting in prompt hydraulic sealing, a crucial requisite for an effective caprock or seal rock.

DATA AVAILABILITY STATEMENT

The datasets generated for this study are available on request to the corresponding author.

AUTHOR CONTRIBUTIONS

MV planned and executed the measurement, performed morphometric analysis and flow simulations, and wrote/edited the final manuscript. JA-F conceptualized the experiment, provided the sample, and wrote/edited the manuscript.

FUNDING

This work was supported as part of the Center for Nanoscale Control of Geologic CO_2 (NCGC), an Energy Frontier Research Center funded by the U.S. Department of Energy, Office of Science, Basic Energy Sciences under Award # DE-AC02-05CH11231. Beamline 8.3.2, at the Advanced Light Source at the Lawrence Berkeley National Laboratory is supported by the U.S. DOE Office of Science, Office of Basic Energy Sciences (DE-AC02-05CH11231).

ACKNOWLEDGMENTS

The SXR-μCT experiment was performed with the assistance of Alastair MacDowell and Dula Parkinson at the Advanced Light Source. The authors acknowledge the reviews of BL and PB, which were very helpful in improving the manuscript.

REFERENCES

Al-Bazali, T. M., Zhang, J., Chenevert, M. E., and Sharma, M. M. (2005). "Measurement of the sealing capacity of shale caprocks," in *Proceedings of the SPE Annual Technical Conference and Exhibition*, Texas.

Bastiaens, W., Bernier, F., and Li, X. L. (2007). SELFRAC: experiments and conclusions on fracturing, self-healing and self-sealing processes in clays. *Phys. Chem. Earth Parts A/B/C* 32, 600–615. doi: 10.1016/j.pce.2006.04.026

Bay, B. K., Smith, T. S., Fyhrie, D. P., and Saad, M. (1999). Digital volume correlation: three-dimensional strain mapping using X-ray tomography. *Exper. Mech.* 39, 217–226. doi: 10.1007/bf02323555

Bock, H., Dehandschutter, B., Martin, C. D., Mazurek, M., De Haller, A., Skoczylas, F., et al. (2010). *Self-Sealing Of Fractures in Argillaceous Formations In The Context Of Geological Disposal Of Radioactive Waste*. OECD/NEA report 6184.

Bossart, P., Bernier, F., Birkholzer, J., Bruggeman, C., Connolly, P., Dewonck, S., et al. (2018). "Mont terri rock laboratory, 20 years of research: introduction, site characteristics and overview of experiments," in *Mont Terri Rock Laboratory, 20 Years. Swiss Journal of Geosciences Supplement*, eds P. Bossart and A. Milnes (Cham: Birkhäuser).

Bourg, I. C. (2015). Sealing shales versus brittle shales: a sharp threshold in the material properties and energy technology uses of fine-grained sedimentary rocks. *Environ. Sci. Technol. Lett.* 2, 255–259. doi: 10.1021/acs.estlett.5b00233

Bourg, I. C., and Ajo-Franklin, J. B. (2017). Clay, water, and salt: controls on the permeability of fine-grained sedimentary rocks. *Acc. Chem. Res.* 50, 2067–2074. doi: 10.1021/acs.accounts.7b00261

Busch, A., Alles, S., Krooss, B. M., Stanjek, H., and Dewhurst, D. (2009). Effects of physical sorption and chemical reactions of CO2 in shaly caprocks. *Energy Proc.* 1, 3229–3235. doi: 10.1016/j.egypro.2009.02.107

Busch, A., Amann-Hildenbrand, A., Bertier, P., Waschbuesch, M., and Krooss, B. M. (2010). "The significance of caprock sealing integrity for CO_2 storage," in *Proceedings of the SPE International Conference on CO2 Capture Storage and Utilization*, Louisiana.

Cnudde, V., and Boone, M. N. (2013). High-resolution X-ray computed tomography in geosciences: a review of the current technology and applications. *Earth Sci. Rev.* 123, 1–17. doi: 10.1016/j.earscirev.2013.04.003

Deng, H., Molins, S., Steefel, C., DePaolo, D., Voltolini, M., Yang, L., et al. (2016). A 2.5 D reactive transport model for fracture alteration simulation. *Environ. Sci. Technol.* 50, 7564–7571. doi: 10.1021/acs.est.6b02184

Deng, H., Voltolini, M., Molins, S., Steefel, C., DePaolo, D., Ajo-Franklin, J., et al. (2017). Alteration and erosion of rock matrix bordering a carbonate-rich shale fracture. *Environ. Sci. Technol.* 51, 8861–8868. doi: 10.1021/acs.est.7b02063

Dierick, M., Masschaele, B., and Van Hoorebeke, L. (2004). Octopus, a fast and user-friendly tomographic reconstruction package developed in LabView®. *Measur. Sci. Technol.* 15:1366. doi: 10.1088/0957-0233/15/7/020

Ellis, B., Peters, C., Fitts, J., Bromhal, G., McIntyre, D., Warzinski, R., et al. (2011). Deterioration of a fractured carbonate caprock exposed to CO2-acidified brine flow. *Greenhouse Gases* 1, 248–260. doi: 10.1002/ghg.25

Heitz, D., Trick, T., and Bühler, C. (2003). Selfrac (SE) experiment: long term plate load experiment. *Mont. Terri. Proj. Techn.* 51:106.

Houben, M. E., Desbois, G., and Urai, J. L. (2013). Pore morphology and distribution in the shaly facies of opalinus clay (Mont Terri, Switzerland): insights from representative 2D BIB–SEM investigations on mm to nm scale. *Appl. Clay Sci.* 71, 82–97. doi: 10.1016/j.clay.2012.11.006

Houben, M. E., Desbois, G., and Urai, J. L. (2014). A comparative study of representative 2D microstructures in shaly and sandy facies of opalinus clay (Mont Terri, Switzerland) inferred form BIB-SEM and MIP methods. *Mar. Petrol. Geol.* 49, 143–161. doi: 10.1016/j.marpetgeo.2013.10.009

Kak, A. C., and Slaney, M. (2001). *Principles of Computerized Tomographic Imaging*. Philadelphia, PA: Society for Industrial and Applied Mathematics.

Laurich, B., Fourrière, A., and Gräsle, W. (2019). LT-A experiment: how fracture wetting leads to closure. *Mont. Terri. Proj. Techn.* TN 2020-29.

Laurich, B., Urai, J. L., Vollmer, C., and Nussbaum, C. (2018). Deformation mechanisms and evolution of the microstructure of gouge in the main fault in opalinus clay in the mont terri rock laboratory (CH). *Solid Earth* 9, 1–24.

Lenoir, N., Bornert, M., Desrues, J., Bésuelle, P., and Viggiani, G. (2007). Volumetric digital image correlation applied to X-ray microtomography images from triaxial compression tests on argillaceous rock. *Strain* 43, 193–205. doi: 10.1111/j.1475-1305.2007.00348.x

Loring, J. S., Schaef, H. T., Thompson, C. J., Turcu, R. V., Miller, Q. R., Chen, J., et al. (2013). Clay hydration/dehydration in dry to water-saturated supercritical CO2: implications for caprock integrity. *Energy Proc.* 37, 5443–5448. doi: 10.1016/j.egypro.2013.06.463

MacDowell, A. A., Parkinson, D. Y., Haboub, A., Schaible, E., Nasiatka, J. R., Yee, C. A., et al. (2012). "X-ray micro-tomography at the advanced light source," in *Proceedings of the Developments in X-Ray Tomography VIII*, San Diego, CA.

Neufelder, R. J., Bowen, B. B., Lahann, R. W., and Rupp, J. A. (2012). Lithologic, mineralogical, and petrophysical characteristics of the Eau Claire Formation: complexities of a carbon storage system sealLithologic, mineralogical, and petrophysical characteristics, eau claire formation. *Environ. Geosci.* 19, 81–104. doi: 10.1306/eg.02081211014

Noiriel, C., Renard, F., Doan, M. L., and Gratier, J. P. (2010). Intense fracturing and fracture sealing induced by mineral growth in porous rocks. *Chem. Geol.* 269, 197–209. doi: 10.1016/j.chemgeo.2009.09.018

Renard, F., Bernard, D., Thibault, X., and Boller, E. (2004). Synchrotron 3D microtomography of halite aggregates during experimental pressure solution creep and evolution of the permeability. *Geophys. Res. Lett.* 31:L07607. doi: 10.1029/2004GL019605

Renard, F., Cordonnier, B., Dysthe, D. K., Boller, E., Tafforeau, P., and Rack, A. (2016). A deformation rig for synchrotron microtomography studies of geomaterials under conditions down to 10 km depth in the Earth. *J. Synchrot. Rad.* 23, 1030–1034. doi: 10.1107/s1600577516008730

Renard, F., Ortoleva, P., and Gratier, J. P. (1997). Pressure solution in sandstones: influence of clays and dependence on temperature and stress. *Tectonophysics* 280, 257–266. doi: 10.1016/s0040-1951(97)00039-5

Tsang, C. F. (1991). Coupled hydromechanical-thermochemical processes in rock fractures. *Rev. Geophys.* 29, 537–551.

Tudisco, E., Andò, E., Cailletaud, R., and Hall, S. A. (2017). TomoWarp2: a local digital volume correlation code. *SoftwareX* 6, 267–270. doi: 10.1016/j.softx.2017.10.002

Voltolini, M., and Ajo-Franklin, J. (2020). Evolution of propped fractures in shales: the microscale controlling factors as revealed by in situ X-Ray microtomography. *J. Petrol. Sci. Eng.* 188:106861. doi: 10.1016/j.petrol.2019.106861

Voltolini, M., Barnard, H., Creux, P., and Ajo-Franklin, J. (2019). A new mini-triaxial cell for combined high-pressure and high-temperature in situ synchrotron X-ray microtomography experiments up to 400° C and 24 MPa. *J. Synchrot. Rad.* 26(Pt 1), 238–243. doi: 10.1107/s1600577518015606

Voltolini, M., Haboub, A., Dou, S., Kwon, T. H., MacDowell, A. A., Parkinson, D. Y., et al. (2017a). The emerging role of 4D synchrotron X-ray microtomography for climate and fossil energy studies: five experiments showing the present capabilities at beamline 8.3. 2 at the Advanced light source. *J. Synchrot. Rad.* 24, 1237–1249. doi: 10.1107/s1600577517012449

Voltolini, M., Kwon, T. H., and Ajo-Franklin, J. (2017b). Visualization and prediction of supercritical CO2 distribution in sandstones during drainage: an in situ synchrotron X-ray micro-computed tomography study. *Intern. J. Greenhouse Gas Control* 66, 230–245. doi: 10.1016/j.ijggc.2017.10.002

Wan, J., Tokunaga, T. K., Ashby, P. D., Kim, Y., Voltolini, M., Gilbert, B., et al. (2018). Supercritical CO2 uptake by nonswelling phyllosilicates. *Proc. Natl. Acad. Sci. U.S.A.* 115, 873–878. doi: 10.1073/pnas.1710853114

Wenk, H. R., Voltolini, M., Mazurek, M., Van Loon, L. R., and Vinsot, A. (2008). Preferred orientations and anisotropy in shales: callovo-oxfordian shale (France) and Opalinus Clay (Switzerland). *Clays Clay Min.* 56, 285–306. doi: 10.1346/ccmn.2008.0560301

Wolter, K. E. (2003). Rock mechanical analyses (RA) experiment: petrophysical analyses of drill cores from the Opalinus clay formation at the Mont Terri laboratory. *Swiss Natl. Hydrol. Geol. Survey*.

Yasuhara, H., and Elsworth, D. (2008). Compaction of a rock fracture moderated by competing roles of stress corrosion and pressure solution. *Pure Appl. Geophys.* 165, 1289–1306. doi: 10.1007/s00024-008-0356-2

Yasuhara, H., Elsworth, D., and Polak, A. (2004). Evolution of permeability in a natural fracture: significant role of pressure solution. *J. Geophys. Res. Solid Earth* 109:B03204.

Zhang, C. L. (2011). Experimental evidence for self-sealing of fractures in claystone. *Phys. Chem. Earth Parts A/B/C* 36, 1972–1980. doi: 10.1016/j.pce.2011.07.030

Zhang, C. L., Wieczorek, K., and Xie, M. L. (2009). "Swelling experiments on mudrocks," in *Proceedings of the International Symposium On Unsaturated Soil Mechanics And Deep Geological Nuclear Waste Disposal (UNSAT-WASTE 2009)*, New York, NY.

Zuo, L., Ajo-Franklin, J. B., Voltolini, M., Geller, J. T., and Benson, S. M. (2017). Pore-scale multiphase flow modeling and imaging of CO2 exsolution in Sandstone. *J. Petrol. Sci. Eng.* 155, 63–77. doi: 10.1016/j.petrol.2016.10.011

Conflict of Interest: The authors declare that the research was conducted in the absence of any commercial or financial relationships that could be construed as a potential conflict of interest.

frontiers in Earth Science

METHODS
published: 21 September 2020
doi: 10.3389/feart.2020.00287

Quantifying Microstructural Evolution in Moving Magma

Katherine J. Dobson[1,2], Anja Allabar[3], Eloise Bretagne[2], Jason Coumans[2], Mike Cassidy[4], Corrado Cimarelli[5], Rebecca Coats[6], Thomas Connolley[7], Loic Courtois[8], Donald B. Dingwell[5], Danilo Di Genova[9,10], Benjamin Fernando[4], Julie L. Fife[11], Frey Fyfe[4], Stephan Gehne[12], Thomas Jones[2,6], Jackie E. Kendrick[6], Helen Kinvig[2], Stephan Kolzenburg[5,13], Yan Lavallée[6], Emma Liu[14], Edward W. Llewellin[2], Amber Madden-Nadeau[4], Kamel Madi[8], Federica Marone[11], Cerith Morgan[15], Julie Oppenheimer[10], Anna Ploszajski[16], Gavin Reid[17], Jenny Schauroth[5,6], Christian M. Schlepütz[11], Catriona Sellick[2], Jérémie Vasseur[5], Felix W. von Aulock[6], Fabian B. Wadsworth[2,5], Sebastian Wiesmaier[5] and Kaz Wanelik[7]*

[1] Department of Civil & Environmental Engineering, University of Strathclyde, Glasgow, United Kingdom, [2] Department of Earth Sciences, Durham University, Durham, United Kingdom, [3] Department of Geosciences, Eberhard Karls University of Tuebingen, Tuebingen, Germany, [4] Department of Earth Sciences, University of Oxford, Oxford, United Kingdom, [5] Department of Earth and Environment Science, Ludwig-Maximilians-Universität, Munich, Germany, [6] Department of Earth, Ocean and Ecological Sciences, University of Liverpool, Liverpool, United Kingdom, [7] Diamond Light Source, Harwell Campus, Didcot, United Kingdom, [8] 3Dmagination, Harwell Campus, Didcot, United Kingdom, [9] Bayerisches Geoinstitut, Universität Bayreuth, Bayreuth, Germany, [10] School of Earth Sciences, University of Bristol, Bristol, United Kingdom, [11] Swiss Light Source, Paul Scherrer Institut, Villigen, Switzerland, [12] School of Earth and Environmental Sciences, University of Portsmouth, Portsmouth, United Kingdom, [13] Department of Geology, University at Buffalo, Buffalo, NY, United States, [14] Department of Earth Sciences, University College London, London, United Kingdom, [15] Lancaster Environment Centre, Lancaster University, Lancaster, United Kingdom, [16] Institute of Making, University College London, London, United Kingdom, [17] Independent Researcher, Aberdeen, United Kingdom

OPEN ACCESS

Edited by:
Margherita Polacci, University of Manchester, United Kingdom

Reviewed by:
Satoshi Okumura, Tohoku University, Japan
Gabriele Lanzafame, University of Catania, Italy

***Correspondence:**
Katherine J. Dobson
katherine.dobson@strath.ac.uk

Specialty section:
This article was submitted to Volcanology, a section of the journal Frontiers in Earth Science

Received: *06 December 2019*
Accepted: *19 June 2020*
Published: *21 September 2020*

Citation:
Dobson KJ, Allabar A, Bretagne E, Coumans J, Cassidy M, Cimarelli C, Coats R, Connolley T, Courtois L, Dingwell DB, Di Genova D, Fernando B, Fife JL, Fyfe F, Gehne S, Jones T, Kendrick JE, Kinvig H, Kolzenburg S, Lavallée Y, Liu E, Llewellin EW, Madden-Nadeau A, Madi K, Marone F, Morgan C, Oppenheimer J, Ploszajski A, Reid G, Schauroth J, Schlepütz CM, Sellick C, Vasseur J, von Aulock FW, Wadsworth FB, Wiesmaier S and Wanelik K (2020) Quantifying Microstructural Evolution in Moving Magma. Front. Earth Sci. 8:287. doi: 10.3389/feart.2020.00287

Many of the grand challenges in volcanic and magmatic research are focused on understanding the dynamics of highly heterogeneous systems and the critical conditions that enable magmas to move or eruptions to initiate. From the formation and development of magma reservoirs, through propagation and arrest of magma, to the conditions in the conduit, gas escape, eruption dynamics, and beyond into the environmental impacts of that eruption, we are trying to define how processes occur, their rates and timings, and their causes and consequences. However, we are usually unable to observe the processes directly. Here we give a short synopsis of the new capabilities and highlight the potential insights that *in situ* observation can provide. We present the XRheo and Pele furnace experimental apparatus and analytical toolkit for the *in situ* X-ray tomography-based quantification of magmatic microstructural evolution during rheological testing. We present the first 3D data showing the evolving textural heterogeneity within a shearing magma, highlighting the dynamic changes to microstructure that occur from the initiation of shear, and the variability of the microstructural response to that shear as deformation progresses. The particular shear experiments highlighted here focus on the effect of shear on bubble coalescence with a view to shedding light on both magma transport and fragmentation processes. The XRheo system is intended to help us understand the microstructural controls on the complex and non-Newtonian evolution of magma rheology, and is therefore

used to elucidate the many mobilization, transport, and eruption phenomena controlled by the rheological evolution of a multi-phase magmatic flows. The detailed, *in situ* characterization of sample textures presented here therefore represents the opening of a new field for the accurate parameterization of dynamic microstructural control on rheological behavior.

Keywords: volcanology, rheology, synchrotron, *in situ*, magma, X-ray tomography

THE NEED FOR *IN SITU* OBSERVATION IN MAGMATIC RESEARCH

Magmas are generally a constantly evolving mixture of silicic melt, crystals, and bubbles, with the magmatic behavior during mobilization, flow, fragmentation, and eruption fundamentally controlled by the evolution of the melt viscosity and interactions between the suspended crystal and bubble phases. Dynamics are key in volcanology. Most of our research focuses on how magmatic systems have, are, and will continue to evolve. We use a wide range of field, laboratory, theoretical, and numerical approaches, but understanding the dynamic and highly heterogeneous nature of magmatic systems, defining the behavioral tipping points, and identifying the markers we should be monitoring remains difficult because we cannot fully interrogate or observe magma at depth. The spatial and temporal heterogeneity of the system means that while empirical relationships can be defined for a given set of conditions, the rheological evolution of magma remains complex and understanding the magmatic and volcanic processes influenced by the rheology requires a knowledge of the interaction microphysics that we currently lack.

The samples we collect in the field inherently contain a complex series of textural and chemical overprints acquired during the entire evolution from formation to eruption/emplacement. The behavior of the magma at any point in time and space will have been influenced by evolution prior to that point. Likewise, when we try to reproduce sub-surface magmatic conditions in the laboratory, experimental charges capture only a small piece of that evolution, usually starting from an ideal condition in order to capture a specific behavior – a condition unlikely to be found in the natural magmatic system. Our inability to observe processes under realistic conditions is a key limitation in developing our understanding. In the natural system, many complex and interacting processes operate simultaneously, and experiments generally aim to simplify and isolate phenomena. However, even if we manage to capture and describe all the individual phenomena, there will still be interactions in the natural system that are missed. The *in situ* approach with both natural and synthetic materials allows us to see what those interacting phenomena look like in a new way.

The Need for *in situ* Observation in Rheological Research

Recent efforts into developing an understanding of the rheology of magmatic suspensions has focused on deriving models that capture the rheology of magmatic suspensions as a function of intrinsic (melt- and crystal-composition, texture, etc.) and extrinsic (temperature, shear rate, etc.) parameters (Ryerson et al., 1988; Spera et al., 1988; Stein and Spera, 1992; Pinkerton, 1994; Sato, 2005; Ishibashi and Sato, 2007; Vona et al., 2011; Vona and Romano, 2013; Chevrel et al., 2015; Campagnola et al., 2016; Soldati et al., 2016; Morrison et al., 2020). We understand that changes in magma viscosity and the transition from Newtonian to non-Newtonian behavior, observed during crystallization and vesiculation, depend fundamentally on the crystal and bubble content, shape, surface texture, and size distribution as well as the imposed strain rates (Mader et al., 2013). However, characterization of sample textures in rheological studies, which is crucial for the derivation of these rheological laws, is, without exception, restricted to snapshots before and after an experiment.

While the importance of disequilibrium effects on crystal growth has inspired recent studies investigating the dynamic rheology of crystallizing silicate melts at conditions close to those expected during emplacement in nature (Kouchi et al., 1986; Ryerson et al., 1988; Giordano et al., 2007; Vona and Romano, 2013), studies under disequilibrium conditions are few, and systematic descriptions of the effects of cooling (Giordano et al., 2007; Kolzenburg et al., 2019; Vetere et al., 2019), deformation (Kolzenburg et al., 2018b; Tripoli et al., 2019), and oxygen fugacity (Kolzenburg et al., 2018a), as well as their interdependence, are limited. Textural characterization of experiments performed under these conditions has been impossible because the high rates of diffusion and crystal growth at high undercooling make it impossible to quench the experimental charges fast enough to preserve the textures under experimental conditions. As a result, dynamic changes in crystallization and vesiculation kinetics, sample textures during flow or during disequilibrium processes, and the associated responses in rheology remain unconstrained.

In recent years, we have seen a dramatic increase in the ability to perform non-destructive observation *in situ* using the high-speed capability of X-ray tomography synchrotron facilities. The development has been largely led by the research needs of the material science community (e.g., Maire and Withers, 2014), but with the development of sample environments suitable for geological materials, and high temperature apparatus we are now capable of making certain key observations. The X-Rheo system described here now permits detailed, *in situ* characterization of these sample textures, a crucial factor for accurate parameterization of the rheological data, and thus opens up an entirely new field of study in magma rheology.

RECENT ADVANCES IN SYNCHROTRON CAPABILITY

Several synchrotron facilities now have the capability to acquire 3D images of geological materials with moderate (10–5 μm) or high (<5 μm) spatial resolution. Several tomography beamlines can achieve fast (defined here as <10 s to collect a single 3D tomographic dataset) tomography of these samples, and those focusing on imaging dynamic systems can routinely perform ultra-fast or real-time (defined here as <1 s to collect a single 3D tomographic dataset) tomography on geological specimens (e.g., Marone et al., 2020). For 3D tomographic acquisition, a frequency of up to 20 tomographies per second (TPS) is now possible (Dobson et al., 2016). These same detector systems can achieve over 5000 fps when used to collect 2D radiography.

Imaging at sub-optimal conditions can lead to a reduction in data quality but can also deliver higher temporal resolution. This usually takes the form of reducing the number of angles from which the 2D projections are acquired and/or underexposing the images. With large volume onboard camera storage this can enable 10s or 100s of high frequency images to be acquired in a single experimental run. Cropped projection image areas can further increase the TPS (reducing data transfer time) and number of tomographies (smaller data volume per image) that can be collected. Data transfer, rather than experimental speed, is now often the bottleneck. This has led to investment in novel continuous read out detectors with real-time data transfer to network storage (Mokso et al., 2017; Marone et al., 2020), and at some beamlines there is no theoretical limit to the number of 3D datasets that can be obtained.

On most systems the sample can be made to rotate continuously in a single direction with acquisition triggered at specific angle(s) by the rotational encoder. For the highest speed experiments, the last projection of the first data set (collected from 0 to 180°) can essentially be the first of the second dataset (collected from 180 to 360°). Alternatively, acquisition "gapped" (e.g., Dobson et al., 2016) can be triggered every time the 0° encoder location is passed, or every *n*-th time it is passed, allowing very high-speed acquisition with a lower image frequency. This method has the added advantage that all the reconstructed tomographies are in the same orientation, removing a registration step from the post processing workflow.

Recent Applications to Volcanology

Areas within volcanology where real-time *in situ* synchrotron X-ray tomography could prove transformative include (but are not limited to) bubble nucleation, growth, and coalescence; crystallization; crystal alignment and physio-chemical interaction; multiphase magma deformation and rheology (including strain localization reactive transport, and fragmentation); magma-rock-fluid interaction; rock mechanics; etc. Work has now begun in some of these areas, such as bubble growth and permeability (Baker et al., 2012, 2019; Colombier et al., 2018; Pleše et al., 2018), gas driven filter pressing (Pistone et al., 2015), deformation (Okumura et al., 2013), sintering (Wadsworth et al., 2016, 2019), and crystallization (Polacci et al., 2018; Arzilli et al., 2019).

When coupled to advances in furnace capability (presented here) (Bai et al., 2008; Fife et al., 2012; Kudrna Prasek et al., 2018; Polacci et al., 2018) and apparatus for tensional and compressional deformation (Kareh et al., 2012; Philippe et al., 2016), experiments that elucidate how volcanic and magmatic processes occur are now possible. We can observe and quantify their rates; we can systematically explore the relationships that control the timing of these events and start to define the critical causes and consequences.

One area where this is critical is in understanding magmatic mobilization, mobility, and flow. Magmas are complex multiphase suspensions with non-Newtonian rheological properties. Testing rheological behavior of natural and synthetic samples is challenging in the laboratory (McBirney and Murase, 1984; Caricchi et al., 2007; Lavalleìe et al., 2007; Cimarelli et al., 2011; Picard et al., 2011; Vona et al., 2011; Pistone et al., 2012, 2013; Chevrel et al., 2015; Vona et al., 2016), but understanding how the microscopic behavior of the suspended phases are controlling the macroscopic behavior remains even more so. As such, analog materials offer an excellent solution to scrutinize key rheological controls properties (Llewellin et al., 2002; Mader et al., 2013; Truby et al., 2014), not permissible during experiments on magma which is commonly enclosed in furnaces and pressure vessels. However, even when working with well controlled analog materials, samples are generally opaque and traditional methods cannot observe the nature or 4D distribution of the suspended phase interactions. Thus, the microphysics controlling fluid behavior is not constrained at the scale of the processes and rheological models remain incomplete. *In situ* X-ray tomography is ideally suited to meet this kind of challenge, as it reveals previously unrecognized phenomena and their temporal relationships.

In situ imaging of deformation experiments is a relatively new technique within the volcanological community, and performing these experiments has many unique challenges. We therefore give an overview of the considerations that must be made when designing or planning volcanological research using *in situ* imaging. We present the XRheo system and associated high temperature furnace for performing *in situ* rheological experiments on magmatic samples: providing cutting edge capabilities for understanding real-time evolution of microstructures and how this affects rheological behavior. We show the quality of the data that can be obtained and highlight the kind of salient features that can be observed before presenting an implementation of new volume correlation analysis methods that enable the extraction of quantitative information on the displacements within deforming samples.

DESIGNING *IN SITU* EXPERIMENTS

In situ imaging can be demanding, especially when working at high temperatures or with complex experimental setups. Careful design to allow integration between synchrotron imaging systems and the *in situ* apparatus is critical to experimental success.

Sample Holders and Encasement

In the volcanic and magmatic context, the high temperatures needed for experiments under natural conditions is a key challenge. Many environmental cells used in standard laboratory experiments are made of substantially thick Pt or stainless steel. These materials have high X-ray attenuation coefficients and cannot easily be used with tomographic imaging. Many materials with low X-ray attenuation have limited thermal stability, cannot accommodate loading, or will react with the melt, changing the composition and behavior of the sample during the experiment. Optimal imaging may result in deviation from optimal experimental conditions, or vice versa.

The need for encasement of molten samples using materials with low X-ray attenuation and good thermal properties makes boron nitride (BN) and Al_2O_3 the widely used materials of choice for high temperature experiments. BN is easy to machine and is stable to temperature of ∼1,000°C. Al_2O_3 can be used to higher temperatures (1,200–1,400°C) and has better mechanical properties under compression, but is harder to machine and can still be susceptible to thermal shock. Graphite could also be used under reducing experimental conditions. For heating schedules typical for volcanic and magmatic experiments (10–20°C/min), the chance of fracture through thermal shock is low. With some natural melt compositions and environments, reaction between the BN or Al_2O_3 sample holder and the enclosed melt may still occur. Where off-line testing is able to demonstrate that some container-sample reaction is tolerable, the progression can usually be observed in real-time during acquisition, or defined *a posteriori* in the reconstructed 3D images. Non-reactive high (or low) temperature magmatic analogs may have to be substituted. In such cases, other experimental parameters (temperature, deformation rate) may also have to be adjusted to allow for investigation of specific phenomena. Other encasement materials such as thin Pt foil (Polacci et al., 2018) and boro-epoxy (Berg et al., 2017) are also possible, but make sample preparation more complex and can limit the range of mechanical experimental conditions that can be tested.

Imaging Moving Magma

When working with changing multiphase materials, easy quantification requires sufficient contrast between melt and the different mineral phases while maintaining low enough overall attenuation to ensure high X-ray fluxes reaching the detector and with good signal quality. In all X-ray tomography, the attenuation differences between the mineral phases should be carefully checked prior to scanning (Hanna and Ketcham, 2017) to ensure the features of interest are visible, and with fast synchrotron tomography it is usually possible to use a monochromatic beam at an energy chosen to maximize the attenuation differences or extract data at two energies bridging an absorption edge. For some minerals it is possible to determine mineral composition from calibrated reconstructed 3D data, even from a polychromatic "white" or "pink" beam (Pankhurst et al., 2018), but this should be considered before starting experimental work so beamline conditions and calibrations standards can be identified.

To achieve the fastest projection acquisition rates for real-time or ultra-fast synchrotron tomography, magmatic sample densities may limit users to a white or pink beam on the lower energy hard X-ray imaging beamlines (e.g., TOMCAT, Swiss Light Source; Marone et al., 2020), but still allow monochromatic imaging on higher energy beamlines (e.g., i12-JEEP, Diamond Light Source; Drakopoulos et al., 2015). The attenuation differences between most rock-forming minerals are greatest at lower energies (Hanna and Ketcham, 2017).

When working with dynamic systems, the changes in total attenuation that will occur during the experiment (nucleation of crystals and associated changes in melt composition can cause a dynamic redistribution and therefore local and bulk attenuation) should also be considered, and the imaging parameters adjusted accordingly to allow adequate image quality at all stages of the experiment. Imaging crystal precipitation from a melt (Polacci et al., 2018), or crystals with a similar density (Arzilli et al., 2016) can be improved if phase contrast retrieval methods are used, but quantitative data analysis is still likely to be challenging and can be time-consuming and hard to automate. The enhanced phase boundaries achieved in phase contrast enhanced topography can make the small volumes of melt between crystals and/or bubbles harder to observe and quantify, and after preliminary testing was not deployed in this study.

THE XRHEO AND HIGH TEMPERATURE APPARATUS

The XRheo system is designed to be compatible with almost all large enclosure laboratory scanning systems and to function on all synchrotron imaging beamlines. Its development was possible by long-term access to both the TOMCAT beamline at the Swiss Light Source and the I12-JEEP beamline at Diamond Light Source. The XRheo takes a standard high precision low-torque rheometric testing apparatus (Di Genova et al., 2016) and integrates it with the high temperature sample environment and the imaging beamline.

The XRheo can perform the same suite of experiments that can be achieved during rotational rheological testing in the laboratory, but does so during 3D X-ray tomography acquisition, allowing the internal structural evolution to be captured *in situ* during the experiment while "traditional" rheological data are being collected. In standard rheological testing, the lower plate or cup is a fixed reference frame and the upper plate or spindle rotates with the torque required to rotate at a given speed recorded. The XRheo uses the rotation needed for 3D image acquisition (i.e., a rotating cup) as the reference frame. In this study, we use the XRheo in a wide gap concentric cylinder (Couette) configuration, but all other rotational rheological testing configurations are possible. The system (**Figure 1**) is conceptually and operationally simple, but technically challenging to design and set up. To acquire 3D data during the deformation, the XRheo uses the beamline rotation stage to control the cup. During the initial period, the rheometer

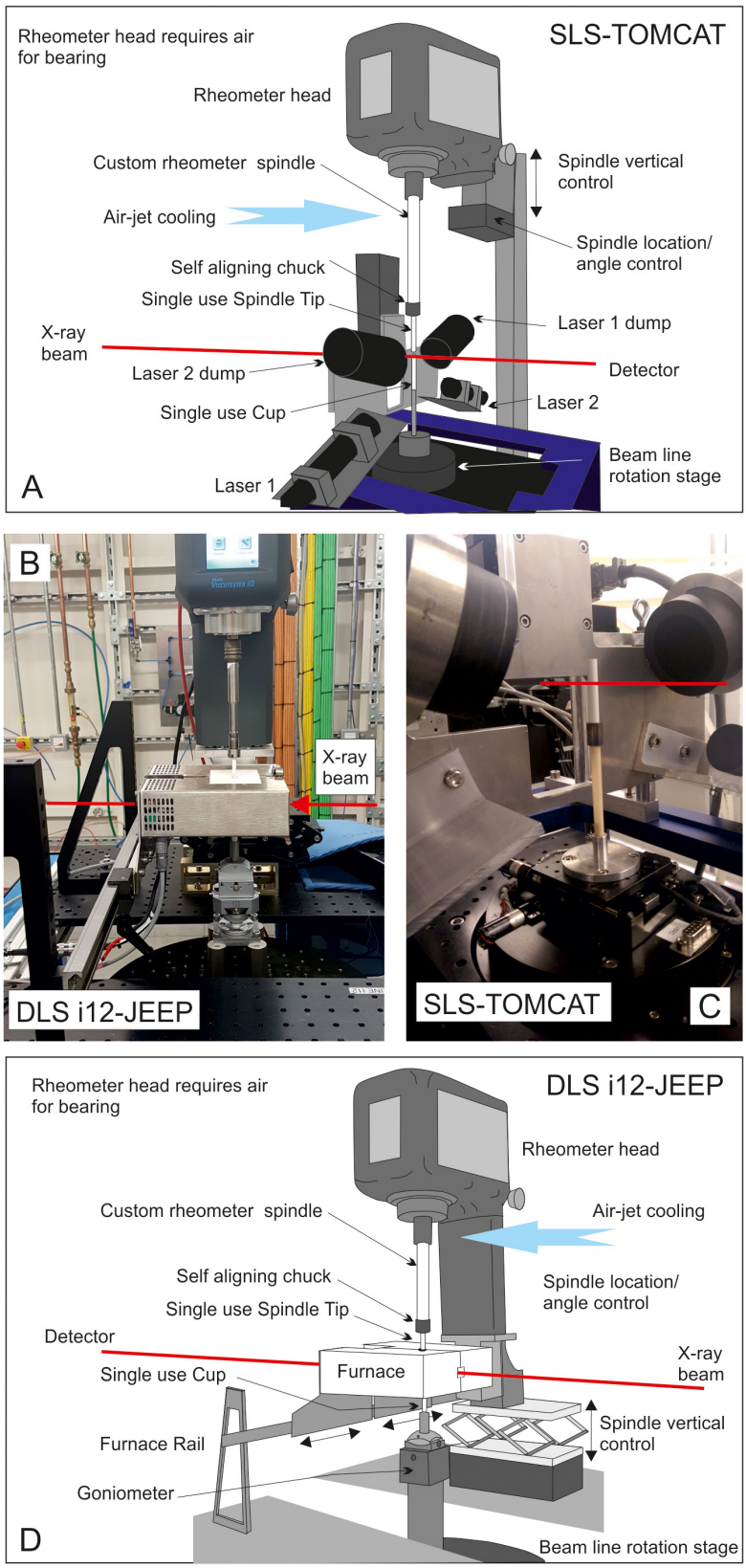

FIGURE 1 | Schematics of the XRheo and its installation at the TOMCAT (Swiss Light Source) **(A,C)** and at i12 (Diamond Light Source) **(D,B)** beamlines. This mounting system can be easily adapted to other synchrotron or laboratory systems, and the system can be used *ex situ* for laboratory bench testing.

head is set to keep a constant value of zero load and the coupled spindle therefore accelerates with and then rotates at the same velocity as the cup (to prevent development of any shear stress and internal deformation ahead of the experiment).

Once the system rotation is established and the desired experiment temperature reached, the beamline rotation stage and cup continue at the same rotation speed, while the rheometer is initiated and the spindle accelerated at a user-defined rate to a differential velocity with respect to the cup. As soon as the acceleration starts, the sample begins to experience internal deformation. Image acquisition from before the start of deformation through to steady state deformation or a given number of relative spindle rotations allows the microstructural evolution to be tracked.

Most rheometer systems allow the torque to be recorded throughout the experiment (both zero deformation and acceleration/constant deformation parts of the sequence) and allow a series of programmable accelerations and decelerations as required by the user. All equipment is safeguarded by an over torque failure condition set at a load well below the maximum operating conditions of the rheometer and beamline rotation stages. Should the load hit this threshold, the rheometer automatically moves back to operating at zero load, returning to the zero-torque condition, i.e., with the spindle rotation the at the velocity as the sample.

The precise setup is somewhat beamline-specific and gives flexibility to adapt to different sample and equipment mounting systems, the size of the sample, and the temperature range over which the system will be operated. Installation and operation of the XRheo system can vary depending on need and the auxiliary furnace equipment available, and the set-ups used at both TOMCAT and I12-JEEP are described here.

The XRheo

The XRheo is highly adaptable and can operate with the rheometer head most suitable for any given experiment, requiring only alteration of the fixing plate. Here we present data acquired using both Anton Paar and Thermo Fisher Scientific air bearing (nNm sensitivity) rheometric testers. The head is mounted on a set of high load manual translation stages that allows adjustment of the location of the rheometer spindle over the center of the beamline rotation stage. A second set of stages can be used to level the spindle. The rheometer is controlled in the beamline control room via a USB connection to a laptop and remote desktop control.

At TOMCAT (**Figures 1A,C**), the rheometer head and translation stages are mounted on a rigid horizontal support bar, which is in turn mounted onto a vertical support bar, which is bolted to the base table. A manual vertical translation stage is included at the bar intersection to allow the head and horizontal bar assembly to be raised for sample changing and then lowered back into imaging position. At I12-JEEP (**Figures 1B,D**) the rheometer mounting block is closer, attached to a split optical breadboard on a frame around the sample stage for mounting custom sample environments. The same breadboard supports the Pele furnace (see **Figures 1B,D**).

Alignment of the rotation axis of the spindle with that of the imaging stage is critical to both imaging and rheological data quality in standard testing. While the tolerances in machining and the alignment of the manufacturer supplied components may be adequate for a spindle or bob on a larger volume laboratory rheological tester, it should be checked before use on a high-resolution imaging beamline. A disposable BN or Al_2O_3 tip is attached to a steel spindle and attached the rheometer head (**Figure 1D**). The spindle tip diameters (and potentially geometry) can be varied according to the experiment. The spindle is lowered to the imaging position with the tip close to the bottom of the field of view and its alignment checked. Initial alignment is achieved using the beamline rotation stage mounting pin, raised to just below the spindle tip, as a visual reference. After that initial alignment, the X-ray hutch is closed, and radiographs taken to quantify any alignment adjustment needed and assessed by eye using multiple micrometer accuracy dial gages.

Samples

Here we use two samples that have already been employed in experimental volcanology. Synthetic magmatic samples formed from sintered soda lime glass beads of known rheological properties (Wadsworth et al., 2016, 2017, 2019) and low temperature magmatic analogs (oils and syrups). Other analog materials could also be used when appropriate to address a specific experimental question. When needed, inert marker crystals are mixed into the fluid. Here we use rutile crystals in the synthetic magma because they have significantly higher density (attenuation) than the molten glass and can be considered nonreactive with the melt under these experimental conditions over the time scale of these experiments. We use olivine or plagioclase as the particles in the low temperature analogs (**Figure 2**). Initial tests showed that there is no measurable settling of the crystals or rise of the bubbles on the timescale of the experiments.

Sinter in place

Some of the synthetic magmas were sintered in place. The beamline mounting pin (fixed to the rotation stage) is then lowered and the sample cup mounted. The cups used here were BN, 5–8 mm internal diameter, 0.5 mm wall thickness, and a 10 mm depth (**Figure 3**). Below the cup, the ceramic extended ∼20 mm to a standard pin for attaching to the rotation stage. The cup is raised and aligned in the field of view of imaging such that the base of the cup is ∼2 mm below the bottom of the image, and the rotation axis of the cup and spindle are aligned. Powdered samples were then loaded into the cup using a pipette tip, taking care not to knock the spindle and to fill the cup evenly from all sides. Once filled to the rim, the cup was tapped gently to allow settling and increase packing tightness.

Pre-sintered or natural samples

Sintered-in-place, powder-loaded samples at 1 bar typically exhibit a minor and variable amount of porosity. Although the porosity can be carefully characterized prior to any deformation, pre-sintered synthetic samples of known crystal and bubble content can often be produced with higher reproducibility *ex situ*.

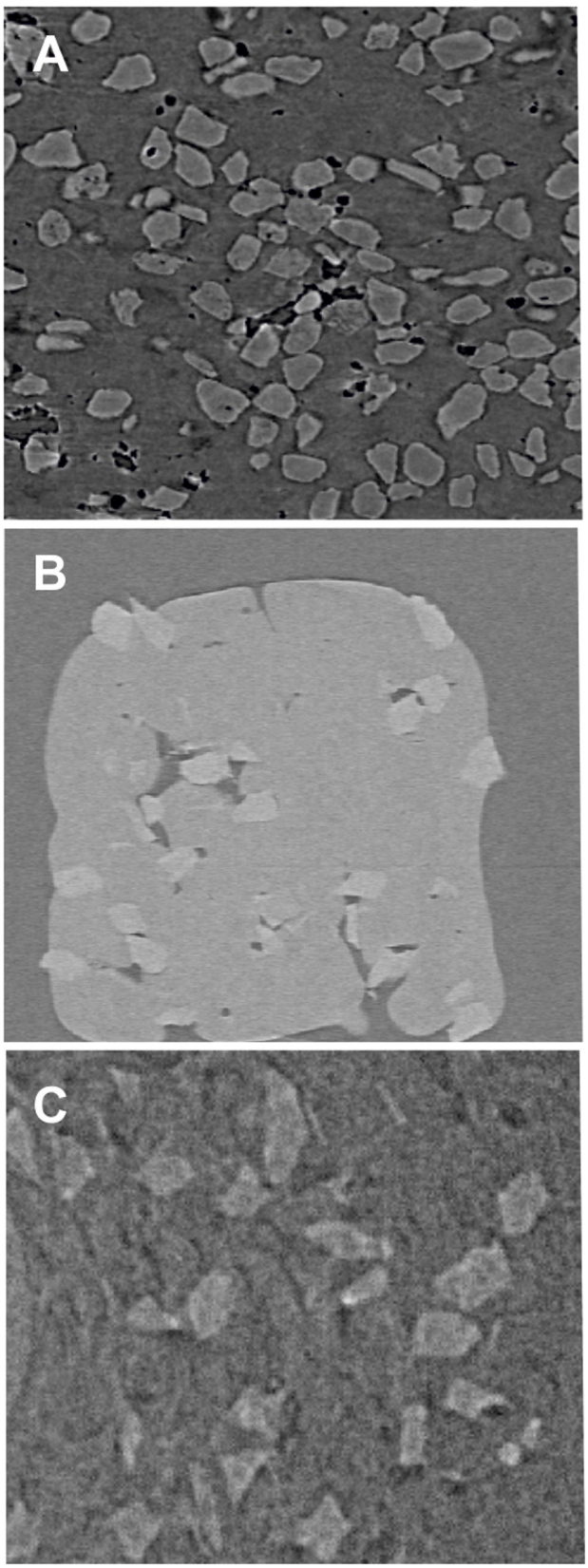

FIGURE 2 | Continued

FIGURE 2 | Two-dimensional slices through 3D datasets showing the contrast between **(A)** rutile in borosilicate (filtered pink beam, SLS-TOMCAT, max energy ~40 keV), **(B)** olivine in the borosilicate (DLS-i12-JEEP, monochromatic beam 53 keV), and **(C)** olivine in Canon N2700000 viscosity standard mineral oil (DLS-i12-JEEP, monochromatic beam 53 keV). The low contrast between olivine and borosilicate (shown in **B**) makes data processing and quantitative analysis extremely challenging when working at short detector distances (minimizing phase contrast to allow accurate rendering of thin bubble wall films). Experiments that have used quartz, wollastonite and feldspars in synthesized haplogranitic and dioritic melts have even lower contrasts, and the particles cannot be observed even with the lower energy at SLS-TOMCAT. The crystals in all three samples are in the 90–180 μm size fraction. Red line shows X-ray beam path.

Small cores cut from natural samples or larger blocks of pre-sintered material can also be used in the XRheo set-up; however, it can be harder to ensure good thermal and mechanical coupling between the cup, sample, and spindle. Cores were ground slightly smaller than the inner diameter of the cup to allow for thermal expansion of the melt during heating without promoting large stresses that may fracture the cup. Finely ground (<60 μm) material of the melt composition was then added to the cup to bridge the sample to the cup and encourage mechanical coupling. In some samples, smaller diameter drills were used to excavate a channel into the center of the core to accommodate the spindle, and additional ground material added over the center of the sample once the spindle was in place.

The best results were achieved when the spindle was raised 10 mm from the spindle imaging position and the cup aligned as for the powdered samples (above). For the drilled samples, the spindle can then be lowered back to image position prior to heating. For the un-drilled samples, the sample is heated prior to the spindle being lowered into the molten material. Immersing the spindle into the sample is done slowly to allow outward movement of the melt and accommodation of the spindle without breaking the tip. Some samples fail to form continuous bubble-free contacts between the melt, the cup, and the spindle. In these cases, large bubbles are usually visible in the reconstructed data and the sample can be changed prior to performing the experiment. In some cases (including some test samples which were loaded into the cups and heated *ex situ* before loading), the samples appear to form a good mechanical contact but decouple from either the cup or spindle as soon as deformation begins. The precise reason for this is unclear, especially when acceleration to deformation speed is low and the sample is thermally equilibrated. It should be noted that the need for rotation during heating means it is not possible to run solid undrilled samples at TOMCAT using the laser system and the current XRheo set-up.

Low temperature analogs

The XRheo can also be used to perform experiments on low temperature magmatic analogs (e.g., oils syrups, waxes). Loading these samples follows the pre-sintered protocol, with the fluids loaded into the sample cup in the laboratory prior to transfer onto beam. While Al_2O_3 and BN cups and spindles can be used for the high temperature experiments, BN cups and spindles are preferred when using low temperature analogs because of the

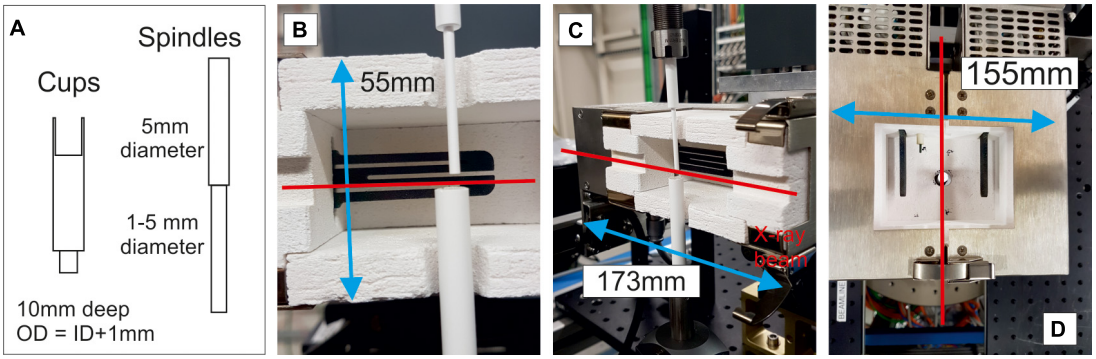

FIGURE 3 | (A) The sample cups and spindles used with the XRheo for high temperature experiments. **(B,C)** The Pele *in situ* furnace (see also **Figure 1**) as mounted and used with the XRheo. **(D)** The Pele *in situ* furnace with the upper insulation plates removed, this also shows the apertures set to accept the spindles/cups (as shown) could also be used as the X-ray window, mounting the sample from the bottom of this image for high temperature (no deformation) scanning in laboratory scanning systems.

lower attenuation of the fluid phase. Use of an encapsulation material that is denser than the sample generally makes image processing more challenging. BN is also lower cost and easier to machine, so more suitable for the shorter experiment times (no long heating periods) when working with analog systems.

Working at Magmatic Temperatures on Synchrotron Beamlines

Maintaining thermal stability across the sample volume can also be difficult in the configurations required on a beamline. Heat losses are largely governed by the geometry of the experimental apparatus and the heating system used. Some beamlines have their own furnaces for direct integration with the beamline controls, and this integration permits accurate and complete capture of the processes under investigation if they are strongly temperature dependent. In most cases, furnace volumes, hot zones, or focused heating spots are relatively small and samples can experience a substantial heat sink through the mounting pin. This effect can be seen and quantified in some tests such as during sintering experiments, where the powder material in contact with the BN mounting plate sinters at a slower rate than the material in the central part of the furnace. The volume of the hot zone and the effect of the heat loss on the experiment can sometimes be tested off beam, but in some experimental geometries, rotation and rotation speed can have an effect that is challenging to test in the laboratory.

At TOMCAT (SLS) the XRheo is compatible with the laser heating system (**Figure 1**; Fife et al., 2012; Marone et al., 2020). This system has two lasers mounted on opposite sides of the sample, each generating a 6 mm × 4 mm portrait spot on the sample holder. The lasers are initiated after rotation has begun and rotation continues while the lasers are heating. The system works well with small volume samples, but high thermal gradients are present away from the laser spot (i.e., above and below the imaging field of view and may affect behaviors for larger samples. The furnace is operated through the beamline control system.

The Pele Furnace

When working at I12-JEEP (DLS), existing beamline furnaces are incompatible with the XRheo; instead we use the bespoke Pele furnace (**Figure 3**), fabricated by Severn Thermal Solutions, who adapted a concept previously developed for a uniaxial deformation press (Lamur et al., 2018) and a rotary-shear apparatus (Wallace et al., 2019). This rail mounted 1 kW furnace has an operating range of 200–1,250°C, and the split design allows easy sample loading and a large hot zone (**Figure 3**) suitable for samples up to 20 mm in diameter. Thermal variability across the 30 mm (vertical) × 30 mm (across split) × 50 mm (along split) hot zone is better than 2°C and thermal stability is better than ±2°C. The furnace is powered and controlled by a Eurotherm programmable control unit (at present operated independently of the beamline control system).

The split design allows the upper and lower insulation panels to be removed (**Figure 3B**) and replaced according to the apertures required for any given experiment. The soft ceramic also allows for insertion of additional thermocouples for monitoring internal temperatures if needed, or fitting of a gas line to allow heating under a controlled atmosphere. In the XRheo setup, the upper and lower insulation plates were drilled to give a central circular aperture, with the diameter of the hole kept to ∼1 mm larger than that of the cup (lower) or spindle (upper) (**Figure 3B**). To minimize heat losses a second pair of insulation plates were placed on the closed furnace at 90° to the furnace closure (not shown in figure). The insulation pieces that allow X-ray transmission, holding the X-ray windows upstream and downstream from the sample, are equally versatile and can be square cut (for tomography) or fanning outward (The Pele furnace has been used for high temperature diffraction studies on i12-JEEP). It is also possible to insert a solid high transmission window into the ceramic insulation should heat losses need to be minimized or atmospheric conditions within the furnace volume controlled.

The height (55 mm), length (173 mm), and width (155 mm) of the furnace enclosure makes it highly versatile. The system can be mounted above or below (as shown here, **Figures 1**, **3**)

the rail, and the rail can be located upstream or downstream (as shown here, **Figures 1**, **3**) of the sample. When mounted below the rail, the thermocouple control and power cables for the furnace connect to the bottom of the unit, allowing space above for user access or additional equipment. The furnace rail can be mounted on the optical breadboard that supports the XRheo or can be integrated with other *in situ* apparatus. The furnace has been successfully mounted on the Deben open frame 10 kN deformation cell. It can also be used in a vertical configuration, hanging from the rail or a custom mounting system. This makes it compatible with laboratory scanning systems. In the vertical orientation the ram apertures and X-ray windows are switched. This enables source-sample and sample-detector distances to be reduced (minimum of 30 mm) to the distances necessary for high resolution laboratory scanners, although additional heat protection for the source and detector would be needed and would increase this distance slightly.

With the heat sinks of the XRheo cup and rams in place, the sample and spindle rotating, and additional air cooling focused on the upper part of the spindle to prevent overheating of the rheometer head air bearing (**Figure 1**) there is a reproducible differential between control loop temperature and sample temperature of ∼50°C for sample temperature of 500–1,200°C. This was calibrated from the rate of sintering in the boro-silicate bead pack, as we have thorough understanding of, and accurate control on, sintering (Wadsworth et al., 2017). This differential will vary with sample and cup materials as should be calibrated for a different experimental set-up.

Heating Schedules With the XRheo

On both beamlines, the hot zone of the furnace system is centered on the imaging field of view. The samples were heated to the chosen dwell temperature at 10–20°C/min and held there until the end of the experiment. In cases where solid samples were loaded the sample was heated to temperatures 1,000°C, usually much higher than target experimental temperatures to increase the speed of equilibration around the spindle and promote coupling. At the end of the experiments, the temperature can be ramped back down or quenched by turning off the furnaces and allowing the samples to cool in place before sample change. All cups and ceramic spindle tips are single use consumables for all high temperature experiments. The two high temperature experiments described here [see sections "Bubble Bearing Magma (High Temperature)" and "Three-Phase Magma (High Temperature)"] were performed at a dwell temperature of 900°C.

IMAGE ACQUISITION

While the tomography acquisition condition can be changed for each sample, this increases the chance of human error, especially when calculating rheometer control in terms of relative difference in rotation speed. Therefore, for simplicity, we define image acquisition parameters (rotation speed, exposure time, and project number) at the start of the experiment using a high-density sample. Reducing the exposure time, or even underexposing, generates more TPS and less motion blur, but this will eventually cause a level of signal to noise that prevents post-processing and accurate analysis of the data. Reducing the number of projections acquired per tomography while keeping slightly longer exposure times can also increase the TPS that can be collected, but again, can lead to degradation of the data quality (although this may be preferable with the latest iterative reconstruction algorithms, see below). The acceptable limit of quality reduction must be defined on a case by case basis.

Typical acquisition schedules showing the link between the beamline, deformation control, and heating is shown in **Figure 4**. This structure was used on the TOMCAT and i12-JEEP beamlines to acquire the data presented below.

We present data collected at TOMCAT for which optimal conditions for high temperature borosilicate melt plus up to 30 vol % rutile crystal cargo were 1s per tomography, collecting 1000 projections per tomography (180° rotation) with an exposure time of 1ms. The data were acquired on the GigaFRoST detector (Mokso et al., 2017), with a 3.7 μm reconstructed voxel (3D equivalent to a pixel) resolution. Up to 150 tomographies were collected in each run. At 1 TPS there was negligible motion blur in the reconstructed data except where coalescence was occurring. Faster rotation is therefore unnecessary for the lower deformation speeds from 0.01 to 1 rotations per minute (rpm) differential speed (equivalent to strain rates of 10^{-3} to 10^{0} s^{-1} at the spindle surface, within the range of those reported for natural systems and experimental studies (Mueller et al., 2011; Vona et al., 2011Pistone et al., 2012; Kendrick et al., 2013; Chevrel et al., 2015; Kolzenburg et al., 2016). To avoid unnecessary post-experiment data processing steps the projections were always collected over the 0–180° arc of the rotation; no data were collected from 180 to 360°. The magnitude of the deformation at the lower strain rates will require less frequent, but not slower, image acquisition. The tomography acquisition rate (TAR) for the data presented (0.15 and 0.3 rpm differential speed) was 0.07/s (1 tomography every 7 rotations, every 14 s, ∼4 tomographies per minute). The data were reconstructed using the standard TOMCAT pipeline.

We also present data collected at i12-JEEP, for which optimal conditions for high temperature borosilicate melt plus rutile crystal cargos were 0.25–0.5 s per tomography (depending on rutile content). We collected 720 projections per tomography (180° rotation) with an exposure time of 150–300 μs. The data were acquired using the MIRO 310M camera using module 3 magnification, giving a 7 μm reconstructed voxel resolution to increase maximum FPS. For the low temperature analog materials acquisition times reduced to 0.125 per tomography, giving a maximum of 8 TPS, and 360 projections per tomography. This enabled imaging of the lower viscosity analogs with deformation speeds of up to 10 rpm differential speed. The projections were always collected over the 0–180° arc of the rotation. The scanning was performed at a minimum sample-detector distance to minimize the phase contrast, which tended to make the bubble bearing samples harder to processes. The gap used depended on the experiment and deformation rate. Data were downloaded between each run, and in each run a maximum of between 43 and 75 tomographies could be collected depending

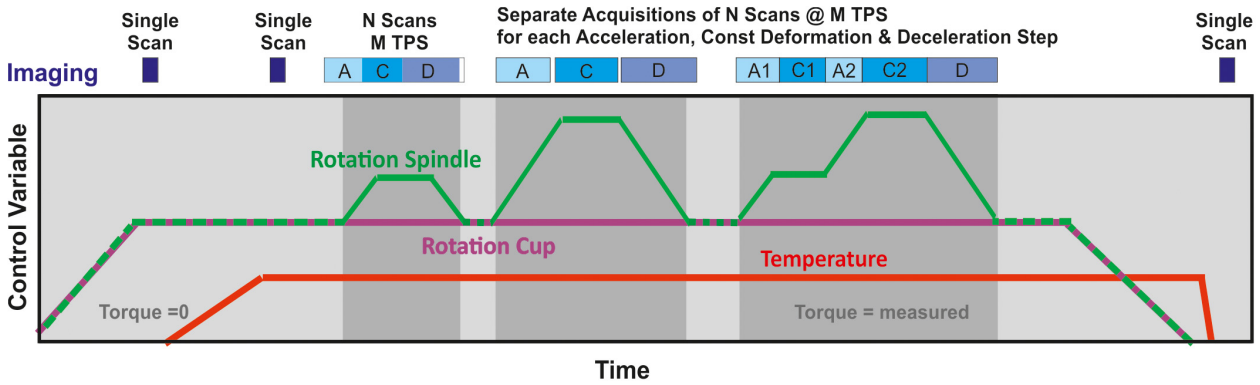

FIGURE 4 | Acquisition schedules typically used with the XRheo, showing how single scans of the sample pre- and post-experiment are collected, and how the timing of the repeated multi-scan acquisitions can fit in a deformation cycle. The full deformation cycle can either be captured as a single scan, or as a series of condition specific data sets for the acceleration (A), constant deformation (C) and deceleration stages (D). The maximum TPS used in an experiment would not usually change, but TAR can be adjusted according to the deformation, as can the total number of tomographies being collected. Some beamlines require time between scans to download the data to network storage. This can be achieved during periods of zero torque (i.e., spindle moving with sample, no deformation) or during extended periods at any of the constant deformation stages. Experiment duration is dependent only on the acquisition capability of the beamline. Heating rates of 20°C/min were used to best control glass behavior (Wadsworth et al., 2019). Cup rotation speed is fixed by image acquisition, and rotation speed of the spindle calculated accordingly with a minimum differential determined by the sensitivity of the rheometer control (0.01 rpm differential at the highest cup rotation speed used in these experiments). The strain rates within the sample are therefore controlled by the spindle rotation speed and the cup and spindle diameters.

on the height of the cropped image. The TAR for the high temperature data presented was 0.07/s (as for TOMCAT) for the same sample deformation conditions. For the low temperature analogs, and faster deformation rates, the maximum TAR was 1/s (1 tomography every 4 rotations, every 1 s). The data were reconstructed using the standard i12 pipeline.

FOUR-DIMENSIONAL OBSERVATIONS: DEFORMATION AND STRAIN LOCALIZATION DURING BUBBLY MAGMATIC FLOW

The focus of this article is technical and methods innovation, and the application of these methods to experiments relevant to volcanological research. Thus, the XRheo system as used here is designed to simulate the conditions of volcanic flow. Detailed analysis of the data and subsequent interpretation will be presented elsewhere. A selection of images and features that show the capability and sensitivity of the method are highlighted in the following sections. Three- and four-dimensional image data are challenging to present on a page; here we show a series of 2D slices through the reconstructed volume along with the relationship of that slice to the data (**Figure 5**). No difference is seen in the general behavior across the height of the sample, and the spindle tip extends well below the field of view. In subsequent images, all 2D slices are the mid-point slice (relative equivalent to the red slice **Figure 5**) and all images have been overlain with a 7 × 7 grid to aid description of the feature locations and visualization of the displacements.

All data have been visualized and processed in Avizo© 2019.2 (Thermo Fisher Scientific™). The data shown have received minimal post processing. The data in **Figures 5–7** have been cropped, down sampled (voxel size now 7.4 μm) and filtered using the Anisotropic Diffusion filter (five iterations) with the default settings as defined by the algorithm from the grayscale distribution. The data in **Figures 8**, **9** have not been processed. These are the raw reconstructed data.

Bubble-Bearing Magma (High Temperature)

Figure 6 shows the evolution and displacement of the bubbles in the middle slice through time. The images are taken from the acceleration phase of the deformation cycle. Deformation starts in the 5th frame collected (#5) and it reaches 0.3 rpm differential speed at #80. The spindle is moving in a clockwise direction faster than the cup, which is stationary in the image reference frame. Three bubbles have been picked out with colored labels (red, blue, yellow). These highlight different behaviors. The red bubble close to the cup (B6, #40) is displaced along a broadly circular path (C7, #47), but as deformation increases, we start to observe an additional component of outward radial displacement (D7, #54). The blue bubbles (E1, E2, #41) undergo coalescence between #42 and 43, then remain nearly stationary for a few frames while the volume around them responds to the change in local stress following the coalescence. The bubble then starts to move and elongate (#42–48) then expands possibly by vertical translation through the plane of the image or by coalescence with bubbles out of the plane of the image, as the bubbles surrounding the blue bubble are not captured. The yellow bubble is almost stationary until frame #46 but then follows a circular displacement path, the bubbles around it showing coalescence and significantly different displacement rates (not the differences in bubble structure in the region between the red and yellow bubbles (#50–56). Substantial microstructural changes are occurring even at the onset of deformation.

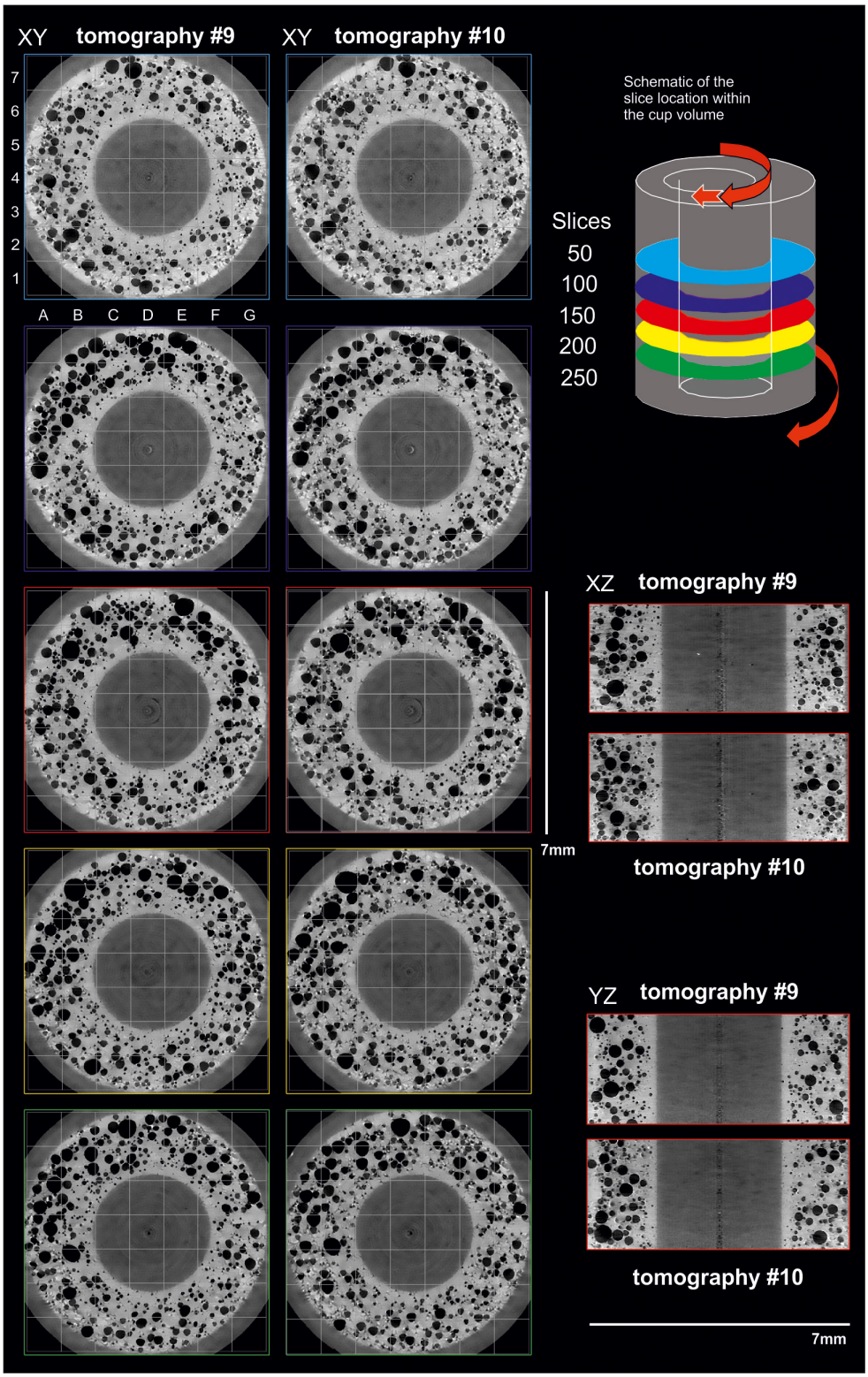

FIGURE 5 | Two-dimensional grayscale slices perpendicular to the rotation axis showing the same slices from the 9th and 10th tomographies at different heights within the sample. The upper right schematic shows the location of the slices within the sample volume: light blue = slice 50, dark blue = slice 100, red = slice 150 (mid-point), yellow = slice 200, green = slice 250, as shown in the image border color. #9 and 10 are at the onset of acceleration when spindle speed = 0.02 rpm clockwise. In the image data, the black regions are bubbles (or air outside the cup), the mid gray is the ceramic of the spindle and cup, and the pale gray is the borosilicate melt. A 7 × 7 gray grid has been overlaid on all XY images to assist in identifying the displacements and the features discussed in the text.

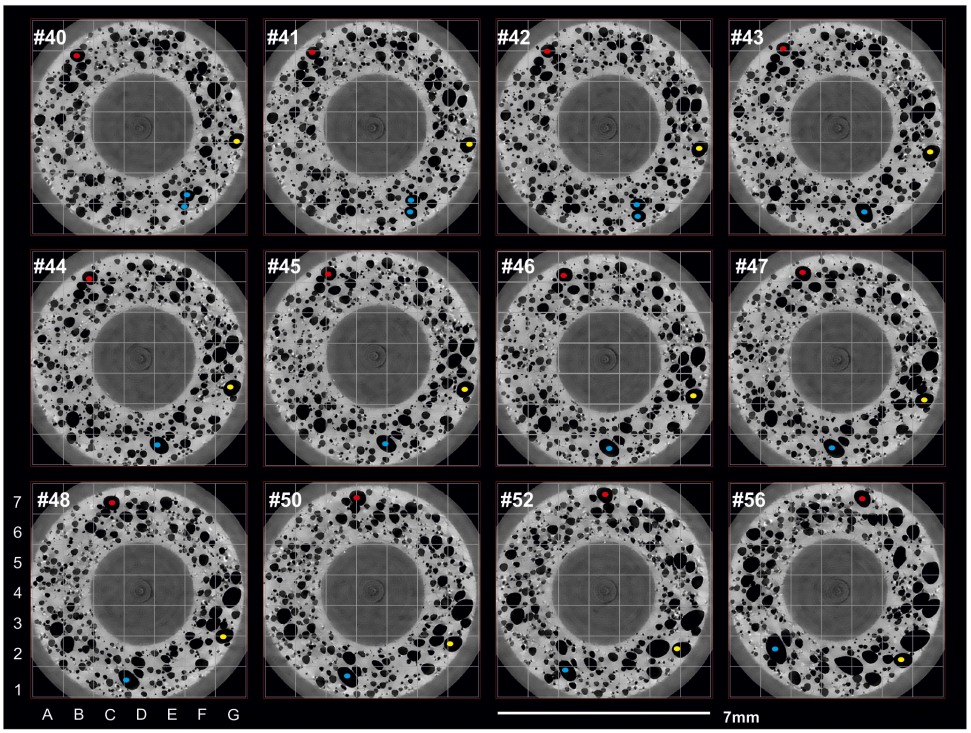

FIGURE 6 | Two-dimensional grayscale slices perpendicular to the rotation axis showing the deformation and coalescence in the mid slice tomographies between #40 and 54 during the acceleration to 0.3 rpm differential rotation. Three bubbles are highlighted (red, yellow, blue) see text for details. Note that bottom row of images shows every other image.

Figure 7 shows the same sample much later in the deformation, during the final part of the acceleration, and the initial stages of the constant rate deformation. The bottom three frames are during the constant deformation stage. Much larger bubbles have formed through coalescence (as seen relative to **Figure 6**), and coalescence continues through the experiment. The higher deformation rate is reflected in the greater elongation of the bubbles, and we see more evidence for shear localization.

Five bubbles have been identified in #60 and tracked through the time series, although the same behaviors can be seen throughout the volume. The blue bubble increases in area from #60 to 65 by movement through the plane of the image and not by coalescence. The blue and red bubbles coalesce, and in #69 we can see the coalesced bubble undergoing relaxation. A higher TAR would have enabled capture of the coalescence events in more detail. The yellow bubble coalesces with the bubble trailing it (not colored) between frames #65 and 66, but does not coalesce with the red, or red-blue bubble pair despite the film thickness between the yellow-red pair and the red-blue pair being similar and tall three bubbles being close in volume. The green and pink bubbles are at the same radial distance but are traveling at different speeds, although both are traveling faster than the yellow-red-blue bubble train. The green bubble "catches up" to the pink, and then both approach a third bubble of similar size and radial position that is moving at an even slower rate. Throughout the volume we can see short lived apparent slip surfaces developing, and the formation of a "nested annular" structure.

Similar to the yellow-red-blue bubble train, two of the three large bubbles in C1, D1, and E1 at #60 coalesce between #62 and 63, but despite having a very thin film between them, do not coalesce until the sample moves from the accelerating to the constant deformation stage. These bubbles are in much closer contact than the red-blue pair that undergo coalescence (#68–70). Many of the bubbles also show deformation that gives an apparent rotation inward toward the spindle, and in some instances the bubbles develop a concave geometry on the spindle-facing bubble surface.

The 2D time series data displayed in **Figures 6**, **7** demonstrate how much deformation can occur at even low strain rates and low total strain. No coalescence was observed when the sample was left undeformed over the same timescales. The bubble number and bubble size distribution at the start of the constant deformation (e.g., #84, **Figure 7**) is significantly different than at the start of the experiment (cf. **Figure 6**). Images from later during the constant deformation continue to show coalescence and elongation throughout the experiment.

This sample will be used to illustrate the more complex quantitative methods applied to the XRheo data set (see section "Quantifying Displacements and Heterogeneity in Flowing Magma").

Three-Phase Magma (High Temperature)

An example of the complexity in 3-phase (melt + crystals + bubbles) deformation can be seen in

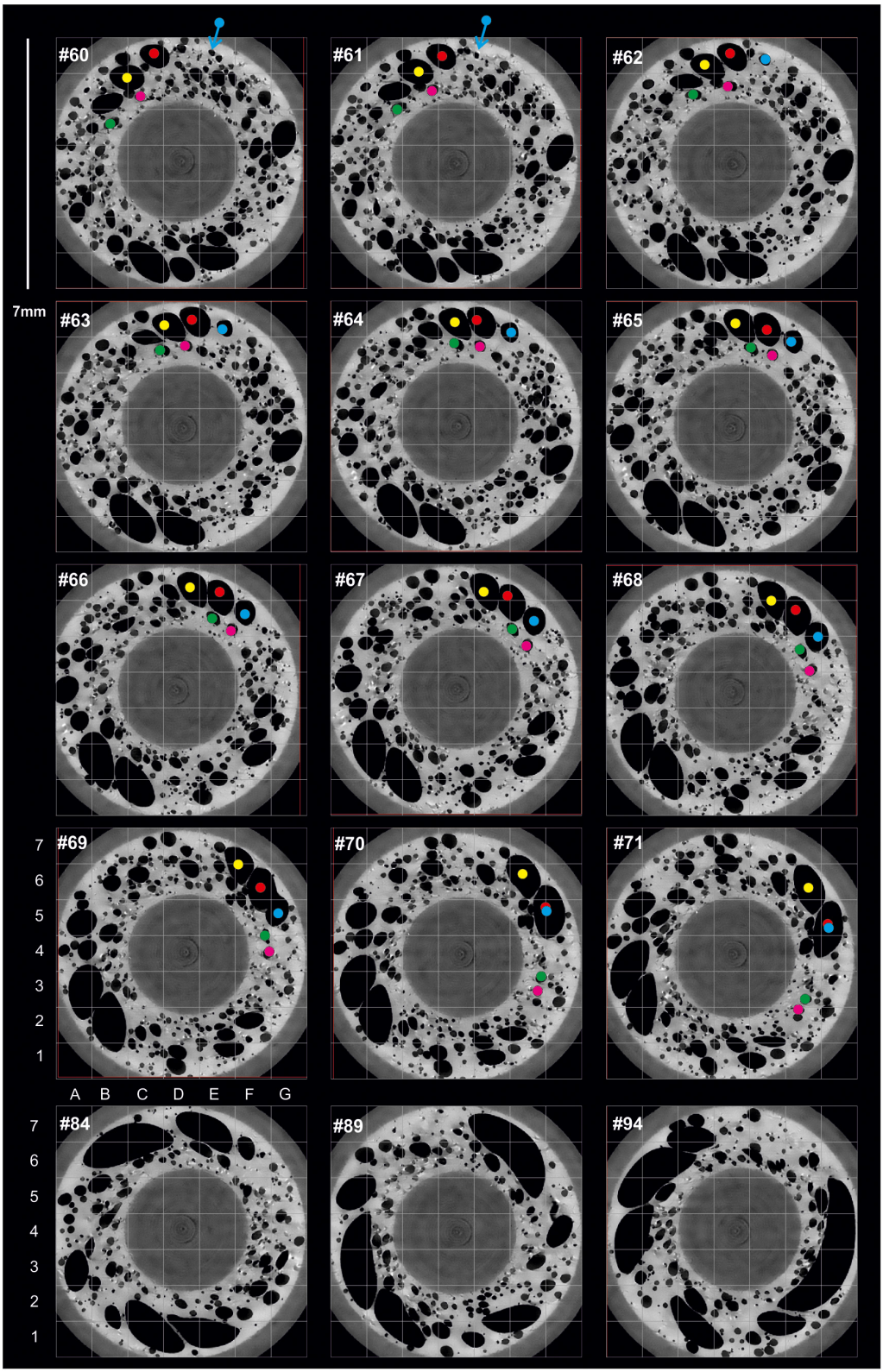

FIGURE 7 | Two-dimensional grayscale slices perpendicular to the rotation axis showing the deformation and coalescence in the mid slice tomographies between #60 and 94 during the end of acceleration and the start of steady state deformation at 0.3 rpm (#80 onward). Five bubbles are highlighted (red, yellow, blue, green, pink) see text for details. Note that the bottom row shows every 5th tomography over the initial part of the constant deformation.

Figure 8. This sample contains a 30 vol % volume crystal load. In this small subset of the acceleration phase, the spindle has accelerated to approximately half the final differential speed of 0.07 rpm. Translation and rotation of crystals is apparent throughout the volume, and the bubbles are both more highly deformed, and undergoing less coalescence than in the crystal-free, bubble-bearing magma (**Figures 6**, **7**). The high density of the rutile grains causes some beam hardening and minor streak artifacts visible in some parts of the data. The formation, deformation, and breaking of chains of crystals can be seen. In the region surrounding B6 and C6, crystals are "rolled" along (migrate with the bubble and show some rotation) one surface of the bubble while the crystals on the opposite surface remain unaffected.

Low Temperature Analog (Room Temperature)

Low temperature analogs are widely used to allow more systematic testing of parameter space, and they often allow more control in the sample preparation or exploration of systems that are unstable in laboratory conditions. The XRheo has been tested with the Canon N2700000 high viscosity standard mineral oil, working at higher deformation rates than used for the magmatic samples above. The data presented in **Figure 9** show a short part of a steady state 5 rpm differential speed deformation step within a longer experiment. These data do show a small and variable amount of motion blur, but this does not prevent qualitative and some quantitative analysis. Like in section "Three-Phase Magma (High Temperature)", this sample has 30 volume % crystals, but the lower viscosity of the sample and the more irregular shapes of the olivine crystals allow observation of crystal rotations. Strain localization is observed but it is generally less focused and less long-lived than seen in the magmatic samples.

QUANTIFYING DISPLACEMENTS AND HETEROGENEITY IN FLOWING MAGMA

The spatial heterogeneity within magma and the highly dynamic (e.g., changes in crystal and bubble fraction, melt viscosity) nature of the system during storage, transport, and eruption makes it extremely challenging to understand how the microstructural evolution effects the macroscopic properties. Understanding this control is the objective of many experiments in the volcanic and magmatic studies that

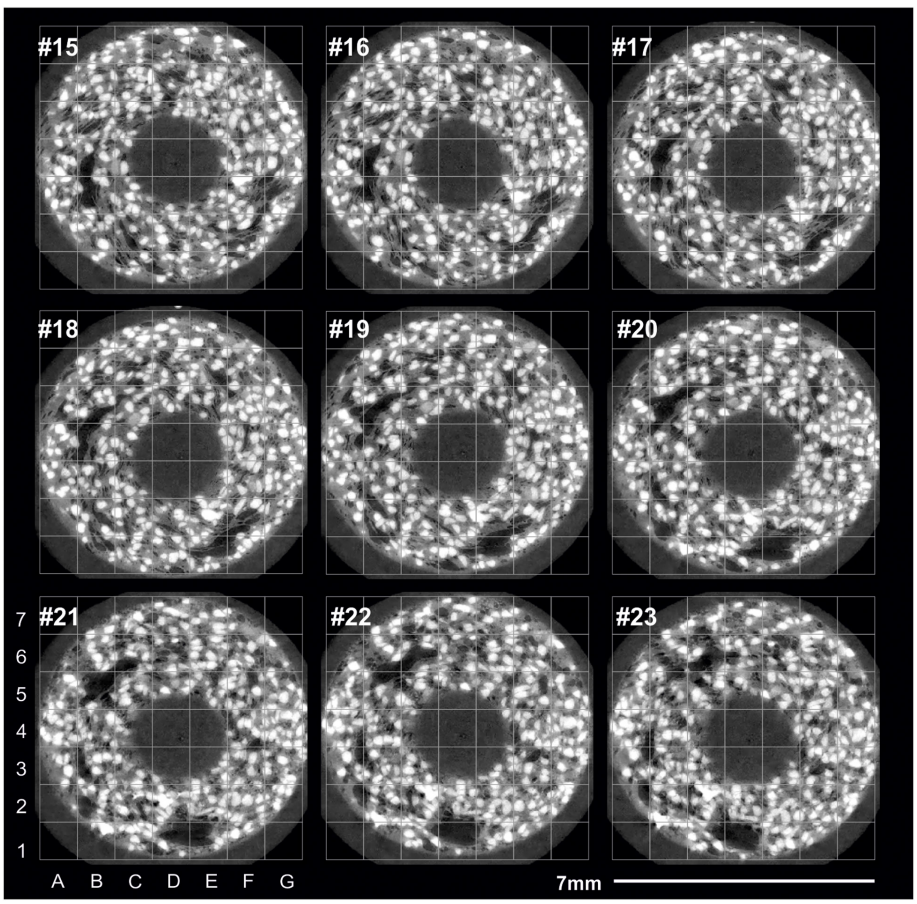

FIGURE 8 | Two-dimensional grayscale slices perpendicular to the rotation axis showing the deformation and coalescence in a selection of slices through a three-phase system. The sample was sintered from the same glass bead pack with 30% rutile crystals. See text for discussion.

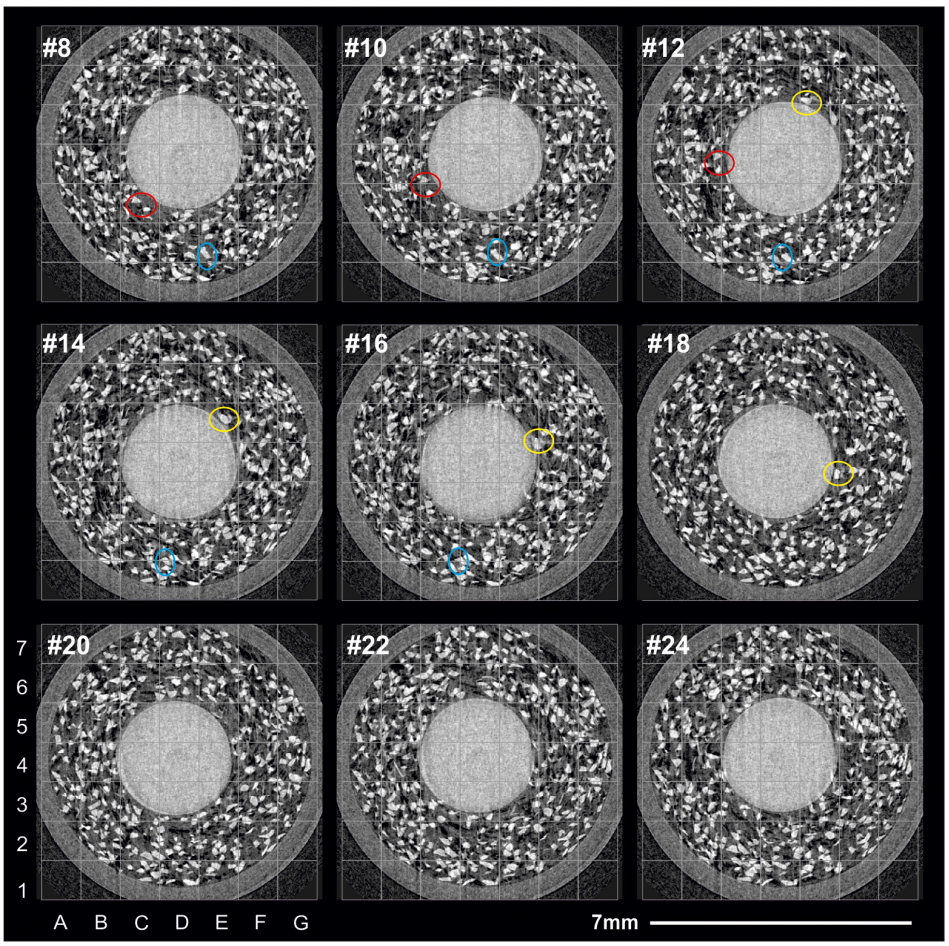

FIGURE 9 | Two-dimensional grayscale slices perpendicular to the rotation axis showing the deformation and coalescence in a selection of slices through a low temperature analog system. N2700000 + 30% by volume olivine crystals. See text for discussion. The red, yellow and blue circles show examples of specific crystals and crystal clusters that can be tracked between frames. Note that rotation of crystals and translation out of the plane of the image makes 2D only tracking challenging.

work to quantify how features move, how deformation is accommodated, how bubbles and crystals interact, and how textures evolve through time. Ultimately, many of the key magmatic and volcanic processes we wish to understand, such as mobilization, mixing, localization, flow, degassing, fragmentation, welding, and many more, are all controlled by the microstructure (and how it is changing) at the time that the process is operating.

Understanding these processes therefore requires thorough *in situ* analysis while those processes are operating under realistic conditions. The experiments presented here focus on using the XRheo to understand bubble deformation, flow localization, and bubble interactions during magmatic flow, focusing on the processes of coalescence and degassing. The data show the processes occurring, but if these data are to be used to build models to predict real world behaviors, a quantitative understanding of the microphysics of the evolving magma is needed. Here we use the 4D XRheo XCT data to develop a new implementation of recently developed Digital Volume Correlation (DVC) algorithms that enable the local displacements and strains to be calculated and the causes and consequences of the structural and rheological heterogeneity within samples to be quantified. DVC is an optical flow-based image matching technique that can measure displacement and strain fields between two 3D image datasets and can measure displacements smaller than the voxel size (Bay, 2008; Tozzi et al., 2014; Hild et al., 2016; Sloof et al., 2016; Buljac et al., 2018).

Different DVC Approaches

Here we apply a novel DVC approach to the bubble bearing magma discussed in section "Bubble Bearing Magma (High Temperature)" and shown in **Figures 6**, **7**.

The established "local" subset-based DVC approach divides the reference and the deformed images into smaller volumes that are then individually correlated (Bay et al., 1999; Smith et al., 2002; Madi et al., 2013; Buljac et al., 2018). This method generally yields displacement fields with small random errors (high

precision) but high systematic errors (low accuracy) because the sub-volumes are treated independently and there is a loss of displacement continuity at the boundaries. The more recently developed "global" DVC approach assumes that a measured displacement field is continuous, and so yields more accurate and robust results close to the solution, but this approach is more computationally costly. Here we employ a protocol which uses the "local" approach to define an initial displacement field, which is then used as the initialization for the more robust global DVC.

Although the data are collected over the same angular interval, and are therefore pre-registered, the location of the cup and spindle drift slightly within the image volume over the time series. To interpret the displacement field within the melt, this rigid body motion was removed using the *Registration* algorithm in Avizo©, prior to running a DVC analysis. A single melt volume was then defined and this "sample mask" used to both remove the cup and spindle from the images and generate the 3D meshes that define the individual elements for the DVC.

Quantitative Analysis of Displacements on XRheo 4D Data

The overall workflow is presented in **Figure 10**. First, the "local" approach was applied to a simple cubic mesh defined within the DVC algorithm in Avizo©. The DVC algorithm them calculates the displacement field, and this is used to initiate the "global" approach across a coarse tetragonal mesh [Global Course (G_C) mesh elements 79 voxels] generated from the sample mask (see **Figure 10** for detail of the steps undertaken in this method). The displacement field output from that correlation (global course mesh, images 1 and 2 = $G_C{}^{1-2}$) is then used as the initialization for $G_C{}^{2-3}$. The output from $G_C{}^{2-3}$ used as the initialization for $G_C{}^{3-4}$ and on through the entire time series (**Figure 10**).

The heterogeneity observed by this process suggests that the G_C mesh was smoothing some of the smaller scale displacements, and so a second iteration using a finer mesh (G_M) with mesh elements of 55 voxels was then completed. Here $G_C{}^{1-2}$ was used to initialize $G_M{}^{1-2}$, and then $G_M{}^{1-2}$ used to initialize $G_M{}^{2-3}$ and on through the data (**Figure 10**). Throughout this process, the G_C and G_M outputs are broadly similar and show no evidence for divergence. At several time points the $G_M{}^{X-(X+1)}$ generated from $G_M{}^{(X-1)-X}$ was compared to that generated from $G_C{}^{X-(X+1)}$. While there are some small differences, the overall variations in the displacement field are small, confirming the validity of applying the G_M (**Figure 10**). At the end of the processing, the DVC outputs were rendered as a volume color wash over the grayscale volumes. This comparison showed that some small-scale deformations were still not captured. A finer global mesh (G_F) iteration with mesh elements of 35 voxels was then completed (up to #69 when the displacements become too large for the finer mesh and the data diverge). Finer meshes were not generated as these would generate a high number of mesh elements without textural information preventing accurate tracking. For each DVC output the displacement fields can be visualized as a 3D color wash volume, or as a vector field (**Figures 11**, **12**) shown here with the vectors color coded by displacement magnitude. Tangential and radial magnitudes can also be extracted.

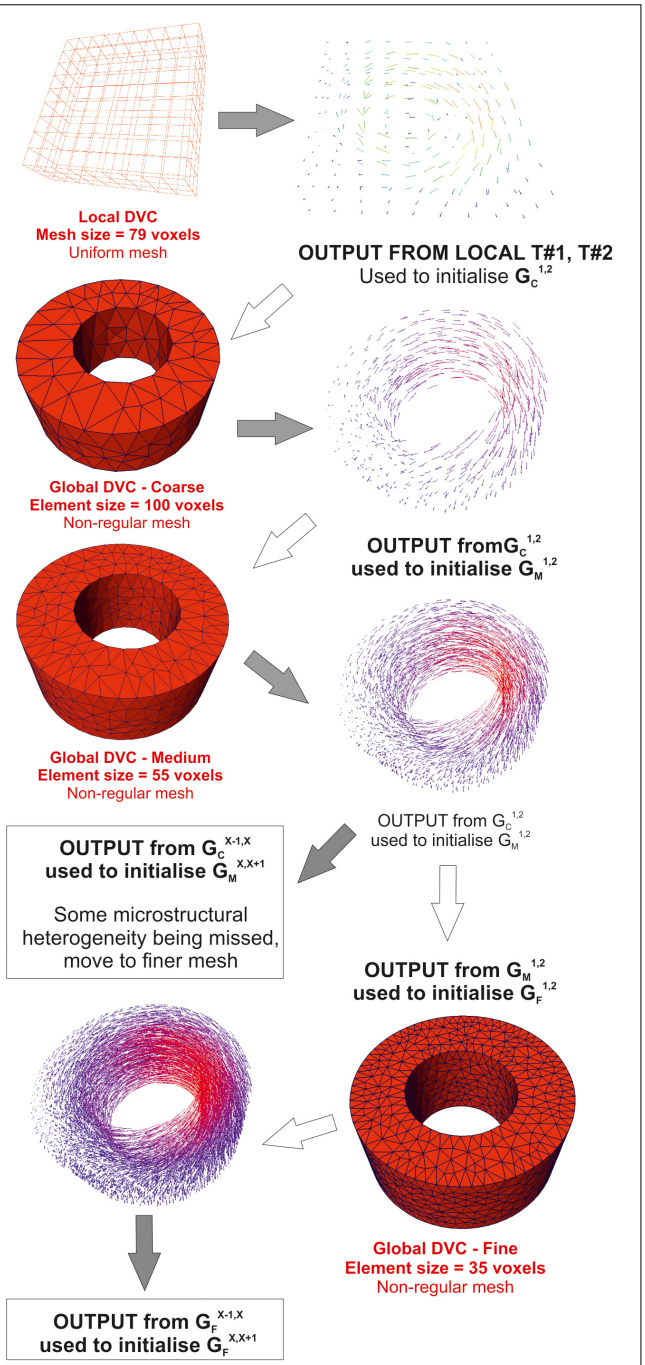

FIGURE 10 | The local-global integrated DVC approach showing how the outputs from one iteration and scale can be used to initiate the calculation at the next spatial or temporal step. G, global; C, coarse; M, medium; F, fine. The size of the regular and irregular meshes should be adjusted to the sample structure and material texture under consideration. The meshes shown were those applied to the experiment discussed in section "Bubble Bearing Magma (High Temperature)" and shown in **Figures 6**, **7**.

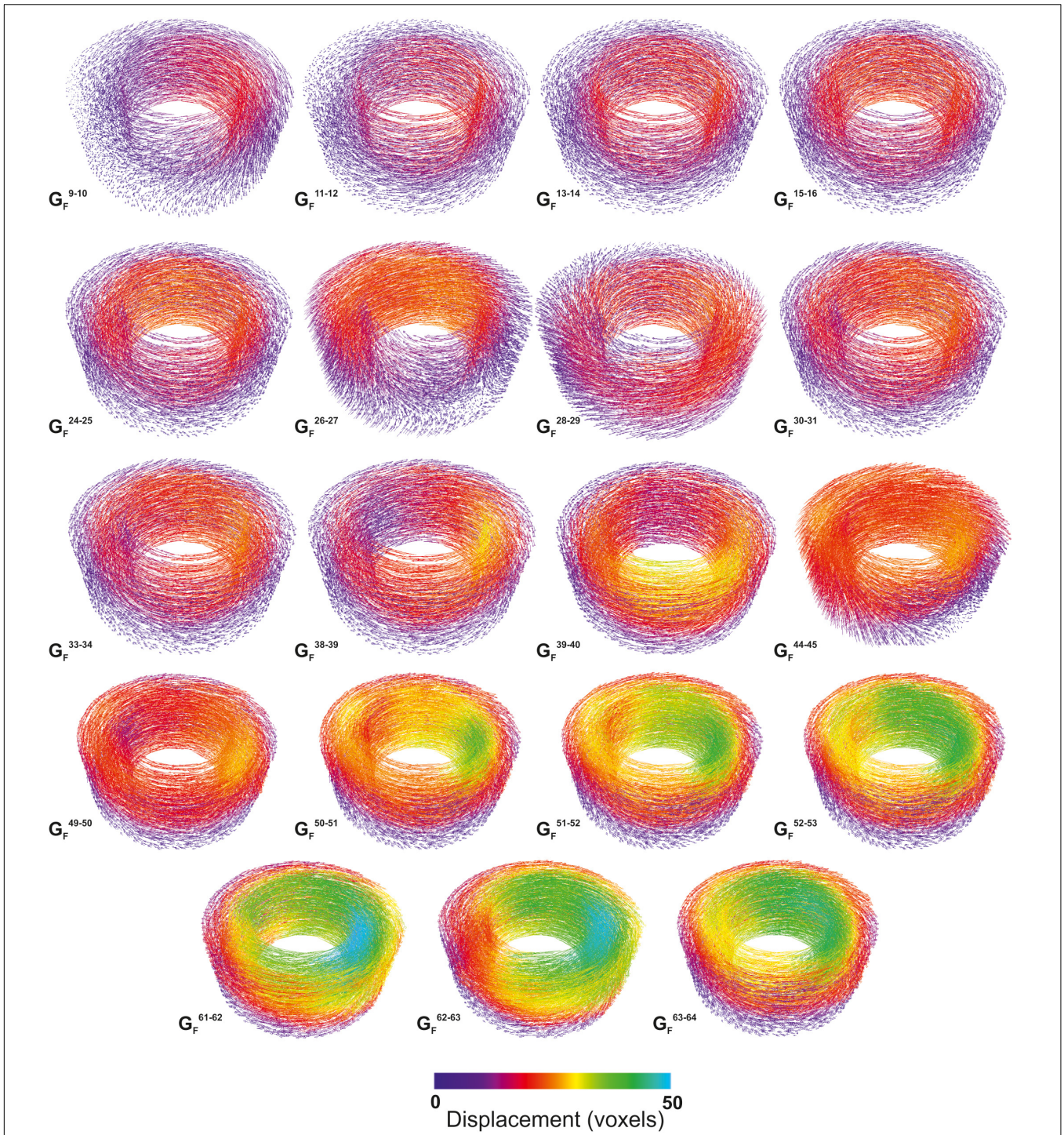

FIGURE 11 | DVC outputs from the start of the acceleration phase. Note the discontinuous time steps shown. Workflow for iterations as shown in **Figure 10**. The outputs shown were those generated on the experiment discussed in section "Bubble Bearing Magma (High Temperature)" and shown in **Figures 6**, **7**.

Observing Heterogeneity in Rheological Test Samples

During the initial acceleration (G_F^{8-9}–G_F^{15-16}, **Figure 11**) we see a gradual radial propagation of the displacement field. As the deformation continues, we start to see the development of heterogeneity in the displacement field. Initially the heterogeneity is angular, with some sectors showing faster motion than others, but as this develops some vertical variability also appears. At this point in the series (see also **Figure 6**), coalescence and bubble deformation are limited, but are observed. The sectoral nature

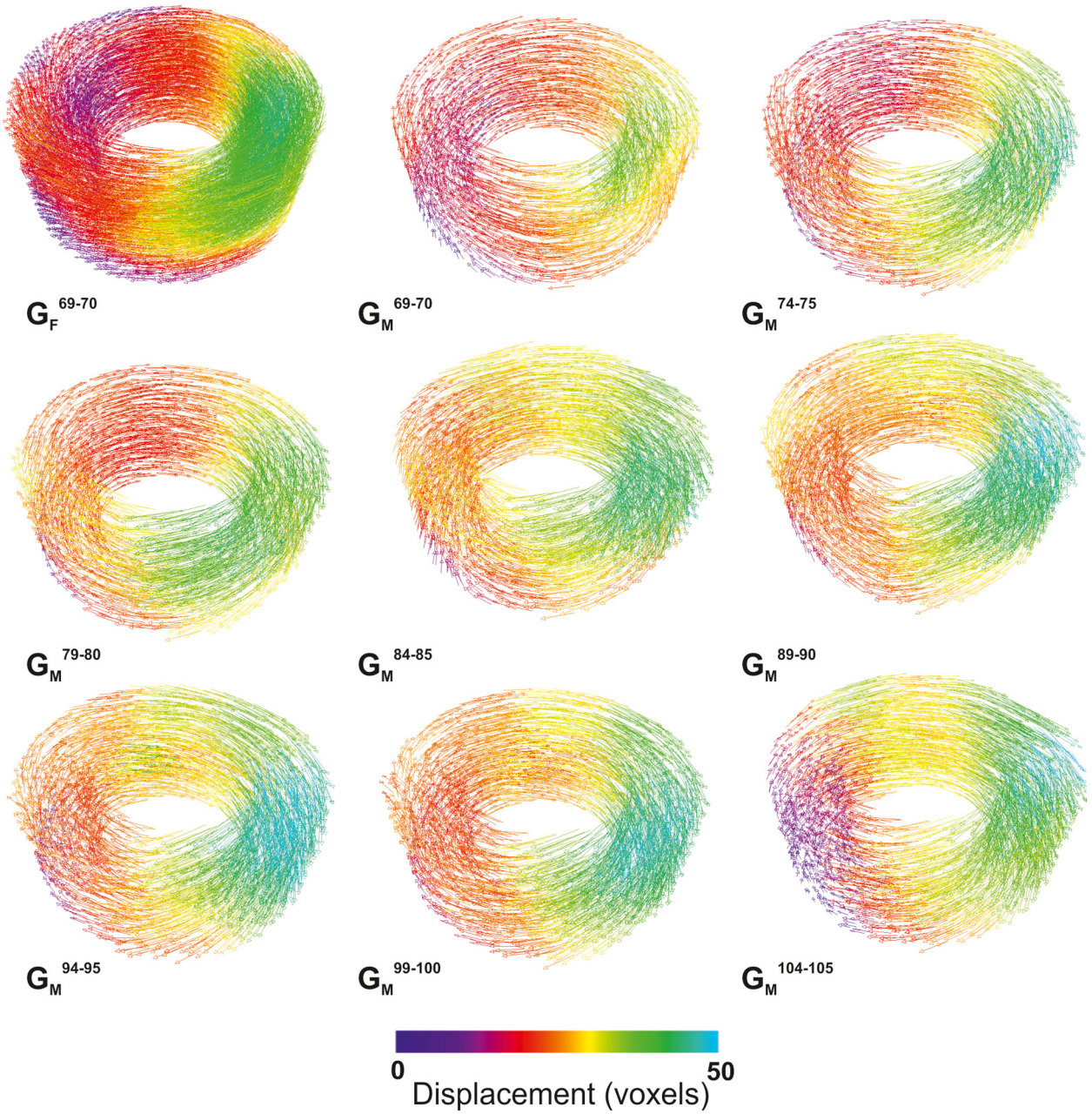

FIGURE 12 | DVC outputs from the end of the acceleration and constant deformation phase. Note the discontinuous time steps shown. The first two frames show the last G_F and the equivalent G_M. After this the large displacements meant the G_F iteration was unnecessary. Workflow for iterations as shown in **Figure 10**. The outputs shown were those generated on the experiment discussed in section "Bubble Bearing Magma (High Temperature)" and shown in **Figures 6**, **7**.

of the heterogeneity might suggest that the cause may be a misalignment between the rotation axes of the spindle and the cup. However, if this was the case, we should expect the sector showing the maximal deformation to rotate with the spindle, tracking the narrowest gap distance. This is not observed, and the region showing the greatest displacement shows no systematic larger scale migration. In fact, the high deformation region is generally fixed at one part of the sample volume or fluctuates between 3 o'clock and 12 o'clock regions (as the data are displayed in **Figures 11**, **12**). From G_F^{25-26} we start to see an increase in the magnitude of the displacement in two regions. From G_F^{38-39} there is a rapid increase in displacement in one sector of the sample, with a noticeable lack of a radial position dependence on the displacement speed. Once coalescence becomes more common in the volume from about G_F^{45-46} onward (see also ∼#45 onward, **Figure 6**), we see another rapid increase in the magnitude of the displacements. There is substantial fluctuation however, especially from G_F^{48-49} to G_F^{52-53} and G_F^{60-61} to

G_F^{63-64} part of the series, where we see a maximum displacement (∼50 voxels) well away from the spindle. This displacement is substantially higher than the velocity of the spindle surface, and corresponds to the major coalescence event shown in #61–64 (**Figure 7**).

As the 0.3 rpm differential speed is reached at #80 (**Figure 7**), the system might be expected to equilibrate and the displacements to become more homogenously distributed. However, the ongoing coalescence and the established heterogeneity and focused displacements continue (**Figure 12**). There is little change immediately after the acceleration ceases (#79–90) despite the ongoing coalescence events and changes in the bubble distribution that can be seen (**Figure 7**). Also, at this time we start to see larger local decelerations in the region opposite the highest displacements (e.g., #69, 74, 104) suggesting there may be some far field effects becoming visible once the deformation rate is constant. Clearly the data are showing an extremely complex behavior and suggest that any bulk viscosity measurement on this sample may contain contributions that are intrinsically tied to the heterogeneity and localization that is present.

The DVC approach presented here has been successfully applied to all three sample types presented in this study (crystal-bearing, bubble-bearing, and three-phase), and has the potential to be useful for most *in situ* magmatic analysis, provided that the geometrical changes (bubble deformation) and displacements are not extreme between the frames being correlated. Better understanding of rotational crystal motions is achieved with non-spherical particles. More traditional versions of the DVC method have been used in other geological systems (e.g., McBeck et al., 2018) but the approach taken here could also make the approach invaluable to experimental volcanology as well, where heterogeneity and local environment can be critical controls on behavior.

BROADER CHALLENGES AND FUTURE DIRECTIONS

There are always improvements to be made, and in tomographic analysis, better quality data can significantly reduce processing and analysis duration. In these experiments motion blur still exists in some regions of some images, showing that we may need yet faster FPS and similar overall experiment durations (meaning an increase in data volume) if we want to investigate behaviors higher strain rates or lower viscosities.

Faster exposure times result in less motion blur, but will generate projection data with high levels of noise, making data harder to analyses. Advances in iterative reconstruction methods can provide increased data quality from reduced number of projections, and therefore mitigate this challenge. Methods that use "structural prior" to enhance the reconstruction processes can yield data of comparable quality from 10 times fewer projections. These methods take a high spatial-low temporal resolution data set collected prior to the dynamic experiment to provide additional structural information and tune the reconstruction of the under-sampled (low projection numbers) and high noise data from the high TPS part of the experiment (Kazantsev et al., 2014, 2015). Where areas of the image volume remain largely unchanged (e.g., fluid flow in porous media experiments and some crystallization experiments) data from non-changing areas in the high TPS part of the experiment can be used instead of that from a high spatial-low temporal resolution data (Eyndhoven et al., 2015). Where contrasts are high and the features of interest are large relative to the voxel size, this could result in data of sufficient quality for quantitative analysis from as little as 18 projections (Eyndhoven et al., 2015). Applying iterative algorithms can be used to achieve three objectives: (i) increase data quality for a given FPS/projection number acquisition protocol, (ii) enable higher FPS to reduce motion blur and experiments with higher strain rates, or (iii) allow longer duration experiments where there are hardware-based limitations on the total number of projections that can be acquired. These iterative methods are becoming routinely available at high-speed imaging beamlines, but may not improve data quality in all experimental scenarios.

Another way to improve data quality is to increase the signal-to-noise in the projection data, usually by increasing the X-ray flux reaching the detector. Many synchrotron facilities are planning or implementing upgrades to existing infrastructure that will deliver this, with increasing beam brilliance (X-ray flux) key among many of the development plans. More brilliance could be used to increase the TPS rate maintaining current data quality or to obtain better quality data for the same TPS.

The experiments shown here are of shorter duration than some *ex situ* laboratory rheological tests and shorter than is necessary for rheological analysis during crystallization, so longer experiments may be needed. DVC algorithms and other particle tracking techniques require relatively small displacements between images, so we cannot achieve longer experimental durations by reducing the TAR. More data are required. Even with current data collection protocols, high speed acquisition can generate vast amounts of data (TB/day), especially when the processes under investigation are poorly understood. Experiments need to start collecting images before the start of the processes, and in some cases the occurrence of the processes themselves are hard to identify until after the reconstruction step. This demonstrates the need to reconstruct ever increasing amounts of data before leaving the synchrotron, the need to transfer ever larger data volumes, and the need to develop more automated processing algorithms.

The final challenge to *in situ* experiments is always in the amount of post processing and data analysis required to interpret the results. The DVC approach applied here removes the need for segmentation or labeling of individual phases, particles, or bubbles, but in most experiments, there will be a need for an additional image processing workflow to extract quantitative information. Rapid advances in automated and machine learning algorithms for application to tomographic image analysis, but these can still be challenging to apply to low contrast geological materials and can be more difficult to implement when changes in sample structure (e.g., clustering of crystals, growth of bubbles) affect local or bulk attenuation. Further work in this area is

needed before fully automated image processing workflows can be achieved on most geological materials.

The data presented here showcase the capabilities we currently possess, and shows how real-time *in situ* tomography can provide useful and extensive information about volcanic and magmatic processes of flow and deformation. The data here are far from optimal by the standards typical for high (spatial) resolution laboratory or synchrotron acquisition but are still more than sufficient to perform complex quantitative analysis of dynamic processes. As multi-scale and correlative imaging techniques (linking to other 2D, 3D, and 4D imaging modalities) become more widely available, the incorporation of data from phase contrast imaging (grain boundaries/crystallization), k-edge imaging (chemical information), simultaneous CT and XRD, and diffraction imaging and diffraction contrast tomography will continue to increase the detailed understanding of microstructural evolution that can be extracted from such *in situ* studies. This, coupled with the continued widening of laboratory scanner access, a diversification and expansion of the *in situ* apparatus available within the community, and plans for beams of higher brilliance at several of the European synchrotron facilities in years to come, means the future of *in situ* magmatic and volcanic flow research looks bright.

CONCLUSION

The XRheo is one example of the rapid development of new experimental apparatus that has been driven by the expansion of *in situ* and real-time X-ray computed tomography. When coupled to the Pele furnace, it enables *in situ* observation of the internal microstructural evolution of samples during rheological experiments. By using the appropriate analog, synthetic, and natural materials as experimental charges and operating under a range of temperature and deformation conditions, it allows us to interrogate the processes occurring in magmas moving in the shallow crust and on the Earth's surface. Studies assessing the microstructural controls on rheological behaviors and the critical microstructural conditions that enable, accelerate, or arrest flow are now being undertaken. By implementing the latest DVC methods to allow quantitative assessment of displacements and strains and the heterogeneity in the displacement fields, we provide an exemplar workflow for the level of quantification that can now be achieved. These tools provide the ability to significantly improve our understanding of the key processes that control the behavior of natural magmas. Specifically, they permit the quantitative understanding of the microstructural changes *in situ* while also recording traditional rheological data. This gives us the ability to define, for the first time, how dynamic microstructures (bubble volume and geometry, bubble coalescence or collapse, changes in local crystal content, growth or dissolution of crystals, and the formation and fragmentation of load-bearing crystal networks and other localization features) affect key rheologically controlled processes such as percolation, mobilization, flow, degassing, and fragmentation.

While computed tomography has become an established technique in earth sciences, it is the recent advances at synchrotron beamlines and the environmental cells and apparatus used to perform *in situ* experiments that now allows the volcanology community to exploit the technique to its maximum potential: tackling some of the greatest challenges in the field and addressing the dynamics of magmatic processes in new ways.

DATA AVAILABILITY STATEMENT

All datasets for this manuscript are not publicly available at this time because they are the subject of other manuscripts in preparation. Once published they will be made available through the NERC National Geoscience Data Centre. Access prior to further publication will be granted where possible, and requests should be directed to KD, katherine.dobson@strath.ac.uk.

AUTHOR CONTRIBUTIONS

KD developed the XRheo and the Pele Furnace, managed the beamline experiments, the data acquisition, and analysis, and led the writing of manuscript. All authors (listed alphabetically) contributed to acquiring and processing the data on which this work is based, contributed to the article and approved the submitted version.

FUNDING

KD acknowledges support from NE/M018687/1 & NE/M018687/2 and ERC 2009 ADV Grant 247076 (EVOKES). DD acknowledges the support of ERC 2009 ADV Grant 247076 (EVOKES) and ERC 2018 ADV Grant 834225 (EAVESDROP) during the conduction of these experiments and the preparation of the manuscript, respectively. RC, JK, YL, JS, and FA were supported by ERC 2012 StG Grant (SLiM) 406388. SK acknowledges the support of H2020 Marie Skłodowska-Curie Fellowship 795044 (DYNAVOLC).

ACKNOWLEDGMENTS

We acknowledge the Paul Scherrer Institut, Villigen, Switzerland for provision of synchrotron radiation beamtime at the TOMCAT beamline X02DA of the SLS under proposal 20150413, and Diamond Light Source for time on i12-JEEP under proposal EE15898; and thank all the staff at both beamlines who provided additional support to the beamline activity. We are also grateful to Severn Thermal Solution and everyone who advised and helped with the design and construction of the technologies presented in this work.

REFERENCES

Arzilli, F., La Spina, G., Burton, M. R., Polacci, M., Le Gall, N., Hartley, M. E., et al. (2019). Magma fragmentation in highly explosive basaltic eruptions induced by rapid crystallization. *Nat. Geosci.* 12, 1023–1028. doi: 10.1038/s41561-019-0468-6

Arzilli, F., Polacci, M., Landi, P., Giordano, D., Baker, D. R., and Mancini, L. (2016). A novel protocol for resolving feldspar crystals in synchrotron X-ray microtomographic images of crystallized natural magmas and synthetic analogs. *Am. Mineral.* 101, 2301–2311. doi: 10.2138/am-2016-5788

Bai, L., Baker, D. R., and Rivers, M. (2008). Experimental study of bubble growth in *Stromboli basalt* melts at 1 atm. *Earth Planet. Sci. Lett.* 267, 533–547. doi: 10.1016/j.epsl.2007.11.063

Baker, D. R., Brun, F., Mancini, L., Fife, J. L., LaRue, A., O'Shaughnessy, C., et al. (2019). The importance of pore throats in controlling the permeability of magmatic foams. *Bull. Volcanol.* 81:54.

Baker, D. R., Brun, F., O'Shaughnessy, C., Mancini, L., Fife, J. L., and Rivers, M. (2012). A four-dimensional X-ray tomographic microscopy study of bubble growth in basaltic foam. *Nat. Commun.* 3:1135.

Bay, B. K. (2008). Methods and applications of digital volume correlation. *J. Strain Anal. Eng. Design* 43, 745–760.

Bay, B. K., Smith, T. S., Fyhrie, D. P., and Saad, M. (1999). Digital volume correlation: three-dimensional strain mapping using X-ray tomography. *Exp. Mech.* 39, 217–226. doi: 10.1007/bf02323555

Berg, M. T., Bromiley, G. D., Butler, I. B., Frost, M., Bradley, R., Carr, J., et al. (2017). Deformation-aided segregation of Fe-S liquid from olivine under deep Earth conditions: implications for core formation in the early solar system. *Phys. Earth Planet. Inter.* 263, 38–54. doi: 10.1016/j.pepi.2017.01.004

Buljac, A., Jailin, C., Mendoza, A., Neggers, J., Taillandier-Thomas, T., Bouterf, A., et al. (2018). Digital volume correlation: review of progress and challenges. *Exp. Mech.* 58, 661–708. doi: 10.1007/s11340-018-0390-7

Campagnola, S., Vona, A., Romano, C., and Giordano, G. (2016). Crystallization kinetics and rheology of leucite-bearing tephriphonolite magmas from the Colli Albani volcano (Italy). *Chem. Geol.* 424, 12–29. doi: 10.1016/j.chemgeo.2016.01.012

Caricchi, L., Burlini, L., Ulmer, P., Gerya, T., Vassalli, M., and Papale, P. (2007). Non-Newtonian rheology of crystal-bearing magmas and implications for magma ascent dynamics. *Earth Planet. Sci. Lett.* 264, 402–419. doi: 10.1016/j.epsl.2007.09.032

Chevrel, M. O., Cimarelli, C., deBiasi, L., Hanson, J. B., Lavallée, Y., Arzilli, F., et al. (2015). Viscosity measurements of crystallizing andesite from Tungurahua volcano (Ecuador). *Geochem. Geophys. Geosyst.* 16, 870–889. doi: 10.1002/2014gc005661

Cimarelli, C., Costa, A., Mueller, S., and Mader, H. M. (2011). Rheology of magmas with bimodal crystal size and shape distributions: insights from analog experiments. *Geochem. Geophys. Geosyst.* 12:3606.

Colombier, M., Wadsworth, F., Scheu, B., Dobson, K., Caceres, F., Vasseur, J., et al. (2018). "The role of crystals on vesiculation and outgassing during volcanic eruptions: insights from 4D synchrotron experiments," in *Proceesdings of the EGU General Assembly Conference Abstracts*, (Vienna: EGU General Assembly), 639.

Di Genova, D., Cimarelli, C., Hess, K.-U., and Dingwell, D. B. (2016). An advanced rotational rheometer system for extremely fluid liquids up to 1273 K and applications to alkali carbonate meltsk. *Am. Mineral.* 101, 953–959. doi: 10.2138/am-2016-5537ccbyncnd

Dobson, K. J., Coban, S. B., McDonald, S. A., Walsh, J. N., Atwood, R. C., and Withers, P. J. (2016). 4-D imaging of sub-second dynamics in pore-scale processes using real-time synchrotron X-ray tomography. *Solid Earth* 7:1059. doi: 10.5194/se-7-1059-2016

Drakopoulos, M., Connolley, T., Reinhard, C., Atwood, R., Magdysyuk, O., Vo, N., et al. (2015). I12: the joint engineering, environment and processing (JEEP) beamline at diamond light source. *J. Synchrotr. Radiat.* 22, 828–838. doi: 10.1107/s1600577515003513

Eyndhoven, G. V., Batenburg, K. J., Kazantsev, D., Nieuwenhove, V. V., Lee, P. D., Dobson, K. J., et al. (2015). An iterative CT reconstruction algorithm for fast fluid flow imaging. *IEEE Trans. Image Process.* 24, 4446–4458. doi: 10.1109/tip.2015.2466113

Fife, J. L., Rappaz, M., Pistone, M., Celcer, T., Mikuljan, G., and Stampanoni, M. (2012). Development of a laser-based heating system for in situ synchrotron-based X-ray tomographic microscopy. *J. Synchrotr. Radiat.* 19, 352–358. doi: 10.1107/s0909049512003287

Giordano, D., Polacci, M., Longo, A., Papale, P., Dingwell, D. B., Boschi, E., et al. (2007). Thermo−rheological magma control on the impact of highly fluid lava flows at Mt. Nyiragongo. *Geophys. Res. Lett.* 34:6301.

Hanna, R. D., and Ketcham, R. A. (2017). X-ray computed tomography of planetary materials: a primer and review of recent studies. *Geochemistry* 77, 547–572. doi: 10.1016/j.chemer.2017.01.006

Hild, F., Bouterf, A., Chamoin, L., Leclerc, H., Mathieu, F., Neggers, J., et al. (2016). Toward 4D mechanical correlation. *Adv. Model. Simul. Eng. Sci.* 3:17.

Ishibashi, H., and Sato, H. (2007). Viscosity measurements of subliquidus magmas: *Alkali olivine* basalt from the Higashi-Matsuura district, Southwest Japan. *J. Volcanol. Geother. Res.* 160, 223–238. doi: 10.1016/j.jvolgeores.2006.10.001

Kareh, K. M., Lee, P. D., and Gourlay, C. M. (2012). In situ, time-resolved tomography for validating models of deformation in semi-solid alloys. *IOP Conf. Ser. Mater. Sci. Eng.* 33:012037. doi: 10.1088/1757-899x/33/1/012037

Kazantsev, D., Ourselin, S., Hutton, B. F., Dobson, K. J., Kaestner, A. P., Lionheart, W. R. B., et al. (2014). A novel technique to incorporate structural prior information into multi-modal tomographic reconstruction. *Inverse Probl.* 30:065004. doi: 10.1088/0266-5611/30/6/065004

Kazantsev, D., Van Eyndhoven, G., Lionheart, W. R. B., Withers, P. J., Dobson, K. J., McDonald, S. A., et al. (2015). Employing temporal self-similarity across the entire time domain in computed tomography reconstruction. *Philos. Trans. Ser. A Math. Phys. Eng. Sci.* 373:20140389. doi: 10.1098/rsta.2014.0389

Kendrick, J. E., Lavallée, Y., Hess, K. U., Heap, M. J., Gaunt, H. E., Meredith, P. G., et al. (2013). Tracking the permeable porous network during strain-dependent magmatic flow. *J. Volcanol. Geother. Res.* 260, 117–126. doi: 10.1016/j.jvolgeores.2013.05.012

Kolzenburg, S., Di Genova, D., Giordano, D., Hess, K. U., and Dingwell, D. B. (2018a). The effect of oxygen fugacity on the rheological evolution of crystallizing basaltic melts. *Earth Planet. Sci. Lett.* 487, 21–32. doi: 10.1016/j.epsl.2018.01.023

Kolzenburg, S., Giodano, D., Hess, K. U., and Dingwell, D. B. (2018b). Shear rate-dependent disequilibrium rheology and dynamics of basalt solidification. *Geophys. Res. Lett.* 45, 6466–6475. doi: 10.1029/2018gl077799

Kolzenburg, S., Giordano, D., Cimarelli, C., and Dingwell, D. B. (2016). In situ thermal characterization of cooling/crystallizing lavas during rheology measurements and implications for lava flow emplacement. *Geochim. Cosmochim. Acta* 195, 244–258. doi: 10.1016/j.gca.2016.09.022

Kolzenburg, S., Giordano, D., Di Muro, A., and Dingwell, D. B. (2019). Equilibrium viscosity and disequilibrium rheology of a high magnesium basalt from piton De La Fournaise volcano, La Reunion, Indian Ocean, France. *Ann. Geophys.* 62:218.

Kouchi, A., Tsuchiyama, A., and Sunagawa, I. (1986). Effect of stirring on crystallization kinetics of basalt: texture and element partitioning. *Contribut. Mineral. Petrol.* 93, 429–438. doi: 10.1007/bf00371713

Kudrna Prasek, M., Pistone, M., Baker, D. R., Sodini, N., Marinoni, N., Lanzafame, G., et al. (2018). A compact and flexible induction furnace for in situ X-ray microradiograhy and computed microtomography at Elettra: design, characterization and first tests. *J. Synchrotr. Radiat.* 25, 1172–1181. doi: 10.1107/s1600577518005970

Lamur, A., Lavallée, Y., Iddon, F. E., Hornby, A. J., Kendrick, J. E., von Aulock, F. W., et al. (2018). Disclosing the temperature of columnar jointing in lavas. *Nat. Commun.* 9:1432.

Lavalleie, Y., Hess, K.-U., Cordonnier, B., and Bruce Dingwell, D. (2007). Non-Newtonian rheological law for highly crystalline dome lavas. *Geology* 35, 843–846.

Llewellin, E., Mader, H. M., and Wilson, S. D. R. (2002). The rheology of a bubbly liquid. *Proc. R. Soc. A Math. Phys. Eng. Sci.* 458, 987–1016.

Mader, H. M., Llewellin, E. W., and Mueller, S. P. (2013). The rheology of two-phase magmas: a review and analysis. *J. Volcanol. Geother. Res.* 257, 135–158. doi: 10.1016/j.jvolgeores.2013.02.014

Madi, K., Tozzi, G., Zhang, Q. H., Tong, J., Cossey, A., Au, A., et al. (2013). Computation of full-field displacements in a scaffold implant using digital

volume correlation and finite element analysis. *Med. Eng. Phys.* 35, 1298–1312. doi: 10.1016/j.medengphy.2013.02.001

Maire, E., and Withers, P. J. (2014). Quantitative X-ray tomography. *Int. Mater. Rev.* 59, 1–43.

Marone, F., Schlepuetz, C., Marti, S., Fusseis, F., Velásquez-Parra, A., Griffa, M., et al. (2020). Time resolved in-situ X-ray tomographic microscopy unraveling dynamic processes in geologic systems. *Front. Earth Sci.* 14:346. doi: 10.3389/feart.2019.00346

McBeck, J., Kobchenko, M., Hall, S. A., Tudisco, E., Cordonnier, B., Meakin, P., et al. (2018). Investigating the onset of strain localization within anisotropic shale using digital volume correlation of time-resolved X-ray microtomography images. *J. Geophys. Res. Solid Earth* 123, 7509–7528. doi: 10.1029/2018jb015676

McBirney, A. R., and Murase, T. (1984). Rheological properties of magmas. *Annu. Rev. Earth Planet. Sci.* 12, 337–357. doi: 10.1146/annurev.ea.12.050184.002005

Mokso, R., Schleputz, C. M., Theidel, G., Billich, H., Schmid, E., Celcer, T., et al. (2017). GigaFRoST: the gigabit fast readout system for tomography. *J. Synchrotr. Radiat.* 24, 1250–1259. doi: 10.1107/s1600577517013522

Morrison, A. A., Whittington, A., Smets, B., Kervyn, M., and Sehlke, A. (2020). The rheology of crystallizing basaltic lavas from Nyiragongo and Nyamuragira volcanoes, D.R.C. *Volcanica* 3, 1–28. doi: 10.30909/vol.03.01.0128

Mueller, S., Llewellin, E. W., and Mader, H. M. (2011). The effect of particle shape on suspension viscosity and implications for magmatic flows. *Geophys. Res. Lett.* 38:L13316.

Okumura, S., Nakamura, M., Uesugi, K., Nakano, T., and Fujioka, T. (2013). Coupled effect of magma degassing and rtheology on silicic volcanism. *Earth Planet. Sci. Lett.* 362, 163–170. doi: 10.1016/j.epsl.2012.11.056

Pankhurst, M. J., Vo, N. T., Butcher, A. R., Long, H., Wang, H., Nonni, S., et al. (2018). Quantitative measurement of olivine composition in three dimensions using helical-scan X-ray micro-tomography. *Am. Mineral.* 103, 1800–1811. doi: 10.2138/am-2018-6419

Philippe, J., Le Godec, Y., Mezouar, M., Berg, M., Bromiley, G., Bergame, F., et al. (2016). Rotating tomography Paris–Edinburgh cell: a novel portable press for micro-tomographic 4-D imaging at extreme pressure/temperature/stress conditions. *High Pressure Res.* 36, 512–532. doi: 10.1080/08957959.2016.1221951

Picard, D., Arbaret, L., Pichavant, M., Champallier, R., and Launeau, P. (2011). Rheology and microstructure of experimentally deformed plagioclase suspensions. *Geology* 39, 747–750. doi: 10.1130/g32217.1

Pinkerton, H. (1994). "Rheological and related properties of lavas," in *Etna: Magma and Lava Flow Modeling and Volcanic System Definition Aimed at Hazard Assessment*, ed. F. Dobran (Rome: Global Volcanic and Environmental Systems Simulation), 76–89.

Pistone, M., Arzilli, F., Dobson, K. J., Cordonnier, B., Reusser, E., Ulmer, P., et al. (2015). Gas-driven filter pressing in magmas: insights into in-situ melt segregation from crystal mushes. *Geology* 43, 699–702. doi: 10.1130/g36766.1

Pistone, M., Caricchi, L., Ulmer, P., Burlini, L., Ardia, P., Reusser, E., et al. (2012). Deformation experiments of bubble- and crystal-bearing magmas: Rheological and microstructural analysis. *J. Geophys. Res. Solid Earth* 117:8986.

Pistone, M., Caricchi, L., Ulmer, P., Reusser, E., and Ardia, P. (2013). Rheology of volatile-bearing crystal mushes: mobilization vs. viscous death. *Chem. Geol.* 345, 16–39. doi: 10.1016/j.chemgeo.2013.02.007

Pleše, P., Higgins, M. D., Mancini, L., Lanzafame, G., Brun, F., Fife, J. L., et al. (2018). Dynamic observations of vesiculation reveal the role of silicate crystals in bubble nucleation and growth in andesitic magmas. *Lithos* 296–299, 532–546. doi: 10.1016/j.lithos.2017.11.024

Polacci, M., Arzilli, F., La Spina, G., Le Gall, N., Cai, B., Hartley, M. E., et al. (2018). Crystallisation in basaltic magmas revealed via in situ 4D synchrotron X-ray microtomography. *Sci. Rep.* 8:8377.

Ryerson, F., Weed, H., and Piwinskii, A. (1988). Rheology of subliquidus magmas: 1. Picritic compositions. *J. Geophys. Res. Solid Earth* 93, 3421–3436.

Sato, H. (2005). Viscosity measurement of subliquidus magmas:1707 basalt of Fuji volcano. *J. Mineral. Petrol. Sci.* 100, 133–142. doi: 10.2465/jmps.100.133

Sloof, W. G., Pei, R., McDonald, S. A., Fife, J. L., Shen, L., Boatemaa, L., et al. (2016). Repeated crack healing in MAX-phase ceramics revealed by 4D in situ synchrotron X-ray tomographic microscopy. *Sci. Rep.* 6:23040.

Smith, T. S., Bay, B. K., and Rashid, M. M. (2002). Digital volume correlation including rotational degrees of freedom during minimization. *Exp. Mech.* 42, 272–278. doi: 10.1007/bf02410982

Soldati, A., Sehlke, A., Chigna, G., and Whittington, A. (2016). Field and experimental constraints on the rheology of arc basaltic lavas: the January 2014 Eruption of Pacaya (Guatemala). *Bull. Volcanol.* 78, 1–19.

Spera, F. J., Borgia, A., Strimple, J., and Feigenson, M. (1988). Rheology of melts and magmatic suspensions: 1. Design and calibration of concentric cylinder viscometer with application to rhyolitic magma. *J. Geophys. Res. Solid Earth* 93, 10273–10294. doi: 10.1029/jb093ib09p10273

Stein, D. J., and Spera, F. J. (1992). Rheology and microstructure of magmatic emulsions: theory and experiments. *J. Volcanol. Geother. Res.* 49, 157–174. doi: 10.1016/0377-0273(92)90011-2

Tozzi, G., Zhang, Q.-H., and Tong, J. (2014). Microdamage assessment of bone-cement interfaces under monotonic and cyclic compression. *J. Biomech.* 47, 3466–3474. doi: 10.1016/j.jbiomech.2014.09.012

Tripoli, B., Manga, M., Mayeux, J., and Barnard, H. (2019). The effects of deformation on the early crystallization kinetics of basaltic magmas. *Front. Earth Sci.* 27:250. doi: 10.3389/feart.2019.00250

Truby, J. M., Mueller, S. P., Llewellin, E. W., and Mader, H. M. (2014). The rheology of three-phase suspensions at low bubble capillary number. *Proc. Math. Phys. Eng. Sci.* 471:20140557. doi: 10.1098/rspa.2014.0557

Vetere, F., Murri, M., Alvaro, M., Domeneghetti, M. C., Rossi, S., Pisello, A., et al. (2019). Viscosity of pyroxenite melt and its evolution during cooling. *J. Geophys. Res. Planets* 124, 1451–1469.

Vona, A., and Romano, C. (2013). The effects of undercooling and deformation rates on the crystallization kinetics of Stromboli and Etna basalts. *Contribut. Mineral. Petrol.* 166, 491–509. doi: 10.1007/s00410-013-0887-0

Vona, A., Romano, C., Dingwell, D. B., and Giordano, D. (2011). The rheology of crystal-bearing basaltic magmas from Stromboli and Etna. *Geochim. Cosmochim. Acta* 75, 3214–3236. doi: 10.1016/j.gca.2011.03.031

Vona, A., Ryan, A. G., Russell, J. K., and Romano, C. (2016). Models for viscosity and shear localization in bubble-rich magmas. *Earth Planet. Sci. Lett.* 449, 26–38. doi: 10.1016/j.epsl.2016.05.029

Wadsworth, F. B., Vasseur, J., Llewellin, E. W., Dobson, K. J., Colombier, M., von Aulock, F. W., et al. (2017). Topological inversions in coalescing granular media control fluid-flow regimes. *Phys. Rev. E* 96:033113.

Wadsworth, F. B., Vasseur, J., Llewellin, E. W., Schauroth, J., Dobson, K. J., Scheu, B., et al. (2016). Sintering of viscous droplets under surface tension. *Proc. R. Soc. A Math. Phys. Eng. Sci.* 472:20150780. doi: 10.1098/rspa.2015.0780

Wadsworth, F. B., Vasseur, J., Schauroth, J., Llewellin, E. W., Dobson, K. J., Havard, T., et al. (2019). A general model for welding of ash particles in volcanic systems validated using in situ X-ray tomography. *Earth Planet. Sci. Lett.* 525:115726. doi: 10.1016/j.epsl.2019.115726

Wallace, P. A., Kendrick, J. E., Miwa, T., Ashworth, J. D., Coats, R., Utley, J. E. P., et al. (2019). Petrological architecture of a magmatic shear zone: a multidisciplinary investigation of strain localisation during magma ascent at Unzen Volcano, Japan. *J. Petrol.* 60, 791–826. doi: 10.1093/petrology/egz016

Conflict of Interest: The authors declare that the research was conducted in the absence of any commercial or financial relationships that could be construed as a potential conflict of interest.

Advantages of publishing in Frontiers

OPEN ACCESS
Articles are free to read for greatest visibility and readership

FAST PUBLICATION
Around 90 days from submission to decision

HIGH QUALITY PEER-REVIEW
Rigorous, collaborative, and constructive peer-review

TRANSPARENT PEER-REVIEW
Editors and reviewers acknowledged by name on published articles

Frontiers
Avenue du Tribunal-Fédéral 34
1005 Lausanne | Switzerland

Visit us: www.frontiersin.org
Contact us: info@frontiersin.org | +41 21 510 17 00

REPRODUCIBILITY OF RESEARCH
Support open data and methods to enhance research reproducibility

DIGITAL PUBLISHING
Articles designed for optimal readership across devices

FOLLOW US
@frontiersin

IMPACT METRICS
Advanced article metrics track visibility across digital media

EXTENSIVE PROMOTION
Marketing and promotion of impactful research

LOOP RESEARCH NETWORK
Our network increases your article's readership